UNIVERSITÀ
DEGLI STUDI
DI TRIESTE

Università
Ca'Foscari
Venezia

UNIVERSITÀ DEGLI STUDI DI TRIESTE

e

UNIVERSITÀ CA' FOSCARI VENEZIA

XXXV CICLO DEL DOTTORATO DI RICERCA IN CHIMICA

SYNTHESIS, CHARACTERIZATION AND PHOTOPHYSICAL PROPERTIES OF FIRST-ROW TRANSITION METAL COMPLEXES

Settore scientifico-disciplinare: **CHIM/03**

DOTTORANDA
VALENTINA FERRARO Valentina Ferraro

COORDINATORE
PROF. ENZO ALESSIO

SUPERVISORE DI TESI
PROF. MARCO BORTOLUZZI Marco Bortoluzzi

ANNO ACCADEMICO 2021/2022

Abstract

According to Horizon 2020, Europe's photonics industry is strong (e.g. in laser-based manufacturing, medical photonics, sensing, lighting) and has the possibility to exploit new emerging market opportunities. Advanced lighting technology includes the use of Solid State Lighting (SSL) based on organic light emitting diodes (OLEDs). The advantages involve higher quality lighting in terms of energy efficiency, quality (robustness, longer lifetime, colour tunability), and therefore cost reduction and energy saving. Lighting represents around 19% of electricity consumption worldwide and the replacement of old lighting technologies such as incandescent bulbs with SSL systems will allow to save up to 70% of energy. With all of this in mind, it is evident that the development of light technology based on SSL is of paramount importance. Nowadays most of the luminescent complexes applied in SSL are based on lanthanides and d-block metals of the second and third transition series. Platinum(II) and iridium(III) are commonly used as emitters for OLEDs due to their long-lived triplet states. However, recent studies have demonstrated that it is possible to obtain highly luminescent complexes based on first-row transition elements, such as chromium(III), iron(III), manganese(II), copper(I) and zinc(II). These elements have the advantage to be less expensive and toxic, as well as more abundant.

The main focus of the following PhD thesis is the synthesis and characterization of luminescent manganese(II), copper(I) and zinc(II) complexes. As concerns the first one, the metal-centred emission related to the $^4T_1(^4G) \rightarrow {}^6A_1(^6S)$ transition is strongly dependent upon the coordination sphere: tetrahedral complexes are normally green emitters, while octahedral species emit in the red range. The presence of rigid structures and light harvesting fragments in the ligand skeleton allows to enhance the luminescent features as well as the UV-light absorption. Several [O=P]-donor ligands were considered for the preparation of both tetrahedral and octahedral derivatives, sometimes affording dual emissions in the corresponding manganese(II) complexes due to concurrent metal- and ligand-centred transitions.

As regards copper(I) complexes, derivatives containing polydentate N-donors based on indazole and benzotriazole were synthesized and their emission properties were attributed to metal-to-ligand charge transfer mechanisms involving triplet emitting states. Small changes in the ligand skeleton determined appreciable variations in the

photophysical properties, as testified by the complexes obtained using 2,1,3-benzothiadiazole as N-donor.

The [O=P]-donors previously used for manganese(II) revealed to be suitable ligands also for the preparation of luminescent zinc(II) halide complexes thanks to the enhancement of ligands fluorescence due to coordination. In selected cases intersystem crossing was observed, causing intense green phosphorescence or dual emission.

Contents

1 Introduction

1.1 Luminescence in *d*-block elements

Luminescent complexes of *d*-block elements can be roughly divided in two categories depending upon the origin of the emitted photon. Metal centres such as manganese(II)[1] and chromium(III)[2] belong to the first category, where the emissions are produced from multielectronic wavefunctions deriving from 3*d* orbitals. The orbitals of the ligands are not directly involved in the construction of the excited states, but the coordinated species are implicated in the population of the emitting levels and in the determination of their relative energies.[3] The behaviour of this group of metal centres is somewhat similar to that of lanthanides(III), where spin-orbit levels originating from 4*f* orbitals are involved in the radiative transitions. The main differences between *d*-block metal centres and trivalent lanthanides are due to the core nature of 4*f* orbitals, that do not participate in the formation of bonds. This feature generates peculiar optical proprieties, such as low dependence of absorption and emission frequencies upon the coordination sphere. Consequently, the absence of vibrational structure in the spectra leads to sharp bands and chromatic purities that have made lanthanide(III) complexes very interesting from a technological point of view. Moreover, being Laporte-forbidden, the *f-f* transitions are characterized by micro- or milliseconds-long emissions.[4] On the other hand, the valence nature of *d*-type orbitals in transition metal centres makes properties of the emission such as wavelength maximum, bandwidth and lifetime deeply influenced by the coordination sphere.

The second category is composed by luminescent complexes where the photon is emitted from excited states also involving the molecular orbitals of the ligands. Several coordination compounds with d^6, d^8 and d^{10} metal centres, such as rhenium(I), ruthenium(II), osmium(II), iridium(III), platinum(II), copper(I), silver(I), gold(I) and gold(III) complexes, belong to this group.[5] Their luminescent proprieties are related to charge transfer mechanisms that, for instance, can occur from a filled *d* orbital of the metal centre to the antibonding orbitals of π-acceptor ligands. This process, depicted as a dark yellow arrow in Figure 1, is called “metal to ligand charge transfer” or MLCT. The opposite mechanism, illustrated as orange arrow in Figure 1, is also observable: an electron can be transferred from a π-donor ligand to the metal centre with a mechanism known as “ligand to metal charge transfer” or simply LMCT.

More rarely, the transfer between coordinated ligands, called LLCT or ligand-to-ligand charge transfer, is possible.[6] When the participation of transition metal orbitals is negligible, the luminescence is ligand-centred (LC). The situations initially described, where the ligand orbitals are instead poorly involved, are called metal-centred (MC) transitions. These last two conditions are respectively pictured as blue and red arrows in Figure 1.

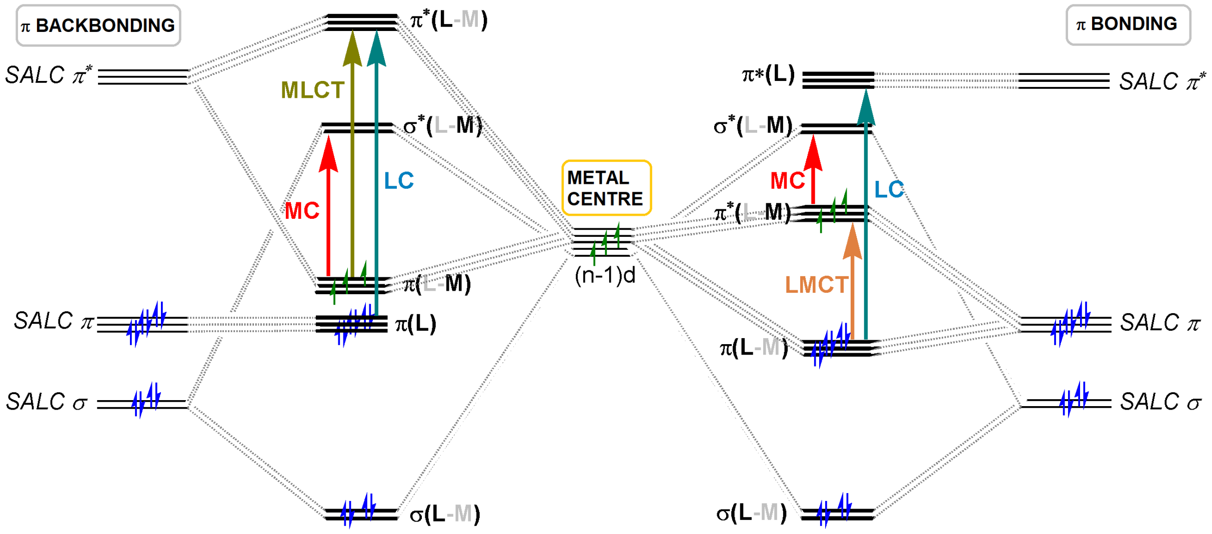

Figure 1. Molecular orbital diagram for a generic octahedral complex ML_6 and possible electronic transitions: MC (red arrow), LMCT (orange arrow), MLCT (dark yellow arrow) and LC (blue arrow) mechanisms.

As regards photoluminescence, two main phenomena can be described: fluorescence and phosphorescence (Figure 2). The former is a spontaneous emission that can be observed few nanoseconds after the exciting radiation is extinguished. It usually occurs at lower frequencies than the incident radiation because the emissive transition takes place after some vibrational energy has been discarded to the surroundings. On the other hand, phosphorescence is a spontaneous emission as well, but it is longer, typically from microseconds to seconds. This difference is mainly attributable to the fact that only transitions having the same multiplicity, as the ones involved in the fluorescence process, are allowed (e.g. singlet → singlet). Instead, phosphorescence is formally forbidden because it involves states of different multiplicity (e.g. triplet → singlet). This selection rule strongly limits the direct population of excited states with different multiplicity. These excited states can be populated when the spin-orbit coupling is large, and consequently when the molecule contains a moderately heavy atom. In fact, if triplet and singlet excited states share a common geometry where their potential energy curves intersect, a molecule can undergo a non-radiative process called “intersystem crossing”, thus turning into a triplet state.[7]

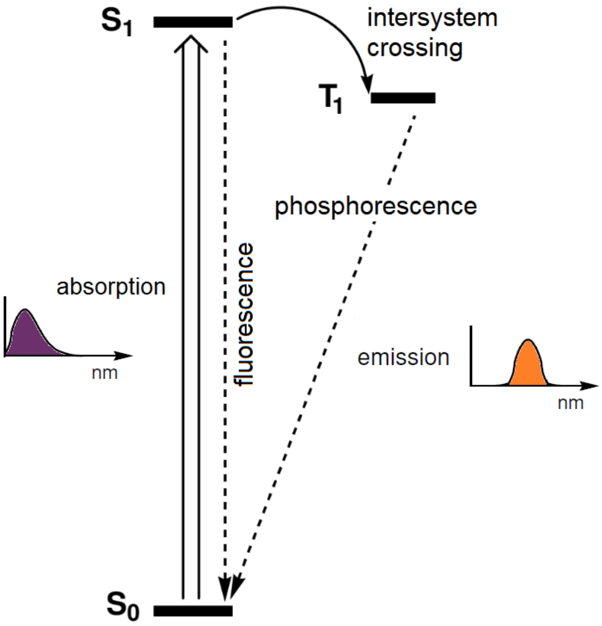

Figure 2. Comparison between the mechanisms leading to fluorescence and phosphorescence.

The first luminescent complexes investigated are based on d^6 metal ions of the second and third transition series, for example ruthenium(II) and osmium(II). Aromatic bi- or tridentate heterocycles, such as 2,2’-bipyridine (bpy), are the most suitable ligands for these elements. One remarkable example is $[Ru(bpy)_3]^{2+}$, that combines high chemical stability, excited state reactivity, well defined redox proprieties, intense luminescent emissions and microseconds-long lifetimes even in solution.[8] Another d^6 metal ion is iridium(III), which can coordinate bidentate cyclometallating ligands, for instance the deprotonated 2-phenylpyridine, to afford the corresponding luminescent complexes. These derivatives were efficiently exploited for the preparation of solid-state lighting devices, such as OLEDs (organic light emitting diodes) and LECs (light-emitting electrochemical cells).[9] Rhenium(I) carbonyl complexes with chelating N-donors were widely investigated for their strong luminescence. Famous examples are tricarbonyl bipyridine derivatives having general formula $[Re(CO)_3(N^\wedge N)X]^{n+}$, where N^N is a diimine and X is a soft halide. Similarly, square-planar d^8 metal ions complexes, such as platinum(II) and gold(III) bearing aromatic polydentate heterocycles and strong σ-donor ligands, showed some interesting emissive features. On the other hand, silver(I) and gold(I) can afford complexes whose luminescent proprieties are attributable to mixed MLCT/MC mechanisms.[5c,6a] Recently, attention has been devoted to d^6 derivatives, in particular platinum(IV) complexes having general formula [Pt(C^N)2MeCl] where C^N is a *ortho*-deprotonated 2-arylpyridine. These species exhibited blue to orange emissions with quantum yields up to 0.81 in solution at room temperature.[10] Selected examples of luminescent second- and third-row transition derivatives are depicted in Figure 3.

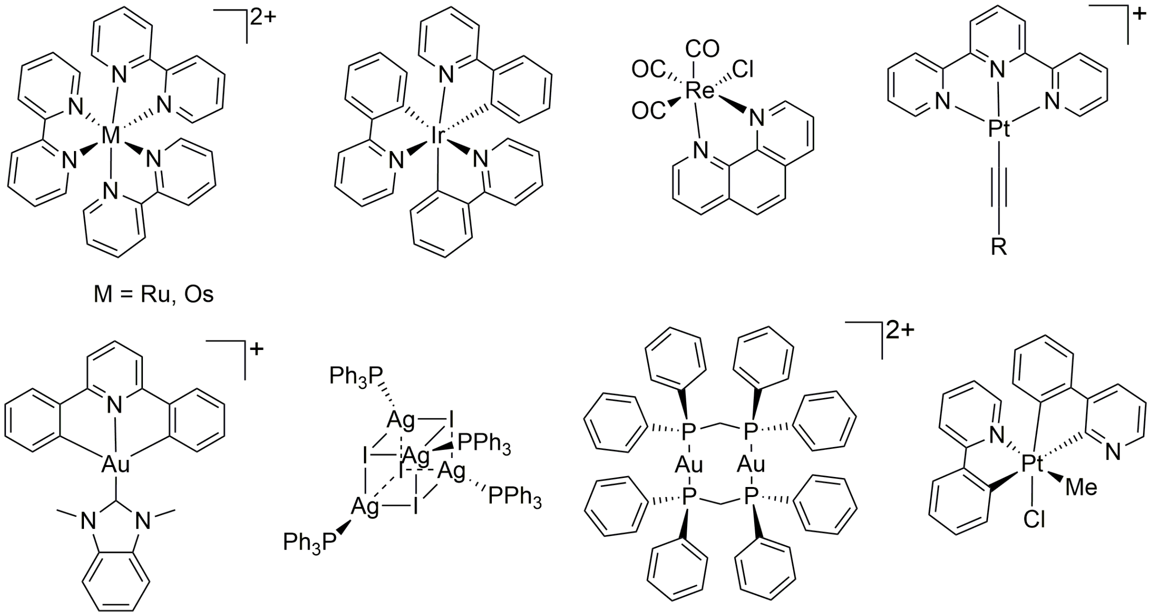

Figure 3. Examples of second and third transition metals luminescent complexes.

In the following pages the attention will be mainly focused on manganese(II), copper(I) and zinc(II) complexes, since they represent possible replacements for lanthanides(III) and *d*-block metals of the second and third transition series currently exploited for solid-state lighting applications. For instance, europium(III), terbium(III) and cerium(III) are commonly used in coatings for fluorescent lamps. However, the recovery of these elements is quite problematic, especially because of the possible contamination by mercury.[11] As regards *d*-block elements, platinum(II) and iridium(III) complexes are commonly used as emitters for OLEDs due to their long-lived triplet states.[12] The possibility of replacing these elements with manganese(II), copper(I) and zinc(II) derivatives could overcome several problems and reduce the cost of the final devices.[13] In fact, among the advantages, these first-row transition elements are less expensive and toxic, as well as more abundant. Highly luminescent derivatives can be synthesized also from other *d*-block elements such as chromium(III) and iron(III). Selected examples are reported in Figure 4.[14]

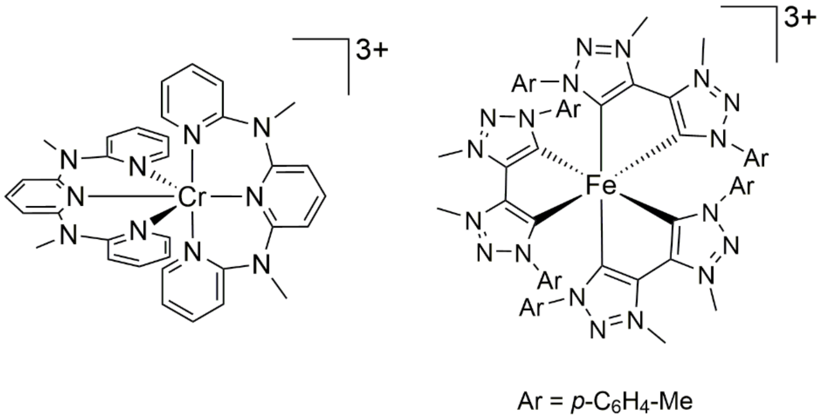

Figure 4. Examples of chromium(III) and iron(III) luminescent complexes bearing respectively *N*,*N′*-dimethyl-*N*,*N′*-dipyridine-2-ylpyridine-2,6-diamine and 3,3-dimethyl-1,1-bis(*p*-tolyl)-4,4-bis(1,2,3-triazol-5-ylidene as ligands.

1.2 Manganese and its luminescence

Manganese is a first-row transition metal element characterized by atomic number 25 and atomic configuration [Ar]$3d^5 4s^2$. It belongs to the group 7 together with technetium and rhenium but, while manganese is the third most abundant transition element on earth after iron and titanium, the other two elements are very rare. Besides as silicate, manganese can typically be found in nature as pyrolusite MnO_2, and more rarely as hausmannite Mn_3O_4 and rhodochrosite $MnCO_3$. Differently from rhenium that has two isotopes, manganese is monoisotopic (^{55}Mn). As regards its oxidation states, the most common are Mn^{II} (d^5) and Mn^{VII} (d^0), but Mn^{III} (d^4), Mn^{IV} (d^3) and Mn^{VI} (d^1) are quite recurrent as well. In some cases manganese can also be characterized by low or formally negative oxidation states in presence of suitable ligands, e.g. $[Mn(NO)_3CO]$ (d^{10}), $[Mn(CO)_5]^-$ (d^8), $[Mn_2(CO)_{10}]$ (d^7) and $[Mn(CH_3)(CO)_5]$ (d^6).

In absence of ligands and in aqueous solution, the reduction potential at 25°C for the reaction $Mn^{2+} + 2e^- \rightarrow Mn^0$ is -1.18 V. The stability of manganese(II) under these conditions is attributable to its d^5 high spin configuration, maximizing the exchange energy. The electronic symmetrical distribution of the *d* orbitals makes it extremely inert towards both oxidation and reduction. On the other hand, the crystal field activation energy equal to zero makes the substitution reactions generally fast. The presence of five unpaired electrons confers paramagnetic properties to the metal centre and determines an expected magnetic momentum μ around 5.92 BM. Manganese(II) forms complexes with coordination numbers usually ranging from four to six. Oxygen-donor ligands are of paramount importance in manganese(II) chemistry, and the affinity towards [O=P]-donor moieties will be further discussed in the next chapters.[15] Further common ligands are halides and molecules containing N-, P- or As- donor moieties.

Manganese ions can act as emitting centres, a feature observable also in minerals. Besides the previously mentioned rhodochrosite, also rhodonite $CaMn_4Si_5O_{15}$, axinite $Ca_2MnAl_2BSi_4O_{15}OH$ and helvine $Mn_4(BiSiO_4)_5S$ exhibit luminescent properties characterized by dark red emissions involving the metal centre. In addition, manganese(II) centres can replace other cations in the lattice determining green, yellow or orange-red luminescence depending upon the coordination geometry of the metal centre. For example, $CaCO_3$ activated with lead, thallium or cerium, and manganese exhibit an orange-red emission after being excited with UV light.[1]

As highlighted in Figure 5, at the ground state the d^5 high spin ion has ^6S as spectroscopic term symbol and the quantum number L is zero, so the electronic distribution around the metal centre is spherical. There is no separation in sublevels due to the crystal field strength (the only level is $^6A_1$) and thus *d-d* absorptions between levels with the same multiplicity are absent. The first excited state is obtained by coupling two electrons in one orbital, so the multiplicity changes from sextet to quartet. Its spectroscopic term is ^4G and it is composed by 9 degenerate sublevels that separate in presence of a crystal field. In particular, in the case of cubic-related symmetries, like tetrahedron and octahedron, the ^4G manifold is separated in $^4T_1$, $^4T_2$, $^4A_1$ and ^4E levels.

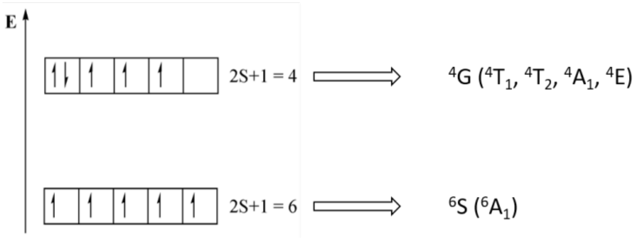

Figure 5. Electronic configuration of the ground and the first excited state in manganese(II) complexes.

Therefore, the absorption spectra of manganese(II) complexes exhibit several peaks, while emissions are normally due to the transition from the low-lying excited state to the ground state, $^4T_1 \rightarrow {}^6A_1$ for tetrahedral and octahedral fields. However, the absorption coefficients are quite small as this transition is forbidden by the selection rules. Because a change in the multiplicity is required, the emission mechanism can be considered a phosphorescence and it is characterized by long lifetimes.

Considering the Tanabe-Sugano diagram for a d^5 ion reported in Figure 6, it is possible to observe two different regions associated to high and low spin configurations. The former is dominant with low crystal field strength, also thanks to the exchange interaction among parallel electrons. The geometry of the complex determines the colour of the emission since the relative stability of the emitting and ground states is different on changing the crystal field strength. Tetrahedral complexes are usually characterized by an emission centred in the green region (500-540 nm), while octahedral ones are typically red emitters with maxima between 590 and 660 nm. This different behaviour can be justified considering that the energy gap between the levels $^4T_1(^4G)$ and $^6A_1(^6S)$ decreases going from four- to hexacoordinated compounds. Examples of these types of complexes will be discussed in the next chapters.

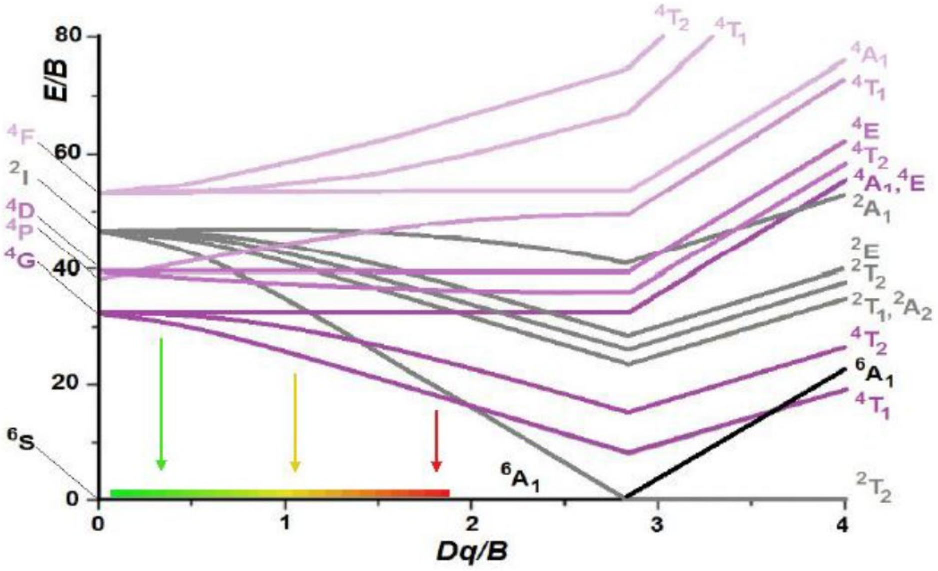

Figure 6. Tanabe-Sugano diagram for d^5 ions.

Transitions in octahedral complexes are both spin and parity forbidden, while in tetrahedral complexes the partial *p*-nature of molecular orbitals makes the emission only spin forbidden, thus characterized by shorter lifetimes.[16]

For what concerns other oxidation states with luminescent behaviour, manganese(V) centres can be found in magmatic apatite, where they replace phosphorous(V) in tetrahedral environments and behave as NIR emitters. In artificial phosphors, manganese(IV) centres exhibit red-orange emissions between 620 and 715 nm, recently exploited for the preparation of warm WLEDs (white light emitting diodes).[17]

These features can easily be understood considering that manganese(IV) is isoelectronic with chromium(III), so similar absorption and emission spectra are expected. It is however worth noting that manganese(IV) luminescence has been mostly studied at the solid state, since complexes are difficult to isolate in a pure form.[1] Manganese(III) and manganese(VI) centres can be also characterized by luminescent properties, observed in artificial phosphors but never in minerals. Recently, the first examples of luminescent manganese(I) complexes have been reported. The metal centre is isoelectronic with iron(II) and in combination with isocyanide chelating ligands afforded air-stable complexes exhibiting emissions in solution and at room temperature due to MLCT mechanisms.[18]

1.2.1 Luminescent manganese(II) complexes

As previously described, the electronic distribution around manganese(II) centres is isotropic, so the coordination geometry is mostly influenced by steric bulks, bite angles and electrostatic repulsions of the ligands. According to Pearson's theory, manganese(II) is a hard Lewis acid, therefore its coordination chemistry is dominated by ligands that establish σ-interactions supported by electrostatic factors, such as halides and polar O- and N-donor ligands.

Green emitting tetrahedral manganese(II) complexes are known since the Sixties, when they were firstly investigated by Cotton and co-workers. Derivatives such as $[MnX_4]^{2-}$ (X = Cl, Br, I), depicted in Figure 7a as pyridinium salt, exhibited both photo- and triboluminescence.[19] These compounds are still under investigation and they are normally called "organic-inorganic hybrids". For instance, the $[NH_2{}^{i}Pr_2]_2[MnBr_4]$ (^{i}Pr = isopropyl) reported in Figure 7b shows a combination of ferroelectricity and luminescence.[20] The tetrabromide manganese(II) complexes depicted in Figure 7c and 7d were respectively exploited for the fabrication of green PhOLEDs (phosphorescent organic light-emitting diodes) through solution process or used as X-ray scintillators.[21] The modulation of zero-dimensional manganese(II) organic-inorganic halides was recently achieved by using structure-directing d^{10} metal ions such as cadmium(II) and zinc(II). The doped systems were isolated as red-emitting octahedra $[(Cd/Mn)Br_6]$ or green-luminescent tetrahedra $[(M/Mn)Br_4]$, where M is cadmium(II) or zinc(II).[22] Manganese(II) complexes are of current interest also thanks to the possibility of combining luminescent and magnetic properties, as reported by Artem'ev's group in the case of homo- and mixed-halomanganates(II) having 1-

methyl-2-(methylthio)pyridin-1-ium as counterion (see Figure 7e).[23] On the other hand, using the cation derived from *trans*-2,5-dimethylpiperazine reversible stimuli-responsible luminescence was achieved. While the dehydrated [$(C_6H_{16}N_2)MnBr_4$] shows a green emission centred at 548 nm, the corresponding hydrated species revealed to be non-emissive. Rewritable paper was prepared by coating filter paper with the complex reported in Figure 7f, that exhibited also high resolution and reversibility. These types of materials are nowadays extremely interesting to be applied in security, for instance in anti-counterfeiting and information encryption.[24] Instead, the protonated *N*,*N*'-dimethylethylene diamide determined the formation of orange-emitting zero-dimensional manganese(II) derivatives (see Figure 7g) characterized by two emission bands, one centred at 516 nm and the other one at 623 nm. The dual-emission is related to the critical distance between Mn-Mn that is around 6.6 Å, originating peculiar luminescent features. The photoluminescence is also characterized by thermochromism; therefore, it is possible to change from orange to green and *vice versa* thanks to the variation of electron coupling coefficients, a propriety that is itself temperature dependent.[25]

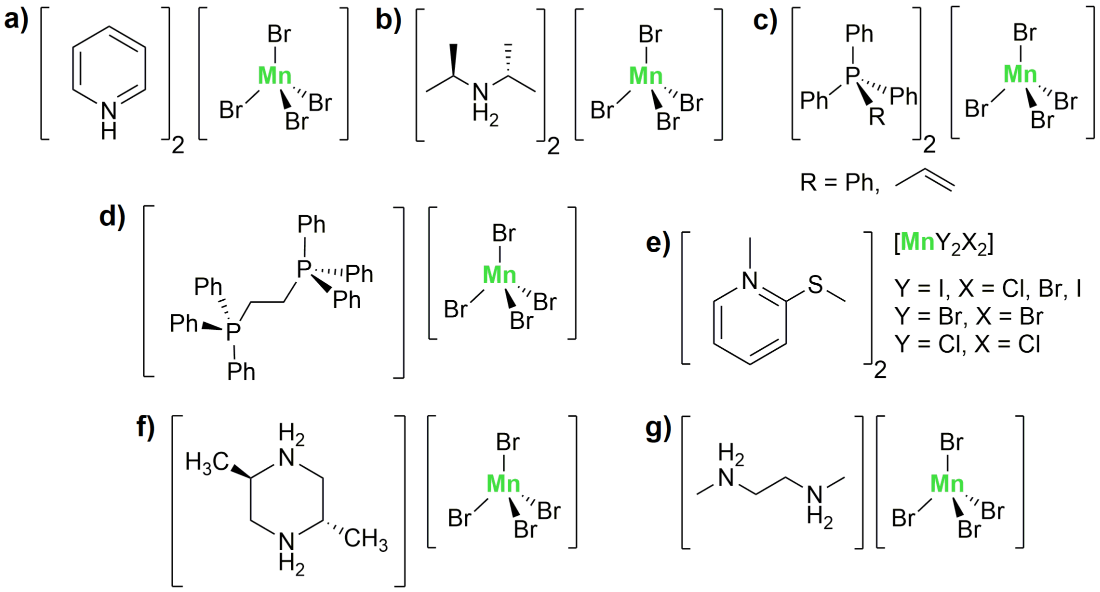

Figure 7. Organic-inorganic hybrid manganese(II) derivatives.

Manganese(II) complexes bearing [O=P]-donor ligands such as triphenylphosphine oxide were also investigated. The functionalization of the phenyl rings with -NMe_2, -OMe or -CF_3 groups (see Figure 8a) afforded complexes that were applied for high-resolution luminescent printing.[26] More recently, ligands such as bis[2-(diphenylphosphino)phenyl]ether dioxide (dpepo) allowed the isolation of green-emitting complexes having general formula [MnX_2(dpepo)] (X = Cl, Br, I) sketched in

Figure 8b.[27] Emission features such as lifetimes are strongly dependent on the halide as the spin-orbit coupling accelerates the radiative decay. This effect can be easily understood considering that their orbitals are energetically close to those involved in the $^4T_1 \rightarrow {}^6A_1$ transition, and it is likely to presume some mixing among the orbitals of metal and ligands.[28] Green emission was observed also using a dibenzofuran- and xanthrene-based biphosphine dioxide (Figure 8c and 8d). Thanks to the high photoluminescent quantum yield, the former was used as dopant to prepare a green OLED characterized by an external quantum efficiency (EQE_{max}) around 11%.[29] Instead, the complex $[MnBr_2(XantphosO_2)]$ exhibited polymorphic luminescence, a rare feature for manganese(II) derivatives. The species crystallizes in two different space groups, *P*-1 and *P*2$_1$/*n*, thus different emissions were detected, in one case green and in other one yellow. Either way, the emission is related to ligand-sensitized $^4T_1 \rightarrow {}^6A_1$ transition.[30]

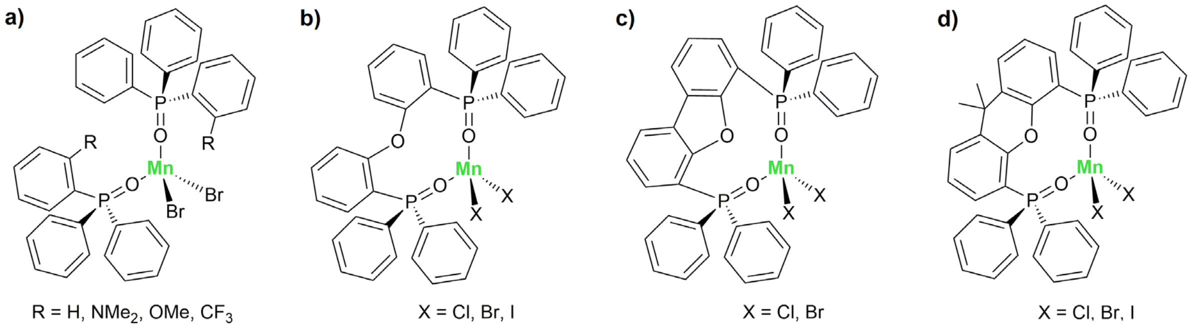

Figure 8. $[MnBr_2(O{=}PPh_3)_2]$ derivatives, $[MnX_2(dpepo)]$, $[MnX_2(dbfdpo)]$ and $[MnX_2(XantphosO_2)]$.

Monodimensional coordination polymers based on the 1,7-$[Ph_2P(O)]_2$-*meta*-carborane ligand exhibiting both green phosphorescence and triboluminescent properties were isolated. The emission colour revealed to be influenced by the temperature and the photoluminescent quantum yield reached up to 60% with the iodo-derivative.[31]

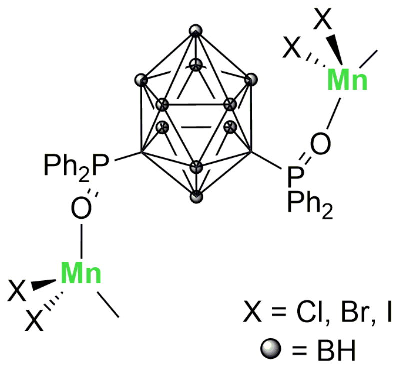

Figure 9. Manganese(II) coordination polymers based on the *meta*-carborane. Boron atoms are indicated as grey spheres.

Crystals of complexes having general formulae $[K(dibenzo\text{-}18\text{-}crown\text{-}6\text{-}ether)]_2[MnX_4]$ (X = Cl or Br) are characterized by green emission and they represent the first examples of manganese(II) derivatives exhibiting circularly polarized luminescence (CPL).[32] CPL is an extremely intriguing property, commonly observed for lanthanide(III) derivatives in a chiral environment. Among the possible applications, complexes characterized by CPL can be exploited in molecular probes, optoelectronics and security inks.[33]

As previously mentioned, octahedral manganese(II) derivatives are characterized by yellow-red emissions, as it was observed in minerals, inorganic materials, coordination polymers and nanoclusters.[34] Recent examples are the ferroelectric $\{[L][MnX_3]\}_n$ complexes (X = Cl, Br and L = pyrrolidinium, 3-pyrrolium and trimethylchloromethyl ammonium).[35] In these species the metal centre is in an octahedral environment, being surrounded by six halide ions. The reaction between manganese(II) halides and tris(2-ammino)ethylamine allowed to isolate both penta- and hexacoordinated compounds with emissions centred between 573 and 590 nm.[36] It is worth noting that five-coordinated manganese(II) complexes are generally quite rare in literature. The reaction between the previously reported $XantphosO_2$ and $MnBr_2\cdot 4H_2O$ afforded $[MnBr(XantphosO_2)_2]Br$ (Figure 10a), characterized by an intense emission peaked at 583 nm and photoluminescent quantum yield Φ up to 93%. Its photophysical features together with the response to X-ray radiation makes it a suitable candidate to be applied for X-ray scintillators.[37] Recently, a new kind of pentacoordinated manganese(II) complex was reported, being the first case of a square-pyramidal derivative, with general formula $[MnL_2X]^+$ [L = $Me_2N\text{-}CH(Ph_2P{=}O)_2$ and X = Cl, Br] (Figure 10b). The remaining positive charge is neutralized by bromide, iodide or $[MnCl_4]^-$ counterions. The so-obtained complexes exhibited a red emission centred at 620 nm due to $^4E(^4G) \rightarrow {}^6A_1(^6S)$ transition.[38] For what concerns other coordination geometries, intense yellow- and red-emitting six- and seven-coordinated derivatives such as $[MnBr_2(18\text{-}crown\text{-}6)]$, $[Mn_3Br_6(18\text{-}crown\text{-}6)_2]$ and $[Mn_3Br_6(18\text{-}crown\text{-}6)]$ were prepared from the reaction between manganese(II) halides and 18-crown-6-ether (see Figure 10c). Similarly, $[Mn_2I_4(18\text{-}crown\text{-}6)]$ and $[Mn_3I_6(18\text{-}crown\text{-}6)_2]$ were synthesized in ionic liquids and exhibit quantum yields between 98 and 100%. In addition, the former is characterized by non-linear optical properties.[39]

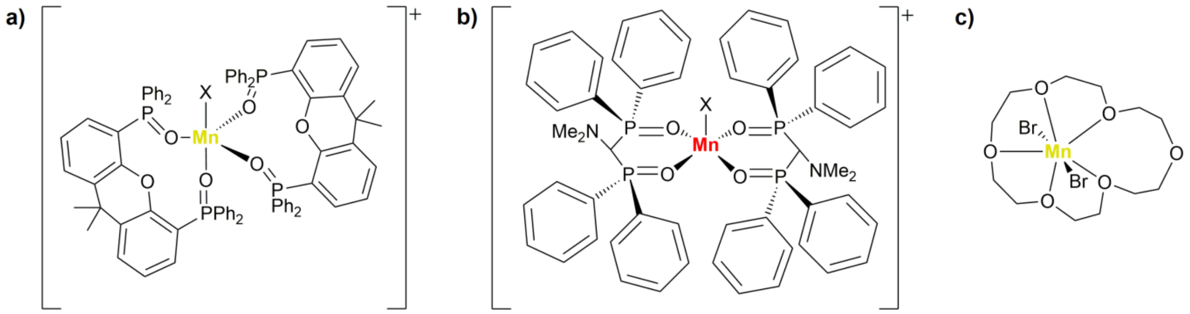

Figure 10. Penta-, six- and seven-coordinated Mn(II) complexes.

Besides dpepo and related ligands, using bis-(diphenylphosphino)methane dioxide (dppmO_2) and 1,2-bis(diphenylphosphino)ethane dioxide (dppeO_2) it was possible to obtain the orange-emitting cationic derivatives $[Mn(dppmO_2)_3]^{2+}$ and $[Mn(dppeO_2)_3]^{2+}$.[40] The reversible coordination of *N*,*N*-dimethylformamide to $[MnBr_2(dppeO_2)]_n$ determined a modification in the coordination geometry, passing from tetrahedral to trigonal-bipyramidal and thus a change from green to red in the luminescence. This phenomenon is known as vapochromism.[41] The structurally related 2,3-bis(diphenylphosphino)-1,3-butadiene dioxide (dppbO_2) in reaction with $MnCl_2$ and $MnBr_2$ allowed the isolation of hybrid organic-inorganic complexes having general formulae $[Mn(dppbO_2)_3][MnX_4]$, where X = Cl or Br (Figure 11a). In these derivatives the manganese(II) ions are in different environments, both octahedral and tetrahedral. For this reason, these complexes are characterized by dual emission, composed by an intense red and a weak green band.[42] Also in the case of 2-(diphenylphosphoryl)-*N*,*N*-diethylacetamide, the corresponding manganese(II) complex reported in Figure 11b shows a deep-red emission, although a weak band related to the $[MnX_4]^{2-}$ counterion is observable.[43] From the reaction between MnI_2 and 1,3-bis(diphenylphosphinyl)propane it was possible to isolate a cage-like complex and a 1D coordination polymer (see Figure 11c). In the first case the atoms surrounding the metal centre define a square-pyramid, so the compound is a red emitter, while in the second case the geometry is tetrahedral, thus determining a green luminescence.[44] An octahedral coordination polymer was prepared starting from 1,2,4,5-tetrakis(diphenylphosphino)benzene tetraoxide (L) and $Mn(ClO_4)_2 \cdot 6H_2O$ in dimethylformamide. The resulting $[MnL(DMF)_2](ClO_4)_2 \cdot DMF$ is characterized by an octahedral MnO_6 structure with four oxygen atoms coming from the ligand and two from the DMF, as depicted in Figure 11d.[45] In the case of the six-coordinated hybrid halide $[(CH_6N_3)_2MnCl_4]$ intense red-emissions centred at 650 nm and photoluminescent quantum yields Φ around 56% were detected. The intriguing photophysical properties were further enhanced by doping with 8% of zinc(II). This material was efficiently exploited for the preparation of a warm WLED in combination with YAG:Ce^{3+} (YAG = yttrium aluminium garnet) and a blue LED chip.[46]

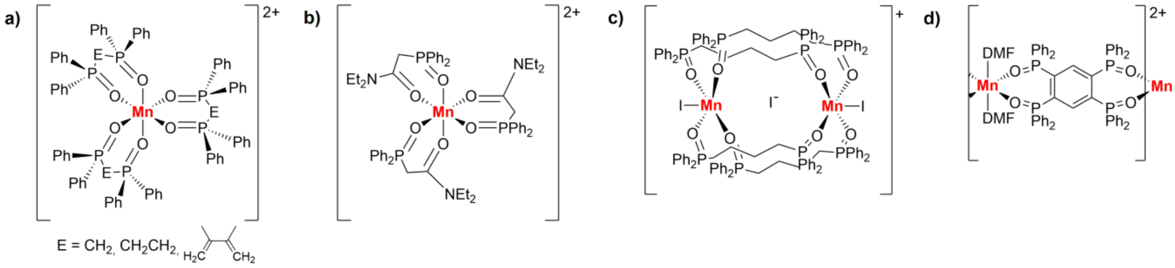

Figure 11. Red-emitting manganese(II) complexes

Finally, $Mn(NCS)_2$ was reacted with bis(phosphine)oxides having general formula $Y(Ph_2P{=}O)_2$ [Y = CH_2, CH_2CH_2, $CH_2CH_2CH_2$, $CH_2C({=}CH_2)CH_2$, $C({=}CH_2)C({=}CH_2)$, C≡C]. Depending on the chosen [O=P]-donor ligand, chelated and ionic complexes or coordination polymers were isolated under the same experimental conditions. $[Mn\{C{\equiv}C(Ph_2P{=}O)_2\}]_n$ and $[Mn\{CH_2C({=}CH_2)CH_2(Ph_2P{=}O)_2\}_2(NCS)_2]$ exhibited extraordinary luminescent features combining intraligand fluorescence and metal-centred phosphorescence. By acting on the excitation wavelength, it was possible to change the ratio of these two contemporary mechanisms and thus tune the colour of the emission from blue (ligand-centred transition) to red (metal-centred transition).[47]

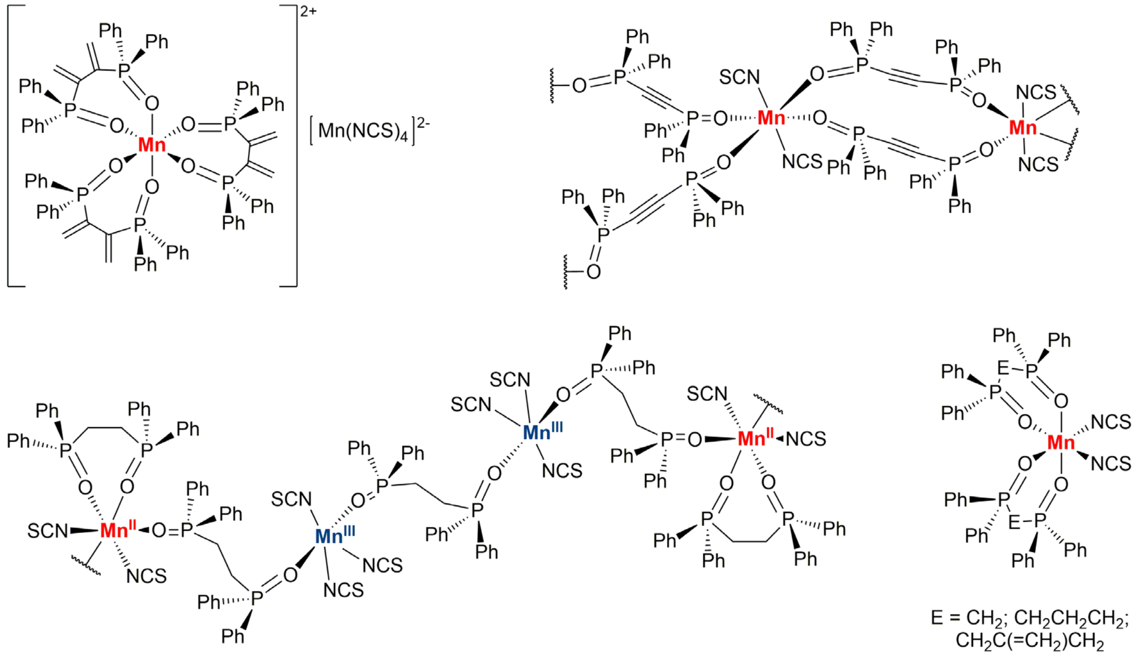

Figure 12. Manganese(II) thiocyanate-based derivatives.

1.3 Copper and its luminescence

Copper is a first-row transition element having 29 as atomic number and it belongs to the group 11 together with silver and gold. Copper has two stable isotopes, ^{63}Cu and ^{65}Cu, whose natural abundances are respectively 69% and 31%. In nature copper is commonly present as sulfide, oxide or carbonate. Half of all the deposits can be found in copper pyrite (chalcopyrite) $CuFeS_2$, followed by copper glance (chalcocite, Cu_2S), cuprite (Cu_2O) and malachite [$Cu_2CO_3(OH)_2$]. The atomic configuration is [Ar]$3d^{10}4s^1$ and the main oxidation states are Cu^I (d^{10}) and Cu^{II} (d^9), even if higher oxidation states were reported in selected cases. The coordination chemistry of Cu^0 is limited, for instance [$Cu(CO)_3$] is stable only at extremely low temperatures. In aqueous solution and in absence of coordinating ligands, the reduction potentials at 25°C are:

$Cu^{2+} + e^- \rightarrow Cu^+$ ($E^0 = 0.15$ V) $Cu^+ + e^- \rightarrow Cu^0$ ($E^0 = 0.52$ V)

Therefore, $2\ Cu^+ \rightarrow Cu^{2+} + Cu^0$ is thermodynamically favourable ($E^0 = 0.37$ V) and the equilibrium constant is around 10^6, that implies that copper(I) is normally unstable in aqueous solution and tends to disproportionate. The instability of copper(I) in water can be ascribed firstly to the smaller size of copper(II) combined with twice the charge. For this reason, it can interact strongly with water molecules and this difference can energetically overcome the second ionization energy.[15] However, poorly soluble compounds such as CuCl, CuI and CuCN are resistant against disproportion and, in general, coordinating ligands can increase the stability of copper(I) in solution. Copper(I) is soluble in organic solvents, such as acetonitrile, where it affords the complex [$Cu(NCCH_3)_4$]$^+$.

Copper(I) derivatives are normally characterized by coordination numbers of 2, 3 and 4. In the last case the geometry is typically tetrahedral to minimize steric repulsions. The completely filled d^{10} configuration determines a symmetrical electronic distribution and prevents *d-d* metal centred transitions. For this reason, besides being diamagnetic, copper(I) compounds are typically colourless, but they can exhibit emitting proprieties associated with MLCT mechanisms in presence of suitable ligands. In fact, after being excited, the metal centre is formally oxidized to copper(II) while the ligands are reduced, therefore π-conjugated systems are of extreme importance.

In minerals copper normally acts as luminescence quencher, being present in the air stable, paramagnetic copper(II) d^9 oxidation state. In this case *d-d* transitions are possible, so the derivatives are commonly characterized by absorptions in the visible or NIR region and they are usually blue-green coloured. However, because of the accessible non-radiative decay from the excited to the fundamental state, these derivatives do not exhibit luminescent proprieties. However, some examples of luminescence regarding copper ions in inorganic solids have been reported and these materials could possibly be applied in tuneable lasers. The presence of copper in $CaO-P_2O_5$ glasses, for example, determines a blue emission, while in doped barite ($BaSO_4$:Cu) a red and a violet band can be observed.[1a]

1.3.1 Luminescent copper(I) complexes

Copper(I) derivatives are interesting from a technological point of view as they can exhibit peculiar emission features, whose lifetime and temperature dependency are deeply influenced by the coordinated ligands. Differently from lanthanides, even small changes in the ligands alter the frontier molecular orbitals and therefore the emission colour. Colour tuning is one of the major driving forces of the recent studies concerning these complexes.[48]

The earliest example of light-emitting complex is $[Cu_4(\mu_3\text{–}I)_4(py)_4]$ (py = pyridine), containing the $\{Cu_4I_4\}$ cubane unit (see Figure 13). Changing the coordinating heterocycle with functionalized pyridines, picoline, quinoline or piperidine allowed the isolation of other Cu_4I_4 clusters. These derivatives are characterized by large Stokes shifts related to interactions among the metal centres in the Cu_4 cluster and to geometry distortions from the ground to the excited state.[49]

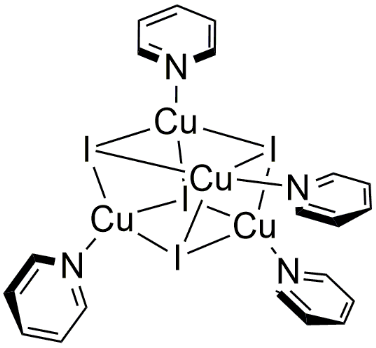

Figure 13. $[Cu_4(\mu_3\text{–}I)_4(py)_4]$ cluster.

However, systematic studies concerning luminescent copper(I) complexes date back to the Nineties due to the difficult harvesting of the $T_1 \rightarrow S_0$ transition associated to long phosphorescence decay. Another complication is related to the non-emissive decay due to the Jahn-Teller flattening distortion after the MLCT excitation and the instability of the complexes at the excited state. As shown in Figure 14, the different geometries of ground (tetrahedral) and excited (distorted tetrahedral or square planar) states can favour non-radiative decay processes with consequent reduction of quantum yield Φ. For this reason, the bulk of the ligands plays a role of paramount importance in the luminescence of copper(I) derivatives. Moreover, the metal can coordinate a new ligand because of the formal change in the oxidation state, namely solvent molecules or counterions, to fulfil an available site in the perpendicular position of the copper(II) square planar excited species, originating a penta-coordinated excited complex, known as "exciplex", that can follow non-radiative decay routes.[48]

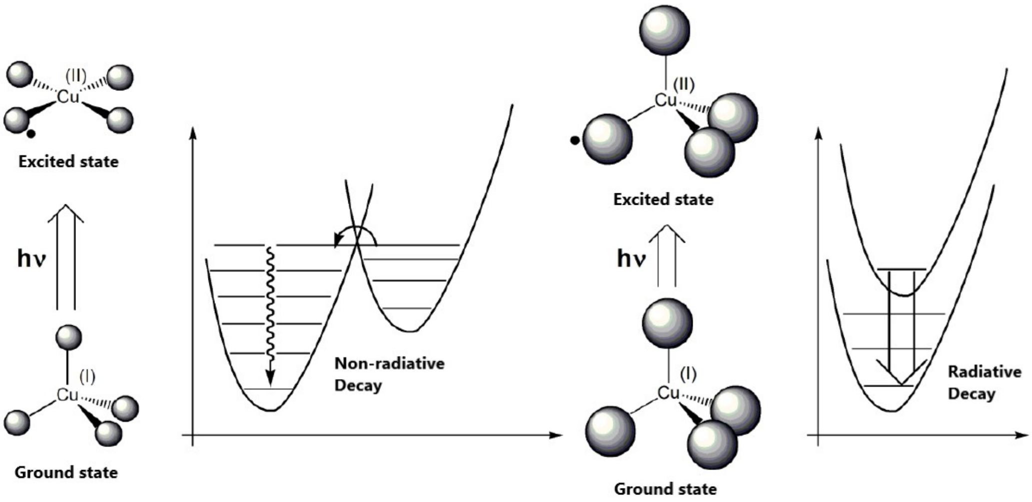

Figure 14. Non-radiative and radiative decay paths in tetrahedral copper(I) complexes.

Unlike d^6 metal complexes that can be strongly affected by the presence of energetically close MC levels causing non-radiative deactivation pathways and photochemical degradation, copper(I) derivatives do not suffer from this kind of problems. Despite that, vibrational modes and distortions of the coordination sphere at the excited state can determine non-radiative deactivation processes. For this reason, emissions are generally weak in solution, even in absence of O_2. Non-radiative pathways can also be favoured by other factors: for example, oxidative quenching can occur in presence of nitroaromatic compounds, cobalt(III) and chromium(III) complexes or bipyridium salt derivatives. Quenching can also be observed as a consequence of energy transfer to molecules with low triplet states like anthracene.[50]

Copper(I) complexes can be mainly divided depending on their charge. Anionic derivatives do not exhibit luminescent properties, whereas neutral and cationic emitting complexes with N- and P-donor ligands are widely studied. 1,10-phenantroline (phen) can be used as chelating imine ligand to afford homoleptic and heteroleptic species such as $[Cu(phen)_2]^+$ and $[Cu(phen)(P^\wedge P)]^+$ where P^P is a mono- or bidentate phosphine. In solution $[Cu(phen)_2]^+$ is non-emissive at room temperature, but the presence of alkyl and aryl groups in the 2,9-positions affords complexes characterized by long-lived triplet-state. This difference is attributable both to the stabilization of the tetrahedral geometry and the increased energy gap between excited and ground states. The most representative complex probably is $[Cu(dmp)_2]^+$ (dmp = 2,9-dimethyl-1,10-phenantroline) that exhibits a broad unstructured emission at λ_{max} = 730 nm and a 85-ns-long excited state. The schematic emission process is depicted in Figure 15.[48]

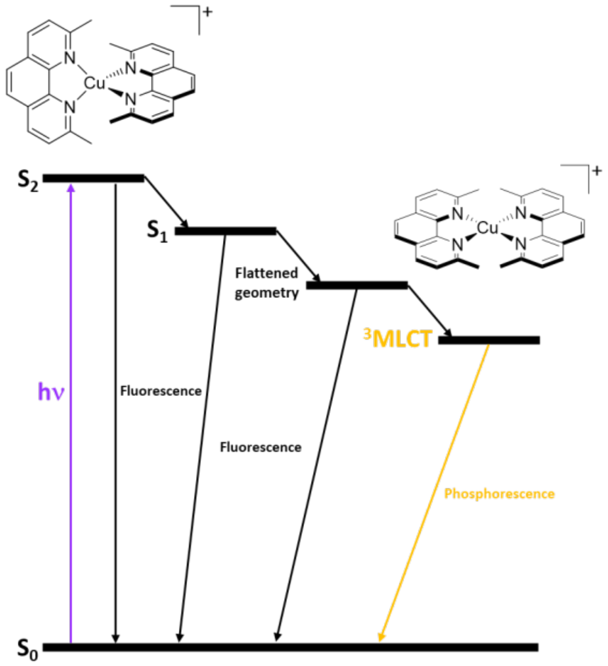

Figure 15. Schematic emission processes of $[Cu(dmp)_2]^+$.

The luminescence of this species is quenched by Lewis bases or coordinating solvents. MLCT lifetimes can be prolonged up to 1200 ns in presence of an organic chromophore characterized by a low-lying triplet state such as anthracene, acting as energy reservoir. On the basis of the results achieved using dmp as ligand, a huge number of 2,9-disubstituted phenanthroline ligands were investigated. Some of them are sketched in Figure 16.[51]

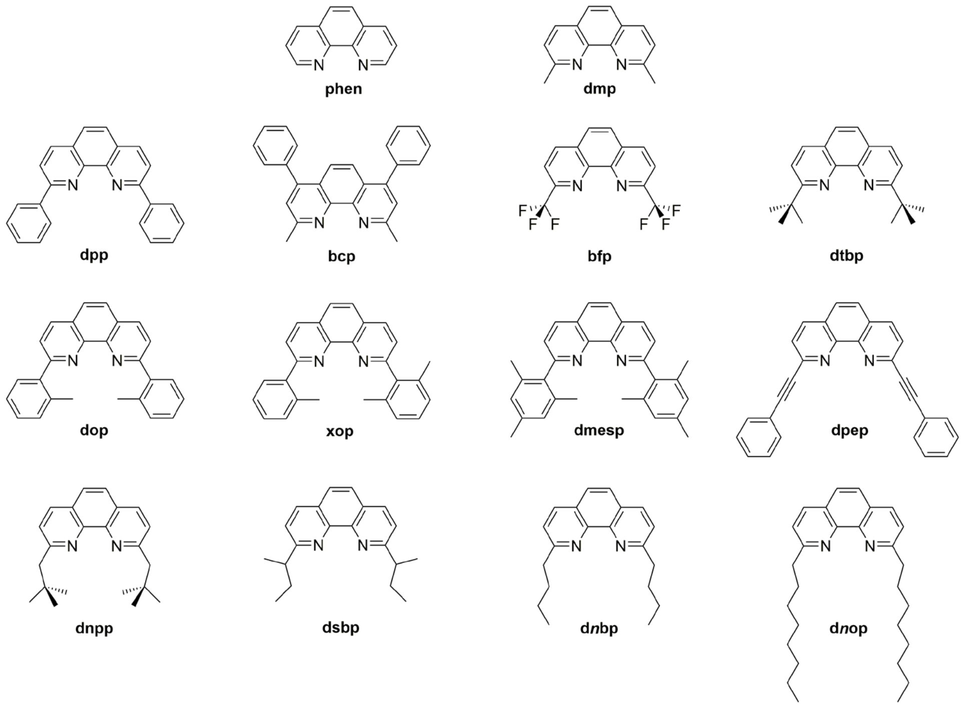

Figure 16. 1,10-phenantroline derivatives and their abbreviations.

Heteroleptic complexes, such as [Cu(N^N)(PPh$_3$)$_2$]$^+$ (N^N = 2,2'-bipyridine, phen or dmp), were widely investigated due to their high luminescence at the solid state and long excited state lifetimes. Computational calculations demonstrated that the HOMO normally involves the lone pairs of the phosphine ligand and copper(I) *d* orbitals, while the LUMO is mainly constituted by the antibonding overlap of the N^N *p* orbitals. The use of a bidentate phosphine like DPEphos affords compounds characterized by enhanced emission proprieties, probably because of the higher stability of the coordination sphere associated to the chelating effect. Moreover, the charge transfer is improved by the presence of a wide P-Cu-P angle, determining the enhancement of the emission lifetimes at room temperature. Examples of DPEphos derivatives are depicted in Figure 17.[52]

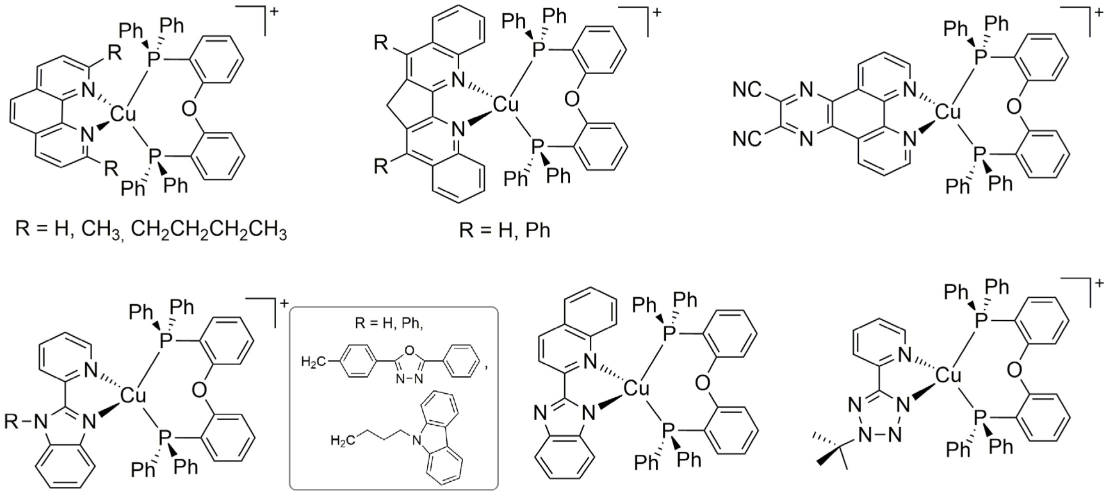

Figure 17. Selected examples of heteroleptic copper(I) complexes bearing DPEphos a P-donor ligand.

As regards the possibility of tuning the emission colour, the introduction of alkyl groups in the N-donor generally causes an hypsochromic (blue) shift of the absorption maxima. For instance, the bands move to shorter wavelengths by introducing in 2,9-positions of the 1,10-phenantoline skeleton methyl (dmp) and *n*-butyl (dnbp) moieties.[52b] On the other hand, the extension of the π-conjugation achievable with the introduction of phenyl groups (dpp) causes the shift of the spectral maxima to longer wavelengths, determining the so-called bathochromic or red shift. As an example, heteroleptic complexes bearing PPh_3 or DPEphos have been investigated with biquinoline (bq) derivatives as N-donors. The coordination of species such as dpbq (4,4'-diphenyl-2,2'-biquinoline) and mdpbp (3,3'-methyl-4,4'-di-phenyl-2,2'-biquinoline) afforded orange- and red-emitting complexes, whose luminescent features appeared to be favoured by the rigid structure, reducing the structural reorganization upon photoexcitation.[52e]

Besides the long-lasting luminescence and the large Stokes shifts, another significant aspect of copper(I) complexes is the possibility of influencing the emission proprieties with external *stimuli*, such as temperature. The previously reported $[Cu_4(\mu_3\text{–}I)_4(py)_4]$ cluster (see Figure 13) exhibits thermochromic proprieties, being the emission characterized by two bands, one at high and the other at low energy. The two emissions are related to excited states of similar energies but involving different orbitals. Regardless the nature of the ligand, at room temperature the emission is dominated by the low energy band that can be assigned to an excited state with mixed halide-to-metal charge transfer (^{3}XMCT) and cluster-centred (^{3}CC) character. The last component is observable only if the Cu-Cu distances are lower than the orbital interaction radius, estimated around 2.8 Å. On the contrary, at low temperature the low energy band is quite weak and red-shifted probably because of the stabilization of the ^{3}CC excited state. In this case, the luminescence is governed by a halide-to-ligand-charge transfer (^{3}XLCT) that involves the antibonding orbitals of the ligand and it can be investigated only if unsaturated systems are present.[53] Similar iodocuprate $[Cu_xI_y]^{(y-x)-}$ (x = 2, 4, 6; y = 4, 6, 10) anions were used in combination with previously reported octahedral manganese(II) complexes having dppmO$_2$, dppeO$_2$ and dppbO$_2$ as chelating ligands for the preparation of dual-emitting organic inorganic hybrids. The phosphorescence is related both to the $^4T_1(^4G) \rightarrow {}^6A_1(^6S)$ transition of manganese(II) centred between 605 and 648 nm, and to the ^{3}CC excited state in the 480-728 nm range. The ratio of the emission bands can be tuned on changing the $[Cu_xI_y]^{(y-x)-}$ cluster.[54]

In the halide-free tetranuclear cluster $[Cu_4(pyz)_4]$, where pyz is 3,5-di-*tert*-butylpyrazolate, the choice of the substituent in position 4 of the pyrazole ring (R = H, F, Cl, Br, I, CH_3) deeply influenced the emission thanks to rigidochromic effects. The emission moves from yellow (R = H), to green (R = F) to deep blue (R = Cl, Br and CH_3) as a consequence of the compression of the {Cu_4} core that avoids the rearrangement of the structure at the excited state and maintains the high energy ^{3}CC state. When R = Br, ^{3}MLCT transitions may be involved due to increased spin-orbit coupling effect related to the heavy atom.[55]

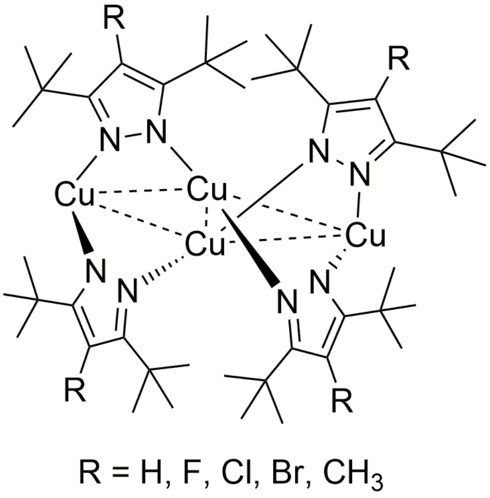

Figure 18. Deep-blue emitting $[Cu_4(pyz)_4]$ cluster.

Other common ways to trigger the luminescence in copper(I) complexes are vapochromism and mechanochromism. The former is particularly useful to detect VOCs (volatile organic compounds). The changes in the luminescence features are attributable to reversible rearrangements catalysed by solvent vapour, or by interstitial solvation affecting the interactions among the copper ions, the π–π stacking and the hydrogen bonding. VOC molecules can also react with the complexes forming metal-solvent bonds. All these aspects modify the energy of the excited state and therefore the emission. For instance, vapochromic properties were observed for [CuI(py)(PPh_3)$_2$] (py = pyridine) in presence of 2-methylpyrazine. To facilitate the observation of changes even with small amounts of vapour molecules, the complex was embedded in a polyvinylpyrrolidone thin film via spin-coating. The emission moves from 510 to 575 nm after being exposed to 2-methylpyrazine. The exchange mechanism proposed is reported in Scheme 1.[56]

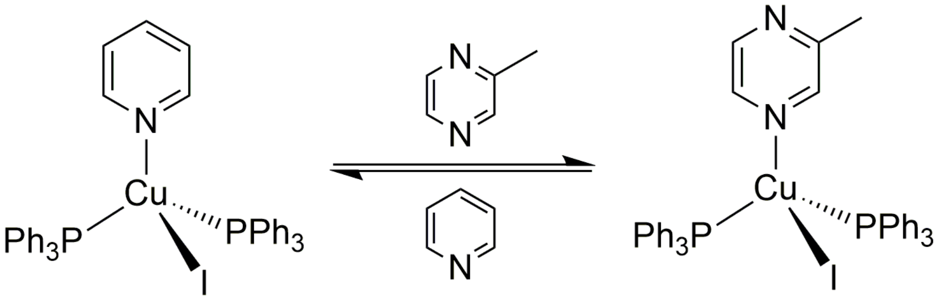

Scheme 1. Vapochromic exchange mechanism for [CuI(py)(PPh_3)$_2$].

Although mechanochromism was investigated mainly for gold(I) and platinum(II) derivatives, few examples of copper(I) complexes exhibiting this property were reported. Mechanically triggered luminescence is attributable to the disruption of internuclear Cu-Cu contacts, π–π stacking or changes in the molecular conformation. Thermal treatment or recrystallization can be used to return to the original emission. Mechanochromic complexes can be applied in various fields, such as mechanosensors, indicators or optoelectronic devices.[57]

Five-membered N-donors such as imidazole (Him) proved to be suitable candidates for the preparation of luminescent copper(I) complexes. [CuBr(PPh_3)$_2$(Him)] (see Figure 19a) was synthesized and its luminescent proprieties were fully investigated and rationalized on the basis of time-dependent DFT (TD-DFT) calculations. In this case, the Cu-Br σ-bond plays a role of paramount importance in the emission since it is associated to the HOMO of the compound. As observable in Figure 19b and 19c, pyrazole heterocycles can be included in polydentate N-donor ligands containing pyridine units. The complexes [Cu(PPh_3)X]$_2$(μ–N^N), where X is I or Br and N^N is 3,5-bis[6-(2,2-dipyridyl)]pyrazole, are characterized by emissive proprieties attributable to interligand charge transfer (ILCT) and MLCT transitions. The formal substitution of Br with I implicates a bathochromic shift of the emission peak. Other examples of copper(I) complexes with pyrazole-based ligands are $[\{Cu_2(N^\wedge N)\}_2(\mu\text{-}dppb)_2]^{2+}$, where N^N = 3-(2'-pyridyl)pyrazole, 5-tert-butyl-3-(2'-pyridyl)pyrazole or 5-trifluoromethyl-3-(2'-pyridyl)pyrazole and dppb = 1,4-bis(diphenylphosphino)butane. The comparison of these species shows an enhancement of the luminescent proprieties as a consequence of the substitution in the 5-position of the pyrazole ring with the electron-withdrawing group CF_3.[58]

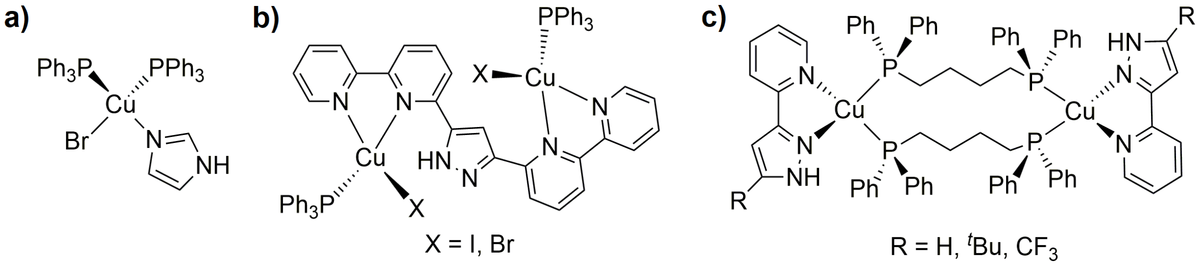

Figure 19. $[CuBr(PPh_3)_2Him]$, $[Cu(PPh_3)X]_2(\mu\text{-}N^\wedge N)$ and $[\{Cu_2(N^\wedge N)\}_2(\mu\text{-}dppb)_2]^{2+}$.

N-functionalized heterocycles such as pyridine-benzimidazole, -triazole, -tetrazole and their conjugated bases were systematically investigated in combination with phosphine moieties, such as PPh_3, dppm and DPEphos. Neutral chelating ligands originated mononuclear cationic complexes both with PPh_3 and DPEphos, characterized by blue to green emissions due to MLCT transitions. On the other hand, with the corresponding deprotonated ligand neutral mononuclear species were achieved only with DPEphos. In neutral complexes the luminescent properties were enhanced by the presence of tetrazole derivatives rather than benzimidazole- or triazole-based ligands. Selected examples of heteroleptic complexes are depicted in Figure 20.[59]

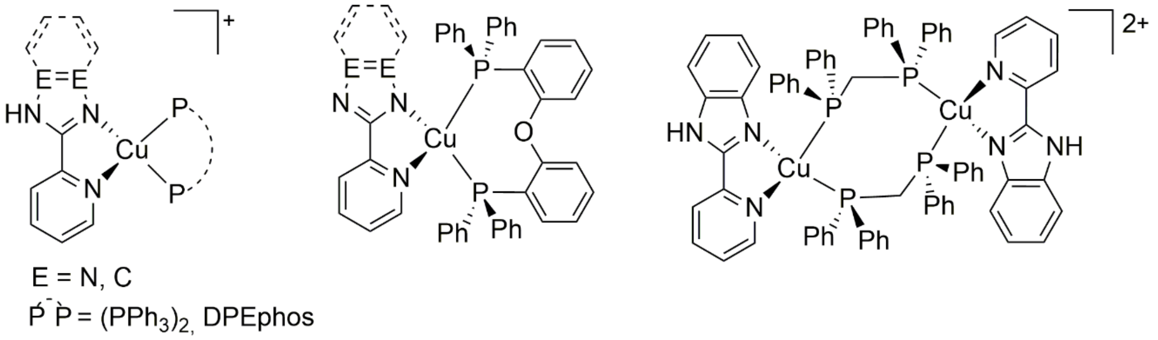

Figure 20. Examples of copper(I) complexes with five-membered N-donor ligands.

In presence of chiral ligands, it was possible to isolate complexes characterized by circularly polarized luminescence. For instance, orange-emitting chiral copper(I) clusters having general formula [(R/S-MBA)$_4$Cu$_4$I$_4$] were isolated from the reaction between CuI and R/S-methylbenzylamine (R/S-MBA). The crystallized complexes exhibited a helical arrangement responsible of the CPL activity at room temperature.[60] Instead, cyclic (alkyl)(amino)carbenes (CAACs) derived from enantiopure menthol (see Figure 21) allowed the preparation of the first examples of C$_1$-symmetrical copper(I) complexes characterized by circularly polarized yellow luminescence. In this case, the architecture of the derivatives is simpler than the example reported above because it does not require helical or axial chirality. The circularly polarized luminescence appeared to be influenced by the size of the other ligand: almost no CPL was observed in the case of X = I, while the other halides follow the trend Br < Cl < F. Despite the fact that fluorine and borohydrides have similar sizes, the magnitude of CPL was not as strong for the latter derivatives, probably because of different σ-interactions.[61]

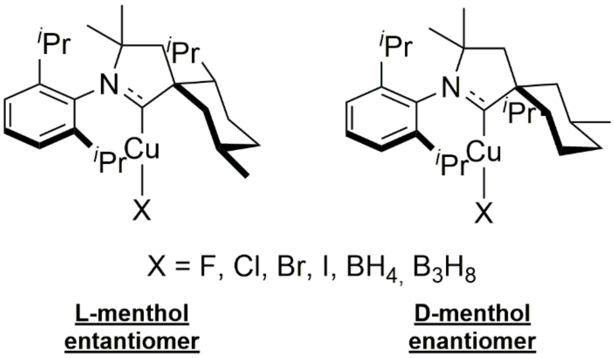

Figure 21. Examples of copper(I) derivatives exhibiting CPL.

1.3.2 Copper coordination polymers

Another reason of interest concerning luminescent copper(I) compounds is given by the fact that, in presence of suitable ligands such as halides, polynuclear species and coordination polymers characterized by unique electronic features can be isolated. In presence of a porous structure where a small molecule can be hosted they are called MOFs or “metal-organic frameworks”. The structural rigidity of MOFs leads to unusual luminescent proprieties characterized by long lifetimes and high quantum efficiencies. MOFs can be widely used as sensors if they show a detectable and reversible change in response to a specific analyte or if the luminescence is quenched as a result of exciplex formation. An example is the Cu_6L_6 (L = 5,6-diphenyl-1,2,4-triazine-3-thiolate) cluster depicted in Figure 22 that can be used to detect aromatic molecules (*i.e.* toluene, nitrobenzene, aniline, *o*-, *m*- and *p*-dimethylbenzene) in water. Copper(I) ions are coordinated to two sulphurs and one nitrogen atom belonging to three different ligands. A bidimensional structure is obtained thanks to Van de Waals interactions among the phenyl rings. As regards the detection of the analytes in water, the distinct response of Cu_6L_6 to benzene-based species is attributable to π-π stacking interactions that, in presence of monosubstituted benzene molecules and *o*-dimethylbenzene, can enlarge the Cu-Cu separation causing the efficient quenching of the luminescence. On the contrary, with *p*- and *m*-dimethylbenzene the aromatic-aromatic interactions in the cluster are only weakened, thus causing a less effective quenching.[62]

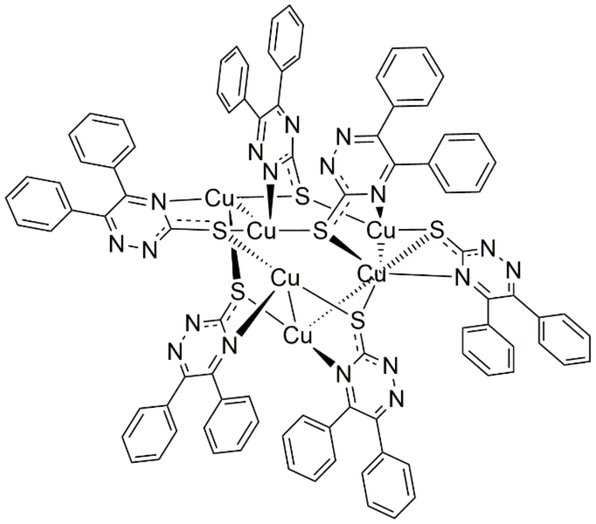

Figure 22. The Cu_6L_6 (L = 5,6-diphenyl-1,2,4-triazine-3-thiolate) cluster.

Coordination polymers can be synthesized from copper(I) halides like CuCl, CuBr and CuI. The first two salts are air-unstable and they can be easily oxidized, so their dissolution in presence of O_2 can lead to the formation of mixed-valence copper(I/II) halide or copper(II) halide complexes. CuX salts are poorly soluble in common organic solvents, but they are moderately soluble in CH_3CN and CH_3CH_2CN. Phosphines can both stabilize copper(I) centres and facilitate the solubilization of its salts.

Moreover, to increase the solubility of copper(I) halides in solvents like water it is possible to dissolve the solid into the corresponding saturated alkali metal halide aqueous solution, e.g. CuI in saturated KI solution. This technique was used to afford luminescent inks based on copper iodide clusters with 1-propyl-1,4-7-diazabicyclo[2.2.2]octan-1-ium (pr-ted) salt. The corresponding complex [Cu_4I_6(pr-ted)$_2$] reported in Figure 23 forms yellow luminescent nanoparticles in presence of a solution containing polyvinylpyrrolidone (PVP) in ethanol. Besides the stability, this cluster is characterized by a photoluminescence quantum yield Φ over 98% thanks to the strong spin-orbit coupling inside the structure.[63]

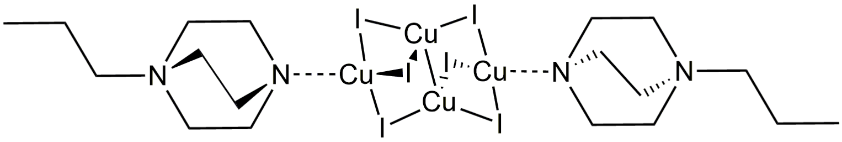

Figure 23. Complex [Cu_4I_6(pr-ted)$_2$].

Recently, hydro(solvo)thermal methods were applied for the synthesis of new copper(I) halide derivatives. In this case, the reactions are conducted in sealed Teflon reactors at 100-200°C and under 10-30 atm of autogenous pressure. These conditions contribute to lower viscosity, facilitate crystal growth and enhance the rate of solvent extraction, partially solving the solubility problems. As an example, this synthetic procedure was used to obtain the complex reported in Figure 24. The bridging mode of the I^- ions leads to a CuI_2Cu rhomboid dimer where PPh_3 and 2,4,5-tri(4-pyridyl)-imidazole (Htpim) are in *trans* positions. The resulting zig-zag chained structure is obtained as the dimer is further connected to the nitrogen atoms of the ligand. The coordination polymer shows a moderately intense red emission after being excited with near UV light.[64]

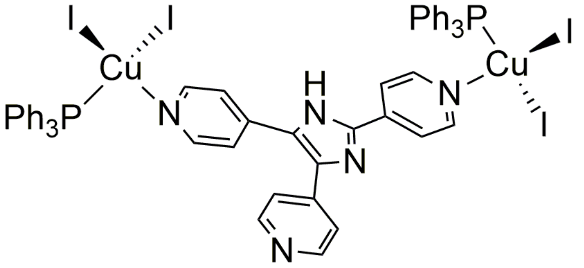

Figure 24. Copper(I) complex with Htpim.

Oxidation and reduction routes can also be followed to afford copper(I) halide clusters respectively from copper(0) and copper(II). These coordination polymers can have a large number of possible structures, depending upon factors such as inner-core variability, outer-shell cooperativity and kinetic tunability. The first feature is connected to the fact that, as previously reported, copper(I) can have different coordination numbers and geometries, as well as the halide ions. Moreover, the organic ligands can influence the structure by acting as bridges among the metal centres. Then, the formation of CuX aggregates is controlled by kinetically fast associative/dissociative equilibria that can be tuned by changing the stoichiometric ratios of the reactants. As the crystallization process is normally slow, the isolated species may not be the most predominant in solution, whose structure can hardly be predicted.

Coordination polymers can be zero-, one-, two- or three-dimensional, and by varying the reaction conditions, in terms of solvent, temperature and template agents, it is possible to obtain coordination polymers having different dimensionality. For instance, several copper(I) halide aggregates were isolated using the triimidazole ligand depicted in Figure 25. The luminescent properties are attributable to concomitant fluorescence and ultralong phosphorescence connected to the formation of π–π stacking interactions in the crystal structure.[65]

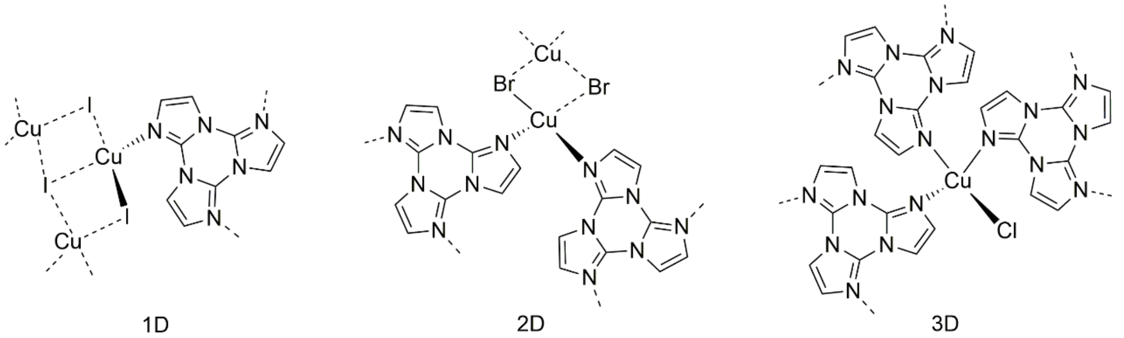

1D 2D 3D

Figure 25. Examples of coordination polymers with triimidazole as ligand.

The direct influence of the halide in the emission colour was observed with complexes having general formula $[Cu_4X_4L_2]_n$ where X is Cl, Br or I (see Figure 26) obtained from the reaction between copper(I) halides and tris[2-(pyridin-2-yl)ethyl]phosphine (L). The emission colour sweeps from deep blue in presence of the iodo-species to green with the chloro-derivative. Such outcome can be justified on considering the active role of the halide in charge transfer process responsible of the emission, being a ^{3}(M+X)LCT.[66] The same ligand was later used to prepare other complexes where tris[2-(pyridin-2-yl)ethyl]phosphine coordinates three different copper(I) centres with the phosphorous atom. This is the first case of a triple bridging phosphine. As regards the photophysical properties, the complexes are blue-emitting species characterized by dual-luminescence. The mechanism responsible of the emission is ^{3}(M+X)LCT and ^{3}CC respectively for the high and the low energy band. Their contribution in the emission can be modified on changing the temperature, as previously observed for [Cu$_4$(μ_3–I)$_4$(py)$_4$].[53] Besides thermochromism, the iodo-derivative exhibits also mechanochromism: grinding at room temperature determines a green emission that can be reversed with the addition of acetonitrile.[67]

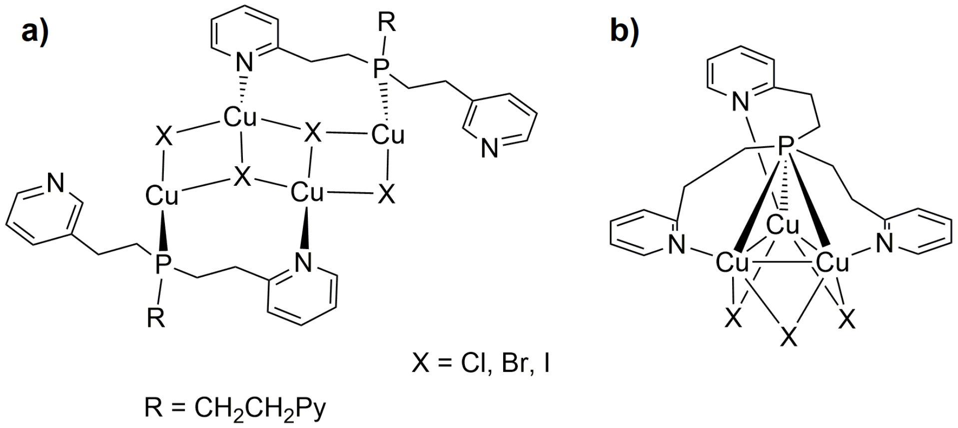

Figure 26. Complexes [Cu$_4$X$_4$L$_2$]$_n$ and [Cu$_3$(μ_2–X)$_3$L].

1.3.3 Copper(I) complexes with TADF properties

Thermally activated delayed fluorescence (TADF) is a photophysical property that was firstly observed in organic compounds such as eosin (Figure 27a) at the beginning of the Sixties.[68] Since then, these features have received growing interest as they could be exploited for optoelectronic applications. The emission of these materials is composed by two separate mechanisms: promoted (PF) and delayed fluorescence (DF). The former corresponds to an immediate fast decay emission from the S$_1$ to the S$_0$ state. On the contrary, during the latter, triplet excitons have to be converted into singlets through a mechanism called “reversed intersystem crossing” (RISC), as shown in Figure 27b. For this reason, the luminescent process is delayed. However, RISC (T$_1$ → S$_1$) has to be efficient in order to harvest triplet excitons and a small energy difference ($\Delta E < 1000$ cm^{-1}) at room temperature between the two excited states is the key feature of the whole process. To achieve this condition, it is necessary to reduce the exchange interaction between HOMO and LUMO, meaning that they have to be spatially separated. Moreover, the rate constant of the RISC process must be higher than that of the phosphorescent decay.[69] Cationic homo- and heteroleptic copper(I) complexes are widely studied for the possibility of tuning the TADF properties.[70] The first metal-based thermally activated delayed fluorescent material investigated was [Cu(phen)(PPh$_3$)$_2$]$^+$, reported in Figure 27c.[71] More recently the neutral complexes reported in Figure 27d having 2-

(diphenylphosphino)-6-methylpyridine as mixed N^P donor ligand were studied for their photophysical properties, attributed to the combination of TADF and short-lived phosphorescence. At room temperature the derivatives exhibited an intense emission centred in blue-green region mostly related to the singlet transition, with quantum yields up to 90%.[72]

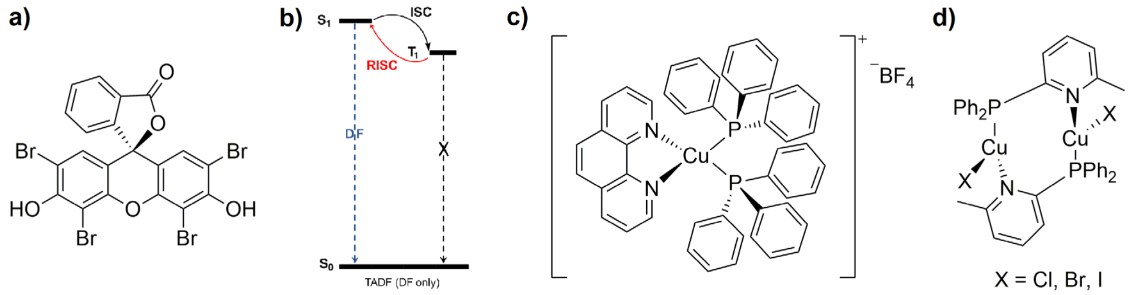

Figure 27. TADF (DF only) luminescence process and the first compounds exhibiting TADF.

TADF properties potentially allow to achieve 100% of internal quantum efficiency (IQE) as both singlet and triplet excitons can be exploited. One of the highest IQE ever reported was reached with the blue-emitting complex $[Cu(PNP\text{-}^{t}Bu)]_2$ [PNP-^{t}Bu = bis(2-diisobutylphosphinophenyl)amide)] depicted in Figure 28a. The vapour-deposited OLED containing this derivative exhibited an external quantum efficiency (EQE) of 16%.[73]

Thermally activated delayed fluorescence revealed to be particularly appealing for solid-state lighting devices.[74] OLED devices are typically composed by three separated emitting layers: a red, a green and a blue one. While the first two are normally highly efficient cyclometallated iridium(III) complexes (second generation OLED), the blue emitter is an organic compound. In fact, blue-emitting second generation OLEDs are not as capable in terms of stability, colour purity and brightness. The first generation OLED is higher energy-demanding than the other two components. In this sense, TADF materials represent a possible solution to overcome this problem and they constitute the so-called third generation OLED.[75]

As observable in the blue emitting complexes reported in Figure 28b and 28c, the emission lifetimes of TADF materials are characterized by two components: one shorter (usually ns-long) referred to the $S_1 \leftarrow S_0$ transition, and one longer (usually μs-long) responsible of the $T_1 \leftarrow S_0$ transition. For instance, emission lifetimes of $[Cu(pz_2BPh_2)(DPEphos)]$ [pz_2BPh_2 = bis(pyrazol-1-yl)-biphenyl-borate] are 120 ns and 480 μs; whereas for $[Cu(\mu\text{–}I)\{PhNMe_2Ph_2P\}]_2$ ($PhNMe_2Ph_2P$ = *N*,*N*-dimethyl-2-(diphenylphosphino)aniline) $\tau(T_1 \leftarrow S_0)$ is 290 μs and $\tau(S_1 \leftarrow S_0)$ is 90 ns.[76] Only more recently intersystem crossing was directly investigated in TADF derivatives through time-dependent photoluminescence. Besides being characterized by an average lifetime around 12 μs, [Cu(PyrTet)(DPEphos)] [PyrTet = 5-(2-pyridyl)tetrazolate] (see Figure 28d) exhibited a 27-ps-long ISC mechanism with a rate of $3.7 \cdot 10^{10}$ s^{-1}. Comparing this value with the typical iridium(III) time constants (~100 fs) it is possible to observe how the process is much slower due to the lower SOC effect.[77]

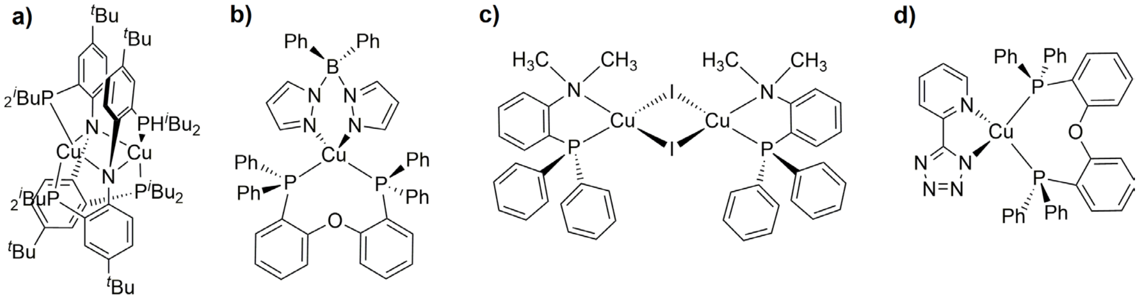

Figure 28. Examples of copper(I) complexes with TADF.

To prove if a complex is characterized by TADF properties it is sufficient to investigate the emission lifetimes on varying the temperature. Lifetimes decay curves are typically registered at 77 and 300 K. On lowering the temperature in TADF materials lifetimes should increase, as only the triplet state T_1 is effectively taking part in the emission. On the contrary, following the Boltzmann distribution the population of the higher energy S_1 state increases on rising the temperature. The general reduction in the emission lifetimes is a consequence of the shorter decay from S_1 compared to T_1. This phenomenon is usually combined with a blue shift in the emission. Besides the complexes previously mentioned, also the derivatives [Cu(py$_2$-BMe$_2$)(IPr)] [py$_2$-BMe$_2$ = di(2-pyridyl)dimethylborate; IPr = 1,3-bis(2,6-diisopropylphenyl)imidazol-2-ylidene] and [Cu(3-R-pypz)(DPEphos)][BF$_4$] [pypz = 1-(2-pyridyl)pyrazole; R = H, CH_3, CF_3] proved to be TADF materials following the considerations described above together with the complexes having general formula [$Cu_2(Py_2PPh)_2X_2$], where X = Cl, Br, I (Figure 29a-c).[78] The use of the analogue pyridylarsine-based ligands afforded derivatives characterized by TADF but with shorter emission lifetimes. This outcome can be justified considering two important aspects: the broadening of the gap between S_1 and T_1 and the increased rate constant between T_1 and S_0 due to the higher spin-orbit coupling of arsenic with respect to phosphorus.[79] Recently the modulation of TADF and phosphorescence was observed in complexes having general formula [$Cu_2(PPy_3)_2X_2$] [PPy_3 = tris-(2-pyridyl)phosphine; X = Cl, Br, I], sketched in Figure 29d. At room temperature these derivatives exhibited dual luminescence between 520 and 550 nm attributable to ^{1}(M+X)LCT and ^{3}(M+X)LCT. The contribution of TADF and phosphorescence depends on the coordinated halide: passing from the chloride to the iodide, the participation of the former becomes dominant at expense of the latter. This outcome can be rationalized considering that the energy gap between S_1 and T_1 decreases thus promoting the TADF mechanism.[80]

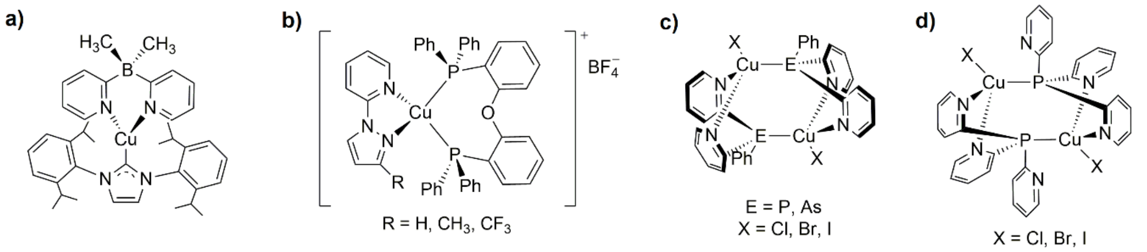

Figure 29. [Cu(py$_2$-BMe$_2$)(IPr)], [Cu(3-R-pypz)(DPEphos)][BF_4], [$Cu_2(Py_2PPh)_2X_2$] and [$Cu_2(PPy_3)_2X_2$].

The combination between photophysical and photocatalytic properties was reported by Xu and co-workers. Photocatalytic H_2 evolution was observed under visible light using [$Cu_6I_6(ppda)_2$] {ppda = 2-[2-(dimethylamino)phenyl(phenyl)phosphino]-*N*,*N*-dimethylaniline} (see Figure 30a) as photocatalyst and methanol as electron scavenger. Besides being characterized by TADF properties, the hexanuclear nanocluster, as powder, is the first example of white emitting complex. A bathochromic shift in the emission is also noticeable passing from crystal to powder to film state, with maxima respectively centred at 476, 535 and 563 nm.[81]

Finally, the carbene-copper-amine complexes exhibiting TADF properties sketched in Figure 30b proved to be efficient materials for the preparation of vacuum-deposited OLEDs characterized by device lifetimes up to 1300 hours at 1000 cd m^{-2} and EQE around 24%. Changes on the bulky pyrazine- (PzIPr) or pyridine-fused N-heterocyclic carbene (PyIPr*) and carbazole (Cz) ligands allowed the preparation of OLEDs with emission centred between 474 and 619 nm.[82]

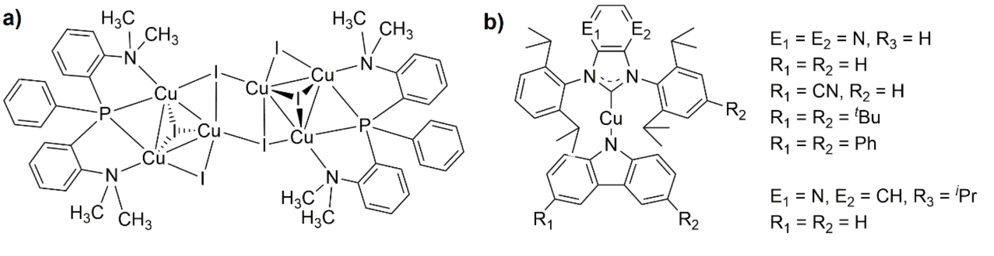

Figure 30. [$Cu_6I_6(ppda)_2$] and carbene-copper-amine complexes.

1.4 Zinc and its luminescence

Zinc is characterized by an atomic number of 30 and belongs to the group 12 together with cadmium and mercury. It has five naturally occurring isotopes, but the most common is ^{64}Zn, that represents around the 49%.

The group 12 elements are known also as "chalcophiles" because their most important ores are sulfides (e.g., HgS or cinnabar). Besides ZnS (zinc blende or sphalerite), zinc can be found also as $ZnCO_3$ (calamine or smithsonite), and more rarely as $Zn_4Si_2O_7(OH)_2\cdot H_2O$ (hemimorphite) and $(Zn,Fe)O\cdot Fe_2O_3$ (franklinite).

Its atomic configuration is $[Ar]3d^{10}4s^2$ and the main oxidation state is Zn^{II} (d^{10}). Zn^{I} also exists, but it requires to be stabilized by bulky ligands. Having the *d* shell completely filled, zinc(II) is similar to magnesium(II) and in some cases its compounds are isomorphous with those of the group 2 element. However, zinc(II) tends to form more covalent bonds with respect to magnesium(II), with the isolation of stable complexes with O-, N- and S-donor ligands, as well as with halides and cyanide. Similarly to magnesium(II), zinc(II) derivatives are generally diamagnetic and colourless, being the spectroscopic term S equal to zero in both cases. Therefore, the symmetrical electronic distribution prevents *d-d* metal centred transitions.[15] Some zinc(II)-based minerals show luminescent properties, but in most of the cases the emissions are due to the substitution of zinc(II) ions with manganese(II) or lead(II), as it was observed in Zn_2SiO_4 (willemite), $ZnAl_2O_4$ (gahnite), $ZnCO_3$ (smithsonite) and $Be_3Zn_4(SiO_4)_3S$ (genthelvite).[1a]

In presence of suitable activators such as silver, copper or manganese, ZnS can exhibit strong phosphorescence that is commonly exploited for cathode ray tubes, X-ray screens or glow-in-the-dark products. Silver-doped zinc sulfide is characterized by short lifetimes and a bright blue emission caused by the recombination at interstitially incorporated silver(I) centres. On the other hand, copper-activated ZnS has an intense and long-lasting phosphorescence, characterized by a green and a blue band whose intensity depends on the composition. The former is due to the substitution of zinc(II) with copper(I) ions, while the latter is a combination of the same phenomenon and interstitially incorporated copper(I) ions. Doping zinc sulfide with manganese(II) determines an emission band centred in the yellow region due to the $^4T_1(^4G) \rightarrow {}^6A_1(^6S)$ transition. At higher concentrations the interactions between manganese(II) ions move the band towards longer wavelengths.[83]

ZnS is commonly exploited for the preparation of quantum dots (QDs) together with ZnSe, CdSe and CdS. These nanoparticles are commonly composed by a semiconductor embedded in a shell functionalized with organic ligands. The dimensions are normally comprised between 1 and 10 nm and they determine different photoluminescent properties associated to the quantum confinement. This phenomenon is observable when the radius of the semiconductor is comparable to the Bohr exciton radius, that is the average distance between holes and electrons inside the material. Under this dimension the material can be considered in high confinement regimen. The band gap increases when the QD dimensions decrease, and discrete energetic levels are originated in the valence and in the conduction bands. The reduction of the size results in an ipsochromic shift of the emission maxima, as it can be observed in Figure 31. The direct dependence between photoluminescent properties and dimensions of the QDs makes them suitable candidates for the preparation of LEDs, lasers, solar cells and sensors.[84]

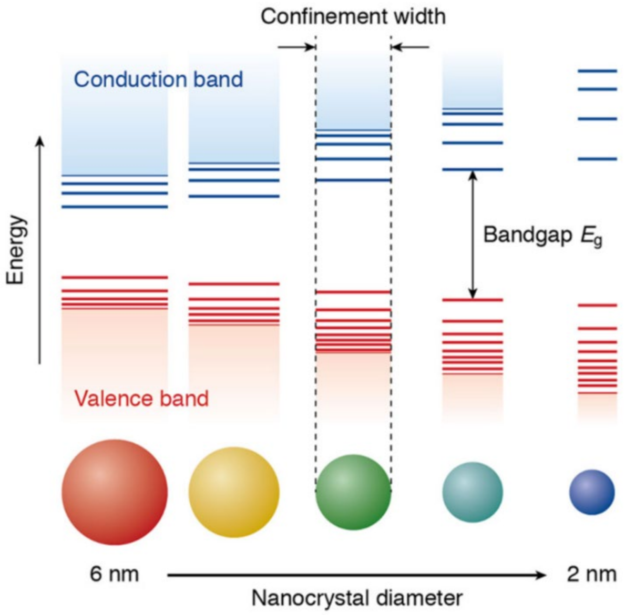

Figure 31. Direct dependence between dimensions and photoluminescence in QDs.

1.4.1 Luminescent zinc(II) complexes

As *d-d* transitions are not expected for zinc(II) complexes, their emissive properties are related in most of the cases to LC or LLCT mechanisms. However, LMCT transitions involving the low-lying zinc(II) empty orbitals were reported. Moreover, empty σ*-antibonding orbitals derived from the overlap of zinc(II) and ligand orbitals can be involved in the LMCT process. Therefore, the lowest excited states could be more accurately described in some cases by a mixed LMCT/LLCT as depicted in Figure 32.

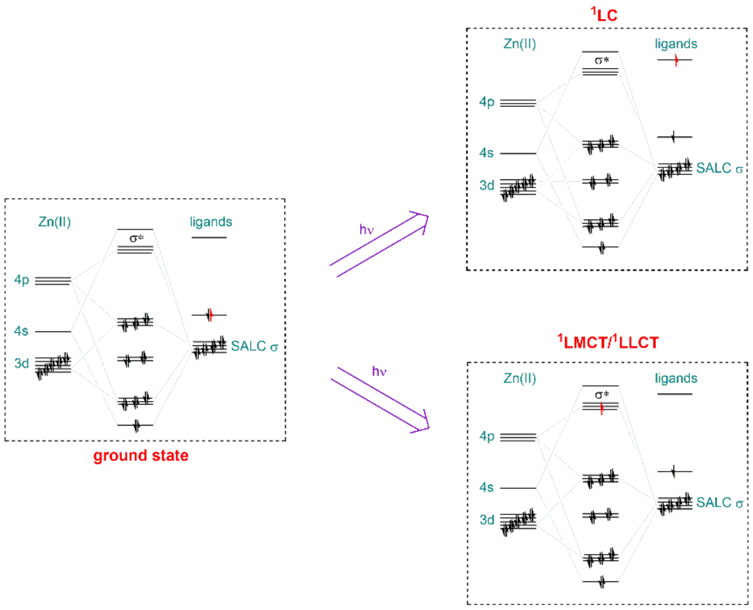

Figure 32. SALCs involved in charge transfer mechanisms for zinc(II) complexes.

Zinc(II) complexes exhibit intense fluorescence related to $\pi^* \leftarrow \pi$ ligand-centred transitions when the metal centre has just the role to provide stability to the ligand at the excited state. Thanks to their unique photophysical properties, zinc(II) derivatives were used to prepare fluorescence-based OLEDs.[51c] Their first application dates back to the early 2000s when derivatives such as bis(8-hydroxyquinolinato), bis(*N*-methylsalicylideneamino), (*N*,*N'*-disalicylidenehexane-1,6-diaminato) and bis[2-(2-hydroxyphenyl)benzothiazolato]zinc(II) complexes were first applied.[85] The first compound (Figure 33a) was used as alternative to the 8-hydroquinolinate aluminium complex Alq_3 and it is characterized by a strong yellow fluorescence. The two imine complexes depicted in Figures 33b and 33c exhibit a blue fluorescence, while the 2-hydroxyphenyl benzothiazole derivative shown in Figure 33d has a broad emission that extends from 430 to 700 nm.[86]

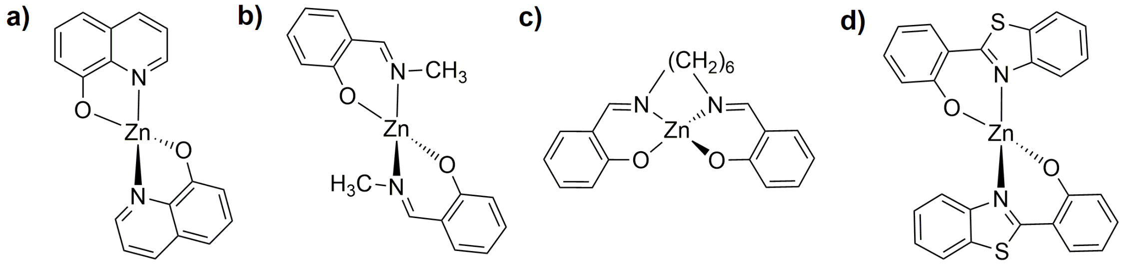

Figure 33. Bis(8-hydroxyquinolinato), bis(*N*-methylsalicylideneaminato), (*N*,*N'*-disalicylidenehexane-1,6-diaminato) and bis[2-(2-hydroxyphenyl)benzothiazolato]zinc(II) complexes.

It is worth noting that the short emission lifetimes typical of singlet excited states limit the possible applications of zinc(II) complexes in OLEDs. Fluorescent zinc(II) complexes based on the benzamidine N-oxide skeleton were used as dopants to prepare solution processed greenish-white OLEDs (see Figure 34). It is the first reported case of preparation of devices with derivatives characterized by aggregation-induced emission. The emission is centred at 556 nm at room temperature, and it is observable only at the solid state.[87]

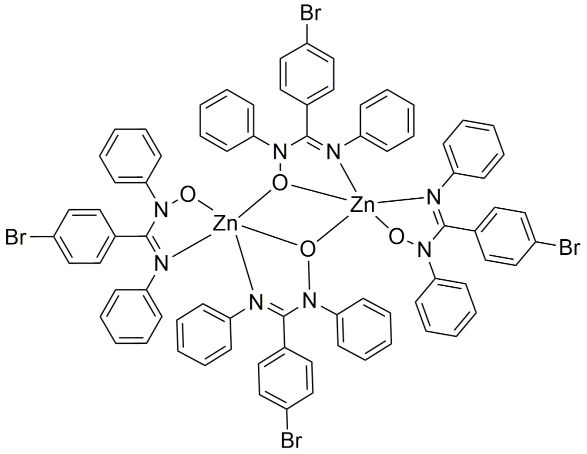

Figure 34. Zinc(II) complexes with 4-bromo-*N*,*N′*-diphenylbenzamidinate *N*-oxide as chelating ligand.

A possible solution to overcome the short emission lifetimes is to exploit zinc(II) derivatives characterized by TADF properties. Selected examples are depicted in Figure 35. In particular, the complex sketched in Figure 35c exhibits excitation-wavelength-dependent emission and excited state intramolecular proton transfer.[88]

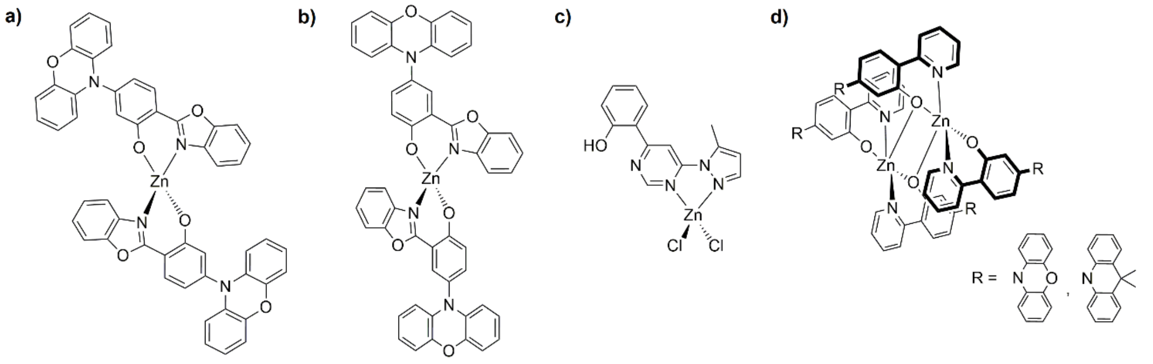

Figure 35. Zinc(II) complexes exhibiting TADF properties.

Ligands such as dipyrrinato derivatives allowed the isolation of the homoleptic zinc(II) complexes depicted in Figures 36a and 36b, characterized by intense fluorescence between 490 and 630 nm with quantum yields up to 66%.[89] The heteroleptic derivatives obtained with the same ligands exhibited intense emission in the far-red region also in polar solvents. In this case the absorption is originated from both the ligands (see Figure 36c), but the emission is only related to the π-extended dipyrrin determining a *pseudo*-Stokes Shift of around 4600 cm^{-1}. These photoluminescent properties were efficiently exploited in cell imaging.[90]

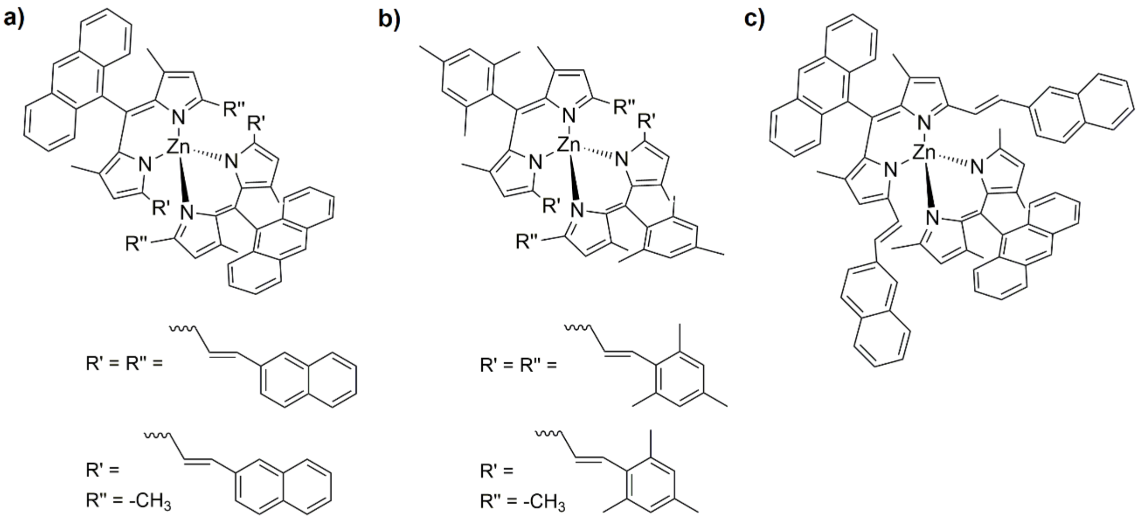

Figure 36. Bis(dipyrrinato)zinc(II) complexes.

Phosphorescence is generally observed only for low-temperature glasses, probably because the high energy potential of zinc(II) forbids its participation to frontier molecular orbitals in the lowest excited states. Consequently, intersystem crossing from singlet to triplet excited state is not favoured.[88c] Recently, however, the two blue-phosphorescent complexes sketched in Figure 37a and 37b were synthesized. Their emission at room temperature was characterized by μs-long lifetimes and it was later assigned to ligand-centred $\pi^* \leftarrow \pi$ transition.[91] A phosphorescent coordination polymer based on the 6-aminonicotinic acid (H6ani) was reported as well (Figure 37c). Specifically, the complex exhibits a bright blue emission and a pale-green afterglow that lasts for few seconds after the UV excitation source is removed. The compound therefore belongs to the group of long-lasting phosphors.[92] Almost identical considerations can be made considering the zero-dimensional organic-inorganic hybrids obtained with 1,4-bis(3-ammoniopropyl)piperazinium (BAPP), having general formula [BAPP][$Zn_2(Cl_yBr_{1-y})_8$] (y = 0-1). Ultra-long phosphorescence and afterglow related to the heavy-atom effect were detected. The emissive properties were exploited for the preparation of anti-counterfeiting materials.[93] Similarly to what previously observed for manganese(II), the reaction between zinc(II) halides and 18-crown-6 in ionic liquids affords the complexes sketched in Figure 37d. It is interesting to observe that [ZnX_2(18-crown-6)] is characterized by an intense emission with a quantum yield of 54%. On the basis of DFT calculations the phosphorescence is attributed to a charge-transfer mechanism between a halide n*p* orbital and an empty 4*s* orbital of the zinc(II) ion.[39b]

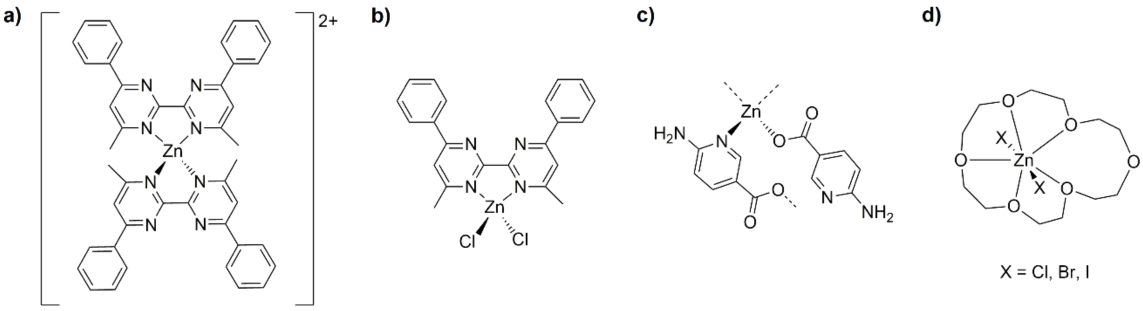

Figure 37. $[Zn(pmbp)_2]^{2+}$, $[ZnCl_2(pmbp)_2]$ (pmbp = 4,4′-diphenyl-6,6′-dimethyl-2,2′-bipyrimidine), the repeating unit of $[Zn(\mu\text{–}6ani)_2]_n$ (H6ani = 6-aminonicotinic acid) and $[ZnX_2(18\text{-crown-}6)]$.

An analogous effect was observed also for the $[Zn_3(HPO_3)_2(tib)_2]X_2$ [X = Cl, Br, I; tib = 1,3,5-tris(1-imidazolyl)-benzene] complex reported in Figure 38, which is characterized by a cationic host structure and an anionic X^- guest. In this case the complex exhibits an almost pure room temperature phosphorescence due to the restricted molecular vibrations/rotations of the tib ligand and the heavy atom effect of the guest X^-. In fact, passing from chlorine to bromine and iodine the fluorescent band at 370 nm almost disappears, leaving only the phosphorescence centred around 470 nm. Computational calculations confirmed that the strong halide-π interactions enable the intersystem crossing and at the same time also the charge transfer from the *n* orbitals of the counterion to the π^* orbitals of the tib ligand.[94]

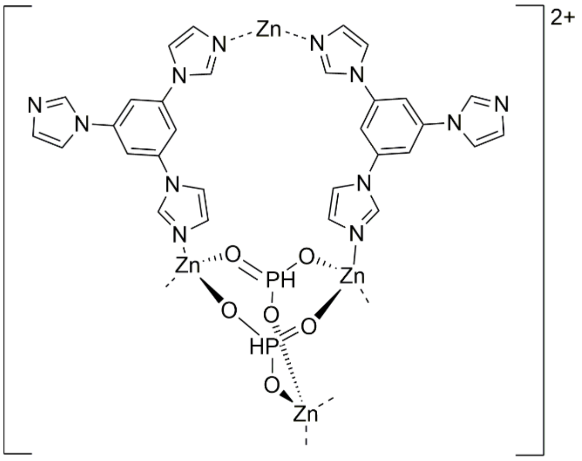

Figure 38. $[Zn_3(HPO_3)_2(tib)_2]^{2+}$.

Besides being used as emitters, zinc(II) complexes can also be used as host for OLEDs. The previously mentioned luminescent bis(2-(2-hydroxyphenyl)benzothiazolato)zinc(II) (see Figure 33d) was used as host for the red emitting 5,6,11,12-tetraphenylnaphthacene (rubrene) in order to prepare a bright white OLED. This complex was chosen thanks to the superimposition between the emission of the host and the absorption of the dopant, inducing a Förster energy transfer from the host to the guest.[95] Moreover, the complexes sketched in Figure 39a were studied as hosts for the red phosphorescent dopant [Ir(piq)$_3$] (piq = 2-phenylisoquinolinate). These species were chosen because their relatively high energy excited states match the energy of the iridium(III) dopant.[96]

Finally, the last possible application of zinc(II) complexes in OLED technology is related to their use in the electron transport layers. For instance, the use of [Zn(phen)q]$^+$ (where phen = 1,10-phenantroline and q = 8-hydroxyquinolinate, Figure 39b) implicated a decrease in the driving voltage of OLEDs.[97]

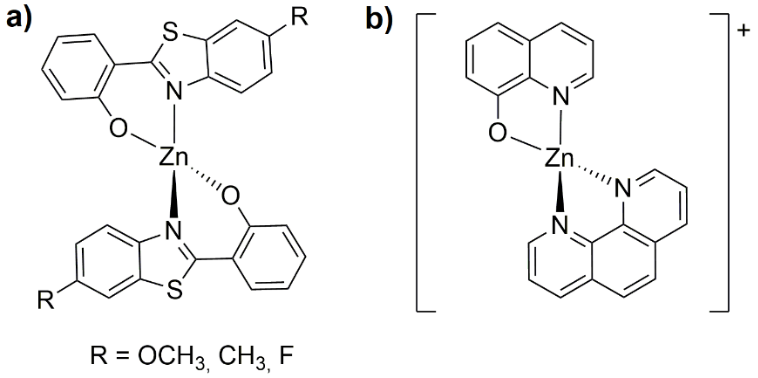

Figure 39. Derivatives of bis(2-(2-hydroxyphenyl)benzothiazolato)zinc(II) and [Zn(phen)q]$^+$.

1.5 Aim of the thesis

The aim of the thesis is the synthesis and characterization of new luminescent manganese(II), copper(I) and zinc(II) complexes for solid-state lighting applications (e.g. OLEDs), following the results previously reported by the research group.[40,98]

The investigation on manganese(II) derivatives will be focused on the coordination of [O=P]-donor ligands characterized by structural rigidity and light-harvesting substituents in order to overcome the limited direct excitation of the metal centre. Since the investigation of [O=P]-donors with zinc(II) is limited to triphenylphosphine oxide (TPPO) and non-linear optical properties were observed for $[ZnCl_2(TPPO)_2]$,[99] the same ligands used for manganese(II) will be considered for the synthesis of luminescent zinc(II) complexes.

On the other hand, the research on copper(I) complexes will be centred on the isolation of mono- and polynuclear species with N-donor ligands. In particular, the focus will be on heterocycles like benzotriazole and benzothiadiazole since their photophysical properties are not extensively explored compared to other aromatic azoles such as pyrazole, imidazole and benzimidazole. In order to enhance the luminescent properties, the investigation will be mostly focused on heteroleptic complexes also having a phosphine in the coordination sphere.

The new derivatives will be characterized from a structural point of view by means of heteronuclear NMR and IR spectroscopy, elemental analysis, single-crystal X-ray diffraction and conductivity measurements. In the case of manganese(II) complexes, magnetic susceptibility will also be measured. The emissive features will be investigated by means of UV-VIS absorption, emission (PL) and excitation (PLE) spectra together with lifetimes decays curves and photoluminescent quantum yields Φ. The photophysical properties of the most promising derivatives will be rationalized by means of computational calculations and electrochemical measurements.

2 Experimental part

2.1 Reagents and solvents

All the reagents employed are from Merck, Carlo Erba, Alfa Aesar, Fluorochem or TCI and they were used without further purification. Carbon monoxide was purchased from SIAD. Anhydrous $CoCl_2$ was obtained from the corresponding hexahydrated salt using an Abderhalden's drying pistol heated in presence of P_4O_{10} with refluxing toluene. The solvents employed for the reactions inside the glove-box were dried according to literature procedures.[100] The complexes $[Cu_4(\mu–N_3)_4(CNXyl)_6]$ and $[Cu(\mu–NCO)(CNXyl)_2]_2$ (CNXyl = 2,6-dimethylphenylisocyanide) were provided by the University of Alcalá (Spain), synthesized on the basis of an unpublished procedure.

Safety disclaimer: perchlorate salts of transition metal complexes, mixtures of acetic acid and hydrogen peroxide, and nitromethane solutions are potentially explosive.

2.2 Instruments

All the reactions under controlled atmosphere were conducted inside a MBraun Labstar glove box equipped with automatic pressure control and suitable for inorganic syntheses.

Elemental analyses (C, H, N, S) were carried out using an Elementar Unicube microanalyzer. The halide content was determined using the Mohr’s method.[101] Conductivity measurements were carried out at 298 K using a Radiometer Copenhagen CDM83 instrument and they were interpreted according to literature.[102] Magnetic susceptibilities for manganese(II) complexes were measured on solid samples at room temperature using a MK1 magnetic susceptibility balance (Sherwood Scientific Ltd) and corrected for diamagnetic contribution using tabulated Pascal’s constants.[103] Specific rotation $[\alpha]^{20}_D$ was measured in $5\cdot10^{-2}$ M acetone solutions using a Optech Polarimeter model PL1 LED (λ = 589.3 nm). Melting points were registered employing a FALC 360 D instrument equipped with a video recording device. DSC-TGA measurements were carried out under N_2 atmosphere with a Linseis STA PT 1000 instrument. The heating rate was set at 10°C min^{-1}. Further TGA measurements were performed with a Q5000 instrument v.3.17 Built 265 at AIMPLAS (Valencia). In this case, the heating rate was set at 20°C min^{-1} from 30°C up to 500°C. ESI-MS analyses for the catalytic tests were performed using a Finnigan LCQ-Duo ion-trap instrument, operating in positive ion mode (sheath gas N_2, source voltage 4.0 KV, capillary voltage 21 V, capillary temperature 200°C). GC-MS analyses were performed using an MSD Agilent Technologies 5977B (electron impact) coupled with Agilent Technologies 7720 gas chromatographer and a HP5-MS 19091S-433UI capillary column (30 m × 0.32 mm × 0.25 μm). The experimental conditions required 1.2 mL min^{-1} helium flow and an initial temperature of 100°C that was kept for 2 minutes. Then the heating rate was set to 20°C min^{-1} until 300°C and this temperature was kept for 15 minutes.

Infrared (IR) spectra were registered using a Perkin-Elmer SpectrumOne spectrophotometer between 4000 and 400 cm^{-1} using KBr as dispersing matrix for solid samples and KBr windows for oils. Mono- and bidimensional nuclear magnetic resonance (NMR) spectra were collected at variable temperature employing Bruker Avance 300 and Avance 400 instruments operating respectively at 300.13 MHz and 400.13 MHz of ^{1}H resonance. ^{1}H and ^{13}C NMR spectra are referred to the partially non-deuterated fraction of the solvent, itself referred to tetramethyl silane. ^{31}P{^{1}H} NMR and ^{11}B NMR resonances are respectively referred to 85% H_3PO_4 in water and $BF_3 \cdot Et_2O$ complex in $CDCl_3$. ^{19}F chemical shifts are referred to CCl_3F.

Cyclic voltammetry measurements were performed using an eDAQ ET014-199 instrument using tetrabutylammonium hexafluorophosphate or lithium perchlorate as supporting electrolytes. Solvents were purified according to literature procedures.[100] The working electrodes were a 1 mm glassy carbon (ET074-1) or platinum disk (ET075-1), while the auxiliary electrode was a 1.6 mm diameter Pt-coated titanium rod (ET078-1). All the electrodes were provided by eDAQ. Ferrocene was introduced as internal standard and a Pt wire was used as pseudo-reference electrode. The Fc/Fc^+ couple was used as internal standard and all the measurements were carried out at room temperature under argon atmosphere.

Absorption spectra were collected in the range 235-700 nm employing Perkin-Elmer Lambda 35 and Lambda 40 spectrophotometers. Photoluminescence emission (PL) and excitation (PLE) spectra as well as lifetime decay curves were registered on solid samples at room temperature using a Horiba Jobin Yvon Fluorolog-3 spectrofluorometer. Air-tight quartz sample holders were used and filled in the glove box to avoid interactions of the air-sensible complexes with moisture. A continuous wave xenon arc lamp was used as source and the excitation wavelength was selected using a double Czerny–Turner monochromator. Suitable long pass filters were placed in front of the acquisition systems. The detector was composed by a single monochromator iHR320 and a photomultiplier tube Hamamatsu R928. Excitation and emission spectra were corrected for the instrumental functions. Time-resolved analyses were performed in Multi Channel Scaling modality (MCS) by using pulsed UV LED sources (SpectraLED) centred at 265, 290, 377 and 454 nm. Lifetimes in the nanoseconds range were collected using a Horiba NanoLED centred at 373 nm in Time Correlated Single-Photon Counting (TCSPC) mode. Luminescence quantum yields Φ were collected using an integrating sphere coupled to an OceanOptics detector HR4000CG operating in the UV-NIR range. The same spectrometer, coupled with an OceanOptics fibre QR400-7-SR-BX and an OceanOptics DH-2000-BAL deuterium-halogen lamp was used to record reflectance spectra at room temperature. Photochemical reactions were performed using a UV LED (ILH-XT01-S365-SC11-WIR200) centred at 375 nm purchased by RS components.

2.3 DFT calculations

The ground-state geometry optimizations were carried out using the range-separated hybrid ωB97X, the *meta*-GGA hybrid TPSSh and the global-hybrid *meta*-NGA MN15 DFT functionals in combination with Alhrichs and Weigend's def2-SVP basis set, with ECP including 28 electrons for iodine.[104] In some cases the C-PCM implicit solvation model was added to calculations, considering dichloromethane as continuous medium.[105] The relative energies of the excited states were obtained by carrying out TD-DFT (time-dependent DFT) calculations at the same theoretical level using the ground state geometries.[106] For copper(I) complexes, the same approach was extended to the geometry optimization of the first singlet and triplet excited states. The software used were Gaussian 16 [107] and ORCA 4.2.0.[108] When needed, the output files were analysed with Multiwfn, version 3.5.[109] The same software was also used for the determination of bond critical points by means of AIM analyses.[110] Cineca (Bologna) is sincerely acknowledged for the availability of high-performance computer resources (class C projects COLUMN, COLUMN21 and COLUMN22).

2.4 Crystal structure determination

Crystallographic data were collected at CACTI (University of Vigo) at 100 K (CryoStream 800) using a Bruker D8 Venture Photon 100 CMOS detector and Mo-Kα radiation (λ = 0.71073 Å) generated by a Incoatec Microfocus Source IμS. The software APEX3 was used for collecting frames of data, indexing reflections, and the determination of lattice parameters, SAINT for integration of intensity of reflections, and SADABS for scaling and empirical absorption correction.[111] The crystallographic treatment was performed with the Oscail program,[112] solved using the SHELXT program.[113] The structure was subsequently refined by a full-matrix least-squares based on F^2 using the SHELXL program.[114] Non-hydrogen atoms were refined with anisotropic displacement parameters. Hydrogen atoms were included in idealized positions and refined with isotropic displacement parameters. The supplementary crystallographic data for each structure can be obtained free of charge from the Cambridge Crystallographic Data Centre via www.ccdc.cam.ac.uk/data_request/cif. PLATON (version 60720)[115] was used to obtain some geometrical parameters of the cif file, and specially the hydrogen bonds and other weak intermolecular interactions.[116] The following CCDC contain the supplementary crystallographic data: 956316-1956317 for [MnX$_2${O=P(MeNCH$_2$CH$_2$NMe)Ph}$_2$] (X = Cl, Br); 1999745-1999746 and 1973290 for [MnX$_2${O=P(NMe$_2$)$_2$Ind}$_2$] (X = Cl, Br, I); 2042163-2042165 for [MnX$_2${O=P(NMe$_2$)$_2$(2-Naph)}$_2$] (X = Cl, Br, I); 2094660-2094662 for [MnX$_2${O=P(NMe$_2$)$_2$Cbz}$_2$] (X = Cl, Br, I); 2077265 and 2045025 for [MnX$_2${O=P(OPh)$_2$(NMe$_2$)}$_2$] (X = Br, I); 2077266 and 2045026 for [MnX$_2${μ-O=P(NMe$_2$)$_2$(res)(NMe$_2$)$_2$P=O}$_2$] (X = Br, I); 2106874 for [Cu(κ^2–BH$_4$)(DPEphos)]; 1963590 for CHPh(btz)$_2$; 1985082 for CH(btz)$_3$; 1984517 for [Cu{CHPh(ind)$_2$}$_2$]$^+$; 2111460 and 2111461 for trz^{OMe}-btz and trz^{OPh}-btz; 2100419 and 2100421 for [CuL(PPh$_3$)$_2$][BF$_4$] (L = py-btz and pym-btz); 2100420 and 2100422 for [Cu(py-btz)(DPEphos)][BF$_4$] and [Cu(pym-btz)(P^{i}Pr$_3$)$_2$][BF$_4$]; 2100423 for [Cu(pym-btz)(dppe)]$_2$[BF$_4$]$_2$; 2111462 for [Cu(trz^{OMe}-btz)(P^{i}Pr$_3$)$_2$][BF$_4$]; 2111463-2111464 for [Cu(trz^{OR}-btz)(DPEphos)][BF$_4$] (R = Et, Ph); 2094664-2094666 for [ZnX$_2${O=P(NMe$_2$)$_2$Ind}$_2$] (X = Cl, Br, I); 2177563 for [ZnBr$_2$(DOPO)$_2$]; 2073393 for [Cu(CNXyl)$_3$][BF$_4$]. Figures were made with ORTEP, POV-Ray or Mercury.[117] Crystal data and structure refinement for all the ligands and complexes are collected in Appendix A. Selected bond lengths and angles are set out in Appendix B.

2.5 Synthesis of ligands

2.5.1 [O=P]-donor ligands

2.5.1.1 Synthesis of triphenylphosphine oxide, TPPO

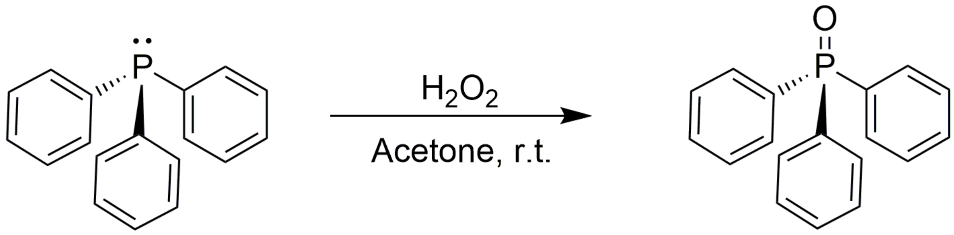

Scheme 2. Synthesis of TPPO.

2.000 g of triphenylphosphine (7.6 mmol) were dissolved in 40 mL of acetone, then 750 μL of H_2O_2 1 M were slowly added under stirring. After 20 minutes 15 mL of distilled water were added, and the acetone was removed under reduced pressure. The white solid that separated was filtered, washed with 2x15 mL of distilled water, 5 mL of ethanol and dried *in vacuo*. Quantitative yield.

2.5.1.2 Synthesis of 1,3-dimethyl-2-phenyl-1,3-diazaphospholidine-2-oxide, O=P(MeNCH$_2$CH$_2$NMe)Ph

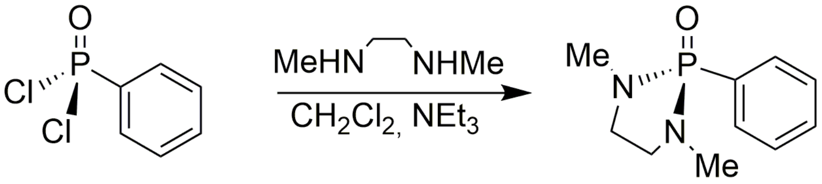

Scheme 3. Synthesis of O=P(MeNCH$_2$CH$_2$NMe)Ph.

The synthesis was performed in glove box under N_2 inert atmosphere, following a reported procedure.[118] A solution of 1.5 mL of *N*,*N'*-dimethylethylenediamine (14.1 mmol) in 10 ml of dichloromethane was slowly added to a flask containing 2 mL of phenylphosphonic dichloride (14.1 mmol) and 3.9 mL of triethylamine (28.2 mmol) dissolved in 20 mL of the same solvent. After stirring overnight, the work-up of the reaction was conducted outside the glovebox. Firstly, the reaction was quenched with water to eliminate the by-product triethylammonium chloride, and the product was extracted with dichloromethane. The organic solution was than dried over anhydrous Na_2SO_4 and filtered. The solvent was eliminated under reduced pressure and the same procedure was then repeated using ethanol. The evaporation of the solvent gave an oily product which was finally dissolved in a small amount of dichloromethane. The slow evaporation of the solvent afforded pale-yellow crystals. Yield > 70%.

Characterization of O=P(MeNCH$_2$CH$_2$NMe)Ph. ^{1}H NMR (CDCl$_3$, 298 K) δ 7.55 (m, 2H, Ph-*m*-H), 7.30 (m, 1H, Ph-*p*-H), 7.27 (m, 2H, Ph-*o*-H), 3.22 (m, 2H, CH$_2$), 3.07 (m, 2H, CH$_2$), 2.35 (d, 6H, $^3J_{PH}$ = 10.0 Hz, N-Me). ^{31}P{^{1}H} NMR (CDCl$_3$, 298 K) δ 29.29 (FWHM = 2 Hz). ^{13}C NMR (acetone-d$_6$, 298 K) δ 132.36 (d, $^3J_{CP}$ = 9.8 Hz, Ph-*m*-C), 131.37 (d, $^4J_{CP}$ = 2.9 Hz, Ph-*p*-C), 130.10 (d, $^1J_{CP}$ = 156.3 Hz, Ph-C$_{ipso}$), 128.27 (d, $^2J_{CP}$ = 13.6 Hz, Ph-*o*-C), 31.45 (d, $^2J_{CP}$ = 5.6 Hz, -CH$_2$CH$_2$-), 48.29 (d, $^2J_{CP}$ = 8.8 Hz, N-Me). IR (KBr, cm^{-1}): 3100-3000 m (aromatic $\nu_{C\text{-}H}$), 2990-2800 m ($\nu_{C\text{-}H}$), 1700-1450 w (aromatic $\nu_{C\text{-}C}$), 1186 s ($\nu_{P=O}$), 1100-1050 m ($\nu_{C\text{-}N}$), 998 s ($\nu_{P\text{-}N}$). UV-VIS (CH$_2$Cl$_2$, r.t., nm): < 350, 266 (max), 273 (sh).

2.5.1.3 Synthesis of *N,N,N',N'*-tetramethyl-*P*-azolylphosphonic diamide [azolyl = indol-1-yl, L = O=P(NMe$_2$)$_2$Ind; carbazol-9-yl, L = O=P(NMe$_2$)$_2$Cbz]

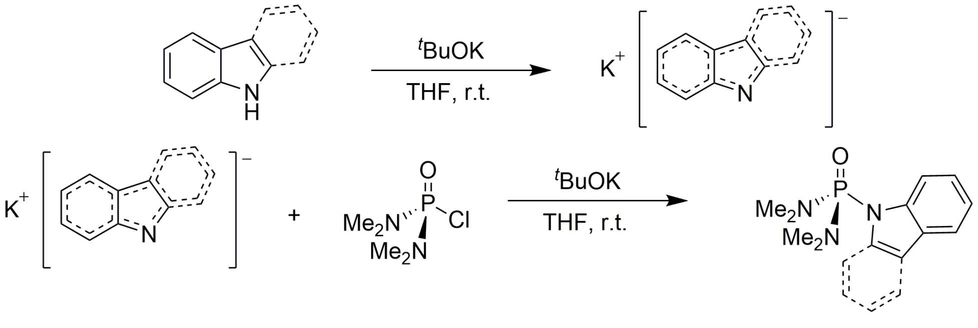

Scheme 4. Synthesis of O=P(NMe$_2$)$_2$Ind and O=P(NMe$_2$)$_2$Cbz.

The ligands were prepared inside the glove box following a reported procedure.[119] 10.0 mmol of the proper azole were dissolved in 20 mL of dry THF. A stochiometric amount of potassium *tert*-butoxide (1.122 g, 10.0 mmol) was then slowly added to the solution under stirring. The suspension was gradually added to the another flask containing 1.5 mL of *N*,*N*,*N'*,*N'*-tetramethylphosphorodiamidic chloride (1.706 g, 10.0 mmol) in dry THF. After stirring overnight at room temperature, the solvent was evaporated under reduced pressure and the so-obtained product was dissolved in 20 mL of dichloromethane. The solution was cleared by centrifugation in order to eliminate the KCl formed as by-product during the reaction. The dichloromethane was removed under reduced pressure and the pale-yellow solid, precipitated with hexane, was then recovered by filtration and dried *in vacuo*. Yield > 60% in both of the cases. Characterization data are in agreement with those reported by Van de Ros and Katritzsky.

2.5.1.4 Synthesis of (Indol-1-yl)diphenylphosphine oxide, O=PPh2Ind (Ind = indole)

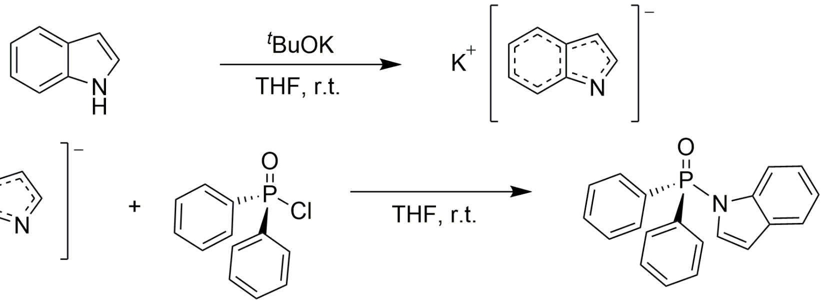

Scheme 5. Synthesis of O=PPh2Ind.

1.172 g of indole (10.0 mmol) were dissolved in 20 mL of dry THF. A stochiometric amount of potassium *tert*-butoxide (1.122 g, 10.0 mmol) was then slowly added to the solution under stirring. The suspension was stirred for 30 minutes and then gradually added to the another flask containing 1.9 mL of diphenylphosphonic chloride (2.366 g, 10.0 mmol) in dry THF. After stirring overnight, the solvent was evaporated. Dichloromethane was added and the by-products were eliminated by centrifugation. The solvent was evaporated to afford an oil that was precipitated by adding diethyl ether. Yield > 70%. Characterization data are in agreement with those reported for the same compound obtained with the different synthetic methods.[120]

2.5.1.5 Synthesis of *N,N,N',N'*-tetramethyl-P-naphtalen-2-yl phosphonic diamide, O=P(NMe2)2(2-Naph)

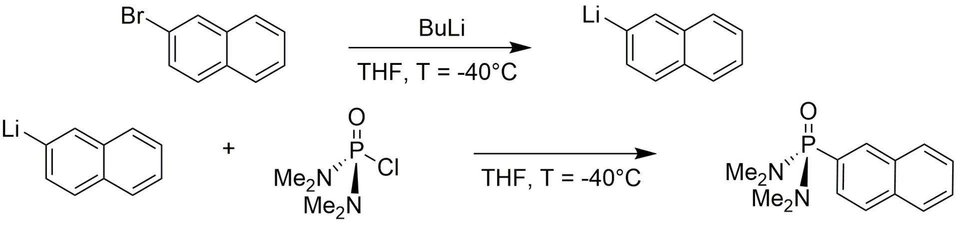

Scheme 6. Synthesis of O=P(NMe2)2(2-Naph).

The synthesis was performed following a reported procedure in a glove box under nitrogen atmosphere.[121] In a double-wall reactor, 2.795 g (13.5 mmol) of 2-bromonaphthalene were dissolved in 30 mL of THF. Cold gaseous N_2 was continuously fluxed in the outer part of the reactor. Once the system reached −40°C, 8.5 mL of 1.6 M butyllithium solution (13.5 mmol) in hexane were slowly added to the mixture. The so-formed 2-naphthenyllithium suspension was then slowly added into a second double-wall reactor, containing a stochiometric amount (2 mL) of *N*,*N*,*N′*,*N′*-tetramethylphosphorodiamidic chloride in 20 mL of THF cooled at −40°C. After the mixture warmed up to room temperature, cold water was added outside the glove box to quench the reaction. Subsequently most of the THF was evaporated under reduced pressure and the product was extracted with diethyl ether (3x10 mL). The organic fraction was dried over anhydrous Na_2SO_4, filtered and washed with cyclohexane to afford a pale-yellow oil. Yield > 80%.

2.5.1.6 Synthesis of diphenyl *N*-dimethylamidophosphate, $O=P(OPh)_2(NMe_2)$

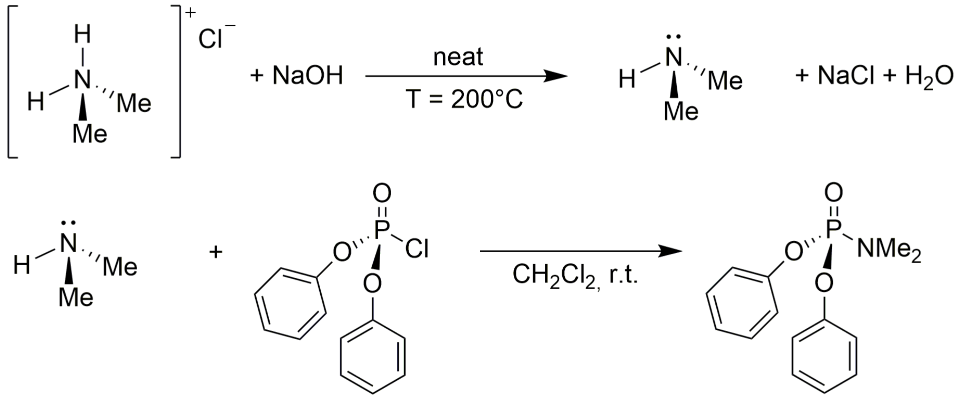

Scheme 7. Synthesis of $O=P(OPh)_2(NMe_2)$.

The compound here reported was prepared following a reported procedure.[122] The synthesis was conducted with a sodium hydroxide trap and under N_2 atmosphere. 10.000 g of dimethylammonium chloride (122.6 mmol) were stirred with a stochiometric amount of NaOH and the mixture was heated to 200°C. The stream of gaseous $NHMe_2$ was allowed to enter in a second flask containing a solution of diphenyl phosphoryl chloride (5.373 g; 20.0 mmol) in 30 mL of dichloromethane. Once the evolution of dimethyl amine from the first flask had stopped, the solution was stirred at room temperature for 5 hours and the solvent was evaporated under reduced pressure. Diethyl ether was added and the by-products were removed by filtration. The final product was obtained after evaporation of the solvent as colourless liquid. Yield: 95%.

2.5.1.7 Synthesis of 1,3-(*N,N,N',N'*-tetramethyldiamidophosphoryloxy benzene), $O{=}P(NMe_2)_2(res)(NMe_2)_2P{=}O$

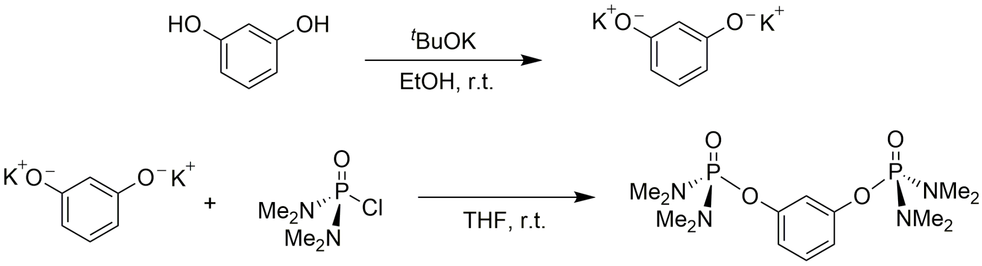

Scheme 8. Synthesis of $O{=}P(NMe_2)_2(res)(NMe_2)_2P{=}O$.

A solution of 0.330 g (3.0 mmol) of 1,3-dihydroxybenzene (resorcinol) in 50 mL of EtOH was slowly added to a flask containing two equivalents of potassium *tert*-butoxide (0.673 g; 6.0 mmol) in 20 mL of EtOH under stirring. After 4 hours the solvent was evaporated under reduced pressure. In order to completely eliminate all the ethanol, few mL of THF were added and the solvent was then evaporated again. The oil thus obtained was then dissolved in 50 mL of THF and 1.023 g of *N*,*N*,*N'*,*N'*-tetramethylphosphorodiamidic chloride (6.0 mmol) was added to the solution under stirring. After 12 hours the cloudy solution was purified by centrifugation. The solvent was evaporated under reduced pressure and the resulting light brown oil was purified with toluene and hexane. Yield > 70%.

Characterization of $O{=}P(NMe_2)_2(res)(NMe_2)_2P{=}O$*.* ^{1}H NMR ($CDCl_3$, 298 K): δ 7.21 (t, 1H, $^3J_{HH}$ = 8.1 Hz, Ar-H_5), 7.11 (s, 1H, Ar-H_2), 6.93 (d, 2H, $^3J_{HH}$ = 8.1 Hz, Ar-H_4/H_6), 2.74 (d, 24H, $^3J_{PH}$ = 10.0 Hz, N-Me). ^{31}P{^{1}H} NMR ($CDCl_3$, 298 K) δ 16.20 (FWHM = 4 Hz). ^{13}C NMR ($CDCl_3$, 298 K): δ 152.02 (d, $^1J_{CP}$ = 6.2 Hz, Ar-C_1/C_3), 129.95 (Ar-C_5), 115.91 (d, $^2J_{CP}$ = 5.2 Hz, Ar-C_4/C_6), 112.53 (t, $^2J_{CP}$ = 5.0 Hz, Ar-C_2), 36.63 (d, $^2J_{CP}$ = 4.2 Hz, N-Me). IR (cm^{-1}): 3070-3000 m/w (aromatic $\nu_{C\text{-}H}$), 2930-2820 m ($\nu_{C\text{-}H}$), 1590-1490 m (aromatic $\nu_{C\text{-}C}$ and $\nu_{C\text{-}N}$), 1320 m ($\nu_{C\text{-}O}$), 1270-1160 s ($\nu_{P=O}$ and $\nu_{C\text{-}O}$), 1133 s ($\nu_{C\text{-}N}$), 1010 m ($\nu_{P\text{-}O}$), 925 s ($\nu_{P\text{-}N}$). UV-VIS (CH_2Cl_2, r.t., nm): < 300, 266 (sh), 272 (max).

2.5.1.8 Synthesis of dibenzo[d,f][1,3,2]dioxaphosphepine 6-oxide, BPPO

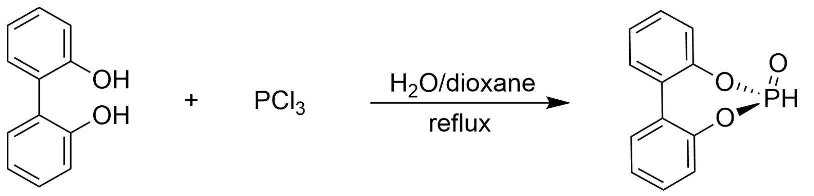

Scheme 9. Synthesis of BPPO.

The ligand was prepared following a reported procedure.[123] 15.0 g of 2,2'-biphenol (80.6 mmol) and 1.5 mL water (80.6 mmol) were dissolved in 50 mL of 1,4-dioxane and heated to reflux. A continuous flow of nitrogen was passed through the solution. A dropping funnel was charged with 7.0 mL of phosphorus trichloride (80.6 mmol), that was slowly added to the boiling reaction mixture within 3 hours. The generated HCl gas was absorbed in a gas bubbler containing water. After the complete addition of PCl_3, the mixture was heated to reflux for an additional hour. The solvent was removed under reduced pressure and a viscous oil was obtained, that solidified after few hours. The solid product was washed three times with diethyl ether and dried *in vacuo*. Yield > 80%. Characterization data are in agreement with those reported by Lenz *et al*.

2.5.1.9 Synthesis of 6-phenyldibenzo[*d,f*][1,3,2]dioxaphosphepine 6-oxide, BPPP, and (4R/S)-4-phenyldinaphtho[2,1-*d*:1',2'-*f*][1,3,2]dioxaphosphepine 4-oxide, O=PPh(R/S-BINOL) (R/S-BINOL = R/S-1,1'-bi-2-naphthol)

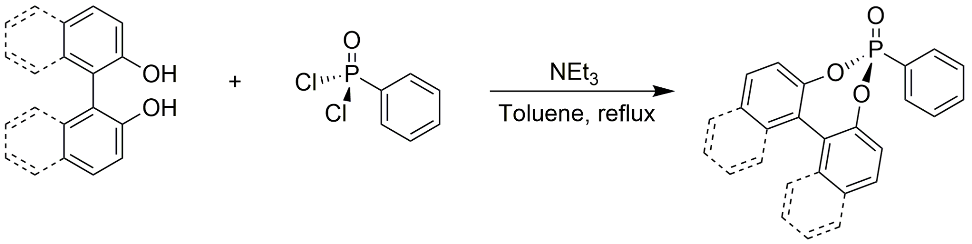

Scheme 10. Synthesis of aryl-substituted dioxaphosphepine oxides.

The ligand was prepared inside the glove box modifying a reported procedure.[124] To a solution containing 5.0 mmol of aryl diol and 0.7 mL of dichlorophenylphosphine oxide (0.975 g, 5.0 mmol) in dry toluene, 2.8 mL of triethylamine (2.024 g, 20.0 mmol) were slowly added. The mixture was then refluxed for 8 hours and stirred overnight. Subsequently the triethylammonium chloride was separated by centrifugation and the solution was filtered on cotton. The solvent was evaporated under reduced pressure to afford an oil that was precipitated with diethyl ether for

O=PPh(R/S-BINOL) and with hexane for BPPP. The white solid was filtered, washed with fresh solvent and dried *in vacuo*. Yield > 80%. Characterization data for BPPP are in agreement with the one reported for the same compound obtained with the different synthetic methods.[125]

Characterization of O=PPh(R/S-BINOL). ^{1}H NMR (CDCl$_3$, 298 K): δ 8.10 (d, 1H, $^{3}J_{HH}$ = 8.8 Hz, BINOL), 8.01 (d, 1H, $^{3}J_{HH}$ = 8.4 Hz, BINOL), 7.96 (d, 1H, $^{3}J_{HH}$ = 8.4 Hz, BINOL), 7.87 (d, 1H, $^{3}J_{HH}$ = 8.8 Hz, BINOL), 7.69 (d, 1H, $^{3}J_{HH}$ = 8.8 Hz, BINOL), 7.68-7.57 (m, 3H, BINOL+Ph), 7.56-7.50 (m, 2H, BINOL+Ph), 7.49 (d, 1H, $^{3}J_{HH}$ = 9.1 Hz, BINOL), 7.44-7.30 (m, 5H, BINOL+Ph), 7.04 (dd, 1H, $^{3}J_{HH}$ = 8.8 Hz, $^{4}J_{HH}$ = 0.7 Hz, BINOL). ^{31}P{^{1}H} NMR (CDCl$_3$, 298 K) δ 27.12 (FWHM = 2 Hz). ^{13}C NMR (CDCl$_3$, 298 K): δ 147.60 (d, J_{CP} = 10.2 Hz, C$_{ipso}$), 145.83 (d, J_{CP} = 9.6 Hz, C$_{ipso}$), 133.56 (d, J_{CP} = 3.0 Hz, CH), 132.52 (s, CH), 132.49 (d, J_{CP} = 1.4 Hz, C$_{ipso}$), 132.45 (d, J_{CP} = 1.6 Hz, C$_{ipso}$), 132.42 (s, CH), 131.94 (d, J_{CP} = 1.1 Hz, CH), 131.56 (d, J_{CP} = 1.1 Hz, CH), 131.37 (d, J_{CP} = 1.1 Hz, CH), 130.72 (s, CH), 128.64 (d, J_{CP} = 9.6 Hz, C$_{ipso}$), 128.53 (d, J_{CP} = 81.3 Hz, CH), 128.45 (d, J_{CP} = 15.6 Hz, CH), 127.32 (s, CH), 127.01 (s, CH), 126.73 (s, CH), 125.76 (s, CH), 123.92 (s, C$_{ipso}$), 121.89 (d, J_{CP} = 2.6 Hz), 121.75 (d, J_{CP} = 2.0 Hz), 121.28 (d, J_{CP} = 2.2 Hz), 120.89 (d, J_{CP} = 3.3 Hz). IR (cm^{-1}): 3110-3020 m/w (aromatic ν_{C-H}), 1620-1510 m (aromatic ν_{C-C} and ν_{C-N}), 1325 m (ν_{C-O}), 1230-1180 s ($\nu_{P=O}$ and ν_{C-O}), 1070 m (ν_{P-O}). $[\alpha]^{20}_{D}$: 320 (R); -320 (S). UV-VIS (CH$_2$Cl$_2$, r.t., nm): < 340, 238 (max), 264 (sh), 273 (sh), 305, 315, 322. PL (solid, r.t., $\lambda_{excitation}$ = 350 nm, nm): 397. PLE (solid, r.t., $\lambda_{emission}$ = 390 nm, nm): < 350.

2.5.1.10 Synthesis of methyl 2,3-bis(6-oxidodibenzo[*c*,*e*][1,2]oxaphosphophinin-6-yl)propanoate (MeDOPOPr) and diethyl 2,3-bis(6-oxidodibenzo[*c*,*e*][1,2]oxaphosphophinin-6-yl)succinate (EtDOPOSuc)

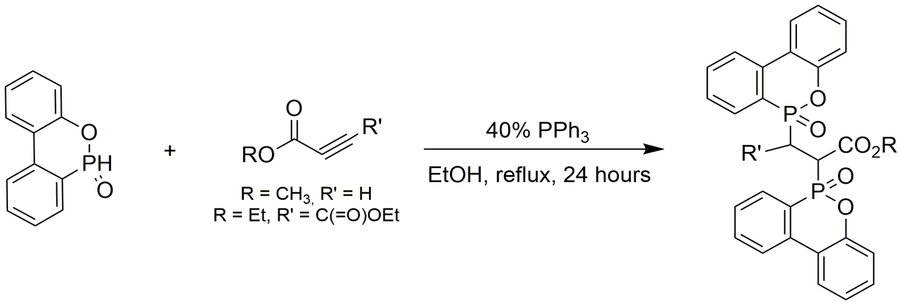

Scheme 11. Synthesis of MeDOPOPr and EtDOPOSuc.

The ligand was prepared modifying a reported procedure.[126] 1.000 g of 9,10-dihydro-9-oxa-10-phosphaphenanthrene-10-oxide (DOPO, 4.6 mmol) and 0.243 g of triphenylphosphine (0.9 mmol) were dissolved in 10 mL of dry ethanol. 2.3 mmol of methyl propiolate (0.194 g, 0.2 mL) or diethyl acetylenedicarboxylate (0.396 g, 0.4 mL) were dissolved in 10 mL of dry ethanol and added to the previous solution under stirring. The mixture was heated at reflux for 24 hours, then the solvent was evaporated under reduced pressure. In the case of MeDOPOPr, the so-obtained oil was treated with 2x20 mL of pentane to remove the unreacted PPh_3 and subsequently it was extracted with hot cyclohexane (3x20 mL) to remove the unreacted DOPO. The product was isolated as white solid after the addition of diethyl ether, washed and dried *in vacuo*. In the case of EtDOPOSuc, the product precipitated from the ethanol solution. Yield: 70% for MeDOPOPr and 85% for EtDOPOSuc.

Characterization of methyl 2,3-bis(6-oxidodibenzo[c,e][1,2]oxaphosphophinin-6-yl)propanoate (MeDOPOPr). ^{1}H NMR ($CDCl_3$, 298 K): δ 8.32-7.09 (m, 16H, DOPO-H), 3.85-3.52 (m, 1H, CH), 3.38-3.13 (m, 3H, O-CH_3), 3.06-2.55 (m, 2H, CH_2). $^{31}P\{^1H\}$ NMR ($CDCl_3$, 298 K): δ 34.74 (d, $^3J_{PP}$ = 56.0 Hz), 34.36 (d, $^3J_{PP}$ = 55.7 Hz), 33.94 (d, $^3J_{PP}$ = 59.3 Hz), 33.43 (d, $^3J_{PP}$ = 60.0 Hz), 30.14 (d, $^3J_{PP}$ = 55.7 Hz), 28.87 (d, $^3J_{PP}$ = 57.1 Hz), 28.67 (d, $^3J_{PP}$ = 57.1 Hz). IR (KBr, cm^{-1}): 3090-2990 m/w (aromatic ν_{C-H}), 2970-2830 m/w (ν_{C-H}), 1738 s ($\nu_{C=O}$), 1610-1560 m (aromatic ν_{C-C} and ν_{C-N}), 1260-1190 s ($\nu_{P=O}$). UV-VIS (CH_2Cl_2, r.t., nm): < 330, 241, 261, 269 (max), 295. PL (solid, r.t., $\lambda_{excitation}$ = 270 nm, nm): 344 (FWHM = 3500 cm^{-1}). PLE (solid, r.t., $\lambda_{emission}$ = 420 nm, nm): < 380. τ (solid, r.t., $\lambda_{excitation}$ = 373 nm, $\lambda_{emission}$ = 410 nm, ns): 6.

Characterization of diethyl 2,3-bis(6-oxidodibenzo[c,e][1,2]oxaphosphophinin-6-yl)succinate (EtDOPOSuc). ^{1}H NMR ($CDCl_3$, 298 K): δ 8.42-7.07 (m, 16H, DOPO-H), 4.63-3.29 (m, 6H, O-CH_2 and CH), 0.95-0.82 (m, 6H, -CH_3). $^{31}P\{^1H\}$ NMR ($CDCl_3$, 298 K): δ 30.22 (d, $^3J_{PP}$ = 49.6 Hz), 29.62, 26.74 (d, $^3J_{PP}$ = 49.6 Hz), 26.30. IR (KBr, cm^{-1}): 3070-2980 m/w (aromatic ν_{C-H}), 2960-2870 m/w (ν_{C-H}), 1723 s ($\nu_{C=O}$), 1610-1530 m (aromatic ν_{C-C} and ν_{C-N}), 1295-1204 s ($\nu_{P=O}$). UV-VIS (CH_2Cl_2, r.t., nm): < 330, 241, 261, 269 (max), 295. PL (solid, r.t., $\lambda_{excitation}$ = 350 nm, nm): 399. PLE (solid, r.t., $\lambda_{emission}$ = 410 nm, nm): < 370. τ (solid, r.t., $\lambda_{excitation}$ = 373 nm, $\lambda_{emission}$ = 410 nm, ns): 5.

2.5.2 [N-O]-donor ligands

2.5.2.1 Synthesis of 2,2'-bipyidine-*N,N'*-dioxide, bpyO2

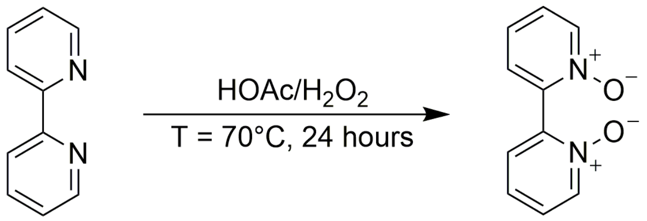

Scheme 12. Synthesis of bpyO2.

The ligand was prepared following a reported procedure.[127] A solution containing 5.000 g of 2,2'-bipiridine (bpy, 32.0 mmol) in 40 mL of glacial acetic acid and 6 mL of hydrogen peroxide 30% v/v was heated at 70°C for 3 hours. Then other 4.5 mL of H_2O_2 were added to the mixture and the reaction was heated for 20 hours. The product was precipitated with acetone and then recrystallized from hot water by adding a large excess of acetone. The white solid was filtered, washed with acetone (2x15 mL) and dried *in vacuo*. Yield: 90%. Characterization data are in agreement with those reported in literature for the same compound obtained with different synthetic approaches.[128]

2.5.3 Mixed [N-O,P=O]-donor ligands

2.5.3.1 Synthesis of 2-(diphenylphosphino)pyridine-N,P-dioxide, NPO2

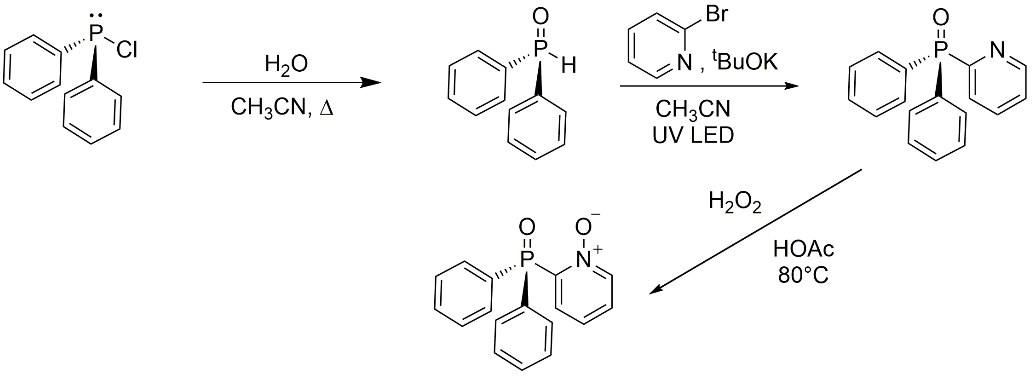

Scheme 13. Synthesis of NPO2.

<u>*Synthesis of diphenylphosphine oxide:*</u> The compound was prepared following a reported method.[129] 2.3 mL of chlorodiphenylphosphine (5.516 g, 25.0 mmol) were dissolved in 20 mL of acetonitrile and the solution was put under nitrogen atmosphere. 2.3 mL of deaerated water (2.300 g, 250.0 mmol) were added through a

syringe and the mixture was refluxed for 6 hours. The solvent was then evaporated under reduced pressure and the so-obtained oil was extracted with dichloromethane (3x20 mL) and distilled water. The solution was dried on Na_2SO_4, that was filtered to afford a clear oil after the evaporation of the solvent. Yield: 50%.

Synthesis of diphenyl(pyridin-2-yl)phosphine oxide: The ligand was prepared following a reported procedure.[130] 1.896 g of 2-bromopyridine (1.2 mL, 12.0 mmol) and 2.022 g of diphenylphosphine oxide (10.0 mmol) were dissolved in dry acetonitrile and put under nitrogen atmosphere. Then 1.683 g of potassium *tert*-butoxide (15.0 mmol) were added and the mixture was stirred at room temperature for 8 hours under the irradiation of a near-UV LED (375 nm, output power 1.2 W). The by-products and the excess of potassium *tert*-butoxide were filtered off to afford a dark orange solution. The solvent was evaporated under reduced pressure and the product was extracted from hot hexane as a yellowish solid. Yield: 75%.

Synthesis of 2-(diphenylphosphino)pyridine-N,P-dioxide, NPO_2: The ligand was prepared dissolving 2.000 g of diphenyl(pyridin-2-yl)phosphine oxide (7.2 mmol) in 18 mL of acetic acid (HOAc, 314.7 mmol). 1.8 mL of hydrogen peroxide 30% w/w in water (17.6 mmol) were slowly added to the mixture which was then heated at 80°C for 7 hours. Then 1.2 mL of further H_2O_2 (11.7 mmol) were added and the mixture was heated at the same temperature overnight. Once the solution returned at room temperature, it was quenched by slow addition of 16.683 g of Na_2CO_3 (157.4 mmol) and then it was extracted with 3x20 mL of dichloromethane. After the anhydrification with Na_2SO_4, the solvent was evaporated under reduced pressure to afford a beige solid. Yield: 50%.

Characterization of NPO_2. ^1H NMR ($CDCl_3$, 298 K): δ 8.33 (td, 1H, $^3J_{HH}$ = 7.2 Hz, $^3J_{PH}$ = 3.0 Hz, py), 8.11 (m, 1H, py), 7.94 (dt, 4H, $^3J_{HH}$ = 7.9 Hz, $^2J_{PH}$ = 1.3 Hz, *o*-Ph), 7.73 (m, 1H, py), 7.57 (td, 2H, $^3J_{HH}$ = 7.6 Hz, $^4J_{HH}$ = 1.7 Hz, *p*-Ph), 7.50-7.42 (m, 5H, *m*-Ph+py). $^{31}P\{^1H\}$ NMR ($CDCl_3$, 298 K) δ 22.94 (FWHM = 8 Hz). ^{13}C NMR ($CDCl_3$, 298 K): δ 144.52 (d, $^1J_{CP}$ = 116.1 Hz, C_{ipso}-py), 139.64 (d, $^2J_{CP}$ = 2.0 Hz, C_{ortho}-py), 133.00 (d, $^3J_{CP}$ = 9.9 Hz, C_{meta}-py), 132.50 (d, $^4J_{CP}$ = 3.0 Hz, C_{para}-Ph), 132.23 (d, $^2J_{CP}$ = 11.0 Hz, C_{ortho}-Ph), 130.52 (d, $^3J_{CP}$ = 9.9 Hz, C_{meta}-py), 128.36 (d, $^3J_{CP}$ = 13.4 Hz, C_{meta}-Ph), 125.30 (d, $^4J_{CP}$ = 8.2 Hz, C_{para}-py). C_{ipso} of the phenyl rings not detected. IR (KBr, cm^{-1}): 3090-2990 m/w (aromatic ν_{C-H}), 1620-1550 m (aromatic ν_{C-C} and ν_{C-N}), 1275 m (ν_{N-O}), 1185 s ($\nu_{P=O}$). UV-VIS (CH_2Cl_2, r.t., nm): < 350, 280 (max), 321 (sh), 332 (sh).

2.5.4 N-donor ligands

2.5.4.1 Synthesis of bis(azolyl)phenylmethane [azolyl = benzotriazolyl, L = CHPh(btz)$_2$; azolyl = indazolyl, L = CHPh(ind)$_2$]

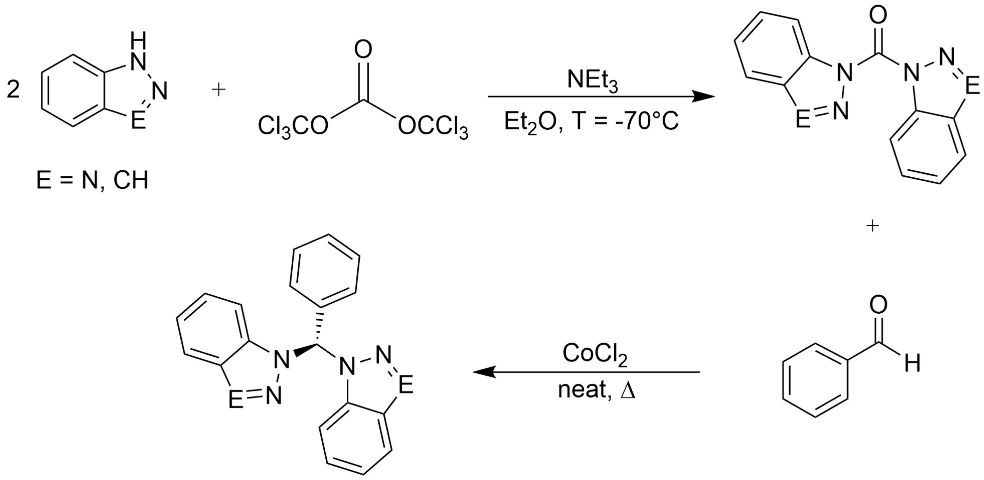

Scheme 14. Synthesis of bis(azol-1-yl)phenylmethane.

Synthesis of bis(azol-1-yl)methanone: The reactions were conducted inside the glove box for safety reasons. In a jacketed reactor cooled down with liquid nitrogen 1.246 g of triphosgene (4.2 mmol) were placed and dissolved in 50 mL of dry diethyl ether. 3.5 mL of triethylamine (2.541 g, 25.2 mmol) were added, then 25.2 mmol of the chosen azole were slowly introduced into the reactor when the temperature had reached −70°C. Particular attention had to be devoted to the temperature especially when indazole was involved in the synthesis. The solution was left under stirring and allowed to slowly reach room temperature, then the work-up was conducted outside the glove box. The white precipitate, mostly composed by the product and tetraethylammonium chloride, was filtered and dried *in vacuo*. The solid was then dissolved in dichloromethane and extracted with distilled water. The aqueous phase was washed three times with 15 mL of dichloromethane and the organic fractions were collected together and then dried with Na_2SO_4. The solution was filtered, and the solvent was concentrated *in vacuo* to give a brown oil, that was precipitated with ether to afford a white solid. Yield: 65% in both the cases.

Synthesis of bis(azolyl)phenylmethane: The ligands were obtained on the basis of a general procedure reported in the literature.[131] The reaction was conducted in a

Schlenk apparatus under nitrogen atmosphere, and it was catalysed by anhydrous $CoCl_2$. In the Schlenk apparatus 2.0 mmol of 1,1'-carbonylbis-azole, 2.0 mmol of benzaldehyde (0.20 mL) and a catalytic amount (approx. 0.004 g) of $CoCl_2$ were added. The solids were heated to 150°C until they melted, and the formation of CO_2 was observed. The solution was stirred at this temperature for 2 hours, then it was left to cool down. Once the mixture reached room temperature, the solid was dissolved in dichloromethane and the solution was extracted with distilled water. The aqueous phase was subsequently washed three times with 15 mL of dichloromethane and, after all the organic fractions were collected, the solution was dried with Na_2SO_4. The organic phase was filtered and the solvent was concentrated *in vacuo* to give a brown oil. The addition of few mL of diethyl ether afforded a white solid, that was collected by filtration. Yield: 40%. Characterization data coincide with those reported for the same compounds prepared on the basis of different procedures.[132]

2.5.4.2 Synthesis of tris(benzotriazol-1-yl)methane, CH(btz)$_3$

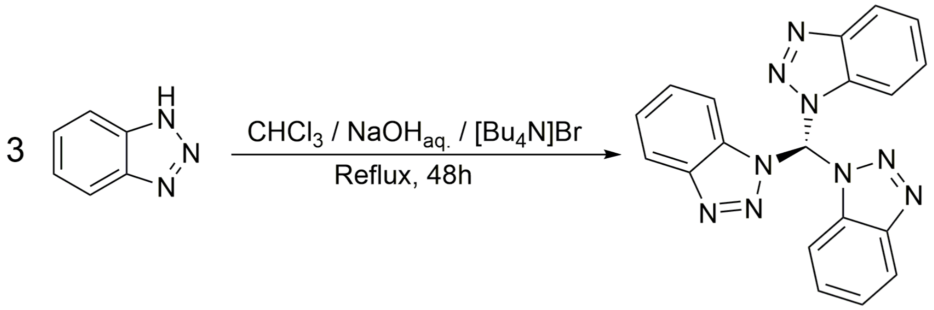

Scheme 15. Synthesis of tris(benzotriazol-1-yl)methane

The ligand was obtained following a procedure reported in literature.[133] To a heterogeneous mixture containing 5.956 g of benzotriazole (50.0 mmol) in 5 mL of $CHCl_3$, 5 mL of a concentrated solution of NaOH aq. 40% were added. 0.160 g of $[Bu_4N]Br$ (0.5 mmol) as phase transfer catalyst were added. The solution was heated under reflux for 48 hours and, once it had cooled down to room temperature, it was extracted twice with 5 mL of chloroform. The organic phase was washed five times with 5 mL of distilled water, dried with Na_2SO_4, filtrated and concentrated *in vacuo*. The oil was finally treated with methanol to afford the desired product as a white precipitate. Characterization data coincide with those reported in literature. Crystals suitable for X-ray diffraction were collected from the slow evaporation of dichloromethane solutions. Yield: 50%.

2.5.4.3 Synthesis of 1-(pyridin-2-yl)benzotriazole and 1-(pyrimidin-2-yl)benzotriazole, py-btz and pym-btz

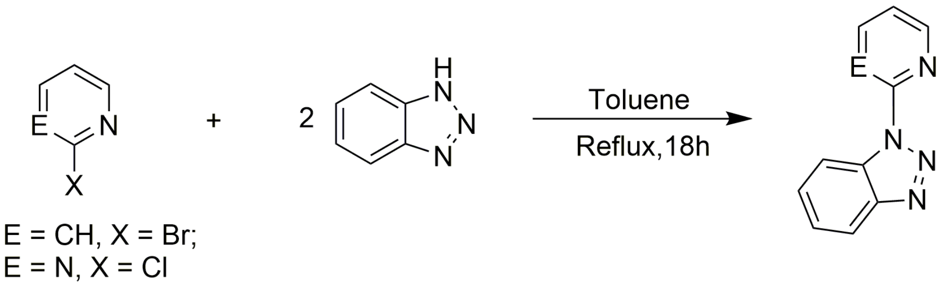

Scheme 16. Synthesis of 1-(pyridin-2-yl)benzotriazole and 1-(pyrimidin-2-yl)benzotriazole.

The ligands were prepared following a procedure reported in literature.[134] A solution containing 15.0 mmol of 2-bromopyridine or 2-chloropyrimidine and 3.574 g of benzotriazole (30.0 mmol) in 20 mL of dry toluene was refluxed for 18 hours under N_2 atmosphere. After cooling down to room temperature, the mixture was dissolved in 250 mL of ethyl acetate for py-btz and 200 mL of diethyl ether for pym-btz. 150 mL of cold KOH 10% were added and the mixture was extracted. In the case of pym-btz, a foam formed so the solvents were evaporated under reduced pressure and the so-obtained oil was treated with diethyl ether. The organic phases were collected and dried with Na_2SO_4. The solvent was evaporated under reduced pressure to isolate the product as pale solid. Characterization data are in agreement with those reported in literature. Yield > 60% in both the cases.

2.5.4.4 Synthesis of 1-(4,6-alkoxy-1,3,5-triazin-2-yl)benzotriazole, trz^{OR}-btz (R = Me, Et, Ph)

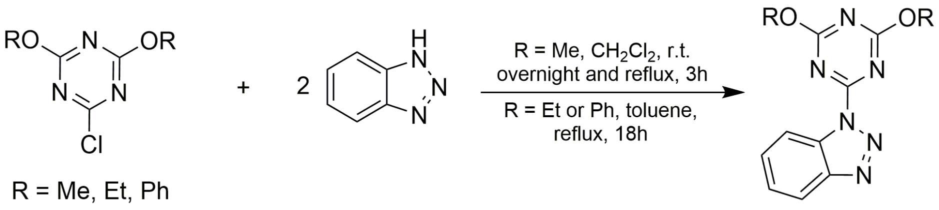

Scheme 17. Synthesis of 1-(4,6-alkoxy-1,3,5-triazin-2-yl)benzotriazole

Following a reported procedure, cyanuric chloride (2,4,6-trichloro-1,3,5-triazine, TCT) was reacted with methanol or ethanol in presence of $NaHCO_3$ to afford the corresponding 2-chloro-4,6-dialkoxy-1,3,5-triazine (CDMT and CDET).[135] 2-chloro-4,6-phenoxy-1,3,5-triazine (CDPhT) was instead prepared by reacting TCT with sodium phenate at 0°C in acetone/water solution.[136] The ligands were prepared by reacting 15.0 mmol of the chosen 2-chlorotriazine and 3.574 g of benzotriazole (30.0 mmol) in 20 mL of dry CH_2Cl_2 for CDMT or toluene for CDET and CDPhT. To prepare trz^{OMe}-btz, the reaction mixture was stirred at room temperature overnight and heated to reflux for the last 3 hours. For trz^{OEt}-btz and trz^{OPh}-btz, the reaction mixture was refluxed for 18 hours under N_2 atmosphere. After cooling down to room temperature, trz^{OMe}-btz and trz^{OPh}-btz were extracted with dichloromethane, while trz^{OEt}-btz was treated with diethyl ether. The so-obtained mixture was washed with 2x50 mL of cold NaOH 10% and 2x50 mL of water. The organic fractions were collected and dried with Na_2SO_4. The solvents were evaporated under reduced pressure to afford the products as white solids. Yield > 80 % in all the cases.

Characterization of 1-(4,6-methoxy-1,3,5-triazin-2-yl)benzotriazole, trz^{OMe}-btz. ^{1}H NMR ($CDCl_3$, 298 K) δ 8.58 (d, 1H, $^3J_{HH}$ = 8.4 Hz, btz), 8.20 (d, 1H, $^3J_{HH}$ = 8.3 Hz, btz), 7.70 (dd, 1H, $^3J_{HH}$ = 8.4 Hz, $^3J_{HH}$ = 7.1 Hz, btz), 7.54 (dd, 1H, $^3J_{HH}$ = 8.3 Hz, $^3J_{HH}$ = 7.1 Hz, btz), 4.25 (s, 6H, $-CH_3$). ^{13}C NMR ($CDCl_3$, 298 K) δ 173.42 (ipso-trz), 146.85 (ipso-trz), 140.56 (ipso-btz), 131.71 (ipso-btz), 129.91 (btz), 125.76 (btz), 120.56 (btz), 115.10 (btz), 56.04 ($-CH_3$). IR (KBr, cm^{-1}): 3120-3020 m/w (aromatic ν_{C-H}), 2960-2850 m (ν_{C-H}), 1610-1540 m (aromatic ν_{C-C} and ν_{C-N}). UV-VIS (CH_2Cl_2, r.t., nm): < 340, 241 (max), 262 (sh), 271 (sh), 304 (sh).

Characterization of 1-(4,6-ethoxy-1,3,5-triazin-2-yl)benzotriazole, trz^{OEt}-btz. ^{1}H NMR ($CDCl_3$, 298 K) δ 8.57 (d, 1H, $^3J_{HH}$ = 8.4 Hz, btz), 8.19 (d, 1H, $^3J_{HH}$ = 8.7 Hz, btz), 7.69 (t, 1H, $^3J_{HH}$ = 7.2 Hz, btz), 7.53 (t, 1H, $^3J_{HH}$ = 7.8 Hz, btz), 4.67 (q, 4H, $^3J_{HH}$ = 7.1 Hz, $-CH_2$), 1.55 (t, 6H, $^3J_{HH}$ = 7.1 Hz, $-CH_3$). ^{13}C NMR ($CDCl_3$, 298 K) δ 172.84 (ipso-trz), 164.66 (ipso-trz), 146.83 (ipso-btz), 131.70 (ipso-btz), 129.81 (btz), 125.66 (btz), 120.50 (btz), 115.08 (btz), 65.22 ($-CH_2$), 14.25 ($-CH_3$). IR (KBr, cm^{-1}): 3120-3000 m/w (aromatic ν_{C-H}), 2990-2880 m (ν_{C-H}), 1660-1600 m (aromatic ν_{C-C} and ν_{C-N}). UV-VIS (CH_2Cl_2, r.t., nm): < 340, 241 (max), 257 (sh), 270 (sh), 303 (sh).

Characterization of 1-(4,6-phenoxy-1,3,5-triazin-2-yl)benzotriazole, trz^{OPh}-btz. ^{1}H NMR ($CDCl_3$, 298 K) δ 8.13 (d, 1H, $^3J_{HH}$ = 8.0 Hz, btz), 7.69 (d, 1H, $^3J_{HH}$ = 8.1 Hz, btz), 7.51 (t, 4H, $^3J_{HH}$ = 7.9 Hz, Ph-H_{meta}), 7.45 (dd, 1H, $^3J_{HH}$ = 8.1 Hz, $^3J_{HH}$ = 7.1 Hz, btz), 7.40 (m, 1H, btz), 7.38 (m, 2H, Ph-H_{para}), 7.30 (m, 4H, Ph-H_{ortho}). ^{13}C NMR

($CDCl_3$, 298 K) δ 173.54 (ipso-trz), 164.81 (ipso-trz), 151.71 (ipso-Ph), 146.72 (ipso-btz), 131.54 (ipso-btz), 129.82 (Ph-C_{meta}), 129.80 (btz), 126.51 (Ph-C_{para}), 125.79 (btz), 121.55 (Ph-C_{ortho}), 120.50 (btz), 115.00 (btz). IR (KBr, cm^{-1}): 3100-3015 m/w (aromatic ν_{C-H}), 1600-1550 m (aromatic ν_{C-C} and ν_{C-N}). UV-VIS (CH_2Cl_2, r.t., nm): < 340, 244 (max), 267 (sh), 308 (sh).

2.6 Synthesis of copper(I) precursors

2.6.1 Synthesis of CuCl

$$2\ CuCl_2 \cdot H_2O + Na_2SO_3 \xrightarrow[H_2O,\ r.t.]{} 2\ CuCl + H_2SO_4 + 2\ NaCl$$

Scheme 18. Synthesis of CuCl.

Copper(I) chloride was prepared according to literature procedures using sodium sulphite as reducing agent.[137] At room temperature a mixture of 3.800 g of Na_2SO_3 in 25 mL of distilled water is added dropwise under stirring to a solution containing 4.995 g of $CuCl_2 \cdot 2\ H_2O$ (29.3 mmol) in 5 mL of distilled water. The mixture becomes first dark brown and then white CuCl slowly separates. The precipitate and the surnatant liquid are subsequently poured into a solution containing 500 mL of water, 0.500 g of Na_2SO_3 and 1 mL of concentrated HCl. Then the mixture is stirred and after sedimentation the surnatant liquid is decanted. The solid is washed with diluted H_2SO_4 and it must always be covered by a layer of this acid solution to prevent its oxidation. Copper(I) chloride is then washed four times with 10 mL of glacial acetic acid, three times with 15 mL of dry ethanol and finally six times with 8 mL of anhydrous ether. Due to its air instability, CuCl is stored inside the glove box. Quantitative yield.

2.6.2 Synthesis of [Cu(κ^2–BH_4)(PPh_3)$_2$]

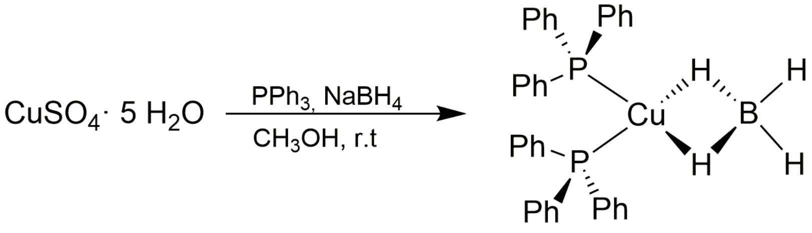

Scheme 19. Synthesis of [Cu(κ^2–BH_4)(PPh_3)$_2$].

This precursor was prepared following a procedure reported in the literature.[138] A stirred solution containing 0.500 g of copper(II) sulfate pentahydrate (2.0 mmol), 2.500 g of triphenylphosphine (9.5 mmol) and 100 mL of methanol was heated until the dissolution of the solids. After the mixture had cooled down to room temperature, sodium borohydride (0.500 g, 13.2 mmol) was added in small amounts. The formation of H_2 was observed. The white precipitated was filtered and purified by dissolution in 20 mL of dichloromethane. After the filtration of the solution, 25 mL of methanol were added and CH_2Cl_2 was concentrated *in vacuo* until the precipitation of a white solid was observed. Quantitative yield.

2.6.3 Synthesis of [Cu(κ^2–BH_4)(DPEphos)]

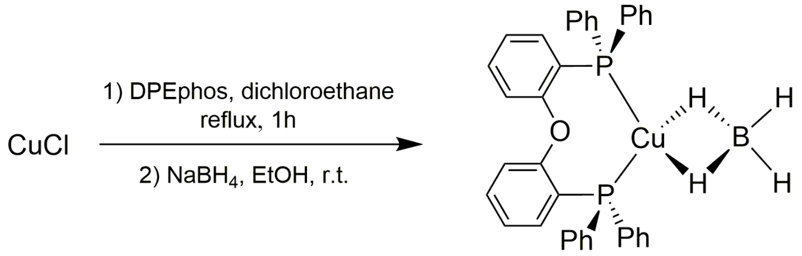

Scheme 20. Synthesis of [Cu(κ^2–BH_4)(DPEphos)].

A stirred solution containing 0.500 g of CuCl (5.0 mmol) and 2.692 g of DPEphos (5.0 mmol) in dichloroethane was heated at reflux under N_2 atmosphere for one hour. After the mixture had cooled down to room temperature, a solution of $NaBH_4$ (0.378 g, 10.0 mmol) in ethanol was added dropwise to the previous one. The solution was left under stirring at room temperature overnight, then the solvent was evaporated under reduced pressure. The complete precipitation of [Cu(κ^2–BH_4)(DPEphos)] was obtained by adding ethanol. The white solid was filtered, washed with ethanol and dried *in vacuo*. The purification was performed by dissolving the complex in dichloromethane and subsequently precipitating it with ethanol. Crystals suitable for X-ray diffraction were collected from dichloromethane/diethyl ether solutions. Yield: 60%

Characterization of [Cu(κ^2–BH_4)(DPEphos)]. Anal. calcd for $C_{36}H_{32}BCuOP_2$ (616.95 g mol^{-1}, %): C, 70.09; H, 5.23. Found (%): C, 69.81; H, 5.25. M.p. > 230 °C (dec., TGA mass loss > 297 °C). ^1H NMR ($CDCl_3$, 298 K) δ 7.53-7.43 (m, 8H, DPEphos), 7.40-7.27 (m, 12H, DPEphos), 7.20 (td, 2H, $^3J_{HH}$ = 8.0 Hz, $^4J_{HH}$ = 1.5 Hz, DPEphos), 6.96-

6.86 (m, 4H, DPEphos), 6.74-6.68 (m, 2H, DPEphos), 1.52-0.66 (m, 4H, BH_4). $^{31}P\{^1H\}$ NMR ($CDCl_3$, 298 K) δ -15.48 (FWHM = 36 Hz). ^{13}C NMR ($CDCl_3$, 298 K) δ 157.86 (t, J_{CP} = 6.0 Hz), 134.26, 134.16 (t, J_{CP} = 8.6 Hz), 131.14, 129.99, 128.58 (t, J_{CP} = 5.0 Hz), 124.44 (t, J_{CP} = 2.2 Hz), 119.88 (t, J_{CP} = 1.9 Hz). P-bonded carbons not detected. ^{11}B NMR ($CDCl_3$, 298 K) δ -32.13 (quint, br, $^1J_{BH}$ = 74 Hz). IR (KBr, cm^{-1}): 3050-3005 w (aromatic $\nu_{C\text{-}H}$), 1690-1560 (aromatic $\nu_{C\text{-}C}$), 2402 sh, 2371 m ($\nu_{B\text{-}H,terminal}$), 1992 m, 1947 m ($\nu_{B\text{-}H,bridging}$). UV-VIS ($CH_2Cl_2$, r.t., nm): < 350, 250 (max), 273 (sh). PL (solid, r.t., $\lambda_{excitation}$ = 290 nm, nm): 465 (FWHM = 3400 cm^{-1}). PLE (solid, r.t., $\lambda_{emission}$ = 470 nm, nm): < 390. τ (r.t., $\lambda_{excitation}$ = 373 nm, $\lambda_{emission}$ = 470 nm, ns): 2.2. Φ (solid, r.t., $\lambda_{excitation}$ = 365 nm): 12%.

2.6.4 Synthesis of $[Cu(NCCH_3)_4][BF_4]$

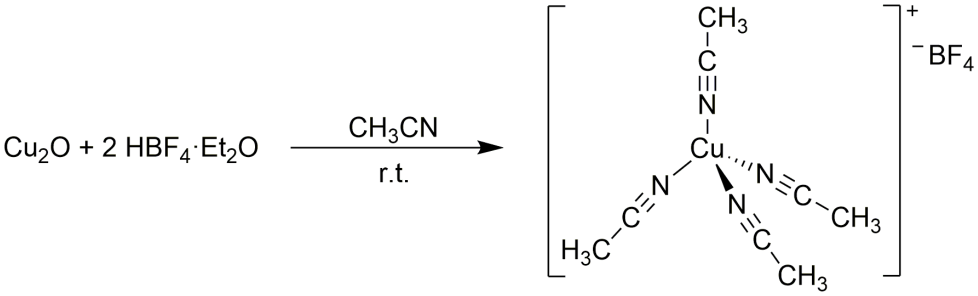

Scheme 21. Synthesis of $[Cu(NCCH_3)_4][BF_4]$.

The complex was obtained following a procedure reported in literature.[139] Due to its air instability, the synthesis was conducted inside the glove box. To a stirred solution of 0.500 g of copper(I) oxide (3.5 mmol) in 20 mL of acetonitrile, 1.0 mL of $HBF_4 \cdot Et_2O$ was added. The evolution of the reaction was indicated by the dissolution of the red solid Cu_2O. After the disappearance of the solid, the solvent was evaporated under reduced pressure to give a brownish solid that was purified. The precipitate was firstly dissolved in dichloromethane and then the solid impurities were eliminated by centrifugation. This procedure was repeated twice, and all the organic fractions were filtered on cotton and collected together. The solvent was concentrated under low pressure, the complex was precipitated with diethyl ether and stored inside the glove box. Yield: 60%.

2.7 Synthesis of the complexes

2.7.1 Manganese(II) complexes

2.7.1.1 Synthesis of [$MnX_2\{O=P(MeNCH_2CH_2NMe)Ph\}_2$] and [$MnX_2\{O=P(NMe_2)_2(2\text{-}Naph)\}_2$], X = Cl, Br, I

The complexes were prepared by slowly adding a solution containing 2.1 mmol of [O=P]-donor ligand dissolved in 10 mL of EtOH into another solution of the proper anhydrous manganese salt MnX_2 (1 mmol) dissolved in 20 mL of EtOH. The reaction mixture was stirred overnight inside the glove-box at room temperature. The solvent was then evaporated under reduced pressure and the so-obtained solid was dissolved in the minimum amount of dichloromethane. The solution was cleared by centrifugation and the solvent was removed under reduced pressure. The product isolated by adding diethyl ether was then filtered and dried *in vacuo*. Crystals of [$MnCl_2\{O=P(MeNCH_2CH_2NMe)Ph\}_2$] and [$MnBr_2\{O=P(MeNCH_2CH_2NMe)Ph\}_2$] suitable for X-ray diffraction were collected from the slow evaporation of acetone/toluene solutions, while crystals of [$MnCl_2\{O=P(NMe_2)_2(2\text{-}Naph)\}_2$] and [$MnBr_2\{O=P(NMe_2)_2(2\text{-}Naph)\}_2$] were collected from acetone/hexane solutions. Crystals of [$MnI_2\{O=P(NMe_2)_2(2\text{-}Naph)\}_2$] were collected from dichloromethane/diethyl ether solutions. Yield > 80% in all the cases.

Characterization of [$MnCl_2\{O=P(MeNCH_2CH_2NMe)Ph\}_2$]. Anal. calcd for $C_{20}H_{30}Cl_2MnN_4O_2P_2$ (546.27 g mol^{-1}, %): C, 43.97; H, 5.54; N, 10.26; Cl, 12.98. Found (%): C, 44.14; H, 5.57; N, 10.30; Cl, 13.03. M.p. 114°C (DSC peak 125.5°C). χ_M^{corr} (c.g.s.u.): $1.47\cdot10^{-2}$. Λ_M (CH_2Cl_2, 298 K) < 2 $ohm^{-1}mol^{-1}cm^2$. IR (KBr, cm^{-1}): 3060-3020 w (aromatic $\nu_{C\text{-}H}$), 2960-2800 w ($\nu_{C\text{-}H}$), 1630-1480 w (aromatic $\nu_{C\text{-}C}$), 1170-1150 s ($\nu_{P=O}$), 1043 m ($\nu_{C\text{-}N}$), 981 s ($\nu_{P\text{-}N}$). UV-VIS (CH_2Cl_2, r.t., nm): < 400, 266 (max), 273 (sh). PL (solid, r.t., $\lambda_{excitation}$ = 280 nm, nm): 508 (FWHM = 2100 cm^{-1}), $^4T_1(^4G) \rightarrow {}^6A_1(^6S)$. PLE (solid, r.t., $\lambda_{emission}$ = 508 nm, nm): < 320, $^4F \leftarrow {}^6A_1(^6S)$ and ligands excitation; 338–384, $^4P,^4D \leftarrow {}^6A_1(^6S)$. τ (solid, r.t., $\lambda_{excitation}$ = 377 nm, $\lambda_{emission}$ = 508 nm, μs): 916.

Characterization of [$MnBr_2\{O=P(MeNCH_2CH_2NMe)Ph\}_2$]. Anal. calcd for $C_{20}H_{30}Br_2MnN_4O_2P_2$ (635.17 g mol^{-1}, %): C, 37.82; H, 4.76; N, 8.82; Br, 25.16. Found (%): C, 37.67; H, 4.80; N, 8.78; Br, 25.06. M.p. 116°C (DSC peak 125.8°C). χ_M^{corr} (c.g.s.u.): $1.46\cdot10^{-2}$. Λ_M (CH_2Cl_2, 298 K) < 2 $ohm^{-1}mol^{-1}cm^2$. IR (KBr, cm^{-1}): 3060-3020 w (aromatic $\nu_{C\text{-}H}$) 2970-2820 w ($\nu_{C\text{-}H}$), 1620-1480 w (aromatic $\nu_{C\text{-}C}$), 1165-1150 s ($\nu_{P=O}$), 1040 m (ν_{C-N}), 983 s (ν_{P-N}). UV-VIS (CH_2Cl_2, r.t., nm): < 400, 266 (max), 275 (sh). PL (solid, r.t., $\lambda_{excitation}$ = 280 nm, nm): 509 (FWHM = 2500 cm^{-1}), $^4T_1(^4G) \rightarrow {}^6A_1(^6S)$. PLE (solid, r.t., $\lambda_{emission}$ = 530 nm, nm): < 320, $^4F \leftarrow {}^6A_1(^6S)$ and ligands excitation; 336–391, $^4P,^4D \leftarrow {}^6A_1(^6S)$. τ (solid, r.t., $\lambda_{excitation}$ = 377 nm, $\lambda_{emission}$ = 508 nm, μs): 683.

Characterization of [MnI₂{O=P(MeNCH₂CH₂NMe)Ph}₂]. Anal. calcd for $C_{20}H_{30}I_2MnN_4O_2P_2$ (729.17 g mol^{-1}, %): C, 32.94; H, 4.15; N, 7.68; I, 34.81. Found (%): C, 32.81; H, 4.18; N, 7.71; I, 34.67. M.p. 86°C (DSC peak 98.7°C). χ_M^{corr} (c.g.s.u.): $1.49 \cdot 10^{-2}$. Λ_M (CH_2Cl_2, 298 K) < 2 $ohm^{-1}mol^{-1}cm^2$. IR (KBr, cm^{-1}): 3080-3055 w (aromatic ν_{C-H}) 2960-2820 w (ν_{C-H}), 1590-1480 w (aromatic ν_{C-C}), 1160-1150 s ($\nu_{P=O}$), 1120-1040 m (ν_{C-N}), 986 s (ν_{P-N}). UV-VIS (CH_2Cl_2, r.t., nm): < 400, 266 (max), 275 (sh), 365. PL (solid, r.t., $\lambda_{excitation}$ = 280 nm, nm): 512 (FWHM = 2400 cm^{-1}), $^4T_1(^4G) \rightarrow {}^6A_1(^6S)$. PLE (solid, r.t., $\lambda_{emission}$ = 510 nm, nm): < 325, $^4F \leftarrow {}^6A_1(^6S)$ and ligands excitation; 340–396, $^4P,^4D \leftarrow {}^6A_1(^6S)$. τ (solid, r.t., $\lambda_{excitation}$ = 377 nm, $\lambda_{emission}$ = 508 nm, μs): 137.

Characterization of [MnCl₂{O=P(NMe₂)₂(2-Naph)}₂]. Anal. calcd for $C_{28}H_{38}Cl_2MnN_4O_2P_2$ (650.42 g mol^{-1}, %): C, 51.71; H, 5.89; N, 8.61; Cl 10.90. Found (%): C, 51.92; H, 5.91; N, 8.64; Cl, 10.85. M.p. 75°C (DSC peak 81.4°C). χ_M^{corr} (c.g.s.u.): $1.46 \cdot 10^{-2}$. IR (KBr, cm^{-1}): 3050-3000 m (aromatic ν_{C-H}), 2930-2800 w (ν_{C-H}), 1630-1480 w (aromatic ν_{C-C}), 1168 s ($\nu_{P=O}$), 1130-1090 m (ν_{C-N}), 986 s (ν_{P-N}). UV-VIS (CH_2Cl_2, r.t., nm): < 350; 269 (sh), 279 (max), 290 (sh), 309 (sh), 316 (sh), 324 (sh). PL (solid, r.t., $\lambda_{excitation}$ = 325 nm, nm): 513 weak (FWHM = 1800 cm^{-1}), $^4T_1(^4G) \rightarrow {}^6A_1(^6S)$; 641 (FWHM = 2600 cm^{-1}), ^{3}LC. PLE (solid, r.t., $\lambda_{emission}$ = 640 nm, nm): < 350, ligands excitation. τ (solid, r.t., $\lambda_{excitation}$ = 290 nm, $\lambda_{emission}$ = 640 nm, μs): 982 (average); 1415 (61%), 313 (39%).

Characterization of [MnBr₂{O=P(NMe₂)₂(2-Naph)}₂]. Anal. calcd for $C_{28}H_{38}Br_2MnN_4O_2P_2$ (739.32 g mol^{-1}, %): C, 45.49; H, 5.18; N, 7.58; Br, 21.62. Found (%): C, 45.31; H, 5.20; N, 7.55; Br, 20.54. M.p. 95°C (DSC peak 98.4°C). χ_M^{corr} (c.g.s.u.): $1.72 \cdot 10^{-2}$. Λ_M (CH_2Cl_2, 298 K) < 2 $ohm^{-1}mol^{-1}cm^2$. IR (KBr, cm^{-1}): 3050-3000 m (aromatic ν_{C-H}), 2930-2800 w (ν_{C-H}), 1630-1480 w (aromatic ν_{C-C}), 1168 s

($\nu_{P=O}$), 1130-1090 m (ν_{C-N}), 986 s (ν_{P-N}). UV-VIS (CH_2Cl_2, r.t., nm): < 350; 269 (sh), 279 (max), 290 (sh), 310 (sh), 317 (sh), 325 (sh). PL (solid, r.t., $\lambda_{excitation}$ = 325 nm, nm): 520 (31%, FWHM = 1900 cm^{-1}), $^4T_1(^4G) \rightarrow {}^6A_1(^6S)$; 643 (69%, FWHM = 2600 cm^{-1}), ^{3}LC. PL (solid, r.t., $\lambda_{excitation}$ = 375 nm, nm): 520 (FWHM = 1900 cm^{-1}), $^4T_1(^4G) \rightarrow {}^6A_1(^6S)$; 643 very weak, ^{3}LC. PLE (solid, r.t., $\lambda_{emission}$ = 513 nm, nm): < 345 weak, ligands excitation; 350–400, $^4P,^4D \leftarrow {}^6A_1(^6S)$; 435, 452, 472 $^4G \leftarrow {}^6A_1(^6S)$. PLE (solid, r.t., $\lambda_{emission}$ = 640 nm, nm): < 345, ligands excitation; 350–400 weak, $^4P,^4D \leftarrow {}^6A_1(^6S)$. τ (solid, r.t., $\lambda_{excitation}$ = 290 nm, $\lambda_{emission}$ = 513 nm, μs): 38 (average); 37 (99%), 223 (1%). τ (solid, r.t., $\lambda_{excitation}$ = 290 nm, $\lambda_{emission}$ = 640 nm, μs): 172 (average); 86 (87%), 747 (13%).

Characterization of $[MnI_2\{O{=}P(NMe_2)_2(2\text{-}Naph)\}_2]$. Anal. calcd for $C_{28}H_{38}I_2MnN_4O_2P_2$ (833.32 g mol^{-1}, %): C, 40.36; H, 4.60; N, 6.72; I, 30.46. Found (%): C, 40.20; H, 4.62; N, 6.75; I, 30.54. M.p. 95°C (DSC peak 104.7°C). χ_M^{corr} (c.g.s.u.): $1.68\cdot10^{-2}$. Λ_M (CH_2Cl_2, 298 K) < 2 ohm^{-1}mol^{-1}cm^2. IR (KBr, cm^{-1}): 3050-3000 m (aromatic ν_{C-H}), 2940-2810 w (ν_{C-H}), 1600-1460 w (aromatic ν_{C-C}), 1164 s ($\nu_{P=O}$), 1120-1060 m (ν_{C-N}), 984 s (ν_{P-N}). UV-VIS (CH_2Cl_2, r.t., nm): < 400; 269 (sh), 280 (max), 289 (sh), 308 (sh), 317 (sh), 325 (sh). PL (solid, r.t., $\lambda_{excitation}$ = 325 nm, nm): 514 (31%, FWHM = 2300 cm^{-1}), $^4T_1(^4G) \rightarrow {}^6A_1(^6S)$; 637 (69%, FWHM = 2900 cm^{-1}), ^{3}LC. PL (solid, r.t., $\lambda_{excitation}$ = 375 nm, nm): 514 (31%, FWHM = 2300 cm^{-1}), $^4T_1(^4G) \rightarrow {}^6A_1(^6S)$; 637 (69%, FWHM = 2900 cm^{-1}), ^{3}LC. PLE (solid, r.t., $\lambda_{emission}$ = 513 nm, nm): < 345, ligands excitation; 350–400 weak, $^4P,^4D \leftarrow {}^6A_1(^6S)$. PLE (solid, r.t., $\lambda_{emission}$ = 640 nm, nm): < 345, ligands excitation; 350–400 weak, $^4P,^4D \leftarrow {}^6A_1(^6S)$. τ (solid, r.t., $\lambda_{excitation}$ = 290 nm, $\lambda_{emission}$ = 513 nm, μs): 28. τ (solid, r.t., $\lambda_{excitation}$ = 290 nm, $\lambda_{emission}$ = 640 nm, μs): 29.

2.7.1.2 Synthesis of $[MnX_2\{O{=}P(NMe_2)_2R\}_2]$, R = Ind, Cbz and X = Cl, Br, I, and $[MnX_2\{O{=}PPh_2Ind\}_2]$, O=PPh$_2$Ind = (Indol-1-yl)diphenylphosphine oxide and X = Br, I

The syntheses were carried out following the procedure described above for $[MnX_2\{O{=}P(MeNCH_2CH_2NMe)Ph\}_2]$. Crystal of $[MnCl_2\{O{=}P(NMe_2)_2Ind\}_2]$ and $[MnBr_2\{O{=}P(NMe_2)_2Ind\}_2]$ suitable for X-ray diffraction were collected from the slow evaporation of acetone/toluene solutions, while $[MnI_2\{O{=}P(NMe_2)_2Ind\}_2]$ and all the $[MnX_2\{O{=}P(NMe_2)_2Cbz\}_2]$ derivatives were crystallized from dichloromethane/diethyl ether solutions. Yield > 80% in all the cases.

Characterization of [MnCl$_2${O=P(NMe$_2$)$_2$Ind}$_2$]. Anal. calcd for $C_{24}H_{36}Cl_2MnN_6O_2P_2$ (628.37 g mol^{-1}, %): C, 45.87; H, 5.77; N, 13.37; Cl, 11.28. Found (%): C, 45.69; H, 5.79; N, 13.32; Cl, 11.28. M.p. 122°C (DSC peak 125 °C). χ_M^{corr} (c.g.s.u.): $1.48 \cdot 10^{-2}$. Λ_M (CH_2Cl_2, 298 K) < 2 ohm^{-1}mol^{-1}cm^2. IR (KBr, cm^{-1}): 3150-3000 m/w (aromatic $\nu_{C\text{-}H}$), 2980-2785 m ($\nu_{C\text{-}H}$), 1550-1390 m (aromatic $\nu_{C\text{-}C}$ and $\nu_{C\text{-}N}$), 1245-1095 s ($\nu_{P=O}$ and $\nu_{C\text{-}N}$), 1040-920 s ($\nu_{P\text{-}N}$). UV-VIS (CH_2Cl_2, r.t., nm): < 300, 260 (max), 276 (sh), 287 (sh). PL (solid, r.t., $\lambda_{excitation}$ = 280 nm, nm): 527 (FWHM = 2800 cm^{-1}), $^4T_1(^4G) \rightarrow {}^6A_1(^6S)$. PLE (solid, r.t., $\lambda_{emission}$ = 530 nm, nm): < 315, 290 sh, $^4F \leftarrow {}^6S$ and ligands excitation; 334–391, $^4P,^4D \leftarrow {}^6A_1(^6S)$; 420–480, $^4G \leftarrow {}^6A_1(^6S)$. τ (solid, r.t., $\lambda_{excitation}$ = 290 nm, $\lambda_{emission}$ = 530 nm, μs): 2198.

Characterization of [MnBr$_2${O=P(NMe$_2$)$_2$Ind}$_2$]. Anal. calcd for $C_{24}H_{36}Br_2MnN_6O_2P_2$ (717.28 g mol^{-1}, %): C, 40.19; H, 5.06; N, 11.72; Br, 22.28. Found (%): C, 40.03; H, 5.10; N, 11.77; Br, 22.19. M.p. 120°C (DSC peak 124°C). χ_M^{corr} (c.g.s.u.): $1.47 \cdot 10^{-2}$. Λ_M (CH_2Cl_2, 298 K) < 2 ohm^{-1}mol^{-1}cm^2. IR (KBr, cm^{-1}): 3150-3000 m/w (aromatic $\nu_{C\text{-}H}$), 2980-2785 m ($\nu_{C\text{-}H}$), 1550-1390 m (aromatic $\nu_{C\text{-}C}$ and $\nu_{C\text{-}N}$), 1245-1095 s ($\nu_{P=O}$ and $\nu_{C\text{-}N}$), 1040-920 s ($\nu_{P\text{-}N}$). UV-VIS (CH_2Cl_2, r.t., nm): < 300, 257 (max), 276 (sh), 287 (sh). PL (solid, r.t., $\lambda_{excitation}$ = 280 nm, nm): 535 (FWHM = 2500 cm^{-1}), $^4T_1(^4G) \rightarrow {}^6A_1(^6S)$. PLE (solid, r.t., $\lambda_{emission}$ = 530 nm, nm): < 315, 290 sh, $^4F \leftarrow {}^6S$ and ligands excitation; 336–392, $^4P,^4D \leftarrow {}^6A_1(^6S)$; 420–480, $^4G \leftarrow {}^6A_1(^6S)$. τ (solid, r.t., $\lambda_{excitation}$ = 290 nm, $\lambda_{emission}$ = 530 nm, μs): 576.

Characterization of [MnI$_2${O=P(NMe$_2$)$_2$Ind}$_2$]. Anal. calcd for $C_{24}H_{36}I_2MnN_6O_2P_2$ (811.28 g mol^{-1}, %): C, 35.53; H, 4.47; N, 10.36; I, 31.29. Found (%): C, 35.39; H, 4.50; N, 10.32; I, 31.42. M.p. 99°C (DSC peak 106°C). χ_M^{corr} (c.g.s.u.): $1.49 \cdot 10^{-2}$. Λ_M (CH_2Cl_2, 298 K): < 2 ohm^{-1}mol^{-1}cm^2. IR (KBr, cm^{-1}): 3150-3000 m/w (aromatic $\nu_{C\text{-}H}$), 2980-2785 m ($\nu_{C\text{-}H}$), 1550-1390 m (aromatic $\nu_{C\text{-}C}$ and $\nu_{C\text{-}N}$), 1245-1095 s ($\nu_{P=O}$ and $\nu_{C\text{-}N}$), 1040-920 s ($\nu_{P\text{-}N}$). UV-VIS (CH_2Cl_2, r.t., nm): < 300, 257 (max), 275 (sh), 287 (sh). PL (solid, r.t., $\lambda_{excitation}$ = 280 nm, nm): 519 (FWHM 2100 cm^{-1}), $^4T_1(^4G) \rightarrow {}^6A_1(^6S)$. PLE (solid, r.t., $\lambda_{emission}$ = 530 nm, nm): < 315, 290 sh, $^4F \leftarrow {}^6S$ and ligands excitation; 336-392, $^4P,^4D \leftarrow {}^6A_1(^6S)$; 420–480, $^4G \leftarrow {}^6A_1(^6S)$. τ (solid, r.t., $\lambda_{excitation}$ = 290 nm, $\lambda_{emission}$ = 530 nm, μs): 76.

Characterization of [MnCl$_2${O=P(NMe$_2$)$_2$Cbz}$_2$]. Anal. calcd for $C_{32}H_{40}Cl_2MnN_6O_2P_2$ (728.50 g mol^{-1}, %): C, 52.76; H, 5.53; N, 11.54; Cl, 9.73. Found (%): C, 52.55; H, 5.55; N, 11.49; Cl, 9.77. M.p. 205°C. χ_M^{corr} (c.g.s.u.): $1.48 \cdot 10^{-2}$. Λ_M (CH_2Cl_2, 298 K) < 2 $ohm^{-1}mol^{-1}cm^2$. IR (KBr, cm^{-1}): 3120-3000 m/w (aromatic ν_{C-H}), 2930-2800 m (ν_{C-H}), 1650-1600 m (aromatic ν_{C-C} and ν_{C-N}), 1200-1120 s ($\nu_{P=O}$ and ν_{C-N}), 1030-970 s (ν_{P-N}). UV-VIS (CH_2Cl_2, r.t., nm): < 263, 280 (sh), 288 (ε = 27800 M^{-1} cm^{-1}), 306, 320. PL (solid, r.t., $\lambda_{excitation}$ = 270 nm, nm): 396, 415, 441 ligands, 526 (max) $^4T_1(^4G) \rightarrow {}^6A_1(^6S)$, 546 (sh), 595 (sh), 649 (sh) ligands. PL (solid, r.t., $\lambda_{excitation}$ = 350 nm, nm): 396, 415, 441 ligands, 526 (sh) $^4T_1(^4G) \rightarrow {}^6A_1(^6S)$, 546 (max), 558 (sh), 595, 614 (sh), 649 ligands. PLE (solid, r.t., $\lambda_{emission}$ = 520 nm, nm): < 345 (max 265), 355, 370 ligands and $^4F,^4P,^4D \leftarrow {}^6A_1(^6S)$; 422, 438, 460 $^4G \leftarrow {}^6A_1(^6S)$. PLE (solid, r.t., $\lambda_{emission}$ = 650 nm, nm): < 360 (max 349), 370 ligands and $^4F,^4P,^4D \leftarrow {}^6A_1(^6S)$; 422, 438, 460 $^4G \leftarrow {}^6A_1(^6S)$. τ (solid, r.t., $\lambda_{excitation}$ = 290 nm, $\lambda_{emission}$ = 520 nm, μs): 305. Φ (solid, r.t., $\lambda_{excitation}$ = 365 nm): 5%.

Characterization of [MnBr₂{O=P(NMe₂)₂Cbz}₂]. Anal. calcd for $C_{32}H_{40}Br_2MnN_6O_2P_2$ (817.41 g mol^{-1}, %): C, 47.02; H, 4.93; N, 10.28; Br, 19.55. Found (%): C, 46.83; H, 4.95; N, 10.32; Br, 19.47. M.p. 210°C. χ_M^{corr} (c.g.s.u.): $1.57 \cdot 10^{-2}$. Λ_M (CH_2Cl_2, 298 K) < 2 $ohm^{-1}mol^{-1}cm^2$. IR (KBr, cm^{-1}): 3080-3000 m/w (aromatic ν_{C-H}), 2980-2820 m (ν_{C-H}), 1640-1390 m (aromatic ν_{C-C} and ν_{C-N}), 1200-1120 s ($\nu_{P=O}$ and ν_{C-N}), 1030-970 s (ν_{P-N}). UV-VIS (CH_2Cl_2, r.t., nm): < 263, 280 (sh), 288 (ε = 28700 M^{-1} cm^{-1}), 306, 320. PL (solid, r.t., $\lambda_{excitation}$ = 270 nm, nm): 520 (max), $^4T_1(4G) \rightarrow {}^6A_1(^6S)$; 625, ligands. PL (solid, r.t., $\lambda_{excitation}$ = 350 nm, nm): 520, $^4T_1(4G) \rightarrow {}^6A_1(^6S)$; 544 (max), 593, 645 ligands. PLE (solid, r.t., $\lambda_{emission}$ = 520 nm, nm): < 340 (max 321), 351, 370 ligands and $^4F,^4P,^4D \leftarrow {}^6A_1(^6S)$; 420, 441, 460 $^4G \leftarrow {}^6A_1(^6S)$. PLE (solid, r.t., $\lambda_{emission}$ = 650 nm, nm): < 340 (max 321), 351, 370 ligands and $^4F,^4P,^4D \leftarrow {}^6A_1(^6S)$; 420, 441, 460 $^4G \leftarrow {}^6A_1(^6S)$. τ (solid, r.t., $\lambda_{excitation}$ = 290 nm, $\lambda_{emission}$ = 520 nm, μs): 182. Φ (solid, r.t., $\lambda_{excitation}$ = 365 nm): 10%.

Characterization of [MnI₂{O=P(NMe₂)₂Cbz}₂]. Anal. calcd for $C_{32}H_{40}I_2MnN_6O_2P_2$ (911.41 g mol^{-1}, %): C, 42.17; H, 4.42; N, 9.22; I, 27.85. Found (%): C, 42.01; H, 4.44; N, 9.18; I, 27.74. M.p. 165°C. χ_M^{corr} (c.g.s.u.): $1.51 \cdot 10^{-2}$. Λ_M (CH_2Cl_2, 298 K): < 2 $ohm^{-1}mol^{-1}cm^2$. IR (KBr, cm^{-1}): 3060-3000 m/w (aromatic ν_{C-H}), 2970-2820 m (ν_{C-H}), 1640-1580 m (aromatic ν_{C-C} and ν_{C-N}), 1203-1120 s ($\nu_{P=O}$ and ν_{C-N}), 1030-930 s (ν_{P-N}). UV-VIS (CH_2Cl_2, r.t., nm): < 263, 280 (sh), 288 (ε = 26400 M^{-1} cm^{-1}), 306, 320. PL (solid, r.t., $\lambda_{excitation}$ = 270 nm, nm): 519 (max), $^4T_1(4G) \rightarrow {}^6A_1(^6S)$; 645, ligands. PL (solid, r.t., $\lambda_{excitation}$ = 350 nm, nm): 519 (max); $^4T_1(^4G) \rightarrow {}^6A_1(^6S)$, 645, ligands. PLE (solid, r.t., $\lambda_{emission}$ = 520 nm, nm): < 340 (max 319), 340-395 ligands and $^4F,^4P,^4D \leftarrow {}^6A_1(^6S)$; 429, 446, 466 $^4G \leftarrow {}^6A_1(^6S)$. PLE (solid, r.t., $\lambda_{emission}$ = 650 nm, nm): < 340 (max 319), ligands and $^4F \leftarrow {}^6A_1(^6S)$. τ (solid, r.t., $\lambda_{excitation}$ = 290 nm, $\lambda_{emission}$ = 520 nm, μs): 71. Φ (solid, r.t., $\lambda_{excitation}$ = 365 nm): 5%.

Characterization of [MnBr$_2$(O=PPh$_2$Ind)$_2$]. Anal. calcd for $C_{40}H_{32}Br_2MnN_2O_2P_2$ (849.40 g mol^{-1}, %): C, 56.56; H, 3.80; N, 3.30; Br, 18.81. Found (%): C, 56.33; H, 3.82; N, 3.29; Br, 18.89. M.p. 170°C. χ_M^{corr} (c.g.s.u.): $1.50 \cdot 10^{-2}$. Λ_M (CH_2Cl_2, 298 K) < 2 ohm^{-1}mol^{-1}cm^2. IR (KBr, cm^{-1}): 3150-2980 m (aromatic ν_{C-H}), 1640-1570 w (aromatic ν_{C-C} and ν_{C-N}), 1210-1130 s ($\nu_{P=O}$ and ν_{C-N}), 997 m (ν_{P-N}). UV-VIS (CH_2Cl_2, r.t., nm): < 300, 259 (max), 288. PL (solid, r.t., $\lambda_{excitation}$ = 265 nm, nm): 520 (max), $^4T_1(^4G) \rightarrow {}^6A_1(^6S)$. PLE (solid, r.t., $\lambda_{emission}$ = 525 nm, nm): < 340, $^4F \leftarrow {}^6A_1(^6S)$, ligands excitation; 350, 371, $^4P,^4D, \leftarrow {}^6A_1(^6S)$; 421, 439, 458, $^4G \leftarrow {}^6A_1(^6S)$. τ (solid, r.t., $\lambda_{excitation}$ = 265 nm, $\lambda_{emission}$ = 520 nm, μs): 288. Φ (solid, r.t., $\lambda_{excitation}$ = 365 nm): 15%.

Characterization of [MnI$_2$(O=PPh$_2$Ind)$_2$]. Anal. calcd for $C_{40}H_{32}I_2MnN_2O_2P_2$ (943.40 g mol^{-1}, %): C, 50.93; H, 3.42; N, 2.97; I, 26.90. Found (%): C, 50.73; H, 3.43; N, 2.96; I, 27.01. M.p. 155°C. χ_M^{corr} (c.g.s.u.): $1.49 \cdot 10^{-2}$. Λ_M (CH_2Cl_2, 298 K) < 2 ohm^{-1}mol^{-1}cm^2. IR (KBr, cm^{-1}): 3140-2970 m (aromatic ν_{C-H}), 1640-1575 w (aromatic ν_{C-C} and ν_{C-N}), 1210-1130 s ($\nu_{P=O}$ and ν_{C-N}), 996 m (ν_{P-N}). UV-VIS (CH_2Cl_2, r.t., nm): < 400, 254 (max), 288, 367. PL (solid, r.t., $\lambda_{excitation}$ = 265 nm, nm): 519 (max), $^4T_1(^4G) \rightarrow {}^6A_1(^6S)$. PLE (solid, r.t., $\lambda_{emission}$ = 520 nm, nm): < 330, $^4F \leftarrow {}^6A_1(^6S)$, ligands excitation; 351, 360, 369, 381, $^4P,^4D, \leftarrow {}^6A_1(^6S)$; 427, 448, 470, $^4G \leftarrow {}^6A_1(^6S)$. τ (solid, r.t., $\lambda_{excitation}$ = 265 nm, $\lambda_{emission}$ = 520 nm, μs): 56. Φ (solid, r.t., $\lambda_{excitation}$ = 365 nm): 6%.

2.7.1.3 Synthesis of [MnX$_2${O=P(OPh)$_2$(NMe)}$_2$], X = Br, I

The syntheses were carried out following the procedure described above for [MnX$_2${O=P(MeNCH$_2$CH$_2$NMe)Ph}$_2$]. Crystals suitable for X-ray diffraction were collected from a solution of dichloromethane/diethyl ether for the bromo-species and ethanol/dichloromethane/toluene for the iodo-species. Yield > 50% in both of the cases.

Characterization of [MnBr$_2${O=P(OPh)$_2$(NMe)}$_2$]. Anal. calcd for $C_{28}H_{32}Br_2MnN_2O_6P_2$ (769.26 g mol^{-1}, %): C, 43.72; H, 4.19; N, 3.64; Br, 20.77. Found (%): C, 43.54; H, 4.22; N, 3.60; Br, 20.85. M.p. 125°C. χ_M^{corr} (c.g.s.u.): $1.42 \cdot 10^{-2}$. Λ_M (CH_2Cl_2, 298 K) < 2 ohm^{-1}mol^{-1}cm^2. IR (KBr, cm^{-1}): 3060-3000 m/w (aromatic ν_{C-H}), 2980-2830 m (ν_{C-H}), 1590-1480 m (aromatic ν_{C-C} and ν_{C-N}), 1320 (ν_{C-O}), 1230-1150 s ($\nu_{P=O}$ and ν_{C-O}), 1070 m (ν_{C-N}), 1010 m (ν_{P-O}), 950 s (ν_{P-N}). UV-VIS (CH_2Cl_2, r.t., nm): < 330, 264 (sh), 270 (max), 280 (sh). PL (solid, r.t., $\lambda_{excitation}$ = 350 nm, nm): 520 (FWHM = 2500 cm^{-1}), $^4T_1(^4G) \rightarrow {}^6A_1(^6S)$. PLE (solid, r.t., $\lambda_{emission}$ = 560 nm, nm): < 290, $^4F \leftarrow {}^6A_1(^6S)$, ligands excitation; 349, 370, $^4P,^4D \leftarrow {}^6A_1(^6S)$; 421, 438, 458, $^4G \leftarrow {}^6A_1(^6S)$. τ (solid, r.t., $\lambda_{excitation}$ = 265 nm, $\lambda_{emission}$ = 520 nm, μs): 173. Φ (solid, r.t., $\lambda_{excitation}$ = 365 nm): 58%.

Characterization of [MnI$_2${O=P(OPh)$_2$(NMe)}$_2$]. Anal. calcd for $C_{28}H_{32}I_2MnN_2O_6P_2$ (863.26 g mol^{-1}, %): C, 38.96; H, 3.74; N, 3.25; I, 29.40. Found (%): C, 38.79; H, 3.75; N, 3.23; I, 29.52. M.p. 107°C. χ_M^{corr} (c.g.s.u.): $1.54 \cdot 10^{-2}$. Λ_M (CH_2Cl_2, 298 K): < 2 ohm^{-1}mol^{-1}cm^2. IR (KBr, cm^{-1}): 3060-3000 m/w (aromatic ν_{C-H}), 2970-2820 m (ν_{C-H}), 1640-1580 m (aromatic ν_{C-C} and ν_{C-N}), 1203-1120 s ($\nu_{P=O}$ and ν_{C-O}), 1070 m (ν_{C-N}), 1030-930 s (ν_{P-N}). UV-VIS (CH_2Cl_2, r.t., nm): < 330, 256 (sh), 262 (max), 268 (sh). PL (solid, r.t., $\lambda_{excitation}$ = 270 nm, nm): 515 (FWHM = 2200 cm^{-1}), $^4T_1(^4G) \rightarrow {}^6A_1(^6S)$. PLE (solid, r.t., $\lambda_{emission}$ = 560 nm, nm): < 305, $^4F \leftarrow {}^6A_1(^6S)$, ligands excitation; 348, 357, 370, 382, $^4P,^4D \leftarrow {}^6A_1(^6S)$; 426, 438-489, $^4G \leftarrow {}^6A_1(^6S)$. τ (solid, r.t., $\lambda_{excitation}$ = 265 nm, $\lambda_{emission}$ = 515 nm, μs): 93. Φ (solid, r.t., $\lambda_{excitation}$ = 365 nm): 84%.

2.7.1.4 Synthesis of [MnX$_2${μ–O=P(NMe$_2$)$_2$(res)(NMe$_2$)$_2$P=O}], X = Br, I

The syntheses were carried out following the procedure described above for [MnX$_2${O=P(MeNCH$_2$CH$_2$NMe)Ph}$_2$], but the ligand was added in ratio 1:1 with respect to the metal centre. Crystals suitable for X-ray diffraction were collected from a solution of dichloromethane/diethyl ether (X = Br) or ethanol/dichloromethane/toluene (X = I). Yield > 50% in both the cases.

Characterization of [MnBr$_2${μ–O=P(NMe$_2$)$_2$(res)(NMe$_2$)$_2$P=O}$_2$]$_2$. Anal. calcd for $C_{14}H_{28}Br_2MnN_4O_4P_2$ (593.09 g mol^{-1}, %): C, 28.35; H, 4.76; N, 9.45; Br, 26.94. Found (%): C, 28.25; H, 4.80; N, 9.39; Br, 27.05. M.p. 167°C. χ_M^{corr} (c.g.s.u.): $1.47 \cdot 10^{-2}$. Λ_M (CH_2Cl_2, 298 K) < 2 ohm^{-1}mol^{-1}cm^2. IR (KBr, cm^{-1}): 3080-3000 m/w (aromatic ν_{C-H}), 2980-2820 m (ν_{C-H}), 1600-1460 m (aromatic ν_{C-C} and ν_{C-N}), 1310 (ν_{C-O}), 1180-1130 s ($\nu_{P=O}$ and ν_{C-O}), 1069 m (ν_{C-N}), 1010 m (ν_{P-O}), 980 s (ν_{P-N}). UV-VIS (CH_2Cl_2, r.t., nm): < 420, 263 (max), 269 (sh), 315 (sh), 415 (sh). PL (solid, r.t., $\lambda_{excitation}$ = 270 nm, nm): 521 (FWHM = 2100 cm^{-1}), $^4T_1(^4G) \rightarrow {}^6A_1(^6S)$. PLE (solid, r.t., $\lambda_{emission}$ = 560 nm, nm): < 300, $^4F \leftarrow {}^6A_1(^6S)$, ligands excitation; 346, 354, 372, ^4P,^4D, $\leftarrow {}^6A_1(^6S)$; 423, 440, 461, $^4G \leftarrow {}^6A_1(^6S)$. τ (solid, r.t., $\lambda_{excitation}$ = 377 nm, $\lambda_{emission}$ = 522 nm, μs): 468. Φ (solid, r.t., $\lambda_{excitation}$ = 365 nm): 17%.

Characterization of [MnI$_2${μ–O=P(NMe$_2$)$_2$(res)(NMe$_2$)$_2$P=O}$_2$]$_n$. Anal. calcd for $C_{14}H_{28}I_2MnN_4O_4P_2$ (687.09 g mol^{-1}, %): C, 24.47; H, 4.11; N, 8.15; I, 36.94. Found (%): C, 24.37; H, 4.09; N, 8.20; I, 37.00. M.p. 149°C. χ_M^{corr} (c.g.s.u.): $1.49 \cdot 10^{-2}$. Λ_M (CH_2Cl_2, 298 K): < 2 ohm^{-1}mol^{-1}cm^2. IR (KBr, cm^{-1}): 3015-3000 m/w (aromatic ν_{C-H}), 2970-2810 m (ν_{C-H}), 1580-1480 m (aromatic ν_{C-C} and ν_{C-N}), 1360 (ν_{C-O}), 1170-1120 s ($\nu_{P=O}$ and ν_{C-O}), 1063 m (ν_{C-N}), 982 m (ν_{P-O}), 930 s (ν_{P-N}). UV-VIS (CH_2Cl_2, r.t., nm): < 410, 262 (sh), 270 (sh), 295 (max), 365 (sh). PL (solid, r.t., $\lambda_{excitation}$ = 270 nm, nm): 524 (FWHM = 2300 cm^{-1}), $^4T_1(^4G) \rightarrow {}^6A_1(^6S)$. PLE (solid, r.t., $\lambda_{emission}$ = 550 nm, nm): 262, 269, 282, $^4F \leftarrow {}^6A_1(^6S)$; 345-388 ^4P,^4D, $\leftarrow {}^6A_1(^6S)$; 427, 444, 466 $^4G \leftarrow {}^6A_1(^6S)$. τ (solid, r.t., $\lambda_{excitation}$ = 265 nm, $\lambda_{emission}$ = 520 nm, μs): 40. Φ (solid, r.t., $\lambda_{excitation}$ = 365 nm): 15%.

2.7.1.5 Synthesis of [MnX$_2${DOPO}$_2$], DOPO = 9,10-dihydro-9-oxa-10-phosphaphenanthrene-10-oxide and X = Cl, Br, I

The complexes were prepared by slowly adding a solution containing 2.1 mmol (0.455 g) of 9,10-dihydro-9-oxa-10-phosphaphenanthrene-10-oxide (DOPO) dissolved in 20 mL of CH_2Cl_2 into another solution of the proper anhydrous manganese salt MnX_2 (1.0 mmol) dissolved in 20 mL of EtOH. The reaction mixture was stirred inside the glove box overnight. The solvent was then evaporated under reduced pressure and the so-obtained oil was precipitated by adding diethyl ether. The product was then filtered and dried *in vacuo*. Yield > 80% in all the cases.

Characterization of [MnCl$_2$(DOPO)$_2$]. Anal. calcd for $C_{24}H_{18}Cl_2MnO_4P_2$ (558.19 g mol^{-1}, %): C, 51.64; H, 3.25; Cl, 12.70. Found (%): C, 51.44; H, 3.26; Cl, 12.65. M.p. 190°C. χ_M^{corr} (c.g.s.u.): $1.68 \cdot 10^{-2}$. IR (KBr, cm^{-1}): 3060-3020 w (aromatic ν_{C-H}), 2414 m (ν_{P-H}), 1620-1560 w (aromatic ν_{C-C}), 1240-1170 s ($\nu_{P=O}$ and ν_{C-O}), 1044 w (ν_{P-O}).

UV-VIS (EtOH, r.t., nm): < 300, 259 (sh), 267 (max), 294. PL (solid, r.t., $\lambda_{excitation}$ = 325 nm, nm): 635, ^{3}LC. PL (solid, r.t., $\lambda_{excitation}$ = 440 nm, nm): 535, $^4T_1(^4G) \rightarrow {}^6A_1(^6S)$; 635, ^{3}LC. PLE (solid, r.t., $\lambda_{emission}$ = 640 nm, nm): < 400 ligands excitation and $^4P,^4D,^4F \leftarrow {}^6A_1(^6S)$; 405-470, $^4G \leftarrow {}^6A_1(^6S)$. PLE (solid, r.t., $\lambda_{emission}$ = 500 nm, nm): 335-400 $^4P,^4D \leftarrow {}^6A_1(^6S)$; 405-470 $^4G \leftarrow {}^6A_1(^6S)$. τ (solid, r.t., $\lambda_{excitation}$ = 290 nm, $\lambda_{emission}$ = 650 nm, ms): 8.2 (average). Φ (solid, r.t., $\lambda_{excitation}$ = 365 nm): 65%.

Characterization of [MnBr₂(DOPO)₂]. Anal. calcd for $C_{24}H_{18}Br_2MnO_4P_2$ (647.10 g mol^{-1}, %): C, 44.55; H, 2.80; Br, 24.70. Found (%): C, 44.37; H, 2.81; Br, 24.60. M.p. 210°C. χ_M^{corr} (c.g.s.u.): $1.43 \cdot 10^{-2}$. IR (KBr, cm^{-1}): 3060-3020 w (aromatic ν_{C-H}), 2427 m (ν_{P-H}), 1620-1560 w (aromatic ν_{C-C}), 1212-1199 s ($\nu_{P=O}$ and ν_{C-O}), 1044 w (ν_{P-O}). UV-VIS (EtOH, r.t., nm): < 300, 259 (sh), 267 (max) 294. PL (solid, r.t., $\lambda_{excitation}$ = 325 nm, nm): 536, $^4T_1(^4G) \rightarrow {}^6A_1(^6S)$; 625, ^{3}LC. PL (solid, r.t., $\lambda_{excitation}$ = 440 nm, nm): 536, $^4T_1(^4G) \rightarrow {}^6A_1(^6S)$; 625, ^{3}LC. PLE (solid, r.t., $\lambda_{emission}$ = 625 nm, nm): < 340 ligands excitation and $^4F \leftarrow {}^6A_1(^6S)$; 345-415 $^4P,^4D \leftarrow {}^6A_1(^6S)$; 415-505, $^4G \leftarrow {}^6A_1(^6S)$. PLE (solid, r.t., $\lambda_{emission}$ = 505 nm, nm): < 340 ligands and $^4F \leftarrow {}^6A_1(^6S)$; 345-415 $^4P,^4D \leftarrow {}^6A_1(^6S)$; 415-480 $^4G \leftarrow {}^6A_1(^6S)$. τ (solid, r.t., $\lambda_{excitation}$ = 290 nm, $\lambda_{emission}$ = 505 nm, μs): 83. τ (solid, r.t., $\lambda_{excitation}$ = 290 nm, $\lambda_{emission}$ = 650 nm, ms): 35.2. Φ (solid, r.t., $\lambda_{excitation}$ = 365 nm): 77%.

Characterization of [MnI₂(DOPO)₂]. Anal. calcd for $C_{24}H_{18}I_2MnO_4P_2$ (741.10 g mol^{-1}, %): C, 38.90; H, 2.45; I, 34.25. Found (%): C, 38.74; H, 2.46; I, 34.11. M.p. 80°C. χ_M^{corr} (c.g.s.u.): $1.52 \cdot 10^{-2}$. IR (KBr, cm^{-1}): 3060-3020 w (aromatic ν_{C-H}), 2410 m (ν_{P-H}), 1620-1560 w (aromatic ν_{C-C}), 1240-1170 s ($\nu_{P=O}$ and ν_{C-O}), 1044 w (ν_{P-O}). UV-VIS (EtOH, r.t., nm): < 300, 259 (sh), 267 (max) 294. PL (solid, r.t., $\lambda_{excitation}$ = 325 nm, nm): 538, $^4T_1(^4G) \rightarrow {}^6A_1(^6S)$; 640, ^{3}LC. PL (solid, r.t., $\lambda_{excitation}$ = 440 nm, nm): 538, $^4T_1(^4G) \rightarrow {}^6A_1(^6S)$; 640, ^{3}LC. PLE (solid, r.t., $\lambda_{emission}$ = 640 nm, nm): < 350 ligands excitation and $^4F \leftarrow {}^6A_1(^6S)$; 355-420 $^4P,^4D \leftarrow {}^6A_1(^6S)$; 425-515 $^4G \leftarrow {}^6A_1(^6S)$. PLE (solid, r.t., $\lambda_{emission}$ = 510 nm, nm): < 350 ligands excitation and $^4F \leftarrow {}^6A_1(^6S)$; 355-420 $^4P,^4D \leftarrow {}^6A_1(^6S)$; 425-480 $^4G \leftarrow {}^6A_1(^6S)$. τ (solid, r.t., $\lambda_{excitation}$ = 290 nm, $\lambda_{emission}$ = 505 nm, μs): 13. τ (solid, r.t., $\lambda_{excitation}$ = 290 nm, $\lambda_{emission}$ = 650 nm, ms): 15.3. Φ (solid, r.t., $\lambda_{excitation}$ = 365 nm): 18%.

2.7.1.6 Synthesis of $[MnX_2\{BPPO\}_2]_n$, BPPO = dibenzo[*d,f*][1,3,2]dioxaphosphepine 6-oxide and X = Cl, Br, I

The syntheses were carried out following the procedure described above for $[MnX_2\{O=P(MeNCH_2CH_2NMe)Ph\}_2]$, but acetonitrile was used as solvent instead of EtOH. The complexes were centrifuged from acetonitrile because of their insolubility in dichloromethane. Yield > 80% in all the cases.

Characterization of $[MnCl_2(BPPO)_2]_n$. Anal. calcd for $C_{24}H_{18}Cl_2MnO_6P_2$ (590.18 g mol^{-1}, %): C, 48.84; H, 3.25; Cl, 12.70. Found (%): C, 48.64; H, 3.26; Cl, 12.65. M.p. 75°C (dec.). χ_M^{corr} (c.g.s.u.): $1.60 \cdot 10^{-2}$. IR (cm^{-1}): 3060-2970 w (aromatic ν_{C-H}), 2443 m (ν_{P-H}), 1630-1570 w (aromatic ν_{C-C}), 1200-1180 s ($\nu_{P=O}$ and ν_{C-O}), 1047 w (ν_{P-O}). UV-VIS (ACN, r.t., nm): < 315, 244 (max), 276. PL (solid, r.t., $\lambda_{excitation}$ = 350 nm, nm): 644, ^{3}LC. PL (solid, r.t., $\lambda_{excitation}$ = 430 nm, nm): 537, $^4T_1(^4G) \rightarrow {}^6A_1(^6S)$; 637, ^{3}LC. PLE (solid, r.t., $\lambda_{emission}$ = 525 nm, nm): < 350 ligands excitation and $^4F \leftarrow {}^6A_1(^6S)$; 345-480 $^4P,^4D,^4G \leftarrow {}^6A_1(^6S)$. PLE (solid, r.t., $\lambda_{emission}$ = 630 nm, nm): < 350 ligands excitation and $^4F \leftarrow {}^6A_1(^6S)$; 345-480 $^4P,^4D,^4G \leftarrow {}^6A_1(^6S)$. τ (solid, r.t., $\lambda_{excitation}$ = 290 nm, $\lambda_{emission}$ = 625 nm, μs): 331. Φ (solid, r.t., $\lambda_{excitation}$ = 310 nm): 19%.

Characterization of $[MnBr_2(BPPO)_2]_n$. Anal. calcd for $C_{24}H_{18}Br_2MnO_6P_2$ (590.18 g mol^{-1}, %): C, 42.45; H, 2.67; Br, 23.53. Found (%): C, 42.28; H, 2.68; Br, 23.44. M.p. >230°C. χ_M^{corr} (c.g.s.u.): $1.56 \cdot 10^{-2}$. IR (cm^{-1}): 3070-2980 w (aromatic ν_{C-H}), 2445 m (ν_{P-H}), 1610-1570 w (aromatic ν_{C-C}), 1235-1180 s ($\nu_{P=O}$ and ν_{C-O}), 1046 w (ν_{P-O}). UV-VIS (ACN, r.t., nm): < 310, 244 (max), 265 (sh). PL (solid, r.t., $\lambda_{excitation}$ = 350 nm, nm): 531, $^4T_1(^4G) \rightarrow {}^6A_1(^6S)$; 625, ^{3}LC. PL (solid, r.t., $\lambda_{excitation}$ = 430 nm, nm): 539, $^4T_1(^4G) \rightarrow {}^6A_1(^6S)$; 617, ^{3}LC. PLE (solid, r.t., $\lambda_{emission}$ = 525 nm, nm): < 340 ligands and $^4F \leftarrow {}^6A_1(^6S)$; 345-470 $^4P,^4D,^4G \leftarrow {}^6A_1(^6S)$. PLE (solid, r.t., $\lambda_{emission}$ = 630 nm, nm): < 340 ligands and $^4F \leftarrow {}^6A_1(^6S)$; 345-415 $^4P,^4D \leftarrow {}^6A_1(^6S)$; 415-480 $^4G \leftarrow {}^6A_1(^6S)$. τ (solid, r.t., $\lambda_{excitation}$ = 290 nm, $\lambda_{emission}$ = 630 nm, μs): 563. Φ (solid, r.t., $\lambda_{excitation}$ = 310 nm): 15%.

Characterization of $[MnI_2(BPPO)_2]_n$. Anal. calcd for $C_{24}H_{18}I_2MnO_6P_2$ (773.79 g mol^{-1}, %): C, 37.29; H, 2.35; I, 32.83. Found (%): C, 37.14; H, 2.34; I, 32.70. M.p. 70°C (dec.). χ_M^{corr} (c.g.s.u.): $1.42 \cdot 10^{-2}$. IR (cm^{-1}): 3070-2980 w (aromatic ν_{C-H}), 2470 m (ν_{P-H}), 1610-1570 w (aromatic ν_{C-C}), 1260-1180 s ($\nu_{P=O}$ and ν_{C-O}), 1047 w (ν_{P-O}). UV-VIS (ACN, r.t., nm): < 300, 246 (max), 268 (sh). PL (solid, r.t., $\lambda_{excitation}$ = 350 nm, nm): 538, $^4T_1(^4G) \rightarrow {}^6A_1(^6S)$; 630, ^{3}LC. PL (solid, r.t., $\lambda_{excitation}$ = 430 nm, nm): 540, $^4T_1(^4G) \rightarrow {}^6A_1(^6S)$; 638, ^{3}LC. PLE (solid, r.t., $\lambda_{emission}$ = 525 nm, nm): < 340 ligands and $^4F \leftarrow {}^6A_1(^6S)$; 345-415 $^4P,^4D \leftarrow {}^6A_1(^6S)$; 415-480 $^4G \leftarrow {}^6A_1(^6S)$. PLE (solid, r.t., $\lambda_{emission}$ = 630 nm, nm): < 340 ligands and $^4F \leftarrow {}^6A_1(^6S)$; 345-415 $^4P,^4D \leftarrow {}^6A_1(^6S)$; 415-480 $^4G \leftarrow {}^6A_1(^6S)$. τ (solid, r.t., $\lambda_{excitation}$ = 290 nm, $\lambda_{emission}$ = 625 nm, μs): 563. Φ (solid, r.t., $\lambda_{excitation}$ = 310 nm): 16%.

2.7.1.7 Synthesis of [MnX$_2$(BPPP)$_2$] and [MnX$_2${O=PPh(R/S-BINOL)}$_2$], BPPP = 6-phenyldibenzo[*d,f*][1,3,2]dioxaphosphepine 6-oxide and O=PPh(R/S-BINOL) = (4R/S)-4-phenyldinaphtho[2,1-*d*:1',2'-*f*][1,3,2]dioxaphosphepine 4-oxide, X = Cl, Br, I

The syntheses were carried out following the procedure described above for [MnX$_2${O=P(MeNCH$_2$CH$_2$NMe)Ph}$_2$]. [MnI$_2$(BPPP)$_2$] was synthesized using acetonitrile as solvent instead of ethanol. [MnI$_2${O=PPh(R/S-BINOL)}$_2$] precipitates from hexane, while the corresponding chloro- and bromo-derivatives were filtered from diethyl ether. Yield > 80% in all the cases.

Characterization of [MnCl$_2$(BPPP)$_2$]. Anal. calcd for $C_{36}H_{26}Cl_2MnO_6P_2$ (724.38 g mol^{-1}, %): C, 58.24; H, 3.53; Cl, 9.55. Found (%): C, 58.01; H, 3.54; I, 9.51. M.p. 70°C (dec.). χ_M^{corr} (c.g.s.u.): $1.54 \cdot 10^{-2}$. IR (cm^{-1}): 3060-2980 w (aromatic ν_{C-H}), 1610-1570 w (aromatic ν_{C-C}), 1265-1180 s ($\nu_{P=O}$ and ν_{C-O}), 1040 w (ν_{P-O}). UV-VIS (CH_2Cl_2, r.t., nm): < 315, 245 (max), 270 (sh). PL (solid, r.t., $\lambda_{excitation}$ = 350 nm, nm): 643, ^{3}LC. PL (solid, r.t., $\lambda_{excitation}$ = 430 nm, nm): 537, $^4T_1(^4G) \rightarrow {}^6A_1(^6S)$; 640, ^{3}LC. PLE (solid, r.t., $\lambda_{emission}$ = 525 nm, nm): < 345 ligands and $^4F \leftarrow {}^6A_1(^6S)$; 415-470 $^4G \leftarrow {}^6A_1(^6S)$. PLE (solid, r.t., $\lambda_{emission}$ = 630 nm, nm): < 340 ligands and $^4F \leftarrow {}^6A_1(^6S)$; 345-415 $^4P,^4D \leftarrow {}^6A_1(^6S)$; 415-470 $^4G \leftarrow {}^6A_1(^6S)$. τ (solid, r.t., $\lambda_{excitation}$ = 265 nm, $\lambda_{emission}$ = 630 nm, μs): 1214. Φ (solid, r.t., $\lambda_{excitation}$ = 365 nm): 5%.

Characterization of [MnBr$_2$(BPPP)$_2$]. Anal. calcd for $C_{36}H_{26}Br_2MnO_6P_2$ (831.28 g mol^{-1}, %): C, 52.01; H, 3.15; Br, 19.22. Found (%): C, 51.80; H, 3.16; I, 19.14. M.p. 70°C (dec.). χ_M^{corr} (c.g.s.u.): $1.57 \cdot 10^{-2}$. IR (cm^{-1}): 3060-2980 w (aromatic ν_{C-H}), 1610-1570 w (aromatic ν_{C-C}), 1270-1180 s ($\nu_{P=O}$ and ν_{C-O}), 1045 w (ν_{P-O}). UV-VIS (CH_2Cl_2, r.t., nm): < 300, 245 (max), 270 (sh). PL (solid, r.t., $\lambda_{excitation}$ = 350 nm, nm): 540, $^4T_1(^4G) \rightarrow {}^6A_1(^6S)$; 625, ^{3}LC. PL (solid, r.t., $\lambda_{excitation}$ = 430 nm, nm): 538, $^4T_1(^4G) \rightarrow$

$^6A_1(^6S)$; 627, ^{3}LC. PLE (solid, r.t., $\lambda_{emission}$ = 525 nm, nm): < 340 ligands and $^4F \leftarrow {}^6A_1(^6S)$; 345-405 $^4P,^4D \leftarrow {}^6A_1(^6S)$; 410-470 $^4G \leftarrow {}^6A_1(^6S)$. PLE (solid, r.t., $\lambda_{emission}$ = 630 nm, nm): < 340 ligands and $^4F \leftarrow {}^6A_1(^6S)$; 345-415 $^4P,^4D \leftarrow {}^6A_1(^6S)$; 415-470 $^4G \leftarrow {}^6A_1(^6S)$. τ (solid, r.t., $\lambda_{excitation}$ = 265 nm, $\lambda_{emission}$ = 525 nm, μs): 141. τ (solid, r.t., $\lambda_{excitation}$ = 265 nm, $\lambda_{emission}$ = 630 nm, μs): 637. Φ (solid, r.t., $\lambda_{excitation}$ = 365 nm): 8%.

Characterization of [MnI$_2$(BPPP)$_2$]. Anal. calcd for $C_{36}H_{26}I_2MnO_6P_2$ (925.29 g mol^{-1}, %): C, 46.73; H, 2.83; I, 27.43. Found (%): C, 46.54; H, 2.82; I, 27.32. M.p. 100°C (dec.). χ_M^{corr} (c.g.s.u.): $1.47 \cdot 10^{-2}$. IR (cm^{-1}): 3060-2975 w (aromatic ν_{C-H}), 1610-1570 w (aromatic ν_{C-C}), 1270-1170 s ($\nu_{P=O}$ and ν_{C-O}), 1045 w (ν_{P-O}). UV-VIS (CH_2Cl_2, r.t., nm): < 320, 245 (max), 270 (sh), 290 (sh). PL (solid, r.t., $\lambda_{excitation}$ = 350 nm, nm): 540, $^4T_1(^4G) \rightarrow {}^6A_1(^6S)$; 625, ^{3}LC. PL (solid, r.t., $\lambda_{excitation}$ = 430 nm, nm): 536, $^4T_1(^4G) \rightarrow {}^6A_1(^6S)$; 618, ^{3}LC. PLE (solid, r.t., $\lambda_{emission}$ = 525 nm, nm): < 340 ligands and $^4F \leftarrow {}^6A_1(^6S)$; 345-410 $^4P,^4D \leftarrow {}^6A_1(^6S)$; 415-470 $^4G \leftarrow {}^6A_1(^6S)$. PLE (solid, r.t., $\lambda_{emission}$ = 610 nm, nm): < 345 ligands and $^4F \leftarrow {}^6A_1(^6S)$; 350-410 $^4P,^4D \leftarrow {}^6A_1(^6S)$; 415-510 $^4G \leftarrow {}^6A_1(^6S)$. τ (solid, r.t., $\lambda_{excitation}$ = 290 nm, $\lambda_{emission}$ = 525 nm, μs): 19. τ (solid, r.t., $\lambda_{excitation}$ = 290 nm, $\lambda_{emission}$ = 610 nm, μs): 174. Φ (solid, r.t., $\lambda_{excitation}$ = 365 nm): 2%.

Characterization of [MnCl$_2${O=PPh(R/S-BINOL)}$_2$]. Anal. calcd for $C_{52}H_{34}Cl_2MnO_6P_2$ (941.84 g mol^{-1}, %): C, 66.26; H, 3.64; Cl, 7.52. Found (%): C, 66.01; H, 3.65; Br, 15.37. M.p. 160°C. χ_M^{corr} (c.g.s.u.): $1.39 \cdot 10^{-2}$. IR (cm^{-1}): 3070-2980 w (aromatic ν_{C-H}), 1620-1590 w (aromatic ν_{C-C}), 1290-1190 s ($\nu_{P=O}$ and ν_{C-O}). UV-VIS (CH_2Cl_2, r.t., nm): < 345, 267 (sh), 273 (sh), 292 (max), 305 (sh), 316 (sh), 323 (sh). PL (solid, r.t., $\lambda_{excitation}$ = 350 nm, nm): 395, ^{1}LC; 650, ^{3}LC. PLE (solid, r.t., $\lambda_{emission}$ = 650 nm, nm): < 395 ligands and $^4P,^4D,^4F \leftarrow {}^6A_1(^6S)$; 400-460 $^4G \leftarrow {}^6A_1(^6S)$. τ (solid, r.t., $\lambda_{excitation}$ = 290 nm, $\lambda_{emission}$ = 650 nm, μs): 203, 623. Φ (solid, r.t., $\lambda_{excitation}$ = 365 nm): 48%.

Characterization of [MnBr$_2${O=PPh(R/S-BINOL)}$_2$]. Anal. calcd for $C_{52}H_{34}Br_2MnO_6P_2$ (1030.92 g mol^{-1}, %): C, 60.55; H, 3.32; Br, 15.49. Found (%): C, 60.31; H, 3.33; Br, 15.43. M.p. 180°C (dec.). χ_M^{corr} (c.g.s.u.): $1.45 \cdot 10^{-2}$. IR (cm^{-1}): 3070-2970 w (aromatic ν_{C-H}), 1610-1590 w (aromatic ν_{C-C}), 1270-1190 s ($\nu_{P=O}$ and ν_{C-O}). UV-VIS (CH_2Cl_2, r.t., nm): < 340, 264 (sh), 273 (sh), 295 (sh), 304 (max), 315 (sh), 323 (sh). PL (solid, r.t., $\lambda_{excitation}$ = 350 nm, nm): 395, ^{1}LC; 640, ^{3}LC. PLE (solid, r.t., $\lambda_{emission}$ = 640 nm, nm): < 340 ligands and $^4F \leftarrow {}^6A_1(^6S)$; 345-410 $^4P,^4D \leftarrow {}^6A_1(^6S)$; 410-490 $^4G \leftarrow {}^6A_1(^6S)$. τ

(solid, r.t., $\lambda_{excitation}$ = 290 nm, $\lambda_{emission}$ = 640 nm, μs): 207; 512. Φ (solid, r.t., $\lambda_{excitation}$ = 365 nm): 14%.

Characterization of [MnI$_2${O=PPh(R/S-BINOL)}$_2$]. Anal. calcd for $C_{52}H_{34}I_2MnO_6P_2$ (1124.75 g mol^{-1}, %): C, 55.49; H, 3.04; I, 22.55. Found (%): C, 55.27; H, 3.05; I, 22.46. M.p. 65°C (dec.). χ_M^{corr} (c.g.s.u.): 1.49·10^{-2}. IR (cm^{-1}): 3070-2980 w (aromatic ν_{C-H}), 1620-1590 w (aromatic ν_{C-C}), 1270-1130 s ($\nu_{P=O}$ and ν_{C-O}). UV-VIS (CH_2Cl_2, r.t., nm): < 350, 267 (sh), 278 (max), 290 (sh), 315 (sh), 323 (sh), 333 (sh). PL (solid, r.t., $\lambda_{excitation}$ = 350 nm, nm): 395, ^{1}LC; 650, ^{3}LC. PLE (solid, r.t., $\lambda_{emission}$ = 650 nm, nm): < 340 ligands and $^4F \leftarrow {}^6A_1({}^6S)$; 345-405 $^4P,^4D \leftarrow {}^6A_1({}^6S)$; 410-500 $^4G \leftarrow {}^6A_1({}^6S)$. τ (solid, r.t., $\lambda_{excitation}$ = 290 nm, $\lambda_{emission}$ = 650 nm, μs): 85; 329. Φ (solid, r.t., $\lambda_{excitation}$ = 365 nm): 8%.

2.7.1.8 Synthesis of [MnX$_2$(MeDOPOPr)] and [MnX$_2$(EtDOPOSuc)], X = Cl, Br, I

The complexes were synthesized following the same procedure reported for [MnX$_2${μ−O=P(NMe$_2$)$_2$(res)(NMe$_2$)$_2$P=O}]. In the case of EtDOPOSuc, the reaction was performed in dichloromethane/ethanol solutions due to the insolubility of the ligand in alcohols. Yield > 80% in all the cases.

Characterization of [MnCl$_2$(MeDOPOPr)]. Anal. calcd for $C_{28}H_{22}Cl_2MnO_6P_2$ (642.26 g mol^{-1}, %): C, 52.36; H, 3.45; Cl, 11.04. Found (%): C, 52.15; H, 3.46; Cl, 11.01. M.p. 140°C. χ_M^{corr} (c.g.s.u.): 1.60·10^{-2}. IR (cm^{-1}): 3070-2950 w (aromatic ν_{C-H}), 2920-2830 w (ν_{C-H}), 1737 s ($\nu_{C=O}$), 1610-1560 w (aromatic ν_{C-C}), 1275-1200 s ($\nu_{P=O}$ and ν_{C-O}). UV-VIS (CH_2Cl_2, r.t., nm): < 330, 239, 261, 269 (max), 293. PL (solid, r.t., $\lambda_{excitation}$ = 350 nm, nm): 641, ^{3}LC. PLE (solid, r.t., $\lambda_{emission}$ = 630 nm, nm): < 350 ligands and $^4F \leftarrow {}^6A_1({}^6S)$; 355-415 $^4P,^4D \leftarrow {}^6A_1({}^6S)$; 410-470 $^4G \leftarrow {}^6A_1({}^6S)$. τ (solid, r.t., $\lambda_{excitation}$ = 290 nm, $\lambda_{emission}$ = 630 nm, μs): 587. Φ (solid, r.t., $\lambda_{excitation}$ = 310 nm): 15%.

Characterization of [MnBr$_2$(MeDOPOPr)]. Anal. calcd for $C_{28}H_{22}Br_2MnO_6P_2$ (731.17 g mol^{-1}, %): C, 46.00; H, 3.03; Br, 21.86. Found (%): C, 45.82; H, 3.04; Br, 21.77. M.p. 110°C. χ_M^{corr} (c.g.s.u.): 1.51·10^{-2}. IR (cm^{-1}): 3100-2950 w (aromatic ν_{C-H}), 2900-2830 w (ν_{C-H}), 1740 s ($\nu_{C=O}$), 1610-1560 w (aromatic ν_{C-C}), 1270-1150 s ($\nu_{P=O}$ and ν_{C-O}). UV-VIS (CH_2Cl_2, r.t., nm): < 330, 239, 261, 269 (max), 293. PL (solid, r.t., $\lambda_{excitation}$ = 350 nm, nm): 630, ^{3}LC. PLE (solid, r.t., $\lambda_{emission}$ = 550 nm, nm): < 350 ligands and ^{4}F

← $^6A_1(^6S)$; 355-405 $^4P,^4D$ ← $^6A_1(^6S)$; 420-510 ^4G ← $^6A_1(^6S)$. PLE (solid, r.t., $\lambda_{emission}$ = 630 nm, nm): < 350 ligands and ^4F ← $^6A_1(^6S)$; 355-415 $^4P,^4D$ ← $^6A_1(^6S)$; 420-510 ^4G ← $^6A_1(^6S)$. τ (solid, r.t., $\lambda_{excitation}$ = 290 nm, $\lambda_{emission}$ = 550 nm, μs): 324. τ (solid, r.t., $\lambda_{excitation}$ = 290 nm, $\lambda_{emission}$ = 630 nm, μs): 525. Φ (solid, r.t., $\lambda_{excitation}$ = 310 nm): 25%.

Characterization of [MnI$_2$(MeDOPOPr)]. Anal. calcd for $C_{28}H_{22}I_2MnO_6P_2$ (825.17 g mol^{-1}, %): C, 40.76; H, 2.69; I, 30.76. Found (%): C, 40.60; H, 2.70; I, 30.64. M.p. 140°C. χ_M^{corr} (c.g.s.u.): $1.30 \cdot 10^{-2}$. IR (cm^{-1}): 3080-2950 w (aromatic ν_{C-H}), 2905-2830 w (ν_{C-H}), 1741 s ($\nu_{C=O}$), 1610-1560 w (aromatic ν_{C-C}), 1280-1150 s ($\nu_{P=O}$ and ν_{C-O}). UV-VIS (CH_2Cl_2, r.t., nm): < 330, 261, 269 (max), 292. PL (solid, r.t., $\lambda_{excitation}$ = 350 nm, nm): 543, $^4T_1(^4G) \rightarrow {}^6A_1(^6S)$; 626, ^{3}LC. PLE (solid, r.t., $\lambda_{emission}$ = 525 nm, nm): < 350 ligands and ^4F ← $^6A_1(^6S)$; 355-415 $^4P,^4D$ ← $^6A_1(^6S)$; 420-480 ^4G ← $^6A_1(^6S)$. PLE (solid, r.t., $\lambda_{emission}$ = 630 nm, nm): < 350 ligands and ^4F ← $^6A_1(^6S)$; 355-415 $^4P,^4D$ ← $^6A_1(^6S)$; 420-540 ^4G ← $^6A_1(^6S)$. τ (solid, r.t., $\lambda_{excitation}$ = 290 nm, $\lambda_{emission}$ = 520 nm, μs): 15. τ (solid, r.t., $\lambda_{excitation}$ = 290 nm, $\lambda_{emission}$ = 630 nm, μs): 390. Φ (solid, r.t., $\lambda_{excitation}$ = 310 nm): 63%.

Characterization of [MnCl$_2$(EtDOPOSuc)]. Anal. calcd for $C_{32}H_{28}Cl_2MnO_8P_2$ (728.36 g mol^{-1}, %): C, 52.77; H, 3.88; Cl, 9.73. Found (%): C, 52.56; H, 3.90; Cl, 9.69. M.p. 180°C. χ_M^{corr} (c.g.s.u.): $1.42 \cdot 10^{-2}$. IR (cm^{-1}): 3100-2940 w (aromatic ν_{C-H}), 2915-2870 w (ν_{C-H}), 1737 s ($\nu_{C=O}$), 1610-1560 w (aromatic ν_{C-C}), 1280-1150 s ($\nu_{P=O}$ and ν_{C-O}). UV-VIS (CH_2Cl_2, r.t., nm): < 320, 243, 262, 270 (max), 287. PL (solid, r.t., $\lambda_{excitation}$ = 350 nm, nm): 630, ^{3}LC. PLE (solid, r.t., $\lambda_{emission}$ = 630 nm, nm): < 350 ligands and ^4F ← $^6A_1(^6S)$; 355-400 $^4P,^4D$ ← $^6A_1(^6S)$; 405-480 ^4G ← $^6A_1(^6S)$. τ (solid, r.t., $\lambda_{excitation}$ = 290 nm, $\lambda_{emission}$ = 630 nm, μs): 1289. Φ (solid, r.t., $\lambda_{excitation}$ = 310 nm): 19%.

Characterization of [MnBr$_2$(EtDOPOSuc)]. Anal. calcd for $C_{32}H_{28}Br_2MnO_8P_2$ (817.26 g mol^{-1}, %): C, 47.03; H, 3.45; Br, 19.55. Found (%): C, 46.84; H, 3.46; Br, 19.48. M.p. 110°C. χ_M^{corr} (c.g.s.u.): $1.31 \cdot 10^{-2}$. IR (cm^{-1}): 3090-2940 w (aromatic ν_{C-H}), 2910-2860 w (ν_{C-H}), 1738 s ($\nu_{C=O}$), 1610-1560 w (aromatic ν_{C-C}), 1280-1160 s ($\nu_{P=O}$ and ν_{C-O}). UV-VIS (CH_2Cl_2, r.t., nm): < 320, 241, 260, 270 (max), 297. PL (solid, r.t., $\lambda_{excitation}$ = 350 nm, nm): 626, ^{3}LC. PLE (solid, r.t., $\lambda_{emission}$ = 630 nm, nm): < 350 ligands and ^4F ← $^6A_1(^6S)$; 355-400 $^4P,^4D$ ← $^6A_1(^6S)$; 405-500 ^4G ← $^6A_1(^6S)$. τ (solid, r.t., $\lambda_{excitation}$ = 290 nm, $\lambda_{emission}$ = 630 nm, μs): 621. Φ (solid, r.t., $\lambda_{excitation}$ = 310 nm): 33%.

Characterization of [MnI$_2$(EtDOPOSuc)]. Anal. calcd for $C_{32}H_{28}I_2MnO_8P_2$ (911.27 g mol^{-1}, %): C, 42.18; H, 3.18; I, 27.85. Found (%): C, 42.01; H, 3.19; I, 27.74. M.p. 165°C. χ_M^{corr} (c.g.s.u.): $1.30 \cdot 10^{-2}$. IR (cm^{-1}): 3090-2940 w (aromatic ν_{C-H}), 2910-2870 w (ν_{C-H}), 1736 s ($\nu_{C=O}$), 1610-1560 w (aromatic ν_{C-C}), 1280-1160 s ($\nu_{P=O}$ and ν_{C-O}). UV-VIS (CH_2Cl_2, r.t., nm): < 320, 261, 270 (max), 296. PL (solid, r.t., $\lambda_{excitation}$ = 350 nm, nm): 550, $^4T_1(^4G) \rightarrow {}^6A_1(^6S)$; 620, ^{3}LC. PLE (solid, r.t., $\lambda_{emission}$ = 525 nm, nm): < 350 ligands and $^4F \leftarrow {}^6A_1(^6S)$; 360-420 $^4P,^4D \leftarrow {}^6A_1(^6S)$; 430-480 $^4G \leftarrow {}^6A_1(^6S)$. PLE (solid, r.t., $\lambda_{emission}$ = 630 nm, nm): < 350 ligands and $^4F \leftarrow {}^6A_1(^6S)$; 360-420 $^4P,^4D \leftarrow {}^6A_1(^6S)$; 425-540 $^4G \leftarrow {}^6A_1(^6S)$. τ (solid, r.t., $\lambda_{excitation}$ = 290 nm, $\lambda_{emission}$ = 530 nm, μs): 15. τ (solid, r.t., $\lambda_{excitation}$ = 290 nm, $\lambda_{emission}$ = 620 nm, μs): 352. Φ (solid, r.t., $\lambda_{excitation}$ = 310 nm): 51%.

2.7.1.9 Synthesis of [Mn(MeDOPOPr)$_3$][ClO$_4$]$_2$ and [Mn(EtDOPOSuc)$_3$][ClO$_4$]$_2$

The complexes were prepared by dissolving 0.362 g (1.0 mmol) of $Mn(ClO_4)_2 \cdot 6H_2O$ in 20 mL ethanol and 3.2 mmol of the chosen ligand (1.652 g for MeDOPOPr and 1.928 g of EtDOPOSuc) were added. In the case of EtDOPOSuc, 10 mL of dichloromethane were used as co-solvent due to the insolubility of the compound in the reaction medium. After stirring overnight, the solvent was evaporated under reduced pressure and the product was precipitated by adding diethyl ether. The white solid was filtered, washed with 2x15 mL of Et_2O and dried *in vacuo*. Yield > 80% in both the cases.

Characterization of [Mn(MeDOPOPr)$_3$][ClO$_4$]$_2$. Anal. calcd for $C_{84}H_{66}Cl_2MnO_{26}P_6$ (1803.10 g mol^{-1}, %): C, 55.95; H, 3.69; Cl, 3.93. Found (%): C, 55.73; H, 3.70; Cl, 3.91. M.p. 130°C. χ_M^{corr} (c.g.s.u.): $9.04 \cdot 10^{-3}$. Λ_M (acetone, 298 K): 162 ohm^{-1}mol^{-1}cm^2. IR (KBr, cm^{-1}): 3120-2950 w (aromatic ν_{C-H}), 2920-2830 w (ν_{C-H}), 1738 s ($\nu_{C=O}$), 1610-1560 w (aromatic ν_{C-C}), 1280-1040 s ($\nu_{P=O}$ and ν_{ClO4}). UV-VIS (CH_2Cl_2, r.t., nm): < 330, 263 (sh), 268 (max), 280 (sh). PL (solid, r.t., $\lambda_{excitation}$ = 265 nm, nm): 611 (FWHM = 2400 cm^{-1}), $^4T_1(^4G) \rightarrow {}^6A_1(^6S)$. PLE (solid, r.t., $\lambda_{emission}$ = 610 nm, nm): < 390, ligands. τ (solid, r.t., $\lambda_{excitation}$ = 290 nm, $\lambda_{emission}$ = 610 nm, ms): 13.1. Φ (solid, r.t., $\lambda_{excitation}$ = 310 nm): 39%.

Characterization of [Mn(EtDOPOSuc)$_3$][ClO$_4$]$_2$. Anal. calcd for $C_{96}H_{84}Cl_2MnO_{32}P_6$ (2061.40 g mol^{-1}, %): C, 55.94; H, 4.11; Cl, 3.44. Found (%): C, 55.72; H, 4.13; Cl, 3.42. M.p. 138°C. χ_M^{corr} (c.g.s.u.): $1.14 \cdot 10^{-2}$. Λ_M (acetone, 298 K): 187 $ohm^{-1}mol^{-1}cm^2$. IR (KBr, cm^{-1}): 3100-2940 w (aromatic ν_{C-H}), 2910-2830 w (ν_{C-H}), 1734 s ($\nu_{C=O}$), 1610-1560 w (aromatic ν_{C-C}), 1290-1060 s ($\nu_{P=O}$ and ν_{ClO4}). UV-VIS (CH_2Cl_2, r.t., nm): < 330, 263 (sh), 268 (max), 280 (sh). PL (solid, r.t., $\lambda_{excitation}$ = 265 nm, nm): 611 (FWHM = 2500 cm^{-1}), $^4T_1(^4G) \rightarrow {}^6A_1(^6S)$. PLE (solid, r.t., $\lambda_{emission}$ = 610 nm, nm): < 390 ligands. τ (solid, r.t., $\lambda_{excitation}$ = 290 nm, $\lambda_{emission}$ = 610 nm, ms): 14.3. Φ (solid, r.t., $\lambda_{excitation}$ = 310 nm): 67%.

2.7.1.10 Synthesis of $[Mn(bpyO_2)_3][ClO_4]_2$ and $[Mn(NPO_2)_3][ClO_4]_2$

The complex were synthesized by dissolving 0.362 g (1.0 mmol) of $Mn(ClO_4)_2 \cdot 6H_2O$ in the minimum amount of distilled water. In a separate beaker 3.2 mmol of $bpyO_2$ were dissolved in the smallest amount of distilled water. In the case of NPO_2, acetone was used instead of H_2O. This solution was slowly added drop by drop to the previous one. After the complete addition, $[Mn(bpyO_2)_3][ClO_4]_2$ as an orange solid started to separate, that was filtered, washed with 2x15 mL of ethanol and dried *in vacuo*. In the case of $[Mn(NPO_2)_3][ClO_4]_2$, the solvent was evaporated under reduced pressure to afford an oil that was precipitated as yellow solid by adding diethyl ether. Crystals of $[Mn(bpyO_2)_3][ClO_4]_2$ suitable for X-ray diffraction were collected from the slow evaporation of water solutions. Yield > 80% in both the cases.

Characterization of $[Mn(bpyO_2)_3][ClO_4]_2$. Anal. calcd for $C_{30}H_{24}Cl_2MnN_6O_{14}$ (818.39 g mol^{-1}, %): C, 44.03; H, 2.96; N, 10.27; Cl, 8.66. Found (%): C, 43.85; H, 2.97; N, 10.31; Cl, 8.63. M.p. > 230°C. χ_M^{corr} (c.g.s.u.): $1.30 \cdot 10^{-2}$. Λ_M (acetone, 298 K): 203 $ohm^{-1}mol^{-1}cm^2$. UV-VIS (CH_2Cl_2, r.t., nm): < 500, 243 (max), 269 (sh), 440.

Characterization of $[Mn(NPO_2)_3][ClO_4]_2$. Anal. calcd for $C_{51}H_{42}Cl_2MnN_3O_{14}P_3$ (1139,66 g mol^{-1}, %): C, 53.75; H, 3.71; N, 3.69; Cl, 6.22. Found (%): C, 53.53; H, 3.72; N, 3.70; Cl, 6.20. M.p.: 115°C. χ_M^{corr} (c.g.s.u.): $1.25 \cdot 10^{-2}$. Λ_M (acetone, 298 K): 192 $ohm^{-1}mol^{-1}cm^2$. UV-VIS (CH_2Cl_2, r.t., nm): < 350, 275 (max), 320 (sh).

2.7.2 Copper(I) complexes

2.7.2.1 Synthesis of [Cu(κ^2–BD_4)(DPEphos)]

The synthetic procedure is the same followed to afford Cu(κ^2–BH_4)(DPEphos). 0.100 g of CuCl (1.0 mmol) and 0.543 g of DPEphos (1.0 mmol) were heated at 83 °C under stirring in dichloroethane for one hour. Once the mixture had cooled down to room temperature, a solution of $NaBD_4$ (0.085 g, 2.0 mmol) in ethanol was added dropwise to the previous one. The solution was left stirring at room temperature overnight and the following day the solvent was concentrated under reduced pressure. The product was filtered from ethanol, washed and dried *in vacuo*. The white solid was purified with dichloromethane and precipitated from ethanol. The purified product was filtered, washed with ethanol and dried *in vacuo*. Yield: 60%

Characterization of [Cu(κ^2–BD_4)(DPEphos)]. ^{1}H NMR ($CDCl_3$, 298 K) δ 7.55-7.40 (m, 8H, DPEphos), 7.40-7.27 (m, 12H, DPEphos), 7.21 (td, 2H, $^3J_{HH}$ = 7.8 Hz, $^4J_{HH}$ = 1.4 Hz, DPEphos), 6.95-6.85 (m, 4H, DPEphos), 6.78-6.69 (m, 2H, DPEphos). ^{31}P{^{1}H} NMR ($CDCl_3$, 298 K) δ -15.44 (FWHM = 42 Hz). ^{11}B NMR ($CDCl_3$, 298 K) δ -32.37 (FWHM = 144 Hz). IR (KBr, cm^{-1}): 3070-3000 w (aromatic $\nu_{C\text{-}H}$), 1680-1560 m (aromatic $\nu_{C\text{-}C}$), 1807 m, 1740 m ($\nu_{B\text{-}D}$). PL (solid, r.t., $\lambda_{excitation}$ = 290 nm, nm): 465. PLE (solid, r.t., $\lambda_{emission}$ = 470 nm, nm): < 390. τ (r.t., $\lambda_{excitation}$ = 373 nm, $\lambda_{emission}$ = 470 nm, ns): 4.5. Φ (solid, r.t., $\lambda_{excitation}$ = 365 nm): 12%.

2.7.2.2 Synthesis of [Cu_2(μ–BH_4)($DPEphos)_2$][OTf]

The complex was synthesized on the basis of a reported procedure.[140] [Cu(κ^2–BH_4)(DPEphos)] (0.617 g, 1.0 mmol) was dissolved in 20 mL dichloromethane. The solution was put under nitrogen atmosphere and frozen with a liquid nitrogen bath. Trifluoromethanesulfonic acid (HOTf, 44 μL, 0.5 mmol) was added with a microsyringe and the mixture was allowed to warm at room temperature under stirring. After 30 minutes the solvent was evaporated under reduced pressure and the product was precipitated by addition of 10 mL of diethyl ether. The white solid was filtered, washed with diethyl ether and dried *in vacuo*. Yield: 60%.

Characterization of [Cu_2(μ-BH_4)($DPEphos)_2$][OTf]. Anal. calcd for (1219.07 g mol^{-1}, %): C, 70.94; H, 4.96. Found (%): C, 70.66; H, 4.98. M.p. > 503 K (dec.). TGA mass loss > 620 K. Λ_M (acetone, 298 K): 124 ohm^{-1}mol^{-1}cm^2. ^{1}H NMR ($CDCl_3$, 298 K) δ

7.55-7.20 (m, 22H, DPEphos), 6.99 (t, 2H, $^3J_{HH}$ = 7.5 Hz, DPEphos), 6.89 (m, 2H, DPEphos), 6.78-6.71 (m, 2H, DPEphos), 1.87 (quart, 4H, $^1J_{BH}$ = 76 Hz, BH_4). $^{31}P\{^1H\}$ NMR ($CDCl_3$, 298 K) δ -13.96 (FWHM = 112 Hz). ^{11}B NMR ($CDCl_3$, 298 K) δ -30.38 (quint, $^1J_{BH}$ = 76 Hz). ^{19}F NMR ($CDCl_3$, 298 K) δ -77.78 (FWHM = 13 Hz). IR (KBr, cm^{-1}): 3070-3005 w (aromatic $\nu_{C\text{-}H}$), 2121 m ($\nu_{B\text{-}H,bridging}$), 1590-1560 m/w (aromatic $\nu_{C\text{-}C}$), 1030 m ($\nu_{S=O}$). PL (solid, r.t., $\lambda_{excitation}$ = 350 nm, nm): 476. PLE (solid, r.t., $\lambda_{emission}$ = 470 nm, nm): < 390. τ (r.t., $\lambda_{excitation}$ = 373 nm, $\lambda_{emission}$ = 470 nm, ns): 5.0. Φ (solid, r.t., $\lambda_{excitation}$ = 365 nm): 14%.

2.7.2.3 Synthesis of $[Cu\{CHPh(btz)_2\}(PP)][BF_4]$ [PP = $(PPh_3)_2$, DPEphos]

Bis(benzotriazolyl)phenylmethane (0.490 g, 1.5 mmol) was first protonated with $HBF_4 \cdot Et_2O$ (0.4 mL, 3.0 mmol) to afford the corresponding salt in 15 mL of dichloromethane. The solvent was evaporated under reduced pressure and the product was used as an oil. 1.0 mmol of the corresponding $[Cu(BH_4)(PP)]$ precursor was added and the reagents were put under inert atmosphere and cooled at 77 K with a liquid nitrogen bath. Dichloromethane (20 mL) was then slowly added through a syringe and the reaction mixture was allowed to slowly warm up to room temperature. After stirring overnight, the solution was purified by filtration and dichloromethane was evaporated under reduced pressure. The addition of diethyl ether (20 mL) caused the separation of a solid, that was filtered, washed with 5 mL of diethyl ether and dried *in vacuo*. Yield > 75% in all the cases.

Characterization of $[Cu\{CHPh(btz)_2\}(PPh_3)_2][BF_4]$. Anal. calcd for (1001.29 g mol^{-1}, %): C, 65.97; H, 4.43; N, 8.39. Found (%): C, 65.70; H, 4.45; N, 8.36. M.p. 105°C (dec.). Λ_M (acetone, 298 K): 142 $ohm^{-1}mol^{-1}cm^2$. ^1H NMR ($CDCl_3$, 298 K) δ 9.17 (s, 1H, CH; ^{13}C HSQC 65.86), 8.40-8.00 (m, 4H, btz), 7.90-6.95 (m, 35H, Ph and PPh_3). $^{31}P\{^1H\}$ NMR ($CDCl_3$, 208 K) δ 0.08 (FWHM = 115 Hz). IR (KBr, cm^{-1}): 3100-3040 m/w (aromatic $\nu_{C\text{-}H}$), 2980-2850 m/w ($\nu_{C\text{-}H}$), 1600-1570 m (aromatic $\nu_{C\text{-}C}$ and $\nu_{C\text{-}N}$), 1170-1000 s (ν_{BF4}). UV-VIS (CH_2Cl_2, r.t., nm): < 310, 255 (max), 262 (sh), 274 (sh). PL (solid, r.t., $\lambda_{excitation}$ = 375 nm, nm): 565 (FWHM = 4100 cm^{-1}). PLE (solid, r.t., $\lambda_{emission}$ = 586 nm, nm): < 460. τ (solid, r.t., $\lambda_{excitation}$ = 377 nm, $\lambda_{emission}$ = 565 nm, μs): < 0.5, ≈ 30 (slow component).

Characterization of [Cu{CHPh(btz)$_2$}(DPEphos)][BF$_4$]. Anal. calcd for (1015.26 g mol^{-1}, %): C, 65.07; H, 4.17; N, 8.28. Found (%): C, 64.81; H, 4.19; N, 8.25. M.p. 160°C (dec. > 230°C). Λ_M (acetone, 298 K): 169 ohm^{-1}mol^{-1}cm^2. ^{1}H NMR (CDCl$_3$, 298 K) δ 9.06 (s, 1H, CH), 7.80-6.50 (m, br, 41H, btz and Ph and DPEphos). ^{31}P{^{1}H} NMR (CDCl$_3$, 298 K) δ -15.45 (FWHM = 94 Hz). IR (KBr, cm^{-1}): 3100-3060 m/w (aromatic ν_{C-H}), 2970-2850 m/w (ν_{C-H}), 1610-1570 m/s (aromatic ν_{C-C} and ν_{C-N}), 1160-1000 m (ν_{BF4}). UV-VIS (CH$_2$Cl$_2$, r.t., nm): < 400, 260 (max), 270 (sh). PL (solid, r.t., $\lambda_{excitation}$ = 375 nm, nm): 555 (FWHM = 4100 cm^{-1}). PLE (solid, r.t., $\lambda_{emission}$ = 600 nm, nm): < 460. τ (solid, r.t., $\lambda_{excitation}$ = 377 nm, $\lambda_{emission}$ = 575 nm, μs): < 0.5, ≈ 40 (slow component).

2.7.2.4 Synthesis of [Cu{CH(btz)$_3$}(PR$_3$)][BF$_4$], PR$_3$ = PPh$_3$, P^{i}Pr$_3$

0.472 g of [Cu(NCCH$_3$)$_4$][BF$_4$] (1.5 mmol) were dissolved in 20 mL of dry dichloromethane inside the glove box. A stoichiometric amount of phosphine was added to the solution and the blueish mixture was stirred at room temperature for 4 hours. After that time, 0.476 g (1.5 mmol) of CH(btz)$_3$ were added and the solution was left stirring overnight. The solvent was then evaporated under reduced pressure and, after adding diethyl ether, the solid was filtered, washed and dried *in vacuo*. Yield > 50 %.

Characterization of [Cu{CH(btz)$_3$}(PPh$_3$)][BF$_4$]. Anal. calcd for (780.02 g mol^{-1}, %): C, 51.72; H, 3.26; N, 14.54. Found (%): C, 51.26; H, 3.23; N, 14.48. Λ_M (acetone, 298 K): 126 ohm^{-1}mol^{-1}cm^2. M.p. 175°C (dec. > 180°C). ^{1}H NMR (CDCl$_3$, 298 K) δ 10.64 (s, 1H, br, CH), 7.75 (d, 3H, br, btz), 7.45-7.15 (m, 15H, br, phosphine), 6.67 (t, 3H, br, btz), 6.42 (t, 3H, br, btz), 6.06 (d, br). ^{31}P{^{1}H} NMR (DMSO-d$_6$, 298 K) δ 2.74. IR (KBr, cm^{-1}): 3100-3005 m/w (aromatic ν_{C-H}), 2970-2850 m/w (ν_{C-H}), 1630-1560 m (aromatic ν_{C-C} and ν_{C-N}), 1170-1000 s (ν_{BF4}). UV-VIS (CH$_2$Cl$_2$, r.t., nm): < 375, 262 (max), 269 (sh). PL (solid, r.t., $\lambda_{excitation}$ = 375 nm, nm): 582 (FWHM = 4200 cm^{-1}). PLE (solid, $\lambda_{emission}$ = 600 nm, nm): < 500. τ (solid, r.t., $\lambda_{excitation}$ = 460 nm, $\lambda_{emission}$ = 600 nm, μs): < 0.5, ≈ 140 (slow component).

Characterization of [Cu{CH(btz)$_3$}(P^{i}Pr$_3$)][BF$_4$]. Anal. calcd for (677.97 g mol^{-1}, %): C, 49.61; H, 5.06; N, 18.59. Found (%): C, 49.41; H, 5.08; N, 18.52. Λ_M (acetone, 298 K): 162 ohm^{-1}mol^{-1}cm^2. M.p. 140°C (dec.). ^{1}H NMR (CDCl$_3$, 313 K) δ 10.59 (s, 1H, CH), 8.64 (s, 3H, br, btz), 8.10 (d, 3H, $^3J_{HH}$ = 8.0 Hz, btz), 7.84 (t, 3H, $^3J_{HH}$ = 8.0 Hz, btz), 7.54 (t, 3H, $^3J_{HH}$ = 8.0 Hz, btz), 2.38 (m, 3H, CH-phosphine), 1.44 (m, 18H, CH_3-phosphine). $^{31}P\{^1H\}$ NMR ($CDCl_3$, 298 K) δ 37.57 (FWHM = 360 Hz, br). IR (KBr, cm^{-1}): 3100-3010 m/w (aromatic $\nu_{C\text{-}H}$), 2970-2850 m/w ($\nu_{C\text{-}H}$), 1640-1590 m (aromatic $\nu_{C\text{-}C}$ and $\nu_{C\text{-}N}$), 1250-1150 s (ν_{BF4}). UV-VIS (CH_2Cl_2, r.t., nm): < 375, 257 (sh), 262 (max), 279 (sh). PL (solid, r.t., $\lambda_{excitation}$ = 375 nm, nm): 599 (FWHM = 4100 cm^{-1}). PLE (solid, $\lambda_{emission}$ = 630 nm, nm): < 500. τ (solid, r.t., $\lambda_{excitation}$ = 460 nm, $\lambda_{emission}$ = 630 nm, μs): < 0.5, ≈ 120 (slow component).

2.7.2.5 Synthesis of $[Cu\{CHPh(ind)_2\}_2][X]$ (X = BF_4, Cl)

To a solution containing 1.5 mmol of $[Cu(NCCH_3)_4][BF_4]$ (0.472 g) in 50 mL of dichloromethane, the ligand $CHPh(ind)_2$ (0.973 g, 3.0 mmol) was added and the mixture was stirred inside the glove box overnight. The solid that slowly separated from CH_2Cl_2 was then filtered, washed with dichloromethane (10 mL) and dried *in vacuo*. Yield: 80%.

Characterization of $[Cu\{CHPh(ind)_2\}_2][BF_4]$. Anal. calcd for $C_{42}H_{32}BCuF_4N_8$ (799.11 g mol^{-1}, %): C, 63.13; H, 4.04; N, 14.02. Found (%): C, 62.88; H, 4.06; N, 13.96. M.p. 235°C (dec.). Λ_M (CH_3NO_2, 298 K): 113 $ohm^{-1}mol^{-1}cm^2$. ^1H NMR (DMSO-d_6, 298 K) δ 9.23 (s, br, 1H, CH), 8.18 (s, br, 2H, ind), 8.00-7.70 (m, br, 4H, arom), 7.70-7.15 (m, 7H, arom), 6.78 (m, br, 2H, arom). ^1H NMR (DMSO-d_6, 338 K) δ 8.99 (s, 1H, CH), 8.04 (s, 2H, ind), 7.94 (d, 2H, $^3J_{HH}$ = 8.6 Hz, ind), 7.82 (d, 2H, $^3J_{HH}$ = 8.0 Hz, ind), 7.55-7.40 (m, 5H, arom), 7.24 (t, 2H, $^3J_{HH}$ = 7.7 Hz, arom), 6.97 (m, br, 2H, arom). IR (KBr, cm^{-1}): 3050-3030 m/w (aromatic $\nu_{C\text{-}H}$), 2980-2850 m/w ($\nu_{C\text{-}H}$); 1620-1550 m (aromatic $\nu_{C\text{-}C}$ and $\nu_{C\text{-}N}$); 1180-1050 s (ν_{BF4}). UV-VIS (DMSO, r.t., nm): < 410, 291 (max), 298 (sh), 311 (sh). PL (solid, r.t., $\lambda_{excitation}$ = 375 nm, nm): 565 (FWHM = 4600 cm^{-1}). PLE (solid, $\lambda_{emission}$ = 600 nm, nm): < 450, 389 (max).

The same complex with a different counterion was obtained from the reaction between CuCl and twice the amount of $CHPh(ind)_2$. Yield 75%. The characterization of the product is reported below for completeness. Crystals suitable for X-ray diffraction were obtained by slow evaporation of dichloromethane solutions.

Characterization of $[Cu\{CHPh(ind)_2\}_2]Cl$. Anal. calcd for $C_{42}H_{32}ClCuN_8$ (747.76 g mol^{-1}, %): C, 67.46; H, 4.31; N, 14.99; Cl, 4.74. Found (%): C, 67.19; H, 4.33; N, 15.05; Cl, 4.72. M.p. 155°C (dec.). Λ_M (acetone, 298 K): 148 $ohm^{-1}mol^{-1}cm^2$. ^1H NMR

(DMSO-d_6, 298 K) δ 9.19 (s, br, 1H, CH), 8.12 (s, br, 2H, ind), 7.94 (s, br, 2H, arom), 7.83 (d, 2H, $^3J_{HH}$ = 8.1 Hz, arom), 7.57 (m, br, 2H, arom), 7.45 (m, 3H, arom), 7.28 (t, 2H, $^3J_{HH}$ = 7.6 Hz, arom), 6.82 (s, br, 2H, arom). ^{1}H NMR ($CDCl_3$, 213 K) δ 8.57 (s, br, 1H, CH), 8.17 (s, br, 2H, arom), 7.78 (m, br, 2H, arom), 7.56 (s, br, 2H, arom), 7.41 (m, br, 3H, arom), 7.23 (s, br, 2H, arom), 7.11 (s, br, 2H, arom), 6.61 (s, br, 2H, arom). IR (KBr, cm^{-1}): 3060-3030 m/w (aromatic ν_{C-H}), 2970-2850 m/w (ν_{C-H}), 1615-1520 m (aromatic ν_{C-C} and ν_{C-N}). UV-VIS (CH_2Cl_2, r.t., nm): < 410, 288 (max), 329 (sh). PL (solid, r.t., $\lambda_{excitation}$ = 375 nm, nm): 565 (FWHM = 4600 cm^{-1}). PLE (solid, $\lambda_{emission}$ = 600 nm, nm): < 450, 389 (max). τ (solid, r.t., $\lambda_{excitation}$ = 317 nm, $\lambda_{emission}$ = 635 nm, μs): 12 (63%), 73 (37%).

2.7.2.6 Synthesis of [CuL(PPh$_3$)$_2$][BF$_4$], L = py-btz, pym-btz, trz^{OR}-btz (R = Me, Et, Ph)

The compounds were prepared following the procedure above described for [Cu{CHPh(btz)$_2$}(PPh$_3$)$_2$][BF$_4$]. Crystal suitable for X-ray diffraction were obtained from dichloromethane/diethyl ether and dichloromethane/ethanol solutions respectively for [Cu(py-btz)(PPh$_3$)$_2$][BF$_4$] and [Cu(pym-btz)(PPh$_3$)$_2$][BF$_4$]. Yield > 70% in all the cases.

Characterization of [Cu(py-btz)(PPh$_3$)$_2$][BF$_4$]. Anal. calcd for $C_{47}H_{38}BCuF_4N_4P_2$ (871.15 g mol^{-1}, %): C, 64.80; H, 4.40; N, 6.43. Found (%): C, 64.54; H, 4.42; N, 6.40. M.p. 195°C (dec.). Λ_M (acetone, 298 K): 166 ohm^{-1}mol^{-1}cm^2. ^{1}H NMR ($CDCl_3$, 233 K) δ 8.55 (t, 1H, $^3J_{HH}$ = 7.7 Hz, py), 8.46 (d, 1H, $^3J_{HH}$ = 8.4 Hz, py), 8.34 (d, 1H, $^3J_{HH}$ = 8.6 Hz, btz), 8.08 (d, 1H, $^3J_{HH}$ = 8.5 Hz, btz), 8.04 (d, 1H, $^3J_{HH}$ = 4.8 Hz, py), 7.87 (t, 1H, $^3J_{HH}$ = 8.0 Hz, btz), 7.58 (t, 1H, $^3J_{HH}$ = 7.6 Hz, btz), 7.43 (t, 1H, J_{HH} = 6.5 Hz, py), 7.34 (t, 6H, J_{HH} = 7.0 Hz, phosphine), 7.25-7.05 (m, 24H, br, phosphine). ^{31}P{^{1}H} NMR ($CDCl_3$, 298 K) δ 2.40 (FWHM = 98 Hz). IR (KBr, cm^{-1}): 3130-3005 m/w (aromatic ν_{C-H}), 1610-1570 m/s (aromatic ν_{C-C} and ν_{C-N}), 1130-1000 s (ν_{BF4}). UV-VIS (CH_2Cl_2, r.t., nm): < 430, 262 (max), 270 (sh), 285 (sh), 307 (sh), 360 (sh). PL (solid, r.t., $\lambda_{excitation}$ = 375 nm, nm): 538 (FWHM = 4100 cm^{-1}). PLE (solid, r.t., $\lambda_{emission}$ = 535 nm, nm): < 440. τ (solid, r.t., $\lambda_{excitation}$ = 290 nm, $\lambda_{emission}$ = 535 nm, μs): 164. Φ (solid, r.t., $\lambda_{excitation}$ = 365 nm): 26%.

Characterization of [Cu(pym-btz)(PPh$_3$)$_2$][BF$_4$]. Anal. calcd for $C_{46}H_{37}BCuF_4N_5P_2$ (872.13 g mol^{-1}, %): C, 63.35; H, 4.28; N, 8.03. Found (%): C, 63.10; H, 4.30; N, 8.01. M.p. 155°C. Λ_M (acetone, 298 K): 155 ohm^{-1}mol^{-1}cm^2. ^{1}H NMR (CDCl$_3$, 298 K) δ 9.20-7.50 (broad signals, pym and btz), 7.40-7.15 (m, br, PPh$_3$). ^{31}P{^{1}H} NMR (CDCl$_3$, 298 K) δ 3.00 (FWHM = 94 Hz). IR (KBr, cm^{-1}): 3100-3060 m/w (aromatic ν_{C-H}), 1640-1570 m (aromatic ν_{C-C} and ν_{C-N}), 1120-1000 m (ν_{BF4}). UV-VIS (CH$_2$Cl$_2$, r.t., nm): < 450, 263 (max), 310 (sh), 350 (sh). PL (solid, r.t., $\lambda_{excitation}$ = 350 nm, nm): 558 (FWHM = 4100 cm^{-1}). PLE (solid, r.t., $\lambda_{emission}$ = 570 nm, nm): < 500. τ (solid, r.t., $\lambda_{excitation}$ = 445 nm, $\lambda_{emission}$ = 555 nm, μs): 20. Φ (solid, r.t., $\lambda_{excitation}$ = 365 nm): 35%.

Characterization of [Cu(trz^{OMe}-btz)(PPh$_3$)$_2$][BF$_4$]. Anal. calcd for $C_{47}H_{40}BCuF_4N_6O_2P_2$ (933.17 g mol^{-1}, %): C, 60.49; H, 4.32; N, 9.01. Found (%): C, 60.25; H, 4.34; N, 8.97. M.p. 115°C. Λ_M (acetone, 298 K): 165 ohm^{-1}mol^{-1}cm^2. ^{1}H NMR (CDCl$_3$, 243 K) δ 8.48 (d, 1H, $^3J_{HH}$ = 8.4 Hz, btz), 8.15 (d, 1H, $^3J_{HH}$ = 8.4 Hz, btz), 7.89 (t, 1H, $^3J_{HH}$ = 7.7 Hz, btz), 7.66 (t, 1H, $^3J_{HH}$ = 7.7 Hz, btz), 7.40-7.16 (m, br, 30H, PPh$_3$), 4.35 (s, 3H, -CH$_3$), 3.91 (s, 3H, -CH$_3$). ^{31}P{^{1}H} NMR (CDCl$_3$, 298 K) δ 2.89 (FWHM = 97 Hz). IR (KBr, cm^{-1}): 3120-3005 (aromatic ν_{C-H}), 2990-2880 m/w (ν_{CH}), 1620-1545 m (aromatic ν_{C-C} and ν_{C-N}), 1140-980 s (ν_{BF4}). UV-VIS (CH$_2$Cl$_2$, r.t., nm): < 450, 260 (max). PL (solid, r.t., $\lambda_{excitation}$ = 350 nm, nm): 557 (FWHM = 3600 cm^{-1}). PLE (solid, r.t., $\lambda_{emission}$ = 555 nm, nm): < 460. τ (solid, r.t., $\lambda_{excitation}$ = 290 nm, $\lambda_{emission}$ = 555 nm, μs): 32. Φ (solid, r.t., $\lambda_{excitation}$ = 365 nm): 7%.

Characterization of [Cu(trz^{OEt}-btz)(PPh$_3$)$_2$][BF$_4$]. Anal. calcd for $C_{49}H_{44}BCuF_4N_6O_2P_2$ (961.23 g mol^{-1}, %): C, 61.23; H, 4.61; N, 8.74. Found (%): C, 60.59; H, 4.63; N, 8.71. M.p. 185°C. Λ_M (acetone, 298 K): 160 ohm^{-1}mol^{-1}cm^2. ^{1}H NMR (CDCl$_3$, 243 K) δ 8.46 (d, 1H, $^3J_{HH}$ = 8.4 Hz, btz), 8.14 (d, 1H, $^3J_{HH}$ = 8.4 Hz, btz), 7.90 (t, 1H, $^3J_{HH}$ = 7.7 Hz, btz), 7.66 (t, 1H, $^3J_{HH}$ = 7.7 Hz, btz), 7.40-7.15 (m, br, 30H, PPh$_3$), 4.77 (q, 2H, $^3J_{HH}$ = 7.2 Hz, -CH$_2$), 4.39 (q, 2H, $^3J_{HH}$ = 7.1 Hz, -CH$_2$), 1.60 (t, 3H, $^3J_{HH}$ = 7.2 Hz, -CH$_3$), 1.14 (t, 3H, $^3J_{HH}$ = 7.2 Hz, -CH$_3$). ^{31}P{^{1}H} NMR (CDCl$_3$, 298 K) δ 2.57 (FWHM = 84 Hz). IR (KBr, cm^{-1}): 3105-3000 m/w (aromatic ν_{C-H}), 2980-2850 m/w (ν_{C-H}), 1640-1580 m (aromatic ν_{C-C} and ν_{C-N}), 1110-995 s (ν_{BF4}). UV-VIS (CH$_2$Cl$_2$, r.t., nm): < 450, 259 (max), 305 (sh), 350 (sh). PL (solid, r.t., $\lambda_{excitation}$ = 350 nm, nm): 577 (FWHM =

3400 cm^{-1}). PLE (solid, r.t., $\lambda_{emission}$ = 575 nm, nm): < 520. τ (solid, r.t., $\lambda_{excitation}$ = 290 nm, $\lambda_{emission}$ = 575 nm, μs): 5. Φ (solid, r.t., $\lambda_{excitation}$ = 365 nm): 17%.

Characterization of [Cu(trz^{OPh}-btz)(PPh$_3$)$_2$][BF$_4$]. Anal. calcd for $C_{57}H_{44}BCuF_4N_6O_2P_2$ (1057.32 g mol^{-1}, %): C, 64.75; H, 4.19; N, 7.95. Found (%): C, 64.49; H, 4.21; N, 7.92. M.p. 90°C. Λ_M (acetone, 298 K): 149 ohm^{-1}mol^{-1}cm^2. ^{1}H NMR (CDCl$_3$, 243 K) δ 8.14 (d, 1H, $^3J_{HH}$ = 8.3 Hz, btz), 8.10 (d, 1H, $^3J_{HH}$ = 8.1 Hz, btz), 7.80-6.50 (m, 42H, btz, Ph and PPh$_3$). ^{31}P{^{1}H} NMR (CDCl$_3$, 298 K) δ 3.01 (FWHM = 184 Hz). IR (KBr, cm^{-1}): 3105-3010 m/w (aromatic ν_{CH}); 1620-1550 m (aromatic $\nu_{C\text{-}C}$ and $\nu_{C\text{-}N}$); 1115-1000 m (ν_{BF4}). UV-VIS (CH$_2$Cl$_2$, r.t., nm): < 470, 259 (max), 319 (sh), 392. PL (solid, r.t., $\lambda_{excitation}$ = 350 nm, nm): 615 (FWHM = 3700 cm^{-1}). PLE (solid, r.t., $\lambda_{emission}$ = 620 nm, nm): < 500. τ (solid, r.t., $\lambda_{excitation}$ = 445 nm, $\lambda_{emission}$ = 615 nm, μs): 23. Φ (solid, r.t., $\lambda_{excitation}$ = 365 nm): 2%.

2.7.2.7 Synthesis of [CuL(PP)][BF$_4$], L = py-btz, pym-btz, OR-trz-btz (R = Me, Et, Ph); PP = (P^{i}Pr$_3$)$_2$, dppe, DPEphos

The compounds were prepared following the procedure described above for [Cu{CH(btz)$_3$}PR$_3$][BF$_4$]. To a solution containing 0.472 g of [Cu(NCCH$_3$)$_4$][BF$_4$] (1.5 mmol) in 20 mL of dry dichloromethane, 3.0 mmol of triisopropylphosphine (4.81 g of 10% solution in hexane) or 1.5 mmol of dppe (0.598 g) or DPEphos (0.808 g) were added. After 4 hours, 1.5 mmol of the proper ligand were added. After stirring overnight, the solvent was evaporated under reduced pressure. The product was precipitated by addition of diethyl ether and the solid was filtered, washed and dried *in vacuo*. Crystal suitable for X-ray diffraction were isolated from dichloromethane/diethyl ether solutions for [Cu(pym-btz)(P^{i}Pr$_3$)$_2$][BF$_4$], [Cu(pym-btz)(dppe)]$_2$[BF$_4$]$_2$, [Cu(trz^{OMe}-btz)(P^{i}Pr$_3$)$_2$][BF$_4$] and [Cu(trz^{OPh}-btz)(DPEphos)][BF$_4$]. Instead, crystals of [Cu(py-btz)(DPEphos)][BF$_4$] and [Cu(trz^{OEt}-btz)(DPEphos)][BF$_4$] were respectively collected from dichloromethane/ethanol and from the slow evaporation of dichloromethane solutions. Yield > 75% in all the cases.

Characterization of [Cu(py-btz)(P^{i}Pr$_3$)$_2$][BF$_4$]. Anal. calcd for $C_{29}H_{50}BCuF_4N_4P_2$ (667.04 g mol^{-1}, %): C, 52.22; H, 7.56; N, 8.40. Found (%): C, 52.01; H, 7.59; N, 8.37. M.p. 135°C (dec.). Λ_M (acetone, 298 K): 148 ohm^{-1}mol^{-1}cm^2. ^{1}H NMR (CDCl$_3$, 298 K) δ 8.71 (d, 1H, $^3J_{HH}$ = 4.6 Hz, py), 8.60 (d, 1H, $^3J_{HH}$ = 8.3 Hz, btz), 8.36 (d, 1H, $^3J_{HH}$

= 8.5 Hz, py), 8.23 (t, 1H, $^{3}J_{HH}$ = 8.0 Hz, py), 8.19 (d, 1H, $^{3}J_{HH}$ = 8.3 Hz, btz), 7.76 (t, 1H, $^{3}J_{HH}$ = 7.7 Hz, btz), 7.59-7.51 (m, 2H, btz and py), 2.27 (m, br, 3H, CH-phosphine), 1.29 (m, 18H, CH_3-phosphine). $^{31}P\{^{1}H\}$ NMR ($CDCl_3$, 298 K) δ 27.87 (FWHM = 75 Hz). IR (KBr, cm^{-1}): 3110-2870 m/w (aromatic ν_{C-H} and ν_{C-H}), 1640-1560 m (aromatic ν_{C-C} and ν_{C-N}), 1160-1020 m (ν_{BF4}). UV-VIS (CH_2Cl_2, r.t., nm): < 350, 238, 247 (sh), 272 (max), 282 (sh). PL (solid, r.t., $\lambda_{excitation}$ = 350 nm, nm): 575 (FWHM = 3800 cm^{-1}). PLE (solid, r.t., $\lambda_{emission}$ = 575 nm, nm): < 470. τ (solid, r.t., $\lambda_{excitation}$ = 290 nm, $\lambda_{emission}$ = 575 nm, μs): 34. Φ (solid, r.t., $\lambda_{excitation}$ = 365 nm): 10%.

Characterization of [Cu(py-btz)(μ−dppe)]$_2$[BF$_4$]$_2$. Anal. calcd for $C_{74}H_{64}B_2Cu_2F_8N_8P_4$ (1489.98 g mol^{-1}, %): C, 59.65; H, 4.33; N, 7.52. Found (%): C, 59.42; H, 4.35; N, 7.49. M.p. 115°C (dec.). Λ_M (acetone, 298 K): 316 $ohm^{-1}mol^{-1}cm^{2}$. ^{1}H NMR ($CDCl_3$, 213 K) δ 8.76 (d, 1H, $^{3}J_{HH}$ = 8.4 Hz, py), 8.70-8.55 (m, 2H, py and btz), 8.37 (d, 1H, $^{3}J_{HH}$ = 8.2 Hz, btz), 8.05 (d, 1H, $^{3}J_{HH}$ = 5.0 Hz, py), 8.00 (t, 1H, $^{3}J_{HH}$ = 8.1 Hz, btz), 7.73 (t, 1H, $^{3}J_{HH}$ = 7.7 Hz, btz), 7.67-7.13 (m, 21H, btz and Ph), 2.66 (m, 2H, dppe), 2.50 (m, 2H, dppe). $^{31}P\{^{1}H\}$ NMR ($CDCl_3$, 213 K) δ -4.55 (FWHM = 30 Hz). IR (KBr, cm^{-1}): 3070-2850 m/w (aromatic ν_{C-H} and ν_{C-H}), 1640-1560 m (aromatic ν_{C-C} and ν_{C-N}), 1140-1020 m (ν_{BF4}). UV-VIS (CH_2Cl_2, r.t., nm): < 475, 266 (sh), 272, 289 (max), 404. PL (solid, r.t., $\lambda_{excitation}$ = 350 nm, nm): 580 (FWHM = 3800 cm^{-1}). PLE (solid, r.t., $\lambda_{emission}$ = 570 nm, nm): < 450. τ (solid, r.t., $\lambda_{excitation}$ = 290 nm, $\lambda_{emission}$ = 570 nm, μs): 47. Φ (solid, r.t., $\lambda_{excitation}$ = 365 nm): 4%.

Characterization of [Cu(py-btz)(DPEphos)][BF$_4$]. Anal. calcd for $C_{47}H_{36}BCuF_4N_4OP_2$ (885.13 g mol^{-1}, %): C, 63.78; H, 4.10; N, 6.33. Found (%): C, 63.52; H, 4.12; N, 6.31. M.p. 215°C (dec.). Λ_M (acetone, 298 K): 166 $ohm^{-1}mol^{-1}cm^{2}$. ^{1}H NMR ($CDCl_3$, 233 K) δ 8.53 (t, 1H, $^{3}J_{HH}$ = 8.0 Hz, py), 8.47 (d, 1H, $^{3}J_{HH}$ = 8.3 Hz, py), 8.32 (d, 1H, $^{3}J_{HH}$ = 8.6 Hz, btz), 8.02 (d, 1H, $^{3}J_{HH}$ = 8.7 Hz, btz), 7.93 (d, 1H, $^{3}J_{HH}$ = 4.5 Hz, py), 7.82 (t, 1H, $^{3}J_{HH}$ = 7.7 Hz, btz), 7.60-7.55 (m, 30H, br, btz and py and DPEphos). $^{31}P\{^{1}H\}$ NMR ($CDCl_3$, 273 K) δ -11.30 (FWHM = 78 Hz). IR (KBr, cm^{-1}): 3070-3015 m/w (aromatic ν_{C-H}), 1610-1560 m/s (aromatic ν_{C-C} and ν_{C-N}), 1130-1020 s (ν_{BF4}). UV-VIS (CH_2Cl_2, r.t., nm): < 475, 264 (sh), 272 (sh), 288 (max), 380. PL (solid, r.t., $\lambda_{excitation}$ = 350 nm, nm): 561 (FWHM = 3700 cm^{-1}). PLE (solid, r.t., $\lambda_{emission}$ = 570 nm, nm): < 470. τ (solid, r.t., $\lambda_{excitation}$ = 290 nm, $\lambda_{emission}$ = 560 nm, μs): 14. Φ (solid, r.t., $\lambda_{excitation}$ = 365 nm): 13%.

Characterization of [Cu(pym-btz)(P^{i}Pr$_3$)$_2$][BF$_4$]. Anal. calcd for $C_{28}H_{49}BCuF_4N_5P_2$ (668.03 g mol^{-1}, %): C, 50.34; H, 7.39; N, 10.48. Found (%): C, 50.14; H, 7.42; N, 10.44. M.p. 115°C (dec.). Λ_M (acetone, 298 K): 88 ohm^{-1}mol^{-1}cm^2. ^{1}H NMR (CDCl$_3$, 298 K) δ 9.17 (d, 2H, $^3J_{HH}$ = 5.0 Hz, pym), 8.74 (d, 1H, $^3J_{HH}$ = 8.4 Hz, btz), 8.24 (d, 1H, $^3J_{HH}$ = 8.4 Hz, btz), 7.98 (t, 1H, $^3J_{HH}$ = 5.0 Hz, pym), 7.83 (td, 1H, $^3J_{HH}$ = 7.9 Hz, btz), 7.65 (td, 1H, $^3J_{HH}$ = 8.0 Hz, btz), 2.15 (m, br, 3H, CH-phosphine), 1.20 (m, br, 18H, CH$_3$-phosphine). ^{31}P{^{1}H} NMR (CDCl$_3$, 298 K) δ 21.80 (FWHM = 120 Hz). IR (KBr, cm^{-1}): 3100-2870 m/w (aromatic ν_{C-H} and ν_{C-H}), 1640-1570 m (aromatic ν_{C-C} and ν_{C-N}), 1150-1000 m (ν_{BF4}). UV-VIS (CH$_2$Cl$_2$, r.t., nm): < 380, 238 (max), 245 (sh), 261 (sh), 268 (sh), 298. PL (solid, r.t., $\lambda_{excitation}$ = 350 nm, nm): 588 (FWHM = 3600 cm^{-1}). PLE (solid, r.t., $\lambda_{emission}$ = 590 nm, nm): < 475. τ (solid, r.t., $\lambda_{excitation}$ = 445 nm, $\lambda_{emission}$ = 590 nm, μs): 23. Φ (solid, r.t., $\lambda_{excitation}$ = 365 nm): 7%.

Characterization of [Cu(pym-btz)(μ−dppe)]$_2$[BF$_4$]$_2$. Anal. calcd for $C_{72}H_{62}B_2Cu_2F_8N_{10}P_4$ (1491.96 g mol^{-1}, %): C, 57.96; H, 4.19; N, 9.39. Found (%): C, 57.73; H, 4.21; N, 9.35. M.p. 189°C (dec.). Λ_M (acetone, 298 K): 308 ohm^{-1}mol^{-1}cm^2. ^{1}H NMR (CDCl$_3$, 298 K) δ 9.18 (s, 1H, pym), 9.06 (s, 1H, pym), 8.80 (d, 1H, $^3J_{HH}$ = 8.2 Hz,btz), 8.33 (d, 1H, $^3J_{HH}$ = 8.3 Hz, btz), 7.95 (t, 1H, $^3J_{HH}$ = 4.7 Hz, pym), 7.89 (t, 1H, $^3J_{HH}$ = 7.9 Hz, btz), 7.72 (t, 1H, $^3J_{HH}$ = 7.9 Hz, btz), 7.68-7.10 (m, 20H, dppe), 2.71 (m, 2H, dppe), 2.45 (m, 2H, dppe). ^{31}P{^{1}H} NMR (CDCl$_3$, 298 K) δ -3.61 (FWHM = 129 Hz). IR (KBr, cm^{-1}): 3100-3025 m/w (aromatic ν_{C-H}), 2970-2850 w (ν_{C-H}), 1640-1570 m (aromatic ν_{C-C} and ν_{C-N}), 1120-1000 m (ν_{BF4}). UV-VIS (CH$_2$Cl$_2$, r.t., nm): < 475, 267 (sh), 273, 287 (max), 408. PL (solid, r.t., $\lambda_{excitation}$ = 350 nm, nm): 561 (FWHM = 3500 cm^{-1}). PLE (solid, r.t., $\lambda_{emission}$ = 570 nm, nm): < 460. τ (solid, r.t., $\lambda_{excitation}$ = 445 nm, $\lambda_{emission}$ = 560 nm, μs): 23. Φ (solid, r.t., $\lambda_{excitation}$ = 365 nm): 6%.

Characterization of [Cu(pym-btz)(DPEphos)][BF$_4$]. Anal. calcd for $C_{46}H_{35}BCuF_4N_5OP_2$ (886.12 g mol^{-1}, %): C, 62.35; H, 3.98; N, 7.90. Found (%): C, 62.10; H, 4.00; N, 7.87. M.p. > 230°C. Λ_M (acetone, 298 K): 158 ohm^{-1}mol^{-1}cm^2. ^{1}H NMR (CDCl$_3$, 298 K) δ 9.18 (s, br, 1H, pym), 8.60 (d, 1H, $^3J_{HH}$ = 8.2 Hz, btz), 8.38 (s, br, 1H, pym), 8.11 (d, 1H, $^3J_{HH}$ = 8.5 Hz, btz), 7.79 (t, 1H, $^3J_{HH}$ = 7.7 Hz, btz), 7.74 (t, 1H, $^3J_{HH}$ = 5.0 Hz, pym), 7.60 (t, 1H, $^3J_{HH}$ = 7.8 Hz, btz), 7.50-6.80 (m, 28H, br, DPEphos). ^{31}P{^{1}H} NMR (CDCl$_3$, 298 K) δ -11.10 (FWHM = 98 Hz). IR (KBr, cm^{-1}): 3100-3010 m/w (aromatic

$\nu_{C\text{-}H}$), 1640-1570 m (aromatic $\nu_{C\text{-}C}$ and $\nu_{C\text{-}N}$), 1130-1020 m (ν_{BF4}). UV-VIS (CH_2Cl_2, r.t., nm): < 475, 273 (max), 282 (sh), 388. PL (solid, r.t., $\lambda_{excitation}$ = 375 nm, nm): 557 (FWHM = 4200 cm^{-1}). PLE (solid, r.t., $\lambda_{emission}$ = 570 nm, nm): < 500. τ (solid, r.t., $\lambda_{excitation}$ = 445 nm, $\lambda_{emission}$ = 555 nm, μs): 37. Φ (solid, r.t., $\lambda_{excitation}$ = 365 nm): 36%.

Characterization of [Cu(trz^{OMe}*-btz)(P*^{i}*Pr*$_3$*)*$_2$*][BF*$_4$*].* Anal. calcd for $C_{29}H_{52}BCuF_4N_6O_2P_2$ (729.07 g mol^{-1}, %): C, 47.78; H, 7.19; N, 11.53. Found (%): C, 47.59; H, 7.22; N, 11.48. M.p. 155°C (dec.). Λ_M (acetone, 298 K): 195 $ohm^{-1}mol^{-1}cm^2$. ^1H NMR ($CDCl_3$, 243 K) δ 8.59 (d, 1H, $^3J_{HH}$ = 8.4 Hz, btz), 8.23 (d, 1H, $^3J_{HH}$ = 8.4 Hz, btz), 7.78 (t, 1H, $^3J_{HH}$ = 7.8 Hz, btz), 7.61 (t, 1H, $^3J_{HH}$ = 7.8 Hz, btz), 4.29 (s, 6H, -CH_3), 2.18 (m, 3H, CH-phosphine), 1.28 (m, 18H, CH_3-phosphine). $^{31}P\{^1H\}$ NMR ($CDCl_3$, 298 K) δ 40.12 (FWHM = 3 Hz). IR (KBr, cm^{-1}): 3078 w (aromatic $\nu_{C\text{-}H}$), 2960-2870 m/w ($\nu_{C\text{-}H}$), 1615-1540 m (aromatic $\nu_{C\text{-}C}$ and $\nu_{C\text{-}N}$), 1140-1020 (ν_{BF4}). UV-VIS (CH_2Cl_2, r.t., nm): < 350, 237 (max), 263 (sh), 270 (sh), 299. PL (solid, r.t., $\lambda_{excitation}$ = 415 nm, nm): 637 (FWHM = 4000 cm^{-1}). PLE (solid, r.t., $\lambda_{emission}$ = 630 nm, nm): < 500. τ (solid, r.t., $\lambda_{excitation}$ = 445 nm, $\lambda_{emission}$ = 600 nm, μs): 21. Φ (solid, r.t., $\lambda_{excitation}$ = 365 nm): 2%.

Characterization of [Cu(trz^{OMe}*-btz)(*μ*–dppe)]*$_2$*[BF*$_4$*]*$_2$*.* Anal. calcd for $C_{74}H_{68}B_2Cu_2F_8N_{12}O_4P_4$ (1614.04 g mol^{-1}, %): C, 55.07; H, 4.25; N, 10.41. Found (%): C, 54.85; H, 4.27; N, 10.37. M.p. 217°C (dec.). Λ_M (acetone, 298 K): 332 $ohm^{-1}mol^{-1}cm^2$. ^1H NMR ($CDCl_3$, 298 K) δ 9.00-7.00 (m, br, 24H, btz and dppe), 4.37 (s, 3H, -CH_3), 4.25 (s, 3H, -CH_3), 2.90-2.30 (m, 4H, dppe). $^{31}P\{^1H\}$ NMR ($CDCl_3$, 298 K) δ -3.36 (FWHM = 117 Hz). IR (KBr, cm^{-1}): 3110-3005 m/w (aromatic $\nu_{C\text{-}H}$), 2960-2850 m/w ($\nu_{C\text{-}H}$), 1620-1530 m/s (aromatic $\nu_{C\text{-}C}$ and $\nu_{C\text{-}N}$), 1120-995 s (ν_{BF4}). UV-VIS (CH_2Cl_2, r.t., nm): < 500, 267 (sh), 273, 290 (max), 433. PL (solid, r.t., $\lambda_{excitation}$ = 415 nm, nm): 598 (FWHM = 4500 cm^{-1}). PLE (solid, r.t., $\lambda_{emission}$ = 590 nm, nm): < 500. τ (solid, r.t., $\lambda_{excitation}$ = 445 nm, $\lambda_{emission}$ = 600 nm, μs): 11. Φ (solid, r.t., $\lambda_{excitation}$ = 365 nm): 6%.

Characterization of [Cu(trz^{OMe}*-btz)(DPEphos)][BF*$_4$*].* Anal. calcd for $C_{47}H_{38}BCuF_4N_6O_3P_2$ (947.16 g mol^{-1}, %): C, 59.60; H, 4.04; N, 8.87. Found (%): C, 59.36; H, 4.06; N, 8.83. M.p. 225°C (dec.). Λ_M (acetone, 298 K): 118 $ohm^{-1}mol^{-1}cm^2$. ^1H NMR ($CDCl_3$, 243 K) δ 8.53 (d, 1H, $^3J_{HH}$ = 8.3 Hz, btz), 8.16 (d, 1H, $^3J_{HH}$ = 8.3 Hz, btz), 7.89 (t, 1H, $^3J_{HH}$ = 7.7 Hz, btz), 7.65 (t, 1H, $^3J_{HH}$ = 7.7 Hz, btz), 7.45-7.15 (m, br, 22H, DPEphos), 7.05-6.90 (m, br, 4H, DPEphos), 6.80-6.70 (m, br, 2H, DPEphos), 4.37 (s, 6H, -CH_3). $^{31}P\{^1H\}$ NMR ($CDCl_3$, 298 K) δ -11.43 (FWHM = 103 Hz). IR (KBr, cm^{-1}): 3120-3005 m/w (aromatic $\nu_{C\text{-}H}$), 2980-2860 m/w ($\nu_{C\text{-}H}$), 1620-1540 m/s (aromatic $\nu_{C\text{-}C}$ and $\nu_{C\text{-}N}$), 1130-1000 s (ν_{BF4}). UV-VIS (CH_2Cl_2, r.t., nm): < 490, 265 (sh), 273 (max), 405. PL (solid, r.t., $\lambda_{excitation}$ = 350 nm, nm): 604 (FWHM = 5000 cm^{-1}). PLE (solid, r.t., $\lambda_{emission}$ = 630 nm, nm): < 500. τ (solid, r.t., $\lambda_{excitation}$ = 445 nm, $\lambda_{emission}$ = 600 nm, μs): 65. Φ (solid, r.t., $\lambda_{excitation}$ = 365 nm): 6%.

Characterization of [Cu(trz^{OEt}-btz)(P^{i}Pr$_3$)$_2$][BF$_4$]. Anal. calcd for $C_{31}H_{56}BCuF_4N_6O_2P_2$ (757.13 g mol^{-1}, %): C, 49.18; H, 7.46; N, 11.10. Found (%): C, 48.98; H, 7.49; N, 11.07. M.p. 145°C (dec.). Λ_M (acetone, 298 K): 207 $ohm^{-1}mol^{-1}cm^2$. ^1H NMR ($CDCl_3$, 298 K) δ 8.59 (d, 1H, $^3J_{HH}$ = 8.4 Hz, btz), 8.16 (d, 1H, $^3J_{HH}$ = 8.4 Hz, btz), 7.83 (t, 1H, $^3J_{HH}$ = 7.8 Hz, btz), 7.63 (t, 1H, $^3J_{HH}$ = 7.7 Hz, btz), 4.76 (q, 4H, $^3J_{HH}$ = 7.4 Hz, -CH_2), 2.29 (m, 3H, CH-phosphine), 1.56 (t, 6H, $^3J_{HH}$ = 7.4 Hz, -CH_3), 1.38 (m, br, 18H, CH_3-phosphine). $^{31}P\{^1H\}$ NMR ($CDCl_3$, 298 K) δ 37.65 (FWHM = 83 Hz). IR (KBr, cm^{-1}): 3120-3070 m/w (aromatic $\nu_{C\text{-}H}$), 2980-2870 m/w ($\nu_{C\text{-}H}$), 1620-1540 m/s (aromatic $\nu_{C\text{-}C}$ and $\nu_{C\text{-}N}$), 1180-1020 s (ν_{BF4}). UV-VIS (CH_2Cl_2, r.t., nm): < 350, 261, 270 (sh), 297 (max), 328 (sh). PL (solid, r.t., $\lambda_{excitation}$ = 350 nm, nm): 600 (FWHM = 3600 cm^{-1}). PLE (solid, r.t., $\lambda_{emission}$ = 610 nm, nm): < 515. τ (solid, r.t., $\lambda_{excitation}$ = 290 nm, $\lambda_{emission}$ = 600 nm, μs): 43. Φ (solid, r.t., $\lambda_{excitation}$ = 365 nm): 14%.

Characterization of [Cu(trz^{OEt}-btz)(μ–dppe)]$_2$[BF$_4$]$_2$. Anal. calcd for $C_{78}H_{76}B_2Cu_2F_8N_{12}O_4P_4$ (1670.14 g mol^{-1}, %): C, 56.09; H, 4.59; N, 10.06. Found (%): C, 55.87; H, 4.61; N, 10.02. M.p. 220°C (dec.). Λ_M (acetone, 298 K): 328 $ohm^{-1}mol^{-1}cm^2$. ^1H NMR ($CDCl_3$, 233 K) δ 8.70 (d, 1H, $^3J_{HH}$ = 8.4 Hz, btz), 8.41 (d, 1H, $^3J_{HH}$ = 8.4 Hz, btz), 8.00 (t, 1H, $^3J_{HH}$ = 7.8 Hz, btz), 7.79 (t, 1H, $^3J_{HH}$ = 7.8 Hz, btz), 7.65-7.05 (m, br, 40H, dppe), 4.83 (q, 2H, $^3J_{HH}$ = 7.0 Hz, -CH_2), 4.01 (q, 2H, $^3J_{HH}$ = 7.0 Hz, -CH_2), 2.66 (m, br, 4H, dppe), 2.43 (m, br, 4H, dppe), 1.62 (t, 3H, $^3J_{HH}$ = 7.1 Hz, -CH_3), 0.58 (t, 6H, J_{HH} = 7.1 Hz, -CH_3). $^{31}P\{^1H\}$ NMR ($CDCl_3$, 298 K) δ -3.60 (FWHM = 111 Hz). IR (KBr, cm^{-1}): 3075-2850 m/w (aromatic $\nu_{C\text{-}H}$ and $\nu_{C\text{-}H}$), 1620-1530 m/s (aromatic $\nu_{C\text{-}C}$ and $\nu_{C\text{-}N}$), 1180-950 s (ν_{BF4}). UV-VIS (CH_2Cl_2, r.t., nm): < 500, 267 (max), 272 (sh), 289, 429. PL (solid, r.t., $\lambda_{excitation}$ = 350 nm, nm): 578 (FWHM = 3300 cm^{-1}). PLE (solid, r.t., $\lambda_{emission}$ = 575 nm, nm): < 475. τ (solid, r.t., $\lambda_{excitation}$ = 290 nm, $\lambda_{emission}$ = 575 nm, μs): 11. Φ (solid, r.t., $\lambda_{excitation}$ = 365 nm): 17%.

Characterization of [Cu(trz^{OEt}-btz)(DPEphos)][BF$_4$]. Anal. calcd for $C_{49}H_{42}BCuF_4N_6O_3P_2$ (975.21 g mol^{-1}, %): C, 60.35; H, 4.34; N, 8.62. Found (%): C, 60.11; H, 4.36; N, 8.59. M.p. > 230 °C. Λ_M (acetone, 298 K): 170 ohm^{-1}mol^{-1}cm^2. ^{1}H NMR (CDCl$_3$, 243 K) δ 8.47 (d, 1H, $^3J_{HH}$ = 8.3 Hz, btz), 8.19 (d, 1H, $^3J_{HH}$ = 8.3 Hz, btz), 7.89 (t, 1H, $^3J_{HH}$ = 7.7 Hz, btz), 7.66 (t, 1H, $^3J_{HH}$ = 7.7 Hz, btz), 7.50-6.70 (m, br, 28H, DPEphos), 4.79 (q, 2H, $^3J_{HH}$ = 7.0 Hz, -CH$_2$), 4.03 (q, 2H, $^3J_{HH}$ = 7.0 Hz, -CH$_2$), 1.62 (t, 3H, $^3J_{HH}$ = 7.0 Hz, -CH$_3$), 0.64 (t, 6H, $^3J_{HH}$ = 7.0 Hz, -CH$_3$). ^{31}P{^{1}H} NMR (CDCl$_3$, 298 K) δ -11.83 (FWHM = 83 Hz). IR (KBr, cm^{-1}): 3070-3050 m/w (aromatic ν_{C-H}), 2980-2850 m/w (ν_{C-H}), 1620-1540 m/s (aromatic ν_{C-C} and ν_{C-N}), 1110-995 s (ν_{BF4}). UV-VIS (CH$_2$Cl$_2$, r.t., nm): < 460, 265 (sh), 272 (max), 404. PL (solid, r.t., $\lambda_{excitation}$ = 350 nm, nm): 550 (FWHM = 4200 cm^{-1}). PLE (solid, r.t., $\lambda_{emission}$ = 525 nm, nm): < 475. τ (solid, r.t., $\lambda_{excitation}$ = 290 nm, $\lambda_{emission}$ = 575 nm, μs): 43. Φ (solid, r.t., $\lambda_{excitation}$ = 365 nm): 92%.

Characterization of [Cu(trz^{OPh}-btz)(μ–dppe)]$_2$[BF$_4$]$_2$. Anal. calcd for $C_{94}H_{76}B_2Cu_2F_8N_{12}O_4P_4$ (1862.32 g mol^{-1}, %): C, 60.63; H, 4.11; N, 9.03. Found (%): C, 60.39; H, 4.13; N, 8.99. M.p. 140°C (dec.). Λ_M (acetone, 298 K): 314 ohm^{-1}mol^{-1}cm^2. ^{1}H NMR (CDCl$_3$, 213 K) δ 8.26 (d, 1H, $^3J_{HH}$ = 8.3 Hz, btz), 7.90-7.05 (m, br, 31H, btz, dppe and Ph), 6.39 (d, 2H, $^3J_{HH}$ = 7.6 Hz, Ph), 2.67 (m, br, 2H, dppe), 2.37 (m, br, 2H, dppe). ^{31}P{^{1}H} NMR (CDCl$_3$, 298 K) δ -3.74 (FWHM = 86 Hz). IR (KBr, cm^{-1}): 3100-3020 m/w (aromatic ν_{C-H}), 2920-2850 m/w (ν_{C-H}), 1620-1550 m/s (aromatic ν_{C-C} and ν_{C-N}), 1110-1000 m (ν_{BF4}). UV-VIS (CH$_2$Cl$_2$, r.t., nm): < 530, 268, 273, 293 (max), 442. PL (solid, r.t., $\lambda_{excitation}$ = 365 nm, nm): 571 (FWHM = 4800 cm^{-1}). PLE (solid, r.t., $\lambda_{emission}$ = 630 nm, nm): < 470. τ (solid, r.t., $\lambda_{excitation}$ = 290 nm, $\lambda_{emission}$ = 630 nm, μs): 14. Φ (solid, r.t., $\lambda_{excitation}$ = 365 nm): 3%.

Characterization of [Cu(trz^{OPh}-btz)(DPEphos)][BF$_4$]. Anal. calcd for $C_{57}H_{42}BCuF_4N_6O_3P_2$ (1071.28 g mol^{-1}, %): C, 63.91; H, 3.95; N, 7.84. Found (%): C, 63.65; H, 3.97; N, 7.81. M.p. 150°C (dec.). Λ_M (acetone, 298 K): 155 ohm^{-1}mol^{-1}cm^2. ^{1}H NMR (CDCl$_3$, 313 K) δ 8.11 (m, 1H, btz), 7.80-6.50 (m, 41H, btz, Ph and DPEphos). ^{31}P{^{1}H} NMR (CDCl$_3$, 298 K) δ -11.70 (FWHM = 95 Hz). IR (KBr, cm^{-1}): 3070-3050 m/w (aromatic ν_{C-H}), 1620-1560 m/s (aromatic ν_{C-C} and ν_{C-N}), 1115-1000 m (ν_{BF4}). UV-VIS (CH_2Cl_2, r.t., nm): < 500, 274 (max), 318 (sh), 415. PL (solid, r.t., $\lambda_{excitation}$ = 365 nm, nm): 598 (FWHM = 4000 cm^{-1}). PLE (solid, r.t., $\lambda_{emission}$ = 630 nm, nm): < 510. τ (solid, r.t., $\lambda_{excitation}$ = 290 nm, $\lambda_{emission}$ = 630 nm, μs): 4. Φ (solid, r.t., $\lambda_{excitation}$ = 365 nm): 7%.

2.7.2.8 Synthesis of [CuL_2][BF_4], L = py-btz, trz^{OR}-btz (R = Me, Et, Ph)

0.472 g of [$Cu(NCCH_3)_4$][BF_4] (1.5 mmol) were dissolved in 20 mL of dry dichloromethane inside the glove box. 3.0 mmol of the proper bidentate heterocycle were added and the yellowish solution was stirred at room temperature overnight. The solvent was then evaporated under reduced pressure and the so-obtained oil was precipitated with diethyl ether. The solid was washed with the same solvent and dried *in vacuo*. Yield > 50 %.

Characterization of [Cu(py-btz)$_2$][BF$_4$]. Anal. calcd for $C_{22}H_{16}BCuF_4N_8$ (542.76 g mol^{-1}, %): C, 48.68; H, 2.97; N, 20.64. Found (%): C, 48.49; H, 2.98; N, 20.56. M.p. 80 °C (dec. > 125 °C). Λ_M (acetone, 298 K): 123 $ohm^{-1}mol^{-1}cm^2$. ^1H NMR ($CDCl_3$, 298 K) δ 8.68 (m, 4H, br, py), 8.33 (d, 2H, $^3J_{HH}$ = 8.6 Hz, btz), 8.16 (d, 2H, $^3J_{HH}$ = 8.3 Hz, btz), 8.01 (t, 2H, $^3J_{HH}$ = 7.9 Hz, py), 7.76 (t, 2H, $^3J_{HH}$ = 7.7 Hz, btz), 7.50 (t, 2H, $^3J_{HH}$ = 7.7 Hz, btz), 7.40 (m, 2H, br, py). IR (KBr, cm^{-1}): 3100-3030 m/w (aromatic ν_{C-H}), 2960-2850 m/w (ν_{C-H}), 1610-1570 m (aromatic ν_{C-C} and ν_{C-N}), 1160-990 s (ν_{BF4}). UV-VIS (CH_2Cl_2, r.t., nm): < 470, 264 (sh), 271, 285 (sh), 304 (max), 360.

Characterization of [Cu(trz^{OEt}-btz)$_2$][BF$_4$]. Anal. calcd for $C_{26}H_{28}BCuF_4N_{12}O_4$ (722.94 g mol^{-1}, %): C, 43.20; H, 3.90; N, 23.25. Found (%): C, 43.13; H, 3.92; N, 23.16. M.p. 85°C (dec.). Λ_M (acetone, 298 K): 142 $ohm^{-1}mol^{-1}cm^2$. ^1H NMR ($CDCl_3$, 323 K) δ 8.62 (d, 2H, $^3J_{HH}$ = 8.4 Hz, btz), 8.23 (d, 2H, $^3J_{HH}$ = 8.1 Hz, btz), 7.85 (t, br, 2H, btz), 7.65 (t, 2H, br, btz), 4.66 (q, 8H, $^3J_{HH}$ = 7.1 Hz, $-CH_2$), 1.39 (t, 12H, $^3J_{HH}$ = 7.1 Hz, $-CH_3$). IR (KBr, cm^{-1}): 3010-3080 m/w (aromatic ν_{C-H}), 2990-2870 m/w (ν_{C-H}), 1620-1550 m/s (aromatic ν_{C-C} and ν_{C-N}), 1150-1030 s (ν_{BF4}). UV-VIS (CH_2Cl_2, r.t., nm): < 480, 241 (max), 266 (sh), 273 (sh), 304, 395.

Characterization of [Cu(trz^{OPh}-btz)$_2$][BF$_4$]. Anal. calcd for $C_{42}H_{28}BCuF_4N_{12}O_4$ (915.12 g mol^{-1}, %): C, 55.13; H, 3.08; N, 18.37. Found (%): C, 54.91; H, 3.09; N, 18.31. M.p. 115°C. Λ_M (acetone, 298 K): 158 $ohm^{-1}mol^{-1}cm^2$. ^1H NMR ($CDCl_3$, 213 K) δ 8.55-6.70 (m, br, 14H, btz and Ph). IR (KBr, cm^{-1}): 3100-3015 m/w (aromatic ν_{C-H}), 1610-1550 m/s (aromatic ν_{C-C} and ν_{C-N}), 1160-990 s (ν_{BF4}). UV-VIS (CH_2Cl_2, r.t., nm): < 500, 243 (max), 269 (sh), 277 (sh), 309, 395.

2.7.2.9 Synthesis of [Cu(BTD)(PP)][BF_4] [BTD = 2,1,3-benzothiadiazole; PP = $(PPh_3)_2$, DPEphos]

0.3 mmol of [Cu(κ^2–BH_4)(PP)] [PP = $(PPh_3)_2$, DPEphos] and 0.045 g of 2,1,3-benzothiadiazole (0.3 mmol, BTD) were dissolved in 50 mL of dichloromethane. The solution was cooled at 77 K with a nitrogen bath and put under inert atmosphere. 45 μL of $HBF_4 \cdot Et_2O$ (0.3 mmol) were added through a syringe and the reaction mixture was allowed to slowly warm up to room temperature. After stirring overnight, the solution was purified by filtration and dichloromethane was evaporated under reduced pressure. The addition of diethyl ether (20 mL) caused the separation of a solid, that was filtered, washed with 5 mL of diethyl ether and dried *in vacuo*. Crystals of [Cu(BTD)$(PPh_3)_2$][BF_4] suitable for X-ray diffraction were collected from the evaporation of diethyl ether solutions. Yield > 60% in all the cases.

Characterization of [Cu(BTD)(PPh$_3$)$_2$][BF$_4$]. Anal. calcd for $C_{42}H_{34}BCuF_4N_2P_2S$ (811.11 g mol^{-1}, %): C, 62.19; H, 4.23; N, 3.45; S, 3.95. Found (%): C, 61.94; H, 4.25; N, 3.44; S, 3.93. M. p. 155 °C (dec.). Λ_M (acetone, 298 K): 149 ohm^{-1}mol^{-1}cm^2. ^1H NMR ($CDCl_3$, 213 K) δ 8.01 (m, 2H, btd), 7.65 (m, 2H, btd), 7.40 (t, $^3J_{HH}$ = 7.5 Hz, 6H, Ph), 7.15 (t, $^3J_{HH}$ = 7.4 Hz, 12H, Ph), 6.90 (m, 12H, Ph). $^{31}P\{^1H\}$ NMR ($CDCl_3$, 298 K) δ 0.44 (FWHM = 85 Hz). IR (KBr, cm^{-1}): 3100-3020 m/w (aromatic ν_{C-H}), 2980-2850 m/w (ν_{C-H}); 1480-1385 m/w (aromatic ν_{C-C} and ν_{C-N}); 1085 s (ν_{BF4}). UV-VIS (CH_2Cl_2, r.t., nm): < 360, 311, 305, 299, 257 (sh). PL (solid, r.t., $\lambda_{excitation}$ = 350 nm, nm): 646 (FWHM = 3400 cm^{-1}). PLE (solid, r.t., $\lambda_{emission}$ = 630 nm, nm): < 500. τ (solid, r.t., $\lambda_{excitation}$ = 290 nm, $\lambda_{emission}$ = 640 nm, μs): 1310. Φ (solid, r.t., $\lambda_{excitation}$ = 365 nm): 46%.

Characterization of [Cu(BTD)(DPEphos)][BF$_4$]. Anal. calcd for $C_{42}H_{32}BCuF_4N_2OP_2S$ (825.09 g mol^{-1}, %): C, 61.14; H, 3.91; N, 3.40; S, 3.89. Found (%): C, 60.90; H, 3.93; N, 3.41; S, 3.74. M. p. > 230 °C (dec.). Λ_M (acetone, 298 K): 150 ohm^{-1}mol^{-1}cm^2. ^1H NMR ($CDCl_3$, 298 K) δ 8.03 (m, 2H, btd), 7.62 (m, 2H, btd), 7.37-7.16 (m, 20H, DPEphos), 6.98 (t, $^3J_{HH}$ = 7.4 Hz, 2H, DPEphos), 6.71 (m, br, 6H, DPEphos). $^{31}P\{^1H\}$ NMR ($CDCl_3$, 298 K) δ -17.57 (FWHM = 105 Hz). IR (KBr, cm^{-1}): 3070-3010 m/w (aromatic ν_{C-H}), 2980-2920 m/w (ν_{C-H}); 1480-1440 m/w (aromatic ν_{C-C} and ν_{C-N}); 1085 s (ν_{BF4}). UV-VIS (CH_2Cl_2, r.t., nm): < 360, 290. PL (solid, r.t., $\lambda_{excitation}$ = 350 nm, nm): 675 (FWHM = 3400 cm^{-1}). PLE (solid, r.t., $\lambda_{emission}$ = 630 nm, nm): < 600. τ (solid, r.t., $\lambda_{excitation}$ = 290 nm, $\lambda_{emission}$ = 670 nm, μs): 70. Φ (solid, r.t., $\lambda_{excitation}$ = 365 nm): 30%.

2.7.2.10 Synthesis of $[Cu(BTD)(CH_3CN)(PPh_3)_2][BF_4]$ and $[Cu_2(BTD)(CH_3CN)(\mu\text{–}dppm)_2][BF_4]_2$ [BTD = 2,1,3-benzothiadiazole; dppm = bis(diphenylphosphino)methane]

The compounds were prepared following the procedure described above for $[Cu\{CH(btz)_3\}(PR_3)][BF_4]$. Crystals of $[Cu_2(BTD)(CH_3CN)(\mu\text{–}dppm)_2][BF_4]_2$ suitable for X-ray diffraction were collected from dichloromethane/diethyl ether solutions. Yield > 60% in both of the cases.

Characterization of $[Cu(BTD)(CH_3CN)(PPh_3)_2][BF_4]$. Anal. calcd for $C_{44}H_{37}BCuF_4N_3P_2S$ (852.16 g mol^{-1}, %): C, 62.02; H, 4.38; N, 4.93; S, 3.76. Found (%): C, 61.77; H, 4.40; N, 4.91; S, 3.74. M.p. 130 °C (dec.). Λ_M (acetone, 298 K): 193 ohm^{-1}mol^{-1}cm^2. ^{1}H NMR ($CDCl_3$, 298 K) δ 7.99 (m, 2H, BTD), 7.62 (m, 2H, BTD), 7.47 (m, 6H, Ph), 7.42-7.24 (m, 24H, Ph), 2.29 (s, 3H, CH_3CN). ^{1}H NMR ($CDCl_3$, 213 K) δ 7.90 (m, 2H, BTD), 7.65 (m, 2H, BTD), 7.41 (m, 6H, Ph), 7.27 (m, 12H, Ph), 7.11 (m, 12H, Ph), 2.32 (s, 3H, CH_3CN). ^{31}P{^{1}H} NMR ($CDCl_3$, 213 K) δ -0.86 (FWHM = 35 Hz). IR (KBr, cm^{-1}): 3070-3000 m/w (aromatic ν_{C-H}), 1480-1440 m/s (aromatic ν_{C-C} and ν_{C-N}), 1120-1000 m (ν_{BF4}). UV-VIS (CH_2Cl_2, r.t., nm): < 360, 312, 305, 300, 255 (sh). PL (solid, r.t., $\lambda_{excitation}$ = 350 nm, nm): 638 (FWHM = 3100 cm^{-1}). PLE (solid, r.t., $\lambda_{emission}$ = 630 nm, nm): < 500. τ (solid, r.t., $\lambda_{excitation}$ = 290 nm, $\lambda_{emission}$ = 640 nm, μs): 1242. Φ (solid, r.t., $\lambda_{excitation}$ = 365 nm): 18%.

Characterization of $[Cu_2(BTD)(CH_3CN)(\mu\text{–}dppm)_2][BF_4]_2$. Anal. calcd for $C_{58}H_{51}B_2Cu_2F_8N_3P_4S$ (1246.72 g mol^{-1}, %): C, 55.88; H, 4.12; N, 3.37; S, 2.57. Found (%): C, 55.66; H, 4.14; N, 3.36; S, 2.56. M.p. 145 °C (dec.). Λ_M (acetone, 298 K): 257 ohm^{-1}mol^{-1}cm^2. ^{1}H NMR ($CDCl_3$, 298 K) δ 8.02 (m, br, 2H, BTD), 7.65 (m, br, 2H, BTD), 7.25-6.88 (m, 40H, dppm), 3.45 (s, br, 4H, dppm), 2.18 (s, 6H, CH_3CN). ^{31}P{^{1}H} NMR ($CDCl_3$, 298 K) δ -12.33 (FWHM = 20 Hz). IR (KBr, cm^{-1}): 3100-3000 m/w (aromatic ν_{C-H}), 2990-2850 m/w (ν_{C-H}), 2280 w ($\nu_{C\equiv N}$), 1480-1440 m/s (aromatic

$\nu_{C\text{-}C}$ and $\nu_{C\text{-}N}$), 1100-995 m (ν_{BF4}). UV-VIS (CH_2Cl_2, r.t., nm): < 360, 312, 306. PL (solid, r.t., $\lambda_{excitation}$ = 350 nm, nm): 623 (FWHM = 3500 cm^{-1}). PLE (solid, r.t., $\lambda_{emission}$ = 630 nm, nm): < 500. τ (solid, r.t., $\lambda_{excitation}$ = 290 nm, $\lambda_{emission}$ = 630 nm, μs): 1789. Φ (solid, r.t., $\lambda_{excitation}$ = 365 nm): 35%.

2.7.2.11 Synthesis of [Cu(BTD)(PP)][ClO_4] and [Cu(BTD)(μ−dppm)]$_2$[ClO_4]$_2$ [BTD = 2,1,3-benzothiadiazole; PP = (PPh_3)$_2$, DPEphos]

0.100 g of CuCl (1.0 mmol) were suspended in 15 mL of dry dichloromethane and 1.0 mmol of DPEphos or dppm, or 2.0 mmol of triphenyl phosphine were added. After the complete dissolution of CuCl, a stoichiometric amount of benzothiadiazole (0.136 g, 1.0 mmol) was added and the solution suddenly becomes yellow coloured. Then 0.207 g of $AgClO_4$ (1.0 mmol) were then added and the mixture was left stirring overnight. AgCl precipitated and it was separated by centrifugation. The solvent was evaporated under reduced pressure to afford an oil that was precipitated with diethyl ether. The so-obtained solid was filtered, washed with diethyl ether and dried *in vacuo*. Yield > 70% in all the cases.

Characterization of [Cu(BTD)(PPh_3)$_2$][ClO_4]. Anal. calcd for $C_{42}H_{34}ClCuN_2O_4P_2S$ (823.75 g mol^{-1}, %): C, 61.24; H, 4.16; N, 3.40; S, 3.89; Cl, 4.30. Found (%): C, 61.22; H, 4.18; N, 3.27; S, 3.74; Cl, 4.32. M.p. 162 °C (dec.). Λ_M (acetone, 298 K): 149 $ohm^{-1}mol^{-1}cm^2$. ^1H NMR ($CDCl_3$, 298 K) δ 7.91 (m, 2H, BTD), 7.55 (m, 2H, BTD), 7.47-7.21 (m, br, 30H, PPh_3). $^{31}P\{^1H\}$ NMR ($CDCl_3$, 298 K) δ -0.14 (FWHM = 180 Hz). IR (KBr, cm^{-1}): 3090-2990 m/w (aromatic $\nu_{C\text{-}H}$), 1535-1440 m/s (aromatic $\nu_{C\text{-}C}$ and $\nu_{C\text{-}N}$), 1120 s (ν_{ClO4}). PL (solid, r.t., $\lambda_{excitation}$ = 350 nm, nm): 660 (FWHM = 3600 cm^{-1}). PLE (solid, r.t., $\lambda_{emission}$ = 630 nm, nm): < 540. τ (solid, r.t., $\lambda_{excitation}$ = 290 nm, $\lambda_{emission}$ = 630 nm, μs): 1572. Φ (solid, r.t., $\lambda_{excitation}$ = 365 nm): 15%.

Characterization of [Cu(BTD)(DPEphos)][ClO_4]. Anal. calcd for $C_{42}H_{32}ClCuN_2O_5P_2S$ (837.73 g mol^{-1}, %): C, 60.22; H, 3.85; N, 3.34; S, 3.83; Cl, 4.23. Found (%): C, 60.15; H, 3.87; N, 3.35; S, 3.81; Cl, 4.21. M.p. 200 °C (dec.). Λ_M (acetone, 298 K): 90 $ohm^{-1}mol^{-1}cm^2$. ^1H NMR ($CDCl_3$, 298 K) δ 7.97 (m, 2H, BTD), 7.56 (m, 2H, BTD), 7.37-7.26 (m, br, 12H, DPEphos), 7.21 (m, br, 8H, DPEphos), 6.98 (t, 2H, $^3J_{HH}$ = 7.6 Hz, DPEphos), 6.69 (m, br, 6H, DPEphos). $^{31}P\{^1H\}$ NMR ($CDCl_3$, 298 K) δ -16.14 (FWHM = 192 Hz). IR (KBr, cm^{-1}): 3080-2990 m/w (aromatic $\nu_{C\text{-}H}$), 1525-1385 m/s (aromatic $\nu_{C\text{-}C}$ and $\nu_{C\text{-}N}$), 1140-1050 s (ν_{ClO4}). PL (solid, r.t., $\lambda_{excitation}$ = 350 nm, nm): 680 (FWHM = 3400 cm^{-1}). PLE (solid, r.t., $\lambda_{emission}$ = 630 nm, nm): < 590. τ (solid, r.t., $\lambda_{excitation}$ = 290 nm, $\lambda_{emission}$ = 670 nm, μs): 81. Φ (solid, r.t., $\lambda_{excitation}$ = 365 nm): 26%.

Characterization of [Cu(BTD)(μ–dppm)]$_2$[ClO$_4$]$_2$. Anal. calcd for $C_{62}H_{52}Cl_2Cu_2N_4O_8P_4S_2$ (1367.12 g mol^{-1}, %): C, 54.47; H, 3.83; N, 4.10; S, 4.69; Cl, 5.19. Found (%): C, 54.26; H, 3.85; N, 4.08; S, 4.67; Cl, 5.21. M.p. 200 °C (dec.). Λ_M (acetone, 298 K): 196 $ohm^{-1}mol^{-1}cm^2$. ^1H NMR ($CDCl_3$, 298 K) δ 7.98 (m, br, 2H, BTD), 7.59 (m, br, 4H, BTD), 7.34 (m, 2H, BTD), 7.22-7.08 (m, 24H, dppm), 7.01 (t, 16H, $^3J_{HH}$ = 7.6 Hz, dppm), 3.40 (m, br, 4H, dppm). $^{31}P\{^1H\}$ NMR ($CDCl_3$, 298 K) δ -13.04 (FWHM = 30 Hz). IR (KBr, cm^{-1}): 3090-2990 m/w (aromatic $\nu_{C\text{-}H}$), 2950-2900 ($\nu_{C\text{-}H}$), 1530-1440 m/s (aromatic $\nu_{C\text{-}C}$ and $\nu_{C\text{-}N}$), 1160-1030 s (ν_{ClO4}). UV-VIS (CH_2Cl_2, r.t., nm): < 340, 250, 267 (sh), 275 (sh), 285 (sh), 296 (sh), 302 (sh), 309 (sh). PL (solid, r.t., $\lambda_{excitation}$ = 350 nm, nm): 683 (FWHM = 4000 cm^{-1}). PLE (solid, r.t., $\lambda_{emission}$ = 630 nm, nm): < 570. τ (solid, r.t., $\lambda_{excitation}$ = 290 nm, $\lambda_{emission}$ = 670 nm, μs): 1283. Φ (solid, r.t., $\lambda_{excitation}$ = 365 nm): 10%.

2.7.3 Zinc(II) complexes

2.7.3.1 Synthesis of [ZnX$_2$(TPPO)$_2$], X = Cl, Br, I

The complexes were prepared by slowly adding a solution containing 2.1 mmol of triphenylphosphine oxide (TPPO) into a solution of the proper anhydrous ZnX_2 (1 mmol) dissolved in 20 ml of EtOH. The reaction mixture was stirred overnight inside the glove-box at room temperature. The solvent was then evaporated under reduced pressure and the product was isolated by adding diethyl ether. The solid was then filtered, washed with 2x15 mL of diethyl ether and dried *in vacuo*. Yield > 70% in all the cases.

Characterization of [ZnCl$_2$(TPPO)$_2$]. Anal. calcd for $C_{36}H_{30}Cl_2O_2P_2Zn$ (692.86 g mol^{-1}, %): C, 62.41; H, 4.36; Cl, 10.23. Found (%): C, 62.16; H, 4.38; Cl, 10.19. ^1H NMR ($CDCl_3$, 298 K) δ 7.72-7.61 (m, 6H, *o*-Ph), 7.56 (t, 3H, $^3J_{HH}$ = 7.4 Hz, *p*-Ph), 7.41 (m, br, 6H, *m*-Ph). $^{31}P\{^1H\}$ NMR ($CDCl_3$, 298 K) δ 37.10 (FWHM = 66 Hz). IR (KBr, cm^{-1}): 1587 m, 1485 m, 1438 m (ν_{arom}), 1155 s ($\nu_{P=O}$). P.f. > 230 °C. UV-VIS (CH_2Cl_2, r.t., nm): < 285, 261, 266 (max), 274. PL (solid, r.t., $\lambda_{excitation}$ = 350 nm, nm): 399 (max), 510 (sh). PLE (solid, r.t., $\lambda_{emission}$ = 400 nm, nm): < 350. τ (solid, r.t., $\lambda_{excitation}$ = 373 nm, $\lambda_{emission}$ = 410, ns): 6. τ (solid, r.t., $\lambda_{excitation}$ = 373 nm, $\lambda_{emission}$ = 520 nm, ns): 10.

Characterization of [ZnBr$_2$(TPPO)$_2$]. Anal. calcd for $C_{36}H_{30}Br_2O_2P_2Zn$ (781.77 g mol^{-1}, %): C, 55.31; H, 3.87; Br, 20.44. Found (%): C, 55.09; H, 3.89; Br, 20.32. ^{1}H NMR (CDCl$_3$, 298 K) δ 7.72-7.64 (m, 6H, *o*-Ph), 7.57 (m, 3H, *p*-Ph), 7.42 (m, br, 6H, *m*-Ph). ^{31}P{^{1}H} NMR (CDCl$_3$, 298 K) δ 36.97 (FWHM = 67 Hz). IR (KBr, cm^{-1}): 1592 m, 1485 m, 1436 s (ν_{arom}), 1153 ($\nu_{P=O}$). P.f. 218 °C (dec.). UV-VIS (CH$_2$Cl$_2$, r.t., nm): < 280, 254 (sh), 261, 267 (max), 274. PL (solid, r.t., $\lambda_{excitation}$ = 350 nm, nm): 403 (max), 515 (sh). PLE (solid, r.t., $\lambda_{emission}$ = 520 nm, nm): < 350, 296 (max). τ (solid, r.t., $\lambda_{excitation}$ = 373 nm, $\lambda_{emission}$ = 450 nm, ns): 6.

Characterization of [ZnI$_2$(TPPO)$_2$]. Anal. calcd for $C_{36}H_{30}I_2O_2P_2Zn$ (875.77 g mol^{-1}, %): C, 49.37; H, 3.45; I, 28.98. Found (%): C, 49.17; H, 3.46; I, 28.86. ^{1}H NMR (CDCl$_3$, 298 K) δ 7.75-7.63 (m, 12H, *o*-Ph), 7.56 (t, 6H, $^3J_{HH}$ = 7.8 Hz, *p*-Ph), 7.42 (m, br, 12H, *m*-Ph). ^{31}P{^{1}H} NMR (CDCl$_3$, 298 K) δ 36.76 (FWHM = 26 Hz). IR (KBr, cm^{-1}): 1590 m, 1485 m, 1436 m (ν_{arom}), 1150 s ($\nu_{P=O}$). P.f. 229 °C (dec.). UV-VIS (CH$_2$Cl$_2$, r.t., nm): < 290, 261, 267 (max), 273.

2.7.3.2 Synthesis of [ZnX$_2${O=P(NMe$_2$)$_2$R}$_2$], R = Ind, Cbz and X = Cl, Br, I

The complexes were prepared following the same synthetic procedure reported for [ZnX$_2$(TPPO)$_2$] (X = Cl, Br, I). Crystals of [ZnX$_2${O=P(NMe$_2$)$_2$Ind}$_2$] derivatives suitable for X-ray diffraction were collected from dichloromethane/diethyl ether solutions. Yield > 70% in all the cases.

Characterization of [ZnCl$_2${O=P(NMe$_2$)$_2$Ind}$_2$]. Anal. calcd for $C_{24}H_{36}Cl_2N_6O_2P_2Zn$ (638.83 g mol^{-1}, %): C, 45.12; H, 5.68; N, 13.16; Cl, 11.10. Found (%): C, 44.94; H, 5.70; N, 13.11; Cl, 11.07. M.p. 125°C (dec.). Λ_M (acetone, 298 K): 24 ohm^{-1}mol^{-1}cm^2. ^{1}H NMR (CDCl$_3$, 298 K) δ 7.84 (d, 1H, $^3J_{HH}$ = 8.2 Hz, Ind), 7.60 (d, 1H, $^3J_{HH}$ = 7.6 Hz, Ind), 7.28-7.11 (m, 3H, Ind), 6.64 (m, 1H, Ind), 2.77 (d, 12H, $^3J_{PH}$ = 10.5 Hz, N-Me). ^{31}P{^{1}H} NMR (CDCl$_3$, 298 K) δ 17.20 (FWHM = 7 Hz). IR (KBr, cm^{-1}): 3140-3005 m (aromatic ν_{C-H}), 2990-2820 m (ν_{C-H}), 1530-1450 m (aromatic ν_{C-C} and ν_{C-N}), 1180-1120 s ($\nu_{P=O}$ and ν_{C-N}), 1010-1000 s (ν_{P-N}). UV-VIS (CH$_2$Cl$_2$, r.t., nm): < 300, 257 (max), 274 (sh), 287 (sh).

Characterization of $[ZnBr_2\{O{=}P(NMe_2)_2Ind\}_2]$. Anal. calcd for $C_{24}H_{36}Br_2N_6O_2P_2Zn$ (727.74 g mol^{-1}, %): C, 39.61; H, 4.99; N, 11.55; Br, 21.96. Found (%): C, 39.45; H, 5.01; N, 11.50; Br, 22.05. M.p. 205°C (dec.). Λ_M (acetone, 298 K): 8 $ohm^{-1}mol^{-1}cm^2$. ^1H NMR ($CDCl_3$, 298 K) δ 7.86 (d, 1H, $^3J_{HH}$ = 8.2 Hz, Ind), 7.60 (d, 1H, $^3J_{HH}$ = 7.6 Hz, Ind), 7.30-7.08 (m, 3H, Ind), 6.64 (m, 1H, Ind), 2.78 (d, 12H, $^3J_{PH}$ = 10.5 Hz, N-Me). $^{31}P\{^1H\}$ NMR ($CDCl_3$, 298 K) δ 17.11 (FWHM = 7 Hz). IR (KBr, cm^{-1}): 3130-3005 m (aromatic $\nu_{C\text{-}H}$), 2950-2820 m ($\nu_{C\text{-}H}$), 1525-1450 m (aromatic $\nu_{C\text{-}C}$ and $\nu_{C\text{-}N}$), 1210-1120 s ($\nu_{P=O}$ and $\nu_{C\text{-}N}$), 1010-950 s ($\nu_{P\text{-}N}$). UV-VIS (CH_2Cl_2, r.t., nm): < 300, 260 (max), 276 (sh), 287 (sh). PL (solid, r.t., $\lambda_{excitation}$ = 290 nm, nm): 531 (FWHM = 2900 cm^{-1}). PLE (solid, r.t., $\lambda_{emission}$ = 520 nm, nm): < 310. τ (solid, r.t., $\lambda_{excitation}$ = 290 nm, $\lambda_{emission}$ = 520 nm, ms): 0.7. Φ (solid, r.t., $\lambda_{excitation}$ = 310 nm): 19%.

Characterization of $[ZnI_2\{O{=}P(NMe_2)_2Ind\}_2]$. Anal. calcd for $C_{24}H_{36}I_2N_6O_2P_2Zn$ (821.73 g mol^{-1}, %): C, 35.08; H, 4.42; N, 10.23; I, 30.89. Found (%): C, 34.94; H, 4.46; N, 10.19; I, 30.77. M.p. 122°C (dec.). Λ_M (acetone, 298 K): 12 $ohm^{-1}mol^{-1}cm^2$. ^1H NMR ($CDCl_3$, 298 K) δ 7.89 (d, 1H, $^3J_{HH}$ = 8.2 Hz, Ind), 7.59 (d, 1H, $^3J_{HH}$ = 7.8 Hz, Ind), 7.26-7.09 (m, 3H, Ind), 6.64 (m, 1H, Ind), 2.78 (d, 12H, $^3J_{PH}$ = 10.6 Hz, N-Me). $^{31}P\{^1H\}$ NMR ($CDCl_3$, 298 K) δ 16.36 (FWHM = 7 Hz). IR (KBr, cm^{-1}): 3130-3005 m/w (aromatic $\nu_{C\text{-}H}$), 2950-2820 m ($\nu_{C\text{-}H}$), 1525-1450 m (aromatic $\nu_{C\text{-}C}$ and $\nu_{C\text{-}N}$), 1210-1120 s ($\nu_{P=O}$ and $\nu_{C\text{-}N}$), 1010-950 s ($\nu_{P\text{-}N}$). UV-VIS (CH_2Cl_2, r.t., nm): < 300, 257 (max), 275 (sh), 287 (sh). PL (solid, r.t., $\lambda_{excitation}$ = 290 nm, nm): 487 (sh), 521 (max), 559, 604 (sh), 655 (sh). PLE (solid, r.t., $\lambda_{emission}$ = 525 nm, nm): < 330. τ (solid, r.t., $\lambda_{excitation}$ = 290 nm, $\lambda_{emission}$ = 520 nm, ms): 2.6. Φ (solid, r.t., $\lambda_{excitation}$ = 310 nm): 7%.

Characterization of $[ZnCl_2\{O{=}P(NMe_2)_2Cbz\}_2]$. Anal. calcd for $C_{32}H_{40}Cl_2N_6O_2P_2Zn$ (738.94 g mol^{-1}, %): C, 52.01; H, 5.46; N, 11.37; Cl, 9.59. Found (%): C, 51.80; H, 5.48; N, 11.32; Cl, 9.55. M.p. 150°C (dec.). Λ_M (acetone, 298 K): 20 $ohm^{-1}mol^{-1}cm^2$. ^1H NMR ($CDCl_3$, 298 K) δ 8.00 (m, 4H, Cbz), 7.91 (m, 2H, Cbz), 7.28 (m, 2H, Cbz), 2.82 (d, 12H, $^3J_{PH}$ = 10.7 Hz, N-Me). $^{31}P\{^1H\}$ NMR ($CDCl_3$, 298 K) δ 17.45 (FWHM = 7 Hz). IR (KBr, cm^{-1}): 3115-2930 m/w (aromatic $\nu_{C\text{-}H}$), 2900-2820 m ($\nu_{C\text{-}H}$), 1620-1590 m (aromatic $\nu_{C\text{-}C}$ and $\nu_{C\text{-}N}$), 1210-1170 s ($\nu_{P=O}$ and $\nu_{C\text{-}N}$), 1000-990 s ($\nu_{P\text{-}N}$). UV-VIS (CH_2Cl_2, r.t., nm): < 340, 246, 256 (sh), 288 (max), 302 (sh), 314 (sh). PL (solid, r.t., $\lambda_{excitation}$ = 350 nm, nm): 397 (sh), 416 (max), 441 (sh), 469 (sh). PLE (solid, r.t.,

$\lambda_{emission}$ = 420 nm, nm): < 360, 340 (max). τ (solid, r.t., $\lambda_{excitation}$ = 373 nm, $\lambda_{emission}$ = 415 nm, ns): 7. Φ (solid, r.t., $\lambda_{excitation}$ = 265 nm): 46%

Characterization of [ZnBr$_2${O=P(NMe$_2$)$_2$Cbz}$_2$]. Anal. calcd for $C_{32}H_{40}Br_2N_6O_2P_2Zn$ (827.85 g mol^{-1}, %): C, 46.43; H, 4.87; N, 10.15; Br, 19.30. Found (%): C, 46.24; H, 4.89; N, 10.11; Br, 19.22. M.p. 145°C (dec.). Λ_M (acetone, 298 K): 5 ohm^{-1}mol^{-1}cm^2. ^{1}H NMR (CDCl$_3$, 298 K) δ 8.00 (m, 4H, Cbz), 7.91 (m, 2H, Cbz), 7.27 (m, 2H, Cbz), 2.82 (d, 12H, $^3J_{PH}$ = 10.6 Hz, N-Me). ^{31}P{^{1}H} NMR (CDCl$_3$, 298 K) δ 17.23 (FWHM = 11 Hz). IR (KBr, cm^{-1}): 3115-2930 m/w (aromatic ν_{C-H}), 2900-2800 m (ν_{C-H}), 1620-1590 m (aromatic ν_{C-C} and ν_{C-N}), 1210-1170 s ($\nu_{P=O}$ and ν_{C-N}), 1000-990 s (ν_{P-N}). UV-VIS (CH$_2$Cl$_2$, r.t., nm): < 340, 247 (max), 254 (sh), 288, 306 (sh), 318 (sh). PL (solid, r.t., $\lambda_{excitation}$ = 350 nm, nm): 396, 410 (sh), 434 (sh), 462 (sh), 545, 554 (sh), 595, 649. PLE (solid, r.t., $\lambda_{emission}$ = 390 nm, nm): < 350, 265 (max). τ (solid, r.t., $\lambda_{excitation}$ = 373 nm, $\lambda_{emission}$ = 415 nm, ns): 7. Φ (solid, r.t., $\lambda_{excitation}$ = 265 nm): 56%

Characterization of [ZnI$_2${O=P(NMe$_2$)$_2$Cbz}$_2$]. Anal. calcd for $C_{32}H_{40}I_2N_6O_2P_2Zn$ (921.85 g mol^{-1}, %): C, 41.69; H, 4.37; N, 9.12; I, 27.53. Found (%): C, 41.52; H, 4.39; N, 9.08; I, 27.42. M.p. 215°C (dec.). Λ_M (acetone, 298 K): 21 ohm^{-1}mol^{-1}cm^2. ^{1}H NMR (CDCl$_3$, 298 K) δ 7.99 (m, 4H, Cbz), 7.91 (m, 2H, Cbz), 7.27 (m, 2H, Cbz), 2.81 (d, 12H, $^3J_{PH}$ = 10.5 Hz, N-Me). ^{31}P{^{1}H} NMR (CDCl$_3$, 298 K) δ 16.39 (FWHM = 8 Hz). IR (KBr, cm^{-1}): 3100-2930 m/w (aromatic ν_{C-H}), 2890-2810 m (ν_{C-H}), 1620-1590 m (aromatic ν_{C-C} and ν_{C-N}), 1210-1150 s ($\nu_{P=O}$ and ν_{C-N}), 998 s (ν_{P-N}). UV-VIS (CH$_2$Cl$_2$, r.t., nm): < 340, 247 (sh), 254 (sh), 288 (max), 300 (sh), 314 (sh). PL (solid, r.t., $\lambda_{excitation}$ = 350 nm, nm): 396 (sh), 416 (max), 442 (sh), 469 (sh). PLE (solid, r.t., $\lambda_{emission}$ = 420 nm, nm): < 350, 331 (sh), 341 (max). τ (solid, r.t., $\lambda_{excitation}$ = 373 nm, $\lambda_{emission}$ = 415 nm, ns): 7. Φ (solid, r.t., $\lambda_{excitation}$ = 265 nm): 5%

2.7.3.3 Synthesis of [ZnX$_2$(O=PPh$_2$Ind)$_2$], O=PPh$_2$Ind = (Indol-1-yl)diphenylphosphine oxide and X = Cl, Br, I

The complexes were prepared following the same synthetic procedure reported for [ZnX$_2${O=P(NMe$_2$)$_2$R}$_2$] (R = Ind, Cbz; X = Cl, Br, I). Differently from the bromo- and iodo-species that were precipitated by adding diethyl ether, [ZnCl$_2${O=PPh$_2$Ind}$_2$] was precipitated from hexane. Yield > 70% in all the cases.

Characterization of $[ZnCl_2(O=PPh_2Ind)_2]$. Anal. calcd for $C_{40}H_{32}Cl_2N_2O_2P_2Zn$ (770.94 g mol^{-1}, %): C, 62.32; H, 4.18; N, 3.63; Cl, 9.20. Found (%): C, 62.07; H, 4.20; N, 3.62; Cl, 9.24. M.p. 70 °C (dec.). Λ_M (acetone, 298 K): 14 ohm^{-1}mol^{-1}cm^2. ^1H NMR ($CDCl_3$, 298 K) δ 7.70 (m, br, 2H, ind), 7.62 (m, 4H, Ph), 7.45 (m, br, 4H, Ph), 7.34 (m, br, 1H, Ph), 7.15 (t, 1H, $^3J_{HH}$ = 7.3 Hz, ind), 6.94 (m, br, 1H, ind), 6.75 (m, br, 1H, ind), 6.62 (m, br, 1H, ind). $^{31}P\{^1H\}$ NMR ($CDCl_3$, 298 K) δ 30.23 (FWHM = 167 Hz). IR (KBr, cm^{-1}): 3140-3000 w (aromatic ν_{C-H}), 2990-2850 w (ν_{C-H}), 1640-1570 m (aromatic ν_{C-C} and ν_{C-N}), 1200-1110 s ($\nu_{P=O}$ and ν_{C-N}), 996 m (ν_{C-N}). UV-VIS (CH_2Cl_2, r.t., nm): < 310, 258 (max), 288. PL (solid, r.t., $\lambda_{excitation}$ = 350 nm, nm): 453 (max), 508 (sh), 562 (sh). PLE (solid, r.t., $\lambda_{emission}$ = 450 nm, nm): < 350. Φ (solid, r.t., $\lambda_{excitation}$ = 365 nm): 54%.

Characterization of $[ZnBr_2(O=PPh_2Ind)_2]$. Anal. calcd for $C_{40}H_{32}Br_2N_2O_2P_2Zn$ (859.84 g mol^{-1}, %): C, 55.88; H, 3.75; N, 3.26; Br, 18.59. Found (%): C, 55.66; H, 3.76; N, 3.25; Br, 18.66. M.p. 165 °C (dec.). Λ_M (acetone, 298 K): 11 ohm^{-1}mol^{-1}cm^2. ^1H NMR ($CDCl_3$, 298 K) δ 7.71 (dd, $^3J_{HH}$ = 7.8 Hz, J_{PH} = 12.9 Hz, 2H, ind), 7.65-7.56 (m, 5H, Ph), 7.43 (m, br, 5H, Ph), 7.15 (t, 1H, $^3J_{HH}$ = 7.4 Hz, ind), 6.91 (t, br, 1H, ind), 6.74 (m, br, 1H, ind), 6.62 (m, br, 1H, ind). $^{31}P\{^1H\}$ NMR ($CDCl_3$, 298 K) δ 30.86 (FWHM = 30 Hz). IR (KBr, cm^{-1}): 3150-3020 w (aromatic ν_{C-H}), 2990-2850 w (ν_{C-H}), 1630-1570 m (aromatic ν_{C-C} and ν_{C-N}), 1215-1110 s ($\nu_{P=O}$ and ν_{C-O}), 996 m (ν_{C-N}). UV-VIS (CH_2Cl_2, r.t., nm): < 315, 255 (max), 288. PL (solid, r.t., $\lambda_{excitation}$ = 350 nm, nm): 445, 534 (sh), 583 (max). PLE (solid, r.t., $\lambda_{emission}$ = 450 nm, nm): < 350. τ (solid, r.t., $\lambda_{excitation}$ = 290 nm, $\lambda_{emission}$ = 585 nm, μs): 310. Φ (solid, r.t., $\lambda_{excitation}$ = 365 nm): 5%.

Characterization of $[ZnI_2(O=PPh_2Ind)_2]$. Anal. calcd for $C_{40}H_{32}I_2N_2O_2P_2Zn$ (953.84 g mol^{-1}, %): C, 50.37; H, 3.38; N, 2.94; I, 26.61. Found (%): C, 50.17; H, 3.39; N, 2.93; I, 26.72. M.p. 140 °C (dec.). Λ_M (acetone, 298 K): 10 ohm^{-1}mol^{-1}cm^2. ^1H NMR ($CDCl_3$, 298 K) δ 7.71 (dd, $^3J_{HH}$ = 7.7 Hz, J_{PH} = 13.4 Hz, 2H, ind), 7.67-7.58 (m, 5H, Ph), 7.44 (m, br, 5H, Ph), 7.16 (t, 1H, $^3J_{HH}$ = 7.5 Hz, ind), 6.92 (t, br, 1H, ind), 6.73 (m, br, 1H, ind), 6.62 (m, br, 1H, ind). $^{31}P\{^1H\}$ NMR ($CDCl_3$, 298 K) δ 30.48 (FWHM = 19 Hz). IR (KBr, cm^{-1}): 3140-3000 w (aromatic ν_{C-H}), 2990-2850 w (ν_{C-H}), 1610-1570 m (aromatic ν_{C-C} and ν_{C-N}), 1210-1100 s ($\nu_{P=O}$ and ν_{C-O}), 997 m (ν_{C-O}). UV-VIS (CH_2Cl_2, r.t., nm): < 320, 254 (max), 289. PL (solid, r.t., $\lambda_{excitation}$ = 350 nm, nm): 455, 535 (sh), 578 (max). PLE (solid, r.t., $\lambda_{emission}$ = 575 nm, nm): < 350. τ (solid, r.t., $\lambda_{excitation}$ = 290 nm, $\lambda_{emission}$ = 593 nm, μs): 409. Φ (solid, r.t., $\lambda_{excitation}$ = 365 nm): 5%.

2.7.3.4 Synthesis of [ZnX$_2$(DOPO)$_2$] and [ZnX$_2$(BPPO)$_2$], DOPO = 9,10-dihydro-9-oxa-10-phosphaphenanthrene-10-oxide, BPPO = dibenzo[*d,f*][1,3,2]dioxaphosphepine 6-oxide and X = Cl, Br

The complexes were prepared following the same synthetic procedure reported for [ZnX$_2$(TPPO)$_2$] (X = Cl, Br, I). Crystal of [ZnBr$_2$(DOPO)$_2$] suitable for X-ray diffraction were collected from toluene/ethanol solutions. As for [MnX$_2$(BPPO)$_2$], acetonitrile was used as solvent for the reaction instead of ethanol. Yield > 70% in all the cases.

Characterization of [ZnCl$_2$(DOPO)$_2$]. Anal. calcd for $C_{24}H_{18}Cl_2O_4P_2Zn$ (568.65 g mol^{-1}, %): C, 50.69; H, 3.19; Cl, 12.47. Found (%): C, 50.49; H, 3.20; Cl, 12.52. M.p. 175°C (dec.). Λ_M (acetone, 298 K): 5 ohm^{-1}mol^{-1}cm^2. ^{1}H NMR (acetone-d$_6$, 298 K) δ 8.87 (s, br, 1H, P-H), 8.24 (d, 2H, J_{HH} = 8.1 Hz, J_{PH} = 5.2 Hz, H$_4$), 8.19 (dd, 1H, J_{HH} = 8.0 Hz, J_{HH} = 1.5 Hz, H$_5$), 8.00 (d, 1H, J_{PH} = 15.0 Hz, J_{HH} = 7.7 Hz, H$_1$), 7.88 (t, 1H, J_{HH} = 7.6 Hz, H$_3$), 7.68 (td, 1H, J_{HH} = 7.4 Hz, J_{PH} = 2.6 Hz, H$_2$), 7.39 (td, 1H, J_{HH} = 7.6 Hz, J_{PH} = 1.0 Hz, H$_7$), 7.37-7.32 (m, 2H, H$_{6,8}$). ^{31}P{^{1}H} NMR (acetone-d$_6$, 298 K) δ 14.31 (FWHM = 186 Hz). IR (KBr, cm^{-1}): 3090-3000 w (aromatic ν_{C-H}), 2429 w (ν_{P-H}), 1610-1560 m (aromatic ν_{C-C}), 1200-1180 s ($\nu_{P=O}$ and ν_{C-O}), 1043 w (ν_{P-O}). PL (solid, r.t., $\lambda_{excitation}$ = 350 nm, nm): 407 (max), 625. PLE (solid, r.t., $\lambda_{emission}$ = 400 nm, nm): < 350. τ (solid, r.t., $\lambda_{excitation}$ = 373 nm, $\lambda_{emission}$ = 410 nm, ns): 7. τ (solid, r.t., $\lambda_{excitation}$ = 290 nm, $\lambda_{emission}$ = 610 nm, ms): 15.0. Φ (solid, r.t., $\lambda_{excitation}$ = 365 nm): 5%.

Characterization of [ZnBr$_2$(DOPO)$_2$]. Anal. calcd for $C_{24}H_{18}Br_2O_4P_2Zn$ (658.56 g mol^{-1}, %): C, 43.84; H, 2.76; Br, 24.30. Found (%): C, 43.68; H, 2.77; Br, 24.21. M.p. 175°C (dec.). Λ_M (acetone, 298 K): 10 ohm^{-1}mol^{-1}cm^2. ^{1}H NMR (CDCl$_3$, 213 K) δ 8.27 (d, 1H, $^1J_{PH}$ = 620 Hz, P-H), 8.07 (dd, 1H, J_{PH} = 15.8 Hz, J_{HH} = 7.6 Hz, H$_1$), 8.02 (dd, 1H, J_{HH} = 8.1 Hz, J_{PH} = 5.6 Hz, H$_4$), 7.96 (dd, 1H, J_{HH} = 8.1 Hz, J_{HH} = 1.6 Hz, H$_5$), 7.80 (t, 1H, J_{HH} = 7.7 Hz, H$_3$), 7.58 (td, 1H, J_{HH} = 7.7 Hz, J_{PH} = 2.9 Hz, H$_2$), 7.44 (t, 1H, J_{HH} = 7.7 Hz, H$_7$), 7.37-7.27 (m, 2H, H$_{6,8}$). ^{31}P{^{1}H} NMR (CDCl$_3$, 213 K) δ 19.44 (FWHM = 35 Hz). IR (KBr, cm^{-1}): 3100-3015 w (aromatic ν_{C-H}), 2418 m (ν_{P-H}), 1640-1560 m (aromatic ν_{C-C}), 1220-1190 s ($\nu_{P=O}$ and ν_{C-O}), 1047 w (ν_{P-O}). UV-VIS (EtOH, r.t., nm): < 300, 259 (sh), 267 (max), 294. PL (solid, r.t., $\lambda_{excitation}$ = 280 nm, nm): 380,

632. PLE (solid, r.t., $\lambda_{emission}$ = 630 nm, nm): < 370 ligands. τ (solid, r.t., $\lambda_{excitation}$ = 373 nm, $\lambda_{emission}$ = 405 nm, ns): 4. τ (solid, r.t., $\lambda_{excitation}$ = 290 nm, $\lambda_{emission}$ = 630 nm, ms): 8.2. Φ (solid, r.t., $\lambda_{excitation}$ = 310 nm): 11%.

Characterization of [ZnCl$_2$(BPPO)$_2$]. Anal. calcd for $C_{24}H_{18}Cl_2O_6P_2Zn$ (600.63 g mol^{-1}, %): C, 47.99; H, 3.02; Cl, 11.80. Found (%): C, 47.81; H, 3.03; Cl, 11.85. M.p. 75°C (dec.). Λ_M (acetone, 298 K): 6 ohm^{-1}mol^{-1}cm^2. ^{1}H NMR (CDCl$_3$, 298 K) δ 7.56 (d, 2H, $^3J_{HH}$ = 7.5 Hz, H$_4$), 7.53 (d, br, 1H, $^1J_{PH}$ = 773 Hz, P-H), 7.53-7.39 (m, 6H, H$_{1-3}$). ^{31}P{^{1}H} NMR (CDCl$_3$, 298 K) δ 14.79 (FWHM = 63 Hz). IR (cm^{-1}): 3120-2985 w (aromatic ν_{C-H}), 2484 w (ν_{P-H}), 1620-1415 w/m (aromatic ν_{C-C}), 1280-1170 s ($\nu_{P=O}$ and ν_{C-O}), 1097 m (ν_{P-O}). UV-VIS (CH$_2$Cl$_2$, r.t., nm): < 290, 244 (max). PL (solid, r.t., $\lambda_{excitation}$ = 265 nm, nm): 396, 606 (max). PLE (solid, r.t., $\lambda_{emission}$ = 610 nm, nm): < 350. τ (solid, r.t., $\lambda_{excitation}$ = 373 nm, $\lambda_{emission}$ = 410 nm, ns): 7. τ (solid, r.t., $\lambda_{excitation}$ = 265 nm, $\lambda_{emission}$ = 610 nm, ms): 17.6. Φ (solid, r.t., $\lambda_{excitation}$ = 310 nm): 13%.

Characterization of [ZnBr$_2$(BPPO)$_2$]. Anal. calcd for $C_{24}H_{18}Br_2O_6P_2Zn$ (689.54 g mol^{-1}, %): C, 41.81; H, 2.63; Br, 23.18. Found (%): C, 41.64; H, 2.64; Br, 23.09. M.p. 55°C (dec.). Λ_M (acetone, 298 K): 9 ohm^{-1}mol^{-1}cm^2. ^{1}H NMR (CDCl$_3$, 298 K) δ 7.72-7.34 (m, 8H, H$_{1-4}$), 7.69 (d, br, 1H, $^1J_{PH}$ = 783 Hz, P-H). ^{31}P{^{1}H} NMR (CDCl$_3$, 298 K) δ 15.31 (FWHM = 195 Hz). IR (cm^{-1}): 3110-2950 w (aromatic ν_{C-H}), 2477 w (ν_{P-H}), 1650-1410 w/m (aromatic ν_{C-C}), 1290-1160 s ($\nu_{P=O}$ and ν_{C-O}), 1097 m (ν_{P-O}). UV-VIS (CH$_2$Cl$_2$, r.t., nm): < 300, 244 (max). PL (solid, r.t., $\lambda_{excitation}$ = 265 nm, nm): 395, 606 (max). PLE (solid, r.t., $\lambda_{emission}$ = 610 nm, nm): < 350. τ (solid, r.t., $\lambda_{excitation}$ = 373 nm, $\lambda_{emission}$ = 410 nm, ns): 5. τ (solid, r.t., $\lambda_{excitation}$ = 265 nm, $\lambda_{emission}$ = 610 nm, ms): 11.8. Φ (solid, r.t., $\lambda_{excitation}$ = 310 nm): 16%.

2.7.3.5 Synthesis of [ZnX$_2$(BPPP)$_2$] and [ZnBr$_2${O=PPh(R/S-BINOL)}$_2$], BPPP = 6-phenyldibenzo[*d*,*f*][1,3,2]dioxaphosphepine 6-oxide, O=PPh(R/S-BINOL) = (4R/S)-4-phenyldinaphtho[2,1-*d*:1',2'-*f*][1,3,2]dioxaphosphepine 4-oxide, and X = Cl, Br, I

The complexes were prepared following the same synthetic procedure reported for [ZnX$_2$(TPPO)$_2$] (X = Cl, Br, I). Yield > 70% in all the cases.

Characterization of [ZnCl$_2$(BPPP)$_2$]. Anal. calcd for $C_{36}H_{26}Cl_2O_6P_2Zn$ (752.83 g mol^{-1}, %): C, 57.44; H, 3.48; Cl, 9.42. Found (%): C, 57.21; H, 3.49; Cl, 9.38. M.p. 225°C (dec.). Λ_M (acetone, 298 K): 4 ohm^{-1}mol^{-1}cm^2. ^{1}H NMR ($CDCl_3$, 298 K) δ 7.78 (dd, 2H, $^3J_{HH}$ = 7.6 Hz, *o*-Ph), 7.63 (t, 1H, $^3J_{HH}$ = 7.8 Hz, *p*-Ph), 7.57 (m, 2H, BP), 7.43 (m, 2H, *m*-Ph), 7.38 (m, 4H, BP), 7.18 (m, br, 2H, BP). ^{31}P{^{1}H} NMR ($CDCl_3$, 298 K) δ 27.28 (FWHM = 22 Hz). IR (cm^{-1}): 3060-2950 w (aromatic ν_{C-H}), 1610-1440 w/m (aromatic ν_{C-C}), 1270-1170 s ($\nu_{P=O}$ and ν_{C-O}), 1045 m (ν_{P-O}). UV-VIS (CH_2Cl_2, r.t., nm): < 350, 244 (max), 271 (sh). PL (solid, r.t., $\lambda_{excitation}$ = 265 nm, nm): 397 (max). PLE (solid, r.t., $\lambda_{emission}$ = 390 nm, nm): < 350, 310 (max). τ (solid, r.t., $\lambda_{excitation}$ = 373 nm, $\lambda_{emission}$ = 410 nm, ns): 6. Φ (solid, r.t., $\lambda_{excitation}$ = 310 nm): 22%.

Characterization of [ZnBr$_2$(BPPP)$_2$]. Anal. calcd for $C_{36}H_{26}Br_2O_6P_2Zn$ (841.73 g mol^{-1}, %): C, 51.37; H, 3.11; Br, 18.99. Found (%): C, 51.57; H, 3.12; Br, 19.07. M.p. 175°C (dec.). Λ_M (acetone, 298 K): 7 ohm^{-1}mol^{-1}cm^2. ^{1}H NMR ($CDCl_3$, 298 K) δ 7.79 (dd, 2H, $^3J_{HH}$ = 7.5 Hz, *o*-Ph), 7.63 (t, 1H, $^3J_{HH}$ = 7.5 Hz, *p*-Ph), 7.57 (m, 2H, BP), 7.44 (m, 2H, *m*-Ph), 7.38 (m, 4H, BP), 7.20 (m, br, 2H, BP). ^{31}P{^{1}H} NMR ($CDCl_3$, 298 K) δ 27.18 (FWHM = 24 Hz). IR (cm^{-1}): 3060-2960 w (aromatic ν_{C-H}), 1630-1430 w/m (aromatic ν_{C-C}), 1280-1170 s ($\nu_{P=O}$ and ν_{C-O}), 1045 m (ν_{P-O}). UV-VIS (CH_2Cl_2, r.t., nm): < 350, 244 (max), 271 (sh). PL (solid, r.t., $\lambda_{excitation}$ = 265 nm, nm): 398, 521 (max), 605 (sh). PLE (solid, r.t., $\lambda_{emission}$ = 520 nm, nm): < 330, 290 (max). τ (solid, r.t., $\lambda_{excitation}$ = 265 nm, $\lambda_{emission}$ = 520 nm, ms): 2.2. Φ (solid, r.t., $\lambda_{excitation}$ = 310 nm): 5%.

Characterization of [ZnI$_2$(BPPP)$_2$]. Anal. calcd for $C_{36}H_{26}I_2O_6P_2Zn$ (935.73 g mol^{-1}, %): C, 46.21; H, 2.80; I, 27.12. Found (%): C, 46.03; H, 2.81; I, 26.91. M.p. 210°C (dec.). Λ_M (acetone, 298 K): 5 ohm^{-1}mol^{-1}cm^2. ^{1}H NMR ($CDCl_3$, 298 K) δ 7.80 (m, br, 2H, *o*-Ph), 7.63 (t, br, 1H, *p*-Ph), 7.56 (m, br, 2H, BP), 7.43 (m, br, 2H, *m*-Ph), 7.36 (m, br, 4H, BP), 7.20 (m, br, 2H, BP). ^{31}P{^{1}H} NMR ($CDCl_3$, 298 K) δ 26.90 (FWHM = 225 Hz). IR (cm^{-1}): 3060-2930 w (aromatic ν_{C-H}), 1605-1435 w/m (aromatic ν_{C-C}), 1260-1170 s ($\nu_{P=O}$ and ν_{C-O}), 1045 m (ν_{P-O}). UV-VIS (CH_2Cl_2, r.t., nm): < 350, 244 (max), 252 (sh), 271 (sh). PL (solid, r.t., $\lambda_{excitation}$ = 265 nm, nm): 513 (max), 605 (sh). PLE (solid, r.t., $\lambda_{emission}$ = 520 nm, nm): < 350, 270 (max). τ (solid, r.t., $\lambda_{excitation}$ = 265 nm, $\lambda_{emission}$ = 515 nm, ms): 2.7. Φ (solid, r.t., $\lambda_{excitation}$ = 310 nm): 6%.

Characterization of [ZnBr$_2${O=PPh(R/S-BINOL)}$_2$]. Anal. calcd for $C_{52}H_{34}Br_2O_6P_2Zn$ (1041.97 g mol^{-1}, %): C, 59.94; H, 3.29; Br, 15.34. Found (%): C, 59.70; H, 3.28; Br, 15.28. M.p. 150°C (dec.). Λ_M (acetone, 298 K): 8 ohm^{-1}mol^{-1}cm^2. ^{1}H NMR ($CDCl_3$, 298 K): δ 8.07 (d, 1H, $^3J_{HH}$ = 7.4 Hz, BINOL), 7.96 (t, 2H, $^3J_{HH}$ = 8.4 Hz, BINOL), 7.83

(m, 2H, BINOL+Ph), 7.64 (m, br, 2H, BINOL), 7.60-7.44 (m, 4H, BINOL+Ph), 7.35 (m, 5H, BINOL+Ph), 6.95 (d, 1H, $^3J_{HH}$ = 8.8 Hz, BINOL). $^{31}P\{^1H\}$ NMR ($CDCl_3$, 298 K) δ 27.97 (FWHM = 44 Hz). IR (cm^{-1}): 3060-2970 m/w (aromatic ν_{C-H}), 1620-1440 m (aromatic ν_{C-C} and ν_{C-N}), 1325 m (ν_{C-O}), 1285-1185 s ($\nu_{P=O}$ and ν_{C-O}), 1070 m (ν_{P-O}). UV-VIS (CH_2Cl_2, r.t., nm): < 350, 237 (max), 262 (sh), 273 (sh), 305, 317, 324. PL (solid, r.t., $\lambda_{excitation}$ = 260 nm, nm): 370. PLE (solid, r.t., $\lambda_{emission}$ = 400 nm, nm): < 350. τ (solid, r.t., $\lambda_{excitation}$ = 373 nm, $\lambda_{emission}$ = 410 nm, ns): 8.

2.8 Additional syntheses and catalytic tests

2.8.1 Synthesis of [Cu(CNXyl)$_3$][BF$_4$] (CNXyl = 2,6-dimethylphenyl isocyanide)

0.472 g of [Cu(NCCH$_3$)$_4$][BF$_4$] (1.5 mmol) were dissolved in 20 mL of dry dichloromethane inside the glove box. 4.5 mmol of 2,6-dimethylphenylisocyanide (CNXyl) were added to the solution and the mixture was stirred overnight. The solvent was then evaporated under reduced pressure and, after adding diethyl ether, the solid formed was filtered, washed and dried *in vacuo*. Crystals suitable for X-ray diffraction were collected from dichloromethane/diethyl ether solutions. Yield > 70%.

Characterization of [Cu(CNXyl)$_3$][BF$_4$]. Anal. calcd for $C_{28}H_{29}BCuF_4N_3$ (543.86 g mol^{-1}, %): C, 60.28; H, 5.24; N, 7.53. Found (%): C, 60.04; H, 5.26; N, 7.50. M.p. 170°C (dec.). Λ_M (acetone, 298 K): 171 $ohm^{-1}mol^{-1}cm^2$. ^1H NMR ($CDCl_3$, 298 K) δ 7.32 (t, J_{HH} = 7.6 Hz, 3H, CH), 7.19 (d, J_{HH} = 7.6 Hz, 6H, CH), 2.51 (s, 18H, CH_3). IR (KBr, cm^{-1}): 3080-2990 m/w (aromatic ν_{C-H}), 2955- 2850 m/w (ν_{C-H}); 2170 s ($\nu_{C\equiv N}$); 1085-985 s (ν_{BF4}).

Catalytic tests with copper(I) complexes: Into a 10 mL vial closed with a screw cap, the organic azide (1.0 mmol), the alkyne (1.1 mmol) and the chosen complex were added in this order. In the case of [Cu(CNXyl)$_3$][BF$_4$] (0.1-1% mol), the reaction was then allowed to proceed under neat conditions and at room temperature.In the cases of [Cu(μ–NCO)(CNXyl)$_2$]$_2$ and [Cu$_4$(μ–N$_3$)$_4$(CNXyl)$_6$] (0.05-5 mol%), 2 mL of methanol or 4 mL of a 1:1 mixture of methanol/dichloromethane were respectively added, and the reaction was performed at 50°C. The full list of azides and alkynes is detailed in Scheme 35 and 37 in the Results and Discussion. The reaction was monitored via TLC and after the total consumption of the starting azide, the product was collected by filtration and washed with hexane. When the corresponding triazole was an oil, the reaction mixture was concentrated under vacuum and the residue was finally purified on silica gel (hexane/ethyl acetate). Yields reported are an average of at least two experiments.

2.8.2 Synthesis of *N,N*-dimethyl-4-amino-2,1,3-benzothiadiazole (BTD^{NMe2})

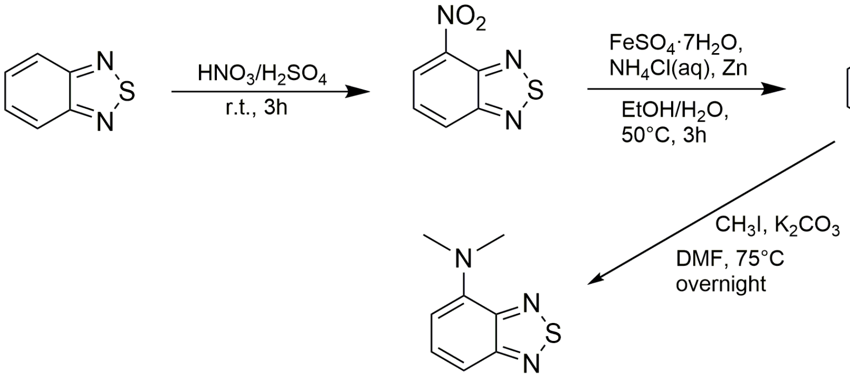

Scheme 22. Synthesis of BTD^{NMe2}.

Synthesis of 4-nitro-2,1,3-benzothiadiazole (BTD^{NO2}): The compound was synthesized by modifying a reported procedure.[141] 24 mL of H_2SO_4 98% and 8 mL of HNO_3 70% were mixed in a flask and frozen with a nitrogen bath. 2,1,3-benzothiadiazole (2.000 g, 14.7 mmol) was added, then the reaction was allowed to warm up at room temperature and stirred for three hours. The reaction mixture was then cooled with an ice bath, and water (15 mL) was slowly added. Subsequently, a solution containing about 18.0 g of NaOH in 40 mL of water was added within an hour. After being removed from the ice bath, $NaHCO_3$ was added in small amounts until a neutral pH was reached. The product was extracted with 2x40 mL of dichloromethane, and the organic fraction was washed with water (2x20 mL), dried over Na_2SO_4, and evaporated under reduced pressure to yield a reddish solid. Yield: 95%. The characterization data agree with those reported for the same product obtained with different synthetic routes.[142]

Synthesis of 4-amino-2,1,3-benzothiadiazole (BTD^{NH2}): The reduction of 4-nitro-2,1,3-benzothiadiazole (BTD^{NO2}) was carried out following a reported procedure with slight modifications.[143] To a solution containing 2.000 g of BTD^{NO2} (11.4 mmol) in 50 mL of ethanol, 9.208 g of $FeSO_4 \cdot 7H_2O$ (34.2 mmol), 4.878 g of ammonium chloride (91.2 mmol), 9 mL of water and 2.243 g of zinc dust (34.2 mmol) were added under vigorous stirring. The mixture was heated at 50 °C for three hours and, after cooling at room temperature, it was cleared by filtration on celite. The solid was washed with 3x10 mL of ethanol. The solution thus obtained was evaporated under reduced pressure. The crude product was dissolved in 40 mL of ethyl acetate, and 30 mL of a 25% aqueous solution of NH_4Cl was added. The organic layer was extracted and washed with water (2x20 mL) and with 30 mL of a saturated aqueous solution of $NaHCO_3$. The organic fraction was then dried over Na_2SO_4 and concentrated under reduced pressure. The product was precipitated with hexane and dried *in vacuo*. Yield: 45%. The characterization data were in agreement with the data reported for the same product prepared with different synthetic routes.[144]

Synthesis of N,N-dimethyl-4-amino-2,1,3-benzothiadiazole, BTD^{NMe2}: The N-methylation of 4-amino-2,1,3-benzothiadiazole (BTD^{NH2}) was carried out by modifying a reported procedure.[145] BTD^{NH2} (0.350 g, 2.3 mmol) was dissolved in 15 mL of *N*,*N*-dimethylformamide (DMF), then 3.179 g of K_2CO_3 (23.0 mmol) and 1.4 mL of CH_3I (23.0 mmol) were added under stirring. The mixture was heated at 75 °C for twelve hours. After cooling at room temperature, water (50 mL) was added, and the product was extracted with 2x80 mL of ethyl acetate. The organic fraction was washed with 100 mL of cold water, dried over Na_2SO_4, and evaporated under reduced pressure. The product was dissolved in 30 mL of pentane, the solution was purified by filtration, and the solvent was removed under nitrogen flow to afford a red oil. Yield: 50%.

Characterization of N,N-dimethyl-4-amino-2,1,3-benzothiadiazole. ^1H NMR ($CDCl_3$, 298 K) δ 7.49-7.40 (m, 2H, BTD), 6.57 (t, 1H, $^3J_{HH}$ = 5.9 Hz, BTD), 3.29 (s, 6H, Me). ^{13}C NMR ($CDCl_3$, 298 K) δ 156.90 BTD-C_{ipso}, 149.29 BTD-C_{ipso}, 144.43 BTD-C_{ipso}, 130.73 BTD-CH, 111.13 BTD-CH, 108.85 BTD-CH, 42.59 Me. IR (KBr disk, cm^{-1}): 1587 m, 1545 s, 1494 m (aromatic ν_{C-N} and ν_{C-C}). UV-VIS (CH_2Cl_2, 298 K, nm): < 530, 253 (max), 300, 306, 314, 432. UV-VIS (hexane, 298 K, nm): < 500, 250 (max), 293 (sh), 299, 304, 312, 425. UV-VIS (CH_3CN, 298 K, nm): < 540, 250 (max), 293 (sh), 299, 305, 312, 429. UV-VIS (DMSO, 298 K, nm): < 549, 295 (sh), 302, 306, 315, 437. UV-VIS (acetone, 298 K, nm): < 534, 433. PL (CH_2Cl_2, 298 K, $\lambda_{excitation}$ = 390 nm, nm): 604. PL (hexane, 298 K, $\lambda_{excitation}$ = 390 nm, nm): 526. PL (CH_3CN, 298 K, $\lambda_{excitation}$ = 390 nm, nm): 630. PL (DMSO, 298 K, $\lambda_{excitation}$ = 390 nm, nm): 642. PL (acetone, 298 K, $\lambda_{excitation}$ = 390 nm, nm): 616.

Synthesis of BTD^{NMe2}@PMMA: 0.250 g of PMMA were dissolved in 6 mL of dichloromethane under slow stirring, then a solution containing 0.010 g of BTD^{NMe2} in

4 mL of dichloromethane was added. The solution was transferred in a cylindrical polyethylene holder (1 cm diameter) and allowed to evaporate at room temperature. The polymeric film thus obtained was finally kept overnight under 10^{-2} torr vacuum to remove traces of solvent.

Characterization of BTD^{NMe2}@PMMA. PL (solid sample, $\lambda_{excitation}$ = 400 nm, nm): 606. PLE (solid sample, $\lambda_{emission}$ = 605 nm, nm): < 560.

2.8.3 Synthesis of palladium(II) complexes with Schiff bases derived from BTD^{NH2}

2.8.3.1 Synthesis of [PdCl$_2$(BTD^{NPy})] and [PdClMe(BTD^{NPy})]

To a solution containing 0.076 g (0.5 mmol) of 4-amino-2,3,1-benzothiadiazole (BTD^{NH2}) in 30 mL of dry dichloromethane a stoichiometric amount of freshly distilled pyridine-2-carboxaldehyde (0.054 g, 48 μL) was added together with 3 Å molecular sieves. The reaction mixture was refluxed for six hours. Once at room temperature, the solution was filtered and added to 0.100 g (0.4 mmol) of [PdCl$_2$(COD)] or [PdClMe(COD)], that were previously synthesized following reported methods.[146] The reaction mixture was stirred overnight, and the product precipitated from CH_2Cl_2 was filtered and dried *in vacuo*. Yield > 80% in both cases.

Characterization of [PdCl$_2$(BTD^{NPy})]. Anal. calcd for $C_{12}H_8Cl_2N_4PdS$ (417.60 g mol^{-1}, %): C, 34.51; H, 1.93; N, 13.42; S, 7.68; Cl, 16.98. Found (%): C, 34.37; H, 1.94; N, 13.37; S, 7.65; Cl, 17.05. M.p. > 230 °C. Λ_M (DMSO, 298 K): 3 ohm^{-1}mol^{-1}cm^2. ^{1}H NMR (CD_3NO_2, 298 K) δ 9.28 (d, 1H, $^3J_{HH}$ = 5.2 Hz, py), 8.80 (s, 1H, CH=N), 8.40 (t, 1H, $^3J_{HH}$ = 7.7 Hz, arom.), 8.23 (d, 1H, $^3J_{HH}$ = 7.3 Hz, arom.), 8.11 (d, 1H, $^3J_{HH}$ = 8.8 Hz, arom.), 7.95 (m, 1H, arom.), 7.82 (t, 1H, $^3J_{HH}$ = 7.7 Hz, arom.), 7.73 (d, 1H, $^3J_{HH}$ = 7.3 Hz, arom.). IR (KBr, cm^{-1}): 3105-2920 m/w (aromatic ν_{C-H}), 1630-1445 m/w (aromatic ν_{C-C} and ν_{C-N}).

Characterization of [PdClMe(BTD^{NPy})]. Anal. calcd for $C_{13}H_{11}ClN_4PdS$ (397.19 g mol^{-1}, %): C, 39.31; H, 2.79; N, 14.11; S, 8.07; Cl, 8.93. Found (%): C, 39.15; H, 2.80; N, 14.05; S, 8.04; Cl, 8.89. M.p. > 230 °C. Λ_M (DMSO, 298 K): 3 ohm^{-1}mol^{-1}cm^2. ^{1}H NMR (DMSO-d$_6$, 298 K) δ 9.27 (s, br, 1H, CH=N), 8.83 (s, br, 1H, py), 8.33 (s, br, 1H, py), 8.25 (d, 1H, $^3J_{HH}$ = 7.4 Hz, BTD), 8.10 (d, 1H, $^3J_{HH}$ = 8.0 Hz, BTD), 7.97 (s, br, 1H, py), 7.85 (t, 1H, $^3J_{HH}$ = 7.5 Hz, BTD), 7.68 (s, br, 1H, py), 1.09-0.00 (m, br, 3H, Pd-Me). ^{1}H NMR (DMSO-d$_6$, 318 K) δ 9.25 (s, 1H, CH=N), 8.84 (d, br, 1H, $^3J_{HH}$ = 4.6 Hz, py), 8.31 (s, br, 1H, py), 8.25 (d, 1H, $^3J_{HH}$ = 7.4 Hz, BTD), 8.07 (d, 1H, $^3J_{HH}$ = 8.0 Hz, BTD), 7.93 (s, br, 1H, py), 7.84 (t, 1H, $^3J_{HH}$ = 7.5 Hz, BTD), 7.67 (s, br, 1H, py), 0.54 (s, br, 3H, Me). IR (KBr, cm^{-1}): 3110-2930 m/w (aromatic $\nu_{C\text{-}H}$), 2890-2815 m/w ($\nu_{C\text{-}H}$), 1620-1450 m/w (aromatic $\nu_{C\text{-}C}$ and $\nu_{C\text{-}N}$).

2.8.3.2 Synthesis of [Pd(COMe)Cl(BTD^{NPy})]

A solution containing 0.100 g (0.3 mmol) of [PdClMe(BTD^{NPy})] in 20 mL of dichloromethane was put under atmosphere of carbon monoxide at room temperature. The solid rapidly dissolved in CH_2Cl_2 and the solution passed from yellow to dark red almost immediately. The solvent was evaporated under reduced pressure and the product was precipitated by adding diethyl ether. The solid was filtered, washed with 2x15 mL of diethyl ether and dried *in vacuo*. Crystals suitable for X-ray diffraction were collected from the slow evaporation of dichloromethane/diethyl ether solutions. Quantitative yield.

Characterization of [Pd(COMe)Cl(BTD^{NPy})]. Anal. calcd for $C_{14}H_{11}ClN_4OPdS$ (425.20 g mol^{-1}, %): C, 39.55; H, 2.61; N, 13.18; S, 7.54; Cl, 8.34. Found (%): C, 39.39; H, 2.62; N, 13.13; S, 7.51; Cl, 8.37. M.p. 160°C (dec.). Λ_M (acetone, 298 K): 3 ohm^{-1}mol^{-1}cm^2. ^{1}H NMR (CDCl$_3$, 298 K) δ 9.62 (s, br, 1H, CH=N), 8.95 (s, br, 1H, py), 8.54 (s, br, 1H, py), 8.47 (s, br, 1H, py), 8.15 (m, br, py), 7.99 (d, 1H, $^3J_{HH}$ = 9.0 Hz, BTD), 7.93 (d, 1H, $^3J_{HH}$ = 7.5 Hz, BTD), 7.71 (dd, 1H, $^3J_{HH}$ = 7.5 Hz, $^3J_{HH}$ = 9.0 Hz, BTD), 2.71 (s, 3H, Pd-C(O)Me). IR (KBr, cm^{-1}): 3130-2970 m/w (aromatic $\nu_{C\text{-}H}$), 2920-2815 m/w ($\nu_{C\text{-}H}$), 1697 s ($\nu_{C=O}$), 1600-1470 m (aromatic $\nu_{C\text{-}C}$ and $\nu_{C\text{-}N}$). UV-VIS (CH_2Cl_2, r.t., nm): < 420, 256, 316 (max), 359, 372 (sh), 395 (sh).

Catalytic tests with [PdCl$_2$(BTD^{NPy})], [PdClMe(BTD^{NPy})] and [Pd(COMe)Cl(BTD^{NPy})]: The reactions were carried out in an autoclave equipped with PTFE insert, and a pressure regulator to maintain constant the reaction pressure. A circulation bath ensured a stable temperature around 120°C. In a typical experiment, 0.002 mmol of palladium(II) complexes, 1.4 mmol of triethylamine and 0.8 mmol of iodobenzene were dissolved in 20 mL of methanol and introduced into the reactor. After that, the reactor was closed, purged before with nitrogen and then with carbon monoxide, pressurized at 50 atm and heated to 120°C under stirring for 2 h. Once cooled down to room temperature, the liquid phase was analysed by GC-MS. Conversion > 97% in all the cases.

3 Results and discussion

3.1 Luminescent manganese(II) complexes

In recent years, the research group exploited [O=P]-donor ligands for the preparation of tetrahedral and octahedral manganese(II) luminescent complexes.[40,98a-b] At the beginning of my PhD I started to use similar derivatives for the synthesis of green-emitting manganese(II) coordination compounds. In particular, the reaction of 1,3-dimethyl-2-phenyl-1,3-diazaphospholidine-2-oxide [$O=P(MeNCH_2CH_2NMe)Ph$] and *N,N,N',N'*-tetramethyl-*P*-indol-1-ylphosphonic diamide [$O=P(NMe_2)_2Ind$] with manganese(II) halides in ethanol and under mild conditions allowed the isolation of the corresponding tetrahedral derivatives having general formulae [MnX_2L_2] (X = Cl, Br, I; L = $O=P(MeNCH_2CH_2NMe)Ph$ or $O=P(NMe_2)_2Ind$), as depicted in Scheme 23.

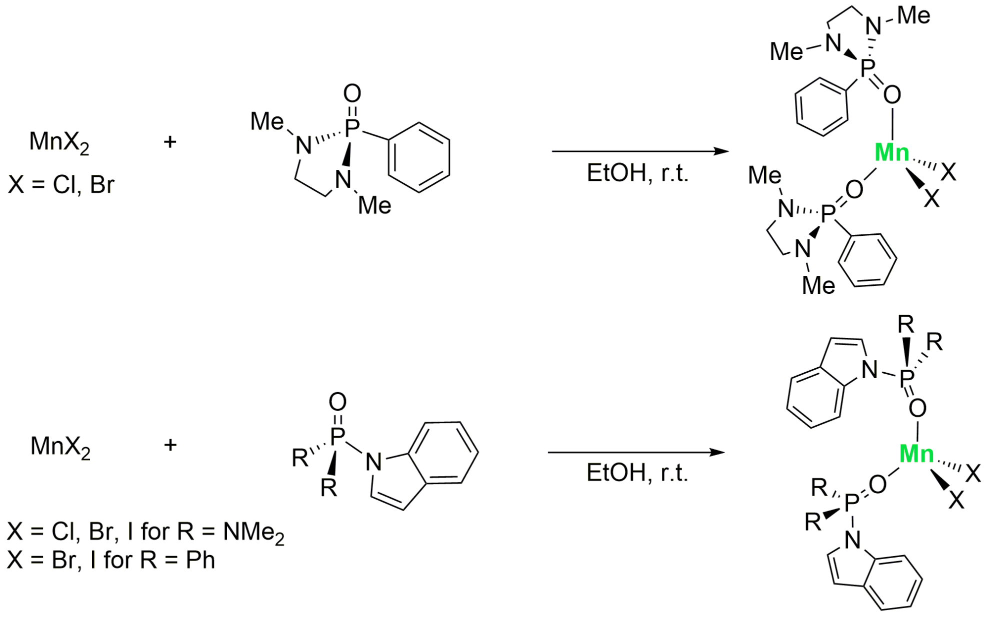

Scheme 23. Synthesis of [$MnX_2\{O=P(MeNCH_2CH_2NMe)Ph\}_2$] (X = Cl, Br) and [$MnX_2\{O=PR_2Ind\}_2$] (X = Cl, Br, I for R = NMe_2; X = Br, I for R = Ph).

In both cases, elemental analyses and conductivity measurements together with the molar magnetic susceptibility values supported the formation of the proposed neutral manganese(II) compounds. The IR spectra showed the bands related to the aromatic ν_{C-H} (3150-3000 cm^{-1}), ν_{C-C} and ν_{C-N} (1620-1390 cm^{-1}), and the $\nu_{P=O}$ (1245-1150 cm^{-1}). As observable in Figure 40, the $\nu_{P=O}$ stretching decreases with respect to the free *N,N,N',N'*-tetramethyl-*P*-indol-1-ylphosphonic diamide because of the coordination to the metal centre, while ν_{P-NMe2} slightly increases, in line with what already detected for other ligands based on the phosphoramide skeleton.[147]

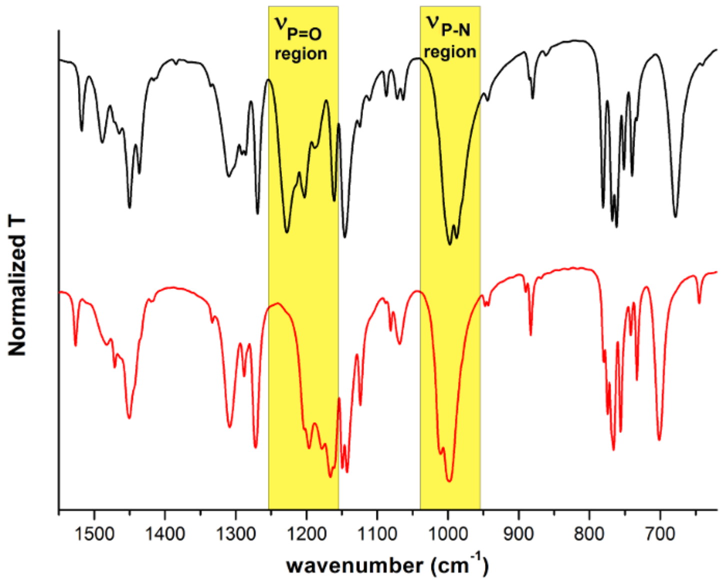

Figure 40. IR spectra of *N,N,N′,N′*-tetramethyl-*P*-indol-1-ylphosphonic diamide (black line) and [MnBr$_2${O=P(NMe$_2$)$_2$Ind}$_2$] (red line).

Single-crystal X-ray diffraction confirmed the formation of the proposed complexes, see for instance the ORTEP plot of the bromo-derivatives reported in Figure 41. The complexes [MnX$_2${O=P(MeNCH$_2$CH$_2$NMe)Ph}$_2$] (X = Cl, Br) and [MnX$_2${O=P(NMe$_2$)$_2$Ind}$_2$] (X = Cl, Br, I) respectively crystallize in the *C*2/*c* and *P*2$_1$/*n* monoclinic space groups. Crystal data and structure refinement are summarized in Table A1 and A2. Selected bond lengths and angles are collected in Table B1 and B2.

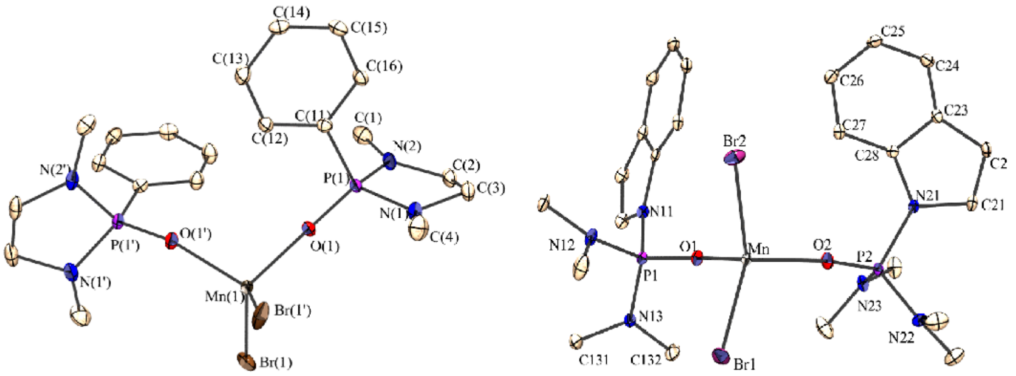

Figure 41. ORTEP plot of [MnBr$_2$L$_2$] where L = O=P(MeNCH$_2$CH$_2$NMe)Ph or O=P(NMe$_2$)$_2$Ind.

As deductible from DSC-TGA measurements conducted on the indolyl derivatives collected in Figure 42, the complexes revealed to be thermally stable up to 200°C. The DSC peaks related to the melting are comprised between 99 and 125 °C for all the six complexes. No significant mass loss occurs below 190°C for

$[MnX_2\{O=P(MeNCH_2CH_2NMe)Ph\}_2]$ and below 230°C for $[MnX_2\{O=P(NMe_2)_2Ind\}_2]$ (X = Cl, Br, I).

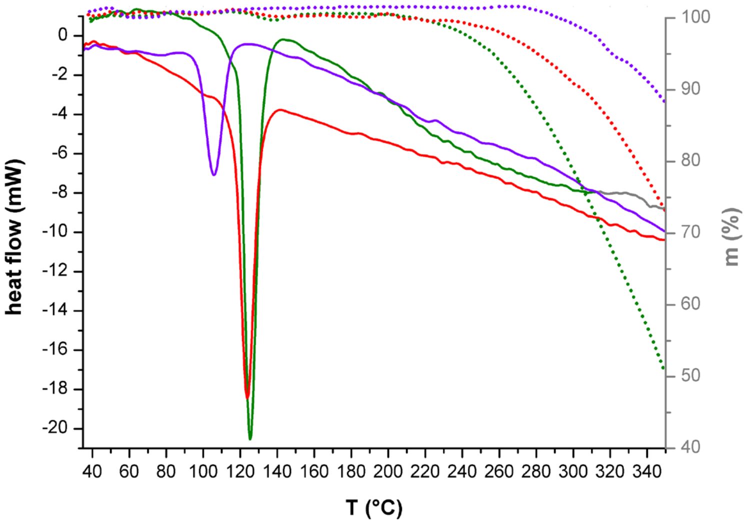

Figure 42. DSC–TGA curves for $[MnX_2\{O=P(NMe_2)_2Ind\}_2]$. DSC, solid lines; TGA, dotted lines. X = Cl, green; X = Br, red; X = I, violet.

As regards the photoluminescent properties, the UV-vis spectra showed in all the cases absorptions below 300 nm, attributable to the $\pi^* \leftarrow \pi$ transitions of the coordinated ligands. The presence of the indolyl instead of the phenyl fragment as light harvesting substituent determines an increased absorption (around 5 times higher) in the UV spectrum of the free ligands as can be observed in Figure 43.

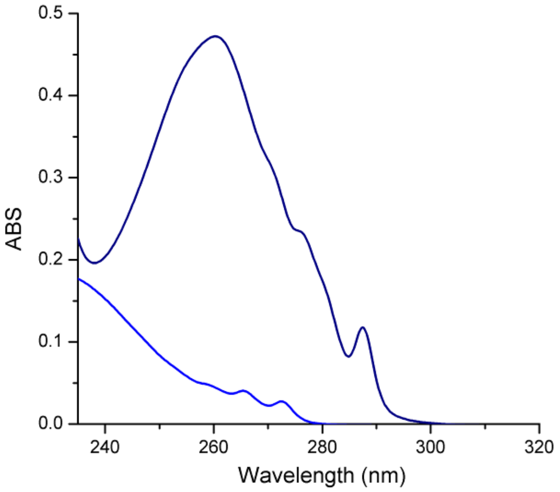

Figure 43. Comparison between the absorption spectra of *N*,*N*,*N*',*N*'-tetramethyl-*P*-indol-1-ylphosphonic (dark blue line) and *N*,*N*,*N*',*N*'-tetramethyl-*P*-phenylphosphonic diamides (blue line). CH_2Cl_2 solution, $5 \cdot 10^{-5}$ M.

At the solid state the tetrahedral derivatives are characterized by appreciable green emission upon excitation with UV and violet-blue light, that is not maintained in solution. The normalized PL and PLE spectra are shown in Figure 44. The PL bands are centred between 508 and 535 nm and attributable to the metal-centred ${}^4T_1({}^4G) \rightarrow {}^6A_1({}^6S)$ transition.[19a,27,29,41,148] No shoulder related to the ground-state vibrational levels is present. The negligible differences among the emission bands suggest a comparable ligand field strength. As observable in the PLE spectra reported in Figure 44, the excitation between 330 and 400 nm is attributable to the ${}^4P,{}^4D \leftarrow {}^6S$ transitions, while below 315 nm it is mainly related to the energy transfer from the coordinated ligands to the excited states of the metal centre, superimposed with the ${}^4F \leftarrow {}^6S$ transitions.[19b] Luminescence lifetimes τ are strongly affected by the choice of the coordinated halide. The increase of the halide atomic number and consequently of the spin-orbit coupling (SOC) effect determines an acceleration of the radiative decay, as observable for the inset in Figure 44. The quantum yield measurements, limited to the bromo-derivatives because of their higher stability under air, are comprised between 22-23%, in line with what reported for $[MnBr_2(O{=}PPh_3)_2]$ and slightly above the 17% measured for $[MnBr_2\{O{=}PPh(NMe_2)_2\}_2]$.[27,98a]

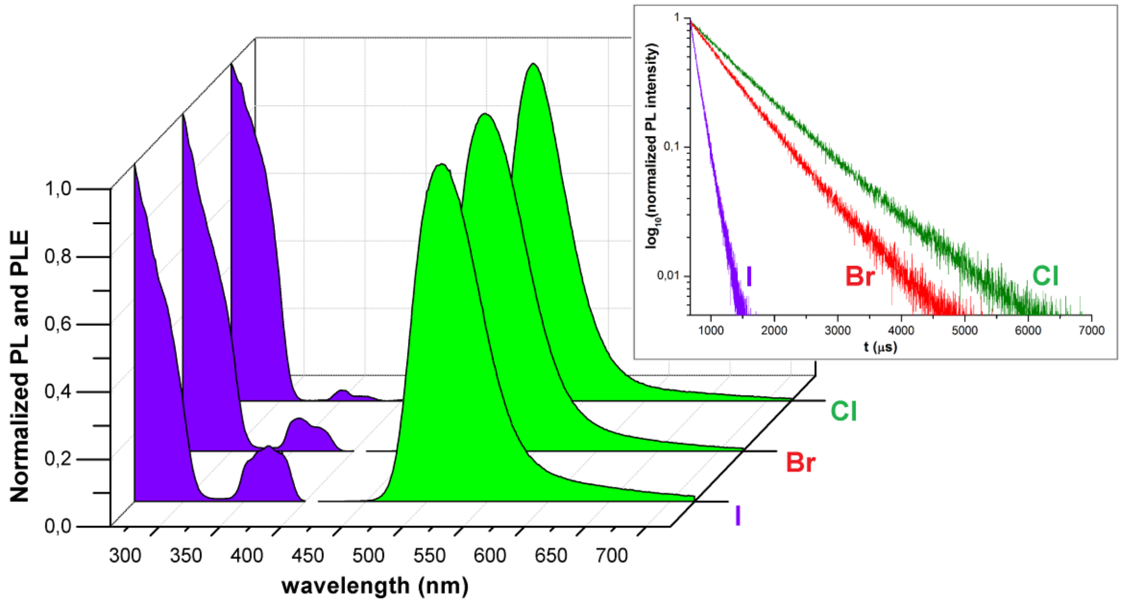

Figure 44. Normalized PL and PLE spectra of $[MnX_2\{O{=}P(MeNCH_2CH_2NMe)Ph\}_2]$ complexes. Inset: Semi-log plot of the luminescence decay curves. Solid samples, r.t.

As previously stated, the absorptions of coordinated ligands fall below 300 nm. On the basis of TD-DFT calculations, they are assigned to $\pi^* \leftarrow \pi$ transitions of the aromatic ring with the participation of the filled oxygen and nitrogen orbitals. Intersystem crossing as the intermediate step between excitation and energy transfer to manganese(II) was considered by modelling the triplet state electronic configuration of $[ZnCl_2L_2]$, L = O=P(MeNCH$_2$CH$_2$NMe)Ph and O=P(NMe$_2$)$_2$Ind. The relative energy of $[ZnCl_2\{O=P(MeNCH_2CH_2NMe)Ph\}_2]$ corresponds to a wavelength around 340 nm, suggesting possible energy transfer towards the ^{4}P, ^{4}D and ^{4}G states of the metal centre. On the other hand, $[ZnCl_2\{O=P(NMe_2)_2Ind\}_2]$ triplet state is in the 382-392 nm wavelength range, overlapping only the ^{4}D levels of tetrahedral manganese(II). The triplet states of the coordinated ligands are localized on the phenyl or indol-1-yl fragments (see Figure 45). The involvement of the ligand triplet state in the sensitization of manganese(II) luminescence was already proposed by Zheng *et al.*[27] The absence of ligand-centred luminescence in $[MnX_2L_2]$ complexes can be explained on supposing that, after the ^{3}LC → ^{4}D energy transfer, fast internal conversion to the ^{4}G levels occurs. The direct energy transfer from excited singlet states located on the ligands to the energetically close manganese(II) ^{4}F manifold and the subsequent internal conversion cannot be however ruled out.

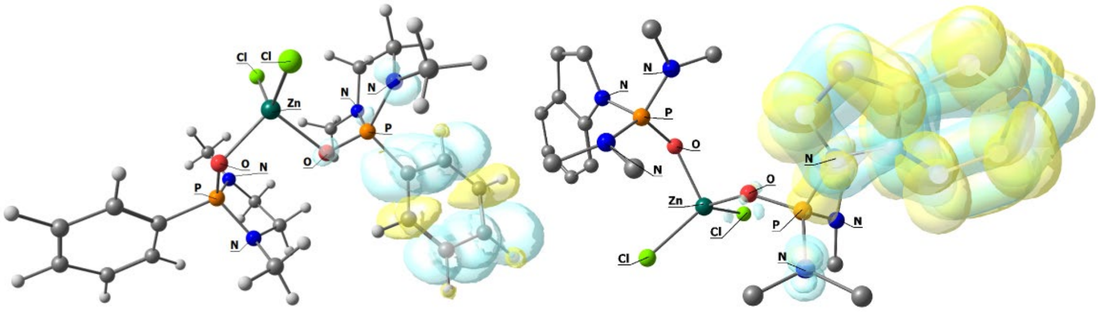

Figure 45. DFT-optimized structure of $[ZnCl_2L_2]$, triplet state and spin density surface (isovalue = 0.003 a.u.). ωB97X/def2-SVP calculations.

These types of derivatives proved that the presence of a rigid structure and a light harvesting substituent can help to overcome the limited directed excitation of manganese(II) metal centre. The formal replacement of the dimethylammino groups with two phenyl moieties was therefore considered, using (indol-1-yl)diphenylphosphine oxide (O=PPh$_2$Ind) as ligand. This species was successfully coordinated to $MnBr_2$ and MnI_2 afforDing the corresponding tetrahedral derivatives having general formulae $[MnX_2(O=PPh_2Ind)_2]$ (X = Br, I). The formation of the proposed complexes was supported by elemental analysis, magnetic momentum and conductivity measurements. The excitation with UV light affords the typical green emission expected for the $^4T_1(^4G) \rightarrow {}^6A_1(^6S)$ transition, centred around 520 nm. Similar to the previously reported tetrahedral complexes, in the PLE spectra the metal centred transitions $^4F \leftarrow {}^6A_1(^6S)$ are superimposed to the excitation of the ligands below 330 nm. At higher wavelengths the $^4P,^4D, \leftarrow {}^6A_1(^6S)$ and $^4G \leftarrow {}^6A_1(^6S)$ transitions can be detected respectively in the 350-380 nm and 420-470 nm ranges. The lifetimes are equal to 288 μs and 56 μs respectively for the bromo- and the iodo-derivative, in line with the increased SOC effect. Despite the fact that on the basis of DFT calculations the triplet states are localized on the indol-1-yl fragment, the emissions are meaningfully less intense than those observed for the related $[MnX_2\{O=P(NMe_2)_2Ind\}_2]$ (X = Br, I) complexes. The formal replacement of $-NMe_2$ with -Ph at pentavalent phosphorus seems therefore to accelerate the ligand-centred non-radiative decay routes, possibly because of a reduced rate of energy transfer to the manganese(II) centre.

I therefore decided to increase the π-conjugated systems by introducing a 2-naphthyl and a carbazolyl fragment in the arylphosphonic diamide skeleton. The corresponding ligands are depicted in Scheme 24.

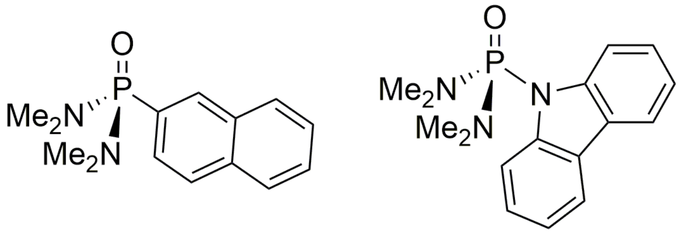

O=P(NMe₂)₂(2-Naph) **O=P(NMe₂)₂Cbz**

Scheme 24. $O=P(NMe_2)_2(2\text{-}Naph)$ and $O=P(NMe_2)_2Cbz$ ligands.

These [O=P]-donor ligands in combination with anhydrous MnX_2 (X = Cl, Br, I) salts allowed the isolation of the corresponding tetrahedral derivatives. The formation of neutral complexes having general formulae $[MnX_2L_2]$ (X = Cl, Br, I; L = *N*,*N*,*N*',*N*'-tetramethyl-*P*-naphtalen-2-ylphosphonic and *N*,*N*,*N*′,*N*′-tetramethyl-*P*-carbazol-9-ylphosphonic diamides) was confirmed by means of elemental analyses, magnetic susceptibility values, conductivity measurements and single-crystal X-ray diffraction (see Figure 46 for the structure of the bromo-derivatives). All the complexes crystallize in monoclinic space groups ($P2_1/n$ for the 2-naphthyl derivatives, the $P2_1/c$ for the chloro- and bromo-carbazolyl species and *P*-1 for the iodo-carbazolyl complex). Crystal data and structure refinement are summarized in Table A3 and A4. Selected bond lengths and angles are collected in Table B3 and B4.

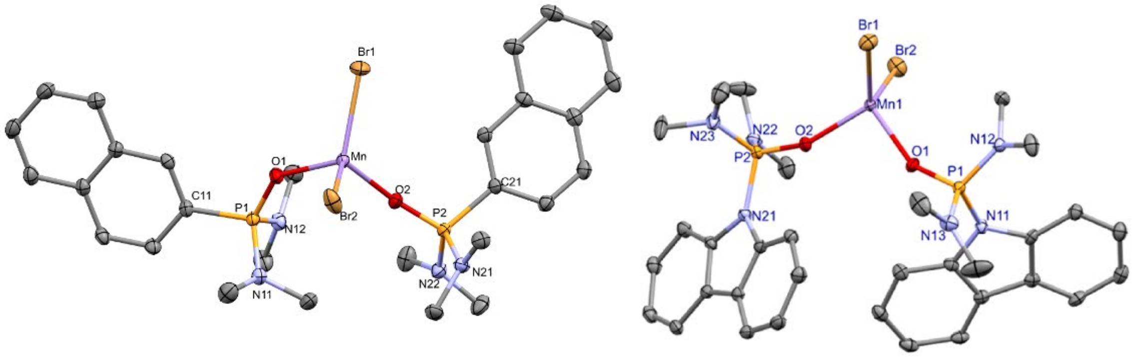

Figure 46. Structure $[MnBr_2L_2]$ where L = O=P(NMe_2)$_2$(2-Naph) or O=P(NMe_2)$_2$Cbz.

Similar to what previously observed from the comparison between the IR spectrum of the free ligand and of [$MnBr_2${O=P(NMe_2)$_2$Ind}$_2$] (see Figure 47), also in the case of O=P(NMe_2)$_2$Cbz the coordination to manganese(II) metal centre determines a lowering of $\nu_{P=O}$ stretchings, as highlighted in Figure 47.

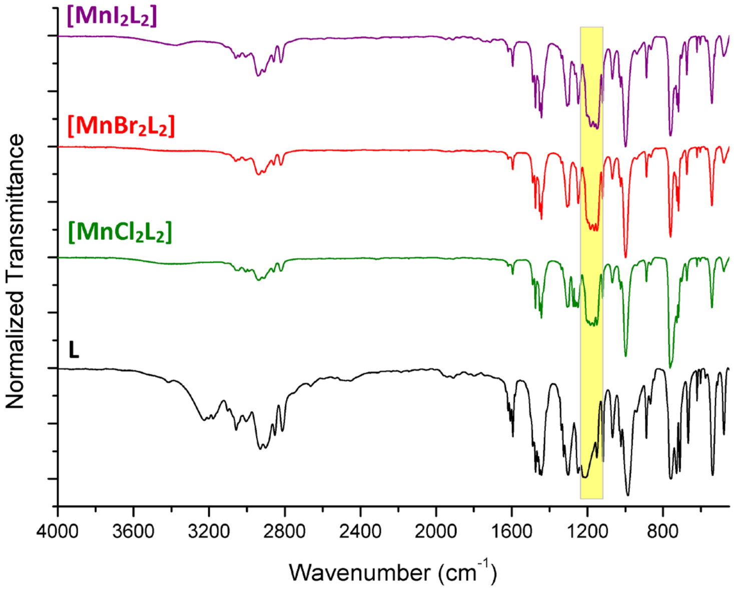

Figure 47. IR spectra of O=P(NMe_2)$_2$Cbz (L) and [MnX_2{O=P(NMe_2)$_2$Cbz}$_2$] (X = Cl, Br, I).

As regards the photoluminescence of the *N*,*N*,*N*',*N*'-tetramethyl-*P*-naphtalen-2-ylphosphonic diamide complexes, the UV-Vis spectra collected in dichloromethane are superimposable, showing bands related to the coordinated ligands below 350 nm. The complexes exhibit appreciable emissions at the solid state upon excitation with UV light. Also in the case of crystallized samples the photoluminescence of the complexes appears to be different to what commonly expected for tetrahedral manganese(II) derivatives. Excitation with wavelengths below 340 nm, mainly attributed to light absorption by the coordinated ligands, affords emission spectra characterized by two bands, the former centred between 513 and 520 nm and attributable to the metal centred transition between the $^4T_1(^4G)$ and the $^6A_1(^6S)$ states (see Figure 48 for the 2-naphthyl derivatives). Instead, the latter band falls in the red region of the visible spectrum, with maximum in the 637-643 nm range. As observable in Figure 48, the relative intensity of the $^4T_1(^4G) \rightarrow {}^6A_1(^6S)$ transition increases by replacing the chlorides with heavier halides. The related PLE spectra are the superimposition of transitions involving the ligands and the direct manganese(II) excitation, in particular the $^4D,^4P \leftarrow {}^6S$ between 350 and 400 nm and the $^4G \leftarrow {}^6S$ in the 405–510 nm range. The intensity of the metal-centred excitation bands is low for the chloro-complex due to the low SOC. On the contrary, the PLE spectra of the bromo- and iodo-derivatives reported in Figure 49 are the superimposition of appreciable metal- and ligand-centred contributions, whose relative intensity remains constant on changing the emission wavelength in the case of the iodo-derivative $[MnI_2\{O{=}P(NMe_2)_2(2\text{-}Naph)\}_2]$. For $[MnBr_2\{O{=}P(NMe_2)_2(2\text{-}Naph)\}_2]$ the ligand-centred contribution is predominant if the emission in the red range is considered, while the metal-centred excitations are enhanced on considering the emission around 510 nm. As a result, the emission of $[MnBr_2\{O{=}P(NMe_2)_2(2\text{-}Naph)\}_2]$ is strongly dependent upon the emission wavelength, as observable from the PL spectra and the CIE 1931 chromaticity diagram in Figure 49.[149] In particular, the excitation of $[MnBr_2\{O{=}P(NMe_2)_2(2\text{-}Naph)\}_2]$ at 375 nm affords a PL spectrum dominated by the highest energy band. Differently, the emission of $[MnI_2\{O{=}P(NMe_2)_2(2\text{-}Naph)\}_2]$ is not excitation dependent, and two bands in the PL spectrum were observed both with $\lambda_{excitation}$ = 325 nm and 375 nm.

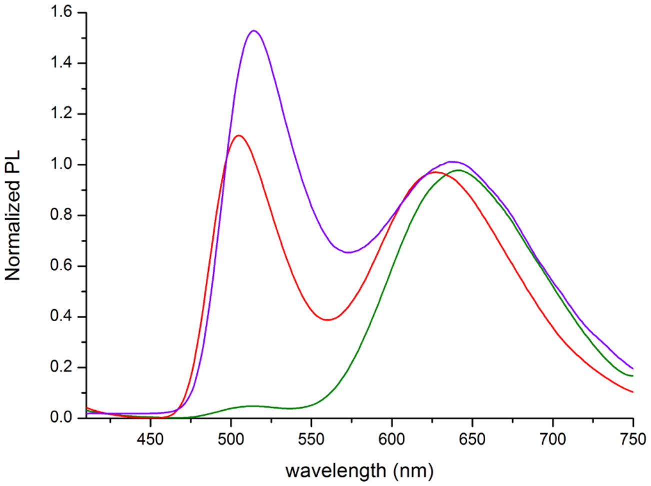

Figure 48. Normalized PL spectra (solid samples, $\lambda_{excitation}$ = 325 nm) of $[MnX_2\{O{=}P(NMe_2)_2(2\text{-}Naph)\}_2]$ complexes. X = Cl, green; X = Br, red; X = I, violet.

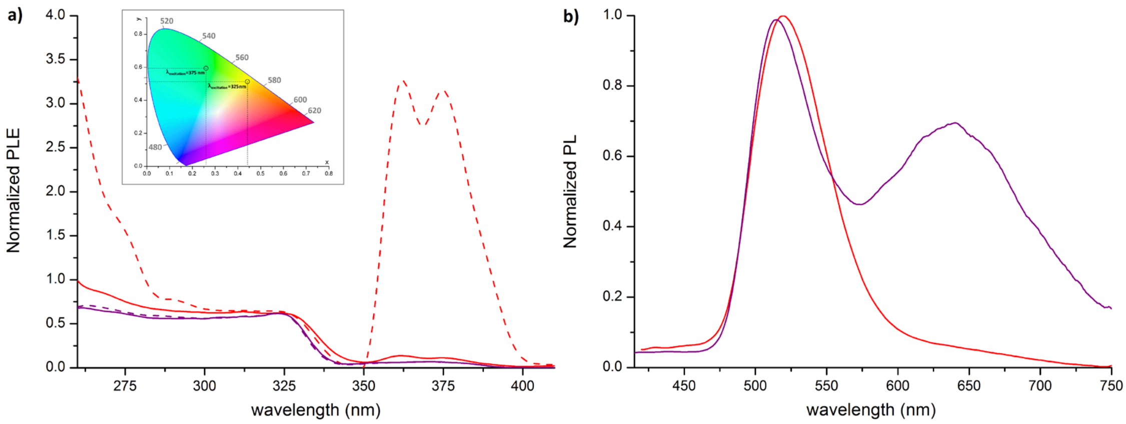

Figure 49. a) Normalized PLE spectra of solid [$MnX_2\{O=P(NMe_2)_2(2\text{-}Naph)\}_2$] complexes. X = Br, red; X = I, violet; $\lambda_{emission}$ = 640 nm, solid line; $\lambda_{emission}$ = 513 nm, dashed line. Inset: CIE 1931 chromaticity diagram of [$MnBr_2\{O=P(NMe_2)_2(2\text{-}Naph)\}_2$], $\lambda_{excitation}$ = 325 nm and 375 nm. b) PL spectra of [$MnX_2\{O=P(NMe_2)_2(2\text{-}Naph)\}_2$] (solid samples, $\lambda_{excitation}$ = 375 nm; X = Br, red; X = I, violet).

Besides working with crystallized samples in order to exclude the presence of octahedral impurities, the interaction with moisture of the [$MnX_2\{O=P(NMe_2)_2(2\text{-}Naph)\}_2$] complexes was carefully avoided, and the compounds underwent heating at 110°C under vacuum for several hours. On considering the free ligand, only the band related to the fluorescence in the greenish blue region was detected also at low temperatures. The nature of the red band was investigated also from a computational point of view. The spin density plots of the sextet and octet states of [$MnBr_2\{O=P(NMe_2)_2(2\text{-}Naph)\}_2$] reported in Figure 50 suggest that the emission at lower energy could be tentatively attributed to a ligand-centred triplet state (^{3}LC), mainly localized on the 2-naphthyl π-system. On admitting this hypothesis, the photoluminescence described for the complexes could be attributed to the competition between metal- and ligand-centred emissions, and the different results obtained on changing the halide can be interpreted in terms of energy transfer between ligands and metal. In the case of X = Cl only the excitation of the ligands causes appreciable luminescence. The absorbed energy is scarcely transferred to manganese(II), therefore the main emission is the ^{3}LC one, falling in the red range. Under the same conditions, part of the energy is instead transferred to manganese(II) when X = Br, and the PL spectrum is the superimposition of $^4T_1(^4G) \rightarrow {}^6A_1(^6S)$ and ^{3}LC transitions. The energy transfer rate must be lower than the manganese(II) luminescence decay rate, since the direct excitation of the metal centre causes an emission with enhanced $^4T_1(^4G) \rightarrow {}^6A_1(^6S)$ transition. Finally, for X = I the ligand-metal energy transfer is efficient with respect to the luminescence decay mechanisms, therefore the same dual band spectrum is obtained on changing the excitation wavelength in a dynamic equilibrium between metal- and ligand-centred emissions.

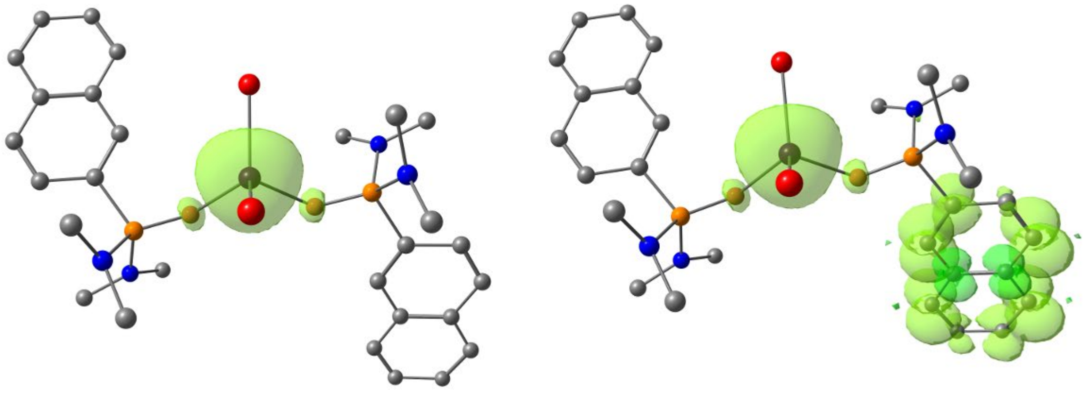

Figure 50. DFT-optimized structures of [$MnBr_2\{O=P(NMe_2)_2(2\text{-}Naph)\}_2$] complexes (sextet and octet state) and spin density surfaces (isovalue = 0.005 a.u.). ωB97X/def2-SVP calculations. Colour map: Mn, violet; Br, dark red; P, orange; O, red; N, blue; C, gray; isosurface, light green tones. Hydrogen atoms are omitted for clarity.

The lifetimes values τ for ${}^4T_1({}^4G) \rightarrow {}^6A_1({}^6S)$ transition follow the expected order X = Cl > X = Br > X = I, but for [$MnBr_2\{O=P(NMe_2)_2(2\text{-}Naph)\}_2$] they are strongly dependent on emission wavelength. The average lifetime at 513 nm, *i.e.* centred on the ${}^4T_1({}^4G) \rightarrow {}^6A_1({}^6S)$ transition, is 38 μs, while it is much longer at 640 nm and equal to 172 μs. The values support the previously proposed excitation-dependent photoluminescence, being the green emission characterized by faster decay with respect to the red one. On the contrary, the lifetime values for [$MnI_2\{O=P(NMe_2)_2(2\text{-}Naph)\}_2$] are almost unaffected by the choice of the emission wavelength.

Focusing the attention on the carbazolyl derivatives, [$MnCl_2\{O=P(NMe_2)_2Cbz\}_2$] shows meaningful changes on varying the excitation wavelength, as highlighted in Figure 51. At shorter excitation wavelengths the PL spectra are dominated by the typical band centred at 526 nm, but additional bands are present for wavelengths below 450 nm and in the red region of the spectrum. The relative intensity of the bands is dependent on the excitation wavelengths, accordingly to emission-dependent PLE spectra and in line with what previously described for the 2-naphthyl derivatives. Possible interactions between manganese(II) centres at the excited state is neglected due to the fact that the distance between the metal centres is between 8 and 10 Å, always above the 6.6 Å reported for the tetrabromomanganates(II) described by Peng and co-workers.[25] The presence of the broad band centred in the red region was previously observed also for the europium(III) nitrato-complex having the same ligand in the coordination sphere.[121] The dual emission of [$MnCl_2\{O=P(NMe_2)_2Cbz\}_2$] was further investigated from an experimental point of view (see Figure 51 for the PL spectra at different wavelengths). As observable in Figure 51, the luminescence decay curves obtained at $\lambda_{emission}$ of 520 nm and 700 nm are roughly parallel in the 700–2000 μs range, indicating that only one species is causing the emission. The observed lifetime τ_{obs} for the $^4T_1(^4G)$ level is estimated around 305 μs. The time shift of the curve at 700 nm suggests that a different emitting level, most likely ligand-centred (^3LC), is populated by the $^4T_1(^4G)$ excited state and that the lifetime of the energy transfer is in the μs range. The parallel decays observed for $\lambda_{emission}$ = 700 nm and $\lambda_{emission}$ = 520 nm also indicate that the lifetime of the lowest energy excited state is longer than the $^4T_1(^4G)$ one. The emission of [$MnCl_2\{O=P(NMe_2)_2Cbz\}_2$] can be tentatively ascribed to a dual phosphorescence[76c,150] similar to what was recently reported for biscarbazole and dibenzothiophene derivatives.[151] The dual emission of [$MnCl_2\{O=P(NMe_2)_2Cbz\}_2$] can be ascribed to a large energy separation between the two emitting states and relatively fast decay from the highest energy level. As for the chloro-complex, the PL spectra of [$MnBr_2\{O=P(NMe_2)_2Cbz\}_2$] and [$MnI_2\{O=P(NMe_2)_2Cbz\}_2$] are composed by two emission bands, even if the dependence of the relative intensity upon the excitation wavelength is poor for the bromo-complex and negligible for the iodo-derivative. The luminescence decay curves of the bromo- and iodo-derivatives are however in line with those reported for [$MnCl_2\{O=P(NMe_2)_2Cbz\}_2$], therefore a strictly comparable mechanism is proposed. The replacement of chloride with heavier halides determines the expected reduction of the observed lifetime values, respectively 182 and 71 μs for bromo- and iodo-derivatives collected at $\lambda_{emission}$ = 520 nm. According to the proposed mechanism, the decay curve of [$MnI_2\{O=P(NMe_2)_2Cbz\}_2$] at $\lambda_{emission}$ = 700 nm is biexponential and, although it was not possible to precisely measure it, the second lifetime appears much longer (in the thousands of μs range) than the τ_{obs} value obtained at 520 nm.

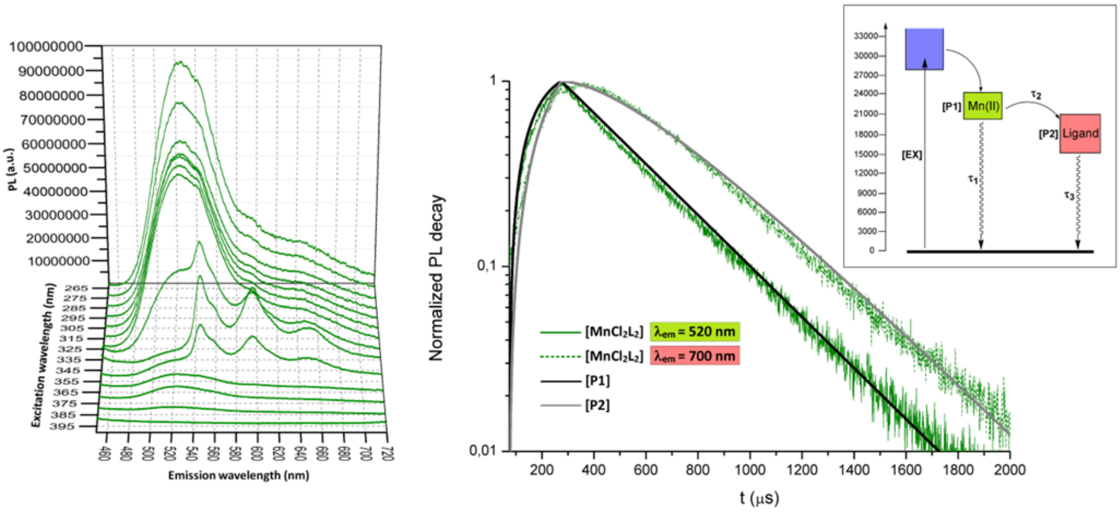

Figure 51. PL spectra of $[MnCl_2\{O{=}P(NMe_2)_2Cbz\}_2]$ at different excitation wavelengths and semi-log plot of the luminescence decay curves of $[MnCl_2\{O{=}P(NMe_2)_2Cbz\}_2]$ (solid sample, r.t., $\lambda_{excitation}$ = 290 nm). Inset: proposed mechanism for the luminescence decay.

In all the cases, the photoluminescent quantum yields Φ are between 5 and 10%, about half of the values obtained with phenyl and indol-1-yl substituents.[40,98a-b] Such an outcome highlights that the introduction of π-conjugated substituents with accessible low-energy excited states favours non-radiative decay routes. These peculiar luminescent features ascribed to wavelength-dependent emission were previously observed for octahedral manganese(II) derivatives but never detected for tetrahedral complexes.[47,152]

The mono- and bidentate amidophosphates depicted in Scheme 25 proved to be other suitable ligands for the preparation of luminescent manganese(II) complexes.

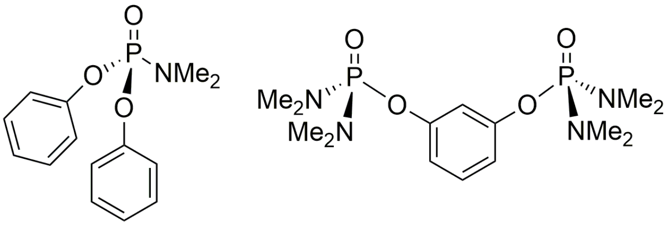

$O{=}P(OPh)_2(NMe_2)$ **$O{=}P(NMe_2)_2(res)(NMe_2)_2P{=}O$**

Scheme 25. $O{=}P(OPh)_2(NMe_2)$ and $O{=}P(NMe_2)_2(res)(NMe_2)_2P{=}O$ ligands.

The reaction of $O{=}P(OPh)_2(NMe_2)$ with two equivalents of anhydrous $MnBr_2$ and MnI_2 afforded the corresponding neutral tetrahedral complexes as suggested by elemental analysis data, conductivity and magnetic measurements, and X-ray diffraction. Crystal data and structure refinements are collected in Table A5 (see Table B5 for selected bond lengths and angles). Instead, in the case of the bidentate resorcinol-based ligand $O{=}P(NMe_2)_2(res)(NMe_2)_2P{=}O$ the X-ray structures of the bromo- and iodo-species are markedly different. The former is a dimer having general formula $[Mn_2Br_4\{\mu–O=P(NMe_2)_2(res)(NMe_2)_2P=O\}_2]$, while the latter is a coordination polymer, as observable in Figure 52. Crystal data and structure refinements are summarized in Table A6 (see Table B6 for selected bond lengths and angles).

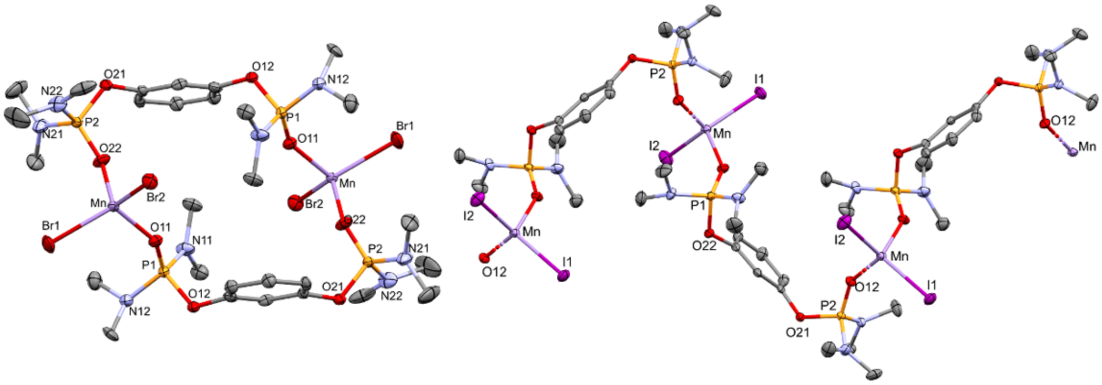

Figure 52. X-ray structures of $[Mn_2Br_4\{\mu–O=P(NMe_2)_2(res)(NMe_2)_2P=O\}_2]$ and $[MnI_2\{\mu–O=P(NMe_2)_2(res)(NMe_2)_2P=O\}_2]_n$.

All the amidophosphate compounds show bright green photoluminescence with maxima between 510 and 524 nm (FWHM 2100–2700 cm^{-1}) upon excitation under UV light in the solid state. As observable in the illustrative PL and PLE spectra reported in Figure 53a, the emission is associated with the direct excitation of the metal centre, in particular the $^4G \leftarrow {}^6A_1(^6S)$ transitions between 400 and 490 nm and the $^4P,^4D \leftarrow {}^6A_1(^6S)$ transitions between 330 and 390 nm. PLE bands are observable also for wavelengths below 300 nm, related to the $^4F \leftarrow {}^6A_1(^6S)$ transitions, superimposed to the excitation of the coordinated ligands. The separation of the ^4G manifold into three groups, $^4T_1$, $^4T_2$ and $^4A_1$ + ^4E, can be easily detected in the PLE spectrum in Figure 53a. The lifetimes τ are all in the tenths of microseconds range, in line with the other tetrahedral derivatives and with the expected decrease passing from Br to I for the $[MnX_2\{O=P(OPh_2)_2(NMe_2)\}_2]$. On the other hand, the differences in the structures of the resorcinol complexes determine noticeable effects in the measured lifetimes (see Figure 53b). The bromo-derivatives has a lifetime equal to 468 μs, up to ten times higher the corresponding iodo-complex where it is equal to 40 μs. This outcome can be justified not only on the basis of the different SOC, but also considering that the former is a roughly centrosymmetric dimer, thus the $^4T_1(^4G) \leftarrow {}^6A_1(^6S)$ transition appears to be much less probable if compared to $[MnI\{\mu–O=P(NMe_2)_2(res)(NMe_2)_2P=O\}_2]_n$.[153]

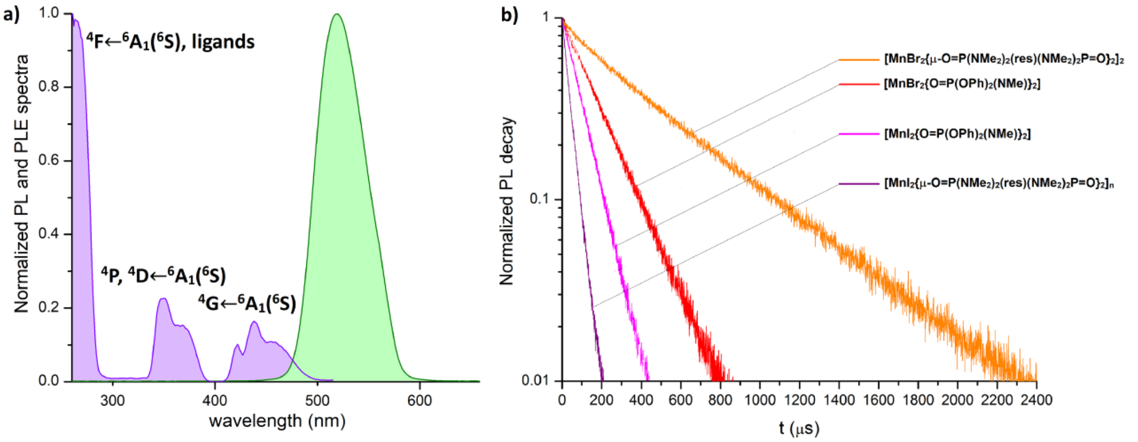

Figure 53. a) Normalized PL and PLE spectra of $[MnBr_2\{O{=}P(OPh)_2(NMe_2)\}_2]$ ($\lambda_{excitation}$ = 350 nm, $\lambda_{emission}$ = 560 nm). b) Semi-log plots of the luminescence decay curves ($\lambda_{excitation}$ = 265 or 377 nm, $\lambda_{emission}$ = 515-522 nm). Solid samples, r.t.

The measured photoluminescence quantum yields Φ for the mononuclear derivatives are respectively around 58% and 84% for the bromo- and iodo-species. Values above 50% for green manganese(II) emitters are commonly observed for tetrahalomanganate(II) derivatives with suitable cations and were detected also for neutral halide complexes with 4,6-bis(diphenylphosphino)dibenzofuran dioxide or bis[2-(diphenylphosphino)phenyl]ether dioxide in the coordination sphere.[18,23,27,29] The dinuclear compounds have Φ values comprised between 15% and 17%, in line with previously reported species. It is likely to suppose that the steric bulk and the rigidity of the coordinated $O{=}P(OPh)_2(NMe_2)$ reduce the probability of non-radiative decay. Moreover, the lack of meaningful conjugation derived by the presence of an oxygen atom between the phosphorus and the aromatic systems prevents the commonly observed antenna effect from the ligands to the metal, but also a back-energy transfer from metal to ligand followed by vibrational decay. This last consideration is supported by the higher quantum yield of $[MnI_2\{O{=}P(OPh)_2(NMe_2)\}_2]$ with respect to the bromo-species. The similar coordination sphere and the quite low wavenumbers of the Mn–X vibrations suggest that the difference is not related to non-radiative decay in the first coordination sphere.[154] On the other hand, it is likely to suppose that the shorter lifetime of the ^4G excited state in the iodo-species probably reduces the possibility of back-energy transfer processes.

It is worth mentioning that the investigation on [O=P]-donor ligands for the preparation of luminescent manganese(II) complexes is actually limited to pentavalent phosphorus. Much less attention was devoted to species containing the phosphorus atom in lower formal oxidation state, such as *H*-phosphinates and *H*-

phosphonates. DOPO or 9,10-dihydro-9-oxa-10-phosphaphenanthrene-10-oxide (see Scheme 26) is a commercially available compound belonging to the first class, commonly used as halogen-free flame retardant.[155] The presence of an extended π-conjugated system in a rigid structure and of an oxygen atom potentially suitable for coordination prompted me to study the reaction of DOPO towards manganese(II) halides.

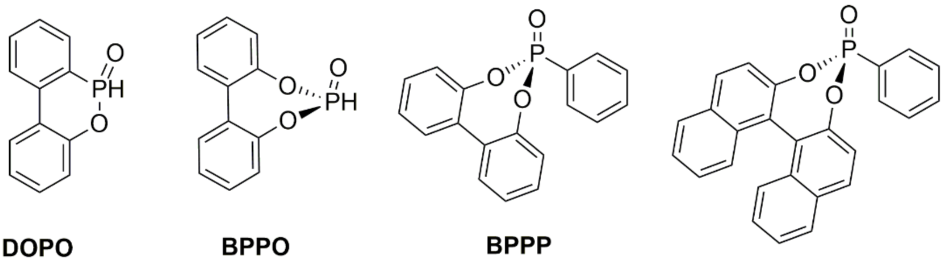

DOPO **BPPO** **BPPP** **O=PPh(R/S-BINOL)**

Scheme 26. DOPO, BPPO, BPPP and O=PPh(R/S-BINOL) ligands.

The reaction between anhydrous MnX_2 (X = Cl, Br, I) salts with two equivalents of DOPO afforded complexes having general formula $[MnX_2(DOPO)_2]$. The proposed formulae were confirmed by elemental analyses and experimental magnetic moments that are in line with the theoretical 5.9 BM expected for high-spin d^5 derivatives of first-row transition elements. As observable in Figure 54, the ν_{P-H} stretchings fall at slightly higher wavenumbers in $[MnBr_2(DOPO)_2]$ with respect to the free ligand,[156] probably because the donation of electronic density from DOPO to manganese(II) makes the phosphorus atom more electrophilic and strengthens the P-H bond. The $\nu_{P=O}$ stretchings are detectable in the 1250-1150 cm^{-1} range, superimposed to other vibrations. Despite the difficulty to precisely assign the $\nu_{P=O}$ stretchings, the comparison with free DOPO suggests a slight weakening of the P=O bonds caused by coordination, as already observed for the previously described [O=P]-donors.

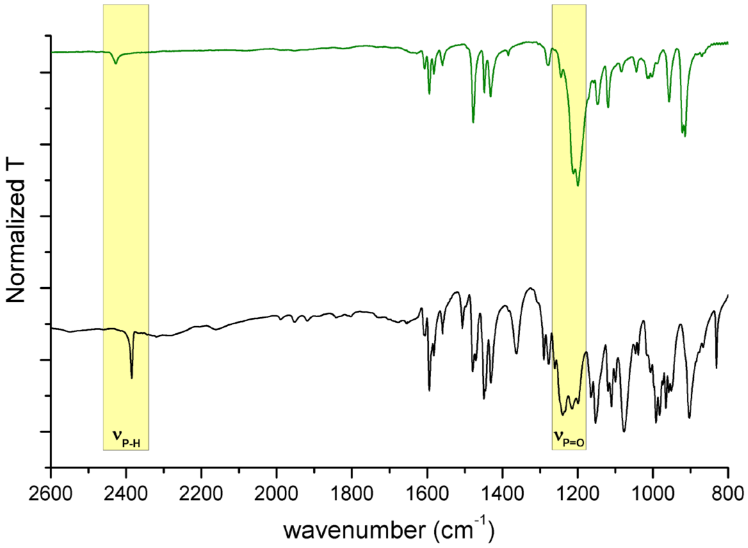

Figure 54. IR spectra in KBr of DOPO (black line) and $[MnBr_2(DOPO)_2]$ (green line).

All the derivatives show absorptions in solution for wavelengths below 325 nm comparable to those of free DOPO and related to the $\pi^* \leftarrow \pi$ transitions. The complexes exhibit appreciable luminescence in the visible range upon excitation with UV light at the solid state. The photoluminescence quantum yields Φ are around 70% for $[MnCl_2(DOPO)_2]$ and $[MnBr_2(DOPO)_2]$ and 18% for $[MnI_2(DOPO)_2]$. As previously described for other compounds, the PL spectra of the manganese(II) derivatives show two bands, the first one in the green region attributable to the $^4T_1(^4G) \rightarrow {}^6A_1(^6S)$ transition of the metal ion in tetrahedral environment, and the other one centred between 625 and 640 nm. The relative intensity of the two bands is dependent upon the choice of the halide and the excitation wavelength. As observable in Figure 55, the red emission (FWHM around 3500 cm^{-1}) dominates the PL spectrum of $[MnCl_2(DOPO)_2]$ and the $^4T_1(^4G) \rightarrow {}^6A_1(^6S)$ transition is detectable only by direct excitation of the metal centre. This wavelength-dependent behaviour is much more pronounced for $[MnBr_2(DOPO)_2]$ (see Figure 56a). The red emission is the most intense only for short excitation wavelengths, while the two bands assume comparable intensity for $\lambda_{excitation}$ > 380 nm. Finally, the PL spectrum of $[MnI_2(DOPO)_2]$ is composed by two bands with relative intensity almost independent upon the excitation wavelength (see Figure 55). The PLE spectra related to the bromo-species reported in Figure 56b indicate that the emissions in the green region are mainly associated to the direct manganese(II) excitation, in particular the $^4G,^4D,^4P \leftarrow {}^6S$ transitions for wavelengths longer than 330 nm. On the other hand, the emission band in the red range appears mostly associated to the excitation of the coordinated ligands, even if the PLE bands related to metal-centred transitions are still detectable.

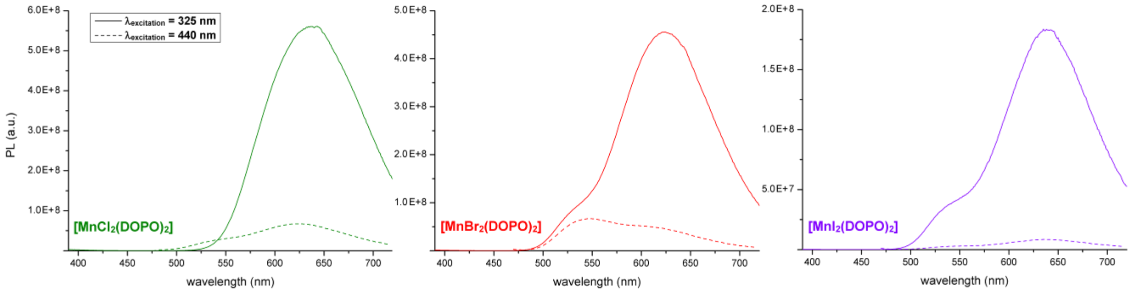

Figure 55. PL spectra of $[MnX_2(DOPO)_2]$ complexes (X = Cl, green; X = Br, red; X = I, violet). Solid samples, r.t., $\lambda_{excitation}$ = 325 nm (solid line) and $\lambda_{excitation}$ = 440 nm (dashed line).

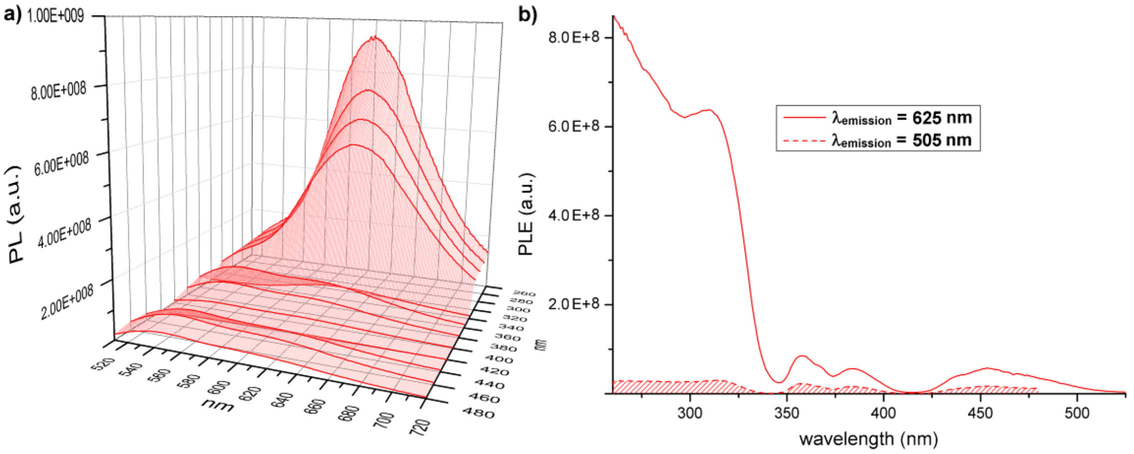

Figure 56. a) 3D PL spectrum of $[MnBr_2(DOPO)_2]$. b) PLE spectra of $[MnBr_2(DOPO)_2]$ complexes, $\lambda_{emission}$ = 625 nm (solid line) and $\lambda_{emission}$ = 505 nm (dashed line). Solid samples, r.t.

It is likely to suppose that the band in the red region is related to a ^{3}LC transition from an excited state localized on the DOPO ligands, similar to what was previously observed for P-bonded 2-naphthyl and 1-carbazolyl substituents. Such an emission falls in the milliseconds range in the luminescence decay curves and it is superimposed to a faster process associated to the metal-centred emission process (see Figure 57). The fast component of the luminescence decay curves of $[MnBr_2(DOPO)_2]$ and $[MnI_2(DOPO)_2]$, measured at $\lambda_{emission}$ = 505 nm, is in the tenths of μs range, as expected for tetrahedral manganese(II) derivatives.[13b,18] Unfortunately, it was not possible to measure the lifetime related to the green emission of $[MnCl_2(DOPO)_2]$ because of its poor relative intensity with the available pulsed excitation sources.

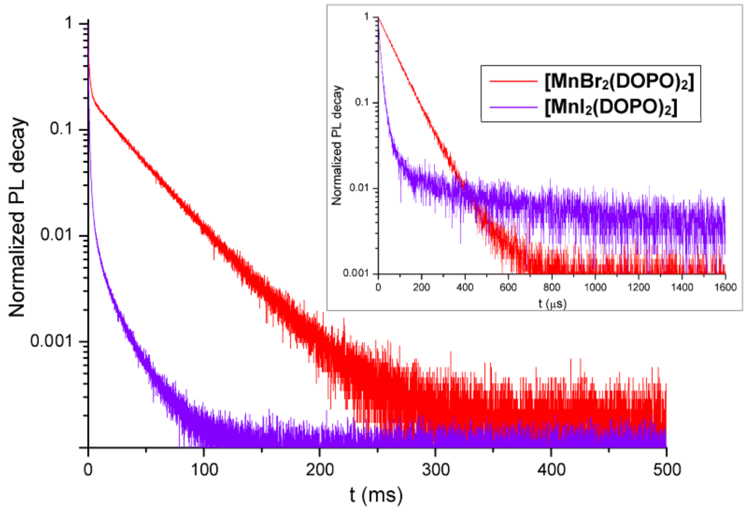

Figure 57. Semi-log plot of the luminescence decay curves of $[MnBr_2(DOPO)_2]$ (red line) and $[MnI_2(DOPO)_2]$ (violet line). Solid samples, r.t., $\lambda_{excitation}$ = 290 nm, $\lambda_{emission}$ = 650 nm. Inset: $\lambda_{emission}$ = 505 nm.

This excitation wavelength-dependent behaviour can be rationalized following the approach proposed for $[MnX_2\{O=P(NMe_2)_2Cbz\}_2]$ derivatives, based on the increased spin-orbit coupling passing from X = Cl to X = I.[28] The ligand-metal energy transfer is probably slow in $[MnCl_2(DOPO)_2]$, therefore the ^{3}LC emission is favoured on exciting the coordinated DOPO and the $^4T_1(^4G) \rightarrow {}^6A_1(^6S)$ transition is detectable only by direct excitation of the metal centre, with relatively weak PLE bands. The same energy transfer is faster in $[MnBr_2(DOPO)_2]$, but emission spectra with different relative intensities of the $^4T_1(^4G) \rightarrow {}^6A_1(^6S)$ and ^{3}LC transitions are observable if the ligands or the metal are preferentially excited. Finally, the ligand-metal energy transfer in $[MnI_2(DOPO)_2]$ is probably so fast that the emission spectrum becomes independent upon the excitation wavelength.

Similar optical properties were observed using the 1,1'-biphenol derivatives BPPO (dibenzo[*d*,*f*][1,3,2]dioxaphosphepine 6-oxide) and BPPP (6-phenyldibenzo[*d*,*f*][1,3,2]dioxaphosphepine 6-oxide) as ligands (see Scheme 26). MnX_2 (X = Cl, Br, I) were reacted with two equivalents of the chosen [O=P]-donor affording the corresponding tetrahedral derivatives. In some cases, acetonitrile was used as solvent because ethanol afforded non-luminescent oils. Elemental analyses and experimental magnetic moments confirmed the formation of the proposed four-coordinated complexes. The non-solubility of the BPPO derivatives in most of the common organic solvents suggests that the species may be coordination polymers. The IR spectra of the ligands and the corresponding bromo-derivatives are collected in Figure 58. It is interesting to observe that the stretching ν_{P-H} is detectable only for the free ligand but in none of the $[MnX_2(BPPO)_2]_n$ complexes (X = Cl, Br, I). Also in this case, the $\nu_{P=O}$ stretchings are superimposed to other vibrations but they fall at lower wavenumbers with respect to the free ligands, as observable in Figure 58 and in the previously reported complexes.

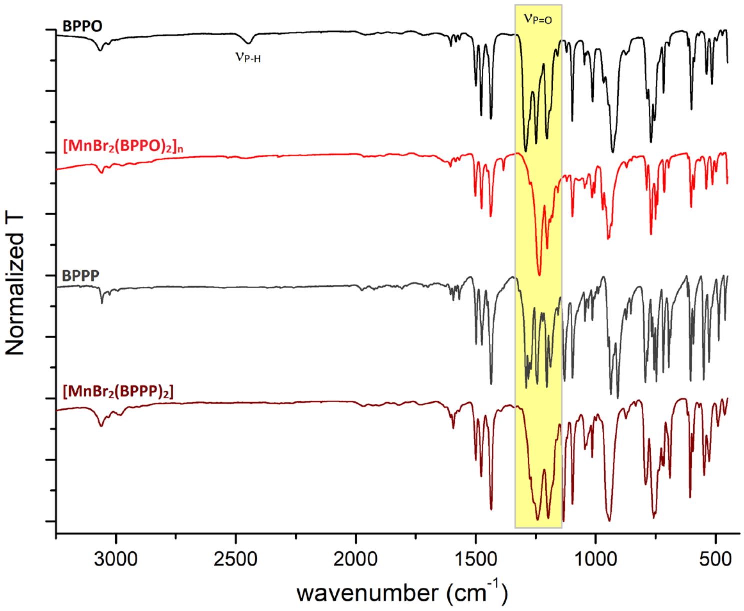

Figure 58. IR spectra in KBr disks of BPPO (black line), $[MnBr_2(DOPO)_2]_n$ (red line), BPPP (dark grey line) and $[MnBr_2(BPPP)_2]$ (wine red line).

The UV-VIS spectra were recorded respectively in acetonitrile and dichloromethane solutions for BPPO and BPPP derivatives. In both the cases the absorptions below 320 nm are related to the $\pi^* \leftarrow \pi$ transitions. The complexes are luminescent at the solid state upon excitation with UV light with photoluminescence quantum yields Φ respectively in the 15-19% and in the 2-8% ranges for $[MnX_2(BPPO)_2]_n$ and $[MnX_2(BPPP)_2]$. As observable in Figure 59, the PL spectra are characterized by two bands, one in the green and the other one in the red region of the spectrum with maximum comprised between 615 and 640 nm. Differently from previously reported complexes, a third band related to the fluorescence of the ligands can sometimes be detected. Both BPPO and BPPP are characterized by emissions centred respectively at 350 and 410 nm at the solid state with lifetimes between 5 and 10 ns. In all the cases, the red band is predominant and the one related to the $^4T_1(^4G) \rightarrow {}^6A_1(^6S)$ transition is detectable only by direct excitation of the metal centre. The two bands are almost independent upon the excitation wavelength, especially in the case of BPPP derivatives (see Figure 59). As previously observed for $[MnX_2(DOPO)_2]$, the band in the red region is mostly related to the excitation of the coordinated ligands, even if the bands attributable to metal-centred transitions are still detectable in the PLE spectra.

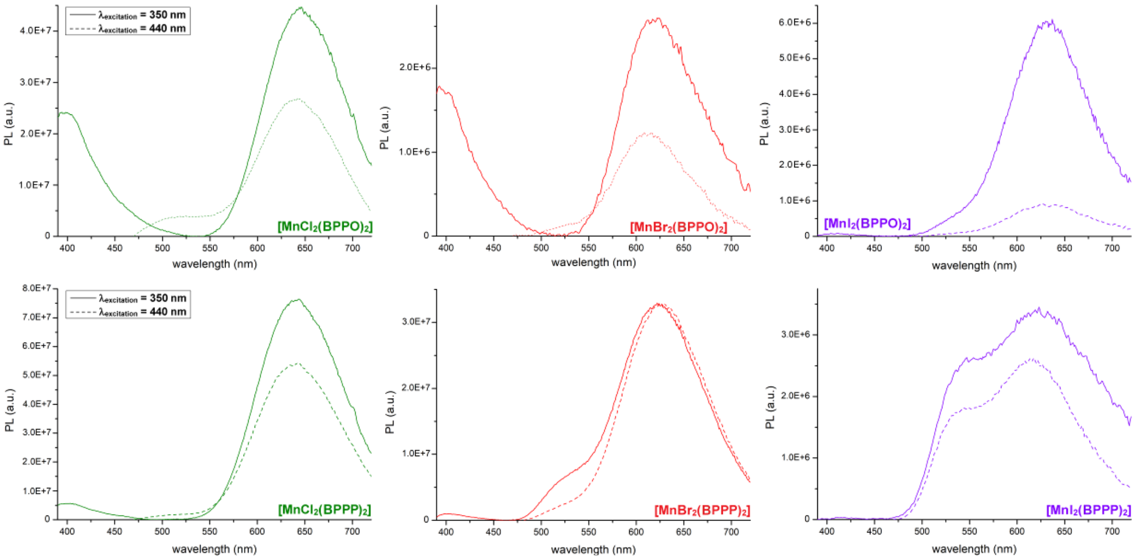

Figure 59. PL spectra of $[MnX_2(BPPO)_2]_n$ and $[MnX_2(BPPP)_2]$ complexes (X = Cl, green; X = Br, red; X = I, violet). Solid samples, r.t., $\lambda_{excitation}$ = 350 nm (solid line) and $\lambda_{excitation}$ = 440 nm (dashed line).

The lifetimes decay curves exhibit the previously described dual-component, one faster and related to the metal-centred process, and the other in the milliseconds range. This behaviour is particularly evident for $[MnX_2(BPPP)_2]$ (X = Br, I) and it is shown in Figure 60. When the lifetime is collected at $\lambda_{emission}$ = 525 nm, the values measured are respectively 141 and 19 μs for the bromo- and the iodo- derivative, as expected for manganese(II) complexes in a tetrahedral environment. On the other hand, the lifetimes for the red bands ($\lambda_{emission}$ = 610 nm) are in the hundreds of μs range, as previously observed for ^{3}LC transitions. Unfortunately, in the case of $[MnX_2(BPPO)_2]_n$ it was not possible to separate the two portions of the lifetimes.

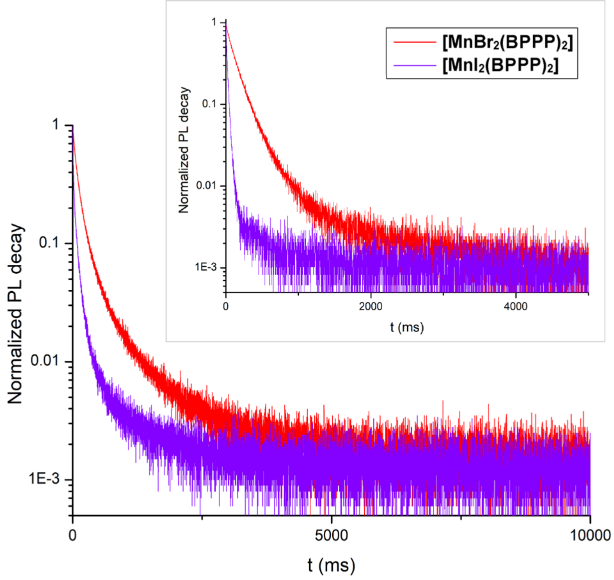

Figure 60. Semi-log plot of the luminescence decay curves of $[MnBr_2(BPPP)_2]$ (red line) and $[MnI_2(BPPP)_2]$ (violet line). Solid samples, r.t., $\lambda_{excitation}$ = 290 nm, $\lambda_{emission}$ = 610 nm. Inset: $\lambda_{emission}$ = 525 nm.

The possible phosphorescent emission from triplet states localized on the BPPO and BPPP ligands was investigated from a computational point of view. The spin density plots of sextet and octet states for the corresponding bromo-derivatives obtained from the optimized geometries are depicted in Figure 61. As it can be observed, in both the cases the spin density plot of the octet state is localized in the 1,1'-biphenol fragments of one of the ligands, supporting the idea that the red emission is originating from a ligand-centred triplet state (^{3}LC).

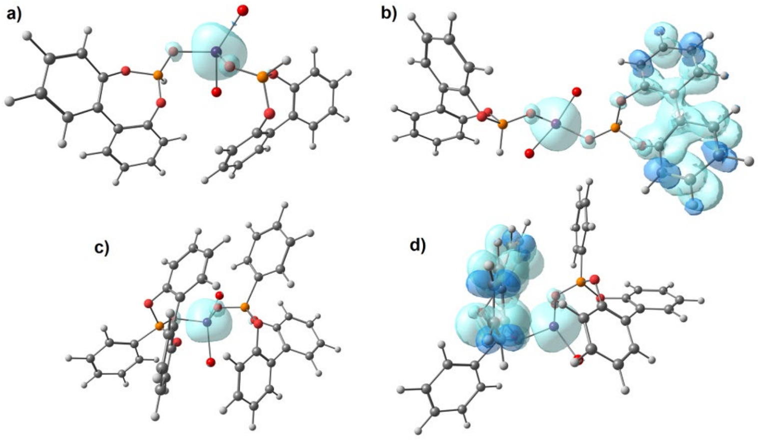

Figure 61. DFT-optimized structures of $\{MnBr_2(BPPO)_2\}$ fragment and of $[MnBr_2(BPPP)_2]$ and spin density surfaces (isovalue = 0.003 a.u.). MN15/def2-SVP calculations. Colour map: Mn, violet; Br, dark red; P, orange; O, red; C, grey; isosurface, light blue tones. a) $\{MnBr_2(BPPO)_2\}$ fragment, sextet state; b) $\{MnBr_2(BPPO)_2\}$ fragment, octet state; c) $[MnBr_2(BPPP)_2]$, sextet state; d) $[MnBr_2(BPPP)_2]$, octet state.

To further extend the π-conjugated systems I decided to use the enantiomerically pure R/S-BINOL fragment. Although the synthesis of the corresponding dioxaphosphepine oxide was reported by Bull and co-workers, the full characterization of the compound was never described.[124] The ^{1}H NMR, ^{31}P{^{1}H} NMR, ^{13}C{^{1}H} NMR and ^{1}H-^{13}C HSQC spectra of O=PPh(S-BINOL) in $CDCl_3$ are reported in Figures 62 and 63. The former is characterized by eight resonances localized in the aromatic region of the spectra that are the superimposition of both phenyl and 1,1'-bi-2-naphthol signals. As expected, the ^{31}P{^{1}H} NMR spectrum presents only one signal at 27.12 ppm. Due to the increased rigidity passing from BINOL to O=PPh(R/S-BINOL), the specific rotation potential $[\alpha]^{20}_{D}$ for the two enantiomers is equal to ± 320, almost ten times higher compared with respect to the precursor ($[\alpha]^{20}_{D} = \pm 36$).[157] The enantiomers crystallized from the slow evaporation of ethanol solutions in the orthorhombic $P2_12_12_1$ space groups (see Table A7 for crystal data and structure refinement and Table B7 for selected bond lengths and angles). The X-ray structure of the S-BINOL derivative with Flack parameter of -0.004(14) is reported in Figure 64.

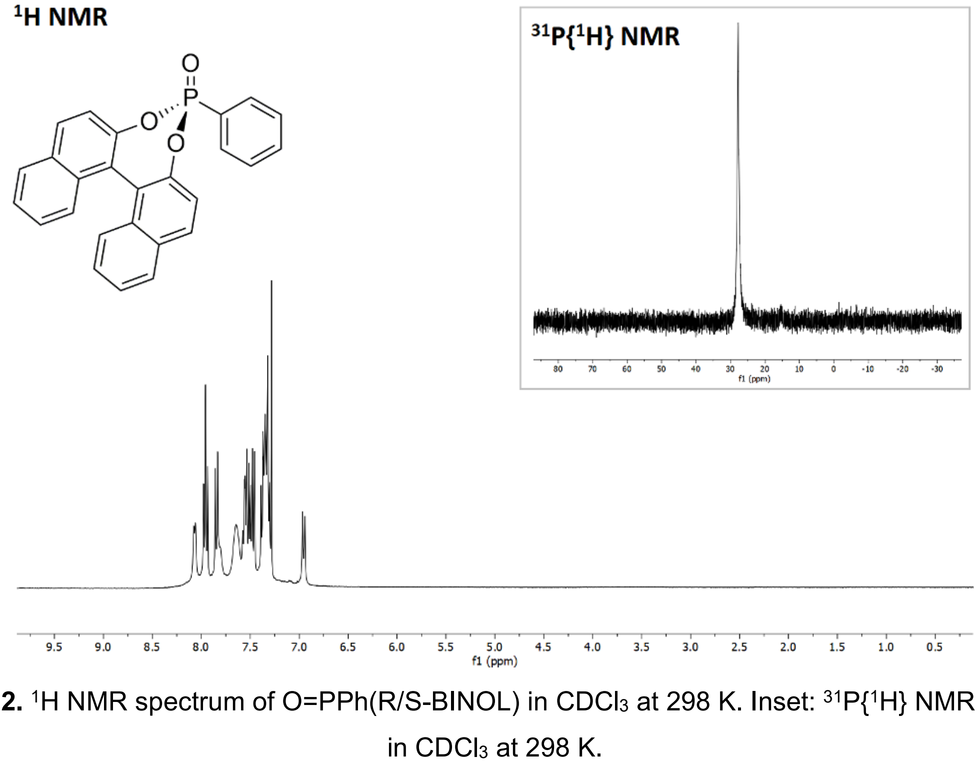

Figure 62. ^{1}H NMR spectrum of O=PPh(R/S-BINOL) in $CDCl_3$ at 298 K. Inset: ^{31}P{^{1}H} NMR spectrum in $CDCl_3$ at 298 K.

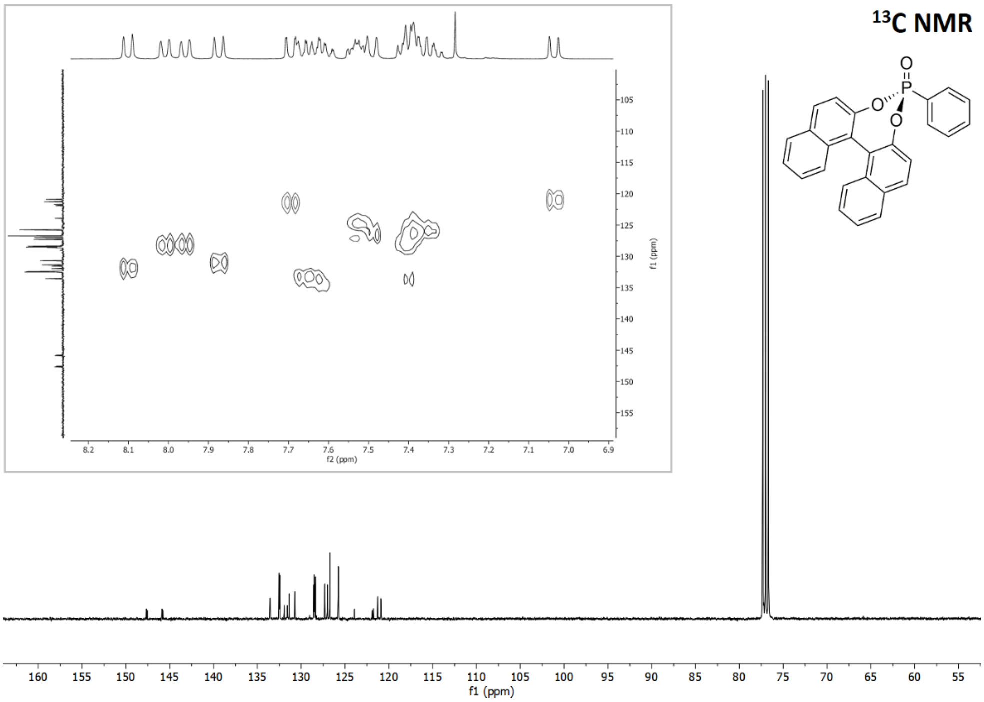

Figure 63. ^{13}C NMR spectrum of O=PPh(R/S-BINOL) in $CDCl_3$ at 298 K. Inset: ^{1}H-^{13}C HSQC spectrum in $CDCl_3$ at 298 K.

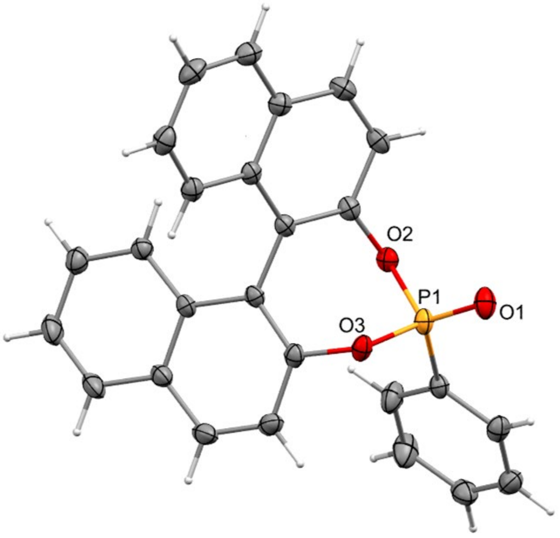

Figure 64. X-ray structure of O=PPh(S-BINOL).

The enantiomers were reacted with manganese(II) halides in ethanol to afford the corresponding tetrahedral derivatives. The proposed formulae $[MnX_2\{O=PPh(R/S\text{-}BINOL)\}_2]$ (X = Cl, Br, I) is confirmed by means of elemental analyses, conductivity measurements and magnetic susceptivity. The IR spectra present the typical decrease in the $\nu_{P=O}$ due to the coordination of the ligand to the metal centre. The UV-VIS spectra recorded in dichloromethane solutions are characterized by absorptions below 350 nm related to the $\pi^* \leftarrow \pi$ transitions and superimposable to that of the free ligands. Although the complexes are tetrahedral, the excitation with UV light on the solid sample determines emission spectra where the predominant band is in the 640-650 nm range. A second band around 400 nm related to the fluorescence of the coordinated ligands is observable and its intensity decreases passing from Cl to I due to the increased SOC effect. Instead, the intensity of the red band grows with heavier halides, as observable in Figure 65. In this case the expected green band attributable to the $^4T_1(^4G) \rightarrow {}^6A_1(^6S)$ transition is not detectable even exciting directly the metal centre. Even if the emission spectra seem to indicate the formation of octahedral complexes, the PLE spectra are characterized by the common $^4P,^4D \leftarrow {}^6A_1(^6S)$ and $^4G \leftarrow {}^6A_1(^6S)$ transitions, that would not be detectable in presence of six-coordinated species.

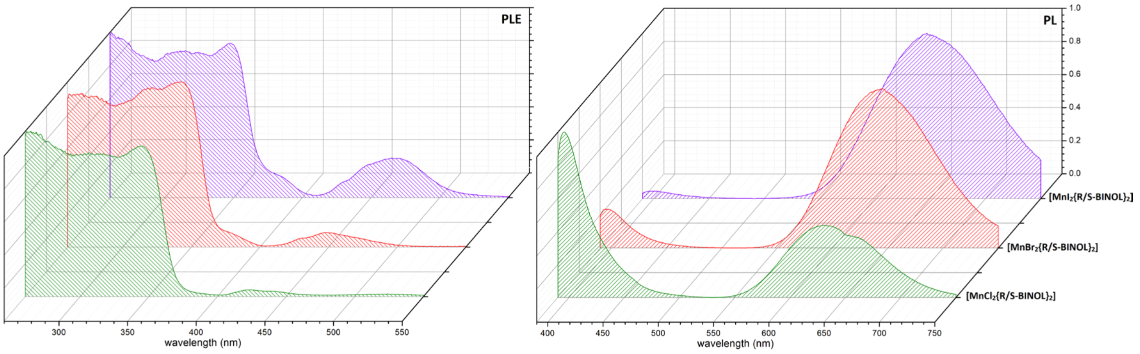

Figure 65. Normalized PL and PLE spectra of $[MnX_2\{O{=}PPh(R/S\text{-}BINOL\}_2]$ (X = Cl, green; X = Br, red; X = I, violet). Solid samples, r.t., $\lambda_{excitation}$ = 350 nm, $\lambda_{emission}$ = 640 nm.

The lifetime decay curves collected in Figure 66 can be fitted with a biexponential function affording two values, one that decreases from 623 to 85 μs passing from Cl to I, and the other one around 200-300 μs for all the complexes. The former follows the expected trend related to the increased SOC effect and can be assigned to the metal-centred transition, even if it is not clearly detectable in the PL spectra. The latter is instead most likely related to triplet-excited states of the BINOL fragment, as supported by DFT calculations (see the spin density plot of the octet state of the $[MnBr_2\{O{=}PPh(R/S\text{-}BINOL\}_2]$ complex reported in Figure 66).

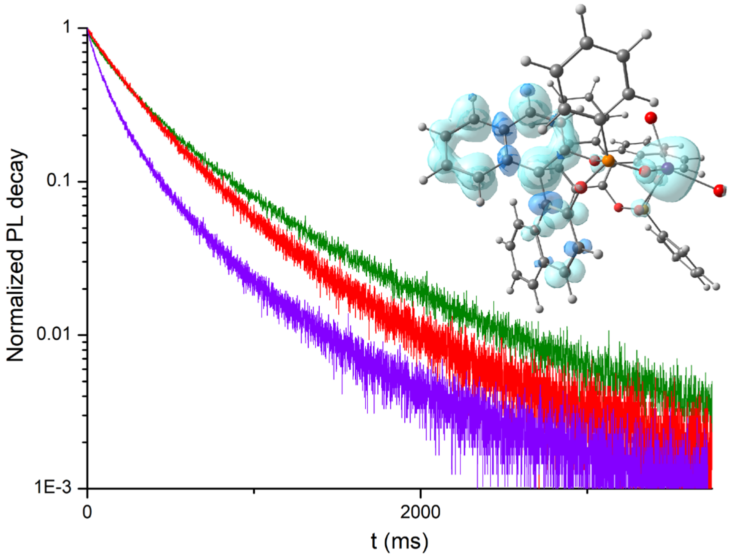

Figure 66. Semi-log plot of the luminescence decay curves of [MnX_2{O=PPh(R/S-BINOL}$_2$] (Cl = green; Br = red; I = violet line). Solid samples, r.t., $\lambda_{excitation}$ = 290 nm, $\lambda_{emission}$ = 640-650 nm. DFT-optimized structure and spin density surfaces (isovalue = 0.003 a.u.) of the octet state. MN15/def2-SVP calculations. Colour map: Mn, violet; Br, dark red; P, orange; O, red; C, grey; isosurface, light blue tones.

The interesting results achieved with DOPO prompted me to synthesize bidentate ligands based on the same skeleton. The method followed was reported by Salin *et al*. and previously tested on dialkyl phosphites and diaryl phosphine oxides in combination with activated alkynes, such as methyl propiolate. Triphenylphosphine was used as organocatalyst (see Scheme 11 in the Experimental Part).[126] Differently from the reported procedure, the experimental conditions required dry ethanol and refluxing. The reaction was then extended to internal alkynes like dimethyl and diethyl acetylenedicarboxylate affording MeDOPOSuc and EtDOPOSuc (see Scheme 27).

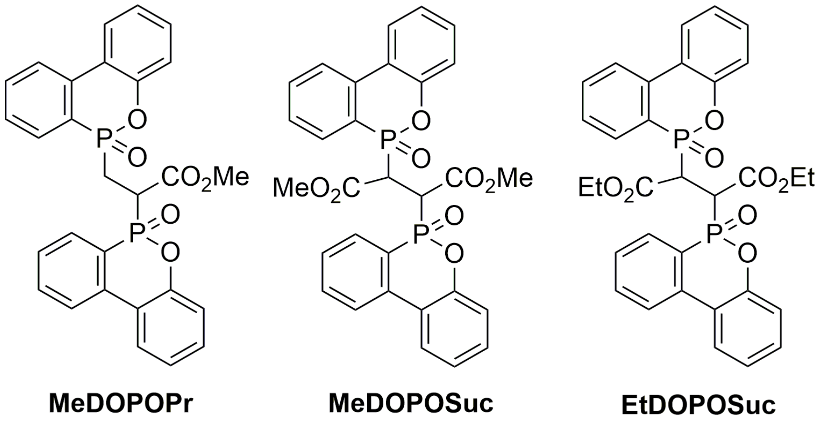

Scheme 27. MeDOPOPr, MeDOPOSuc and EtDOPOSuc ligands.

The insolubility in common organic solvents of the product isolated from the former (MeDOPOSuc) prevented its use as possible ligand. Instead, the presence of a longer alkyl chain in EtDOPOSuc allowed its solubilization in chloroalkanes. The ^{1}H and ^{31}P{^{1}H} NMR spectra of MeDOPOPr and EtDOPOSuc are reported in Figures 67 and 68. It is interesting to observe that the compounds present respectively three and four stereocenters: two on the phosphorus atoms and one or two on carbon atoms. Therefore, a mixture of eight enantiomers was obtained with MeDOPOPr, corresponding to four *AB* spin systems (four diastereoisomers) observable in the ^{31}P{^{1}H} NMR spectrum (see inset of Figure 67). The $^{3}J_{PP}$ coupling is in all the cases in the 55-60 Hz range. Instead, in the case of EtDOPOSuc the symmetry of the molecule and the presence of four stereocentres is associated to potentially eight optically active isomers and two *meso*-compounds. In the ^{31}P{^{1}H} NMR spectrum reported in Figure 68 an *AB* spin system characterized by a $^{3}J_{PP}$ coupling around 50 Hz and two singlets can be detected, the latter attributed to the *meso*-compounds. The different isomers were not isolated, and the compounds were used as mixture.

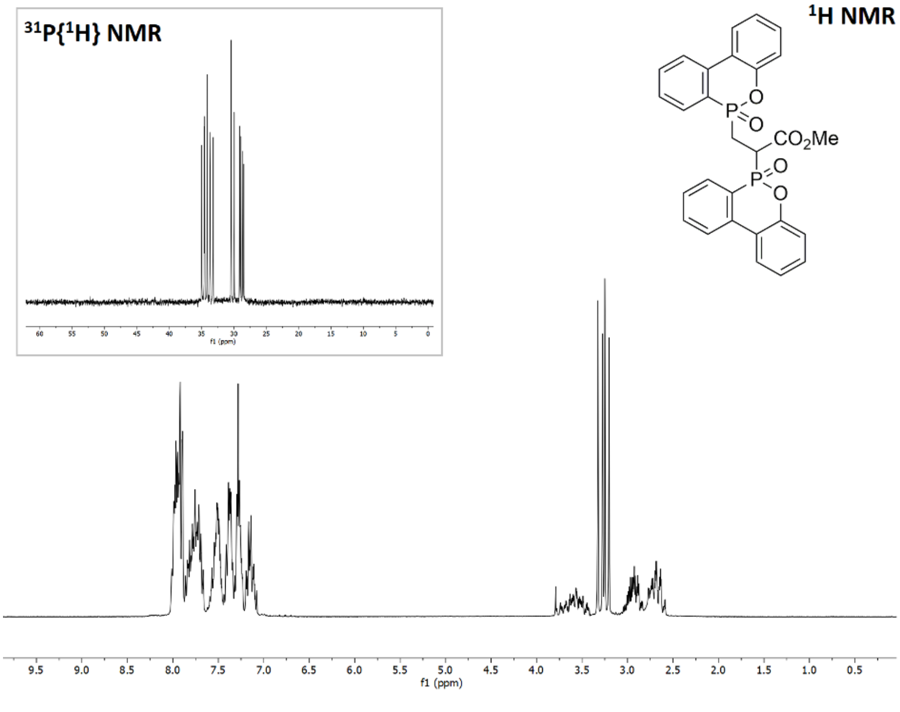

Figure 67. ^{1}H NMR spectrum of MeDOPOPr in $CDCl_3$ at 298 K. Inset: ^{31}P{^{1}H} NMR spectrum in $CDCl_3$ at 298 K.

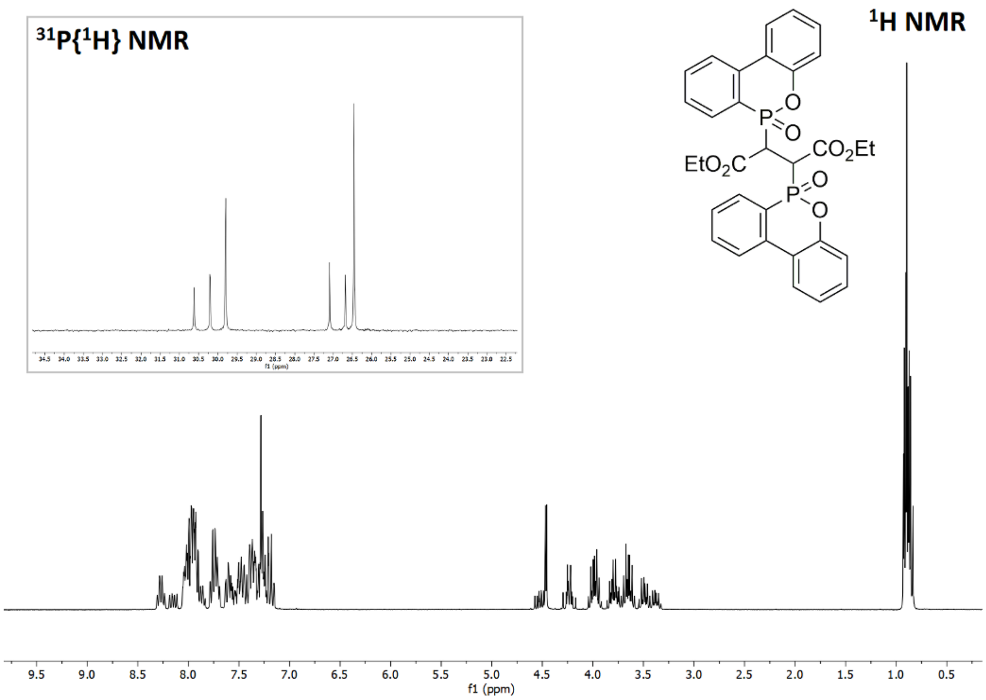

Figure 68. ^1H NMR spectrum of EtDOPOSuc in $CDCl_3$ at 298 K. Inset: $^{31}P\{^1H\}$ NMR spectrum in $CDCl_3$ at 298 K.

The reaction between manganese(II) halides and MeDOPOPr or EtDOPOSuc in ratio 1:1 afforded the corresponding derivatives where the [O=P]-donor acts as bidentate ligand. The proposed formulae [MnX_2(MeDOPOPr)] and [MnX_2(EtDOPOSuc)] (X = Cl, Br, I) are supported by elemental analyses, conductivity measurements and magnetic moments. The coordination of the ligand is further supported by the IR spectra, where the $\nu_{P=O}$ is observable at lower wavenumbers if compared to the free compound. The UV-VIS spectra are superimposable to that of MeDOPOPr and EtDOPOSuc. All the complexes are emissive in the solid state at room temperature with photoluminescent quantum yields Φ that increase passing from Cl to I. The PL spectra of the MeDOPOPr and EtDOPOsuc derivatives are strictly superimposable and comparable to that of the [$MnX_2(DOPO)_2$] (X = Cl, Br, I), as it can be observed for instance in Figure 69. The negligible differences among the emission bands suggest a comparable ligand field strength. The presence of two bands is detectable in the case of the iodo-species, while for the chloro- and the bromo-complexes only the band centred around 630 nm can be observed. The green band was not perceivable even by direct excitation of the metal centre as highlighted by the PL in dashed line and no wavelength-dependent behaviour was noticed.

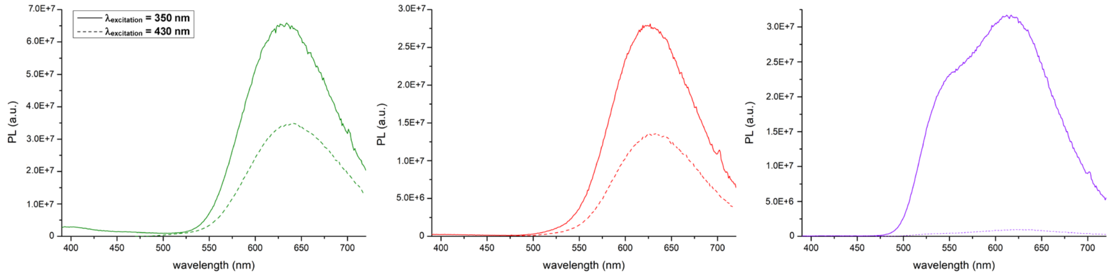

Figure 69. PL spectra of [MnX$_2$(EtDOPOSuc)$_2$] complexes (X = Cl, green; X = Br, red; X = I, violet). Solid samples, r.t., $\lambda_{excitation}$ = 350 nm (solid line) and $\lambda_{excitation}$ = 430 nm (dashed line).

The PLE spectra of [MnI$_2$(MeDOPOPr)] and [MnI$_2$(EtDOPOSuc)] (see for instance Figure 70a) indicate that the emissions in the green region are mostly related to the direct manganese(II) excitation, in particular the ^{4}G,^{4}D,^{4}P ← ^{6}S transitions for wavelengths above 350 nm. As previously observed, the red band is mainly associated to the excitation of the coordinated ligands, but the metal-centred transitions are still detectable in the PLE spectra. As regards the lifetimes, for the chloro- and the bromo-species it was not possible to measure the component associate to the manganese(II) metal-centred transition. Instead, for the iodo-species the lifetimes measured for the green and the red band could be easily extracted. The former is in the tenths of μs range, as expected, whereas the latter is in the 350-390 μs. The semi-log plot of the normalized decays curves for [MnI$_2$(MeDOPOPr)] highlighting the presence of two different lifetimes are collected in Figure 70b.

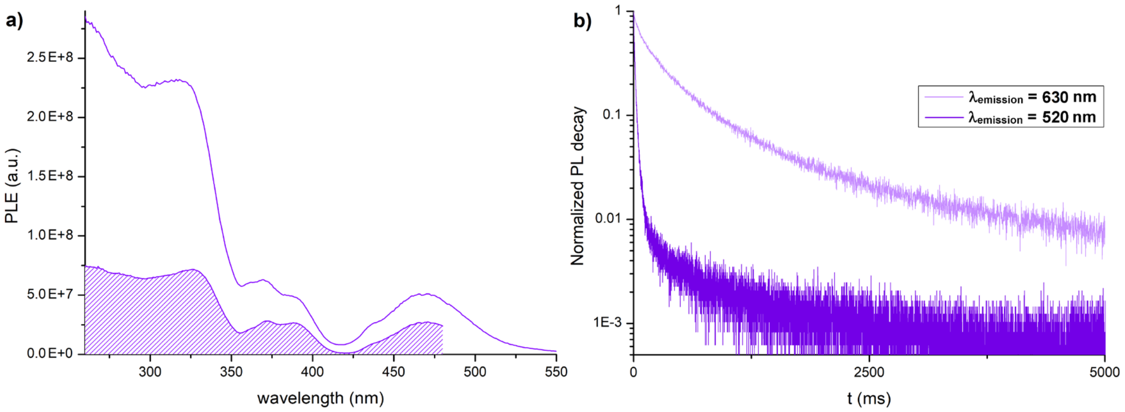

Figure 70. a) PLE spectra of [MnI$_2$(MeDOPOPr)], $\lambda_{emission}$ = 630 nm (solid line) and $\lambda_{emission}$ = 525 nm (filled curve). Solid samples, r.t. b) Semi-log plot of the luminescence decay curves of [MnI$_2$(MeDOPOPr)]. $\lambda_{excitation}$ = 290 nm, $\lambda_{emission}$ = 630 nm (light violet line) and $\lambda_{emission}$ = 520 nm (violet line). Solid samples, r.t.,

Despite this aspect requires to be further investigated, it is likely to suppose that the presence of extended π-conjugated systems in the coordinated ligands favours low-energy ligand-centred triplet emitting states that determine the superimposition of multiple bands in the PL spectra. This outcome is supported also by the dual lifetimes that in some cases can be separated into a fast and a long component with values respectively in the tenths and in the hundreds of μs ranges. Similarly, the photoluminescence quantum yields Φ appear to be lower with respect to pure green derivatives such as [MnX_2{O=P(MeNCH_2CH_2NMe)Ph}$_2$] (X = Cl, Br) and [MnX_2{O=P(NMe_2)$_2$Ind}$_2$] (X = Cl, Br, I) due to the population of ligand-centred excited states that originate non-radiative decay routes.

The same bidentate ligands used to synthesize tetrahedral manganese(II) derivatives were used in combination with $Mn(ClO_4)_2\cdot 6H_2O$ to afford the corresponding octahedral complexes. Conductivity measurements in acetone solutions indicate the formation of bicationic complexes with proposed formulae [Mn(MeDOPOPr)$_3$][ClO_4]$_2$ and [Mn(EtDOPOSuc)$_3$][ClO_4]$_2$, supported also by elemental analyses. As highlighted in Figure 71, the IR spectra are characterized by the strong band around 1740 cm^{-1} related to $\nu_{C=O}$ and the superimposition of $\nu_{P=O}$ and ν_{ClO4} in the 1260-1180 cm^{-1} range.

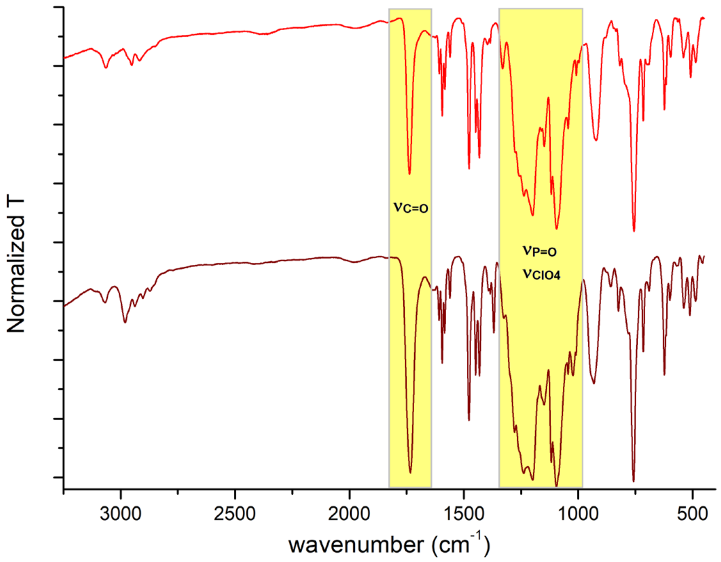

Figure 71. IR spectra of [Mn(MeDOPOPr)$_3$][ClO_4]$_2$ (red line) and [Mn(EtDOPOSuc)$_3$][ClO_4]$_2$ (wine red line).

At the solid state the derivatives are characterized by noticeable orange-red emission centred at 611 nm related to the $^4T_1(^4G) \rightarrow {}^6A_1(^6S)$ transition. The photoluminescent quantum yields Φ measured at 310 nm are respectively equal to 39% and 67% for [Mn(MeDOPOPr)$_3$][ClO_4]$_2$ and [Mn(EtDOPOSuc)$_3$][ClO_4]$_2$. As observable in Figure 72a, the emission maxima and the FWHM around 2500 cm^{-1} do not change passing from MeDOPOPr to EtDOPOSuc, indicating similar crystal field strength. The CIE

1931 chromaticity coordinates are x = 0.596, y = 0.395 in the former and x = 0.590, y = 0.407 for the latter. In both the cases the colour purity is almost unitary (see the inset in Figure 72). Differently from the previously reported octahedral species having general formulae [Mn(dppmO$_2$)$_3$][BF$_4$]$_2$ and [Mn(dppeO$_2$)$_3$][BF$_4$]$_2$ where only $\lambda_{excitation}$ < 300 nm produced emission,[40] the PLE spectra extend up to 350 nm in agreement with the UV-VIS spectra. The absorptions of the two complexes are superimposable and strictly overlap that of the free ligands and of the tetrahedral derivatives described above, being attributable to the $\pi^* \leftarrow \pi$ transitions of the DOPO fragments. The excitation is mainly related to the coordinated ligands and no metal-centred transition is observable in the PLE spectra as shown in Figure 72a. No change in the emission was measured on changing the excitation wavelength. Luminescent lifetimes τ are in the ms range as previously measured for similar derivatives, being $^4T_1(^4G) \rightarrow {}^6A_1(^6S)$ transition both parity and spin forbidden for octahedral complexes. The dominant component is between 13 and 14 ms (Figure 72b).[41-43,45,47]

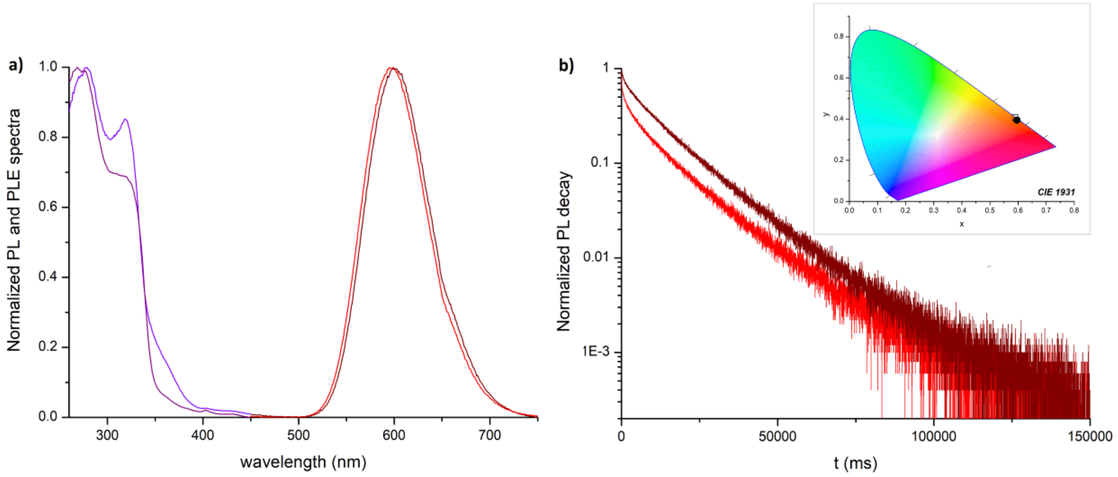

Figure 72. a) PL and PLE spectra of the octahedral derivatives (red and violet line, [Mn(MeDOPOPr)$_3$][ClO$_4$]$_2$; purple and wine red line, [Mn(EtDOPOSuc)$_3$][ClO$_4$]$_2$; solid state, r.t., $\lambda_{excitation}$ = 350 nm, $\lambda_{emission}$ = 610 nm). b) Semi-log plot of the luminescence decay curves (red line, [Mn(MeDOPOPr)$_3$][ClO$_4$]$_2$; wine red line, [Mn(EtDOPOSuc)$_3$][ClO$_4$]$_2$; solid samples, r.t., $\lambda_{excitation}$ = 290 nm, $\lambda_{emission}$ = 610 nm). Inset: CIE 1931 Chromaticity diagram. Blank square, [Mn(MeDOPOPr)$_3$][ClO$_4$]$_2$ (x = 0.596, y = 0.395); dark circle, [Mn(EtDOPOSuc)$_3$][ClO$_4$]$_2$ (x = 0.590, y = 0.407).

The similarity with the {O=P} fragments previously used prompted me to investigate octahedral complexes obtained with 2,2'-bipyridine N-oxide (bpyO$_2$), depicted in Scheme 28. Derivatives with N-oxides as mono- and bidentate ligands were deeply studied for their magnetic properties.[158]

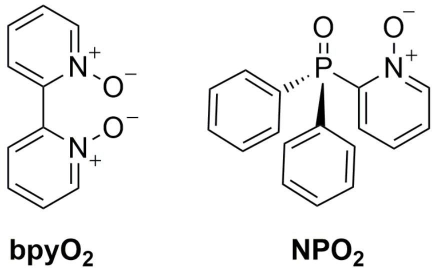

Scheme 28. bpyO_2 and NPO_2 ligands.

It is worth noting that the complex was reported both as perchlorate and as tetrachloroplatinate salt, but the X-ray structure was never described.[127] The complex crystallizes from the slow evaporation of water solutions in the monoclinic $P2_1/n$ space group as depicted in Figure 73. Crystal data and structure refinement are collected in Table A8. Selected bond lengths and angles are summarized in Table B8. $[Mn(bpyO_2)_3][ClO_4]_2$ is intense orange-coloured both at the solid state and in solution due to the presence of a MLCT band around 440 nm, as highlighted in Figure 73. Similar behaviour was detected also for manganese(II) complexes with aromatic amine N-oxides and the analogous $[Mn(bpyO_2)_3][PtCl_4]_2$.[158c,127] As previously highlighted,[158b,127] the bpyO_2 ligand confers light-instability to the corresponding $[Mn(bpyO_2)_3][ClO_4]_2$ complex and the charge-transfer band rapidly disappears irradiating the complex with a near-UV light (see Figure 73). Studies on $[Mn(pyO)_6][ClO_4]_2$ suggested that pyridine was found to be one of the decomposition products, suggesting the oxidation of the metal centre to manganese(III). Similar complexes with N-oxides were investigated also from an electrochemical point of view. One-electron reversible oxidation-reduction and irreversible reduction processes were detected for $[Mn(bpyO_2)_3][ClO_4]_2$ and attributed to the formation of manganese(III) and manganese(IV) species.[159]

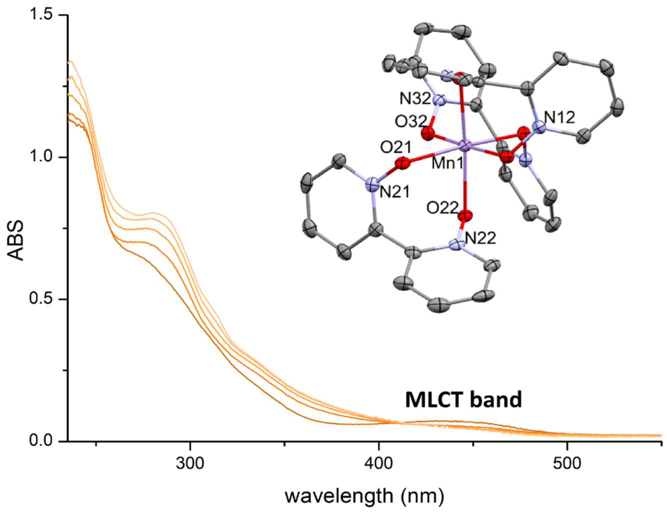

Figure 73. UV-VIS spectra and X-ray structure of $[Mn(bpyO_2)_3][ClO_4]_2$ (acetonitrile solution, $2.5 \cdot 10^{-5}$ M, $\lambda_{near\text{-}UV\ LED}$ = 405 nm).

Despite the outcomes on $[Mn(bpyO_2)_3][ClO_4]_2$ were previously reported in literature, they encourage me to try to synthesize the mixed [N-O,P=O] chelating ligand depicted in Scheme 28, *i.e.* 2-(diphenylphosphino)pyridine-N,P-dioxide (NPO_2). To the best of my knowledge, the full characterization was never reported for this compound, despite the fact that it was used for the preparation of europium(III), samarium(III) and uranyl complexes.[160] ^1H NMR, $^{31}P\{^1H\}$ NMR, ^{13}C NMR and ^1H-^{13}C HSQC NMR spectra in $CDCl_3$ are collected in Figure 74 and 75 for completeness. The $^{31}P\{^1H\}$ NMR is characterized by one singlet centred at 22.94 ppm roughly superimposable to one reported by Vats *et al.*[160b] In the ^1H NMR spectrum the signals related to the pyridinyl and phenyl fragments can be found between 8.35 and 7.40 ppm, but their multiplicity is sometimes complicated by the coupling with ^{31}P nucleus.

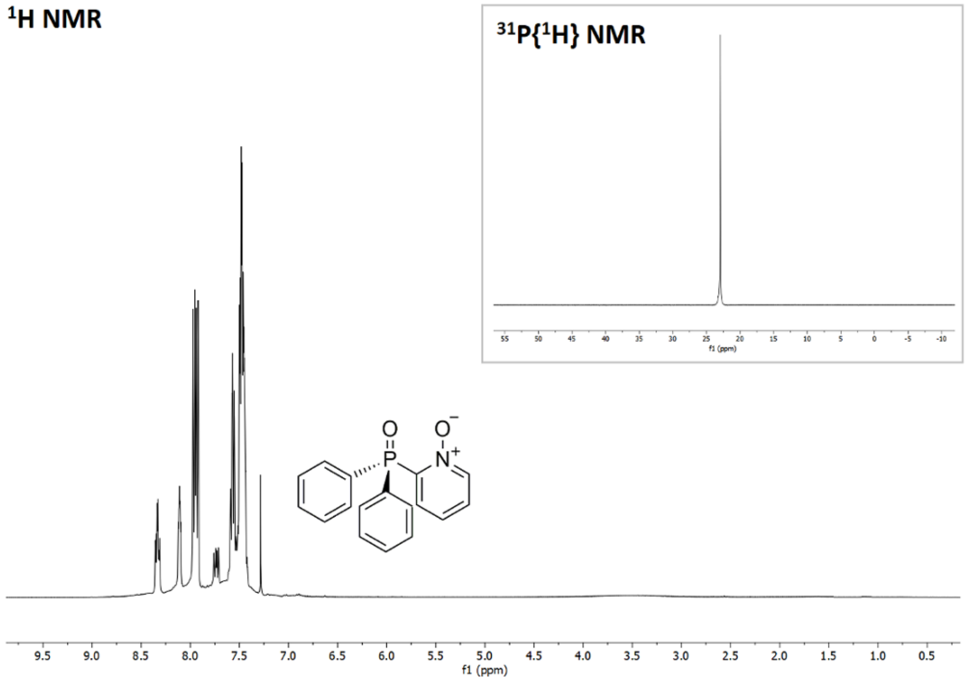

Figure 74. ^{1}H NMR spectrum of NPO$_2$ in CDCl$_3$ at 298 K. Inset: ^{31}P{^{1}H} NMR spectrum in CDCl$_3$ at 298 K.

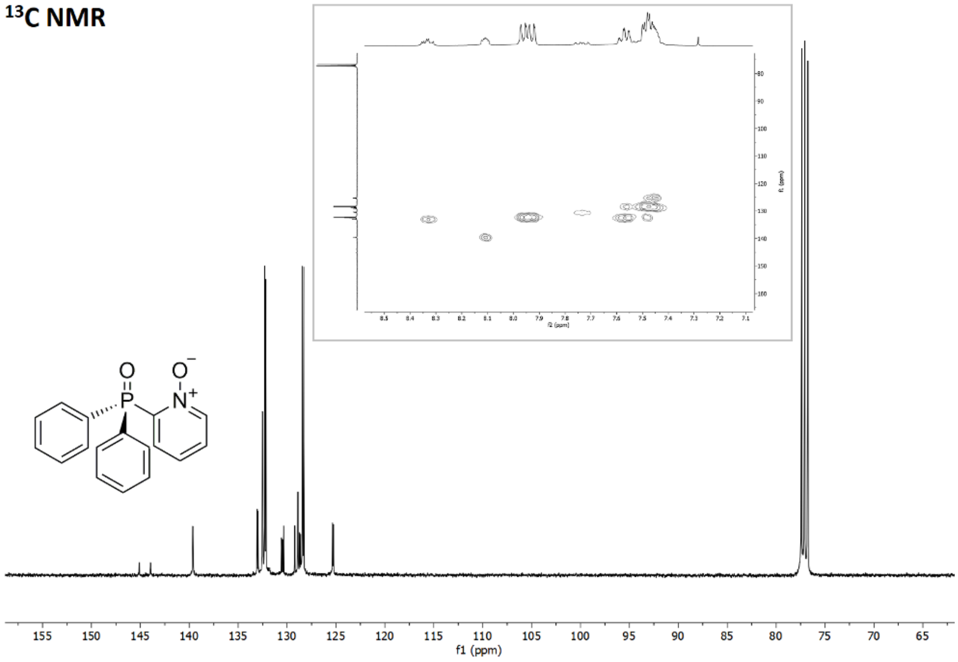

Figure 75. ^{13}C{^{1}H} NMR spectrum of NPO$_2$ in CDCl$_3$ at 298 K. Inset: ^{1}H-^{13}C HSQC spectrum in CDCl$_3$ at 298 K.

The octahedral complex [Mn(NPO$_2$)$_3$][ClO$_4$]$_2$ was prepared starting from manganese(II) perchlorate hexahydrate following Scheme 29. Since two isomers, *fac* and *mer*, can possibly form, computational calculations were exploited to rationalized which one was the more stable. The structures were optimized using dichloromethane a continuous medium. The *mer*-isomer appears to be the most stable in solution thanks to the higher dipole moment, equal to 9.15 Debye. Instead, as highlighted in Figure 76, the *fac*-isomer is characterized by an energy 1.5 kcal mol^{-1} higher being much less polar (μ = 0.08 Debye). Despite being yellow-coloured both at solid state and in solution, in the UV-VIS spectra reported in Figure 77 the band attributed to charge transfer mechanisms can be detected only in high concentrations between 400 and 500 nm (see inset Figure 77) and the complex does not decompose upon photoexcitation with blue light.

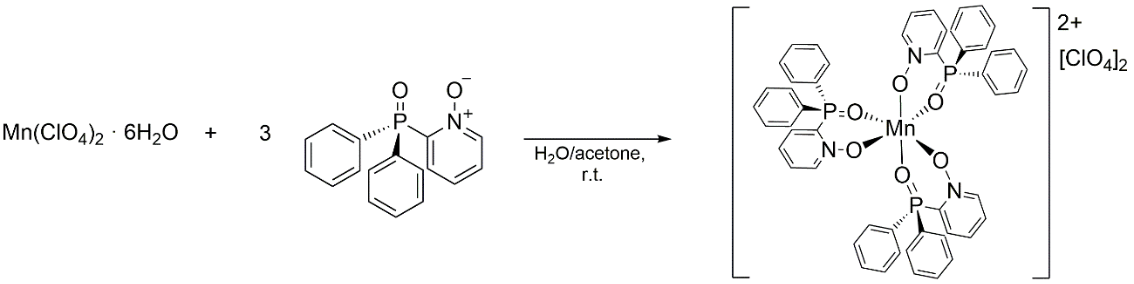

Scheme 29. Synthesis of $[Mn(NPO_2)_3][ClO_4]_2$.

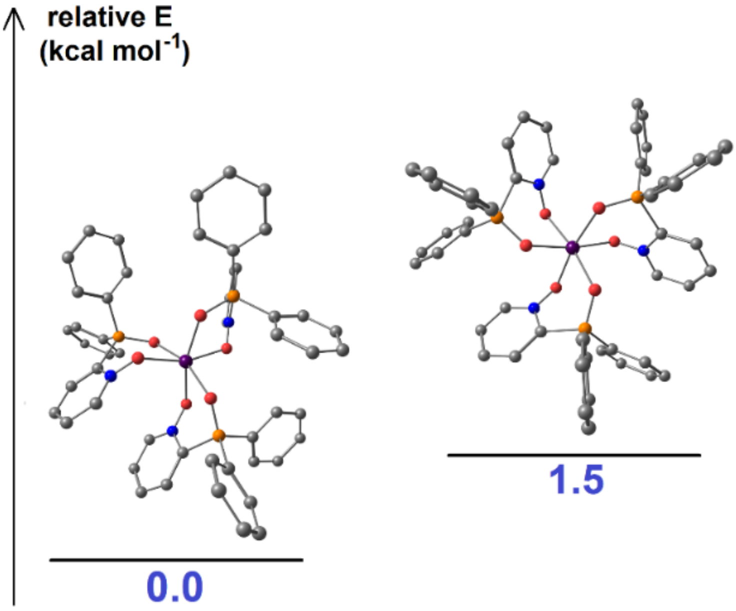

Figure 76. DFT-optimized structures of the *mer*- and *fac*-isomers for $[Mn(NPO_2)_3]^{2+}$ (TPSSh/def2-SVP calculations, C-PCM = dichloromethane).

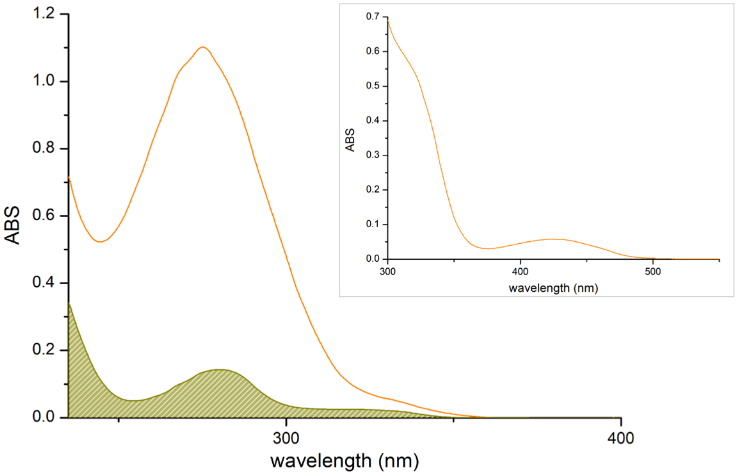

Figure 77. UV-VIS spectra of NPO_2 (dark yellow filled line) and $[Mn(NPO_2)_3][ClO_4]_2$ (orange line). CH_2Cl_2 solution, 10^{-5} M. Inset: UV-vis spectrum of $[Mn(NPO_2)_3][ClO_4]_2$ (orange line), CH_2Cl_2 solution, 10^{-4} M.

Cyclic voltammetry measurements helped to rationalize this outcome. As highlighted in Figure 78 the two ligands exhibit superimposable reversible reduction peaks between -1.8 and 1.9 V *vs* Fc^+/Fc, but the corresponding complexes appear to be different from an electrochemical point of view. For $[Mn(bpyO_2)_3][ClO_4]_2$ two reversible oxidation processes are observable, one around 0.6 V *vs* Fc^+/Fc attributed to the oxidation of manganese(II) to manganese(III) and the other one around 1.3 V *vs* Fc^+/Fc related to the oxidation to manganese(IV). These two processes can be detected also for $[Mn(NPO_2)_3][ClO_4]_2$ but they occur at higher potentials (first oxidation peak at 0.9 V *vs* Fc^+/Fc), thus justifying the higher photostability of the complex since manganese(III) appears to be less easily accessible. As another difference, the metal-centred process are not reversible in $[Mn(NPO_2)_3][ClO_4]_2$.

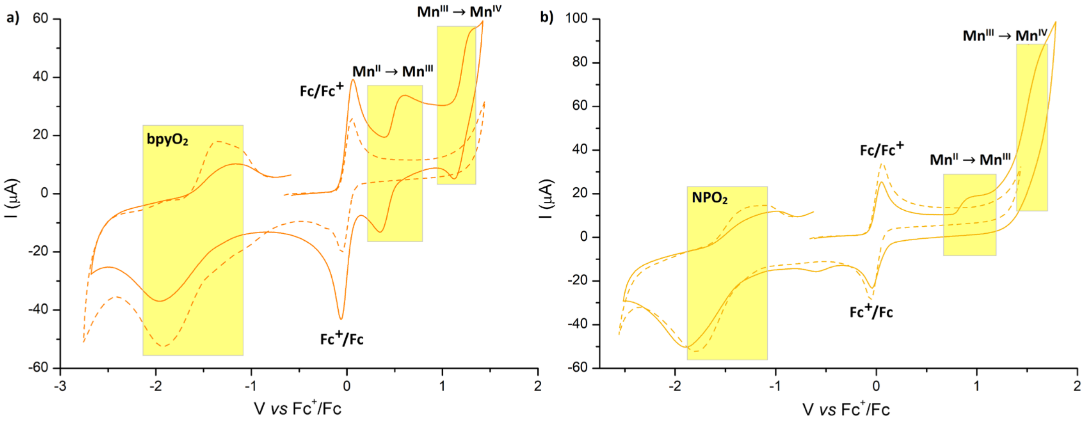

Figure 78. Cyclic voltammetries of: a) $bpyO_2$ (dashed orange line) and $[Mn(bpyO_2)_3][ClO_4]_2$ (continuous orange line); b) NPO_2 (dashed yellow line) and $[Mn(NPO_2)_3][ClO_4]_2$ (continuous yellow line). Platinum electrode, $CH_3CN/LiClO_4$, 1000 mV s^{-1}, ferrocene as internal standard, r.t., Ar atmosphere.

As can be deducted from the last examples, it is possible to conclude that the presence of a {N-O} fragment in the skeleton of the ligands acts as a quencher for the metal-centred $^4T_1(^4G) \rightarrow {^6A_1}(^6S)$ transition in manganese(II) complexes because of a MLCT process, sometimes conferring light-instability to the derivatives.

3.2 Luminescent copper(I) complexes

During my Master's degree thesis I started to use copper(I) borohydride complexes as alternative precursors to the commonly exploited CuCl and $[Cu(NCCH_3)_4]^+$ for the preparation of heteroleptic derivatives. Differently from the previously mentioned species, these complexes are air-stable and do not require to be stored under inert atmosphere. Moreover, the decomposition of the borohydride ligand with an acid avoids the possibility that acetonitrile or chloride remain in copper(I) coordination sphere. Thus, at the beginning of my PhD I decided to synthesize the corresponding complex with bis[(2-diphenylphosphino)phenyl] ether (DPEphos) as chelating ligand. This phosphine is widely recognized for its photophysical properties, related to the rigid structure and the wide P-Cu-P angle able to enhance the luminescent features.[52c] $[Cu(\kappa^2\text{–}BH_4)(DPEphos)]$ was isolated following the scheme reported in the Experimental Part (Scheme 20). First CuCl and DPEphos were heated in dichloroethane at reflux for one hour, then a solution of $NaBH_4$ in ethanol was added. The same reaction was then extended to the corresponding isotopologue $[Cu(\kappa^2\text{–}BD_4)(DPEphos)]$ in order to study the luminescence of these derivatives and the possible influences related to the change of the isotope. It is worth noting that the emission properties of copper(I) borohydride complexes were reported in literature only in the case of triphenylphosphine and 1,3-bis(diphenylphosphino)propane as P-donors.[161] Elemental analyses and non-conductive acetone solutions are in agreement with the proposed formulae. ^1H NMR, $^{31}P\{^1H\}$ NMR and ^{11}B NMR spectra of $[Cu(\kappa^2\text{–}BH_4)(DPEphos)]$ are reported in Figure 79. Besides the signals attributable to the phosphine in the region between 7.47 and 6.68 ppm of the ^1H NMR spectrum, it is possible to observe two broad multiplets of comparable intensity in the high-frequency region attributable to the borohydride moiety, broadened by quadrupolar relaxation. As regards the $^{31}P\{^1H\}$ NMR and the ^{11}B NMR spectra, a singlet at -15.48 ppm and a broad quintet at -32.13 ppm with $^1J_{BH}$ = 74 Hz can be respectively detected. The resonances related to the borohydride ligand are similar to those observed for [Cu(κ^2–BH_4)($(PPh_3)_2$] and agree with κ^2–coordination mode. Instead, no signal at high field was detected in the ^{1}H NMR spectrum of the isotopologue complex as well as no multiplicity in the ^{11}B NMR resonance because of the lower gyromagnetic ratio of deuterium with respect to protium.

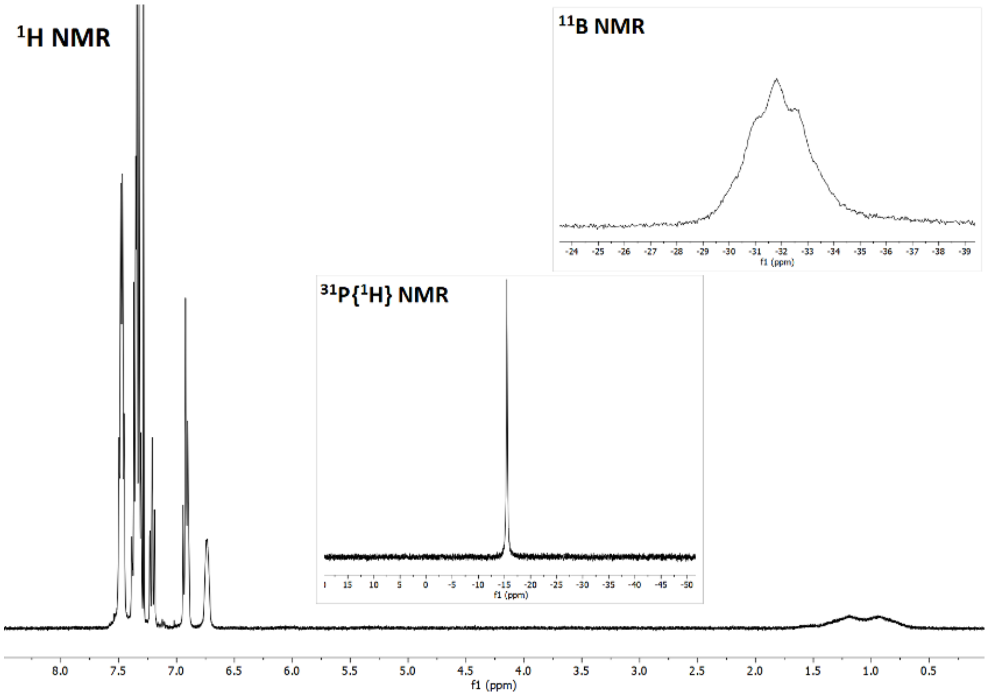

Figure 79. ^{1}H NMR, ^{31}P{^{1}H} NMR and ^{11}B NMR spectra of [Cu(κ^2–BH_4)(DPEphos)] in $CDCl_3$ at 298 K.

The κ^2–coordination mode is further confirmed by the IR spectrum of [Cu(κ^2–BH_4)(DPEphos)] reported in Figure 80, where two groups of signals are observable, one between 2240 and 2370 cm^{-1} and the other one in 1940–1990 cm^{-1} ranges, respectively attributed to the asymmetric and symmetric stretchings of terminal and bridging B-H bonds. Both the groups of signals are shifted at lower wavenumbers in the case of the isotopologue [Cu(κ^2–BD_4)(DPEphos)].

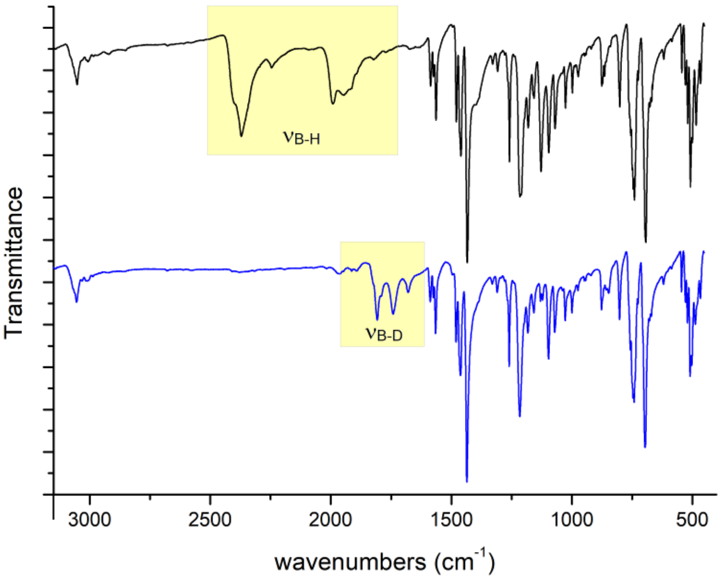

Figure 80. IR spectra of [Cu(κ^2–BH_4)(DPEphos)] (black line) and [Cu(κ^2–BD_4)(DPEphos)] (blue line) in KBr pellets.

[Cu(κ^2–BH_4)(DPEphos)] crystallizes in the *P*-1 triclinic space group by slow perfusion of diethyl ether in dichloromethane solutions. The ellipsoid plot of the two molecules found in the asymmetric unit is depicted in Figure 81. Crystal data and structure refinement are collected in Table A9 (see Table B9 for selected bond lengths and angles).

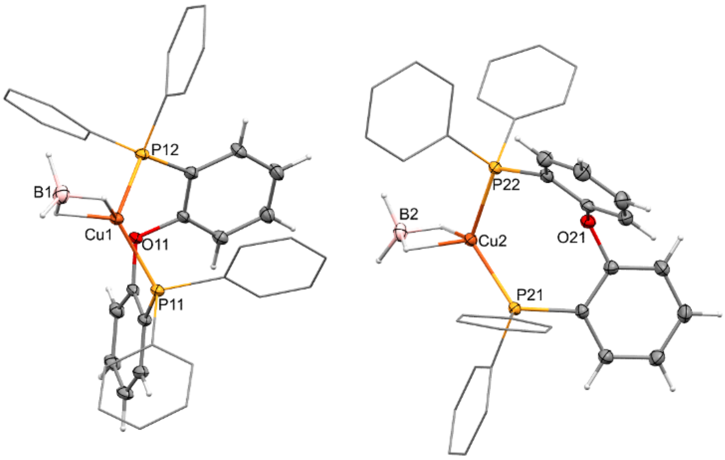

Figure 81. Ellipsoid plot of the asymmetric unit of [Cu(κ^2–BH_4)(DPEphos)].

Following a previously reported approach applied for [Cu(κ^2–BH_4)(PPh_3)$_2$],[140] the borohydride complex [Cu(κ^2–BH_4)(DPEphos)] was reacted with trifluoromethanesulfonic acid (HOTf) in 2:1 ratio in dichloromethane solution at low temperature, obtaining the corresponding dimer [Cu_2(μ–BH_4)(DPEphos)$_2$][OTf]. The formation of a cationic complex was supported by conductivity measurements and the presence of the counter-anion was confirmed both by the $\nu_{S=O}$ at 1030 cm^{-1} in the IR spectrum and by the singlet at -77.78 ppm in the ^{19}F NMR spectrum. Besides the resonances of coordinated DPEphos, the ^{1}H NMR spectrum is characterized by a quartet with 1:1:1:1 intensity ratio centred at 1.87 ppm and with $^{1}J_{BH}$ = 76 Hz. The same coupling constant was detected for the ^{11}B NMR quintet centred at -30.66 ppm. The ^{31}P{^{1}H} NMR showed only one singlet at -13.96 ppm (see Figure 82). As shown in Figure 83, the IR spectrum further confirms the change in the coordination mode of the borohydride since only one band at 2121 cm^{-1} attributable to μ–BH$_4$ was observable. No signal related to terminal ν_{B-H} was noticeable.

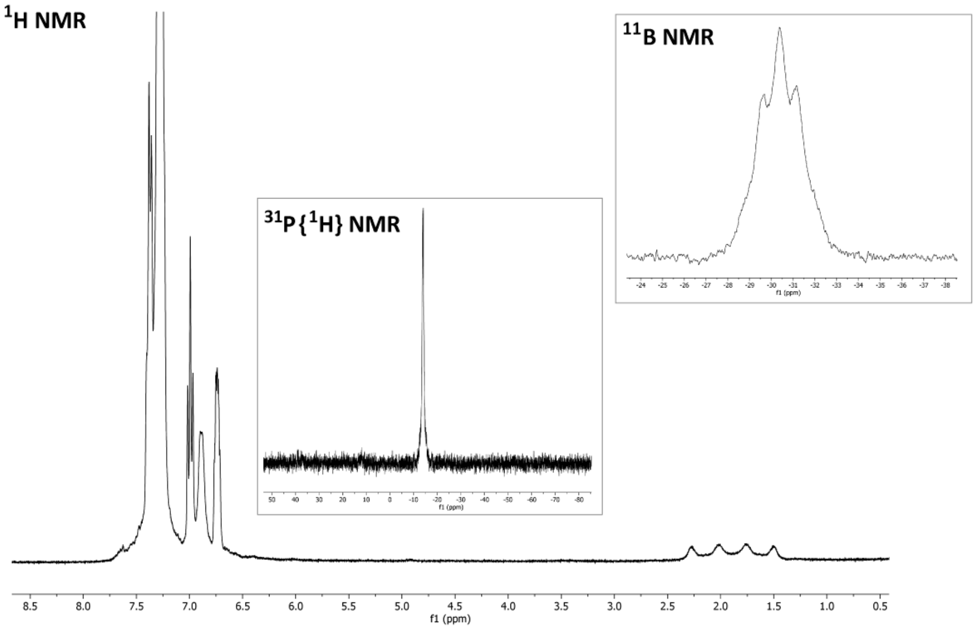

Figure 82. ^{1}H NMR, ^{31}P{^{1}H} and ^{11}B NMR spectra of [Cu$_2$(μ–BH$_4$)(DPEphos)$_2$][OTf] in CDCl$_3$ at 298 K.

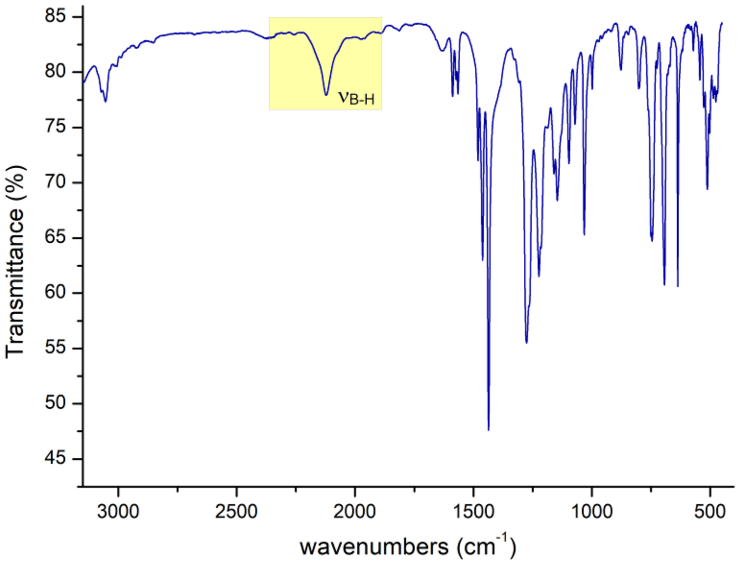

Figure 83. IR spectrum of [Cu$_2$(μ–BH$_4$)(DPEphos)$_2$][OTf] in KBr pellets.

$[Cu(\kappa^2–BH_4)(DPEphos)]$ and $[Cu(\kappa^2–BD_4)(DPEphos)]$ are characterized by absorptions below 350 nm in dichloromethane solutions (inset of Figure 84), in agreement with the bands reported for the free ligand and related to $\pi^* \leftarrow \pi$ transitions of the DPEphos.[76b,162] As shown in Figure 84 for $[Cu(\kappa^2–BH_4)(DPEphos)]$, the excitation of solid samples in the UV region determined an emission in the blue region centred at 465 nm. The photoluminescence quantum yields Φ of the two complexes are roughly the same, around 12%, suggesting that the borohydride ligand is scarcely involved in the non-radiative decay routes from the excited to the ground state. It is worth noting that the free ligand is poorly luminescent at solid state, being characterized by an emission maximum at 443 nm and $\Phi = 3\%$.[163] The photophysical properties of $[Cu_2(\mu–BH_4)(DPEphos)_2][OTf]$ are roughly comparable to those of the other two borohydride complexes here described, with a red-shift of about 10 nm of the emission maximum. The measured photoluminescence quantum yield Φ of the dimer equal to 14% is in line with the values previously reported, confirming a scarce participation of the borohydride ligand in the non-radiative decay routes of the excited states. Therefore, also on the basis of literature data,[163] it is possible to conclude that the photoluminescence of the three complexes is attributable to transitions of DPEphos, enhanced by coordination. The interaction with the metal centre causes a red shift in the emission maximum, more pronounced in the cationic $[Cu_2(\mu–BH_4)(DPEphos)_2][OTf]$ complex.

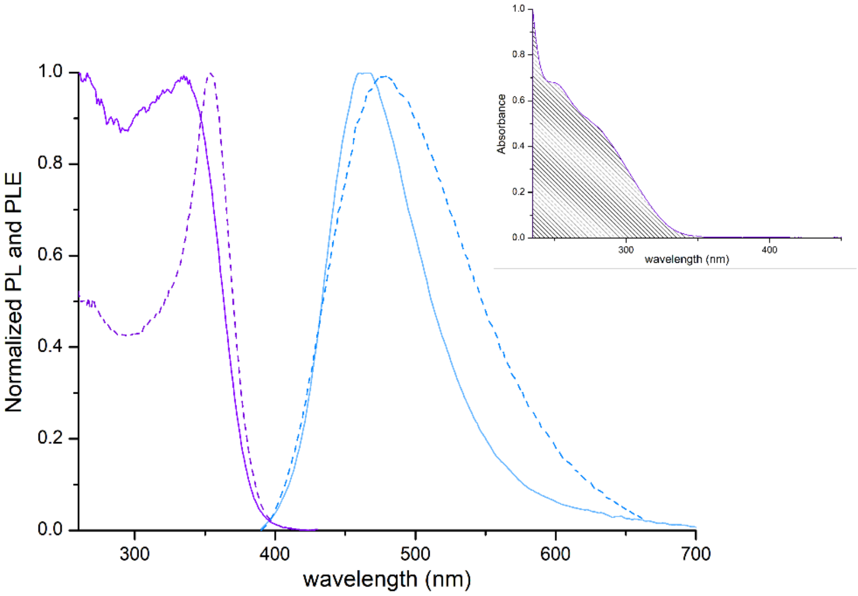

Figure 84. Normalized PL and PLE spectra (solid sample, r.t., $\lambda_{excitation} = 290$ nm, $\lambda_{emission} = 470$ nm) of $[Cu(\kappa^2–BH_4)(DPEphos)]$ (solid line) and $[Cu_2(\mu–BH_4)(DPEphos)_2][OTf]$ (dashed line) Inset: absorption spectrum, 10^{-5} M dichloromethane solution.

The decomposition under acidic conditions of the borohydride moiety prompted me to try to exploit [Cu(κ^2–BH$_4$)(DPEphos)] as precursor to obtain previously reported luminescent heteroleptic copper(I) complexes having general formula [Cu(N^N)(DPEphos)]$^+$.[52a,164] Acetic acid (HOAc) was used in combination with 1,10-phenanthroline (phen), 2,9-dimethyl-1,10-phenanthroline (dmp), 2,2'-bipyridine (bpy) and 4,4'-dimethyl-2,2'-bipyridine (dmbpy) and the complexes were isolated as acetate salts (see Scheme 30). The compounds were prepared in high yields and purity using mild reaction conditions and with and minimal work-up. The characterization data are in agreement with the ones reported in literature for the same complexes obtained with different synthetic methods.[52a,164]

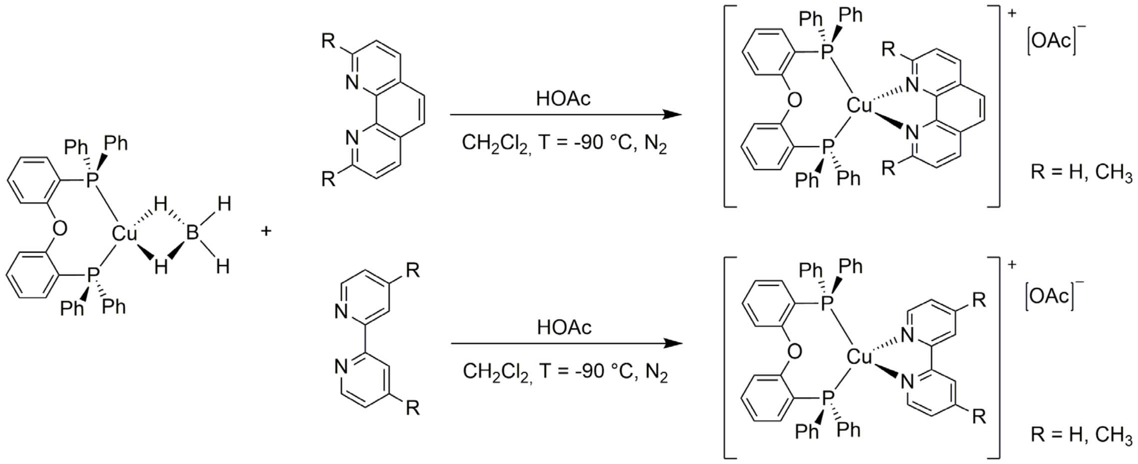

Scheme 30. Synthesis of [Cu(N^N)(DPEphos)][OAc] (N^N = phen, dmp, bpy, dmbpy).

Following these considerations, I decided to prepare bidentate ligands based on the benzotriazole fragment to be reacted with borohydride copper(I) complexes. It is worth mentioning that the benzotriazole heterocycle is widely applied in organic synthesis[165] but its possible use as ligand is much less explored. *N*-methyl benzotriazole was efficiently exploited in the past by the research group for the preparation of a yellow-emitting copper(I) coordination polymer.[98c] Bis(benzotriazol-1-yl)phenylmethane CHPh(btz)$_2$ was synthesised in two steps following the method reported in the Experimental Part (see Scheme 14). First, benzotriazole was treated with triphosgene and triethylamine to afford the corresponding bis(azol-1-yl)methanone, that was subsequently reacted with benzaldehyde in the presence of anhydrous CoCl$_2$. Characterization data are in agreement with those reported in literature for the same compound obtained with different synthetic methods.[132] However, the X-ray structure of this compound was never reported. Despite the fact that it is a commercially available compound and it was described by Katritzky *el al.*

back in the Nineties, a similar situation occurred with tris(benzotriazol-1-yl)methane CH(btz)$_3$.[133] In both the cases, crystals suitable for X-ray diffraction were obtained from slow evaporation of dichloromethane solutions. Both the compounds crystallized in the $P2_1/c$ monoclinic space group and their ORTEP plots are outlined in Figure 85. Crystal data and structure refinement are collected in Table A10 (see Table B10 for selected bond lengths and angles).

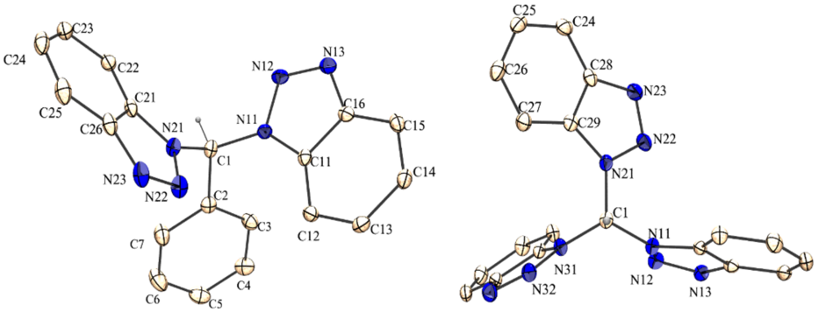

Figure 85. ORTEP plot of CHPh(btz)$_2$ and CH(btz)$_3$. Except in C1 hydrogen atoms are omitted for clarity.

Heteroleptic copper(I) complexes with bis(benzotriazol-1-yl)phenylmethane in the coordination sphere were obtained from the reaction of the proper borohydride complex with the ligand in presence of $HBF_4 \cdot Et_2O$ and under mild conditions. Complexes with tris(benzotriazol-1-yl)methane and phosphines were instead synthesized by the subsequent addition of the ligands to the precursor $[Cu(NCCH_3)_4][BF_4]$ following the scheme reported below.

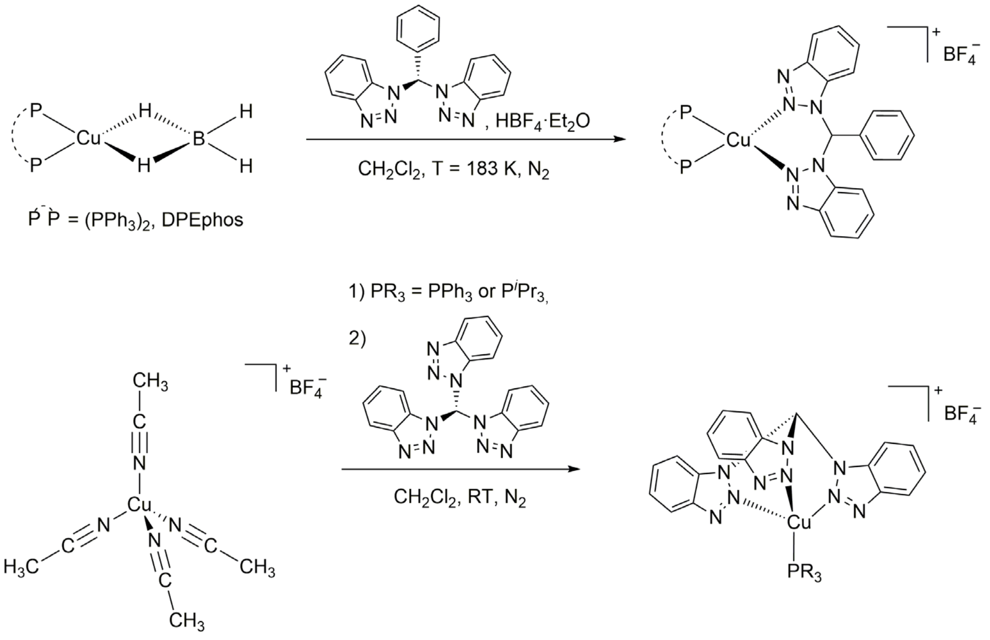

Scheme 31. Synthesis of $[Cu\{CH(btz)_2\}(PP)][BF_4]$ [PP = $(PPh_3)_2$, DPEphos] and $[Cu\{CH(btz)_3\}(PR_3)][BF_4]$ (R = Ph, ^{i}Pr).

Elemental analyses are in agreement with the proposed formulae and conductivity measurements in acetone solutions indicate that the complexes behave as 1:1 electrolytes. The evolution of the reactions was confirmed by the IR spectra, where no signal attributable to coordinated borohydride or acetonitrile is detectable. The IR bands are related to vibrations of the coordinated N- and P-donor ligands, superimposed to ν_{BF4} in the 1000–1170 cm^{-1} range. The presence of the counter-anion is further confirmed by the appearance of a quintet ($^1J_{BF}$ = 0.9 Hz) in the ^{11}B NMR spectra. Diagnostic for the coordination of bis(benzotriazol-1-yl)phenylmethane or tris(benzotriazol-1-yl)methane is the methine ^{1}H NMR resonance, observable at low fields between 9.06 and 10.64 ppm. The remaining ^{1}H NMR signals fall in the aromatic region and are related to the phosphine substituents and to the benzotriazol-1-yl or phenyl substituents of the N-donor ligands. The only exception is the ^{1}H NMR spectrum of [Cu{CH(btz)$_3$}(P^{i}Pr$_3$)][BF$_4$], with multiplets affected by the temperature in the aliphatic region related to the isopropyl substituents of the phosphine. The coordination of mono- and bidentate phosphines is confirmed by the ^{31}P{^{1}H} NMR spectra, showing in all the cases only a broad resonance also at low temperature, this indicating fluxional behaviour in solution.

The complexes are characterized by absorptions for wavelengths below 400 nm in CH_2Cl_2 solutions. Excitation of the solid samples with near-UV and violet light (see the PLE spectra in Figure 86) determines bright yellow and orange emissions centred between 555 and 600 nm, as observable in the PL spectra reported in Figure 86. The emission maxima are red-shifted in the tris(benzotriazol-1-yl)methane derivatives.

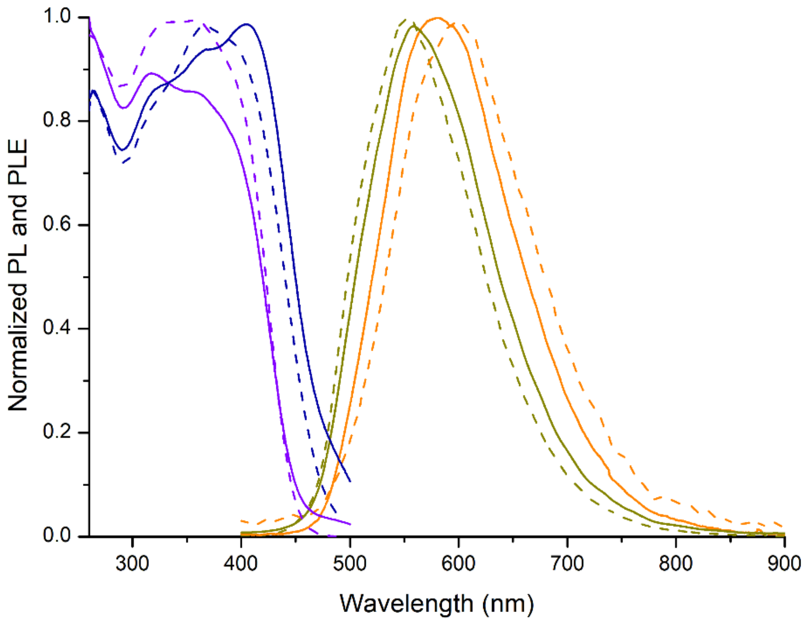

Figure 86. Normalized PL (solid sample, $\lambda_{excitation}$ = 375 nm, r.t.): solid dark yellow line, $[Cu\{CHPh(btz)_2\}(PPh_3)_2][BF_4]$; dashed dark yellow line, $[Cu\{CHPh(btz)_2\}(DPEphos)][BF_4]$; solid orange line, $[Cu\{CH(btz)_3\}(PPh_3)][BF_4]$; dashed orange line, $[Cu\{CH(btz)_3\}(P^iPr_3)][BF_4]$. Normalized PLE (solid sample, $\lambda_{emission}$ = 600 nm, r.t.): solid violet line, $[Cu\{CHPh(btz)_2\}(PPh_3)_2][BF_4]$; dashed violet line, $[Cu\{CHPh(btz)_2\}(DPEphos)][BF_4]$; solid dark blue line, $[Cu\{CH(btz)_3\}(PPh_3)][BF_4]$; dashed dark blue line, $[Cu\{CH(btz)_3\}(P^iPr_3)][BF_4]$.

Despite the comparison of solid samples is only qualitative, the emission intensity grows appreciably by replacing the two triphenylphosphine ligands with DPEphos in $[Cu\{CHPh(btz)_2\}(PP)][BF_4]$ complexes. Such a trend was previously observed for similar compounds,[166] and it is attributable to the rigidity and to the steric hindrance of the chelating phosphine, that contributes to prevent distortions at the excited state. As a further comparison, the emission of $[Cu\{CH(btz)_3\}(P^iPr_3)][BF_4]$ is lower than that of $[Cu\{CH(btz)_3\}(PPh_3)][BF_4]$, perhaps because of the more flexible isopropyl substituents. The large Stokes shifts, about 200 nm, and the wide emission bands (FWHM between 4100 and 4200 cm^{-1}) suggest that the emissions of the complexes could involve triplet excited states. The luminescence lifetimes are in the 2–6 μs range. In order to investigate the transitions from a computational point of view, singlet and triplet state geometries of $[Cu\{CHPh(btz)_2\}(PPh_3)_2]^+$ and $[Cu\{CH(btz)_3\}(PPh_3)]^+$ were optimized (see Figure 87). TD-DFT calculations on the ground states indicate that singlet-singlet light absorption is related to the charge transfer from occupied metal- and phosphine-centred frontier orbitals to unoccupied π* orbitals of the benzotriazole fragments. Therefore, the lowest-energy absorptions have ^{1}MLCT nature. The lowest energy singlet-triplet absorptions implicate the molecular orbitals superimposed in Figure 87. The triplet state emissions are the specular processes and appear based on transitions between benzotriazole-centred orbitals and molecular orbitals localized on the metal centre, the phosphine ligands and also the N-donor ligands. The computed values, respectively 563 and 678 nm for $[Cu\{CHPh(btz)_2\}(PPh_3)_2]^+$ and $[Cu\{CH(btz)_3\}(PPh_3)]^+$, are roughly in agreement with the experimental data. The nature of the emissions assigned on the basis of DFT calculations is therefore ^{3}MLCT/^{3}LC.

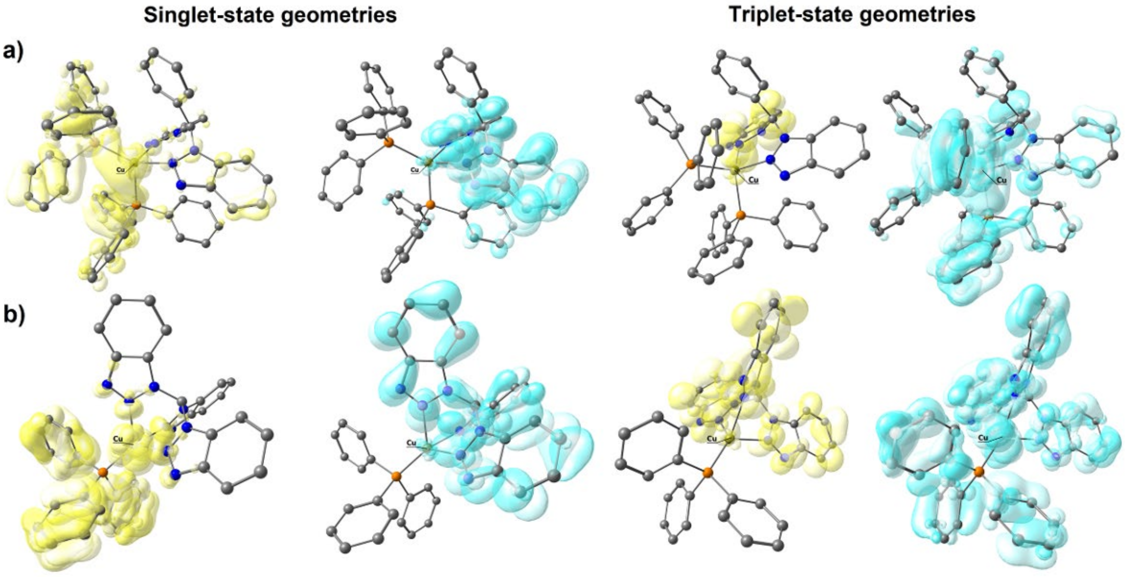

Figure 87. DFT-optimized structures of: a) $[Cu\{CHPh(btz)_2\}(PPh_3)_2]^+$ and b) $[Cu\{CH(btz)_3\}(PPh_3)]^+$, singlet and triplet states. ωB97X/def2-SVP calculations. The orbitals involved in the lowest energy singlet-singlet absorptions (lowest energy singlet geometry) are respectively depicted in yellow (occupied) and turquoise (unoccupied) tones. The orbitals involved in the lowest energy singlet-triplet absorptions (lowest energy triplet geometry) are respectively depicted in turquoise (occupied) and yellow (unoccupied) tones. Surface isovalue = 0.003 a.u.

Yellow-emitting compounds with wide emission bands are of interest for the preparation of white light emitting diodes (WLEDs). A common technological approach is the coating of blue LEDs with yellow-emitting species, used for instance in the case of indium gallium nitride (InGaN) LEDs in combination with cerium-doped yttrium aluminium garnets (YAG:Ce^{3+}).[167] The PL and PLE spectra together with the thermal stability (decomposition starts above 250°C on the basis of TGA data) of the yellow-emitting $[Cu\{CHPh(btz)_2\}(DPEphos)][BF_4]$ suggested its possible application in this field. The complex maintains the luminescence without meaningful alterations once embedded in poly(methyl methacrylate) (PMMA) matrix. The doped polymers obtained from dichloromethane solutions were applied to coat commercial UV LEDs with emission maximum at 385 nm. The emission spectrum of a typical coated LED is reported in Figure 88. White light is conventionally located at coordinates x = y = 0.333, while [Cu{CHPh(btz)$_2$}(DPEphos)][BF$_4$] and the derived WLED are respectively positioned at x = 0.444, y = 0.512 and x = 0.354, y = 0.381 in the CIE 1931 diagram (see the inset in Figure 88). The white emission thus obtained is characterized by a colour temperature of 4800 K, calculated accordingly to McCamy's formula.[168]

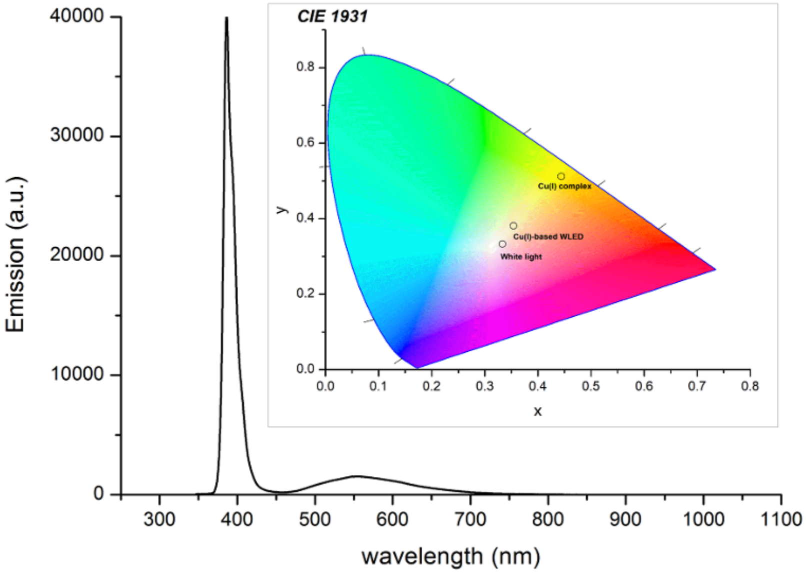

Figure 88. Emission spectrum of copper(I)-based WLED. Inset: CIE 1931 chromaticity diagram with the chromaticity coordinates of white light, [Cu{CHPh(btz)$_2$}(DPEphos)][BF$_4$] and the related WLED.

The same synthetic procedure used to isolate bis(benzotriazol-1-yl)phenylmethane was extended to the indazole heterocycle. As occurs for benzotriazole, also this compound is not commonly applied for the preparation of luminescent copper(I) complexes. Only few examples are reported in literature.[166a,169] Di(1*H*-indazol-1-yl)methane and di(2*H*-indazol-2-yl)methane were exploited by Pettinari and co-workers for the preparation of copper(I) complexes, but the photophysical properties of these derivatives were not investigated.[170]

Bis(indazol-1-yl)phenylmethane was reacted with CuCl and [Cu(NCCH$_3$)$_4$][BF$_4$] under mild conditions. In both the cases the homoleptic complex [Cu{CHPh(ind)$_2$}$_2$][X] (X = Cl, BF$_4$) was isolated. Elemental analyses are in agreement with the proposed formula and conductivity measurements indicate that the complexes are monocationic. The IR spectra show bands comparable to those of the free ligand, with the addition of the ν_{BF4} stretching between 1180 and 1050 cm^{-1} in the case of X = BF$_4$.[156] The most diagnostic signals fall between 1620 and 1450 cm^{-1} and are related to $\nu_{C=N}$ and $\nu_{C=C}$ stretching vibrations. No signal attributed to coordinated acetonitrile is observable in the IR and ^{1}H NMR spectra. The resonances of the coordinated N-donors in DMSO-d$_6$ solution are broad at 298 K, becoming sharp on heating the sample above 330 K and revealing that the two coordinated ligands are equivalent on the NMR timescale (see Figure 89). The singlets related to the methine fragment at 9.23 ppm and to the indazole-CH at 8.18 ppm at 338 K are diagnostic for the coordinated CHPh(ind)$_2$. Broad resonances were detected in CDCl$_3$ solution between 213 K and 318 K for [Cu{CHPh(ind)$_2$}$_2$][Cl], suggesting fluxional behaviour.

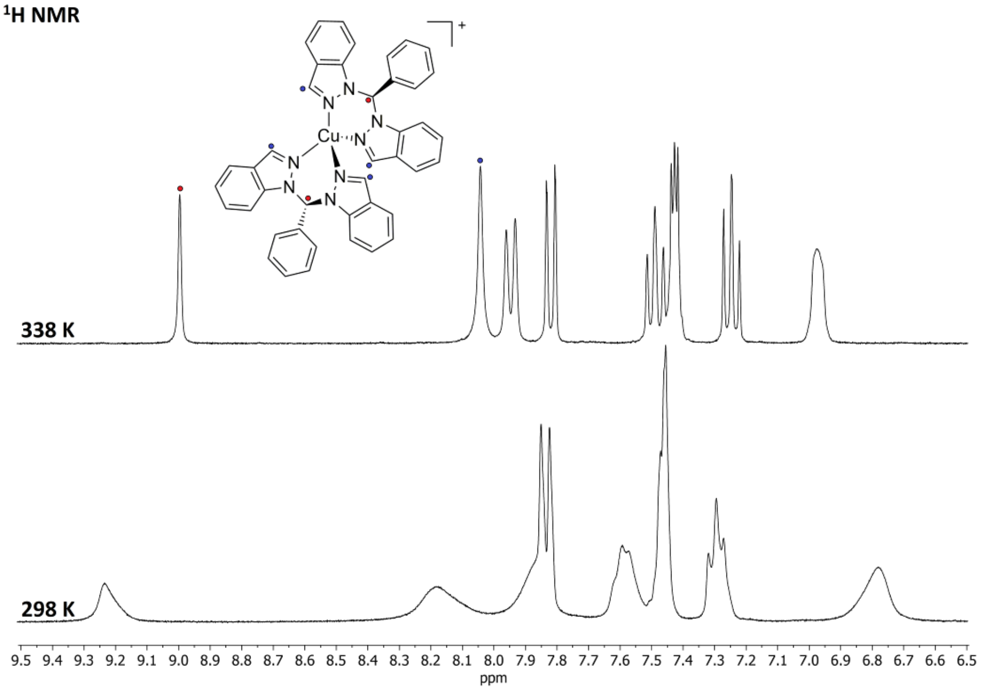

Figure 89. ^{1}H NMR spectra of [Cu{CHPh(ind)$_2$}$_2$][BF$_4$] in DMSO-d$_6$ at 298 and 338 K.

Crystals of [Cu{CHPh(ind)$_2$}$_2$][Cl] suitable for X-ray diffraction were collected from the slow evaporation of dichloromethane solutions. The complex crystallized in the *I*4$_1$*/a* space group. The ORTEP plot of the cation is shown in Figure 90. Crystal data and structure refinement are collected in Table A11. Selected distances and angles are set out in Table B11.

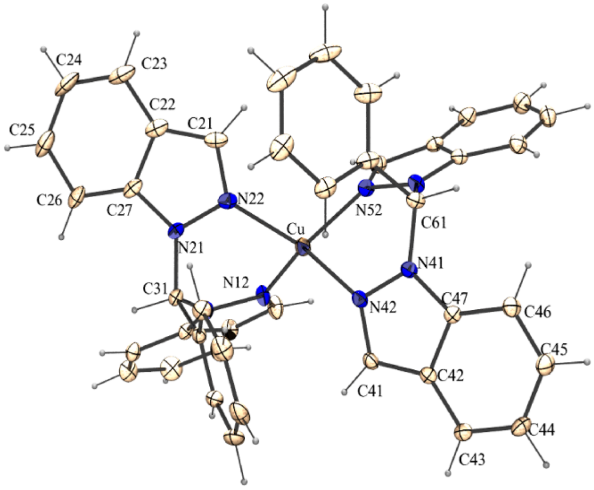

Figure 90. ORTEP view of [Cu{CHPh(ind)$_2$}$_2$]$^+$. Atoms are drawn at 30% probability level.

[Cu{CHPh(ind)$_2$}$_2$]$^+$ absorbs light in dichloromethane and DMSO solution for wavelengths below 410 nm. As observable in Figure 91a, the absorption features are different when using a coordinating solvent, *i.e.* DMSO, being markedly less pronounced the band centred around 329 nm. This outcome suggests that the lowest energy absorption could be related to charge transfer between metal centre and coordinated ligands. This aspect is further confirmed by TD-DFT calculations, that clearly indicate that the lowest energy singlet transition involves the metal-centred occupied molecular orbitals (HOMO, HOMO-1) and unoccupied π^* orbitals localized on the indazol-1-yl fragments (LUMO, LUMO+1, LUMO+12 and LUMO+13). Figure 91a shows the superposition of the HOMO-1 (green) and of the LUMO (yellow) as illustrative example. [Cu{CHPh(ind)$_2$}$_2$][Cl] and [Cu{CHPh(ind)$_2$}$_2$][BF$_4$] are non-luminescent in solution but at the solid state they exhibit bright yellow emissions upon excitation with near-UV and violet light. In both the cases, the emission maximum lies at 565 nm and the FWHM is 4600 cm^{-1} (see Figure 91b). The emission can be obtained for excitation wavelengths below 450 nm with maximum at 386 nm, as observable in the PLE spectrum reported in Figure 91b. No wavelength-dependent behaviour was observed, and the emission appears to be independent upon the nature of the counterion. The photoluminescent properties remain constant on considering powder and crystals samples. The CIE 1931 chromaticity coordinates are x = 0.437, y = 0.477, falling between the yellow and the yellowish orange regions of the diagram (see inset of Figure 91b).

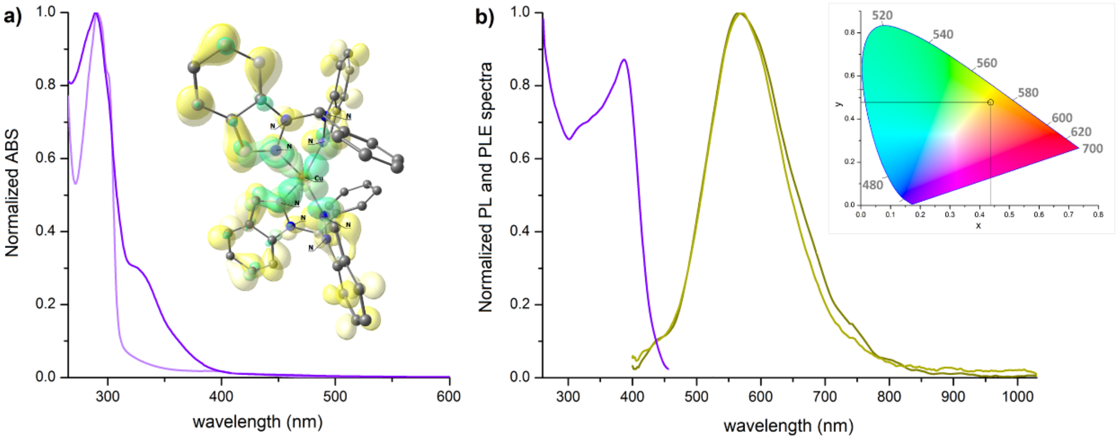

Figure 91. a) Normalized absorption spectra of [Cu{CHPh(ind)$_2$}$_2$]$^+$ in DMSO (light violet line) and CH_2Cl_2 (violet line). DFT-optimized structure with superimposed HOMO-1 (green) and LUMO (yellow). ωB97X/def2-SVP calculation. Surface isovalue = 0.03 a.u. Hydrogen atoms are omitted for clarity. b) Normalized PLE (violet line, $\lambda_{emission}$ = 600 nm) and PL spectra ($\lambda_{excitation}$ = 375 nm) (X = Cl, yellow line; X = BF_4, dark yellow line). Inset: CIE 1931 chromaticity diagram.

As highlighted in the spectrum presented in Figure 92, time-resolved photoluminescent measurement clearly show the presence of two decay components, characterized by τ values of 12 (63%) and 73 μs (37%), respectively. The average lifetime is 35 μs. Biexponential decays were observed for several luminescent copper(I) complexes and assigned to the decays from MLCT and LLCT excited states.[171] The TD-DFT optimized geometries of the first (T1) and second (T2) triplet states of [Cu{CHPh(ind)$_2$}$_2$]$^+$ agree with ^{3}LLCT/^{3}MLCT transitions, being the electronic structures described by the electron transfer from Cu- and indazole-centred molecular orbitals (mainly HOMO, HOMO-1 and HOMO-2) to indazole-localized unoccupied orbitals (mainly LUMO). The most involved orbitals are depicted in Figure 92. T1 and T2 states have quite similar geometry and the energy difference between them is only 470 cm^{-1}, suggesting that both T1 and T2 may be reasonably involved in the emission process. The photoluminescence quantum yield Φ measured at room temperature for powder samples is 1.3%. The radiative (k_r) and non-radiative (k_{nr}) rate constants are estimated on the basis of the equation $\Phi = k_r/(k_r+k_{nr}) = \tau^m k_r$ to be $k_r = 3.7\cdot10^2$ s^{-1} and $k_{nr} = 2.8\cdot10^4$ s^{-1}.[172] The low quantum yield can be explained on considering the scarce rigidity of the molecule and its distortion towards square planar geometry,[173] evident for the T2 excited state, with τ_4 parameter equal to 0.44.[174] Both these factors favour non-radiative decay routes.

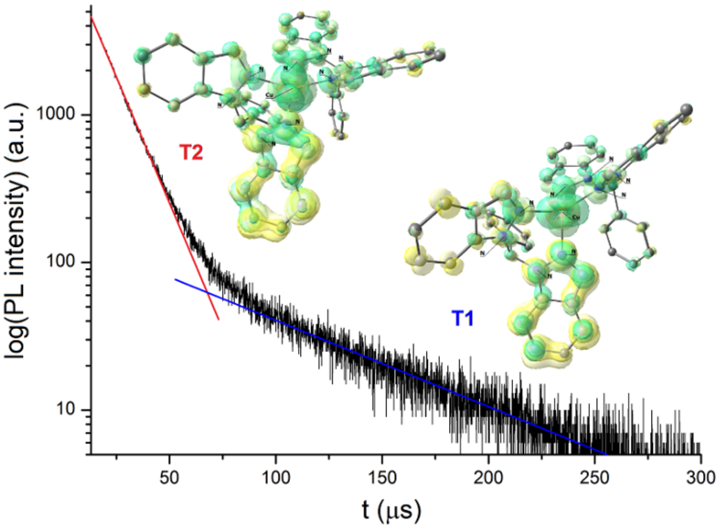

Figure 92. Semi-log plot of the time-resolved luminescence decay of [Cu{CHPh(ind)$_2$}$_2$][Cl]. TD-DFT-optimized structures of T1 and T2 states. ωB97X/def2-SVP calculations. Superimposed orbitals for T1: HOMO-2 and HOMO (green), LUMO (yellow). Superimposed orbitals for T2: HOMO-1 and HOMO (green), LUMO (yellow). Surface isovalue = 0.003 a.u. Hydrogen atoms are omitted for clarity.

The outcomes achieved with the ligands previously described prompt me to try to act on the bulk and on the rigidity of the chelating N-donors in order to improve the radiative decay and thus the photoluminescence. The functionalization of azoles with other heterocycles is a commonly used method to simultaneously obtain rigid bidentate structures and remove high energy oscillators.[52h,58a,58c,59,175] So I decided to functionalize the benzotriazole fragment with pyridine (py), pyrimidine (pym) and alkoxy-substitued triazines (trz^{OR}). The first two ligands, 1-(pyridin-2-yl)benzotriazole (py-btz) and 1-(pyrimidin-2-yl)benzotriazole (pym-btz), were obtained following the method previously reported by Katritzky and co-workers, based on the aromatic nucleophilic substitution of C-bonded halides by benzotriazole.[134] The triazinyl-benzotriazoles trz^{OMe}-btz, trz^{OEt}-btz and trz^{OPh}-btz were obtained by reacting the related 2-chloro-triazines with benzotriazole. The ^{1}H NMR, ^{13}C NMR and ^{1}H-^{13}C HSQC NMR spectra of trz^{OEt} are reported in Figure 93 and 94 as illustrative example. The ^{1}H NMR of the derivatives is characterized by four resonances at high fields related to the benzotriazole fragment. In the case of trz^{OMe} a singlet at 4.25 ppm due to the alkoxy groups is detectable, while for trz^{OEt} the related signals are a quartet at 4.67 ppm and a triplet at 1.55 ppm. Instead, all the signals are observable in the aromatic region for trz^{OPh}-btz, superimposed to those of the benzotriazole heterocycle.

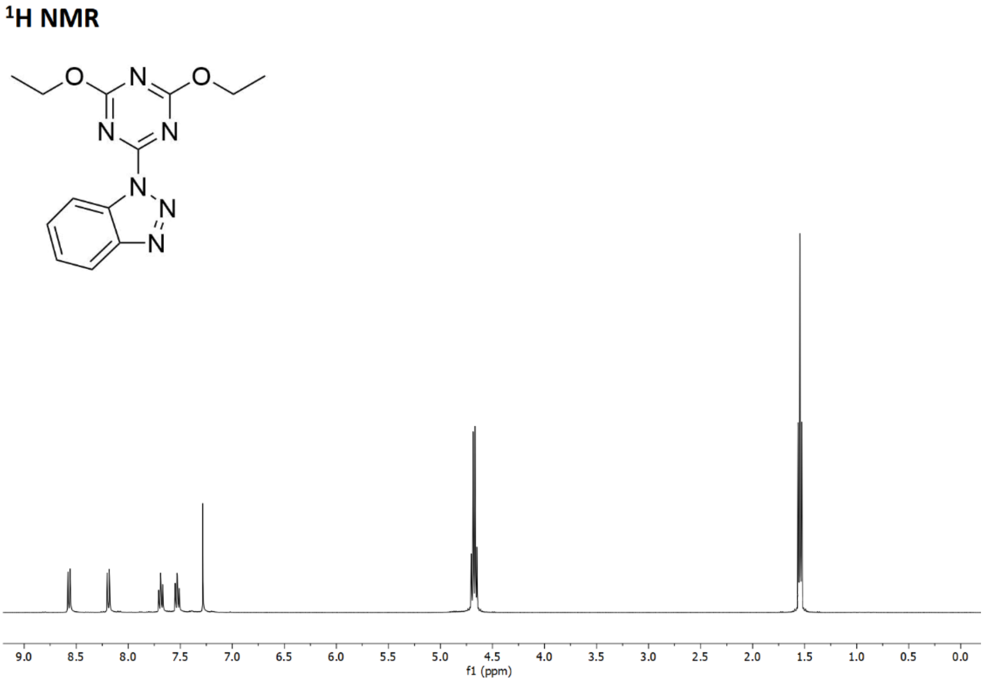

Figure 93. ^{1}H NMR spectrum of trz^{OEt}-btz in $CDCl_3$ at 298 K.

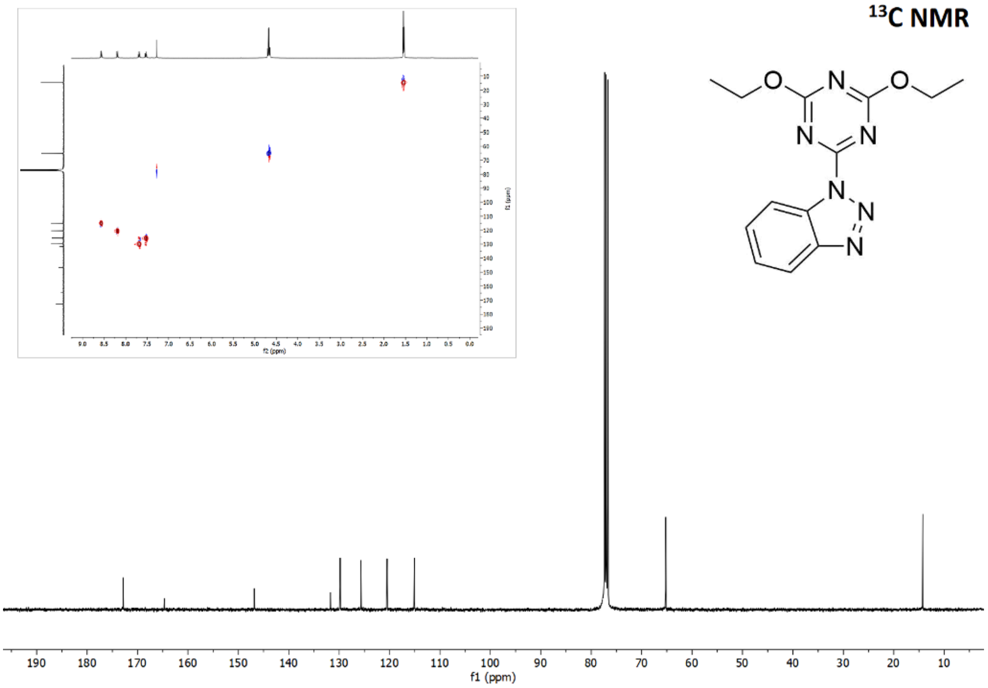

Figure 94. ^{13}C NMR spectrum of trz^{OEt}-btz in $CDCl_3$ at 298 K. Inset: ^{1}H-^{13}C HSQC ($CDCl_3$, 298 K).

In the cases of 1-(4,6-dimethoxy-1,3,5-triazin-2-yl)benzotriazole (trz^{OMe}-btz) and 1-(4,6-diphenoxy-1,3,5-triazin-2-yl)benzotriazole (trz^{OPh}-btz) the structure was further confirmed by single crystal X-ray diffraction obtained from slow evaporation of dichloromethane (trz^{OMe}-btz) or acetone (trz^{OPh}-btz) solutions. The former crystallizes in the monoclinic $P2_1/c$ group with two equivalent molecules in the asymmetric unit, while the latter crystallizes in triclinic P-1 space group. One of the two molecules of trz^{OMe}-btz and the trz^{OPh}-btz found in the asymmetric unit are shown in Figure 95. Crystal data and structure refinement are reported in Table A12. Selected distances and angles are collected in Table B12.

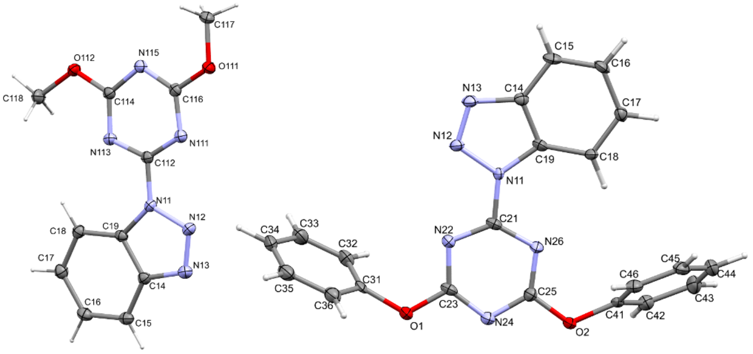

Figure 95. Ellipsoid representation of one of the molecules found in the asymmetric unit of trz^{OMe}-btz and of trz^{OPh}-btz.

The heteroleptic copper(I) complexes with PPh_3 in the coordination sphere were obtained by reaction of the corresponding conjugated acids (obtained *in situ* by adding $HBF_4{\cdot}Et_2O$) with $[Cu(\kappa^2\text{–}BH_4)(PPh_3)_2]$. The same synthetic approach using copper(I) borohydride precursors with other phosphines afforded multiple products, therefore the synthesis of the other complexes prosecuted using $[Cu(NCCH_3)_4][BF_4]$ as precursor. The acetonitrile complex was reacted with the proper phosphine, triisopropylphosphine P^iPr_3, 1,2-bis(diphenylphosphino)ethane dppe or bis[(2-diphenylphosphino)phenyl] ether DPEphos, and subsequently with the chosen chelating N-donor. The procedures followed are summarized in Scheme 32 together with the numbering of the complexes.

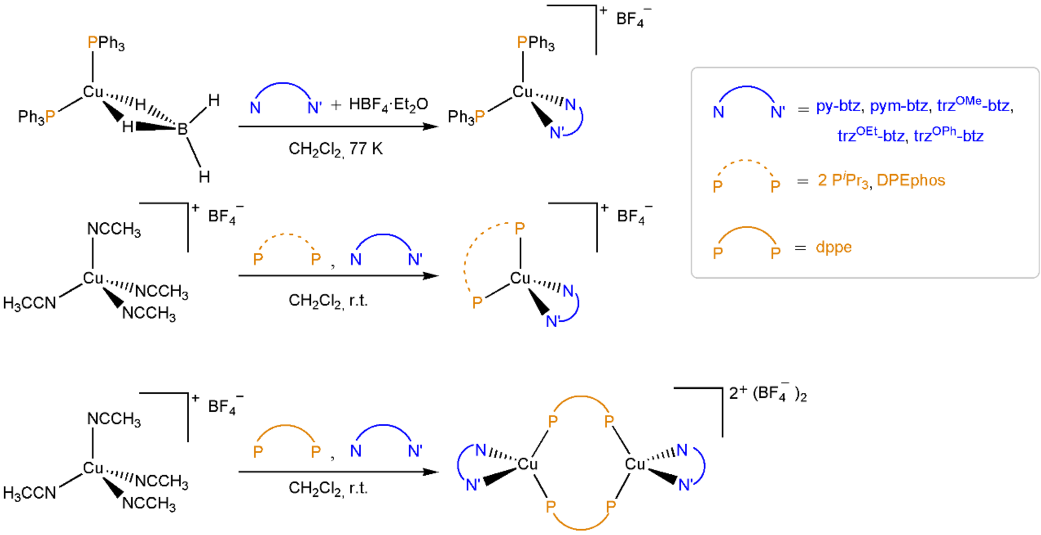

Scheme 32. Synthesis of heteroleptic copper(I) complexes.

In all the cases elemental analyses agree with the proposed formulae and conductivity measurements in acetone solutions indicate that the complexes behave as 1:1 electrolytes, with the exception of the dinuclear dppe derivatives (*vide infra*), acting as 1:2 electrolytes. The IR spectra confirmed the disappearances of both coordinated borohydride and acetonitrile. The observed bands are essentially ascribable to the stretching of coordinated N- and P-donor ligands and to the BF_4^- counterion (ν_{BF4} 1150-950 cm^{-1}).[156] The high frequency region of the ^1H NMR spectra shows, besides the signals related to aromatic phosphines and pyridine, pyrimidine or phenoxytriazine substituents, a set of resonances for the benzotriazole heterocycle. In the aliphatic region the P-bonded $-CH(CH_3)_2$ or $-CH_2CH_2-$ resonances are detectable for the complexes with P^iPr_3 and dppe as P-donors. The methoxy- and ethoxytriazinyl-benzotriazole derivatives show in some cases two distinct groups of resonances for the O-bonded substituents owing to the loss of chemical equivalence caused by coordination (see Figure 96). A single set was however observed at low temperature for selected complexes, depending upon the choice of the phosphine and the bulk of the alkoxy groups. In particular, two separate -OR were detected for the triphenylphosphine and dppe derivatives $[Cu(trz^{OR}\text{-}btz)(PPh_3)_2][BF_4]$ and $[Cu(trz^{OR}\text{-}btz)(\mu\text{–}dppe)]_2[BF_4]_2$ with R = Me or Et. On the other hand, in the ^1H NMR spectra of the triisopropylphosphine complexes $[Cu(trz^{OR}\text{-}btz)(P^iPr_3)_2][BF_4]$ only one set of resonances is present. Finally, the methoxy-substituted DPEphos complex $[Cu(trz^{OMe}\text{-}btz)(DPEphos)][BF_4]$ shows only one singlet for the two -OMe groups at 243 K, while two distinct -OEt fragments are recognizable in the ^1H NMR spectrum of the related ethoxy-substituted species $[Cu(trz^{OEt}\text{-}btz)(DPEphos)][BF_4]$ under the same experimental conditions. The effects of coordination on the chemical equivalence are present also for some pym-btz derivatives, in particular $[Cu(pym\text{-}btz)(\mu\text{–}dppe)]_2[BF_4]_2$ and $[Cu(pym\text{-}btz)(DPEphos)][BF_4]$.

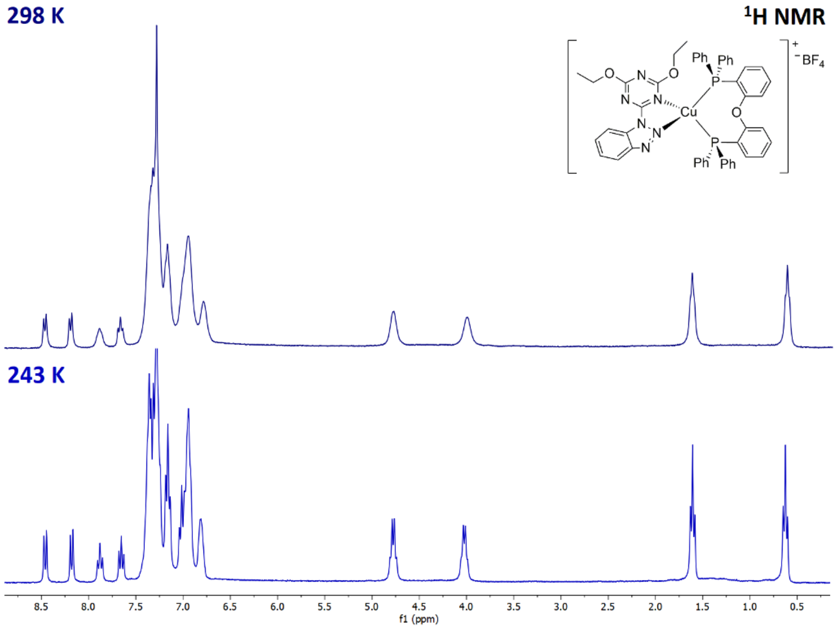

Figure 96. ^{1}H NMR spectra of [Cu(trz^{OEt}-btz)(DPEphos)][BF$_4$] in CDCl$_3$ at variable temperature (navy-blue line, 298 K; blue line, 243 K).

Crystals suitable for X-ray diffraction for the triphenylphosphine complexes [Cu(py-btz)(PPh$_3$)$_2$][BF$_4$] and [Cu(pym-btz)(PPh$_3$)$_2$][BF$_4$] were respectively isolated from dichloromethane/diethyl ether and dichloromethane/ethanol solutions. Both the complexes crystallize in the triclinic *P*-1 group. The structures of the two cations are shown in Figure 97. Crystal data and structure refinement are reported in Table A13 (see Table B13 for selected bond lengths and angles).

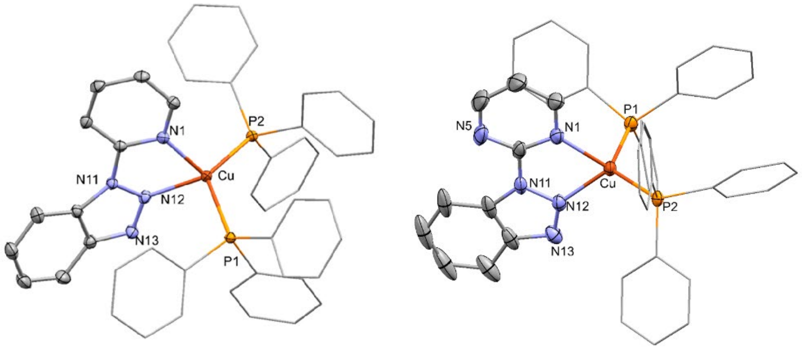

Figure 97. Ellipsoid plot of the cations [Cu(py-btz)(PPh$_3$)$_2$]$^+$ and [Cu(pym-btz)(PPh$_3$)$_2$]$^+$. Hydrogen atoms are omitted for clarity.

Crystal suitable for X-ray diffraction were isolated from dichloromethane/diethyl ether solutions also for [Cu(pym-btz)(P^{i}Pr$_3$)$_2$][BF$_4$], [Cu(pym-btz)(μ–dppe)]$_2$[BF$_4$]$_2$, [Cu(trz^{OMe}-btz)(P^{i}Pr$_3$)$_2$][BF$_4$] and [Cu(trz^{OPh}-btz)(DPEphos)][BF$_4$]. Except for the first complex that crystallizes in the orthorhombic *P*2$_1$2$_1$2$_1$ group, all the other complexes belong to the triclinic *P*-1 group. Instead, crystals for [Cu(py-btz)(DPEphos)][BF$_4$] and

[Cu(trz^{OEt}-btz)(DPEphos)][BF$_4$] were respectively collected from dichloromethane/ethanol and from the slow evaporation of dichloromethane solutions. These two complexes crystallize in the monoclinic groups, *C2/c* for the former (with two molecules in the asymmetric unit) and *P*2$_1$*/c* for the latter. The structures of the compounds are depicted in Figure 98. Crystal data and structure refinement are set out in Table A14-A16. Selected bond distances and angles are set out in Tables B14-B16.

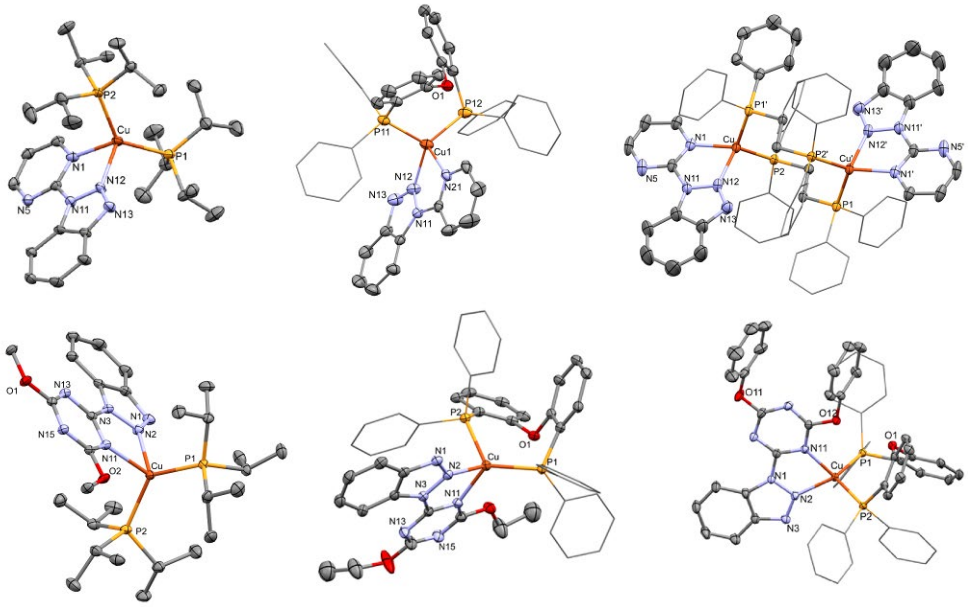

Figure 98. Ellipsoid plot of the cations [Cu(pym-btz)(P^{i}Pr$_3$)$_2$]$^+$, [Cu(py-btz)(DPEphos)]$^+$, [Cu(pym-btz)(μ–dppe)]$_2$$^{2+}$, [Cu(trz^{OMe}-btz)(P^{i}Pr$_3$)$_2$]$^+$ and [Cu(trz^{OR}-btz)(DPEphos)]$^+$ (R = Et or Ph). Hydrogen atoms are omitted for clarity.

The complexes exhibit absorptions below 500 nm in diluted dichloromethane solutions. The maximum molar extinction coefficients are comprised between 30000 and 60000 M^{-1}cm^{-1}. The tails in the visible range account for the yellow colour observed for concentrated solutions and powder samples. The comparison with the free ligands allows to point out that the absorption spectra are almost in part related to the $\pi^* \leftarrow \pi$ transitions of the aromatic fragments. In the case of aromatic phosphine derivatives, it is also possible to notice a band tentatively attributed to MLCT transitions around 400 nm. The same band is present, but with much lower extinction coefficient, also for the triisopropylphosphine complexes, as observable in the superimposition of the UV-VIS spectra of complexes with pym-btz reported in Figure 99.

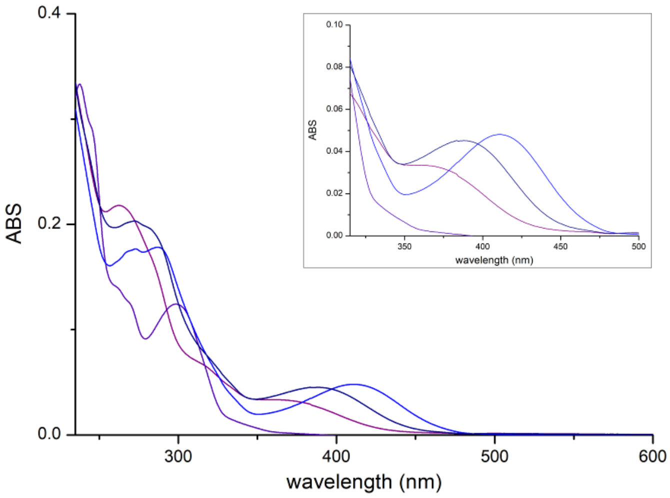

Figure 99. Absorption spectra of complexes 10^{-5} M in CH_2Cl_2. $[Cu(pym\text{-}btz)(PPh_3)_2][BF_4]$, purple line; $[Cu(pym\text{-}btz)(P^{i}Pr_3)_2][BF_4]$, violet line; $[Cu(pym\text{-}btz)(\mu\text{–}dppe)]_2[BF_4]_2$, navy blue line; $[Cu(pym\text{-}btz)(DPEphos)][BF_4]$, blue line).

DFT calculations on $[Cu(py\text{-}btz)(PPh_3)_2]^+$ and $[Cu(trz^{OEt}\text{-}btz)(DPEphos)]^+$ as representative compounds confirmed the MLCT nature of the lowest energy absorption. The computed ground-state stationary points are in good agreement with the X-ray data (RMSD of 0.353 Å and 0.480 Å for $[Cu(py\text{-}btz)(PPh_3)_2]^+$ and $[Cu(trz^{OEt}\text{-}btz)(DPEphos)]^+$, respectively) and the computed wavelength of the lowest energy singlet ← singlet transitions are in line with the absorption spectra (341 nm for $[Cu(py\text{-}btz)(PPh_3)_2]^+$ and 376 nm for $[Cu(trz^{OEt}\text{-}btz)(DPEphos)]^+$). The hole and electron distributions associated to the singlet-singlet transition, depicted in Figure 100, clearly indicate that the electron moves from an occupied orbital centred on the $\{CuP_2\}$ fragment to an unoccupied π^* orbital localized on the N-donor heterocycle. In both the cases the absorption is related to a transition involving the frontier orbitals, and the computed distance between the centres of hole and electron distributions is around 2.9 Å.

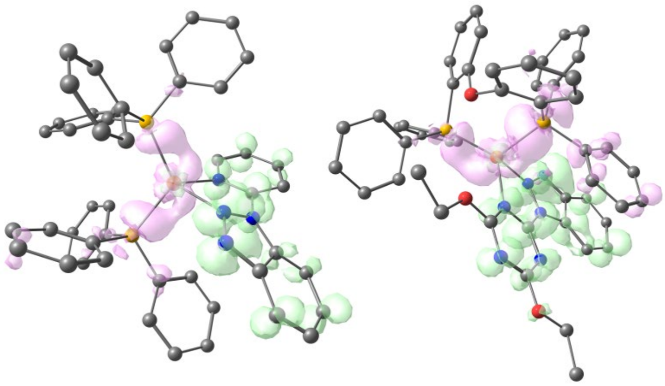

Figure 100. DFT-optimized structures of $[Cu(py\text{-}btz)(PPh_3)_2]^+$ and $[Cu(trz^{OEt}\text{-}btz)(DPEphos)]^+$ (ground singlet states) with hole (pink) and electron (green) distributions related to the lowest energy singlet-singlet transitions (surface isovalue = 0.003 a.u.). MN15/def2-SVP calculations. Colour map: Cu, orange; P, yellowish orange; O, red; N, blue; C; grey. Hydrogen atoms are omitted for clarity.

Electrochemical measurements on $[Cu(py\text{-}btz)(PPh_3)_2][BF_4]$ and $[Cu(trz^{OEt}\text{-}btz)(DPEphos)][BF_4]$ and on the free py-btz and trz^{OEt}-btz ligands show irreversible processes related to the oxidation of the $\{CuP_2\}$ fragment starting around 0.75 V *vs* Fc/Fc^+ (see Figure 101). Several other oxidation processes occur at higher potential, closely comparable to those observed for the free N-donor ligands. The first reduction process is observable for potentials lower than -1.75 V in the case of $[Cu(py\text{-}btz)(PPh_3)_2][BF_4]$ and lower than -1.65 V for $[Cu(trz^{OEt}\text{-}btz)(DPEphos)][BF_4]$. The reduction processes of the free ligands start at lower potentials, in particular in the case of py-btz. This outcome can be ascribed to the σ-donation of electron density to the copper(I) centre, that makes the N-donor heterocycles more electron deficient and therefore more oxidant. The reduction processes are in all the cases irreversible. The potential gap between first oxidation and first reduction is in the 2.6-3.1 V range for $[Cu(py\text{-}btz)(PPh_3)_2][BF_4]$, while it is slightly lower for $[Cu(trz^{OEt}\text{-}btz)(DPEphos)][BF_4]$ (2.4-2.8 V range). Such a result is perfectly in line with the onsets of the MLCT absorptions, about 400 nm for $[Cu(py\text{-}btz)(PPh_3)_2][BF_4]$ and 450 nm for $[Cu(trz^{OEt}\text{-}btz)(DPEphos)][BF_4]$ (see Figure 99).

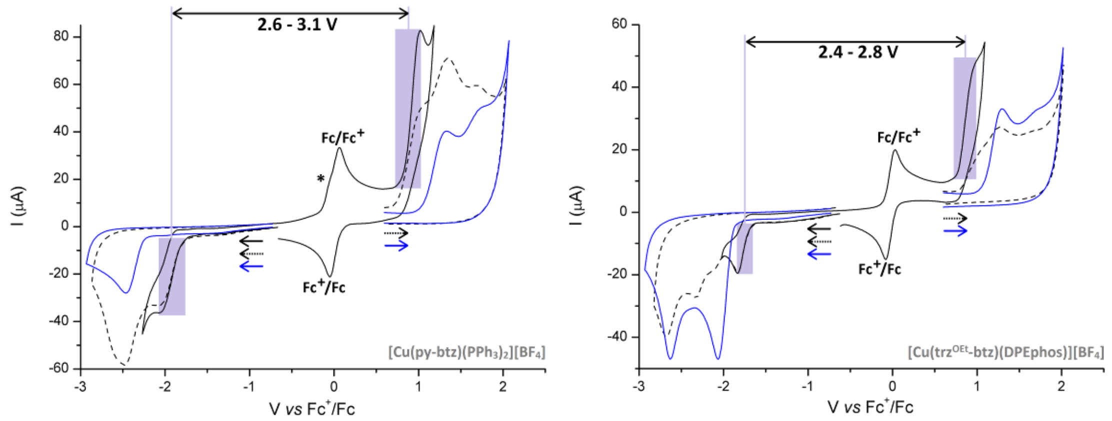

Figure 101. Cyclic voltammetries of $[Cu(py\text{-}btz)(PPh_3)_2][BF_4]$ and $[Cu(trz^{OEt}\text{-}btz)(DPEphos)][BF_4]$ (from the first reduction to the first oxidation, continuous black lines; extended cathodic and anodic scans, dashed black lines) and of py-btz and trz^{OEt}-btz (continuous blue lines). Glassy carbon electrode, acetone/$LiClO_4$, 500 mV s^{-1}, ferrocene as internal standard, r.t., Ar atmosphere. The * symbol highlights the reverse oxidation process related to the first reduction of $[Cu(py\text{-}btz)(PPh_3)_2][BF_4]$.

Excitation of powder samples with near-UV and violet light affords emissions centred between 540 and 640 nm. The normalized PL and PLE spectra are shown in Figure 102. On comparing complexes with the same N-donor chelate, the emission maxima fall at longer wavelengths when P^iPr_3 is used as P-donor ligand. The choice of the N-donor ligands also influences the emission maximum, with longer wavelengths generally observed for the trz^{OPh}-btz derivatives.

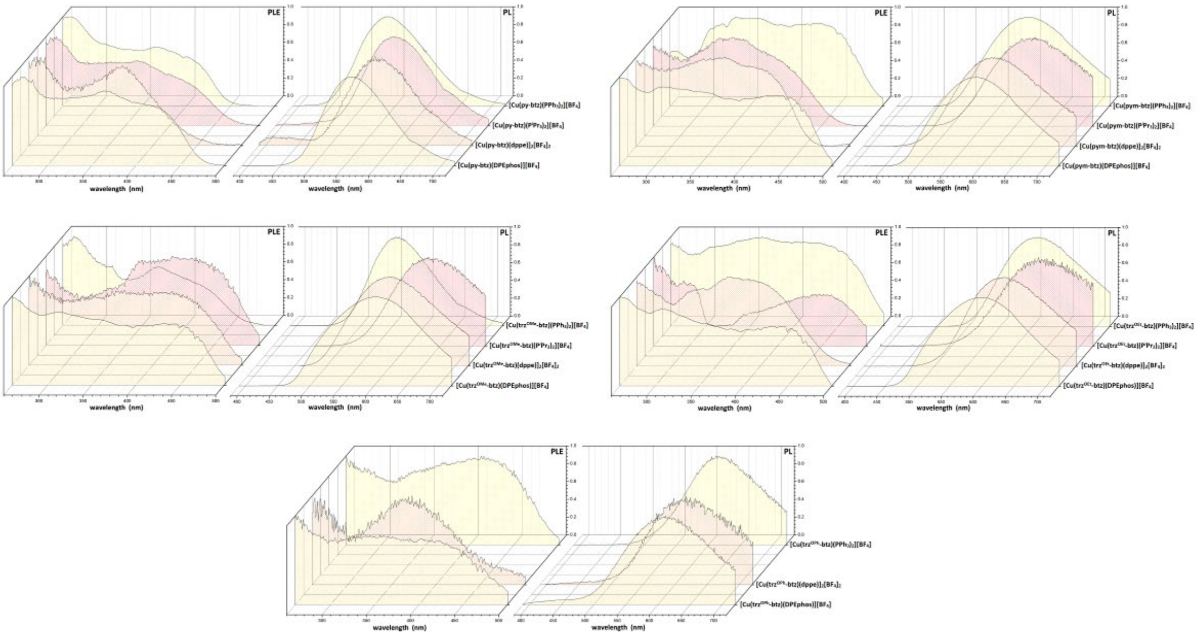

Figure 102. Normalized PL and PLE spectra of the complexes (solid state, r.t.).

Despite the roughly comparable PL and PLE spectra, the photoluminescence quantum yield values (Φ) are markedly different. Weaker emissions were generally observed for the mononuclear P^iPr_3 complexes and the dinuclear dppe derivatives. The flexibility of the isopropyl substituents and of the ethylene bridges probably favours non-radiative decay routes. Moreover, in the P^iPr_3 derivatives there is no possibility of extra-stabilization offered by π-π stacking with the N-donor chelates, differently from the other complexes here considered. For what concerns the N-donor ligands, the worst results were achieved using trz^{OPh}-btz and trz^{OMe}-btz. On the other hand, higher Φ values were surprisingly measured using the comparable trz^{OEt}-btz ligand. The quantum yield values do not however show any evident trend related to the choice of the P- or N-donor ligands. For instance, higher Φ was obtained with py-btz in combination with PPh_3 with respect to DPEphos, while the related pym-btz complex $[Cu(pym\text{-}btz)(PPh_3)_2][BF_4]$ and $[Cu(py\text{-}btz)(DPEphos)][BF_4]$ have very similar quantum yields. The measured Φ for $[Cu(trz^{OEt}\text{-}btz)(PPh_3)_2][BF_4]$ is 17%, while the value rises up to the astonishing value of 92% by replacing the two triphenylphosphine ligands with DPEphos. It is to conclude that the combined electronic and steric features of the coordinated ligands play a hardly predictable role on the stabilization of ground and excited states.

The Stokes shifts around 200 nm and the wide emissions (FWHM between 3500 and 5000 cm^{-1}) suggest that triplet excited states are involved in the luminescence. Such an outcome is confirmed by luminescent lifetimes τ in the microseconds range. The measured τ values depend upon copper(I) coordination sphere, but there is no linear correlation with the photoluminescence quantum yields. For instance, the longest τ, 164 μs, is that of complex $[Cu(py\text{-}btz)(PPh_3)_2][BF_4]$, having Φ equal to 26%, while for the most efficient $[Cu(trz^{OEt}\text{-}btz)(DPEphos)][BF_4]$ complex the τ value is 43 μs (see Figure 103 for the luminescence decay curves). The radiative (k_r) and non-radiative (k_{nr}) constants for $[Cu(trz^{OEt}\text{-}btz)(DPEphos)][BF_4]$, estimated on the basis of the equation $\Phi = k_r/(k_r + k_{nr}) = \tau\ k_r$ are $k_r = 2.1 \cdot 10^4\ s^{-1}$ and $k_{nr} = 1.8 \cdot 10^3\ s^{-1}$. For comparison, the same constants for $[Cu(py\text{-}btz)(PPh_3)_2][BF_4]$ are $k_r = 1.6 \cdot 10^3\ s^{-1}$ and $k_{nr} = 4.6 \cdot 10^3\ s^{-1}$.[172]

The computationally optimized structures of $[Cu(py\text{-}btz)(PPh_3)_2]^+$ and $[Cu(trz^{OEt}\text{-}btz)(DPEphos)]^+$ in triplet state and depicted in Figure 103 are comparable to the relative singlet ground states (RMSD of 0.563 Å for $[Cu(py\text{-}btz)(PPh_3)_2]^+$ and 0.525 Å for $[Cu(trz^{OEt}\text{-}btz)(DPEphos)]^+$). The analysis of the hole and electron distributions related to the lowest energy triplet-singlet transitions gives a picture in line with the previously discussed MLCT absorptions, with the electron moving from a π* orbital localized on the N-donor heterocycle to the {CuP_2} fragment.

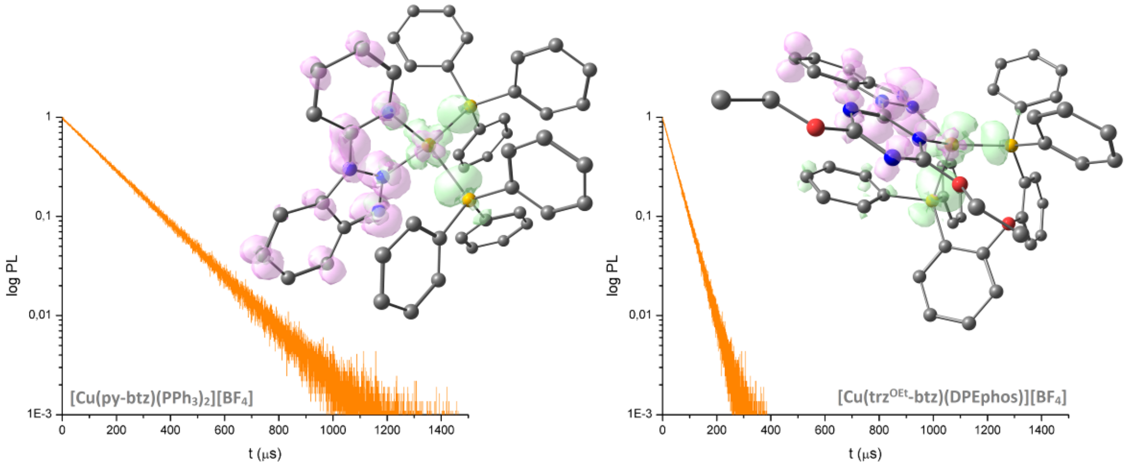

Figure 103. Luminescence decay curves of [Cu(py-btz)(PPh_3)$_2$][BF_4] and [Cu(trz^{OEt}-btz)(DPEphos)][BF_4] and DFT-optimized structures of [Cu(py-btz)(PPh_3)$_2$]$^+$ and [Cu(trz^{OEt}-btz)(DPEphos)]$^+$ (triplet states) with hole (pink) and electron (green) distributions related to the lowest energy triplet-singlet transitions (surface isovalue = 0.003 a.u.). MN15/def2-SVP calculations. Colour map: Cu, orange; P, yellowish orange; O, red; N, blue; C; grey. Hydrogen atoms are omitted for clarity.

On the basis of experimental and computational outcomes the emissions are therefore attributed to ^{3}MLCT transitions. The computed energy gaps between singlet and triplet MLCT states are respectively 4360 and 4000 cm^{-1} for [Cu(py-btz)(PPh_3)$_2$]$^+$, and 3130 and 2750 cm^{-1} [Cu(trz^{OEt}-btz)(DPEphos)]$^+$. These values do not support the possibility of TADF mechanism, usually invoked for energy gaps below 1000 cm^{-1}.[69]

The same bidentate N-donors, *i.e.* py-btz and trz^{OR}-btz (R = Et, Ph) were exploited for the preparation of homoleptic copper(I) complexes. In the case of pym-btz and trz^{OMe}-btz coordination polymers were probably isolated, and their insolubility in common organic solvents prevented the full characterization. The ^{1}H NMR spectra of [Cu(py-btz)$_2$][BF_4] and [Cu(trz^{OEt}-btz)$_2$][BF_4] in $CDCl_3$ are collected in Figure 104. It is worth noting that differently from [Cu(py-btz)$_2$][BF_4], the complexes derived from trz^{OR}-btz (R = Et, Ph) exhibit fluxional behaviour from 298 to 213 K. In the case of [Cu(trz^{OEt}-btz)$_2$][BF_4], recording the ^{1}H NMR spectrum at 323 K allowed to detected the multiplicity of the signals. Differently from the heteroleptic complex, only one quartet and one triplet are observable for the ethoxy chains. Instead, for [Cu(trz^{OPh}-btz)$_2$][BF_4] the signals are extremely broad and they are not separable also on heating the sample.

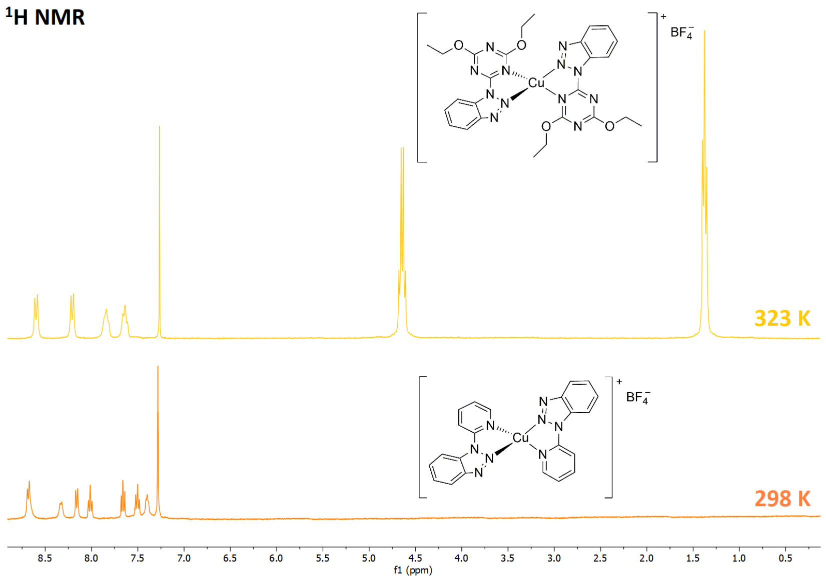

Figure 104. ^{1}H NMR spectra of [Cu(py-btz)$_2$][BF$_4$] (orange line, CDCl$_3$, 298 K) and [Cu(trz^{OEt}-btz)$_2$][BF$_4$] (yellow line, CDCl$_3$, 323 K).

The complexes do not exhibit luminescent properties neither at the solid state nor in solution. Instead, they are intensely yellow or orange coloured both as powder samples and in concentrated solutions due to the MLCT band observable between 400 and 500 nm (see Figure 105). The other bands are attributable to $\pi^* \leftarrow \pi$ transitions of the coordinated N-donors. As it is clearly noticeable in Figure 105, the absorption at longer wavelengths appears to be much more intense for the [Cu(trz^{OPh}-btz)$_2$][BF$_4$] derivative.

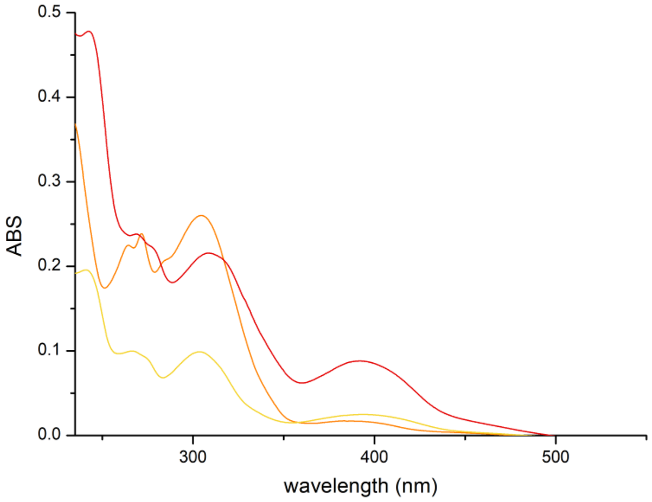

Figure 105. UV-VIS spectra of the homoleptic complexes (10^{-5} M CH$_2$Cl$_2$ solution, r.t.). [Cu(py-btz)$_2$][BF$_4$], orange line; [Cu(trz^{OEt}-btz)$_2$][BF$_4$], yellow line; [Cu(trz^{OPh}-btz)$_2$][BF$_4$], red line.

As highlighted in the previous pages, small modifications on the skeleton of the ligands determined noticeable variations in the photoluminescent properties, also because of the usual localization of the LUMO on the coordinated ligands. It is widely recognized that the presence of a sulphur atom in the ligands skeleton determined enhanced photophysical properties and electric conductivity in the corresponding copper(I) derivatives.[175f,176] Both these aspects are extremely important for the application in OLED technology. Following these considerations, I decided to study 2,1,3-benzothiadiazole (BTD) for the synthesis of luminescent copper(I) derivatives. Thanks to its well-known photophysical properties, BTD is widely applied for the preparation of polymers and liquid crystals to be exploited for advanced applications, such as OLEDs, dyes, solar and photovoltaic cells.[177] The investigation began using borohydrides as precursors following the conditions previously described (see Scheme 33), and three-coordinated species were isolated also using two equivalents of BTD. Instead, when $[Cu(NCCH_3)_4][BF_4]$ was used as precursor one acetonitrile molecule remained in copper(I) coordination sphere, as observable in Scheme 33. In the case of $[Cu_2(BTD)(CH_3CN)(\mu\text{–}dppm)_2][BF_4]_2$ this product was isolated also working in excess of BTD. To avoid the presence of the coordinated acetonitrile, CuCl was exploited. The addition of the chosen phosphine to a mixture of CuCl in dichloromethane determined its solubilization. BTD was then added in presence of silver(I) perchlorate and the by-product AgCl was filtered off, affording the complexes depicted in Scheme 33. In all the cases mono- or bi-cationic complexes were isolated, as supported by conductivity measurements in acetone.

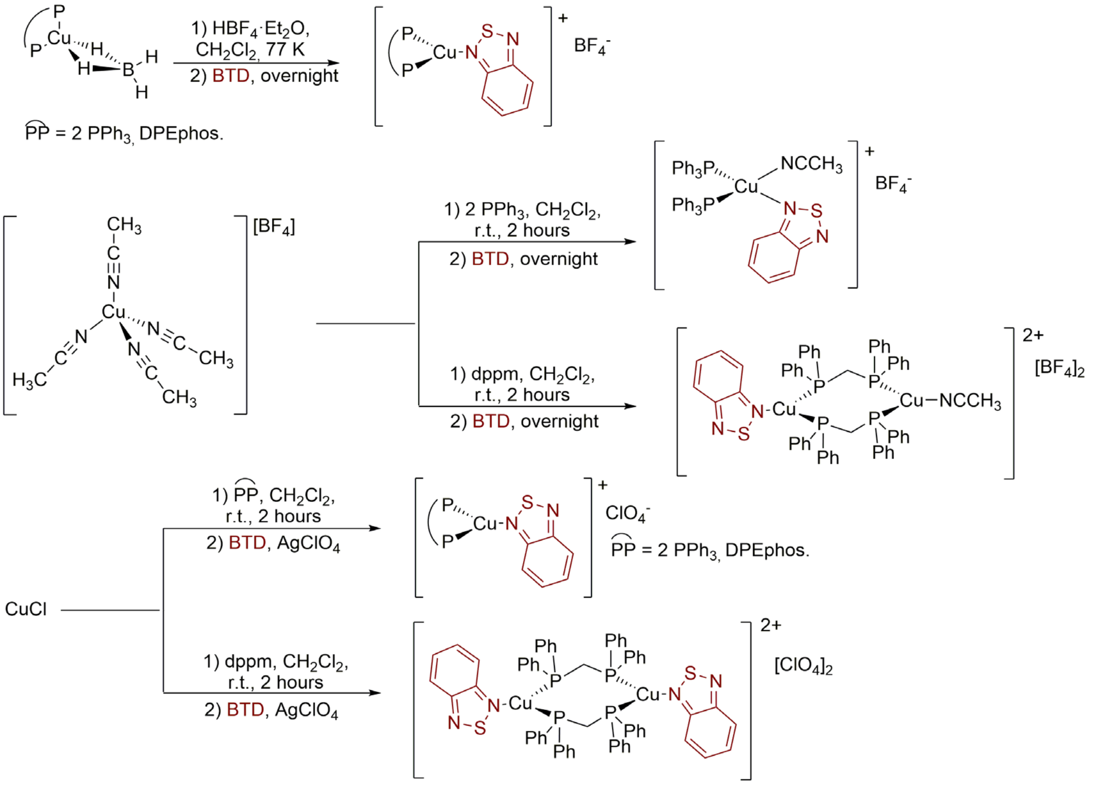

Scheme 33. Synthesis of heteroleptic BTD copper(I) complexes.

The proposed formulae are further confirmed by the IR spectra, where the stretchings of C-H and aromatic C-C- and C-N can be detected. For the complexes [Cu(BTD)(PP)][BF_4] (PP = 2 PPh_3, DPEphos) obtained from borohydride precursors, no evidence of coordinated B-H bonds could be noticed. The stretchings of the BF_4^- and ClO_4^- counterions are observable in the 1100-990 cm^{-1} range. Instead, for the heteroleptic copper(I) complexes containing a coordinated acetonitrile molecule a weak band around 2300 cm^{-1} can be detected for [Cu_2(BTD)(CH_3CN)(μ–dppm)$_2$][BF_4]$_2$.

The ^1H NMR spectra are characterized by two sets of signals attributable to the coordinated BTD, superimposed to that of the phosphines. Only in the case of complexes containing dppm or acetonitrile, signals can be detected also at high fields. The multiplicity of the signals can often be observed only recording the NMR spectra at low temperature due to the fluxionality of both N- and P-donors. For the same reason, broad signals are noticeable in the $^{31}P\{^1H\}$ NMR spectra. The ^1H NMR spectra of the triphenylphosphine derivatives [Cu(BTD)($NCCH_3$)(PPh_3)$_2$][BF_4] and [Cu(BTD)(PPh_3)$_2$][BF_4] are reported in Figure 106 for comparison. It is clearly observable for the second species the presence of a singlet integrating three protons related to the coordinated acetonitrile around 2.55 ppm.

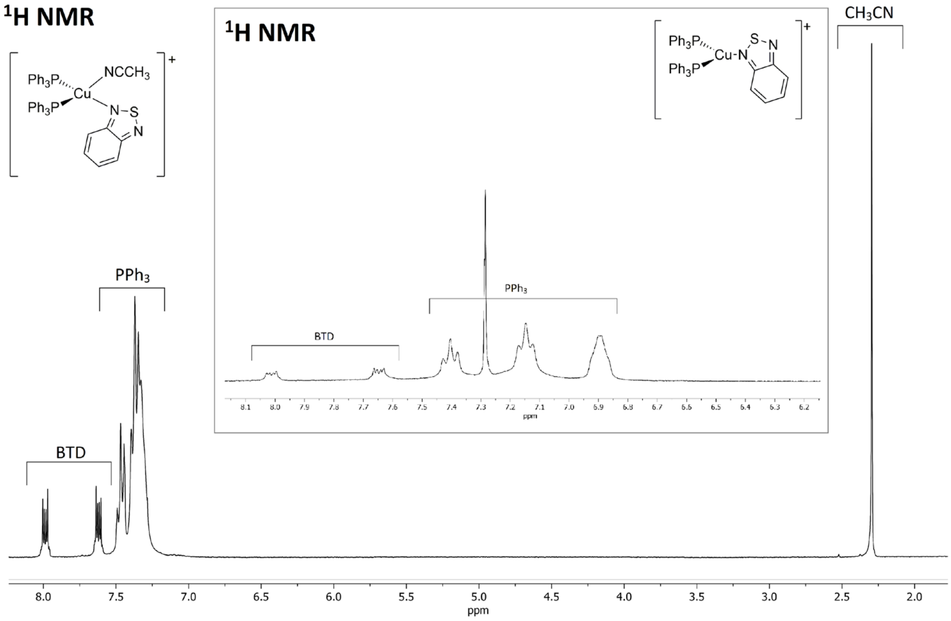

Figure 106. ^1H NMR spectrum of [Cu(BTD)($NCCH_3$)(PPh_3)$_2$][BF_4] in $CDCl_3$ at 298 K. Inset: ^1H NMR spectrum of [Cu(BTD)(PPh_3)$_2$][BF_4] in $CDCl_3$ at 213 K.

The structure of [Cu(BTD)(PPh_3)$_2$][X] where X^- is BF_4^- and ClO_4^- together with [Cu_2(BTD)(CH_3CN)(μ–dppm)$_2$][BF_4]$_2$ was ascertained by means of X-ray diffraction.

Suitable crystals were isolated from dichloromethane/diethyl ether or from the slow evaporation of diethyl ether solutions. All the three complexes crystallized in the monoclinic $P2_1/n$ space group and are depicted in Figure 107. Crystal data and structure refinement are collected in Table A17-A18. Selected bond distances and angles are set out in Tables B17-B18. The two triphenylphosphine derivatives appear to be tetracoordinated at the solid state because the counterions are directly bonded to the metal centre through a fluorine or an oxygen atom.

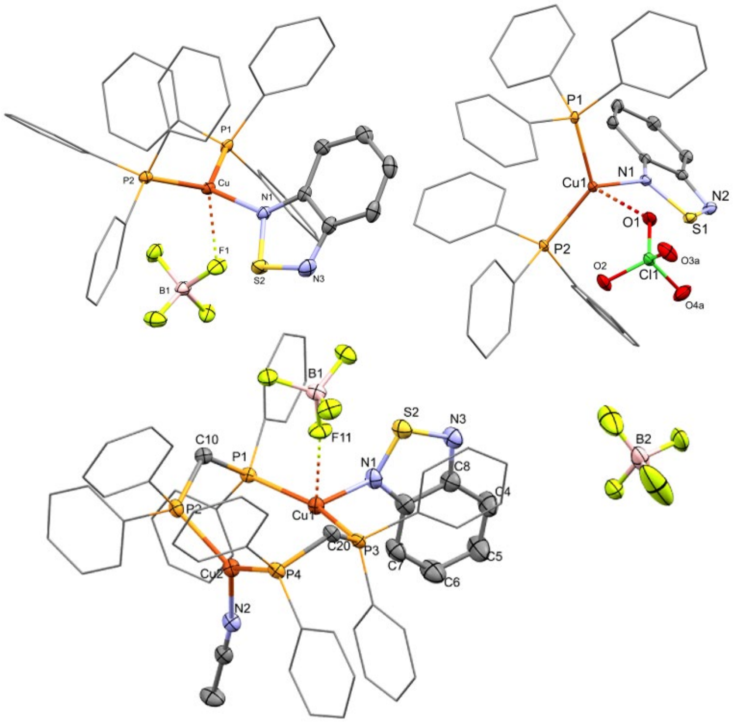

Figure 107. Plot of $[Cu(BTD)(PPh_3)_2][X]$ [X = BF_4, ClO_4] and $[Cu_2(BTD)(CH_3CN)(\mu\text{–}dppm)_2][BF_4]_2$. Hydrogen atoms are omitted for clarity.

The nature on the bond between copper(I) and BF_4^- or ClO_4^- was investigated by means of DFT calculations, carried out both in gas phase and considering dichloromethane as continuous medium. The AIM analysis revealed in the case of $[Cu(BTD)(PPh_3)_2][BF_4]$ the presence of two (3,-1) bond critical points (b.c.p.) between the metal centre and two fluorine atoms of the counter-anion (see Figure 108). Selected computed properties at b.c.p. are reported in Table 1. The electron density (ρ) and potential energy density (V) values indicate that the two Cu---F interactions have different strength, and they become weaker by introducing the implicit solvent. The energy density (E) and Laplacian of electron density ($\nabla^2\rho$) values give information about the nature of the interactions. In particular, the negative sign of E and the positive value of $\nabla^2\rho$ are in agreement with Bianchi's definition of dative bond.[178] The AIM analyses revealed a quite different interaction with the counter-anion in the case of $[Cu(BTD)(PPh_3)_2][ClO_4]$. In fact, only one Cu---O (3,-1) b.c.p. was localized (see Figure 108), and the positive values of both E and $\nabla^2\rho$ collected in Table 1 are in line with an electrostatic interaction.

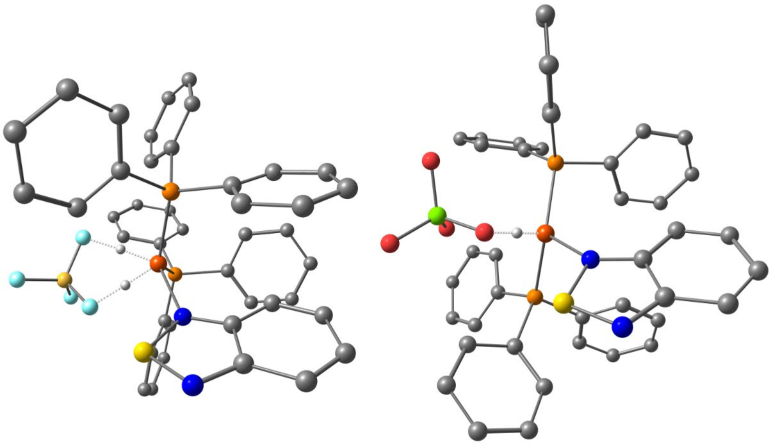

Figure 108. DFT-optimized structure of $[Cu(BTD)(PPh_3)_2][X]$ [X = BF_4, ClO_4]. Colour map: Cu, orange; P, yellowish orange; O, red; N, blue; S, yellow; C, grey; Cl, green; B, yellow; F, turquoise. MN15/def2-SVP calculations. Selected (3,-1) b.c.p. are shown in light grey. Hydrogen atoms are omitted for clarity.

Table 1. Selected computed properties (a.u.) computed at Cu---F and Cu---O (3,-1) b.c.p. for $[Cu(BTD)(PPh_3)_2][BF_4]$ and $[Cu(BTD)(PPh_3)_2][ClO_4]$.

Complex	**Cu---F [Å]**	ρ	**V**	**E**	**$\nabla^2\rho$**
$[Cu(BTD)(PPh_3)_2][BF_4]$	2.441	0.026	-0.031	-0.005	0.087
	2.275	0.035	-0.044	-0.002	0.159
$[Cu(BTD)(PPh_3)_2][BF_4]$ in CH_2Cl_2	2.518	0.022	-0.026	-0.004	0.069
	2.345	0.030	-0.037	-0.003	0.122

Complex	**Cu---O [Å]**	ρ	**V**	**E**	**$\nabla^2\rho$**
$[Cu(BTD)(PPh_3)_2][ClO_4]$	2.162	0.050	-0.064	0.036	0.286
$[Cu(BTD)(PPh_3)_2][ClO_4]$ in CH_2Cl_2	2.194	0.046	-0.058	0.029	0.253

As observable in Figure 109a, the complexes are characterized by absorptions for wavelengths below 400 nm in diluted CH_2Cl_2 solutions. Although the complexes are yellow or orange powders at the solid state, once dissolved in common organic solvents the colour disappears and no tail in the visible range attributable to MLCT transitions is observable even for concentrated solutions. The absorption spectra are almost in part related to the $\pi^* \leftarrow \pi$ transitions of the aromatic fragments. The extension of the absorption range associated to the expected MLCT bands can be detected at the solid state, with MLCT transitions centred around 460 nm, as observable in Figure 109b.

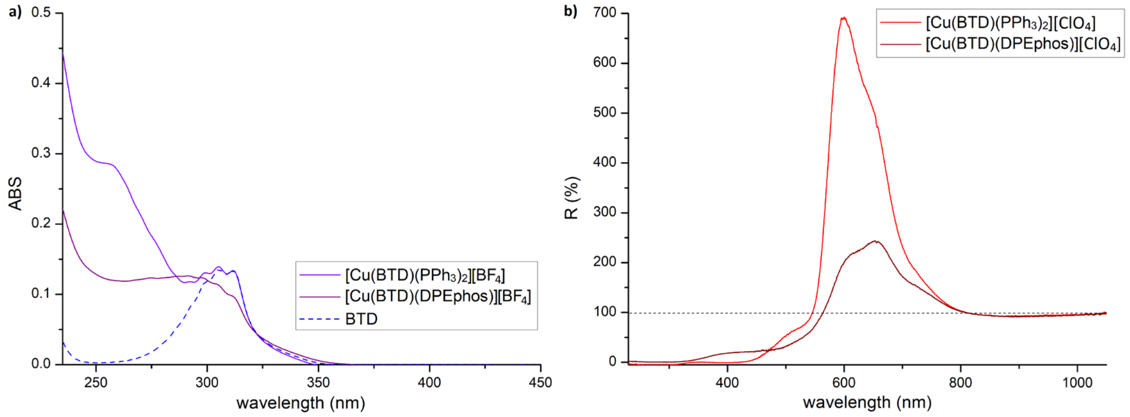

Figure 109. a) UV-VIS spectra of BTD (dashed blue line), [Cu(BTD)(PPh$_3$)$_2$][BF$_4$] (violet line) and [Cu(BTD)(DPEphos)][BF$_4$] (purple line) 10^{-5} M in CH_2Cl_2. b) Reflectance spectra of solid [Cu(BTD)(PPh$_3$)$_2$][ClO$_4$] (red line) and [Cu(BTD)(DPEphos)][ClO$_4$] (wine red line) at room temperature.

Electrochemical measurements were conducted on free BTD, [Cu(BTD)(PPh$_3$)$_2$][ClO$_4$] and [Cu(BTD)(DPEphos)][ClO$_4$] in acetone solutions with lithium perchlorate as supporting electrolyte. Figure 110a highlights two irreversible oxidation processes for the free ligands occurring respectively around 1.23 and 1.67 V *vs* Fc/Fc$^+$. The corresponding reduction peaks can be detected around -1.92 and -2.21 V *vs* Fc/Fc$^+$. The same processes can be observed also for [Cu(BTD)(PPh$_3$)$_2$][ClO$_4$] and [Cu(BTD)(DPEphos)][ClO$_4$] together with the oxidation of the {CuP$_2$} fragment around 0.80 V *vs* Fc/Fc$^+$ (see Figure 110b). The first reduction process is observable for potentials lower than -1.64 V in the case of [Cu(BTD)(PPh$_3$)$_2$][ClO$_4$] and lower than -1.50 V for [Cu(BTD)(DPEphos)][ClO$_4$].

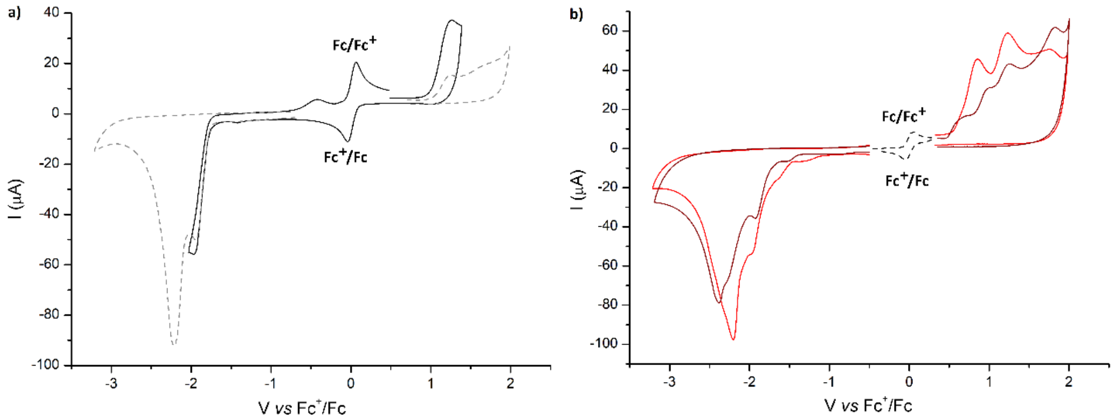

Figure 110. Cyclic voltammetries of: a) free BTD (black line; extended oxidation and reduction processes, dashed grey line) and b) [Cu(BTD)(PPh$_3$)$_2$][ClO$_4$] (red line) and [Cu(BTD)(DPEphos)][ClO$_4$]

(wine red line). Glassy carbon electrode, acetone/$LiClO_4$, 250 mV s^{-1}, ferrocene (Fc) as internal standard, r.t., Ar atmosphere.

Excitation of powder samples with near-UV and violet-blue light affords intense red emissions centred between 620 and 685 nm. The luminescence is not maintained in solution. It is worth mentioning that luminescent trigonal planar copper(I) derivatives are quite rare in literature.[179] Normalized PL and PLE spectra of the perchlorate copper(I) complexes are shown in Figure 111. Passing from triphenylphosphine to DPEphos and dppm the PL and PLE spectra appear to be red shifted, with consequent reduction of photoluminescent quantum yield due to the energy gap law, *i.e.* the increase of k_{nr} related to the vibrational coupling.[180] The emission maximum of the complex $[Cu_2(BTD)(CH_3CN)(\mu\text{–dppm})_2][BF_4]_2$ is instead blue-shifted with respect to $[Cu(BTD)(PPh_3)_2][X]$ (X = BF_4, ClO_4). The photoluminescent quantum yields Φ of the copper(I) BTD complexes are comprised between 10 and 46%, and the highest value was measured for $[Cu(BTD)(PPh_3)_2][BF_4]$. The different Φ values among the complexes here reported are difficult to rationalise, since they depend upon several factors, such as the coordination number, the steric bulk of the phosphines, the P-Cu-P angles, and the nature of the counter-anion. Moreover, it is likely to suppose that π-π stacking interaction could play a stabilizing role at the solid state.

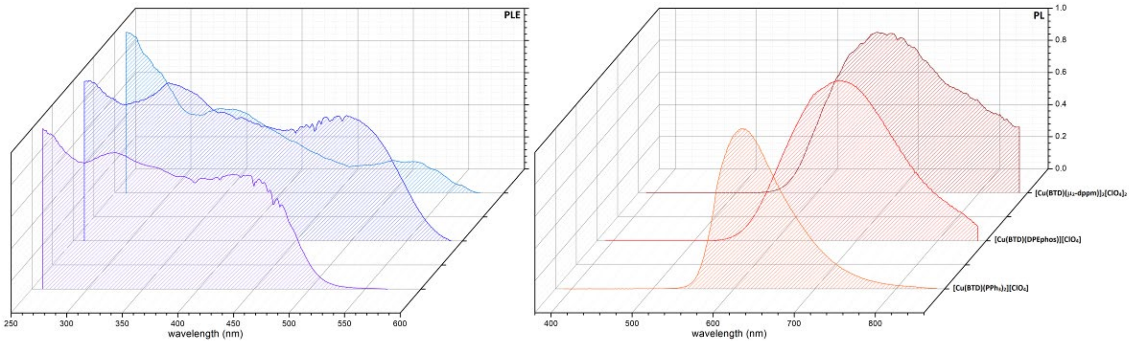

Figure 111. Normalized PL and PLE spectra of perchlorate copper(I) BTD complexes. Powder samples, r.t. $\lambda_{excitation}$ = 350 nm; $\lambda_{emission}$ = 630 nm.

The Stokes shifts around 200 nm and the wide emissions with FWHM between 3000 and 4000 cm^{-1} suggest the involvement of triplet excited states in the emission. This hypothesis is supported by the luminescent lifetimes τ, that are in the micro- and millisecond ranges. Lifetimes in the milliseconds long were reported only in few cases for copper(I) complexes at room temperature.[181] It is worth noting that in this family of compounds the DPEphos derivatives are characterized by shorter lifetimes if compared to triphenylphosphine and dppm complexes. The direct coordination of the counterion to copper(I) metal centres has repercussions on the τ values that are around 15% longer for perchlorates with respect to tetrafluoroborate salts, as highlighted in Figure 112.

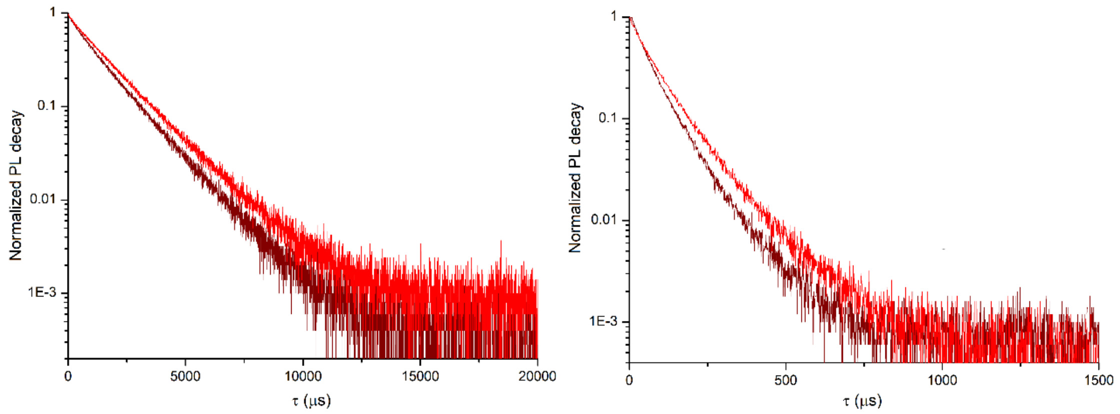

Figure 112. Semi-log plot of luminescence decay curves of $[Cu(BTD)(PPh_3)_2][X]$ and $[Cu(BTD)(DPEphos)][X]$, X = BF_4 (wine red line), ClO_4 (red line). Solid samples, r.t., $\lambda_{excitation}$ = 290 nm; $\lambda_{emission}$ = 640-670 nm.

It is worth mentioning that the photophysical properties of low-coordinated copper(I), silver(I) and gold(I) metal complexes are very sensitive to subtle anion contacts because of the resulting structural distortions both at the ground and at the excited state.[182] TD-DFT calculations were conducted on $[Cu(BTD)(PPh_3)_2][X]$ and $[Cu(BTD)(DPEphos)][X]$ (X = BF_4, ClO_4). The hole and electron distributions associated to the singlet-singlet transition, depicted in Figure 113, clearly indicate that the absorption has MLCT nature, with the electron moves from an occupied orbital centred on the metal centre and on the P-donors to an unoccupied π* orbital localized on the BTD ligand. On the other hand, it is likely to suppose that the emission is a mixed ^{3}MLCT/^{3}LLCT since the electron is moving from a π* orbital localized on the N-donor heterocycle to the $\{CuP_2\}$ fragment but with a non-negligible contribution of the BTD orbitals. Despite the noticeable differences in the lifetime for the DPEphos derivatives, the same mechanism can be proposed on the basis of TD-DFT calculations, and its reduction can be tentatively attributed to the increased k_{nr}, as previously stated. The better photophysical properties of $[Cu(BTD)(PPh_3)_2][X]$ with respect to $[Cu(BTD)(DPEphos)][X]$ can be also tentatively ascribed to the larger P-Cu-P angle, around 130°, greater than what previously observed for similar compounds. This structural parameter has effects on the energy of HOMO and on the HOMO-LUMO gap, as previously observed for similar complexes.[183]

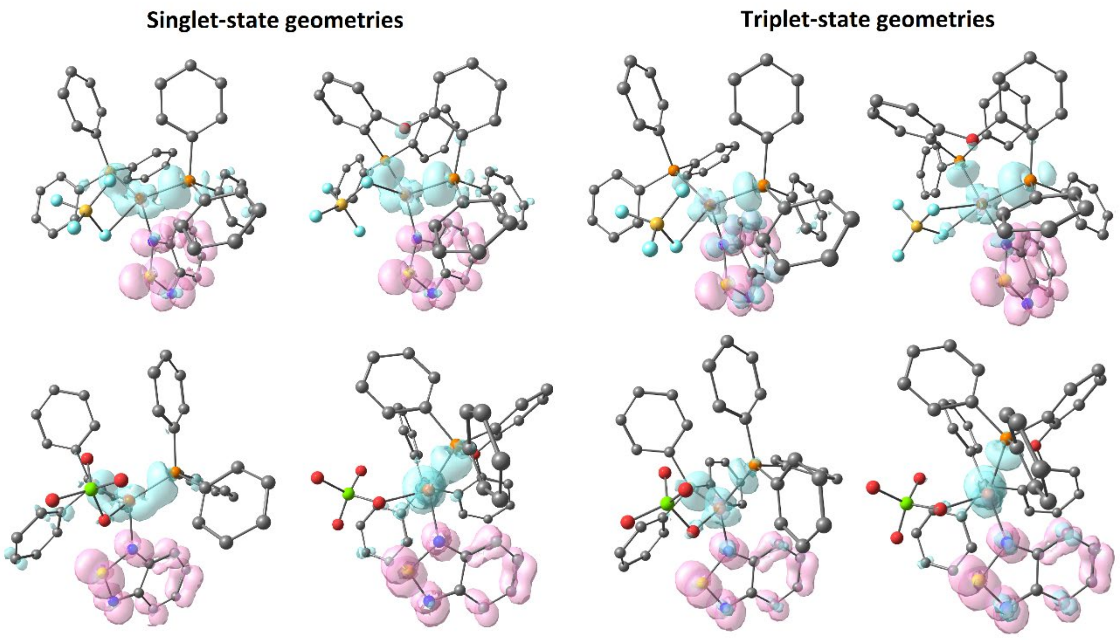

Figure 113. DFT-optimized structures (ground singlet and excited triplet state) of [Cu(BTD)(PPh$_3$)$_2$][X] and [Cu(BTD)(DPEphos)][X] (X = BF$_4$, ClO$_4$) with hole (turquoise) and electron (pink) distribution related to the lowest energy singlet-singlet (singlet state geometries) and singlet-triplet transitions (triplet state geometries). Surface isovalue = 0.003 a.u., MN15/def2-SVP calculations. Colour map: Cu, orange; P, yellowish orange; O, red; N, blue; S, yellow; C, grey; Cl, green, B, yellow, F, turquoise. Hydrogen atoms are omitted for clarity.

To conclude, due to the extremely long lifetimes and the excitation spectra, these complexes could be suitable candidates to be used as photocatalysts. It is worth noting that, besides OLEDs, red-and NIR-emitting complexes are interesting to be applied for security applications, biological therapy, phototherapy and photodynamic therapy.[184]

3.3 Luminescent zinc(II) complexes

Most of the luminescent zinc(II) complexes reported in literature have N- and O-donors derived from phenate moieties as ligands. The investigation on [O=P]-donor species is limited to the use of triphenylphosphine oxide,[99a-c,185] but no luminescent study on the corresponding zinc(II) complexes was ever described. It is however worth noting that [ZnCl$_2$(O=PPh$_3$)$_2$] exhibited non-linear optical properties.[99d] For what concerns phosphoramide zinc(II) complexes, some tetrahedral homoleptic complexes were isolated.[186] Hexamethylphosphoramide is present in the coordination sphere of a dinuclear zinc(II) alkoxide-phenoxide-ketoiminate complex and the interactions in solution of zinc(II) halides and perchlorate and of tetraphenylporphirinatozinc with hexamethylphosphoramide were studied.[187] I started my investigation preparing the previously described triphenylphosphine oxide derivatives. $[ZnI_2(O=PPh_3)_2]$ showed no appreciable photoluminescence and it was not further investigated. On the other hand, the emission spectrum of $[ZnBr_2(O=PPh_3)_2]$ is dominated by a peak at 403 nm, with shoulders at about 440 and 504 nm, and the lifetime is around 5 ns. These weak emissive properties and the similarity between manganese(II) and zinc(II) encouraged me to investigate the effects of the coordination of the previously reported phosphoramides $O=P(NMe_2)_2Ind$ and $O=P(NMe_2)_2Cbz$ to anhydrous zinc(II) halides. The reaction of two equivalent of $O=P(NMe_2)_2R$ (R = Ind or Cbz) with anhydrous ZnX_2 (X = Cl, Br, I) in ethanol under mild conditions afforded the corresponding neutral complexes $[ZnX_2\{O=P(NMe_2)_2R\}_2]$. As observable in Figures 114 and 115, the ^1H NMR spectra of $[ZnBr_2\{O=P(NMe_2)_2R\}_2]$ (R = Ind and Cbz) show a single set of resonances attributable to the coordinated {O=P}-donor ligands, composed by respectively six and three multiplets in the aromatic region and a doublet around 2.8 ppm with $^3J_{PH}$ coupling constant between 10.5 and 10.7 Hz. The $^{31}P\{^1H\}$ NMR spectra are composed by a singlet in the 17.4-16.3 ppm range.

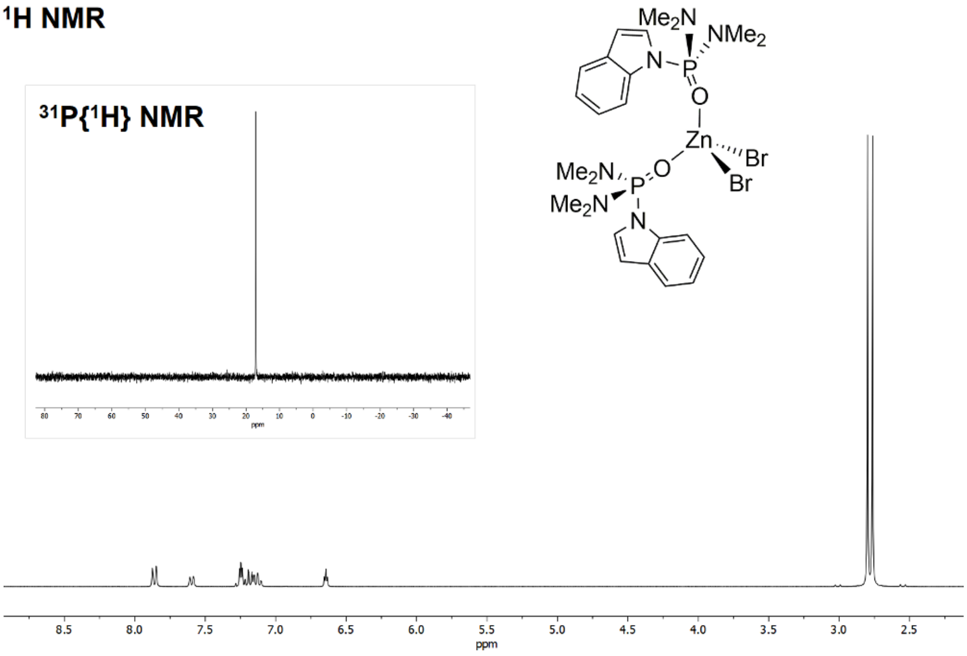

Figure 114. ^1H NMR spectrum of $[ZnBr_2\{O=P(NMe_2)_2Ind\}_2]$ in $CDCl_3$ at 298 K. Inset: $^{31}P\{^1H\}$ NMR spectrum in $CDCl_3$ at 298 K.

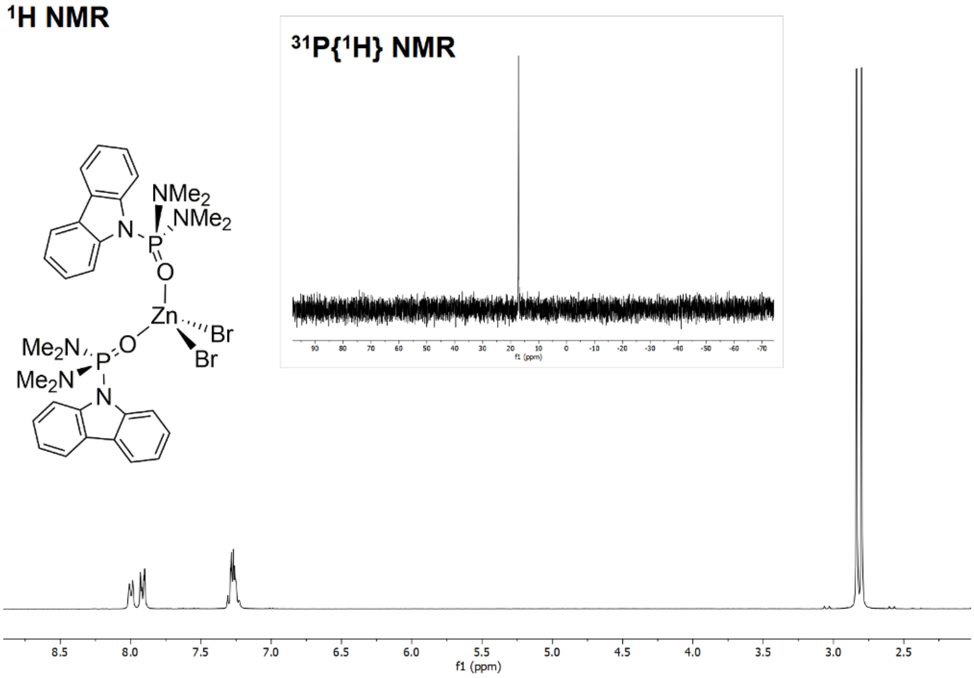

Figure 115. ^{1}H NMR spectrum of [$ZnBr_2\{O{=}P(NMe_2)_2Cbz\}_2$] in $CDCl_3$ at 298 K. Inset: $^{31}P\{^1H\}$ NMR spectrum in $CDCl_3$ at 298 K.

The IR spectra show bands related to the vibrations of the {O=P}-donors. The small shifts in the $\nu_{P=O}$ and $\nu_{P\text{-}N}$ regions with respect to the free ligand are in line with the previously described [$MnX_2\{O{=}P(NMe_2)_2R\}_2$] (R = Ind and Cbz) complexes and are attributable to the weakening of the O=P bond caused by coordination, with consequent slight enforcement of the P-N bonds.[147] Crystals of [$ZnX_2\{O{=}P(NMe_2)_2Ind\}_2$] (X = Cl, Br, I) suitable for X-ray diffraction were collected from dichloromethane/diethyl ether solutions. Crystal data and structure refinement are collected in Table A19 (see Table B19 for selected bond lengths and angles). [$ZnCl_2\{O{=}P(NMe_2)_2Ind\}_2$] and [$ZnBr_2\{O{=}P(NMe_2)_2Ind\}_2$] (depicted in Figure 116) are isomorphs and crystallize in the monoclinic $P2_1/n$ space group. [$ZnI_2\{O{=}P(NMe_2)_2Ind\}_2$] instead crystallizes in the triclinic P-1 space group with two molecules not symmetry related in the asymmetric unit, since one of the NMe_2 groups and the indolyl fragment are interchanged around one of the phosphorus atoms. One of the [$ZnI_2\{O{=}P(NMe_2)_2Ind\}_2$] molecules is however superimposable with the other halide complexes.

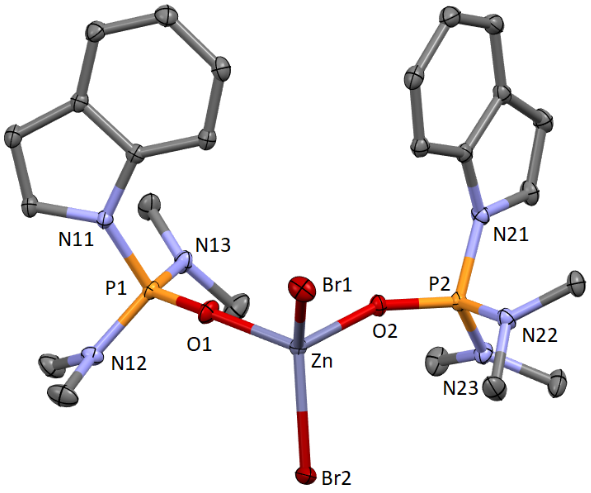

Figure 116. X-ray structure of [$ZnBr_2\{O{=}P(NMe_2)_2Ind\}_2$].

The UV-VIS spectrum of the complexes in dichloromethane solutions is strictly comparable to that of the free ligands, therefore the excitation causing the emission is mainly ascribed to $\pi^* \leftarrow \pi$ absorptions of the coordinated ligands. No absorption in the visible range was detected also for concentrated solutions.

[$ZnX_2\{O{=}P(NMe_2)_2Ind\}_2$] (X = Br and I) exhibited bright green emissions upon excitation with UV light below 300 nm at the solid state. The photoluminescence of [$ZnCl_2\{O{=}P(NMe_2)_2Ind\}_2$] was negligible and not further investigated. This outcome can be justified considering the absence of heavy atoms in the zinc(II) first coordination sphere able to induce strong intersystem crossing. No appreciable luminescence was observed for the compounds in solution, probably because of vibrational coupling with solvent molecules. All the measurements were therefore carried out on crystallized solid samples. Normalized PL and PLE spectra of [$ZnX_2\{O{=}P(NMe_2)_2Ind\}_2$] (X = Br and I) are reported in Figure 117. The PL spectrum of [$ZnBr_2\{O{=}P(NMe_2)_2Ind\}_2$] is composed by a single band centred at 531 nm, with FWHM around 2900 cm^{-1}. Despite the comparable emission range, the PL spectrum of [$ZnI_2\{O{=}P(NMe_2)_2Ind\}_2$] is different, being composed by a set of shoulders and peaks, the most intense falling at 521 nm. The peaks are all separated by about 1300 cm^{-1}, suggesting that the ground-state vibrational structure is subtended by the PL spectrum. The quite high wavenumber is most likely related to vibrations in the $O{=}P(NMe_2)_2Ind$ ligands, since much lower values are expected for vibrations involving the zinc(II) first coordination sphere.[188] Despite the fact that solid samples allow only qualitative comparisons, the bromo-derivative is much more luminescent than the related iodo-complex under the same experimental conditions. The PL spectra do not vary on changing the excitation wavelength and the two compounds have roughly superimposable PLE spectra. The excitation range at the solid state is limited to wavelengths shorter than 330 nm and it is comparable to the UV-VIS absorptions obtained in dichloromethane solutions. As observable in Figure 117, the emissions of both $[ZnBr_2\{O=P(NMe_2)_2Ind\}_2]$ and $[ZnI_2\{O=P(NMe_2)_2Ind\}_2]$ fall in the yellowish green region of the CIE 1931 diagram, with colour purity values around 0.78 and 0.61 for the bromo- and the iodo-complex, respectively. The photoluminescence quantum yields Φ at room temperature are 19% and 7% respectively for $[ZnBr_2\{O=P(NMe_2)_2Ind\}_2]$ and $[ZnI_2\{O=P(NMe_2)_2Ind\}_2]$. The lower value obtained for the iodo-derivative is perhaps related to expansion of the emission band towards higher wavelengths, favouring non-radiative decay routes.

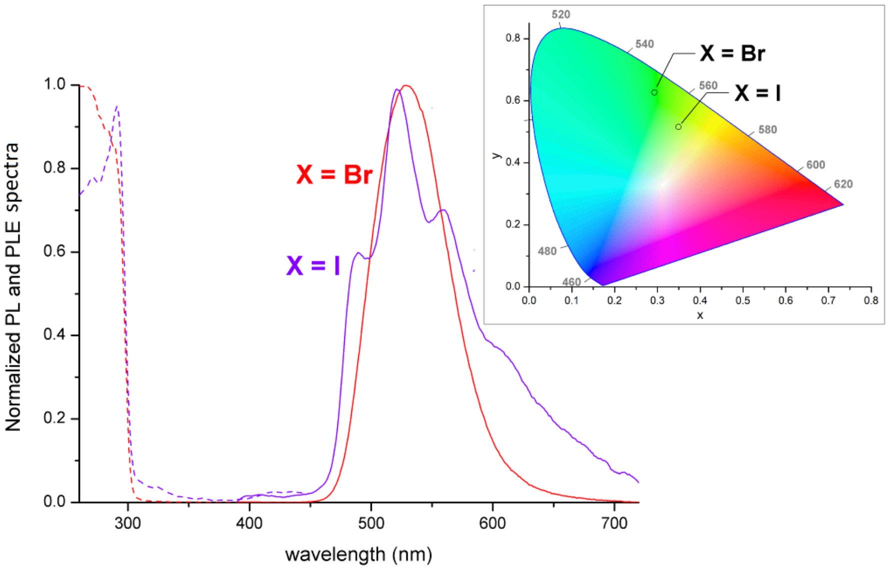

Figure 117. Normalized PL (solid lines) and PLE (dashed lines) spectra of $[ZnBr_2\{O=P(NMe_2)_2Ind\}_2]$ (red lines) and $[ZnI_2\{O=P(NMe_2)_2Ind\}_2]$ (violet lines). Solid samples, r.t., $\lambda_{excitation}$ = 290 nm, $\lambda_{emission}$ = 520 nm. Inset: CIE 1931 chromaticity diagram, $[ZnBr_2\{O=P(NMe_2)_2Ind\}_2]$ (x = 0.293, y = 0.627) and $[ZnI_2\{O=P(NMe_2)_2Ind\}_2]$ (x = 0.349, y = 0.516).

Excitation with UV light below 350 nm determined blue-purple or whitish luminescence for the $[ZnX_2\{O=P(NMe_2)_2Cbz\}_2]$ derivatives. Similar to $[ZnX_2\{O=P(NMe_2)_2Ind\}_2]$ (X = Cl, Br, I), the PLE spectra are almost superimposable to the UV-VIS spectra of the complexes in dichloromethane solutions. The emission bands are related to those of the free ligand, as highlighted in Figure 118. In fact, the PL spectrum of $O=P(NMe_2)_2Cbz$ shows transitions in the blue-violet region and broad bands in the 450–600 nm range with luminescence lifetimes of 15 ns (solid sample, r.t., $\lambda_{emission}$ = 520 nm), in line with emission from excited singlet states. The maxima are red-shifted due to the coordination to zinc(II) metal centre. As previously observed for [$ZnI_2\{O=P(NMe_2)_2Ind\}_2$], all the peaks are separated by roughly the same energy (around 1300 cm^{-1}), and such a separation can be related to the ground-state vibrational structure. The PL and PLE spectra of [$ZnBr_2\{O=P(NMe_2)_2Cbz\}_2$] however present some differences compared to the other two halide derivatives. First, the maximum in the PLE spectra appears to be blue-shifted and the excitation terminates at 350 nm, while for the other two complexes the band ends at longer wavelengths. Then, [$ZnBr_2\{O=P(NMe_2)_2Cbz\}_2$] is characterized by noticeable bands between 550 and 700 nm. This difference in the emission is further stressed by the CIE 1931 chromaticity diagram, where the bromo-species is located in the whitish zone, while the other two complexes are purplish-blue emitters. The photoluminescence quantum yields Φ at room temperature are respectively 46% (X = Cl), 56% (X = Br) and 5% (X = I) for the three [$ZnX_2\{O=P(NMe_2)_2Cbz\}_2$] derivatives. The relatively low Φ of the iodo-species can be tentatively attributed the vibrational decay from excited triplet states, whose population is favoured by the presence of the heavy halides in the coordination sphere.

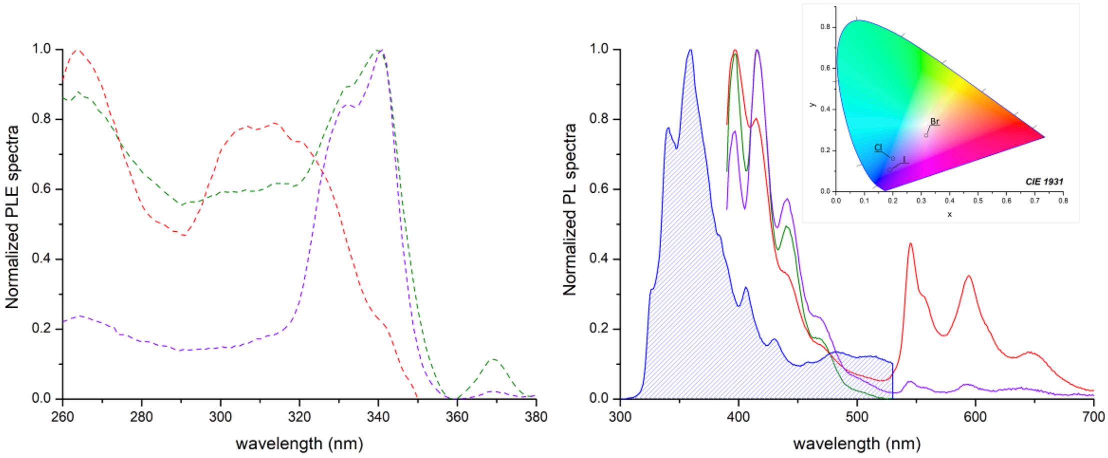

Figure 118. Normalized PL (solid lines) and PLE (dashed lines) spectra of [$ZnX_2\{O=P(NMe_2)_2Cbz\}_2$] (X = Cl, green; X = Br, red; I = violet) and $O=P(NMe_2)_2cbz$ (filled blue line). Solid samples, r.t., $\lambda_{excitation}$ = 280-350 nm, $\lambda_{emission}$ = 390-420 nm. Inset: CIE 1931 chromaticity diagram, [$ZnCl_2\{O=P(NMe_2)_2Cbz\}_2$] (x = 0.201, y = 0.161), [$ZnBr_2\{O=P(NMe_2)_2Cbz\}_2$] (x = 0.317, y = 0.274) and [$ZnI_2\{O=P(NMe_2)_2Cbz\}_2$] (x = 0.191, y = 0.106).

The large Stokes shifts observable for the indolyl derivatives are quite uncommon for zinc(II) luminescent complexes. The lifetimes of the excited states obtained from the monoexponential fit of the luminescence decay curves provided in Figure 119 are in the milliseconds range, respectively 0.7 ms for [$ZnBr_2\{O=P(NMe_2)_2Ind\}_2$] and 2.6 ms for [$ZnI_2\{O=P(NMe_2)_2Ind\}_2$], strongly supporting the idea that triplet excited states are involved in the emissions. This hypothesis is in line with the absence of comparable photoluminescence from the related chloro-complex. The linear semi-log plot of the luminescence decay curves indicate the presence of a single emitting level. The lifetimes here provided are in the same time scale of those recently reported for coordination polymers based on $[Zn_3(HPO_3)_2]^{2+}$ cations linked by 1,3,5-tris(1-imidazolyl)-benzene.[94] On the other hand, shorter Stokes shifts were in general observed for the carbazolyl species and the three $[ZnX_2\{O=P(NMe_2)_2Cbz\}_2]$ (X = Cl, Br, I) derivatives are characterized by superimposable emissions in the 400-500 nm range, with lifetimes all around 7 ns suggesting that the mechanism in this case is ^{1}LC. Emissions at longer wavelengths in line with those previously described for $[ZnX_2\{O=P(NMe_2)_2Ind\}_2]$ are clearly detectable only for the bromo-complex $[ZnBr_2\{O=P(NMe_2)_2Carb\}_2]$, while they are absent for the chloro-species and almost quenched for the iodo-complex. In conclusion, the comparison of the emission spectra suggests that the replacement of the indolyl with the carbazolyl fragment favours the direct fluorescent decay with respect to the intersystem crossing followed by phosphorescence.

The possible nature of the emissions of $[ZnX_2\{O=P(NMe_2)_2Ind\}_2]$ (X = Br, I) was investigated by means of DFT and TD-DFT calculations. The hole and electron distributions[189] associated to the emission transition, plotted in Figure 119, confirm that the electron moves between π-delocalized orbitals of the same indolyl fragment, with negligible contribution of the remaining parts of the molecules. On the basis of the TD-DFT outcomes the transitions are therefore ascribed to ligand-centred processes, not detected for the free *N*,*N*,*N'*,*N'*-tetramethyl-*P*-indol-1-ylphosphonic diamide. The role attributable to the zinc(II) heavy halide fragments is the enhancement of the intersystem crossing between excited singlet and triplet states of the coordinated ligands. On the other hand, the experimental data indicate that the role of the metal centre in $[ZnX_2\{O=P(NMe_2)_2Cbz\}_2]$ is mainly the enhancement of the fluorescence because of the increased rigidity.

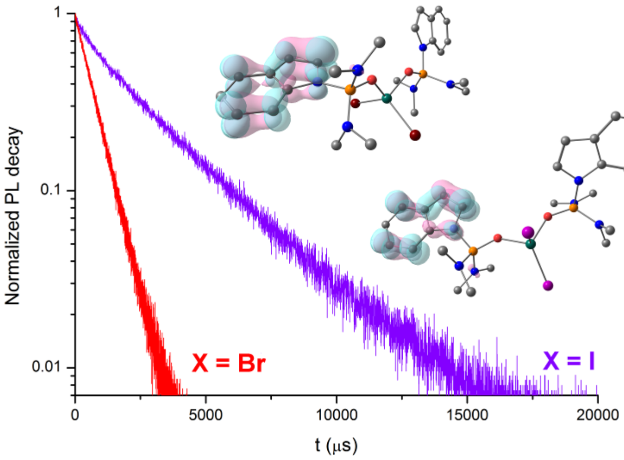

Figure 119. Semi-log plot of the luminescence decay curves of $[ZnBr_2\{O=P(NMe_2)_2Ind\}_2]$ (red line) and $[ZnI_2\{O=P(NMe_2)_2Ind\}_2]$ (violet line). Solid samples, r.t., $\lambda_{excitation}$ = 290 nm, $\lambda_{emission}$ = 520 nm. DFT-optimized triplet state geometries of $[ZnBr_2\{O=P(NMe_2)_2Ind\}_2]$ and $[ZnI_2\{O=P(NMe_2)_2Ind\}_2]$ with hole (light blue) and electron (light pink) distributions related to the $T_1 \rightarrow S_0$ transitions (surface isovalue = 0.003 a.u.). TPSSh/def2-SVP calculations. Colour map: C, grey; N, blue; O, red; P, orange; Zn, dark green; Br, dark red; I, violet. Hydrogen atoms are omitted for clarity.

Electrochemical measurements were conducted on $O=P(NMe_2)_2Ind$ and compared to triphenylphosphine oxide revealing that *N*,*N*,*N'*,*N'*-tetramethyl-*P*-indol-1-ylphosphonic diamide is more reducing than triphenylphosphine oxide. As highlighted by Figure 120a, both the ligands give irreversible oxidation processes, but the onset of the oxidation of $O=P(NMe_2)_2Ind$ falls at potential around 200 mV lower than that of $O=PPh_3$. The oxidation of $O=P(NMe_2)_2Ind$ occurs at lower potential with respect to $ZnBr_2$ and it is more or less coincident with the second oxidation peak of ZnI_2. The cyclic voltammograms of $[ZnBr_2\{O=P(NMe_2)_2Ind\}_2]$ and $[ZnI_2\{O=P(NMe_2)_2Ind\}_2]$, compared to those of the corresponding zinc(II) halides, are shown in Figure 120b. The oxidation process of the bromo-derivative starts around 0.95 V *vs* Fc^+/Fc, roughly at the same potential of the free ligand. An analogous process is observable for the iodo-complex, anticipated by an irreversible oxidation centred at about 0.43 V *vs* Fc^+/Fc related to coordinated iodide. The reduction processes occur at potential lower than -1.4 V *vs* Fc^+/Fc for $[ZnBr_2\{O=P(NMe_2)_2Ind\}_2]$ and -1.5 V *vs* Fc^+/Fc for $[ZnI_2\{O=P(NMe_2)_2Ind\}_2]$ and are comparable to those observed for the related ZnX_2 halides, with little shifts at lower potentials. The onsets of the ligand-centred oxidation and metal-centred reduction processes are separated by about 2.45-2.50 V, corresponding to an energy difference in the same range of the emissions of the complexes. The same energy values for the $T_1 \rightarrow S_0$ transitions at the triplet equilibrium geometries obtained from DFT calculations are 2.06 eV for

$[ZnBr_2\{O{=}P(NMe_2)_2Ind\}_2]$ and 2.36 eV for $[ZnI_2\{O{=}P(NMe_2)_2Ind\}_2]$, in acceptable agreement with the experimental data.

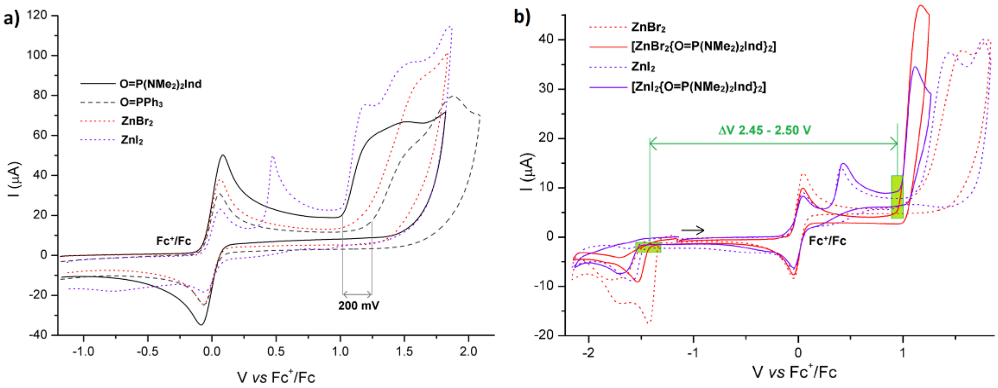

Figure 120. a) Cyclic voltammograms of $O{=}P(NMe_2)_2Ind$ (solid black line), $O{=}PPh_3$ (dashed grey line), $ZnBr_2$ (dotted red line) and ZnI_2 (dotted violet line). b) Cyclic voltammograms of $[ZnBr_2\{O{=}P(NMe_2)_2Ind\}_2]$ (solid red line), $[ZnI_2\{O{=}P(NMe_2)_2Ind\}_2]$ (solid violet line), $ZnBr_2$ (dotted red line) and ZnI_2 (dotted violet line). $CH_3CN/LiClO_4$, r.t., glassy carbon electrode, ferrocene (Fc) as internal reference, scan rate 100 mV/s.

The introduction of phenyl fragments in the ligand skeleton allowed the preparation of (Indol-1-yl)diphenylphosphine oxide, $O{=}PPh_2Ind$. The formation of the corresponding neutral zinc(II) complexes is supported by conductivity measurements and elemental analyses. As observable in Figure 121, the ^1H NMR spectra is characterized by several resonances in the aromatic region attributable to both phenyl and indolyl substituents. The $^{31}P\{^1H\}$ NMR spectra are characterized by a sharp singlet around 30.5 ppm.

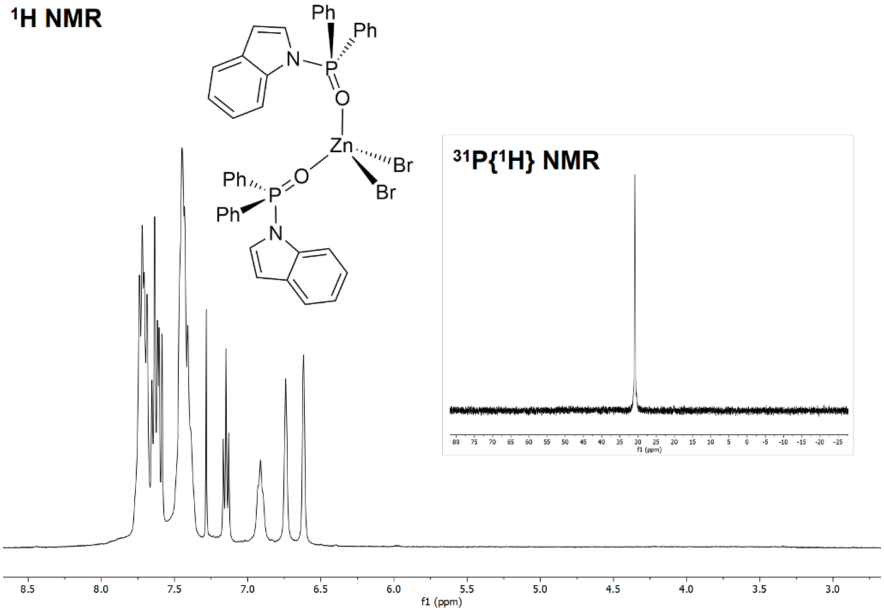

Figure 121. ^1H NMR spectrum of $[ZnBr_2(O{=}PPh_2Ind)_2]$ in $CDCl_3$ at 298 K. Inset: $^{31}P\{^1H\}$ NMR spectrum in $CDCl_3$ at 298 K.

The UV-VIS spectra collected in dichloromethane solutions exhibit absorptions below 320 nm attributable to $\pi^* \leftarrow \pi$ transitions of the coordinated ligands. The complexes are not luminescent in solution but at the solid state they are characterized by emissions strictly comparable to the ones observed for $[ZnX_2\{O=P(NMe_2)_2Ind\}_2]$ (X = Cl, Br, I). The photoluminescence is dependent on the choice of the halide. As highlighted in Figure 122a, moving from Cl to I the band around 400 nm related to the fluorescence of the coordinated ligands decreases with respect to the other one centred at longer wavelengths. This result can be clearly rationalized considering the increased intersystem crossing using heavier halides. The measured photoluminescence quantum yields Φ at room temperature are 54% for the chloro-species and 5% for $[ZnX_2(O=PPh_2Ind)_2]$ (X = Br, I). The Stokes shifts are quite short due to the presence of the fluorescence band, thus complicating the photoluminescent measurements. The fast component of the luminescence decay curves is shorter than the limit of the experimental technique (few microseconds), and a more precise measurement was limited by the available excitation range of the complexes. The presence of a longer component in the 300-400 μs range related to the emission at longer wavelengths was observed for $[ZnX_2(O=PPh_2Ind)_2]$ (X = Br, I). On the basis of DFT and TD-DFT calculations (see for instance Figure 122b), the hole and electron distributions underline how the absorption involves both indolyl and phenyl fragments, while the emission is localized only on the indolyl substituent, suggesting a ^{3}LC/^{3}LLCT nature.

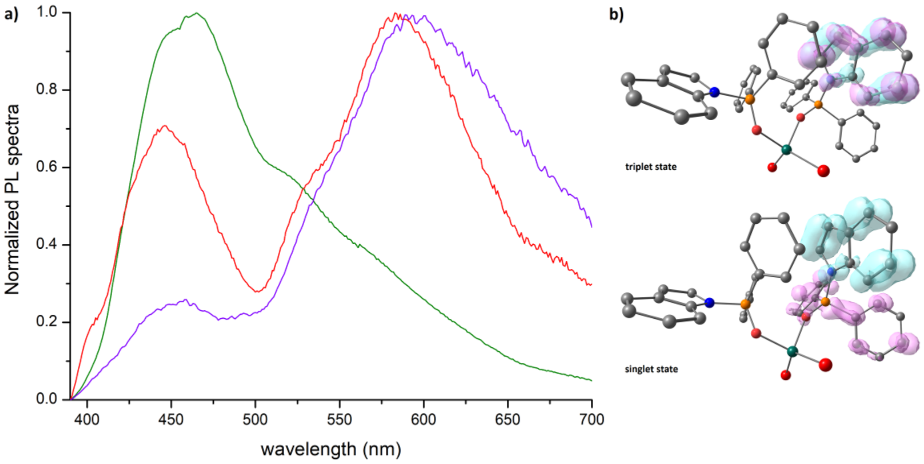

Figure 122. a) Normalized PL spectra of $[ZnX_2(O=PPh_2Ind)_2]$ (X = Cl, green; Br, red; I, violet lines). Solid samples, r.t., $\lambda_{excitation}$ = 350 nm. b) DFT-optimized single and triplet state geometries of $[ZnBr_2(O=PPh_2Ind)_2]$ with hole (light blue) and electron (light pink) distributions (surface isovalue = 0.003 a.u.). MN15/def2-SVP calculations. Colour map: C, grey; N, blue; O, red; P, orange; Zn, dark green; Br, dark red. Hydrogen atoms are omitted for clarity.

The investigation on zinc(II) halide complexes prosecuted with ligands based on trivalent phosphorus, *i.e.* 9,10-dihydro-9-oxa-10-phosphaphenanthrene-10-oxide (DOPO) and dibenzo[*d*,*f*][1,3,2]dioxaphosphepine 6-oxide (BPPO). The reaction on anhydrous ZnX_2 salts with two equivalents of DOPO (X = Cl, Br) or BPPO (X = Cl, Br) afforded the corresponding tetrahedral complexes. The proposed formulae are confirmed by means of elemental analyses and conductivity measurements. The ^1H NMR spectra of $[ZnBr_2(DOPO)_2]$ recorded at variable temperature revealed fluxional behaviour in $CDCl_3$ solution, as clearly observable from the comparison with the NMR spectra of free DOPO (Figure 123). Similar fluxionality was observed also for the chloro-derivatives and in the $^{31}P\{^1H\}$ NMR spectra. The eight aromatic ^1H resonances expected for two equivalent coordinated DOPO ligands can be however detected, while in the case of BPPO derivatives only four aromatic signals are expected since the [O=P]-donor is symmetric. The $^1J_{PH}$ coupling constant raises from the 593 Hz of free DOPO to 620 Hz in $[ZnBr_2(DOPO)_2]$, and from 733 Hz of free BPPO to 770-780 Hz for $[ZnX_2(BPPO)_2]$ (X = Cl, Br). It is likely to suppose that the donation of electronic density from DOPO and BPPO to zinc(II) makes the phosphorus atom more electrophilic and strengthens the P-H bond. The $^{31}P\{^1H\}$ NMR resonances of $[ZnX_2(DOPO)_2]$ and $[ZnX_2(BPPO)_2]$ (X = Cl, Br) are shifted at higher frequency with respect to the free ligands by about 5 ppm and the singlets appear to be broadened, most likely because of fluxional behaviour.

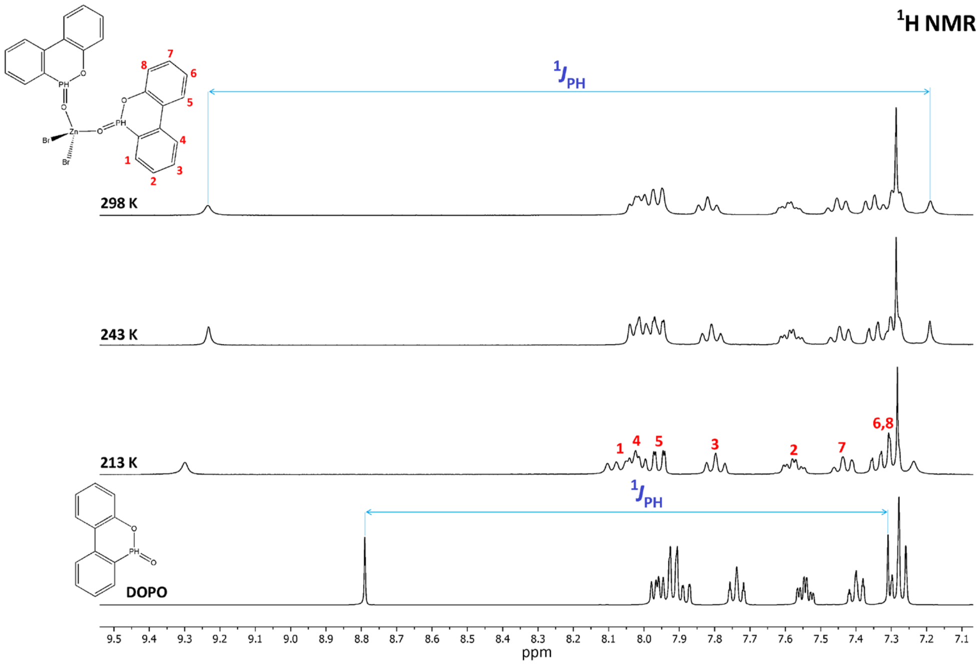

Figure 123. ^1H NMR spectra at variable temperature of $[ZnBr_2(DOPO)_2]$ and of free DOPO in $CDCl_3$.

The IR spectra of the $[ZnX_2(DOPO)_2]$ (X = Cl, Br) and $[ZnX_2(BPPO)_2]$ (X = Cl, Br) complexes are roughly superimposable to the corresponding manganese(II) derivatives. The $\nu_{P\text{-}H}$ stretchings fall at slightly higher wavenumbers in the complexes with respect to the free ligand, in line with the increased $^1J_{PH}$ coupling constant.[156] Similar to $[MnX_2(DOPO)_2]$ (X = Cl, Br, I), the $\nu_{P=O}$ stretchings between 1250 and 1150 cm^{-1} indicate a slight weakening of the P=O bonds due to the coordination. $[ZnBr_2(DOPO)_2]$ crystallized in the *P*-1 space group from ethanol/toluene solutions (see Figure 124). Crystal data and structure refinement are reported in Table A20. Selected bond distances and angles are set out in Table B20.

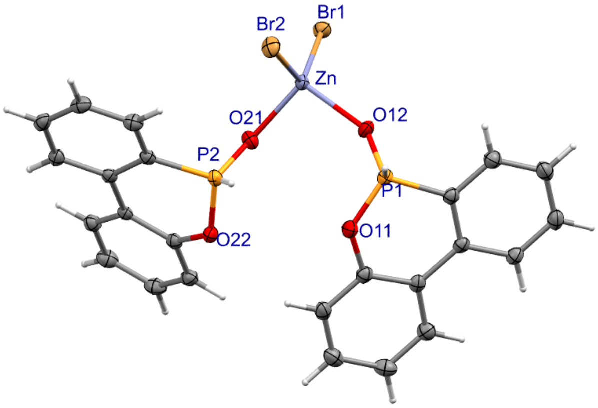

Figure 124. X-ray structure of $[ZnBr_2(DOPO)_2]$.

The $[ZnX_2(DOPO)_2]$ (X = Cl, Br) and $[ZnX_2(BPPO)_2]$ (X = Cl, Br) complexes show absorptions in solution respectively below 325 and 300 nm related to $\pi^* \leftarrow \pi$ transitions. The computed singlet → singlet absorption of $[ZnBr_2L_2]$ (L = DOPO or BPPO) is predicted respectively at 272 and 248 nm, roughly in line with the experimental data. The TD-DFT computed hole and electron distributions for the lowest energy state confirm that the transition involves the π-conjugated system of the DOPO and BPPO ligands. The photoluminescence quantum yield values are in the 5-11% range for $[ZnX_2(DOPO)_2]$ (X = Cl, Br) and 13-16% for $[ZnX_2(BPPO)_2]$ (X = Cl, Br). The excitation of $[ZnX_2(DOPO)_2]$ and $[ZnX_2(BPPO)_2]$ produced strictly comparable emission spectra. In both the cases the PL spectra are composed of two bands, one most likely attributed to fluorescence and the other one to phosphorescence of the coordinated the ligands. It is worth noting that the latter is observable also in the corresponding manganese(II) halide complexes, supporting its ^{3}LC nature (see Figures 125 and 126). This outcome and the decrease in the fluorescent band passing from Cl to Br can be ascribed to the increased intersystem crossing with heavier halides. The lifetime of the highest-energy emission is in the ns range with values strictly comparable to the fluorescent emission of free DOPO and BPPO. The PLE spectra of $[ZnX_2(DOPO)_2]$ (X = Cl, Br) and $[ZnX_2(BPPO)_2]$ (X = Cl, Br) are superimposable to those of the corresponding manganese(II) complexes, with the expected lack of bands related to the direct excitation of the metal centre.

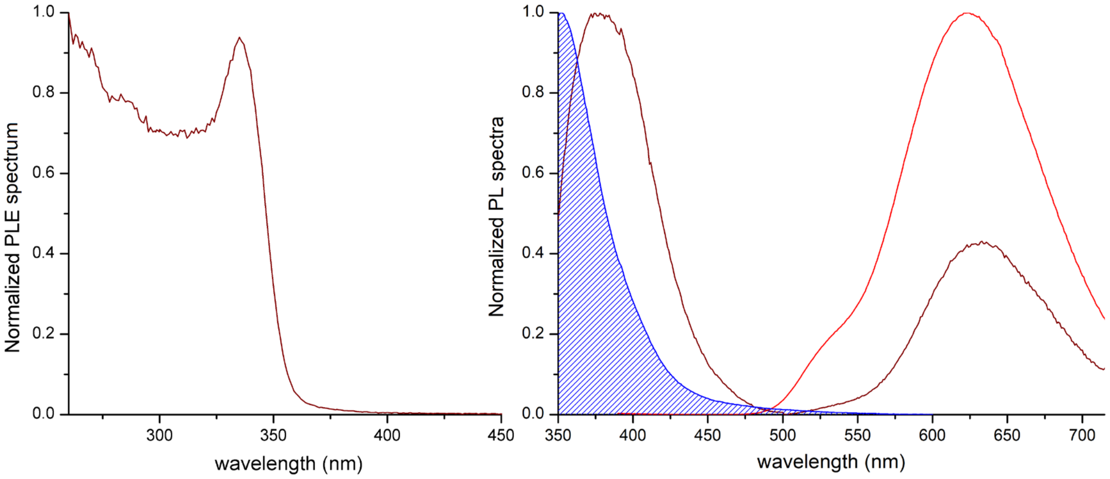

Figure 125. Normalized PL and PLE spectra of $[ZnBr_2(DOPO)_2]$ (wine red line, $\lambda_{excitation}$ = 325 nm, $\lambda_{emission}$ = 630 nm). PL spectra of $[MnBr_2(DOPO)_2]$ (red line, $\lambda_{excitation}$ = 325 nm) and of DOPO (filled blue line, $\lambda_{excitation}$ = 280 nm). Solid samples, r.t.

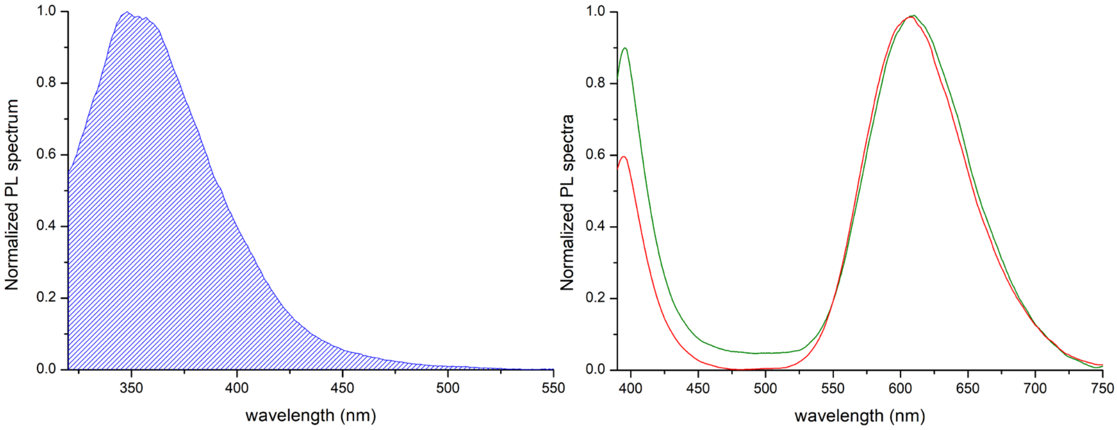

Figure 126. Normalized PL of free BPPO (filled blue line, $\lambda_{excitation}$ = 280 nm) and $[ZnX_2(BPPO)_2]$ (Cl, green; Br, red). Solid samples, r.t., $\lambda_{excitation}$ = 265 nm.

When the emission in the red region is considered, the lifetimes for $[ZnCl_2(BPPO)_2]$ and $[ZnBr_2(BPPO)_2]$ are in the tens of ms long, as observable in Figure 127a. The ^{3}LC nature of the emission in the red region was supported by TD-DFT calculations on the optimized structure of $[ZnBr_2(DOPO)_2]$ and $[ZnBr_2(BPPO)_2]$ (triplet state). The hole and electron distributions for the emission ($\lambda_{predicted}$ = 578 and 633 nm) show that the transition is localized of the π-delocalized orbitals of the coordinated DOPO and BPPO ligands, see for instance Figure 127b.

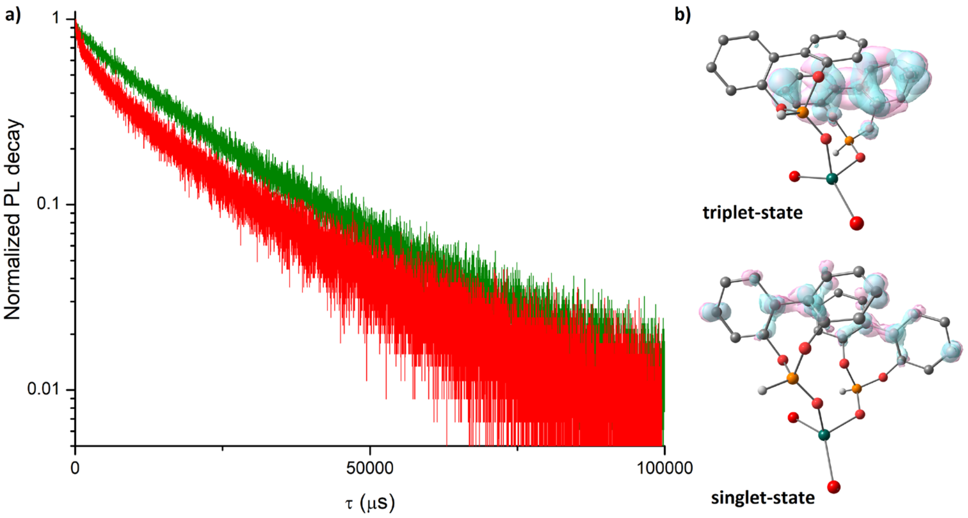

Figure 127. a) Semi-log plot of normalized PL decay curves of [$ZnX_2(BPPO)_2$] (Cl, green line; Br, red line; solid samples, r.t., $\lambda_{excitation}$ = 265 nm; $\lambda_{excitation}$ = 610 nm). b) DFT-optimized triplet state geometries of [$ZnBr_2(BPPO)_2$] with hole (light blue) and electron (light pink) distributions (surface isovalue = 0.003 a.u.). MN15/def2-SVP calculations. Colour map: C, grey; N, blue; O, red; P, orange; Zn, dark green; Br, dark red. Hydrogen atoms (except P-bonded) are omitted for clarity.

Ligand-centred emission was observed also using 6-phenyldibenzo[*d*,*f*][1,3,2]dioxaphosphepine 6-oxide (BPPP) as ligand. Two equivalents of BPPP were reacted with anhydrous ZnX_2 salts affording the corresponding tetrahedral complexes. The proposed formulae are confirmed by means of elemental analyses and conductivity measurements. The ^1H NMR and $^{31}P\{^1H\}$ NMR spectra of [$ZnBr_2(BPPP)_2$] are reported in Figure 128. In the case of the iodo-species, the signals appeared to be broadened due to fluxional behaviour in solution. The expected resonances related to the biphenyl and phenyl fragment can be detected in the aromatic region of the spectra. The $^{31}P\{^1H\}$ NMR signals are slightly moved to higher ppm with respect to the free ligand. Similar to the previously reported BPPO derivatives, the $\nu_{P=O}$ stretchings can be found between 1280 and 1170 cm^{-1} due to the weakening of the coordinated P=O bonds.

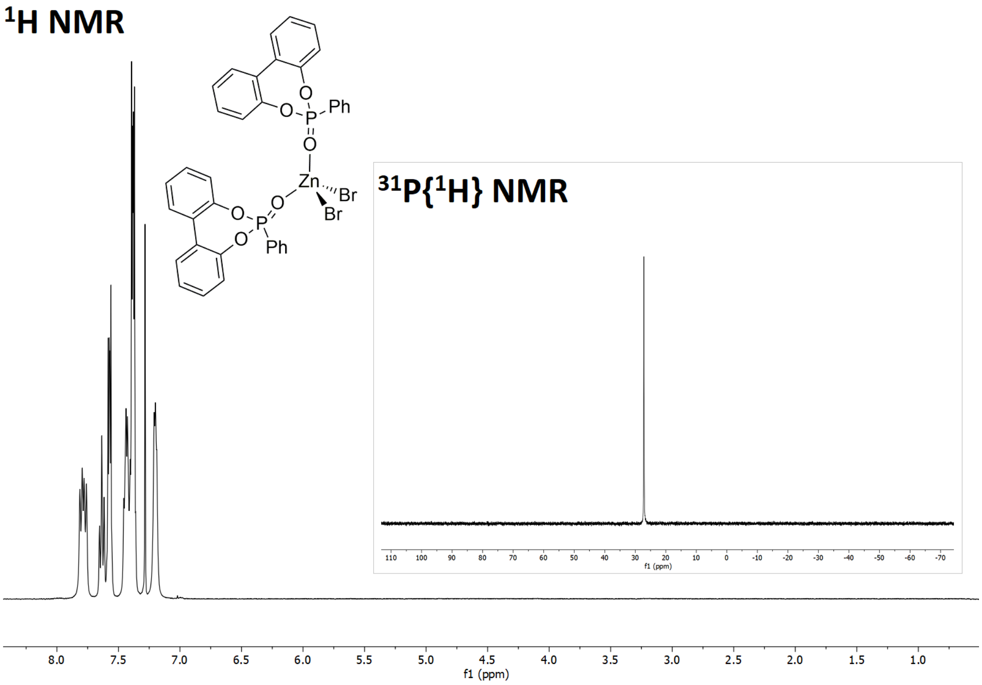

Figure 128. ^{1}H NMR spectrum of $[ZnBr_2(BPPP)_2]$ in $CDCl_3$ at 298 K. Inset: $^{31}P\{^{1}H\}$ NMR spectrum in $CDCl_3$ at 298 K.

The UV-VIS spectra of $[ZnX_2(BPPP)_2]$ (X = Cl, Br, I) in dichloromethane solutions are characterized by absorptions under 350 nm attributable to $\pi^* \leftarrow \pi$ transitions of the 2,2'-biphenol and phenyl fragments. TD-DFT calculations predicted the singlet → singlet absorption at 248 nm, perfectly in agreement with the experimental data. In this case the computed hole and electron distributions for the lowest energy state also indicate the direct involvement of the coordinated bromides together with the π-conjugated system of BPPP (see Figure 129b). The photoluminescence quantum yields are 22% for the chloro-derivative and in the 5-6% range for the green-emitting $[ZnX_2(BPPP)_2]$ (X = Br, I).

The emission spectra of $[ZnX_2(BPPP)_2]$ are strongly dependent upon the choice of the halide. The chloro-species exhibits the classic fluorescence of BPPP enhanced by the coordination to the metal centre with photoluminescent lifetimes τ of 6 ns. Instead, the heavier halides determined an increased intersystem crossing and thus a phosphorescent band in the green region of the spectra, as shown in Figure 129a. The lifetimes for $[ZnX_2(BPPP)_2]$ (X = Br, I) are in the milliseconds range, as previously observed for the BPPO derivatives. TD-DFT calculation performed on the optimized structure of $[ZnBr_2(BPPP)_2]$ support the ^{3}LC nature of the emission with the $\lambda_{predicted}$ at 580 nm. The hole and electron distribution depicted in Figure 129b clearly indicates that the emission is localized on the π-delocalized orbitals of BPPP.

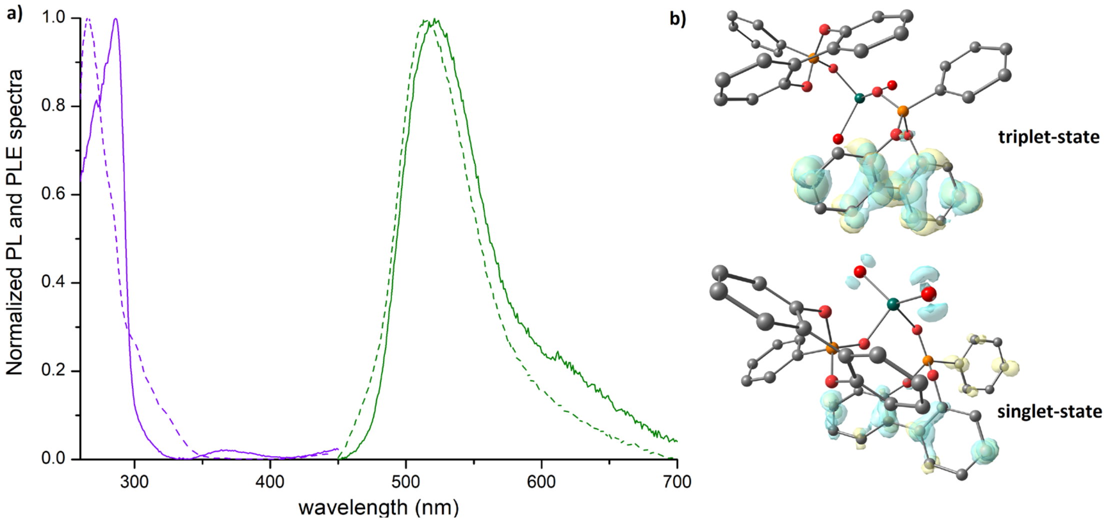

Figure 129. a) Normalized PL and PLE spectra of [$ZnX_2(BPPP)_2$] (Br, continuous line; I, dashed line). Solid samples, r.t., $\lambda_{excitation}$ = 265 nm, $\lambda_{emission}$ = 520 nm. b) DFT-optimized singlet and triplet state geometries of [$ZnBr_2(BPPP)_2$] with hole (light blue) and electron (yellow) distributions (surface isovalue = 0.003 a.u.). MN15/def2-SVP calculations. Colour map: C, grey; N, blue; O, red; P, orange; Zn, dark green; Br, dark red. Hydrogen atoms are omitted for clarity.

With (4R/S)-4-phenyldinaphtho[2,1-*d*:1',2'-*f*][1,3,2]dioxaphosphepine 4-oxide O=P(R/S-BINOL) only $ZnBr_2$ allowed the isolation of the corresponding neutral species, while $ZnCl_2$ and ZnI_2 afforded multiple products. The proposed formulae are supported by elemental analyses and conductivity measurements. ^1H and $^{31}P\{^1H\}$ NMR spectra are strictly superimposable to the free ligands, as well as IR and UV-VIS data. The absorptions below 350 nm are associated to $\pi^* \leftarrow \pi$ transitions of the 1,1′-bi-2-naphthol and phenyl fragments. Unfortunately, due to the extremely short Stokes shift, it was not possible to measure the photoluminescent quantum yields. TD-DFT calculations performed on the ground-state geometry of [$ZnBr_2$\{O=P(R/S-BINOL)\}$_2$] predict the singlet → singlet transition around for 306 nm roughly in line with the experimental data. Despite the extended π-conjugated systems, [$ZnBr_2$\{O=P(R/S-BINOL)\}$_2$] is characterized by only one emission band centred at 370 nm (see Figure 130a) and related to the fluorescence of coordinated ligands as further confirmed by the lifetimes in the nanoseconds range reported in Figure 130b.

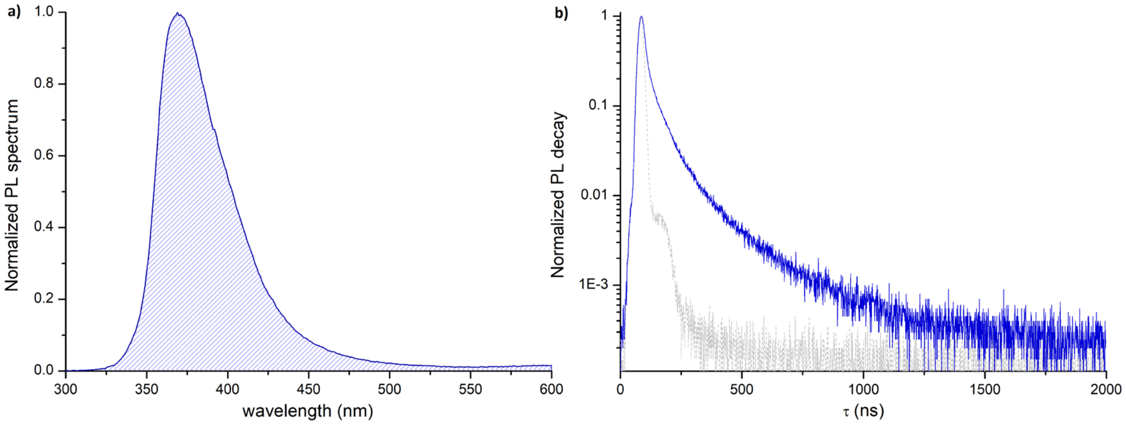

Figure 130. a) Normalized PL spectra of [$ZnBr_2${O=P(R/S-BINOL)}$_2$] (solid sample, r.t., $\lambda_{excitation}$ = 265nm). b) Semi-log plot of the luminescence decay curve (solid sample, r.t., $\lambda_{excitation}$ = 373 nm, $\lambda_{emission}$ = 410 nm). Prompt, grey line; decay, blue line.

4 Other projects

4.1 Copper(I) complexes for CuAAC

The complex [Cu(CNXyl)$_3$][BF$_4$] was serendipitously crystallized in the attempt of obtaining luminescent copper(I) complexes. Crystals suitable for X-ray determination were collected from dichloromethane/diethyl ether solutions. The compound reported in Figure 131 crystallized in the *P*2$_1$/*c* space group. Crystal data and parameters related to the refinement of the structure are collected in Table A21 (see Table B21 for selected bond lengths and angles). It was later prepared by addition of three equivalents of 2,6-dimethylphenyl isocyanide to the acetonitrile complex [Cu(NCCH$_3$)$_4$][BF$_4$] under mild conditions (see Scheme 34).

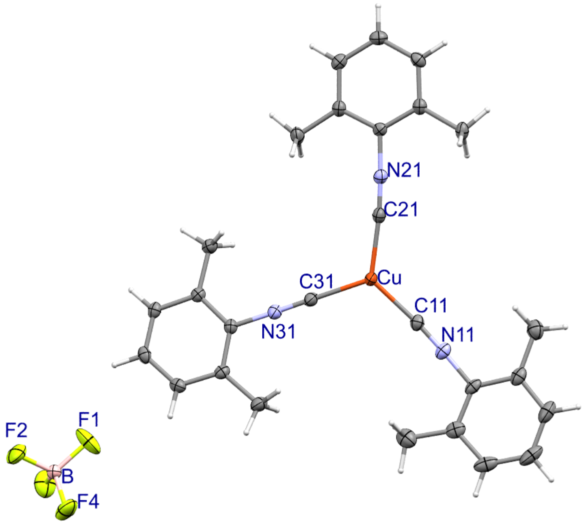

Figure 131. X-ray structure of [Cu(CNXyl)$_3$][BF$_4$].

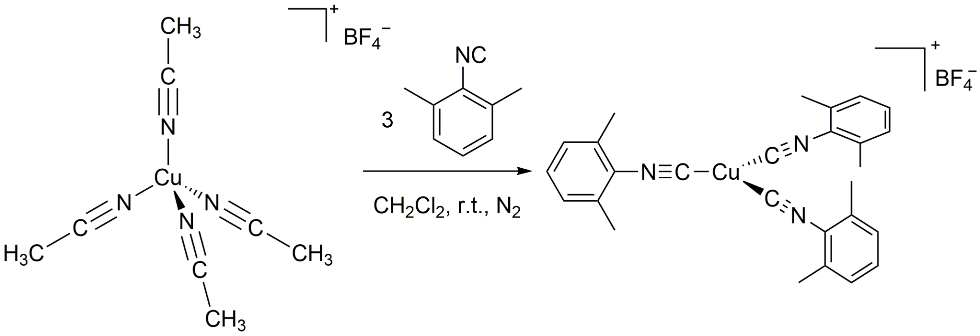

Scheme 34. Synthesis of [Cu(CNXyl)$_3$][BF$_4$].

The elemental analysis supported the proposed formula and conductivity measurements indicated that the complex behaves as 1:1 electrolyte in acetone solutions. IR and ^{1}H NMR spectra (see Figure 132) confirmed the disappearance of the coordinated acetonitrile and the presence of the isocyanides. In particular, the band at 2170 cm^{-1} related to the $\nu_{C\equiv N}$ stretching is diagnostic for their coordination. As regards the ^{1}H NMR spectrum, the methyl protons are associated to a singlet at 2.51 ppm. The aromatic protons generate one doublet centred at 7.19 ppm related to the *meta*-positions and one triplet at 7.32 ppm for the *para*-position. IR and NMR data are in line with those reported for the comparable halide-complex [CuBr(CNXyl)$_3$].[190] The complex exhibits good thermal stability (decomposition starts around 170°C) and no appreciable oxidation could be detected under air at room temperature.

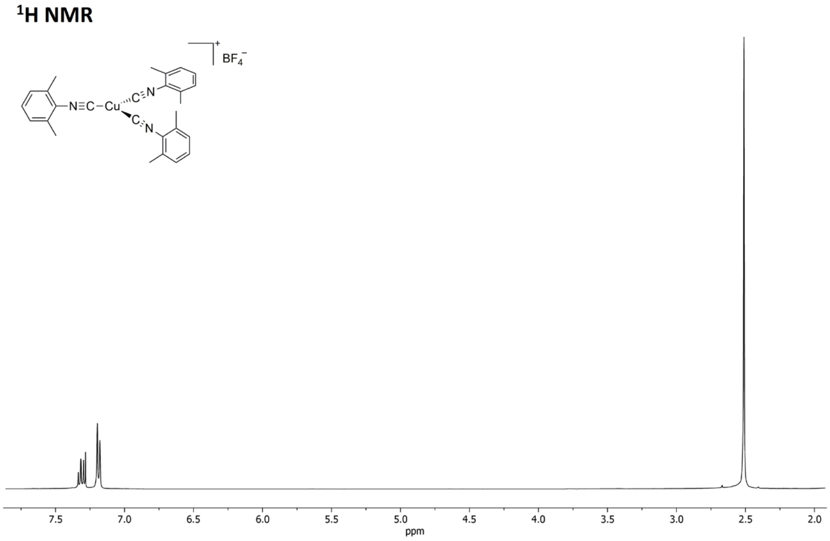

Figure 132. ^{1}H NMR spectrum of [Cu(CNXyl)$_3$][BF$_4$] in CDCl$_3$ at 298 K.

[Cu(CNXyl)$_3$][BF$_4$] was tested towards the copper azide-alkyne cycloaddition (CuAAC) between benzyl azide and phenylacetylene in 1:1 water/methanol solution, and the corresponding 1-benzyl-4-phenyl-1*H*-1,2,3-triazole was prepared in good yields (**T1**, 72%) after 18 hours of reaction time (see Scheme 35).[191] The selectivity towards the 1,4-disubstituted regioisomer was complete and no traces of 1,5 regioisomer were detected. Similar yield was achieved by reducing the reaction time to 6 hours, allowing to set this reaction time as starting point for further optimization experiments. Surprisingly, it was observed that the reaction proceeded faster when no solvent was employed since [Cu(CNXyl)$_3$][BF$_4$] revealed to be soluble in the mixture of azide and alkyne. In absence of solvent, the reaction stopped as the product gradually formed as a white solid. Two hours were sufficient to reach almost quantitative yields of the desired triazole. For comparison, the $CuSO_4\cdot5H_2O$/sodium ascorbate catalytic system under the same experimental conditions afforded 1-benzyl-4-phenyl-1*H*-1,2,3-triazole in 32% yield.

When the catalyst loading was reduced to 0.1 mol% 1-benzyl-4-phenyl-1*H*-1,2,3-triazole was obtained in lower yields after 2 hours, and at least 12 hours were required to reach yield > 90% under these conditions.

Further experiments were carried out in the best reaction conditions, *i.e.* 2 hours reaction time, 1 mol% catalyst loading and solvent-free, to verify the robustness of the optimized catalytic system. Consequently, different azides and terminal alkynes were tested to achieve a wide library of 1,4-disubstituted-1,2,3-triazoles as reported in Scheme 35.

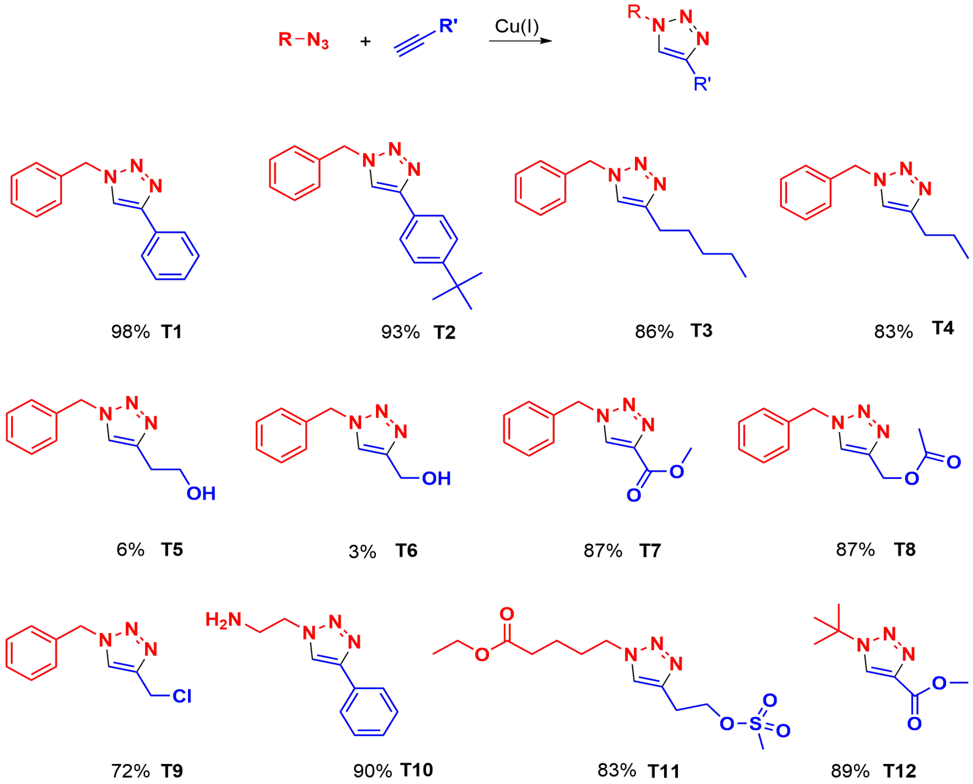

Scheme 35. Triazoles synthesized using [Cu(CNXyl)$_3$][BF$_4$] as catalyst and isolated yields. Reaction conditions: azide = 1 mmol; alkyne = 1.1 mmol; cat. = 1 mol%; r.t., 2 hours.

The presence of a sterically hindered donating group on phenylacetylene and aliphatic alkynes (**T2**-**T4**) did not slow down the reaction and the same performances were maintained. CuAAC failed when alkynes bearing a terminal hydroxyl group were tested (**T5** and **T6**) probably because of coordination of the oxygen atom to the metal centre. A possible explanation is that the hydroxyl-substituted fragments may behave as donor groups towards copper(I) species in the experimental conditions described, thus inhibiting the catalytic activity of the complex. Such an assumption was verified by protection of the -OH moiety with an acetate group allowing to overcome this drawback, as indicated by the high yield of the reaction between benzyl azide and propargyl acetate (**T8**). Additionally, when propargyl chloride was employed, good yields of the corresponding triazole were obtained (72%, **T9**). Different aliphatic azides were also tested, demonstrating that the reaction proceeded with good tolerance towards different functional groups. As a matter of fact, 2-(4-phenyl-1*H*-1,2,3-triazol-1-yl)ethan-1-amine (**T10**) was recovered in excellent yields, despite the fact that amine moieties could display affinity towards copper(I) species, as previously verified for hydroxyl functional groups. Finally, the reaction of ethyl 4-azidopentanoate with but-3-ynyl methanesulfonate and *tert*-butyl azide with propargyl acetate afforded the triazoles **T11** and **T12** (see Scheme 35) with yields above 80%. The activity of the catalyst towards most of the substrates is comparable to similar reports making use of copper(I) catalysts using phosphine ligands and/or amine bases.[192] Finally, the preliminary test carried out with 2-butyne in combination with benzyl azide in neat condition showed no conversion of the substrates, therefore the catalytic study was not further extended to non-terminal alkynes.

The structure of the molecule in a low polar solvent ($\varepsilon = 3.0$) was simulated by means of C-PCM/DFT calculations. The central $\{CuC_3\}$ fragment is roughly superimposable to that determined by X-ray diffraction, as observable in Figure 133. On the other hand, the lack of the intramolecular interactions previously described causes a rotation of the aryl substituents, that are much more perpendicular to the $\{CuC_3\}$ plane with respect to the X-ray structure. The tetrafluoroborate ion is quite close to copper(I), being the shorter Cu---F distance 2.290 Å, but the molecule maintains the trigonal planar arrangement, being the copper(I) only 0.125 Å far from the plane determined by the three coordinated carbon atoms.

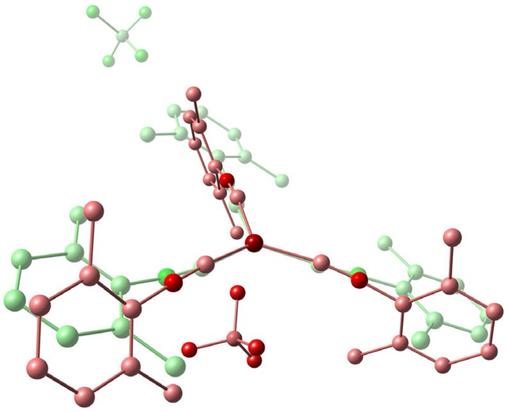

Figure 133. Superimposition of the DFT-optimized (red tones) and X-ray (green tones) structures of $[Cu(CNXyl)_3][BF_4]$.

Since alkynes were used as solvents in most of the catalytic runs described below, the possible complex formed by $[Cu(CNXyl)_3][BF_4]$ with phenylacetylene was computationally investigated. The DFT-optimized structure of $[Cu(CNXyl)_3(HC{\equiv}CPh)][BF_4]$ is reported in Figure 134. The reaction $[Cu(CNXyl)_3][BF_4] + HC{\equiv}CPh \rightarrow [Cu(CNXyl)_3(HC{\equiv}CPh)][BF_4]$ is associated to a negative enthalpy variation equal to -4.6 kcal mol^{-1} but, because of the reduction of molecularity, the estimated Gibbs energy variation is positive, +6.3 kcal mol^{-1}. On the other hand, the high concentration of alkyne in the catalytic runs makes possible the formation in solution of the complex depicted in Figure 134. AIM calculations highlighted the presence of two (3,-1) bond critical points (b.c.p.), connecting the phenylacetylene with copper(I) and the tetrafluoroborate anion. $[Cu(CNXyl)_3(HC{\equiv}CPh)][BF_4]$ is less planar than the precursor, being the Cu(I) centre 0.381 Å far from the plane determined by the isocyanide donor atoms. The H---F interaction is associated to a slight activation of the phenylacetylene C-H bond, longer in the complex (1.089 Å) with respect to the free molecule optimized at the same computational level (1.077 Å). The electron density at (3,-1) C-H b.c.p. decreases upon coordination from 0.279 to 0.274 a.u., and accordingly the potential energy density is less negative (-0.339 a.u. in the complex, -0.343 a.u. in the free phenylacetylene). The (3,-1) C-H b.c.p is closer to the hydrogen atom in the complex (0.332 Å) than in the free molecule (0.368 Å), suggesting an increase of acidity.

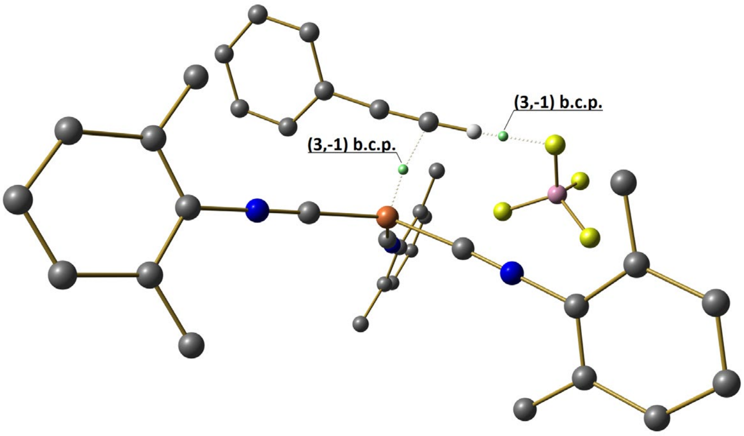

Figure 134. DFT-optimized structure of $[Cu(CNXyl)_3(HC{\equiv}CPh)][BF_4]$. Colour map: Cu, orange; N, blue; C, grey; F, yellow; B, pink. Selected (3,-1) b.c.p. are shown in green. Electron density (ρ) and potential energy density (V) values at b.c.p. (a.u.): Cu---C, ρ = 0.030, V = -0.029; H---F, ρ = 0.026, V = -0.021. Selected computed bond lengths (Å): Cu-$C_{isocyanide}$, 1.966, 1.983, 1.989; Cu-C_{alkyne}, 2.491, 2.652; H---F, 1.891; C≡N, 1.163, 1.164, 1.165. Selected computed angles (°): C-Cu-C, 112.0, 115.3, 122.2.

This study opened up a collaboration with the University of Alcalá to investigate similar compounds towards CuAAC. The complexes are reported in Scheme 36.

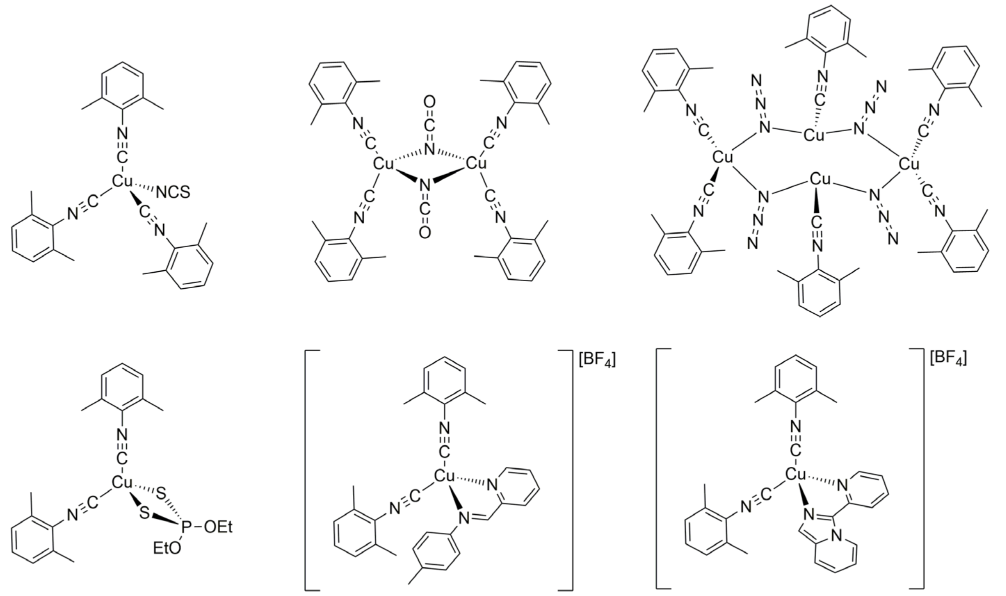

Scheme 36. Isocyanide copper(I) complexes tested for CuAAC.

The investigation began testing all the complexes for the CuAAC between benzyl azide and phenyl acetylene using 5% mol of catalyst in methanol. $[\mathrm{Cu_4(\mu{-}N_3)_4(CNXyl)_6}]$ required a 1:1 solution of MeOH/CH_2Cl_2 due to its insolubility in alcohols. Only $[\mathrm{Cu_4(\mu{-}N_3)_4(CNXyl)_6}]$ and $[\mathrm{Cu(\mu{-}NCO)(CNXyl)_2}]_2$ revealed to be catalytically active. After 6 hours, yields respectively equal to 88% and 64% were detected for the corresponding triazole. Therefore, the catalyst loading was lowered to 0.5% mol, obtaining yields equal to 68% and 61% respectively. In order to further increase the yield, the reaction was performed at 50°C determining after 24 hours yields of 99% for the former and of 98% for the latter. The catalyst loading was reduced to 0.05% mol to test the activity of both the catalysts, affording 25% and 6% of yield for the corresponding triazole.

Since $[\mathrm{Cu_4(\mu{-}N_3)_4(CNXyl)_6}]$ appeared to have a better catalytic activity, the complex was tested also with 0.1% mol affording 43% yield. Instead, reducing the reaction time to 18 hours, 1-benzyl-4-phenyl-1*H*-1,2,3-triazole was obtained in 86% yield. $[\mathrm{Cu_4(\mu{-}N_3)_4(CNXyl)_6}]$ was investigated in combination with other azides and alkynes at the best reaction conditions, *i.e.* 50°C for 24 hours and with 0.5% of catalyst loading. The triazoles obtained and their yields are summarized in Scheme 37.

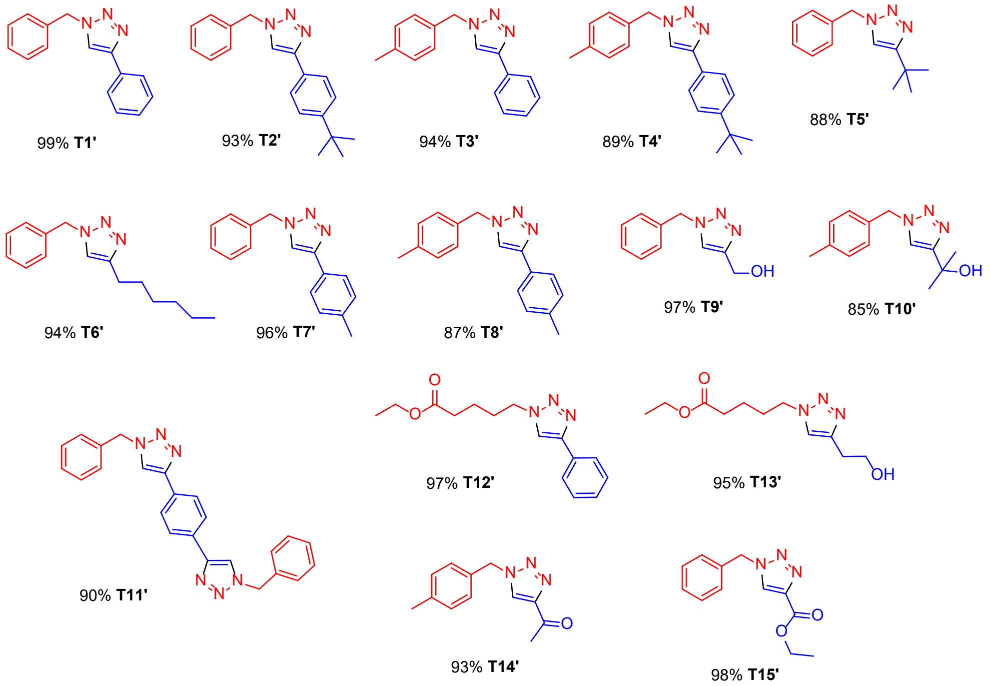

Scheme 37. Triazoles synthesized using $[Cu_4(\mu\text{–}N_3)_4(CNXyl)_6]$ as catalyst and isolated yields. Reaction conditions: azide = 1 mmol; alkyne = 1.1 mmol; cat. = 0.5 mol%; 1:1 MeOH/CH_2Cl_2, 50°C, 24 hours.

Similarly to what previously observed for the $[Cu(CNXyl)_3][BF_4]$ catalyst, the presence of hindered groups on both aromatic and aliphatic alkynes did not affect the reaction performances (see for instance **T1'-T4'**; **T5'-T8'**; **T11'**). Instead, triazoles were obtained in good yields using alkynes with terminal -OH groups (**T9'**, **T10'** and **T15'**). Besides benzyl azide and *p*-methyl benzyl azide, ethyl 5-azidopentanoate was used as aliphatic azide affording the corresponding triazoles **T12'** and **T13'** in yields above 95%. The catalytic system had good tolerance also towards carbonyl groups, as stated by the high yields of **T14'** and **T15'**. On the other hand, the use of substrates containing $-NH_2$, $-SiMe_3$ or S=O, such as 2-azidoethan-1-amine, trimethylsilylacetylene and but-3-yn-1-yl methanesulfonate, determined the rapid decomposition of the catalyst without the formation of any product. On the contrary, $[Cu(CNXyl)_3][BF_4]$ exhibited good catalytic performances in the presence of these groups. $[Cu_4(\mu\text{–}N_3)_4(CNXyl)_6]$ did not catalyse the CuAAC in presence of internal alkynes, such as 1-phenyl-1-propyne, neither increasing the catalyst loading to 5% mol nor the temperature to 80°C.

It is worth noting that only few examples of azido copper(I) complexes were reported in literature.[193] The coordinated N_3^- determined peculiar reactivity in the case of $[CuN_3(IPr)]$ where IPr = *N*,*N*'-bis[(2,6-(di-isopropyl)phenyl)]imidazol-2-ylidene).[193f] Therefore, I decided to test the reactivity of $[Cu_4(\mu\text{–}N_3)_4(CNXyl)_6]$. First of all, the possibility to perform an intramolecular CuAAC by adding a stoichiometric amount of phenylacetylene was checked. Similar to what was observed for [CuN$_3$(IPr)], no reaction occurred even after days and at 50°C. Instead, using an internal alkyne such as dimethyl acetylenedicarboxylate (DMAD) the corresponding triazolate-complex formed, as observed in the ^{1}H NMR reported in Figure 135. The -CH$_3$ groups of DMAD are characterized by a singlet at 3.87 ppm integrating 6 protons. Once added to [Cu$_4$(μ–N$_3$)$_4$(CNXyl)$_6$] a second singlet appear at 3.91 ppm almost immediately. The signal related to free DMAD disappears overnight.

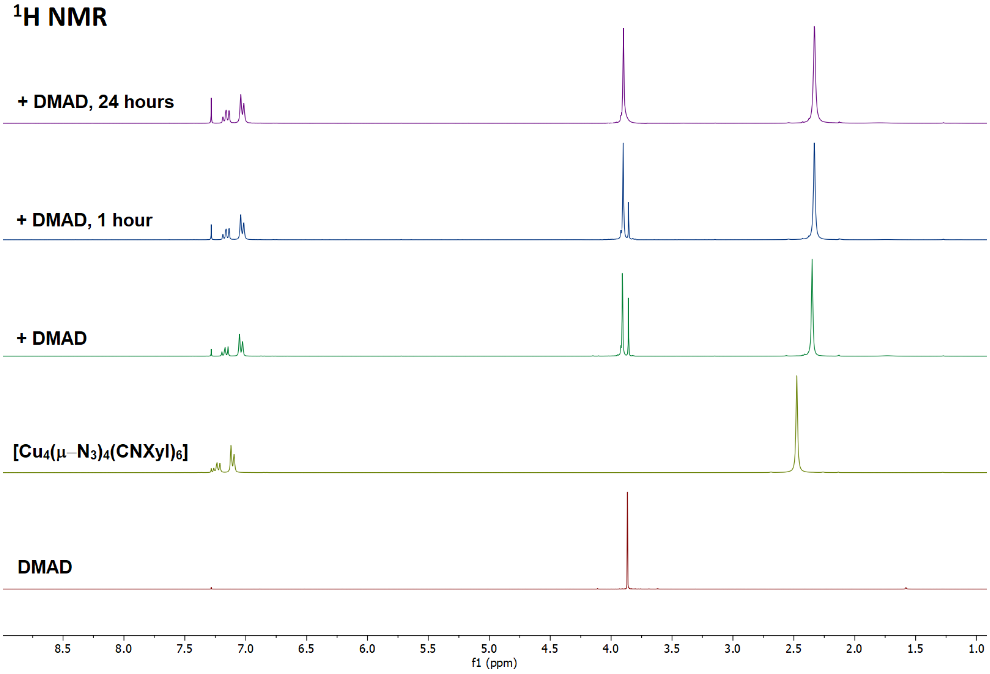

Figure 135. ^{1}H NMR spectra of DMAD, [Cu$_4$(μ–N$_3$)$_4$(CNXyl)$_6$] and after the addition of DMAD (CDCl$_3$, 298 K).

1-benzyl-4-phenyl-1*H*-1,2,3-triazole was obtained in a two-step reaction. A stoichiometric amount of benzyl bromide (BzBr) was added to an NMR tube containing a stoichiometric amount of [Cu$_4$(μ–N$_3$)$_4$(CNXyl)$_6$] and then reacted for two days at room temperature to afford the corresponding benzyl azide derivative. As observable in the ^{1}H NMR reported in Figure 136, after 24 hours from the addition of BzBr a singlet related to the secondary carbons around 4.36 ppm can be detected. For benzyl bromide the same signal is present at 4.52 ppm. After 48 hours it was possible to observe the complete disappearance of the reactant.

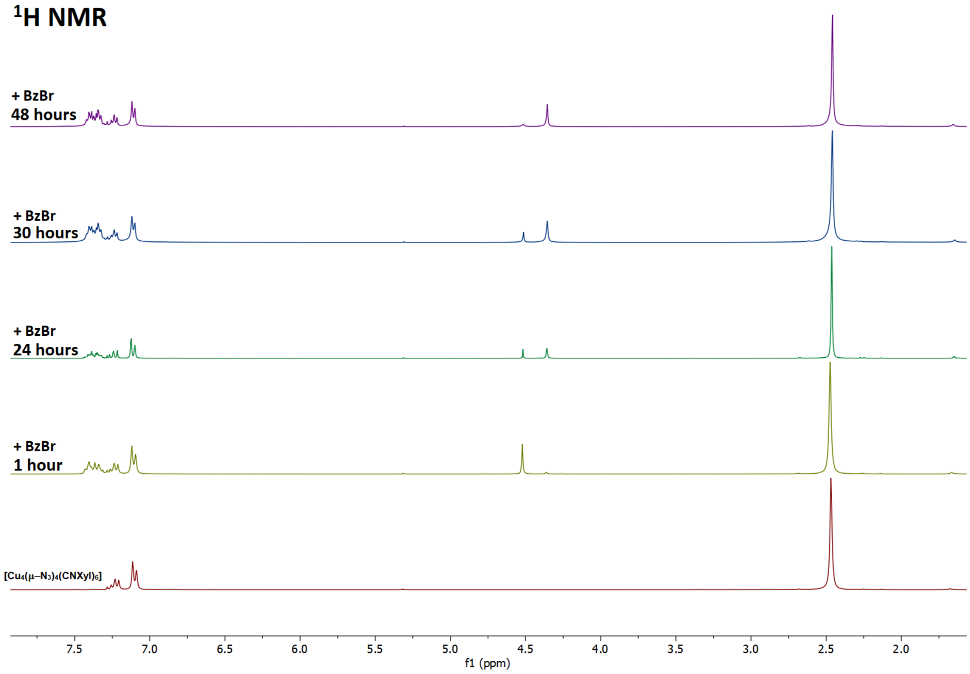

Figure 136. ^{1}H NMR spectra [$Cu_4(\mu{-}N_3)_4(CNXyl)_6$] and after the addition of BzBr ($CDCl_3$, 298 K).

Then phenylacetylene (PhCCH) was added in ratio 1:1 with respect to the copper(I) centre determining the formation of the corresponding triazole. As observable in Figure 137, the singlets at 5.61 ppm and at 7.74 ppm are diagnostic for the formation of the triazole. In fact, the former integrates two protons and is related to the -CH_2 of the benzyl moiety, while the latter is associated with the -CH proton of the five-membered triazole ring.

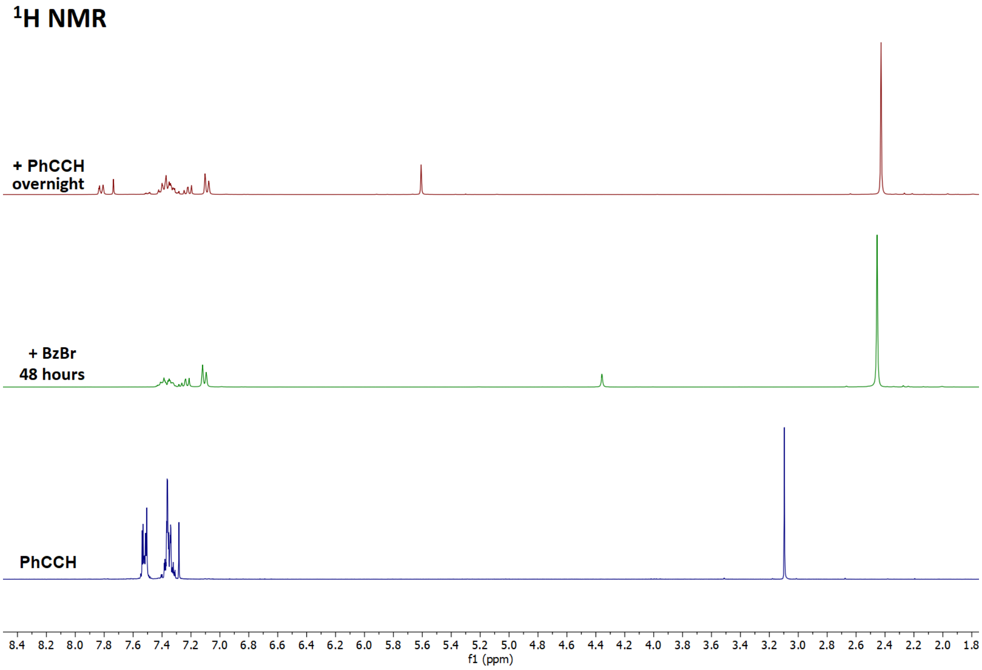

Figure 137. ^{1}H NMR spectra of PhCCH, [$Cu_4(\mu{-}N_3)_4(CNXyl)_6$]+BzBr and after the addition of PhCCH ($CDCl_3$, 298 K).

4.2 Benzothiadiazole-based organic fluorophores

2,3,1-benzothiadiazole (BTD) was functionalized in order to obtain *N*,*N*-dimethyl-4-amino-2,1,3-benzothiadiazole (BTD^{NMe2}) with the aim of coordinating it to copper(I) or zinc(II) metal centres. The synthetic route here proposed for BTD^{NMe2} starts with the nitration of the 2,1,3-benzothiadiazole heterocycle, followed by reduction of the nitro group and subsequent methylation with CH_3I. As observable from the ^1H, ^{13}C and ^1H-^{13}C HSQC NMR spectra reported in Figure 138, the methyl groups are associated with a singlet at 3.29 ppm (^{13}C resonance at 42.59 ppm), while the aromatic protons of the heterocycle resonate in the 7.50-6.50 range (^{13}C resonances at 130.73, 111.13 and 108.85 ppm). The signals attributable to the three ipso-carbons can be detected respectively at 144.43, 149.28 and 156.90 ppm.

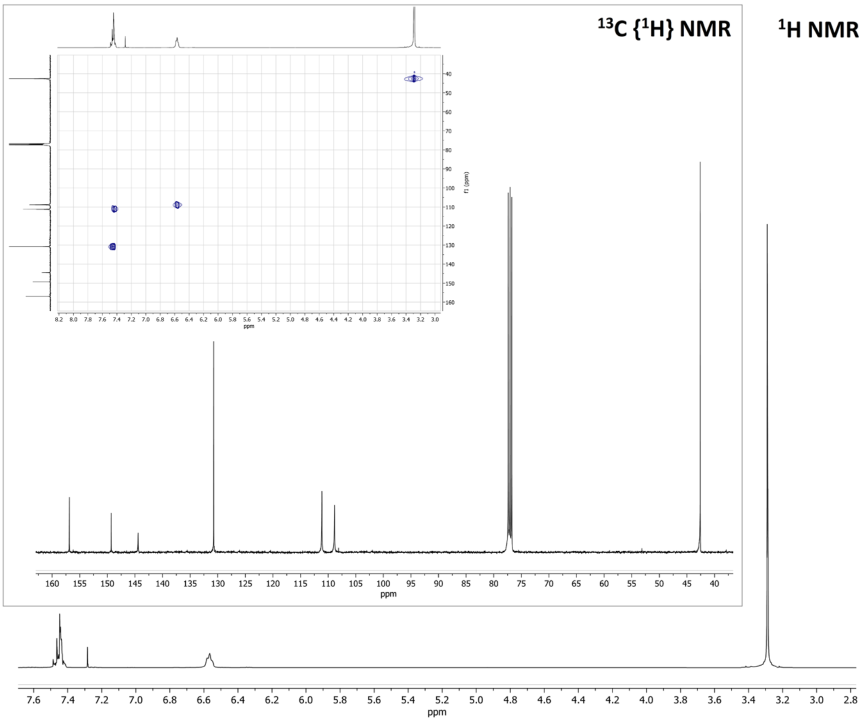

Figure 138. ^1H NMR spectrum of BTD^{NMe2}. Inset: ^{13}C NMR and ^1H-^{13}C HSQC spectra in $CDCl_3$ at 298 K.

Unfortunately, in both cases the corresponding copper(I) and zinc(II) derivatives were intensely coloured as powders but did not exhibit any luminescent property, probably because of concentration quenching. Instead, the compound isolated as a dark red oil exhibited intriguing luminescent properties once dissolved in common organic solvents (see Figure 139). The evident solvatochromism was investigated considering four solvents characterized by different dielectric constants ε (n-hexane, dichloromethane, acetone, and acetonitrile). The absorption and emission spectra are shown in Figure 139.

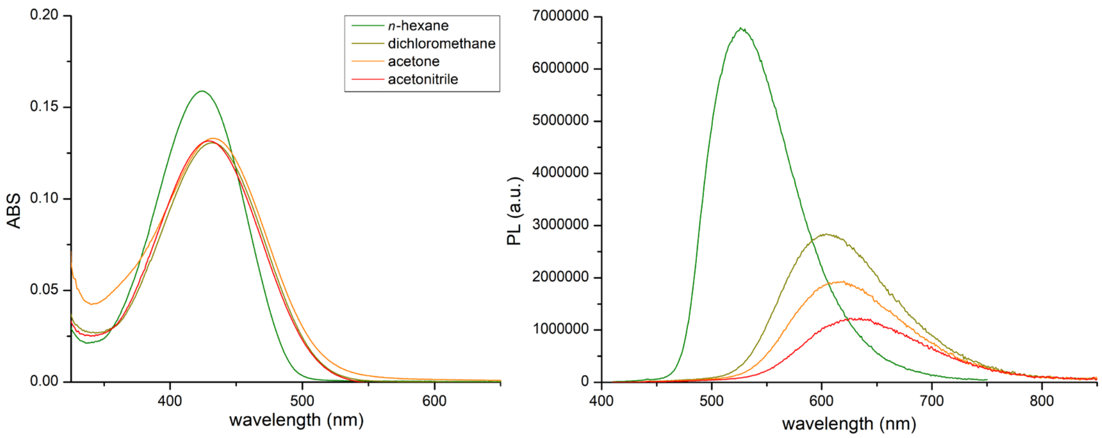

Figure 139. Absorption (left) and emission (right) spectra of $5\cdot10^{-5}$ M solutions of BTD^{NMe2} in different solvents recorded at room temperature. Inset: picture of the solutions under UV light ($\lambda_{excitation}$ = 365 nm).

Selected properties of the solvents, including the orientation polarizability Δf calculated according to Equation (1), are summarized in Table 2. The table also reports absorption and emission maxima of BTD^{NMe2}, Stokes shifts $\tilde{u}_A-\tilde{u}_F$ and Φ_f values, calculated accordingly to Equation (2). Fluorescence quantum yields Φ_f of $5\cdot10^{-5}$ M solutions were calculated using $5\cdot10^{-5}$ M anthracene in ethanol as standard on the basis of Equation (1),[194] where $\Phi_{f,std}$ is the quantum yield of anthracene in ethanol (0.27), F and F_{std} are respectively the areas under the fluorescence emission bands of the sample and of the standard, A and A_{std} are respectively the absorbance values of sample and standard at the excitation wavelength, n is the refractive index of the solvent used for the sample and n_{std} is the refractive index of ethanol.

$$\Delta f = (\varepsilon - 1)(2\varepsilon + 1)^{-1} - (n^2 - 1)(2n^2 + 1)^{-1} \quad (1)$$

$$\Phi_f = \Phi_{f,std}\,(F\,A_{std}\,n^2)(F_{std}\,A\,n_{std}^2)^{-1} \quad (2)$$

As observable both in Figure 139 and in Table 2, the solvents characterized by higher ε values determine a bathochromic shift of the emission maxima in solution together with an increase in the Stokes shift, which varies from 4560 cm^{-1} in hexane to 7450 cm^{-1} in acetonitrile. The greatest variations occur on changing the solvent from hexane to dichloromethane, with a shift of the emission maximum from 526 to 604 nm and a consequent increase of the Stokes shift from 4560 cm^{-1} to 6610 cm^{-1}.

Table 2. Fluorescence data of BTD^{NMe2} in different solvents.

Solvent	ε	**n**	**ABS max (nm)[a]**	**PL max (nm)[b]**	$\tilde{\upsilon}_A$-$\tilde{\upsilon}_F$ **(cm^{-1})**	Φ_F **(%)[c]**	**Δf**
n-hexane	1.9	1.375	424	526	4560	52	0.001
Dichloromethane	8.9	1.424	432	604	6610	41	0.217
Acetone	20.7	1.359	433	616	6870	23	0.284
Acetonitrile	37.5	1.479	430	630	7450	16	0.305

[a] 298 K. [b] $\lambda_{excitation}$ = 390 nm, 298 K. [c] Data obtained using a solution of anthracene in ethanol as standard (Φ_f = 27%).[195]

The CIE 1931 chromaticity coordinates are reported in the diagram in Figure 140, where the change of emission is observable from yellowish-green to reddish-orange on increasing the ε value. The colour purity of the emission of BTD^{NMe2} in hexane is 0.79, while it is almost unitary for the other solvents. The luminescent properties of BTD^{NMe2} were maintained after encapsulation in PMMA matrix. The emission falls in the orange region of the CIE diagram with unitary colour purity, as observable in the CIE 1931 chromaticity diagram and in the picture reported as inset in Figure 140.

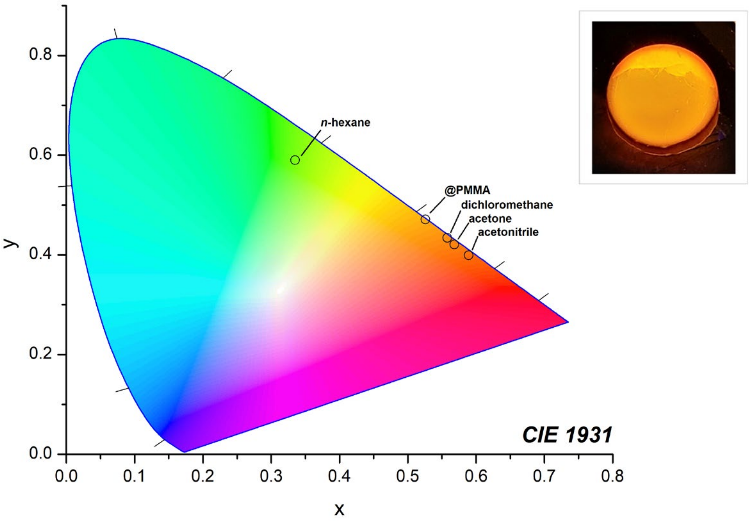

Figure 140. CIE 1931 chromaticity diagram of BTD^{NMe2} in different solvents and in PMMA (*n*-hexane: x = 0.335, y = 0.590; dichloromethane: x = 0.558, y = 0.434; acetone: x = 0.561, y = 0.421; acetonitrile: x = 0.589, y = 0.399; @PMMA: x = 0.526, y = 0.471). Inset: BTD^{NMe2}@PMMA excited at 365 nm.

The increase of the dielectric constant also caused a decrease in the fluorescence quantum yield, from 52% (hexane) to 16% (acetonitrile), probably attributable to the relative increase of non-radiative decay because of the red-shift of the emission.

As observable in Figure 141, the Stokes shift increases roughly linearly with the orientation polarizability Δf (Pearson's coefficient R = 0.99), accordingly to the Lippert–Mataga equation (3).[196] h is Planck's constant, c is the speed of light in a vacuum, as is the radius of the cavity in which the molecule resides, and μ_e and μ_g are the dipole moments of the excited and ground state, respectively. The plot in Figure 141 confirms that the solvatochromic effect is related to specific solute–solvent interactions that involve the polarization.[197]

$$\tilde{\upsilon}_A - \tilde{\upsilon}_F = 2\, h^{-1} c^{-1} (\mu_e - \mu_g)^2\, a_s^{-3}\, \Delta f + constant \qquad (3)$$

The radius obtained from the C-PCM/DFT optimization of the structure of BTD^{NMe2} is 3.92 Å. Based on Equation (3), the increase of dipole moment from the ground to the excited state is about 7 D.

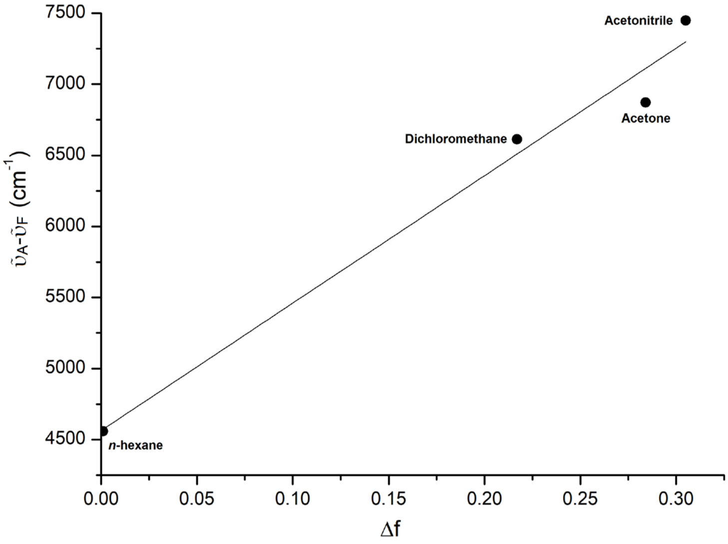

Figure 141. Lippert-Mataga plot.

The photoluminescent properties were justified by means of electrochemical measurements and DFT calculations. As observable from the square wave voltammetry reported in Figure 142, the HOMO–LUMO gap can be estimated at around 2.5 eV, considering the irreversible oxidation and reduction processes. Such an outcome is in agreement with the onset of the absorption spectrum using acetonitrile as solvent. The TD-DFT calculations confirm that the lowest energy transition occurs between HOMO and LUMO, which are the π and π* frontier molecular orbitals mostly localized on the benzothiadiazole skeleton, with a contribution from the molecular orbitals of the *N*,*N*-dimethylamino moiety (Figure 142).

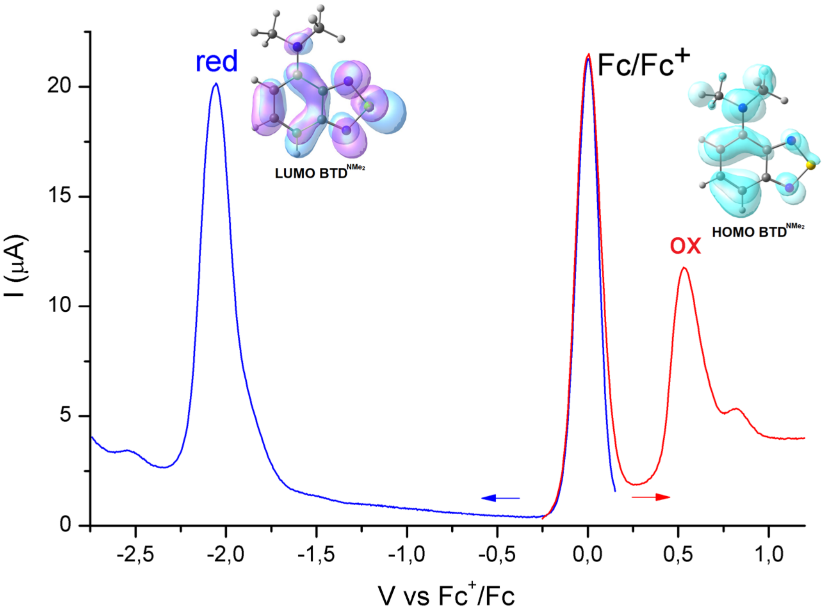

Figure 142. Square wave voltammetry of BTD^{NMe2} ($CH_3CN/LiClO_4$, ferrocene as internal reference, blue line: reduction, red line: oxidation) and frontier molecular orbitals (surface isovalue = 0.003 a.u.). ωB97X/def2-TZVP calculations.

4.3 Palladium(II) complexes with Schiff bases derived from BTD^{NH2}

2,2’:6’,2”-terpyridine (terpy) was deeply investigated as polydentate ligand for d^8 transition metal elements, such as platinum(II) and palladium(II).[198] The corresponding complexes were exploited for a wide variety of applications, that spread from catalysis to supramolecular chemistry.[199] Other N-donors able to act as tridentate ligands and characterized by extended π-conjugated systems are Schiff bases that can be obtained by metal-assisted condensation reaction in presence of *ortho*-substituted aldehydo- or keto-pyridines. The research group previously reported palladium(II) chloro- and methylcomplexes starting from 8-aminoquinoline.[200] The similarity with 4-amino-2,1,3-benzothiadiazole (BTD^{NH2}) prompted me to try to use this amine to prepare the corresponding Schiff base by metal-assisted condensation.

Preliminary tests to verify the reactivity of BTD^{NH2} towards pyridine-2-carboxaldehyde were conducted in CD_3OD. The related ^{1}H NMR spectra are reported in Figure 143. Differently from 8-aminoquinoline, the corresponding hemiaminal did not form immediately after the addition of the two reagents.[200a] However, after reacting overnight, new resonances could be detected. In particular, the singlet at 6.03 ppm is diagnostic for the formation of the hemiaminal (see Figure 143d). These preliminary tests underline how BTD^{NH2} is less reactive towards pyridine-2-carboxaldehyde with respect to 8-aminoquinoline, probably because of the lower nucleophilicity of the NH_2 group associated with the presence of more electron withdrawing groups in the heterocycle. Ignoring the extremely weak resonance at 9.31 ppm, the corresponding Schiff base was never detected, as observable in Figure 143d.

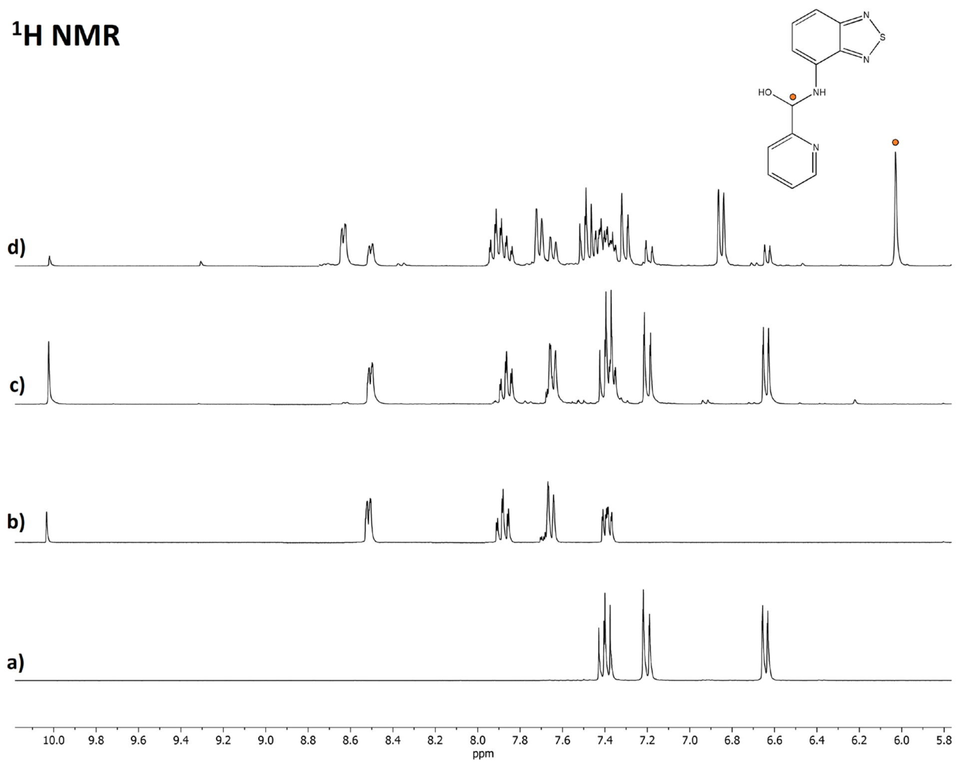

Figure 143. ^{1}H NMR spectra in CD_3OD at 298 K of: a) BTD^{NH2}; b) pyridin-2-carboxaldehyde; c) BTD^{NH2}+pyridin-2-carboxaldehyde after mixing; d) BTD^{NH2}+pyridin-2-carboxaldehyde after 24 hours.

The corresponding Schiff base *N*-((pyridin-2-yl)methylene)-4-amino-2,1,3-benzothiadiazole (BTD^{NPy}) was synthesized after prolonged refluxing in dichloromethane in presence of an excess of 3 Å molecular sieves. Once isolated, the product revealed to be unstable, rapidly decomposing at room temperature.

The first attempts to prepare palladium(II) complexes with BTD^{NPy} were conducted by reacting BTD^{NH2} and pyridine-2-carboxaldehyde in methanol at room temperature and in presence of the chosen precursor. Using [$PdCl_2$(COD)], the corresponding [$PdCl_2$(BTD^{NPy})] rapidly precipitated from the solution. The reaction was improved in terms of yield and purity of the product using the same conditions described above to prepare BTD^{NPy} and then adding this solution to the chosen precursor after filtration.

[PdCl$_2$(BTD^{NPy})] is scarcely soluble in polar organic solvents. In the ^{1}H NMR spectra recorded in CD$_3$NO$_2$ (see Figure 144) the resonances attributable to both the heterocycles can be detected together with a singlet at 8.80 ppm related to the imine fragment. The signal observable at 9.28 is related to the proton in *ortho*-position with respect to the nitrogen atom of the pyridine fragment, as further confirmed by the low $^3J_{HH}$ coupling equal to 5.3 Hz.

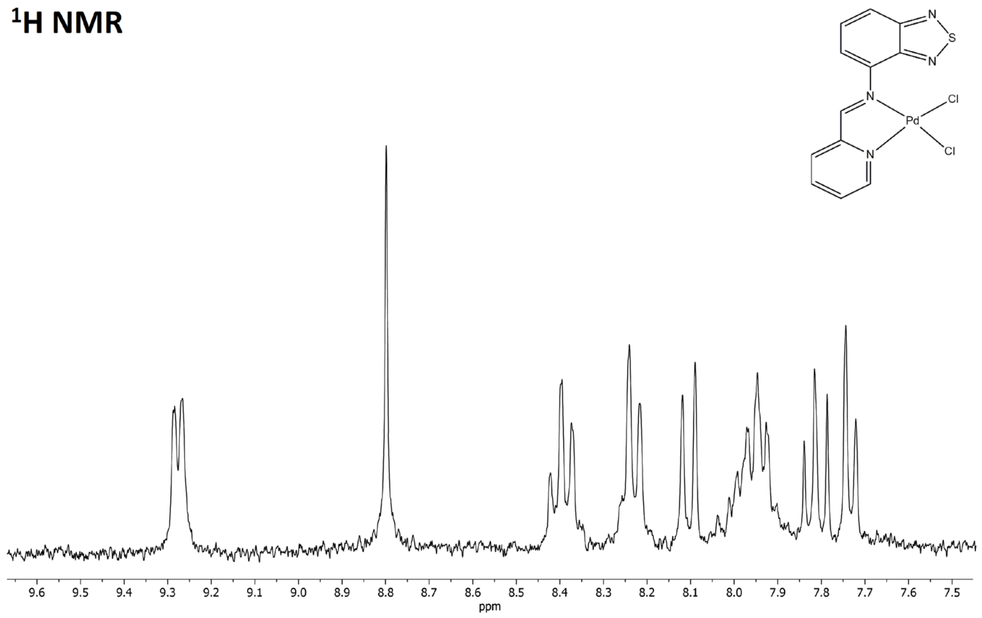

Figure 144. ^{1}H NMR spectrum of [PdCl$_2$(BTD^{NPy})] in CD$_3$NO$_2$ at 298 K.

In the case of 8-aminoquinoline, the product isolated was a cationic palladium(II) complex where the Schiff base acted as tridentate ligand. Instead, DMSO solutions of [PdCl$_2$(BTD^{NPy})] revealed to be non-conductive. The formation of a neutral complex was further confirmed by the reaction with AgClO$_4$, that did not cause the precipitation of AgCl under mild conditions, as expected for complexes having Cl$^-$ as counterion.

The same synthetic approach was extended to [PdClMe(COD)]. In this case, the metal-assisted condensation reaction did not lead to the expected product. Instead, [PdClMe(BTD^{NPy})] was isolated after the *in situ* synthesis of the Schiff base BTD^{NPy}. Similar to [PdCl$_2$(BTD^{NPy})], the product is scarcely soluble in polar organic solvents. The ^{1}H NMR spectrum recorded in DMSO-d$_6$ at 298 K (see Figure 145) is characterized by eight resonances in the aromatic region. Three of them can be attributed to the BTD fragment, while four of the remaining are related to the pyridine moiety and the last one corresponds to the imine proton. The signals are broadened, in particular the ones related to pyridine and imine groups. Surprisingly, at higher fields two broad resonances related to the coordinated methyl group can be detected. Recording the ^{1}H NMR spectrum at 318 K determined sharper signals for the BTD and the imine groups, and larger for the pyridine fragment. The two signals in the aliphatic region related to Pd-Me are almost fused in one resonance. The full merging can be achieved collecting the ^{1}H NMR spectrum at 338 K, but at this temperature the signals related to the pyridine fragment are too large to be detected, as observable in Figure 145. This peculiar behaviour in solution can be tentatively attributed to association/dissociation equilibria between the N-donor ligand and the coordinating DMSO. The presence of different isomers is ruled out due to the presence of only one set of signals related to the Schiff base BTD^{NPy} and also owing to the temperature-dependent reversibility of this process. Similar to what previously observed for [PdCl$_2$(BTD^{NPy})], DMSO solutions of [PdClMe(BTD^{NPy})] revealed to be non-conductive. In both the cases, the formation of the Schiff base was further confirmed by the IR spectra where no signal related to aldehyde $\nu_{C=O}$ could be detected.

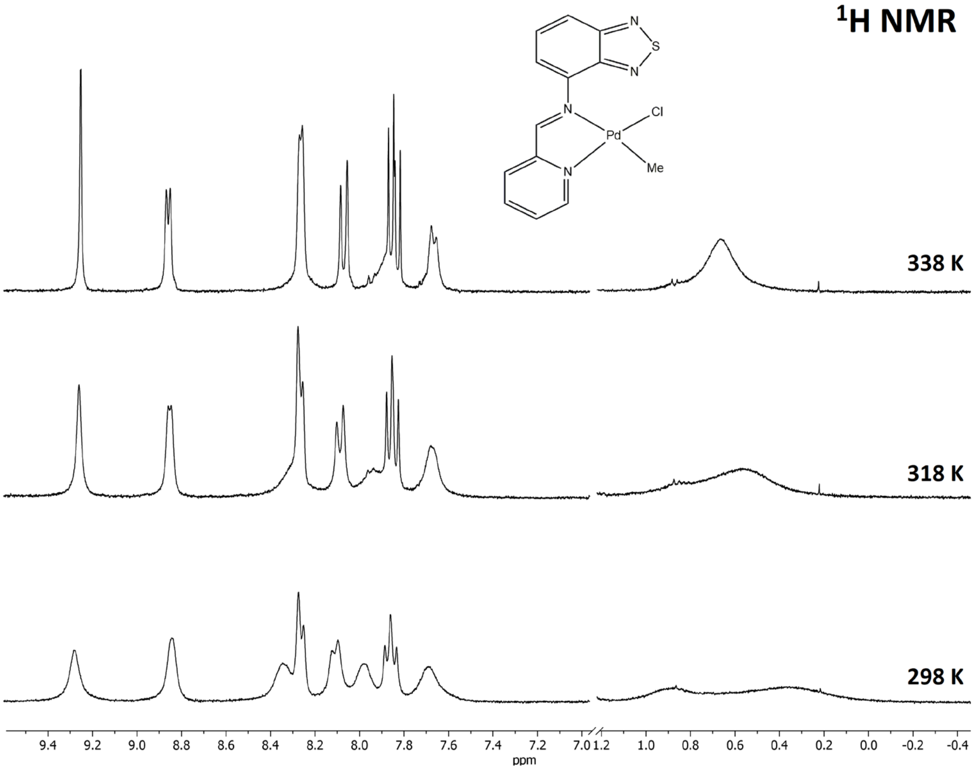

Figure 145. ^{1}H NMR spectrum of [PdClMe(BTD^{NPy})] in DMSO-d$_6$ at variable temperature.

The reaction between [PdClMe(BTD^{NPy})] and CO (1 atm) at room temperature afforded the corresponding [Pd(COMe)Cl(BTD^{NPy})], as highlighted in the ^{1}H NMR and IR spectra reported in Figures 146 and 147. In particular, the presence of a singlet at

2.71 ppm related to the methyl group and the $\nu_{C=O}$ at 1697 cm^{-1} is diagnostic for the insertion of carbon monoxide in the Pd-Me bond. The aromatic region in the ^{1}H NMR spectrum reported in Figure 146 is complicated by the broad signals associated to pyridine and imine fragments, due to fluxional behaviour in solution. [Pd(COMe)Cl(BTD^{NPy})] revealed to be soluble in common organic solvent and conductivity measurements confirmed the formation of a neutral species.

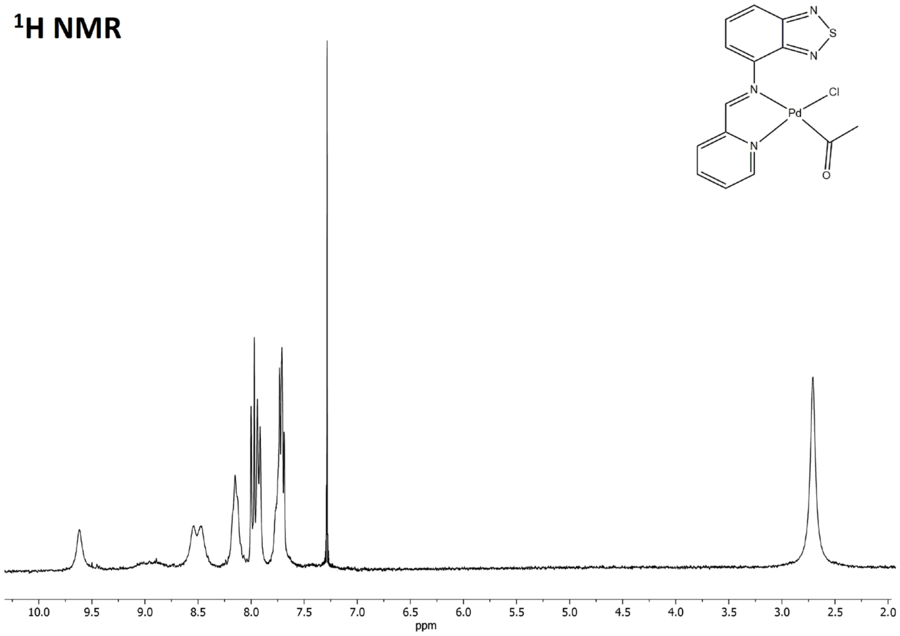

Figure 146. ^{1}H NMR spectra of [Pd(COMe)Cl(BTD^{NPy})] in $CDCl_3$ at 298 K.

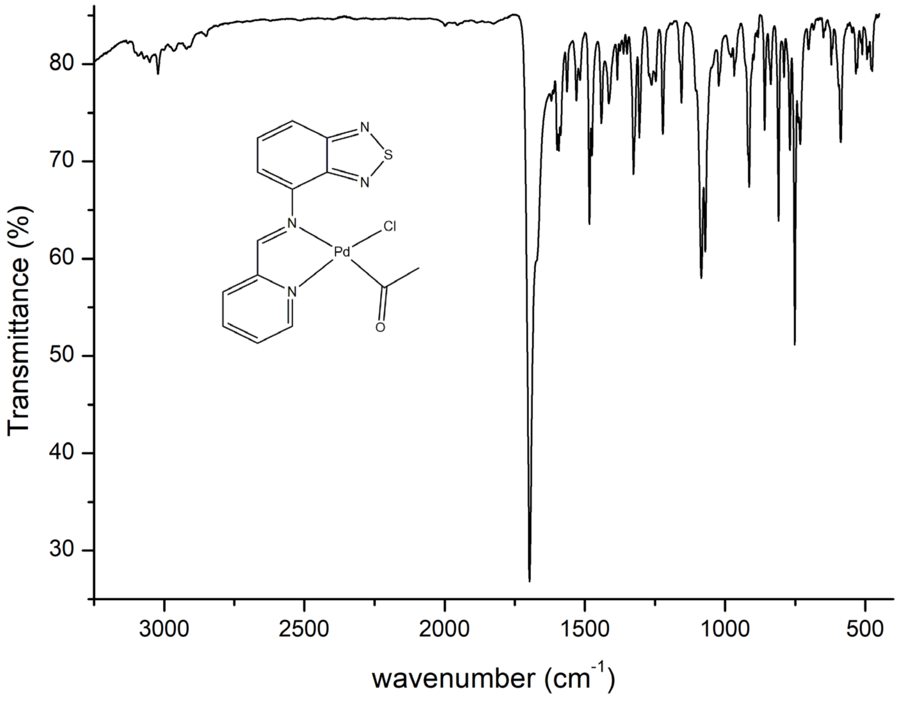

Figure 147. IR spectra of [Pd(COMe)Cl(BTD^{NPy})] in KBr pellets.

Thanks to the increased solubility, it was possible to obtain the X-ray structure of [Pd(COMe)Cl(BTD^{NPy})] reported in Figure 148. Crystals suitable for X-ray diffraction were collected by slow evaporation of dichloromethane/diethyl ether solutions. Crystal data and structure refinement are collected in Table A22. Selected bond lengths and angles are shown in Table B22.

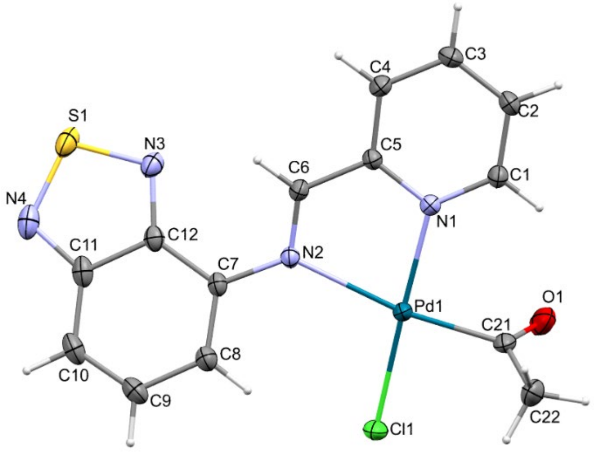

Figure 148. X-ray structure of [Pd(COMe)Cl(BTD^{NPy})].

Following the results on similar palladium(II) chloro-complexes,[201] catalytic tests were conducted on the three complexes for the palladium-catalyzed methoxycarboxylation reaction of iodobenzene to methyl benzoate, as depicted in Scheme 38.

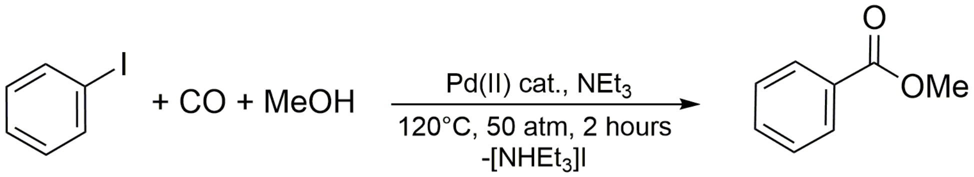

Scheme 38. Palladium-catalyzed methoxycarboxylation of iodobenzene.

The complexes appeared to be active towards this reaction with conversions above 97% in all the cases. The results in terms of conversion and turn-over number (TON, mol ester/mol catalyst) are summarized in Table 3 and compared with the previously reported [Pd(OAc)$_2$] (OAc = acetate), [Pd(OAc)$_2$(phen)] (phen = 1,10-phenantroline) and [Pd(OAc)$_2$(dppp)] [dppp = 1,3-bis(diphenylphosphino)propane]. The three complexes showed closely similar conversion and TON values, respectively comprised between 97% and 100% and between 356 and 379, this suggesting the formation of the same catalytically active species in the reaction mixture. The conversions are close to the 100% obtained for [Pd(OAc)$_2$], but with higher TON values, in line with that obtained for another complex with a N-donor chelate in the coordination sphere, [Pd(OAc)$_2$(phen)]. The TON values are however lower than that obtained for the phosphine-complex [Pd(OAc)$_2$(dppp)].[201]

Table 3. Conversion (mol%) and TON of palladium(II) complexes.

Catalyst	**Conversion, mol%**	**TON**
[Pd(OAc)$_2$]	100	194
[Pd(OAc)$_2$(phen)]	98.0	351
[Pd(OAc)$_2$(dppp)]	99.0	566
[PdCl$_2$(BTD^{NPy})]	98.5	356
[PdClMe(BTD^{NPy})]	100	372
[Pd(COMe)Cl(BTD^{NPy})]	97.0	379

5 Conclusions and future outlooks

The luminescent manganese(II) complexes synthesized during my PhD helped to rationalize how the presence of extended π-conjugated systems in the [O=P]-donors can help to overcome the limited direct excitation of the metal centre. However, in some cases dual emission and wavelength-dependent luminescence were observed when low energy triplet emitting states of the coordinated ligands were involved. Instead, the presence of {N-O} fragments determined the quenching of the $^4T_1(^4G) \rightarrow {}^6A_1(^6S)$ transition also in mixed [N-O,P=O]-ligands. Further studies will be conducted on ligands with aliphatic {N-O} fragments in order to definitely confirm this statement.

As concerns luminescent copper(I) complexes, the azole-based ligands considered afforded several luminescent derivatives. In particular, 2,1,3-benzothiadiazole (BTD) determined a general enhancement of the emissive features both in terms of quantum yields and excited state lifetimes. Additional research will involve the functionalization of this heterocycle to afford chelating N-donor ligands e.g., Schiff bases. Moreover, the sulphur atom in the azole skeleton will be substituted with the heavier selenium to prepare the corresponding 2,1,3-benzoselenadiazole to increase furthermore the spin-orbit coupling and thus the intersystem crossing.

Although the investigation here presented is preliminary and needs to be examined more in depth, it is possible to conclude that [O=P]-donors with well-suited substituents can be efficiently used as ligands for the preparation of luminescent zinc(II) complexes. The widely recognized photophysical properties[202] of pentavalent phosphorous derivatives appeared to be enhanced once coordinated to zinc(II). All these features make luminescent zinc(II) complexes suitable candidates to be applied for third-generation OLEDs.[75] Possible future outlooks involve the extension of the study to other [O=P]-donors and also to ligands based on the {N-O} or {N-O,P=O} fragments.

Finally, another donor fragment electronically related to those here described is the {RN=P} one, scarcely considered for the preparation of luminescent compounds. Ligand based on this donor moiety will be synthesized and reacted with all the metal centres described above, trying to prepare new luminescent coordination compounds.

6 Bibliography

1 (a) M. Gaft, R. Reisfeld, G. Panczer, *Modern Luminescence Spectroscopy of Minerals and Materials*, 2nd ed., Springer, Heidelberg, 2015. (b) A. Harriman, *Coord. Chem. Rev.* **28** (1979) 147.

2 N.A.P. Kane-Maguire, *Top. Curr. Chem.* **280** (2007) 37.

3 J.-C.G. Bünzli, *Chem. Rev.* **110** (2010) 2729.

4 J.P. Leonard, C.B. Nolan, F. Stomeo, T. Gunnlaugsson, *Top. Curr. Chem.* **281** (2007) 1.

5 (a) L. Pereira, *Organic Light-Emitting Diodes. The Use of Rare-Earth and Transition Metals*, CRC Press, Boca Raton, 2012. (b) H. Xu, R. Chen, Q. Sun, W. Lai, Q. Su, W. Huang, X. Liu, *Chem. Soc. Rev.* **43** (2014) 3259. (c) V.W.W. Yam, K.M.C. Wong, *Chem. Commun.* **47** (2011) 11579. (d) P.-T. Chou, Y. Chi, *Chem. Eur. J.* **13** (2007) 380. (e) W.-P. To, Q. Wan, G.S.M. Tong, C.-M. Che, *Trends in Chemistry* **2** (2020) 796.

6 (a) Y. Yue, T. Grusenmeyer, Z. Ma, P. Zhang, R.H. Schmehl, D.N. Beratan, I.V. Rubtsov, *J. Phys. Chem. A* **118** (2014) 10407. (b) V.W.W. Yam, K.K.W. Lo, *Chem. Soc. Rev.* **28** (1999) 323. (c) V.W.W. Yam, A.K.W. Chan, E.Y.H. Hong, *Nat. Rev. Chem.* **4** (2020) 528.

7 P. Atkins, J. De Paola, *Physical Chemistry*, 8th ed., OUP Oxford, 2006.

8 (a) P. Chen, T.J. Meyer, *Chem. Rev.* **98** (1998) 1439. (b) A. Juris, V. Balzani, F. Barigelletti, S. Campagna, P. Belser, A. von Zelewsky, *Coord. Chem. Rev.* **84** (1988) 85. (c) K. Kalyanasundaram, *Coord. Chem. Rev.* **46** (1982) 159.

9 B. Pashaei, S. Karimi, H. Shahroosvand, P. Abbasi, M. Pilkington, A. Bartolotta, E. Fresta, J. Fernandez-Cestau, R.D. Costa, F. Bonaccorso, *Chem. Soc. Rev.* **48** (2019) 5033.

10 F. Juliá, D. Bautista, P. González-Herrero, *Chem. Commun.* **52** (2016) 1657.

11 K. Binnemans, P.T. Jones, *J. Rare Earths* **32** (2014) 195.

12 Q.C. Zhang, H. Xiao, X. Zhang, L.J. Xu, Z.N. Chen, *Coord. Chem. Rev.* **378** (2019) 121.

13 (a) C. Bizzarri, E. Spuling, D.M. Knoll, D. Volz, S. Bräse, *Coord. Chem. Rev.* **373** (2018) 49. (b) P. Tao, S.-J. Liu, W.-Y. Wong, *Adv. Opt. Mater.* **8** (2020) 2000985. (c) L.P. Ravaro, K.P.S. Zanoni, A.S.S.de Camargo, *Energy Rep.* **6** (2020) 37. (d) W. Liu, W.P. Lustig, J. Li, *EnergyChem* **1** (2019) 100008.

14 (a) O.S. Wenger, *J. Am. Chem. Soc.* **140** (2018) 13522. (b) C. Wegeberg, O.S. Wenger, *JACS Au* **1** (2021) 1860.

15 N.N. Greenwood, A. Earnshaw, *Chemistry of the elements*, 2nd ed., Butterworth-Heinemann, Oxford, 1997.

16 Y. Qin, P. She, X. Huang, W. Huang, Q. Zhao, *Coord. Chem. Rev.* **416** (2020) 213331.

17 (a) H. Zhu, C.C. Lin, W. Luo, S. Shu, Z. Liu, Y. Liu, J. Kong, E. Ma, Y. Cao, R.-S. Liu, X. Chen, *Nat. Commun.* **5** (2014) 4312. (b) D. Kim, S. Park, B.C. Choi, S.H. Park, J.H. Jeong, J.H. Kim, *Materials Research Bulletin* **97** (2018) 115. (c) Q. Zhou, L. Dolgov, A.M. Srivastava, L. Zhou, Z. Wang, J. Shi, M.D. Dramićanin, M.G. Brike, M. Wu, *J. Mater. Chem. C* **6** (2018) 2652.

18 P. Herr, C. Kerzig, C.B. Larsen, D. Häussinger, O.S. Wenger, *Nat. Chem.* **13** (2021) 956.

19 (a) D.M.L. Goodgame, F.A. Cotton, *J. Chem. Soc.* (1961) 3735. (b) F.A. Cotton, D.M.L. Goodgame, M. Goodgame, *J. Am. Chem. Soc.* **84** (1962) 167.

20 C. Jiang, N. Zhong, C. Luo, H. Lin, Y. Zhang, H. Peng, C.-G. Duan, *Chem. Commun.* **53** (2017) 5954.

21 (a) L.-J. Xu, C.-Z. Sun, H. Xiao, Y. Wu, Z.-N. Chen, *Adv. Mater.* **29** (2017) 1605739. (b) A. Jana, V.G. Sree, Q. Ba, S.C. Cho, S.U. Lee, S. Cho, Y. Jo, A. Meena, H. Kim, H. Im, *J. Mater. Chem. C* **9** (2021) 11314. (c) P. Fu, Y. Sun, Z. Xia, Z. Xiao, *J. Phys. Chem. Lett.* **12** (2021) 7394. (d) L.-J. Xu, X. Lin, Q. He, M. Worku, B. Ma, *Nat. Commun.* **11** (2020) 4329.

22 D.K. Das, R. Bakthavatsalam, V. Anilkumar, B.P. Mali, M.S. Ahmed, S.S.K. Raavi, R. Pallepogu, J. Kundu, *Inorg. Chem.* **61** (2022) 5363.

23 A.S. Berezin, M.P. Davydova, D.G. Samsonenko, T.S. Sukhikh, A.V. Artem'ev, *J. Lumin.* **236** (2021) 118069.

24 H.-L. Liu, H.-Y. Ru, M.-E. Sun, Z.-Y. Wang, S.-Q. Zang, *Adv. Optical Mater.* **10** (2022) 2101700.

25 H. Peng, T. Huang, B. Zou, Y. Tian, X. Wang, Y. Guo, T. Dong, Z. Yu, C. Ding, F. Yang, J. Wang, *Nano Energy* **87** (2021) 106166.

26 X. Huang, Y. Qin, P. She, H. Meng, S. Liu, Q. Zhao, *Dalton Trans.* **50** (2021) 8831.

27 J. Chen, Q. Zhang, F.-K. Zheng, Z.-F. Liu,S.-H. Wang, A.-Q. Wu, G.-C. Guo, *Dalton Trans.* **44** (2015) 3289.

28 M. Wrighton, D. Ginley, *Chem. Phys.* **4** (1974) 295.

29 Y. Qin, P. Tao, L. Gao, P. She, S. Liu, X. Li, F. Li, H. Wang, Q. Zhao, Y. Miao, W. Huang, *Adv. Opt. Mater.* **7** (2019) 1801160.

30 A.V. Artem’ev, M.P. Davydova, M.I. Rakhmanova, I. Yu. Bagryanskaya, D.P. Pishchur, *Inorg. Chem. Front.* **8** (2021) 3767.

31 A.V. Artem'ev, M.P. Davydova, A.S. Berezin, T.S. Sukhikh, D.G. Samsonenko, *Inorg. Chem. Front.* **8** (2021) 2261.

32 J. Zhao, T. Zhang, X.-Y. Dong, M.-E. Sun, C. Zhang, X. Li, Y S. Zhao, S.-Q. Zang, *J. Am. Chem. Soc.* **141** (2019) 15755.

33 (a) F. Zinna, L. Di Bari, *Chirality* **27** (2015) 1. (b) G. Muller, *Dalton Trans.* (2009) 9692. (c) R. Carr, N.H. Evans, D. Parker, *Chem. Soc. Rev.* **41** (2012) 7673. (d) J. Han, S. Guo, H. Lu, S. Liu, Q. Zhao, W. Huang, *Adv. Opt. Mater.* **6** (2018) 1800538. (e) L.E. MacKenzie, R. Pal, *Nat. Rev. Chem.* **5** (2021) 109.

34 (a) A. Hosseiny, C.A. McAuliffe, K. Minten, M.J. Parrott, R. Pritchard, J. Tames, *Inorg. Chim. Acta* **39** (1980) 221. (b) H. Zhao, R. Clérac, J.-S. Sun, X. Ouyang, J.M. Clemente-Juan, C.J. Gómez-García, E. Coronado, K. R. Dunbar, *J. Solid State Chem.* **159** (2001) 281. (d) S. Gorter, A.D. Van Ingen Schenau, G.C. Verschoor, *Acta Cryst.* **30** (1974) 1867. (e) B.C. Unni Nair, J.E. Sheats, R. Ponteciello, D. Van Engen, V. Petrouleas, G.C. Dismukes, *Inorg. Chem.* **28** (1989) 1582.

35 (a) Y. Zhang, W.-Q. Liao, D.-W. Fu, H.-Y. Ye, C.-M. Liu, Z.-N. Chen, R.-G. Xiong, *Adv. Mater.* **27** (2015) 3942. (b) Y. Zhang, W.-Q. Liao, D.-W. Fu, H.-Y. Ye, Z.-N. Chen, R.-G. Xiong, *J. Am. Chem. Soc.* **137** (2015) 4928. (c) H.-Y. Ye, Q. Zhou, X. Niu, W.-Q. Liao, D.-W. Fu, Y. Zhang, Y.-M. You, J. Wang, Z.-N. Chen, R.-G. Xiong, *J. Am. Chem. Soc.* **137** (2015) 13148. (d) Y.-M. You, W.-Q. Liao, D. Zhao, H.-Y. Ye, Y. Zhang, Q. Zhou, X. Niu, J. Wang, P.-F. Li, D.-W. Fu, Z. Wang, S. Gao, K. Yang, J.-M. Liu, J. Li, Y. Yan, R.-G. Xiong, *Science* **357** (2017) 306.

36 Y. Mei, H. Yu, Z. Wei, G. Mei, H. Cai, *Polyhedron* **127** (2017) 458.

37 H. Meng, W. Zhu, F. Li, X. Huang, Y. Qin, S. Liu, Y. Yang, W. Huang, Q. Zhao, *Laser Photonics Rev.* **15** (2021) 2100309.

38 A.V. Artem'ev, M.P. Davydova, A.S. Berezin, V.K. Brel, V.P. Morgalyuk, I. Yu. Bagryanskaya, D.G. Samsonenko, *Dalton Trans.* **48** (2019) 16448.

39 (a) D. Hausmann, A. Kuzmanoski, C. Feldmann, *Dalton Trans.* **45** (2016) 6541. (b) E. Merzlyakova, S. Wolf, S. Lebedkin, L. Bayarjargal, B.L. Neumeier, D. Bartenbach, C. Holzer, W. Klopper, B. Winkler, M. Kappes, C. Feldmann, *J. Am. Chem. Soc.* **143** (2021) 798.

40 M. Bortoluzzi, J. Castro, E. Trave, D. Dallan, S. Favaretto, *Inorg. Chem. Commun.* **90** (2018) 105.

41 Y. Wu, X. Zhang, L.-J. Xu, M. Yang, Z.-N. Chen, *Inorg. Chem.* **57** (2018) 9175.

42 A.S. Berezin, D.G. Samsonenko, V.K. Brel, A.V. Artem'ev, *Dalton Trans.* **47** (2018) 7306.

43 A.V. Artem’ev, A.S. Berezin, V.K. Brel, V.P. Morgalyuk, D.G. Samsonenko, *Polyhedron* **148** (2018) 184.

44 M.P. Davydova, I.Y. Bagryanskaya, I.A. Bauer, M.I. Rakhmanova, V.P. Morgalyuk, V.K. Brel, A.V. Artem'ev, *Polyhedron* **188** (2020) 114706.

45 A.S. Berezin, M.P. Davydova, I.Y. Bagryanskaya, O.I. Artyushin, V.K. Brel, A.V. Artem'ev, *Inorg. Chem. Commun.* **107** (2019) 107473.

46 S. Wang, X. Han, T. Kou, Y. Zhou, Y. Liang, Z. Wu, J. Huang, T. Chang, C. Peng, Q. Weia, B. Zou, *J. Mater. Chem. C* **9** (2021) 4895.

47 M.P. Davydova, I.A. Bauer, V.K. Brel, M.I. Rakhmanova, I.Y. Bagryanskaya, A.V. Artem'ev, *Eur. J. Inorg. Chem.* (2020) 695.

48 Y. Liu, S. C. Yiu, C.L. Ho, W.Y. Wong, *Coord. Chem. Rev.* **375** (2018) 514.

49 (a) A. Vogler, H. Kunkely, *J. Am. Chem. Soc.* **108** (1986) 7211. (b) K.R. Kyle, P.C. Ford, *J. Am. Chem. Soc.* **111** (1989) 5005. (c) K.R. Kyle, C.K. Ryu, J.A. Di Benedetto, P.C. Ford, *J. Am. Chem. Soc.* **113** (1991) 2954. (d) A. Døssing, C.K. Ryu, S. Kudo, P.C. Ford, *J. Am. Chem. Soc.* **115** (1993) 5132. (e) F. De Angelis, S. Fantacci, A. Sgamellotti, E. Cariati, R. Ugo, P.C. Ford, *Inorg. Chem.* **45** (2006) 10576. (f) P.C. Ford, E. Cariati, J. Bourassa, *Chem. Rev.* **99** (1999) 3625.

50 M. Ruthkosky, C.A. Kelly, F.N. Castellano, G.J. Meyer, *Coord. Chem. Rev.* **171** (1998) 309.

51 (a) D.V. Scaltrito, D.W. Thompson, J.A. O’Callaghan, G.J. Meyer, *Coord. Chem. Rev.* **208** (2000) 243. (b) A. Lavie-Cambot, M. Cantuel, Y. Leydet, G. Jonusauskas, D.M. Bassani, N.D. McClenaghan, *Coord. Chem. Rev.* **252** (2008) 2572. (c) A. Barbieri, G. Accorsi, N. Armaroli, *Chem. Commun.* (2008) 2185.

52 (a) S.M. Kuang, D.G. Cuttell, D.R. McMillin, P.E. Fanwick, R.A. Walton, *Inorg. Chem.* **41** (2002) 3313. (b) Q. Zhang, Q. Zhou, Y. Cheng, L. Wang, D. Ma, X. Jing, F. Wang, *Adv. Mater.* **16** (2004) 432. (c) T. McCormick, W.-L. Jia, S. Wang, *Inorg. Chem.* **45** (2006) 147. (d) G. Che, Z. Su, W. Lia, B. Chu, M. Li, *Chem. Appl. Phys. Lett.* **89** (2006) 103511. (e) Q. Zhang, J. Ding, Y. Cheng, L. Wang, Z. Xie, X. Jing, F. Wang, *Adv. Funct. Mater.* **17** (2007) 2983. (f) Z. Si, J. Li, B. Li, S. Liu, W. Li, *J. Lumin.* **129** (2009) 181. (g) J. Min, Q. Zhang, W. Sun, Y. Cheng, L. Wang, *Dalton Trans.* **40** (2011) 686. (h) C. Femoni, S. Muzzioli, A. Palazzi, S. Stagni, S. Zacchini, F. Monti, G. Accorsi, M. Bolognesi, N. Armaroli, M. Massi, G. Valenti, M. Marcaccio, *Dalton Trans.* **42** (2013) 997.

53 F. Parmeggiani, A. Sacchetti, *J. Chem. Educ.* **89** (2012) 946.

54 A.V. Artem’ev, M.P. Davydova, A.S. Berezin, D.G. Samsonenko, I.Yu. Bagryanskaya, V.K. Brel, X. Hei, K.A. Brylev, O.I. Artyushin, L.E. Zelenkov, I.I. Shishkin, J. Li, *ACS Appl. Mater. Interfaces* **14** (2022) 31000.

55 Y. Watanabe, B.M. Washer, M. Zeller, S. Savikhin, L.V. Slipchenko, A. Wei, *J. Am. Chem. Soc.* **144** (2022) 10186.

56 S. Kondo, N. Yoshimura, M. Yoshida, A. Kobayashi, M. Kato, *Dalton Trans.* **49** (2020) 16946.

57 E. Cariati, E. Lucenti, C. Botta, U. Giovanella, D. Marinotto, S. Righetto, *Coord. Chem. Rev.* **306** (2016) 566.

58 (a) J.L. Chen, P. Song, J. Liao, H.R. Wen, R. Hong, Z.N. Chen, Y. Chi, *Inorg. Chem. Commun.* **13** (2010) 1057. (b) F. Liu, Y. Jin, B. Liu, R. Li, Y. Deng, W. Li, F. Jian, *Chin. J. Chem.* **30** (2012) 1069. (c) J.L. Chen, Z.H. Guo, H.G. Yu, L.H. He, S.J. Liu, H.R. Wen, J.Y. Wang, *Dalton Trans.* **45** (2016) 696.

59 L. Bergmann, C. Braun, M. Nieger, S. Bräse, *Dalton Trans.* **47** (2018) 608.

60 L. Yao, G. Niu, J. Li, L. Gao, X. Luo, B. Xia, Y. Liu, P. Du, D. Li, C. Chen, Y. Zheng, Z. Xiao, J. Tang, *J. Phys. Chem. Lett.* **11** (2020) 1255.

61 (a) M. Deng, N.F.M. Mukthar, N.D. Schley, G. Ung, *Angew. Chem. Int. Ed.* **132** (2020) 1244. (b) E.E. Braker, N.F.M. Mukthar, N.D. Schley, G. Ung, *ChemPhotoChem* **5** (2021) 902.

62 (a) Y. Bai, G.J. He, Y.G. Zhao, C.Y. Duan, D.B. Dang, Q.J. Meng, *Chem. Commun.* (2006) 1530. (b) M.D. Allendorf, C.A. Bauer, R.K. Bhakta, R.J.T. Houk, *Chem. Soc. Rev.* **38** (2009) 1330.

63 J.-J. Wang, C. Chen, W.-G. Chen, J.-S. Yao, J.-N. Yang, K.-H. Wang, Y.-C. Yin, M.-M. Yao, L.-Z. Feng, C. Ma, F.-J. Fan, H.-B. Yao, *J. Am. Chem. Soc.* **142** (2020) 3686.

64 (a) R. Peng, M. Li, D. Li, *Coord. Chem. Rev.* **254** (2010) 1. (b) X.Q. Liang, H.P. Xiao, B.L. Liu, Y.Z. Li, J.L. Zuo, X.Z. You, *Polyhedron* **27** (2008) 2494.

65 E. Lucenti, E. Cariati, A. Previtali, D. Marinotto, A. Forni, V. Bold, V.C. Kravtsov, M.S. Fonari, S. Galli, L. Carlucci, *Cryst. Growth Des.* **19** (2019) 1567.

66 A.V. Artem’ev, A.Y. Baranov, M.I. Rakhmanova, S.F. Malysheva, D.G. Samsonenko, *New J. Chem.* **44** (2020) 6916.

67 A.V. Artem’ev, A.Y. Baranov, E.A. Pritchina, A.S. Berezin, N.P. Gritsan, D.G. Samsonenko, V.P. Fedin, N.A. Belogorlova, *Angew. Chem. Int. Ed.* **60** (2021) 12577.

68 (a) C.A. Parker, C.G. Hatchard, *Trans. Faraday Soc.* **57** (1961) 1894. (b) M.Y. Wong, E. Zysman-Colman, *Adv. Mater.* **29** (2017) 1605444.

69 H. Yersin, *Highly Efficient OLEDs: Materials Based on Thermally Activated Delayed Fluorescence*, Wiley-VCH, Weinheim, 2018.

70 C. Sandoval-Pauker, M. Santander-Nelli, P. Dreyse, *RSC Adv.* **12** (2022) 10653.

71 (a) Y. Tao, K. Yuan, T. Chen, P. Xu, H. Li, R. Chen, C. Zheng, L. Zhang, W. Huang, *Adv. Mater.* **26** (2014) 7931. (b) G. Li, Z.Q. Zhu, Q. Chen, J. Li, *Org. Electron.* **69** (2019) 135.

72 T. Hofbeck, U. Monkowius, H. Yersin, *J. Am. Chem. Soc.* **137** (2015) 399.

73 J.C. Deaton, S.C. Switalski, D.Y. Kondakov, R.H. Young, T.D. Pawlik, D.J. Giesen, S.B. Harkins, A.J.M. Miller, S.F. Mickenberg, J.C. Peters, *J. Am. Chem. Soc.* **132** (2010) 9499.

74 (a) H. Uoyama, K. Goushi, K. Shizu, H. Nomura, C. Adachi, *Nature* **492** (2012) 234. (b) R. Czerwieniec, M.J. Leitl, H.H.H. Homeier, H. Yersin, *Coord. Chem. Rev.* **325** (2016) 2. (c) T.J.

Penfold, F.B. Dias, A.P. Monkman, *Chem. Commun.* **54** (2018) 3926. (d) C. Bizzarri, F. Hundemer, J. Busch, S. Bräse, *Polyhedron* **140** (2018) 51. (e) G.U. Mahoro, J. Fernandez-Cestau, J.-L. Renaud, P.B. Coto, R.D. Costa, S. Gaillard, *Adv. Optical Mater.* **8** (2020) 2000260. (f) C.E. Housecroft, E.C. Constable, *J. Mater. Chem. C* **10** (2022) 4456.

75 G. Hong, X. Gan, C. Leonhardt, Z. Zhang, J. Seibert, J.M. Busch, S. Bräse, *Adv. Mater.* **33** (2021) 2005630.

76 (a) M.J. Leitl, F.R. Küchle, H.A. Mayer, L. Wesemann, H. Yersin, *J. Phys. Chem. A* **117** (2013) 11823. (b) R. Czerwieniec, J. Yu, H. Yersin, *Inorg. Chem.* **50** (2011) 8293. (c) K. Li, Y. Chen, J. Wang, C. Yang, *Coord. Chem. Rev.* **433** (2021) 213755.

77 L. Bergmann, G.J. Hedley, T. Baumann, S. Bräse, I.D.W. Samuel, *Sci. Adv.* **2** (2016) e1500889.

78 (a) X.-L. Chen, R. Yu, Q.-K. Zhang, L.-J. Zhou, X.-Y. Wu, Q. Zhang, C.-Z. Lu, *Chem. Mater.* **25** (2013) 3910. (b) M.J. Leitl, V.A. Krylova, P.I. Djurovich, M. E.Thompson, H. Yersin, *J. Am. Chem. Soc.* **136** (2014) 16032. (c) A. Kobayashi, T. Hasegawa, M. Yoshida, M. Kato, *Inorg. Chem.* **55** (2016) 1978.

79 A.V. Artem’ev, Y.V. Demyanov, M.I. Rakhmanova, I. Yu. Bagryanskaya, *Dalton Trans.* **51** (2022) 1048.

80 A.Y. Baranov, A.S. Berezin, D.G. Samsonenko, A.S. Mazur, P.M. Tolstoy, V.F. Plyusnin, I.E. Kolesnikov, A.V. Artem'ev, *Dalton Trans.* **49** (2020) 3155.

81 K. Xu, B.-L. Chen, R. Zhang, L. Liu, X.-X. Zhong, L. Wang, F.-Y. Li, G.-H. Li, K. A. Alamry, F.-B. Li, W.-Y. Wong, H.-M. Qin, *Dalton Trans.* **49** (2020) 5859.

82 R. Tang, S. Xu, T.-L. Lam, G. Cheng, L. Du, Q. Wan, J. Yang, F.-F. Hung, K.-H. Low, D.L. Phillips, C.-M. Che, *Angew. Chem. Int. Ed.* **61** (2022) e202203982.

83 T. Jüstel, S. Möller, H. Winkler, W. Adam, *Luminescent Materials, Ullman’s Encyclopedia of Industrial Chemistry*, Wiley-VCH, Wienheim, 2012.

84 (a) Q. Sun, Y.A. Wang, L.S. Li, D. Wang, T. Zhu, J. Xu, C. Yang, Y. Li, *Nat. Photonics* **1** (2007) 717. (b) Y. Shirasaki, G. J. Supran, M. G. Bawendi, V. Bulović, *Nat. Photonics* **7** (2013) 13.

85 T. Sano, Y. Nishio, Y. Hamada, H. Takahashi, T. Usukia, K. Shibata, *J. Mater. Chem.* **10** (2000) 157.

86 F. Dumur, *Synthetic Metals* **195** (2014) 241.

87 M. Cibian, A. Shahalizad, F. Souissi, J. Castro, J. G. Ferreira, D. Chartrand, J.-M. Nunzi, G.S. Hanan, *Eur. J. Inorg. Chem.* (2018) 4322.

88 (a) Y. Sakai, Y. Sagara, H. Nomura, N. Nakamura, Y. Suzuki, H. Miyazakiae, C. Adachi, *Chem. Commun.* **51** (2015) 3181. (b) A.S. Berezin, K.A. Vinogradova, V.P. Krivopalov, E.B. Nikolaenkova, V.F. Plyusnin, A.S. Kupryakov, N.V. Pervukhina, D.Y. Naumov, M.B. Bushuev, *Chem. Eur. J.* **24** (2018) 12790. (c) J. Xiong, K. Li, T. Teng, X. Chang, Y. Wei, C. Wu, C. Yang, *Chem. Eur. J.* **26** (2020) 6887.

89 D. Tungulin, J. Leier, A.B. Carter, A.K. Powell, R.Q. Albuquerque, A.N. Unterreiner, C. Bizzarri, *Chem. Eur. J.* **25** (2019) 3816.

90 R. Tabone, D. Feser, E.D. Lemma, U. Schepers, C. Bizzarri, *Front. Chem.* **9** (2021) 754420.

91 Q.-D Liu, R. Wang, S. Wang, *Dalton Trans.* (2004) 2073.

92 J. Cepeda, E. San Sebastian, D. Padro, A. Rodríguez-Diéguez, J.A. García, J.M. Ugalde, J.M. Seco, *Chem. Commun.* **52** (2016) 8671.

93 J.-H. Wei, W.-T. Ou, J.-B. Luo, D.-B. Kuang, *Angew. Chem. Int. Ed.* (2022) e202207985.

94 J.-Q. Wang, Y. Mu, S.-D. Hen, J. Pan, J.-H. Li, G.-M. Wang, *Inorg. Chem.* **58** (2019) 9476.

95 X.-M. Wu, Y.-L. Hua, Z.-Q. Wang, J.-J. Zheng, X.-L. Feng, Y.-Y. Sun, *Chin. Phys. Lett.* **22** (2005) 1797.

96 R. Wang, L. Deng, M. Fu, J. Cheng, J. Li, *J. Mater. Chem.* **22** (2012) 23454.

97 B.-S. Kim, D.-E. Kim, G.-C. Choi, J.-W. Park, B.-J. Lee, Y.-S. Kwon, *J. Electr. Eng. Technol.* **4** (2009) 418.

98 (a) M. Bortoluzzi, J. Castro, F. Enrichi, A. Vomiero, M. Busato, W. Huang, *Inorg. Chem. Commun.* **92** (2018) 145. (b) M. Bortoluzzi, J. Castro, *J. Coord. Chem.* **72** (2019) 309. (c) M. Bortoluzzi, J. Castro, M. Girotto, F. Enrichi, A. Vomiero, *Inorg. Chem. Commun.* **102** (2019) 141.

99 (a) C.A. Kosky, J.P. Gayda, J.F. Gibson, S.F. Jones, D.J. Williams, *Inorg. Chem.* **21** (1982) 3173. (b) J.P. Rose, R.A. Lalancette, J.A. Potenza, H.J. Schugar, *Acta Crystallogr.* **B36** (1980) 2409. (c) X. Liu, G. Wang, Y. Dang, S. Zhang, H. Tian, Y. Ren, X. Tao, *CrystEngComm* **18** (2016) 1818. (d) L. Li, Z.-P. Wang, G.-R. Tian, X.-Y. Song, S.-X. Sun, *J. Cryst. Growth* **310** (2008) 1202.

100 W.L.F. Armarego, D.D. Perrin, *Purification of laboratory chemicals*, 4th ed., Butterworth Heinemann, Oxford, 1996.

101 D.J. Pietrzyk, C.W. Frank, *Analytical Chemistry*, 2nd edn., Academic Press, New York, 2012.

102 W.J. Geary, *Coord. Chem. Rev.* **7** (1971) 81.

103 G.A. Bain, J.F. Berry, *J. Chem. Ed.* **85** (2008) 532.

104 (a) I.C. Gerber, J.G. Ángyán, *Chem. Phys. Lett.* **415** (2005) 100. (b) J.D. Chai, M. Head-Gordon, *Phys. Chem. Chem. Phys.* **10** (2008) 6615. (c) Y. Minenkov, Å. Singstad, G. Occhipinti, V.R. Jensen, *Dalton Trans.* **41** (2012) 5526. (d) V.N. Staroverov, G.E. Scuseria, J. Tao, J.P. Perdew, *J. Chem. Phys.* **19** (2003) 12129. (e) H.S. Yu, X. He, S.L. Li, D.G. Truhlar, *Chem. Sci.* **7** (2016) 5032. (f) F. Weigend, R. Ahlrichs, *Phys. Chem. Chem. Phys.* **7** (2005) 3297.

105 (a) M. Cossi, N. Rega, G. Scalmani, V. Barone, *J. Comput. Chem.* **24** (2003) 669. (b) V. Barone, M. Cossi, *J. Phys. Chem. A* **102** (1998) 1995.

106 C.A. Ullrich, *Time-Dependent Density Functional Theory*, Oxford University Press, New York, 2011.

107 *Gaussian 16, Revision C.01*, M.J. Frisch, G.W. Trucks, H.B. Schlegel, G.E. Scuseria, M.A. Robb, J.R. Cheeseman, G. Scalmani, V. Barone, G.A. Petersson, H. Nakatsuji, X. Li, M. Caricato, A.V. Marenich, J. Bloino, B.G. Janesko, R. Gomperts, B. Mennucci, H.P. Hratchian, J.V. Ortiz, A.F. Izmaylov, J.L. Sonnenberg, D. Williams-Young, F. Ding, F. Lipparini, F. Egidi, J. Goings, B. Peng, A. Petrone, T. Henderson, D. Ranasinghe, V. G. Zakrzewski, J. Gao, N. Rega, G. Zheng, W. Liang, M. Hada, M. Ehara, K. Toyota, R. Fukuda, J. Hasegawa, M. Ishida, T. Nakajima, Y. Honda, O. Kitao, H. Nakai, T. Vreven, K. Throssell, J.A. Montgomery, Jr., J.E. Peralta, F. Ogliaro, M.J. Bearpark, J.J. Heyd, E.N. Brothers, K.N. Kudin, V.N. Staroverov, T.A. Keith, R. Kobayashi, J. Normand, K. Raghavachari, A.P. Rendell, J.C. Burant, S.S. Iyengar, J. Tomasi, M. Cossi, J.M. Millam, M. Klene, C. Adamo, R. Cammi, J.W. Ochterski, R.L. Martin, K. Morokuma, O. Farkas, J.B. Foresman and D.J. Fox, Gaussian, Inc., Wallingford CT, 2016.

108 (a) F. Neese, *WIREs Comput. Mol. Sci.* **2** (2012) 73. (b) F. Neese, *WIREs Comput. Mol. Sci.* **8** (2018) e1327.

109 T. Lu, F. Chen, *J. Comput. Chem.* **33** (2012) 580.

110 R.F.W. Bader, *Chem. Rev.* **91** (1991) 893.

111 Bruker, *APEX3, SMART, SAINT,* Bruker AXS Inc., Madison, Wisconsin, USA, 2015.

112 P. McArdle, K. Gilligan, D. Cunningham, R. Dark, M. Mahon, *CrystEngComm* **6** (2004) 303.

113 G.M. Sheldrick, *Acta Crystallogr.* **A71** (2015) 3.

114 G.M. Sheldrick, *Acta Crystallogr.* **C71** (2015) 3.

115 A.L. Spek, *Acta Crystallogr.* **E76** (2020) 1.

116 (a) S.J. Grabowski, *Crystals* **6** (2016) 59. (b) S.J. Grabowski, *Chem. Rev.* **111** (2011) 2597. (c) R. Taylor, *Growth Des.* **16** (2016) 4165. (d) R. Taylor, *CrystEngComm.* **16** (2014) 6852. (e) C.B. Aakeröy, N.R. Champness, C. Janiak, *CrystEngComm.* **12** (2010) 22.

117 (a) L.J. Farrugia, *J. Appl. Crystallogr.* **30** (1997) 565. (b) *POV-Ray v3.7 for Windows*, Persistence of Vision Pty. Ltd., 2016, Persistence of Vision Raytracer (Version 3.7) http://www.povray.org/documentation. (c) C.F. Macrae, I.J. Bruno, J.A. Chisholm, P.R. Edgington, P. McCabe, E. Pidcock, L. Rodriguez-Monge, R. Taylor, J. van de Streek, P.A. Wood, *J. Appl. Cryst.* **41** (2008) 466.

118 H. Ulrich, B. Tucker, A.A.R. Sayigh, *J. Org. Chem.* **32** (1967) 1360.

119 (a) B.G. Van den Bos, C.J. Schoot, M.J. Koopmans, J. Meltzer, *Recl. Trav. Chim. Pay-B* **80** (1961) 1040. (b) A.R. Katritzky, G.W. Rewcastle, L.M. Vazquez de Miguel, *J. Org. Chem.* **53** (1988) 794.

120 X. Dong, R. Wang, W. Jin, C. Liu, *Org. Lett.* **22** (2020) 3062.

121 M. Bortoluzzi, A. Gobbo, A. Palù, F. Enrichi, A. Vomiero, *Chem. Pap.* **74** (2020) 3693.

122 M. Bortoluzzi, A. Di Vera, L. Pietrobon, J. Castro, *J. Coord. Chem.* **74** (2021) 1466.

123 J. Lenz, D. Pospiech, H. Komber, M. Paven, R. Albach, S. Mentizi, G. Langstein, B. Voit, *Tetrahedron* **75** (2019) 1306.

124 E.O.J. Bull, M.S.R. Naidu, C. Nagaraju, *Indian J. Chem.* **29B** (1990) 688.

125 P. Haranath, V. Sreedhar Kumar, C. Suresh Reddy, C. Naga Raju, C. Devendranath Reddy, *Synth. Commun.* **37** (2007) 1697.

126 A.V. Salin, A.V. Il'in, R.I. Faskhutdinov, R.R. Fayzullin, *Tetrahedron* **75** (2019) 2676.

127 P.G. Simpson, A. Vinciguerra, J.V. Quagliano, *Inorg. Chem.* **2** (1963) 282.

128 X. Peng, P. Huang, L. Jiang, J. Zhu, L. Liu, *Tetrahedron Lett.* **57** (2016) 5223.

129 S. Kosei, M. Akio, T. Masahiko, K. Yoshimitsu, S. Toshiyuki, Y. Yoshinobu, O. Kentaro, *Bull. Chem. Soc. Jpn.* **80** (2007) 743.

130 J. Yuan, W.-P. To, Z.-Y. Zhang, C.-D. Yue, S. Meng, J. Chen, Y. Liu, G.-A. Yu, C.-M. Che, *Org. Lett.* **20** (2018) 7816.

131 B.S. Hammes, C.J. Carrano, *Inorg. Chem.* **38** (1999) 3562.

132 (a) Z. Zhong, R. Hong, X. Wang, *Tetrahedron Lett.* **51** (2010) 6763. (b) P. Ballesteros, J. Elguero, R. M. Claramunt, *Tetrahedron* **41** (1985) 5955.

133 A.R. Katritzky, Z. Yang, J.N. Lam, *Synthesis* (1990) 666.

134 (a) A.R. Katritzky, J. Wu, *Synthesis* **6** (1994) 597. (b) A.R. Katritzky, A.V. Ignatchenko, H. Lang, *Heterocycles* **41** (1995) 131.

135 S. Xie, Z. Yan, Y. Li, Q. Song, M. Ma, *J. Org. Chem.* **83** (2018) 10916.

136 X.-K. Liu, C.-J. Zheng, M.-F. Lo, J. Xiao, Z. Chen, C.-L. Liu, C.-S. Lee, M.-K. Fung, X.-H. Zhang, *Chem. Mat.* **25** (2013) 4454.

137 R.N. Keller, H.D. Wycoff, *Inorg. Synth.* **2** (1946) 1.

138 C. Bianchini, C. A. Ghilardi, A. Meli, S. Midollini, A. Orlandini, *Inorg. Chem.* **24** (1985) 924.

139 G.J. Kubas, B. Monzyk, A.L. Crumblis, *Inorg. Synth.* **28** (1990) 68.

140 (a) F. Cariati, L. Naldini, *J. Nucl. Inorg. Chem.* **28** (1966) 2243. (b) B. E. Green, C. H. L. Kennard, G. Smith, B. D. James, P. C. Healy, A. H. White, *Inorg. Chim. Acta* **81** (1984) 147.

141 A.P. Komin, M. Carmack, *J. Heterocycl. Chem.* **12** (1975) 829.

142 F. Da Silva Miranda, A.M. Signori, J. Vicente, B. de Souza, J.P. Priebe, B. Szpoganicz, N. Sanches Gonçalves, A. Neves, *Tetrahedron* **64** (2008) 5410.

143 Y. Liu, Y. Lu, M. Prashad, O. Repič, T.J. Blacklock, *Adv. Synth. Catal.* **347** (2005) 217.

144 D.A. Bashirov, T.S. Sukhikh, N.V. Kuratieva, E.A. Chulanova, I.V. Yushina, N.P. Gritsan, S.N. Konchenko, A.V. Zibarev, *RSC Adv.* **4** (2014) 28309.

145 M.D. Reddy, F.R. Fronczek, E.B. Watkins, *Org. Lett.* **18** (2016) 5620.

146 (a) J. Chatt, L.M. Vallarino, L.M. Venanzi, *J. Chem. Soc.* **678** (1957) 3413. (b) R.E. Rulke, J.M. Ernsting, A.L. Spek, C.J. Elsevier, P.W. van Leeuwen, K. Vrieze, *Inorg. Chem.* **32** (1993) 5769.

147 S.P. Sinha, T.T. Pakkanen, T.A. Pakkanen, L. Niinistö, *Polyhedron* **1** (1982) 355.

148 Y.-Y. Tang, Z.-X. Wang, P.-F. Li, Y.-M. You, A. Stroppa, R.-G. Xiong, *Inorg. Chem. Front.* **4** (2017) 154.

149 E.F. Schubert, *Light-emitting Diodes*, 2nd edn., Cambridge University Press, Cambridge, 2006.

150 S.K. Behera, S.Y. Park, J. Gierschner, *Angew. Chem. Int. Ed.* **60** (2021) 22624.

151 (a) Z. He, W. Zhao, J.W.Y. Lam, Q. Peng, H. Ma, G. Liang, Z. Shuai, B.Z. Tang, *Nat. Commun.* **8** (2017) 416. (b) T. Wang, X. Su, X. Zhang, X. Nie, L. Huang, X. Zhang, X. Sun, Y. Luo, G. Zhang, *Adv. Mater.* **31** (2019) 1904273. (c) H. Wang, J. Wang, T. Zhang, Z. Xie, X. Zhang, H. Sun, Y. Xiao, T. Yu, W. Huang, *J. Mater. Chem. C* **9** (2021) 10154.

152 A.S. Berezin, K.A. Vinogradova, V.A. Nadolinny, T.S. Sukhikh, V.P. Krivopalov, E.B. Nikolaenkov, M.B. Bushuev, *Dalton Trans.* **47** (2018) 1657.

153 D.C. Harris, M.D. Bertolucci, *Symmetry and Spectroscopy*, Oxford University Press, New York, 1978.

154 H.G.M. Edwards, M.J. Ware, L.A. Woodward, *Chem. Commun.* (1968) 540.

155 (a) Z. Bai, L. Song, Y. Hu, R.K.K. Yuen, *Ind. Eng. Chem. Res.* **52** (2013) 12855. (b) Y. Lin, S. Jiang, Z. Gui, G. Li, X. Shi, G. Chen, X. Peng, *RSC Adv.* **6** (2016) 86632. (c) H. Wang, S. Wang, X. Du, H. Wang, X. Cheng, Z. Du, *RSC Adv.* **9** (2019) 7411. (d) Y.K. Chen, Q.X. Lu, G. Zhong, H.G. Zhang, M.F. Chen, C.P. Liu, *J. Appl. Polym. Sci.* **138** (2021) 49918. (e) K.A. Salmeia, S. Gaan, *Polym. Degrad. Stab.* **113** (2015) 119. (f) J. Vasiljević, M. Čolović, N. Čelan Korošin, M. Šobak, Ž. Štirn, I. Jerman, *Polymers* **12** (2020) 657.

156 K. Nakamoto, *Infrared and Raman Spectra of Inorganic and Coordination Compounds Part B: Applications in Coordination, Organometallic, and Bioinorganic Chemistry*, 6th edn., Wiley, Hoboken, 2009.

157 J. Sathiya Savithri, P. Rajakumar, *RSC Adv.* **9** (2019) 36994.

158 (a) S.K. Madan, W.E. Bull, *J. Inorg. Nucl.* **26** (1964) 2211. (b) R.G. Garveya, J.H. Nelson, R.O. Ragsdale, *Coord. Chem. Rev.* **3** (1968) 375. (c) L.C. Nathan, R.O. Ragsdale, *Inorg. Chim. Acta* **3** (1969) 473. (d) G.B. Aitken, G.P. McQuillan, *J. Chem. Soc., Dalton Trans.* (1973) 2637. (e) I.S. Ahuja, R. Singh, G.L. Yadava, *J. Mol. Struct.* **74** (1981) 143. (f) H.-L. Sun, S. Gao, B.-Q. Ma, G. Su, S.R. Batten, *Cryst. Growth Des.* **5** (2005) 269. (g) J.-M. Shi, Z. Liu, W.-N. Li, H. Y. Zhao, L.-D. Liu, *J. Coord. Chem.* **60** (2007) 1077. (h) H. Alizadeh, M. Mirzaei, A.Sh. Saljooghi, V. Jodaian, M. Bazargan, J.T. Mague, R.M. Gomila, A. Frontera, *RSC Adv.* **11** (2021) 37403.

159 (a) L.C. Nathan, J. Cullen, R.O. Ragsdale, *Inorg. Nucl. Chem. Letters* **12** (1976) 137. (b) M.M. Morrison, D.T. Sawyer, *Inorg. Chem.* **17** (1978) 338.

160 (a) D.J. McCabe, A.A. Russell, S. Karthikeyan, R.T. Paine, R.R. Ryan, B. Smith, *Inorg. Chem.* **26** (1987) 1230. (b) B.G. Vats, S. Kannan, M. Kumar, M.G.B. Drew, *ChemistrySelect* **2** (2017) 3683.

161 D.P. Segers, M.K. DeArmond, P.A. Grutsch, C. Kutal, *Inorg. Chem.* **23** (1984) 2874.

162 (a) C. Wen, G. Tao, X. Xu, X. Feng, R. Luo, *Spectrochim. Acta A* **79** (2011) 1345. (b) C. Zhou, Q. Wang, *Transit. Met. Chem.* **35** (2010) 605.

163 J. Yuasa, M. Dana, T. Kawai, *Dalton Trans.* **42** (2013) 16096.

164 (a) L. Yang, J.-K. Feng, A.-M. Ren, M. Zhang, Y.-G. Ma, X.-D. Liu, *Eur. J. Inorg. Chem.* (2005) 1867. (b) I. Andrés-Tomé, J. Fyson, F. B. Dias, A. P. Monkman, G. Iacobellis, P. Coppo, *Dalton Trans.* **41** (2012) 8669.

165 (a) R. Gérardy, J.C.M. Monbaliu, *Top. Heterocycl. Chem.* **43** (2016) 1. (b) A.R. Katritzky, B.V. Rogovoy, *Chem. Eur. J.* **9** (2003) 4586.

166 (a) A.R. Cabrera, I.A. Gonzalez, D. Cortés-Arriagada, M. Natali, H. Berke, C.G. Daniliuc, M.B. Camarada, A. Toro-Labbé, R.S. Rojasa, C.O. Salasa, *RCS Adv.* **6** (2016) 5141. (b) K. Kubiček, S.T. Veedu, D. Storozhuk, R. Kia, S. Techert, *Polyhedron* **124** (2017) 166. (c) C. Bizzarri, C. Fléchon, O. Fenwick, F. Cacialli, F. Polo, M.D. Gálvez-López, C.H. Yang, S. Scintilla, Y. Sun, R. Fröhlich, L. De Cola, *ECS J. Solid State Sci. Technol.* **5** (2016) R83.

167 A. Kitai, *Luminescent materials and applications*, Wiley, Chichester, 2008.

168 Z. Ghassemlooy, L.N. Alves, S. Zvanovec, M.A. Khalighi, *Visible light communications: theory and applications*, CRC Press, Boca Raton, 2017.

169 I.A. González, M.A. Henríquez, D. Cortés-Arriagada, M. Natali, C. G. Daniliuc, P. Dreyse, J. Maze, R.S. Rojas, C.O. Salas, A.R. Cabrera, *New J. Chem.* **42** (2018) 12576.

170 C. Pettinari, F. Marchetti, S. Orbisaglia, R. Pettinari, J. Ngoune, M. Gómez, C. Santos, E. Álvarez, *CrystEngComm* **15** (2013) 3892.

171 (a) G. Chakkaradhari, T. Eskelinen, C. Degbe, A. Belyaev, A.S. Melnikov, E.V. Grachova, S.P. Tunik, P. Hirva, I.O. Koshevoy, *Inorg. Chem.* **58** (2019) 3646. (b) P. Arce, C. Vera, D. Escudero, J. Guerrero, A. Lappin, A. Oliver, D.H. Jara, G. Ferraudi, L. Lemus, *Dalton Trans.* **46** (2017) 13432. (c) S. Tong, D. Yuan, L. Yi, *Spectrochim. Acta A* **130** (2014) 280.

172 H. Yersin, A. F. Rausch, R. Czerwieniec, T. Hofbeck, T. Fischer, *Coord. Chem. Rev.* **255** (2011) 2622.

173 N. Armaroli, G. Accorsi, F. Cardinali, A. Listorti, *Top. Curr. Chem.* **280** (2007) 69.

174 L. Yang, D.R. Powell, R.P. Houser, *Dalton Trans.* (2007) 955.

175 (a) Y. Zhang, M. Schulz, M. Wächtler, M. Karnahl, B. Dietzek, *Coord. Chem. Rev.* **356** (2018) 127. (b) A. Alconchel, O. Crespo, P. García-Orduña, M. Concepción Gimeno, *Inorg. Chem.* **60** (2021) 18521. (c) K.F. Baranova, A.A. Titov, A.F. Smol'yakov, A.Y. Chernyadyev, O.A. Filippov, E.S. Shubina, *Molecules* **26** (2021) 6869. (d) M. Grupe, P. Boden, P. Di Martino-Fumo, X. Gui, C. Bruschi, R. Israil, M. Schmitt, M. Nieger, M. Gerhards, W. Klopper, C. Riehn, C. Bizzarri, R. Diller, *Chem. Eur. J.* **27** (2021) 15252. (e) Y. Wu, X. Han, Y. Qu, K. Zhao, C. Wang, G. Huang, H. Wu, *J. Mol. Struct.* **1191** (2019) 95. (f) B. Hupp, C. Schiller, C. Lenczyk, M. Stanoppi, K. Edkins, A. Lorbach, A. Steffen, *Inorg. Chem.* **56** (2017) 8996. (g) L. Pathaw, D. Maheshwaran, T. Nagendraraj, T. Khamrang, M. Velusamy, R. Mayilmurugan, *Inorg. Chim. Acta* **514** (2021) 119999. (h) C. Bizzarri, A.P. Arndt, S. Kohaut, K. Fink, M. Nieger, *J. Organomet. Chem.* **871** (2018) 140. (i) G. Li, R.S. Nobuyasu, B. Zhang, Y. Geng, B. Yao, Z. Xie, D. Zhu, G. Shan, W. Che, L. Yan, Z. Su, F.B. Dias, M.R. Bryce, *Chem. Eur. J.* **23** (2017) 11761. (j) Y. Sun, V. Lemaur, J. I. Beltrán, J. Cornil, J. Huang, J. Zhu, Y. Wang, R. Fröhlich, H. Wang, L. Jiang, G. Zou, *Inorg. Chem.* **55** (2016) 5845. (k) Q. Zhang, X.-L. Chen, J. Chen, X.-Y. Wu, R. Yu, C.-Z. Lu, *Dalton Trans.* **44** (2015) 10022. (l) L. Bergmann, J. Friedrichs, M. Mydlak, T. Baumann, M. Nieger, S. Bräse, *Chem. Commun.* **49** (2013) 6501. (m) C.-W. Hsu, C.-C. Lin, M.-W. Chung, Y. Chi, G.-H. Lee, P.-T. Chou, C.-H. Chang, P. Y. Chen, *J. Am. Chem. Soc.* **133** (2011) 12085.

176 (a) P.D. Harvey, M. Knorr, *Macromol. Rapid Commun.* **31** (2010) 808. (b) J. Troyano, J. Perles, P. Amo-Ochoa, F. Zamora, S. Delgado, *CrystEngComm* **18** (2016) 1809. (c) A.V. Artem'ev, E.P. Doronina, M.I. Rakhmanova, O.A. Tarasova, I.Yu. Bagryanskaya, N.A. Nedolya, *Inorg. Chem. Front.* **6** (2019) 671. (d) K.A. Vinogradova, N.A. Shekhovtsov, A.S. Berezin, T.S. Sukhikh, M.I. Rogovoy, A.V. Artem'ev, M.B. Bushuev, *Dalton Trans.* **50** (2021) 9317. (e) I. Nohara, C. Wegeberg, M. Devereux, A. Prescimone, C.E. Housecroft, E.C. Constable, *J. Mater. Chem. C* **10** (2022) 3089.

177 (a) Y. Zhang, J. Song, J. Qu, P.-C. Qian, W.-Y. Wong, *Sci. China Chem.* **64** (2021) 341. (b) I.M. Paczkowski, F.L. Coelho, L.F. Campo, *J. Mol. Liq.* **319** (2020) 114277. (c) C. Wang, F. Liu, Q.-M. Chen, C.-Y. Xiao, Y.-G. Wu, W.-W. Li, *Chin. J. Polym. Sci.* **39** (2021) 525.

178 (a) R. Bianchi, G. Gervasio, D. Marabello, *Inorg. Chem.* **39** (2000) 2360. (b) C. Lepetit, P. Fau, K. Fajerwerg, M.L. Kahn, B. Silvi, *Coord. Chem. Rev.* **345** (2017) 150.

179 (a) M. Hashimoto, S. Igawa, M. Yashima, I. Kawata, M. Hoshino, M. Osawa, *J. Am. Chem. Soc.* **133** (2011) 10348. (b) M. Osawa, M. Hoshino, M. Hashimoto, I. Kawata, S. Igawa, M. Yashima, *Dalton Trans.* **44** (2015) 8369. (c) X. Yin, C. Liu, S. Liu, M. Cao, J.M. Rawson, Y. Xu, B. Zhang, *New J. Chem.* **46** (2022) 6185. (d) S. Liu, J. Zhang, C. Liu, G. Yin, M. Wu, C. Du, B. Zhang, *Polyhedron* **218** (2022) 115761. (e) R. Wang, Y. Wu, J. Wang, H. Huang, Y. Wang, S. Xu, F. Zhao, *J. Mol. Struct.* **1257** (2022) 132642.

180 (a) R. Englman, J. Jortner, *Mol. Phys.* **18** (1970) 145. (b) E.M. Kober, J.V. Caspar, R.S. Lumpkin, T.J. Meyer, *J. Phys. Chem.* **90** (1986) 3722.

181 (a) C.S. Smith, K.R. Mann, *J. Am. Chem. Soc.* **134** (2012) 8786. (b) J.G. Małecki, I. Łakomska, A. Maroń, M. Szala, M. Fandzloch, J.E. Nycz, *J. Lumin.* **161** (2015) 382.

182 (a) V.W.-W. Yam, V. K.-M. Au, S. Y.-L. Leung, *Chem. Rev.* **115** (2015) 7589. (b) B. Hupp, J. Nitsch, T. Schmitt, R. Bertermann, K. Edkins, F. Hirsch, I. Fischer, M. Auth, A. Sperlich, A. Steffen, *Angew. Chem. Int. Ed.* **57** (2018) 13671. (c) A. Liske, L. Wallbaum, T. Hölzel, J. Föller, M. Gernert, B. Hupp, C. Ganter, C.M. Marian, A. Steffen, *Inorg. Chem.* **58** (2019) 5433.

183 (a) D.-D. Wang, L. Song, Y.-Y. Wang, J.-Y. Guo, H.-Y. Shen, X.-R. Wang, W.-X. Chai, *Appl. Organomet. Chem.* **34** (2020) e5561. (b) D. Domyati, B.A. Babgi, A. Jedidi, B. Davaasuren, A.-H.M. Emwas, M. Jaremko, *Polyhedron* **224** (2022) 115975.

184 (a) Y. Jiang, G. Li, W. Che, Y. Liu, B. Xu, G. Shan, D. Zhu, Z. Su, M.R. Bryce, *Chem. Commun.* **53** (2017) 3022. (b) K.Y. Zhang, X. Chen, G. Sun, T. Zhang, S. Liu, Q. Zhao, W. Huang, *Adv. Mater.* **28** (2016) 7137. (c) R. Weissleder, V. Ntziachristos, *Nat. Med.* **9** (2003) 123. (d) A. Zamora, G. Vigueras, V. Rodríguez, D. Santana, J. Ruiz, *Coord. Chem. Rev.* **360** (2018) 34. (e) V. Novohradsky, A. Rovira, C. Hally, A. Galindo, G. Vigueras, A. Gandioso, M. Svitelova, R. Bresolí-Obach, H. Kostrhunova, L. Markova, J. Kasparkova, S. Nonell, J. Ruiz, V. Brabec, V. Marchán, *Angew. Chem. Int. Ed.* **58** (2019) 6311.

185 D.C. Batesky, M.J. Goldfogel, D.J. Weix, *J. Org. Chem.* **82** (2017) 9931.

186 M.W.G. de Bolster, J.F. Scholte, *Z. Anorg. Allg. Chem.* **503** (1983) 201.

187 (a) C. Di Iulio, M. Middleton, G. Kociok-Köhn, M.D. Jones, A.L. Johnson, *Eur. J. Inorg. Chem.* (2013) 1541. (b) J.C. de Queiroz, C. Airoldi, A.P. Chagas, *J. Chem. Soc., Dalton Trans*. (1985) 1103. (c) W. Grzybkowski, M. Pilarczyk, L. Klinszporn, *J. Chem. Soc., Faraday Trans. 1* **84** (1988) 1551. (d) N.Sh. Lebedeva, A.I. V'yugin, K.V. Mikhailovskii, *Russ. J. Gen. Chem.* **73** (2003) 968.

188 Y. Hase, O. L. Alves, *J. Mol. Struct.* **50** (1978) 293.

189 T. Wang, Z. Hu, X. Nie, L. Huang, M. Hui, X. Sun, G. Zhang, *Nat. Commun.* **12** (2021) 1364.

190 A.A. Melekhova, A.S. Novikov, K.V. Luzyanin, N.A. Bokach, G.L. Starova, V.V. Gurzhiy, V.Yu. Kukushkin, *Inorg. Chim. Acta* **434** (2015) 31.

191 (a) R. Sole, M. Bortoluzzi, A. Spannenberg, S. Tin, V. Beghetto, J.G. de Vries, *Dalton Trans.* **48** (2019) 13580. (b) A. Scrivanti, R. Sole, M. Bortoluzzi, V. Beghetto, N. Bardella, A. Dolmella, *Inorg. Chim. Acta* **498** (2019) 119. (c) A. Scrivanti, M. Bortoluzzi, R. Sole, V. Beghetto, *Chem. Pap.* **72** (2018) 799.

192 (a) D. Döhler, P. Michael, W.H. Binder, *Macromolecules* **45** (2012) 3335. (b) M. Schunack, M. Gragert, D. Döhler, P. Michael, W.H. Binder, *Macromol. Chem. Phys.* **213** (2012) 205.

193 (a) J. Green, E. Sinn, S. Woodward, *Inorg. Chim. Acta* **230** (1995) 231. (b) A.A. Mohamed, *Coord. Chem. Rev.* **254** (2010) 1918. (c) F. Guang, Z. Yin-li, Z. Min-yan, S. Jia-juan, *J. Chem. Crystallogr.* **42** (2012) 923. (d) E. Goreshnik, *J. Coord. Chem.* **74** (2021) 1919. (e) A.M. Khalil, C. Xu, V. Delmas, G. Calvez, K. Costuas, M. Haouas, C. Lescop, *Inorg. Chem. Front.* **8** (2021) 4887. (f) M. Trose, F. Nahra, D.B. Cordes, A.M.Z. Slawin, C.S.J. Cazin, *Chem. Commun.* **55** (2019) 12068.

194 S. Fery-Forgues, D. Lavabre, *J. Chem. Educ.* **76** (1999) 1260.

195 D.F. Eaton, *Pure Appl. Chem.* **60** (1988) 1107.

196 (a) B. Valeur, *Molecular Fluorescence: Principles and Applications*, WILEY-VCH, Weinheim, 2002. (b) N. Mataga, Y. Kaifu, M. Koizumi, *Bull. Chem. Soc. Jpn.* **29** (1956) 465.

197 J.R. Lakowicz, *Principles of Fluorescence Spectroscopy*, 3rd edn., Springer, Singapore, 2006.

198 U.S. Schubert, H. Hofmeier, G.R. Newkome, *Modern Terpyridine Chemistry*, Wiley-VCH, Weinheim, 2006.

199 (a) H. Hofmeier, U.S. Schubert, *Chem. Soc. Rev.* **33** (2004) 373. (b) C. Wei, Y. He, X. Shi, Z. Song, *Coord. Chem. Rev.* **385** (2019) 1. (c) A. Winter, G.R. Newkome, U.S. Schubert, *ChemCatChem* **3** (2011) 1384. (d) A. Winter, U.S. Schubert, *ChemCatChem* **12** (2020) 2890.

200 (a) M. Bortoluzzi, G. Paolucci, B. Pitteri, A. Vavasori, *Inorg. Chem. Commun.* **9** (2006) 1301. (b) M. Bortoluzzi, G. Paolucci, B. Pitteri, P. Zennaro, V. Bertolasi, *J. Organomet. Chem.* **696** (2011) 2565. (c) M. Bortoluzzi, L. Agostinis, V. Bertolasi, *Chem. Pap.* **74** (2020) 3673.

201 (a) M. Beller, B. Cornils, C.D. Frohning, C.W. Kohlpaintner, *J. Mol. Catal. A: Chem.* **104** (1995) 17. (b) A. Brennführer, H. Neumann, M. Beller, *Angew. Chem. Int. Ed.* **48** (2009) 4114. (c) B. Cornils, W.A. Herrmann, M. Beller, R. Paciello, *Applied homogeneous catalysis with organometallic compounds, A Comprehensive Handbook in Four Volumes*, 3rd edn., Wiley-VCH, Weinheim, 2018.

202 X. Song, H. Xu, *J. Inf. Disp.* **21** (2020) 149.

7 List of publications and presentations

V. Ferraro, M. Bortoluzzi, J. Castro, Synthesis of bis(benzotriazol-1-yl)methane derivatives by cobalt catalyzed formation of C-C bonds, *Proceedings* **41** (2019) 29. DOI: 10.3390/ecsoc-23-06469

M. Bortoluzzi, J. Castro, A. Gobbo, V. Ferraro, L. Pietrobon, S. Antoniutti, Tetrahedral photoluminescent manganese(II) halide complexes with 1,3-dimethyl-2-phenyl-1,3-diazaphospholidine-2-oxide as a ligand, *New J. Chem.* **44** (2020) 571. DOI: 10.1039/c9nj05083c

V. Ferraro, M. Bortoluzzi, J. Castro, A. Vomiero, S. You, Luminescent Cu(I) complex with bis(indazol-1-yl)phenylmethane as chelating ligand, *Inorg. Chem. Commun.* **116** (2020) 107894. DOI: 10.1016/j.inoche.2020.107894

M. Bortoluzzi, J. Castro, A. Gobbo, V. Ferraro, L. Pietrobon, Light harvesting indolyl-substituted phosphoramide ligand for the enhancement of Mn(II) luminescence, *Dalton Trans.* **49** (2020) 7525. DOI: 10.1039/d0dt01659d

M. Bortoluzzi, V. Ferraro, ^{138}La as a useful isotope for gamma spectroscopy without radioactive sources, *Spectroscopy Europe* **32** (2020) 14.

M. Bortoluzzi, V. Ferraro, J. Castro, Synthesis and photoluminescence of manganese(II) naphtylphosphonic diamide complexes, *Dalton Trans.* **50** (2021) 3132. DOI: 10.1039/d1dt00123j

V. Ferraro, M. Bortoluzzi, Influence of copper(I) halides on the reactivity of aliphatic carbodiimides, *Chemistry Proceedings* **3** (2021) 20. DOI: 10.3390/ecsoc-24-08096

V. Ferraro, J. Castro, L. Agostinis, M. Bortoluzzi, Luminescent heteroleptic copper(I) complexes with polydentate benzotriazolyl-based ligands, *Transit. Met. Chem.* **46** (2021) 391. DOI: 10.1007/s11243-021-00458-4

M. Bortoluzzi, J. Castro, A. Di Vera, A. Palù, V. Ferraro, Manganese(II) bromo- and iodo-complexes with phosphoramidate and phosphonate ligands: synthesis, characterization and photoluminescence, *New J. Chem.* **45** (2021) 12871. DOI: 10.1039/d1nj02053f

M. Bortoluzzi, V. Ferraro, F. Sartor, Photoluminescence of homoleptic lanthanide complexes with tris(benzotriazol-1-yl)borate, *J. Fluoresc.* **31** (2021) 1433. DOI: 10.1007/s10895-021-02772-7

V. Ferraro, R. Sole, M. Bortoluzzi, V. Beghetto, J. Castro, *Tris*-isocyanide copper(I) complex enabling copper azide-alkyne cycloaddition (CuAAC) in neat conditions, *Appl. Organomet. Chem.* **35** (2021) e6401. DOI: 10.1002/AOC.6401

V. Ferraro, J. Castro, E. Trave, M. Bortoluzzi, Preparation, reactivity and photoluminescence of copper(I) borohydride complexes with bis[(2-diphenylphosphino)phenyl] ether as chelating ligand, *J. Organomet. Chem.* **957** (2022) 122171. DOI: 10.1016/j.jorganchem.2021.122171

M. Bortoluzzi, J. Castro, V. Ferraro, Dual emission from Mn(II) complexes with carbazolyl-substituted phosphoramides, *Inorg. Chim. Acta* **536** (2022) 120896. DOI: 10.1016/j.ica.2022.120896

V. Ferraro, F. Baggio, J. Castro, M. Bortoluzzi, Green phosphorescent Zn(II) halide complexes with *N*,*N*,*N'*,*N'*-tetramethyl-*P*-indol-1-ylphosphonic diamide as ligand, *Eur. J. Inorg. Chem.* (2022) e202200119. DOI: 10.1002/ejic.202200119

V. Ferraro, M. Girotto, M. Bortoluzzi, *N*,*N*-Dimethyl-4-amino-2,1,3-benzothiadiazole: synthesis and luminescent solvatochromism, *Chem. Proc.* **8** (2022) 87. DOI: 10.3390/ecsoc-25-11658

J. Castro, V. Ferraro, M. Bortoluzzi, Visible-emitting Cu(I) complexes with N-functionalized benzotriazole-based ligands, *New. J. Chem.* **46** (2022) 18938. DOI: 10.1039/D2NJ03165E

V. Ferraro, M. Bortoluzzi, J. Castro, *Synthesis of bis(benzotriazol-1-yl)methane derivatives by cobalt catalyzed formation of C-C bonds*, lecturer for the 23rd International Electronic Conference on Synthetic Organic Chemistry (ECSOC-23, 15th November-15th December 2019), sciforum-027551.

V. Ferraro, M. Bortoluzzi, *Influence of copper(I) halides on the reactivity of aliphatic carbodiimides*, lecturer for the 24th International Electronic Conference on Synthetic Organic Chemistry (ECSOC-24, 15th November-15th December 2020), sciforum-038596.

V. Ferraro, M. Bortoluzzi, J. Castro, *Copper(I) borohydride complex with bis[(2-diphenylphosphino)phenyl] ether. Structure investigation by single-crystal X-Ray diffraction and DFT calculations,* poster presentation at the "XXIX Simposio del Grupo Especializado en Crístalografia y Crecimiento Cristalino" (GE3C, 19th-22nd January 2021, 3rd prize granted by Malvern Panalytical)".

V. Ferraro, R. Sole, M. Bortoluzzi, V. Beghetto, J. Castro, *Three-coordinated isocyanide copper(I) complex: synthesis, characterization and catalytic activity*, poster presentation at XXIV EuCOMC (Virtual Conference on Organometallic Chemistry, 1st-3rd September 2021, University of Alcalá, Madrid, Spain).

M. Bortoluzzi, M. Busato, V. Ferraro, *Computational studies on mercury halides as ligands in organometallic transition complexes*, poster presentation at XXIV EuCOMC (Virtual Conference on Organometallic Chemistry, 1st-3rd September 2021, University of Alcalá, Madrid, Spain).

V. Ferraro, M. Girotto, M. Bortoluzzi, *N,N-dimethyl-4-amino-2,1,3-benzothiadiazole: synthesis and luminescent solvatochromism* for the 25th International Electronic Conference on Synthetic Organic Chemistry (ECSOC-25, 15th-30th November 2021), sciforum-050043.

V. Ferraro, J. Castro, M. Bortoluzzi, *Green-emitting tetrahedral Mn(II) complexes with [O=P]-donor ligands*, oral communication at Italian Photochemistry Meeting 2021 organized by Gruppo Italiano Fotochimica (16th-18th December 2021, University of Torino).

V. Ferraro, J. Castro, M. Bortoluzzi, *Green-emitting Zn(II) halide complexes with N,N,N',N'-tetramethyl-P-indol-1-ylphosphonic diamide as ligand*, poster presentation at SILQCOM08 (VIII Simposio Latinoamericano de Química de Coordinación y Organometálica, 10th-11th March 2022, awarded best poster for the category "Coordination chemistry").

M. Bortoluzzi, J. Castro, V. Ferraro, *Carbazolyl-substituted phosphoramides as ligands for Mn(II) luminescent complexes*, poster presentation at SILQCOM08 (VIII Simposio Latinoamericano de Química de Coordinación y Organometálica, 10th-11th March 2022).

V. Ferraro, J. Castro, M. Bortoluzzi, *Intense red-emitting three-coordinated benzothiadiazole-based copper(I) complexes*, poster presentation at ICCC22 (44th International Conference on Coordination Chemistry, 28th August-2nd September 2022, Rimini).

V. Ferraro, J. Castro, M. Bortoluzzi, *Synthesis and characterization of luminescent N-functionalized benzotriazole-based heteroleptic copper(I) complexes*, poster presentation at INORG22 (XLVIII Italian Conference of Inorganic Chemistry, 6th-9th September 2022, Pisa).

Appendix A: Crystal data and structure refinement

Table A1. Crystal data and structure refinement of [$MnX_2\{O=P(MeNCH_2CH_2NMe)Ph\}_2$], X = Cl, Br.

Compound	[$MnCl_2\{O=P(MeNCH_2CH_2NMe)Ph\}_2$]	[$MnBr_2\{O=P(MeNCH_2CH_2NMe)Ph\}_2$]
Empirical formula	$C_{20}H_{30}Cl_2MnN_4O_2P_2$	$C_{20}H_{30}Br_2MnN_4O_2P_2$
Formula weight	546.26	635.18
Temperature	100(2) K	100(2) K
Wavelength	0.71073 Å	0.71073 Å
Crystal system	Monoclinic	Monoclinic
Space group	*C2/c*	*C2/c*
Unit cell dimensions	a = 13.4104(6) Å	a = 13.4668(6) Å
	b = 13.4995(6) Å	b = 13.7458(6) Å
	c = 14.4145(7) Å	c = 14.4342(6) Å
	β = 102.687(2)°	β = 101.192(2)°
Volume	2545.8(2) Å^3	2621.1(2) Å^3
Z	4	4
Density (calculated)	1.425 Mg/m^3	1.610 Mg/m^3
Absorption coefficient	0.878 mm^{-1}	3.698 mm^{-1}
F(000)	1132	1276
Crystal size	0.253 x 0.171 x 0.167 mm	0.074 x 0.071 x 0.065 mm
θ range for data collection	2.791 to 28.328°	2.739 to 28.356°
Index ranges	$-17 \leq h \leq 17$	$-17 \leq h \leq 17$
	$-18 \leq k \leq 17$	$-18 \leq k \leq 18$
	$-18 \leq l \leq 19$	$-18 \leq l \leq 19$
Reflections collected	24362	37967
Independent reflections	3182 [R_{int} = 0.0366]	3271 [R_{int} = 0.0426]
Reflections observed (>2σ)	2716	2873
Data Completeness	0.999	0.999
Absorption correction	Semi-empirical from equivalents	Semi-empirical from equivalents
Max. and min. transmission	0.7457 and 0.6883	0.7457 and 0.6870
Refinement method	Full-matrix least-squares on F^2	Full-matrix least-squares on F^2
Data / restraints / parameters	3182 / 0 / 143	3271 / 0 / 143
Goodness-of-fit on F^2	1.100	1.047
Final R indices [$I>2\sigma(I)$]	R_1 = 0.0281; wR_2 = 0.0694	R_1 = 0.0235; wR_2 = 0.0510
R indices (all data)	R_1 = 0.0377; wR_2 = 0.0733	R_1 = 0.0304; wR_2 = 0.0531
Largest diff. peak and hole	0.408 and -0.337 e Å^{-3}	0.687 and -0.632 e Å^{-3}

Table A2. Crystal data and structure refinement of [$MnX_2\{O=P(NMe_2)_2Ind\}_2$], X = Cl, Br, I.

Compound	[$MnCl_2\{O=P(NMe_2)_2Ind\}_2$]	[$MnBr_2\{O=P(NMe_2)_2Ind\}_2$]	[$MnI_2\{O=P(NMe_2)_2Ind\}_2$]
Empirical formula	$C_{24}H_{36}Cl_2MnN_6O_2P_2$	$C_{24}H_{36}Br_2MnN_6O_2P_2$	$C_{24}H_{36}I_2MnN_6O_2P_2$
Formula weight	628.37	717.29	811.27
Temperature	100(2) K	100(2) K	100(2) K
Wavelength	0.71073 Å	0.71073 Å	0.71073 Å
Crystal system	Monoclinic	Monoclinic	Monoclinic
Space group	$P2_1/n$	$P2_1/n$	$P2_1/n$
Unit cell dimensions	a = 10.3500(8) Å	a = 10.4594(5) Å	a = 10.6662(7) Å
	b = 15.7450(13) Å	b = 15.7962(8) Å	b = 15.8451(12) Å
	c = 18.6481(14) Å	c = 19.0025(9) Å	c = 19.6427(15) Å
	β = 99.437(2)°	β = 99.319(2)°	β = 100.640(2)°
Volume	2997.8(4) $Å^3$	3098.1(3) $Å^3$	3262.7(4) $Å^3$
Z	4	4	4
Density (calculated)	1.392 Mg/m^3	1.538 Mg/m^3	1.652 Mg/m^3
Absorption coefficient	0.758 mm^{-1}	3.140 mm^{-1}	2.425 mm^{-1}
F(000)	1308	1452	1596
Crystal size	0.172 x 0.109 x 0.047 mm	0.263 x 0.259 x 0.121 mm	0.235 x 0.226 x 0.169 mm
Θ range for data collection	2.214 to 26.456°	2.357 to 28.368°	2.330 to 28.377°
Index ranges	$-12 \leq h \leq 12$	$-13 \leq h \leq 13$	$-14 \leq h \leq 12$
	$-19 \leq k \leq 19$	$-21 \leq k \leq 20$	$-20 \leq k \leq 21$
	$-19 \leq l \leq 23$	$-24 \leq l \leq 25$	$-25 \leq l \leq 26$
Reflections collected	25091	69466	56685
Independent reflections	6164 [R_{int} = 0.0908]	7731 [R_{int} = 0.0606]	8153 [R_{int} = 0.0373]
Reflections observed (>2σ)	4240	6776	7437
Data Completeness	0.995	0.999	0.998
Absorption correction	Semi-empirical from equivalents	Semi-empirical from equivalents	Semi-empirical from equivalents
Max. and min. transmission	0.7425 and 0.6431	0.7457 and 0.3403	0.7457 and 0.5669
Refinement method	Full-matrix least-squares on F^2	Full-matrix least-squares on F^2	Full-matrix least-squares on F^2
Data / restraints / parameters	6164 / 0 / 342	7731 / 0 / 342	8153 / 0 / 342
Goodness-of-fit on F^2	1.010	1.055	1.090
Final R indices [$I>2\sigma(I)$]	R_1 = 0.0514	R_1 = 0.0302	R_1 = 0.0234
	wR_2 = 0.0840	wR_2 = 0.0655	wR_2 = 0.0509
R indices (all data)	R_1 = 0.0974	R_1 = 0.0380	R_1 = 0.0280
	wR_2 = 0.0959	wR_2 = 0.0680	wR_2 = 0.0522
Largest diff. peak and hole	0.390 and -0.425 e $Å^{-3}$	0.448 and -0.747 e $Å^{-3}$	0.742 and -1.000 e $Å^{-3}$

Table A3. Crystal data and structure refinement of $[MnX_2\{O=P(NMe_2)(2\text{-}Naph)\}_2]$, X = Cl, Br, I.

Compound	$MnCl_2\{O=P(NMe_2)(2\text{-}Naph)\}_2]$	$MnBr_2\{O=P(NMe_2)(2\text{-}Naph)\}_2]$	$MnI_2\{O=P(NMe_2)(2\text{-}Naph)\}_2]$
Empirical formula	$C_{28}H_{38}Cl_2MnN_4O_2P_2$	$C_{28}H_{38}Br_2MnN_4O_2P_2$	$C_{28}H_{38}I_2MnN_4O_2P_2$
Formula weight	650.40	739.32	833.30
Temperature	100(2) K	100(2) K	100(2) K
Wavelength	0.71073 Å	0.71073 Å	0.71073 Å
Crystal system	Monoclinic	Monoclinic	Monoclinic
Space group	$P2_1/n$	$P2_1/n$	$P2_1/n$
Unit cell dimensions	a = 10.9664(3) Å	a = 11.3369(4) Å	a = 11.4408(3) Å
	b = 18.1731(6) Å	b = 16.9218(5) Å	b = 17.2155(4) Å
	c = 16.0050(5) Å	c = 17.2939(6) Å	c = 17.7567(4) Å
	β = 90.3520(10)°	β = 97.1810(10)°	β = 99.6840(10)°
Volume	3189.63(17) Å^3	3291.65(19) Å^3	3447.51(14) Å^3
Z	4	4	4
Density (calculated)	1.354 Mg/m^3	1.492 Mg/m^3	1.605 Mg/m^3
Absorption coefficient	0.713 mm^{-1}	2.956 mm^{-1}	2.296 mm^{-1}
F(000)	1356	1500	1644
Crystal size	0.161 x 0.098 x 0.074 mm	0.243 x 0.231 x 0.122 mm	0.213 x 0.193 x 0.175 mm
Theta range for data collection	2.245 to 28.311°	2.366 to 28.298°	2.159 to 28.288°
Index ranges	$-14 \leq h \leq 14$	$-15 \leq h \leq 15$	$-14 \leq h \leq 15$
	$-24 \leq k \leq 24$	$-22 \leq k \leq 22$	$-22 \leq k \leq 22$
	$-21 \leq l \leq 21$	$-23 \leq l \leq 23$	$-23 \leq l \leq 23$
Reflections collected	86852	77021	73511
Independent reflections	7927 [R_{int} = 0.0554]	8169 [R_{int} = 0.0363]	8554 [R_{int} = 0.0312]
Reflections observed (>2σ)	7002	7498	7967
Data Completeness	0.998	0.999	0.999
Absorption correction	Semi-empirical from equivalents	Semi-empirical from equivalents	Semi-empirical from equivalents
Max. and min. transmission	0.7457 and 0.6905	0.7457 and 0.4625	0.7457 and 0.6319
Refinement method	Full-matrix least-squares on F^2	Full-matrix least-squares on F^2	Full-matrix least-squares on F^2
Data / restraints / parameters	7927 / 7 / 382	8169 / 0 / 360	8554 / 0 / 360
Goodness-of-fit on F^2	1.057	1.035	1.078
Final R indices [$I>2\sigma(I)$]	R_1 = 0.0346	R_1 = 0.0226	R_1 = 0.0181
	wR_2 = 0.0767	wR_2 = 0.0543	wR_2 = 0.0392
R indices (all data)	R_1 = 0.0410	R_1 = 0.0257	R_1 = 0.0206
	wR_2 = 0.0798	wR_2 = 0.0557	wR_2 = 0.0400
Largest diff. peak and hole	0.774 and -0.647 e.Å^{-3}	0.809 and -0.615 e.Å^{-3}	0.597 and -0.526 e.Å^{-3}

Table A4. Crystal data and structure refinement of [MnX$_2${O=P(NMe$_2$)$_2$Cbz}$_2$], X = Cl, Br, I.

Compound	[MnCl$_2${O=P(NMe$_2$)$_2$Carb}$_2$]	[MnBr$_2${O=P(NMe$_2$)$_2$Carb}$_2$]	[MnI$_2${O=P(NMe$_2$)$_2$Carb}$_2$]
Empirical formula	$C_{32}H_{40}Cl_2MnN_6O_3P_2$	$C_{32}H_{40}Br_2MnN_6O_2P_2$	$C_{32}\ H_{40}\ I_2\ Mn\ N_6\ O_2\ P_2$
Formula weight	744.48	817.40	911.38
Temperature	100(2) K	100(2) K	100(2) K
Wavelength	0.71073 Å	0.71073 Å	0.71073 Å
Crystal system	Monoclinic	Monoclinic	Triclinic
Space group	$P2_1/c$	$P2_1/c$	P-1
Unit cell dimensions	a = 13.4553(11) Å	a = 13.6104(12) Å	a = 13.5937(8) Å
	b = 7.5969(6) Å	b = 7.5925(8) Å	b = 16.1525(8) Å
	c = 33.633(3) Å	c = 33.857(4) Å	c = 18.1507(10) Å
	α = 90°	α = 90°	α = 70.450(2)°
	β = 94.306(3)°	β = 94.243(3)°	β = 78.827(2)°
	γ = 90°	γ = 90°	γ = 89.773(2)°
Volume	3428.2(5) Å^3	3489.1(6) Å^3	3676.5(4) Å^3
Z	4	4	4
Density (calculated)	1.442 Mg/m^3	1.556 Mg/m^3	1.647 Mg/m^3
Absorption coefficient	0.677 mm^{-1}	2.799 mm^{-1}	2.162 mm^{-1}
F(000)	1548	1660	1804
Crystal size	0.178 x 0.075 x 0.015 mm	0.213 x 0.092 x 0.015 mm	0.161 x 0.155 x 0.113 mm
Θ range for data collection	1.871 to 27.533°	1.854 to 28.316°	1.967 to 28.352°
Index ranges	$-17 < h \leq 17$	$-18 \leq h \leq 14$	$-17 \leq h \leq 18$
	$-9 \leq k \leq 9$	$-10 \leq k \leq 10$	$-21 \leq k \leq 21$
	$-37 \leq l \leq 43$	$-45 \leq l \leq 45$	$-16 \leq l \leq 24$
Reflections collected	78371	103097	18300
Independent reflections	7861 [R_{int} = 0.1080]	8659 [R_{int} = 0.0510]	18300 [R_{int} = 0.0473]
Reflections observed (>2σ)	6716	7789	17352
Data Completeness	0.996	0.997	0.997
Absorption correction	Semi-empirical from equivalents	Semi-empirical from equivalents	Semi-empirical from equivalents
Max. and min. transmission	0.7456 and 0.6371	0.7457 and 0.6192	0.7455 and 0.6771
Refinement method	Full-matrix least-squares on F^2	Full-matrix least-squares on F^2	Full-matrix least-squares on F^2
Data / restraints / parameters	7861 / 0 / 423	8659 / 0 / 414	18300 / 0 / 837
Goodness-of-fit on F^2	1.226	1.163	1.109
Final R indices [I>2σ(I)]	R_1 = 0.1329	R_1 = 0.0389	R_1 = 0.0377
	wR_2 = 0.2880	wR_2 = 0.0830	wR_2 = 0.0948
R indices (all data)	R_1 = 0.1486	R_1 = 0.0450	R_1 = 0.0398
	wR_2 = 0.2947	wR_2 = 0.0851	wR_2 = 0.0960
Largest diff. peak and hole	3.282 and -1.639 e.Å^{-3}	1.259 and -0.469 e.Å^{-3}	4.223 and -1.842 e.Å^{-3}

Table A5. Crystal data and structure refinement of $[MnX_2\{O{=}P(OPh)_2(NMe_2)\}_2]$, X = Br, I.

Compound	$[MnBr_2\{O{=}P(OPh)_2(NMe_2)\}_2]$	$[MnI_2\{O{=}P(OPh)_2(NMe_2)\}_2]$
Empirical formula	$C_{28}H_{32}Br_2MnN_2O_6P_2$	$C_{28}H_{32}I_2MnN_2O_6P_2$
Formula weight	769.25	863.23
Temperature	100(2) K	100(2) K
Wavelength	0.71073 Å	0.71073 Å
Crystal system	Monoclinic	Monoclinic
Space group	$P2_1/n$	$P2_1/n$
Unit cell dimensions	a = 17.2910(15) Å	a = 10.0153(8) Å
	b = 10.3838(9) Å	b = 17.3133(14) Å
	c = 18.4599(15) Å	c = 19.6665(16) Å
	β = 103.825(3)°	β = 103.495(3)°
Volume	3218.4(5) Å^3	3316.0(5) Å^3
Z	4	4
Density (calculated)	1.588 Mg/m^3	1.729 Mg/m^3
Absorption coefficient	3.035 mm^{-1}	2.398 mm^{-1}
F(000)	1548	1692
Crystal size	0.233 x 0.212 x 0.023 mm	0.191 x 0.091 x 0.069 mm
θ range for data collection	2.267 to 28.320°	2.353 to 28.383°
Index ranges	$-23 \leq h \leq 23$	$-13 \leq h \leq 13$
	$-13 \leq k \leq 13$	$-23 \leq k \leq 23$
	$-24 \leq l \leq 24$	$-11 \leq l \leq 26$
Reflections collected	84590	8310
Independent reflections	7976 [R_{int} = 0.0637]	8310 [R_{int} = 0.0426]
Reflections observed (>2σ)	6849	7024
Data Completeness	0.997	0.992
Absorption correction	Semi-empirical from equivalents	Semi-empirical from equivalents
Max. and min. transmission	0.7457 and 0.5152	0.7457 and 0.6383
Refinement method	Full-matrix least-squares on F^2	Full-matrix least-squares on F^2
Data / restraints / parameters	7976 / 0 / 374	8310 / 0 / 375
Goodness-of-fit on F^2	1.030	1.119
Final R indices [I>2σ(I)]	R_1 = 0.0284	R_1 = 0.0472
	wR_2 = 0.0627	wR_2 = 0.1777
R indices (all data)	R_1 = 0.0377	R_1 = 0.0589
	wR_2 = 0.0660	wR_2 = 0.1889
Largest diff. peak and hole	0.475 and -0.483 e.Å^{-3}	1.321 and -1.744 e.Å^{-3}

Table A6. Crystal data and structure refinement of $[\mathrm{MnX_2\{\mu{-}O{=}P(NMe_2)_2(res)(NMe_2)_2P{=}O\}]_n}$, X = Br (n = 2), I.

Compound	$[\mathrm{MnBr_2\{\mu{-}O{=}P(NMe_2)_2(res)(NMe_2)_2P{=}O\}]_2}$	$[\mathrm{MnI_2\{\mu{-}O{=}P(NMe_2)_2(res)(NMe_2)_2P{=}O\}]_n}$
Empirical formula	$C_{14}H_{28}Br_2MnN_4O_4P_2$	$C_{14}H_{28}I_2MnN_4O_2P_2$
Formula weight	593.10	655.08
Temperature	100(2) K	100(2) K
Wavelength	0.71073 Å	0.71073 Å
Crystal system	Monoclinic	Monoclinic
Space group	$P2_1/n$	$P2_1/n$
Unit cell dimensions	a = 11.7628(14) Å	a = 11.1151(9) Å
	b = 9.0147(10) Å	b = 14.0317(12) Å
	c = 23.078(3) Å	c = 16.0386(14) Å
	β = 103.072(4)°	β = 100.395(3)°
Volume	2383.7(5) Å^3	2460.4(4) Å^3
Z	4	4
Density (calculated)	1.653 Mg/m^3	1.768 Mg/m^3
Absorption coefficient	4.065 mm^{-1}	3.190 mm^{-1}
F(000)	1188	1268
Crystal size	0.133 x 0.115 x 0.071 mm	0.265 x 0.238 x 0.205 mm
θ range for data collection	2.811 to 28.506°	2.362 to 28.345°
Index ranges	$-15 \le h \le 15$	$-14 \le h \le 14$
	$-12 \le k \le 12$	$-18 \le k \le 18$
	$-21 \le l \le 30$	$-20 \le l \le 21$
Reflections collected	5934	50220
Independent reflections	5934 [R_{int} = 0.0736]	6143 [R_{int} = 0.0425]
Reflections observed (>2σ)	5147	5510
Data Completeness	0.989	0.999
Absorption correction	Semi-empirical from equivalents	Semi-empirical from equivalents
Max. and min. transmission	0.7151 and 0.5810	0.7457 and 0.5007
Refinement method	Full-matrix least-squares on F^2	Full-matrix least-squares on F^2
Data / restraints / parameters	5934 / 0 / 255	6143 / 0 / 252
Goodness-of-fit on F^2	1.162	1.093
Final R indices [I>2σ(I)]	R_1 = 0.0906; wR_2 = 0.2264	R_1 = 0.0395; wR_2 = 0.0960
R indices (all data)	R_1 = 0.1004; wR_2 = 0.2304	R_1 = 0.0458; wR_2 = 0.0986
Largest diff. peak and hole	1.512 and -1.732 e.Å^{-3}	1.946 and -2.470 e.Å^{-3}

Table A7. Crystal data and structure refinement of O=PPh(S-BINOL).

Compound	O=PPh(S-BINOL)
Empirical formula	$C_{26}H_{17}O_3P$
Formula weight	408.36
Temperature	100(2) K
Wavelength	0.71073 Å
Crystal system	Orthorhombic
Space group	$P2_12_12_1$
Unit cell dimensions	a = 10.1725(3) Å b = 10.5825(3) Å c = 18.4246(5) Å
Volume	1983.42(10) Å^3
Z	4
Density (calculated)	1.368 Mg/m^3
Absorption coefficient	0.165 mm^{-1}
F(000)	848
Crystal size	0.208 x 0.177 x 0.148 mm
Θ range for data collection	2.211 to 28.315°
Index ranges	$-13 \leq h \leq 13$ $-14 \leq k \leq 14$ $-24 \leq l \leq 24$
Reflections collected	31587
Independent reflections	4932 [R_{int} = 0.0204]
Reflections observed (>2σ)	4866
Data Completeness	0.999
Absorption correction	Semi-empirical from equivalents
Max. and min. transmission	0.7457 and 0.6981
Refinement method	Full-matrix least-squares on F^2
Data / restraints / parameters	4932 / 0 / 271
Goodness-of-fit on F^2	1.091
Final R indices [I>2σ(I)]	R_1 = 0.0273 wR_2 = 0.0731
R indices (all data)	R_1 = 0.0277 wR_2 = 0.0734
Largest diff. peak and hole	0.348 and -0.311 e.Å^{-3}

Table A8. Crystal data and structure refinement of $[Mn(bpyO_2)_3][ClO_4]_2$.

Compound	$[Mn(bpyO_2)_3][ClO_4]_2$
Empirical formula	$C_{90}H_{72}Cl_6Mn_3N_{18}O_{46}$
Moiety formula	$3(C_{30}H_{24}MnN_6O_6)$, $6(ClO_4)$, $4(H_2O)$
Formula weight	2519.17
Temperature	100(2) K
Wavelength	0.71073 Å
Crystal system	Monoclinic
Space group	$P2_1/n$
Unit cell dimensions	a = 21.302(3) Å b = 19.101(3) Å c = 25.487(4) Å β = 90.354(5)°
Volume	10370(2) Å^3
Z	4
Density (calculated)	1.614 Mg/m^3
Absorption coefficient	0.619 mm^{-1}
F(000)	5132
Crystal size	0.198 x 0.153 x 0.112 mm
Θ range for data collection	1.921 to 28.433°
Index ranges	$-28 \leq h \leq 28$ $-25 \leq k \leq 25$ $-33 \leq l \leq 34$
Reflections collected	190740
Independent reflections	25620 [R_{int} = 0.0759]
Reflections observed (>2σ)	20715
Data Completeness	0.980
Absorption correction	Semi-empirical from equivalents
Max. and min. transmission	0.7457 and 0.6008
Refinement method	Full-matrix least-squares on F^2
Data / restraints / parameters	25620 / 0 / 1468
Goodness-of-fit on F^2	1.096
Final R indices [I>2σ(I)]	R_1 = 0.1007 wR_2 = 0.2669
R indices (all data)	R_1 = 0.1162 wR_2 = 0.2747
Largest diff. peak and hole	1.681 and -0.713 e.Å^{-3}

Table A9. Crystal data and structure refinement of [Cu(κ^2–BH$_4$)(DPEphos)].

Identification code	[Cu(κ^2–BH$_4$)(DPEphos)]
Empirical formula	$C_{36}H_{32}BCuOP_2$
Formula weight	616.90
Temperature	100(2) K
Wavelength	0.71073 Å
Crystal system	Triclinic
Space group	*P*-1
Unit cell dimensions	*a* = 13.1770(10) Å
	b = 14.6407(11) Å
	c = 17.4820(12) Å
	α = 108.429(3)°
	β = 107.017(3)°
	γ = 90.579(3)°
Volume	3039.9(4) Å^3
Z	4
Density (calculated)	1.348 Mg/m^3
Absorption coefficient	0.852 mm^{-1}
F(000)	1280
Crystal size	0.273 x 0.166 x 0.075 mm
Θ range for data collection	2.069 to 28.356°
Index ranges	$-17 \le h \le 17$
	$-19 \le k \le 19$
	$-23 \le l \le 23$
Reflections collected	121492
Independent reflections	15155 [R_{int} = 0.0500]
Reflections observed (>2σ)	13338
Data Completeness	0.996
Absorption correction	Semi-empirical from equivalents
Max. and min. transmission	0.7457 and 0.6373
Refinement method	Full-matrix least-squares on F^2
Data / restraints / parameters	15155 / 0 / 771
Goodness-of-fit on F^2	1.029
Final *R* indices [I>2σ(I)]	R_1 = 0.0321
	wR_2 = 0.0807
R indices (all data)	R_1 = 0.0390
	wR_2 = 0.0847
Largest diff. peak and hole	0.649 and -0.654 e.Å^{-3}

Table A10. Crystal data and structure refinement of CHPh(btz)$_2$ and CH(btz)$_3$.

Compound	CHPh(btz)$_2$	CH(btz)$_3$
Empirical formula	$C_{19}H_{18}N_6$	$C_{19}H_{13}N_9$
Formula weight	330.39	367.38
Temperature	100(2) K	100(2) K
Wavelength	0.71073 Å	0.71073 Å
Crystal system	Monoclinic	Monoclinic
Space group	$P2_1/c$	$P2_1/c$
Unit cell dimensions	a = 11.0957(6) Å b = 13.1089(6) Å c = 11.3388(6) Å β = 105.678(2)°	a = 9.8330(8) Å b = 14.6452(10) Å c = 11.9477(9) Å β = 96.571(3)°
Volume	1587.90(14) Å^3	1709.2(2) Å^3
Z	4	4
Density (calculated)	1.382 Mg/m^3	1.428 Mg/m^3
Absorption coefficient	0.087 mm^{-1}	0.094 mm^{-1}
F(000)	696	760
Crystal size	0.158 x 0.149 x 0.132 mm	0.235 x 0.035 x 0.029 mm
Θ range for data collection	2.428 to 28.356 °	2.209 to 28.345°
Index ranges	$-14 \leq h \leq 14$ $-17 \leq k \leq 17$ $-15 \leq l \leq 15$	$-12 \leq h \leq 13$ $-19 \leq k \leq 19$ $-15 \leq l \leq 15$
Reflections collected	26843	32654
Independent reflections	3956 [R_{int} = 0.0447]	4261 [R_{int} = 0.0560]
Reflections observed (>2σ)	3194	3295
Data Completeness	0.997	0.999
Absorption correction	Semi-empirical from equivalents	Semi-empirical from equivalents
Max. and min. transmission	0.7383 and 0.7121	0.7457 and 0.6533
Refinement method	Full-matrix least-squares on F^2	Full-matrix least-squares on F^2
Data / restraints / parameters	3956 / 0 / 226	4261 / 0 / 253
Goodness-of-fit on F^2	1.063	1.055
Final R indices [I>2σ(I)]	R_1 = 0.0440 wR_2 = 0.0937	R_1 = 0.0426 wR_2 = 0.0938
R indices (all data)	R_1 = 0.0621 wR_2 = 0.1010	R_1 = 0.0635 wR_2 = 0.1022
Largest diff. peak and hole	0.238 and -0.308 e.Å^{-3}	0.246 and -0.307 e.Å^{-3}

Table A11. Crystal data and structure refinement of the cation [Cu{CHPh(ind)$_2$}$_2$]$^+$.

Compound	[Cu{CHPh(ind)$_2$}$_2$]$^+$
Empirical formula	$C_{42}H_{32}ClCuN_8$
Formula weight	747.74
Temperature	100(2) K
Wavelength	0.71073 Å
Crystal system	Tetragonal
Space group	$I4_1/a$
Unit cell dimensions	$a = b$ = 20.2702(9) Å
	c = 38.6461(19) Å
Volume	15878.9(16) Å^3
Z	16
Density (calculated)	1.251 Mg/m^3
Absorption coefficient	0.657 mm^{-1}
F(000)	6176
Crystal size	0.152 x 0.146 x 0.042 mm
Theta range for data collection	2.269 to 28.366°
Index ranges	$-27 \leq h \leq 27$
	$-27 \leq k \leq 22$
	$-51 \leq l \leq 50$
Reflections collected	115565
Independent reflections	9916 [R_{int} = 0.0576]
Reflections observed (>2σ)	7401
Data Completeness	0.998
Absorption correction	Semi-empirical from equivalents
Max. and min. transmission	0.7457 and 0.6648
Refinement method	Full-matrix least-squares on F^2
Data / restraints / parameters	9916 / 0 / 460
Goodness-of-fit on F^2	1.026
Final R indices [I>2σ(I)]	R_1 = 0.0517
	wR_2 = 0.1151
R indices (all data)	R_1 = 0.0761
	wR_2 = 0.1263
Largest diff. peak and hole	1.274 and -1.078 e.Å^{-3}

Table A12. Crystal data and structure refinement of 1-(4,6-methoxy-1,3,5-triazin-2-yl) and 1-(4,6-phenoxy-1,3,5-triazin-2-yl)benzotriazole, trz^{OMe}-btz and trz^{OPh}-btz.

Compound	trz^{OMe}-btz	trz^{OPh}-btz
Empirical formula	$C_{11}H_{10}N_6O_2$	$C_{21}H_{14}N_6O_2$
Formula weight	258.25	382.38
Temperature	100(2) K	100(2) K
Wavelength	0.71073 Å	0.71073 Å
Crystal system	Monoclinic	Triclinic
Space group	$P2_1/c$	P-1
Unit cell dimensions	a = 14.3117(9) Å	a = 6.7497(7) Å
	b = 10.6121(6) Å	b = 10.5961(10) Å
	c = 15.8829(10) Å	c = 12.9511(13) Å
	α = 90°	α = 74.696(4)°
	β = 113.323(2)°	β = 82.773(4)°
	γ = 90°	γ = 81.119(4)°
Volume	2215.1(2) Å^3	879.19(15) Å^3
Z	8	2
Density (calculated)	1.549 Mg/m^3	1.444 Mg/m^3
Absorption coefficient	0.114 mm^{-1}	0.098 mm^{-1}
F(000)	1072	396
Crystal size	0.255 x 0.155 x 0.094 mm	0.139 x 0.054 x 0.014 mm
Θ range for data collection	2.467 to 28.301°	2.009 to 26.462°
Index ranges	$-19 \le h \le 19$	$-8 \le h \le 8$
	$-14 \le k \le 14$	$-13 \le k \le 13$
	$-21 \le l \le 21$	$-16 \le l \le 16$
Reflections collected	55418	3627
Independent reflections	5496 [R_{int} = 0.0388]	3627 [R_{int} = 0.1108]
Reflections observed (>2σ)	4781	3209
Data Completeness	0.998	0.994
Absorption correction	Semi-empirical from equivalents	Semi-empirical from equivalents
Max. and min. transmission	0.7376 and 0.7145	0.7454 and 0.5587
Refinement method	Full-matrix least-squares on F^2	Full-matrix least-squares on F^2
Data / restraints / parameters	5496 / 0 / 349	3627 / 0 / 262
Goodness-of-fit on F^2	1.044	1.190
Final R indices [I>2σ(I)]	R_1 = 0.0348	R_1 = 0.0882
	wR_2 = 0.0935	wR_2 = 0.2144
R indices (all data)	R_1 = 0.0409	R_1 = 0.0997
	wR_2 = 0.0978	wR_2 = 0.2223
Largest diff. peak and hole	0.393 and -0.221 e.Å^{-3}	0.416 and -0.444 e.Å^{-3}

Table A13. Crystal data and structure refinement of $[CuL(PPh_3)_2][BF_4]$, L = py-btz and pym-btz.

Compound	$[Cu(py\text{-}btz)(PPh_3)_2][BF_4]$	$[Cu(pym\text{-}btz)(PPh_3)_2][BF_4]$
Empirical formula	$C_{47}H_{38}BCuF_4N_4P_2$	$C_{46}H_{37}BCuF_4N_5P_2$
Moiety formula	$C_{47}H_{38}CuN_4P_2$, BF_4	$C_{46}H_{37}CuN_5P_2$, BF_4
Formula weight	871.10	872.09
Temperature	100(2) K	100(2) K
Wavelength	0.71073 Å	0.71073 Å
Crystal system	Triclinic	Triclinic
Space group	P-1	P-1
Unit cell dimensions	a = 12.5593(9) Å	a = 11.5371(7) Å
	b = 13.8159(9) Å	b = 13.8789(7) Å
	c = 14.4530(9) Å	c = 14.6175(8) Å
	α = 73.092(2)^o	α = 76.379(2)^o
	β = 68.530(2)^o	β = 75.218(2)^o
	γ = 63.003(2)^o	γ = 80.553(2)^o
Volume	2055.9(2) Å^3	2185.9(2) Å^3
Z	2	2
Density (calculated)	1.407 Mg/m^3	1.325 Mg/m^3
Absorption coefficient	0.667 mm^{-1}	0.628 mm^{-1}
F(000)	896	896
Crystal size	0.243 x 0.202 x 0.183 mm	0.214 x 0.076 x 0.034 mm
Theta range for data collection	2.928 to 28.315^o	2.510 to 28.311°
Index ranges	$-16 \le h \le 16$	$-15\le h \le15$
	$-18 \le k \le 18$	$-18\le k \le18$
	$-19 \le l \le 19$	$-19\le l \le19$
Reflections collected	92382	134529
Independent reflections	10220 [Rint = 0.0266]	10868 [R_{int} = 0.0478]
Reflections observed (>2σ)	9675	9733
Data Completeness	0.998	0.997
Absorption correction	Semi-empirical from equivalents	Semi-empirical from equivalents
Max. and min. transmission	0.7457 and 0.6946	0.7388 and 0.6985
Refinement method	Full-matrix least-squares on F^2	Full-matrix least-squares on F^2
Data / restraints / parameters	10220 / 0 / 532	10868 / 0 / 532
Goodness-of-fit on F2	1.041	1.058
Final R indices [I>2σ(I)]	R_1 = 0.0268	R_1 = 0.0443
	wR_2 = 0.0656	wR_2 = 0.1164
R indices (all data)	R_1 = 0.0287	R_1 = 0.0498
	wR_2 = 0.0667	wR_2 = 0.1199
Largest diff. peak and hole	0.395 and -0.373 e.Å-3	1.397 and -0.864 e.Å^{-3}

Table A14. Crystal data and structure refinement of [Cu(py-btz)(DPEphos)][BF$_4$] and [Cu(pym-btz)(P^{i}Pr$_3$)$_2$][BF$_4$].

Compound	[Cu(py-btz)(DPEphos)][BF$_4$]	[Cu(pym-btz)(P^{i}Pr$_3$)$_2$][BF$_4$]
Empirical formula	$C_{47}H_{36}BCuF_4N_4OP_2$	$C_{28}H_{49}BCuF_4N_5P_2$
Moiety formula	$C_{47}H_{36}CuN_4OP_2$, BF_4	$C_{28}H_{49}CuN_5P_2$, BF_4
Formula weight	885.09	668.01
Temperature	100(2) K	100(2) K
Wavelength	0.71073 Å	0.71073 Å
Crystal system	Monoclinic	Orthorhombic
Space group	*C2/c*	$P2_12_12_1$
Unit cell dimensions	a = 29.5710(14) Å	a = 13.5696(6) Å
	b = 22.0467(9) Å	b = 15.0666(7) Å
	c = 25.9445(10) Å	c = 16.2774(8) Å
	β = 91.716(2)°	β = 90°
Volume	16906.8(12) Å^3	3327.9(3) Å^3
Z	16	4
Density (calculated)	1.391 Mg/m^3	1.333 Mg/m^3
Absorption coefficient	0.652 mm^{-1}	0.801 mm^{-1}
F(000)	7264	1408
Crystal size	0.215 x 0.173 x 0.083 mm	0.173 x 0.135 x 0.109 mm
Theta range for data collection	1.931 to 28.304°	1.954 to 28.307°
Index ranges	$-39 \leq h \leq 39$	$-18 \leq h \leq 18$
	$-29 \leq k \leq 29$	$-20 \leq k \leq 20$
	$-34 \leq l \leq 33$	$-21 \leq l \leq 21$
Reflections collected	234094	45415
Independent reflections	20984 [R_{int} = 0.0567]	8263 [R_{int} = 0.0330]
Reflections observed (>2σ)	16754	8088
Data Completeness	0.998	0.999
Absorption correction	Semi-empirical from equivalents	Semi-empirical from equivalents
Max. and min. transmission	0.7336 and 0.6915	0.7457 and 0.6651
Refinement method	Full-matrix least-squares on F^2	Full-matrix least-squares on F^2
Data / restraints / parameters	20984 / 0 / 1177	8263 / 0 / 382
Goodness-of-fit on F^2	1.021	1.089
Final R indices [I>2σ(I)]	R_1 = 0.0415	R_1 = 0.0535
	wR_2 = 0.10208	wR_2 = 0.1396
R indices (all data)	R_1 = 0.0578	R_1 = 0.0543
	wR_2 = 0.1120	wR_2 = 0.1402
Largest diff. peak and hole	0.520 and -0.940 e.Å^{-3}	3.158 and -0.743 e.Å^{-3}

Table A15. Crystal data and structure refinement of [Cu(pym-btz)(μ-dppe)]$_2$[BF$_4$]$_2$ and [Cu(trz$^{\mathrm{OMe}}$-btz)(P^{i}Pr$_3$)$_2$][BF$_4$].

Compound	[Cu(pym-btz)(dppe)]$_2$[BF$_4$]$_2$	[Cu(trz$^{\mathrm{OMe}}$-btz)(P^{i}Pr$_3$)$_2$][BF$_4$]
Empirical formula	$C_{72}H_{62}B_2Cu_2F_8N_{10}P_4$	$C_{29}H_{52}BCuF_4N_6O_2P_2$
Moiety formula	$C_{72}H_{62}Cu_2N_{10}P_4$, 2(BF$_4$)	$C_{29}H_{52}CuN_6O_2P_2$, BF$_4$
Formula weight	1491.89	729.05
Temperature	100(2) K	100(2) K
Wavelength	0.71073 Å	0.71073 Å
Crystal system	Triclinic	Triclinic
Space group	*P*-1	*P*-1
Unit cell dimensions	a = 12.8974(8) Å	a = 10.1027(6) Å
	b = 13.1088(8) Å	b = 12.8600(9) Å
	c = 13.3025(7) Å	c = 13.8962(10) Å
	α = 111.144(2)°	α = 95.446(3)°
	β = 99.259(2)°	β = 100.595(2)°
	γ = 109.024(2)°	γ = 93.419(2)°
Volume	1881.56(19) Å^3	1761.1(2) Å^3
Z	1	2
Density (calculated)	1.317 Mg/m^3	1.375 Mg/m^3
Absorption coefficient	0.717 mm^{-1}	0.768 mm^{-1}
F(000)	764	768
Crystal size	0.173 x 0.121 x 0.063 mm	0.282 x 0.255 x 0.173 mm
Theta range for data collection	2.042 to 28.328°	2.057 to 28.329°
Index ranges	$-17 \leq h \leq 17$	$-13 \leq h \leq 13$
	$-17 \leq k \leq 17$	$-17 \leq k \leq 17$
	$-17 \leq l \leq 17$	$-18 \leq l \leq 18$
Reflections collected	86819	109259
Independent reflections	9358 [R_{int} = 0.0436]	8766 [R_{int} = 0.0418]
Reflections observed (>2σ)	7986	8168
Data Completeness	0.998	0.996
Absorption correction	Semi-empirical from equivalents	Semi-empirical from equivalents
Max. and min. transmission	0.7457 and 0.7013	0.7457 and 0.6550
Refinement method	Full-matrix least-squares on F^2	Full-matrix least-squares on F^2
Data / restraints / parameters	9358 / 39 / 465	8766 / 0 / 420
Goodness-of-fit on F^2	1.043	1.017
Final R indices [I>2σ(I)]	R_1 = 0.0858	R_1 = 0.0291
	wR_2 = 0.2467	wR_2 = 0.0755
R indices (all data)	R_1 = 0.0962	R_1 = 0.0318
	wR_2 = 0.2572	wR_2 = 0.0771
Largest diff. peak and hole	4.207 and -2.328 e.Å^{-3}	0.728 and -0.479 e.Å^{-3}

Table A16. Crystal data and structure refinement of [Cu(trz^{OEt}-btz)(DPEphos)][BF$_4$], and [Cu(trz^{OPh}-btz)(DPEphos)][BF$_4$].

Compound	[Cu(trz^{OEt}-btz)(DPEphos)][BF$_4$]	[Cu(trz^{OPh}-btz)(DPEphos)][BF$_4$]
Empirical formula	$C_{49}H_{42}BCuF_4N_6O_3P_2$	$C_{61}H_{52}BCuF_4N_6O_4P_2$
Moiety formula	$C_{49}H_{42}CuN_6O_3P_2$, BF_4	$C_{57}H_{42}CuN_6O_3P_2$, BF_4, $C_4H_{10}O$
Formula weight	975.17	1145.37
Temperature	100(2) K	100(2) K
Wavelength	0.71073 Å	0.71073 Å
Crystal system	Monoclinic	Triclinic
Space group	$P2_1/c$	P-1
Unit cell dimensions	a = 14.7130(12) Å	a = 11.3664(5) Å
	b = 23.4115(16) Å	b = 12.6813(6) Å
	c = 14.0533(12) Å	c = 20.9098(10) Å
	α = 90°	α = 96.034(2)°
	β = 106.376(3)°	β = 105.307(2)°
	γ = 90°	γ = 106.960(2)°
Volume	4644.3(6) Å^3	2725.9(2) Å^3
Z	4	2
Density (calculated)	1.395 Mg/m^3	1.395 Mg/m^3
Absorption coefficient	0.604 mm^{-1}	0.528 mm^{-1}
F(000)	2008	1184
Crystal size	0.273 x 0.156 x 0.087 mm	0.174 x 0.131 x 0.078 mm
Theta range for data collection	1.972 to 28.304°	1.970 to 28.302°
Index ranges	$-19 \leq h \leq 19$	$-15 \leq h \leq 15$
	$-31 \leq k \leq 31$	$-16 \leq k \leq 16$
	$-18 \leq l \leq 18$	$-27 \leq l \leq 27$
Reflections collected	139660	168957
Independent reflections	11546 [R_{int} = 0.0355]	13508 [R_{int} = 0.0384]
Reflections observed (>2σ)	10628	12432
Data Completeness	0.999	0.999
Absorption correction	Semi-empirical from equivalents	Semi-empirical from equivalents
Max. and min. transmission	0.7457 and 0.6835	0.7447 and 0.7134
Refinement method	Full-matrix least-squares on F^2	Full-matrix least-squares on F^2
Data / restraints / parameters	11546 / 1 / 567	13508 / 0 / 714
Goodness-of-fit on F^2	1.046	1.027
Final R indices [I>2σ(I)]	R_1 = 0.1067	R_1 = 0.0298
	wR_2 = 0.2984	wR_2 = 0.0741
R indices (all data)	R_1 = 0.1132	R_1 = 0.0333
	wR_2 = 0.3056	wR_2 = 0.0761
Largest diff. peak and hole	5.560 and -4.058 e.Å^{-3}	0.354 and -0.417 e.Å^{-3}

Table A17. Crystal data and structure refinement of [Cu(BTD)(PPh_3)$_2$][X], X- = BF_4^-, ClO_4^-.

Compound	[Cu(BTD)PPh_3)$_2$]BF_4	[Cu(BTD)(PPh_3)$_2$][ClO_4]
Empirical formula	$C_{42}H_{34}BCuF_4N_2P_2S$	$C_{42}H_{34}ClCuN_2O_4P_2S$
Moiety formula	$C_{42}H_{34}CuN_2P_2S$, BF_4	$C_{42}H_{34}CuN_2P_2S$, ClO_4
Formula weight	811.06	823.70
Temperature	100(2) K	100(2) K
Wavelength	0.71073 Å	0.71073 Å
Crystal system	Monoclinic	Monoclinic
Space group	$P2_1/c$	$P2_1/n$
Unit cell dimensions	a = 9.8849(5) Å	a = 10.9823(4) Å
	b = 36.9427(18) Å	b = 17.4360(7) Å
	c = 11.1027(6) Å	c = 20.0255(8) Å
	β = 113.293(2)°	β = 105.1040(10)°
Volume	3724.0(3) Å^3	3702.2(2) Å^3
Z	4	4
Density (calculated)	1.447 Mg/m^3	1.478 Mg/m^3
Absorption coefficient	0.783 mm^{-1}	0.852 mm^{-1}
F(000)	1664	1696
Crystal size	0.273 x 0.255 x 0.216 mm	0.294 x 0.273 x 0.261 mm
Theta range for data collection	2.243 to 28.327°	2.248 to 28.303°
Index ranges	$-13 \leq h \leq 13$	$-14 \leq h \leq 14$
	$-49 \leq k \leq 49$	$-23 \leq k \leq 23$
	$-13 \leq l \leq 14$	$-26 \leq l \leq 26$
Reflections collected	89995	95260
Independent reflections	9263 [R_{int} = 0.0377]	9211 [R_{int} = 0.0301]
Reflections observed (>2σ)	8987	8843
Data Completeness	0.998	0.999
Absorption correction	Semi-empirical from equivalents	Semi-empirical from equivalents
Max. and min. transmission	0.7457 and 0.5924	0.7457 and 0.6129
Refinement method	Full-matrix least-squares on F^2	Full-matrix least-squares on F^2
Data / restraints / parameters	9263 / 0 / 478	9211 / 0 / 497
Goodness-of-fit on F^2	1.189	1.070
Final R indices [I>2σ(I)]	R_1 = 0.0425	R_1 = 0.0275
	wR_2 = 0.0929	wR_2 = 0.0653
R indices (all data)	R_1 = 0.0436	R_1 = 0.0288
	wR_2 = 0.0934	wR_2 = 0.0660
Largest diff. peak and hole	1.265 and -0.647 e.Å^{-3}	0.387 and -0.537 e.Å^{-3}

Table A18. Crystal data and structure refinement of [Cu_2(BTD)(CH_3CN)(μ-dppm)$_2$][BF_4]$_2$.

Compound	[Cu_2(BTD)(CH_3CN)(μ_2-dppm)$_2$][BF_4]$_2$
Empirical formula	$C_{58}H_{51}B_2Cu_2F_8N_3P_4S$
Moiety formula	$C_{58}H_{51}BCu_2F_4N_3P_4S$, BF_4
Formula weight	1246.66
Temperature	100(2) K
Wavelength	0.71073 Å
Crystal system	Monoclinic
Space group	$P2_1/n$
Unit cell dimensions	a = 13.8698(14) Å b = 18.7249(18) Å c = 21.727(2) Å β = 92.587(4)°
Volume	5636.9(10) Å^3
Z	4
Density (calculated)	1.469 Mg/m^3
Absorption coefficient	0.973 mm^{-1}
F(000)	2544
Crystal size	0.176 x 0.052 x 0.028 mm
Theta range for data collection	2.369 to 26.411°
Index ranges	$-17 \leq h \leq 17$ $-23 \leq k \leq 23$ $-27 \leq l \leq 27$
Reflections collected	11501
Independent reflections	11501 [R_{int} = 0.0933]
Reflections observed (>2σ)	9210
Data Completeness	0.994
Absorption correction	Semi-empirical from equivalents
Max. and min. transmission	0.7454 and 0.6322
Refinement method	Full-matrix least-squares on F^2
Data / restraints / parameters	11501 / 0 / 705
Goodness-of-fit on F^2	1.063
Final R indices [I>2σ(I)]	R_1 = 0.0526 wR_2 = 0.1228
R indices (all data)	R_1 = 0.0710 wR_2 = 0.1319
Largest diff. peak and hole	0.938 and -0.651 e.Å^{-3}

Table A19. Crystal data and structure refinement of [ZnX$_2${O=P(NMe$_2$)$_2$Ind}$_2$], X = Cl, Br, I.

Compound	[ZnCl$_2${O=P(NMe$_2$)$_2$Ind}$_2$]	[ZnBr$_2${O=P(NMe$_2$)$_2$Ind}$_2$]	[ZnI$_2${O=P(NMe$_2$)$_2$Ind}$_2$]
Empirical formula	$C_{24}H_{36}Cl_2N_6O_2P_2Zn$	$C_{24}\ H_{36}\ Br_2\ N_6\ O_2\ P_2\ Zn$	$C_{24}\ H_{36}\ I_2\ N_6\ O_2\ P_2\ Zn$
Formula weight	638.80	727.72	821.70
Temperature	100(2) K	100(2) K	100(2) K
Wavelength	0.71073 Å	0.71073 Å	0.71073 Å
Crystal system	Monoclinic	Monoclinic	Triclinic
Space group	$P2_1/n$	$P2_1/n$	P-1
Unit cell dimensions	a = 11.3448(5) Å	a = 10.4643(8) Å	a = 10.8525(7) Å
	b = 17.9540(6) Å	b = 15.6926(11) Å	b = 15.4380(12) Å
	c = 15.4009(6) Å	c = 18.9051(13) Å	c = 19.4844(14) Å
	α = 90°	α = 90°	α = 93.015(3)°
	β = 108.205 (1)°	β = 99.883(3)°	β = 101.922(2)°
	γ = 90°	γ = 90°	γ = 90.938(2)°
Volume	2979.9(2) Å^3	3058.4(4) Å^3	3188.4(4) Å^3
Z	4	4	4
Density (calculated)	1.424 Mg/m^3	1.580 Mg/m^3	1.712 Mg/m^3
Absorption coefficient	1.143 mm^{-1}	3.552 mm^{-1}	2.838 mm^{-1}
F(000)	1328	1472	1616
Crystal size	0.293 x 0.275 x 0.233 mm	0.175 x 0.085 x 0.079 mm	0.293 x 0.255 x 0.211 mm
Theta range for data collection	2.204 to 28.308°	2.743 to 28.302°	1.919 to 28.291°
Index ranges	$-15 \le h \le 15$	$-13 \le h \le 13$	$-14 \le h \le 14$
	$-23 \le k \le 23$	$-20 \le k \le 20$	$-20 \le k \le 20$
	$-20 \le l \le 20$	$-25 \le l \le 25$	$-25 \le l \le 25$
Reflections collected	73198	96462	151361
Independent reflections	7392 [R_{int} = 0.0313]	7582 [R_{int} = 0.0369]	15830 [R_{int} = 0.0553]
Reflections observed (>2σ)	6999	7184	15133
Data Completeness	0.998	0.998	0.999
Absorption correction	Semi-empirical from equivalents	Semi-empirical from equivalents	Semi-empirical from equivalents
Max. and min. transmission	0.7457 and 0.6021	0.7457 and 0.5768	0.7457 and 0.4660
Refinement method	Full-matrix least-squares on F^2	Full-matrix least-squares on F^2	Full-matrix least-squares on F^2
Data / restraints / parameters	7392 / 0 / 342	7582 / 0 / 342	15830 / 0 / 683
Goodness-of-fit on F^2	1.084	1.048	1.178
Final R indices [I>2σ(I)]	R_1 = 0.0215; wR_2 = 0.0540	R_1 = 0.0190; wR_2 = 0.0447	R_1 = 0.0246; wR_2 = 0.0557
R indices (all data)	R_1 = 0.0232; wR_2 = 0.0547	R_1 = 0.0206; wR_2 = 0.0452	R_1 = 0.0263; wR_2 = 0.0563
Largest diff. peak and hole	0.321 and -0.430 e.Å^{-3}	0.511 and -0.712 e.Å^{-3}	0.503 and -1.434 e.Å^{-3}

Table A20. Crystal data and structure refinement of [$ZnBr_2(DOPO)_2$].

Empirical formula	$C_{24}H_{18}Br_2O_4P_2Zn$
Formula weight	657.51
Temperature	100(2) K
Wavelength	0.71073 Å
Crystal system	Triclinic
Space group	*P*-1
Unit cell dimensions	a = 7.4593(3) Å
	b = 9.8654(4) Å
	c = 16.7638(8) Å
	α = 85.436(2)°
	β = 87.870(2)°
	γ = 70.289(2)°
Volume	1157.59(9) $Å^3$
Z	2
Density (calculated)	1.886 Mg/m^3
Absorption coefficient	4.682 mm^{-1}
F(000)	648
Crystal size	0.275 x 0.213 x 0.188 mm
Theta range for data collection	2.198 to 28.297°
Index ranges	$-9 \leq h \leq 9$
	$-13 \leq k \leq 13$
	$-22 \leq l \leq 22$
Reflections collected	59106
Independent reflections	5737 [R_{int} = 0.0559]
Reflections observed (>2σ)	5339
Data Completeness	0.999
Absorption correction	Semi-empirical from equivalents
Max. and min. transmission	0.7457 and 0.5188
Refinement method	Full-matrix least-squares on F^2
Data / restraints / parameters	5737 / 0 / 306
Goodness-of-fit on F^2	1.051
Final *R* indices [I>2σ(I)]	R_1 = 0.0207
	wR_2 = 0.0485
R indices (all data)	R_1 = 0.0233
	wR_2 = 0.0496
Largest diff. peak and hole	0.558 and -0.422 e.$Å^{-3}$

Table A21. Crystal data and structure refinement of [Cu(CNXyl)$_3$][BF$_4$].

Identification code	[Cu(CNXyl)$_3$][BF$_4$]
Empirical formula	$C_{27}H_{27}BCuF_4N_3$
Moiety formula	$C_{27}H_{27}CuN_3$, BF_4
Formula weight	543.86
Temperature	100(2) K
Wavelength	0.71073 Å
Crystal system	Monoclinic
Space group	$P2_1/c$
Unit cell dimensions	a = 10.5656(6) Å b = 19.9807(11) Å c = 12.6679(6) Å β = 101.811(2)°
Volume	2617.7(2) Å^3
Z	4
Density (calculated)	1.380 Mg/m^3
Absorption coefficient	0.883 mm^{-1}
F(000)	1120
Crystal size	0.256 x 0.213 x 0.201 mm
Theta range for data collection	1.969 to 28.310°
Index ranges	$-14 \le h \le 14$ $-26 \le k \le 26$ $-16 \le l \le 16$
Reflections collected	79592
Independent reflections	6501 [R_{int} = 0.0415]
Reflections observed (>2σ)	5883
Data Completeness	0.999
Absorption correction	Semi-empirical from equivalents
Max. and min. transmission	0.7457 and 0.5596
Refinement method	Full-matrix least-squares on F^2
Data / restraints / parameters	6501 / 0 / 331
Goodness-of-fit on F^2	1.034
Final R indices [I>2σ(I)]	R_1 = 0.0290 wR_2 = 0.0748
R indices (all data)	R_1 = 0.0334 wR_2 = 0.0772
Largest diff. peak and hole	0.427 and -0.330 e.Å^{-3}

Table A22. Crystal data and structure refinement of [Pd(COMe)Cl(BTD^{NPy})].

Identification code	[Pd(COMe)Cl(BTD^{NPy})]
Empirical formula	$C_{14}H_{11}ClN_4OPdS$
Formula weight	425.18
Temperature	100(2) K
Wavelength	0.71073 Å
Crystal system	Monoclinic
Space group	$P2_1/n$
Unit cell dimensions	a = 11.3051(7) Å
	b = 6.9256(4) Å
	c = 19.3392(10) Å
	β = 100.944(2)°
Volume	1486.62(15) Å^3
Z	4
Density (calculated)	1.900 Mg/m^3
Absorption coefficient	1.574 mm^{-1}
F(000)	840
Crystal size	0.234 x 0.051 x 0.043 mm
Theta range for data collection	3.131 to 28.299°
Index ranges	$-15 \leq h \leq 15$
	$-9 \leq k \leq 9$
	$-25 \leq l \leq 25$
Reflections collected	34408
Independent reflections	3676 [R_{int} = 0.0278]
Reflections observed (>2σ)	3445
Data Completeness	0.996
Absorption correction	Semi-empirical from equivalents
Max. and min. transmission	0.7457 and 0.6534
Refinement method	Full-matrix least-squares on F^2
Data / restraints / parameters	3676 / 0 / 200
Goodness-of-fit on F^2	1.088
Final R indices [I>2σ(I)]	R_1 = 0.0169
	wR_2 = 0.0417
R indices (all data)	R_1 = 0.0187
	wR_2 = 0.0425
Largest diff. peak and hole	0.344 and -0.627 e.Å^{-3}

Appendix B: Selected bond lengths [Å] and angles [°]

Table B1. Selected bond lengths [Å] and angles [°] for [$MnX_2\{O=P(MeNCH_2CH_2NMe)Ph\}_2$], X = Cl, Br.

	X = Cl	X = Br
Mn(1)-X(1)	2.33834(5)	2.4811(3)
Mn(1)-O(1)	2.0463(10)	2.0382(11)
P(1)-O(1)	1.4977(10)	1.4979(12)
P(1)-N(1)	1.6275(13)	1.6279(14)
P(1)-N(2)	1.6422(14)	1.6420(15)
O(1')-Mn(1)-O(1)	102.55(6)	103.90(7)
O(1')-Mn(1)-X(1)	109.31(3)	109.25(3)
O(1)-Mn(1)-X(1)	107.13(3)	106.77(3)
X(1)-Mn(1)-X(1')	120.03(3)	119.801(17)

Table B2. Selected bond lengths [Å] and angles [°] for [$MnX_2\{O=P(NMe_2)_2Ind\}_2$], X = Cl, Br, I.

	X = Cl	X = Br	X = I
Mn(1)-O(1)	2.045(2)	2.0328(14)	2.0237(14)
Mn(1)-O(2)	2.054(2)	2.0479(14)	2.0364(14)
Mn(1)-X(1)	2.3334(9)	2.4727(4)	2.6765(4)
Mn(1)-X(2)	2.3290(10)	2.4656(4)	2.6659(3)
P(1)-O(1)	1.485(2)	1.4884(14)	1.4861(14)
P(1)-N(11)	1.680(3)	1.6786(17)	1.6796(17)
P(1)-N(12)	1.621(3)	1.6230(17)	1.6235(17)
P(1)-N(13)	1.624(3)	1.6257(17)	1.6225(17)
P(2)-O(2)	1.492(2)	1.4912(14)	1.4950(14)
P(2)-N(21)	1.679(3)	1.6764(17)	1.6747(18)
P(2)-N(22)	1.620(3)	1.6230(17)	1.6197(18)
P(2)-N(23)	1.624(3)	1.6251(17)	1.6146(18)
O(1)-Mn(1)-O(2)	106.80(9)	106.75(6)	104.88(6)
X(1)-Mn(1)-X(2)	119.82(4)	118.433(13)	116.111(12)
O(1)-Mn(1)-X(1)	111.59(7)	111.94(4)	113.35(4)
O(2)-Mn(1)-X(1)	106.28(6)	106.54(4)	107.31(4)
O(1)-Mn(1)-X(2)	105.95(7)	105.60(4)	104.72(4)
O(2)-Mn(1)-X(2)	105.60(6)	106.96(4)	109.91(4)
P(1)-O(1)-Mn(1)	165.06(15)	166.86(10)	170.53(10)

P(2)-O(2)-Mn(1)	148.26(13)	148.43(9)	148.86(9)
O(1)-P(1)-N(11)	109.26(13)	109.12(9)	109.20(8)
O(1)-P(1)-N(12)	112.54(13)	111.17(9)	110.99(9)
O(1)-P(1)-N(13)	111.37(13)	112.47(9)	112.45(9)
N(11)-P(1)-N(12)	105.29(13)	107.47(9)	107.33(9)
N(12)-P(1)-N(13)	110.63(14)	110.65(9)	110.88(9)
N(11)-P(1)-N(13)	107.44(14)	105.67(9)	105.71(9)
O(2)-P(2)-N(21)	108.66(13)	108.45(8)	108.34(9)
O(2)-P(2)-N(22)	110.76(13)	114.59(9)	109.93(9)
O(2)-P(2)-N(23)	114.44(13)	110.29(9)	115.06(9)
N(21)-P(2)-N(22)	107.78(14)	104.44(9)	108.52(9)
N(22)-P(2)-N(23)	110.61(14)	110.57(9)	109.79(10)
N(21)-P(2)-N(23)	104.18(13)	108.12(9)	104.92(9)

Table B3. Selected bond lengths [Å] and angles [°] for [MnX$_2${O=P(NMe$_2$)(2-Naph)}$_2$], X = Cl, Br, I.

	X = Cl	X = Br	X = I
Mn-O(1)	2.0487(11)	2.0423(10)	2.0299(11)
Mn-O(2)	2.0534(12)	2.0393(10)	2.0259(11)
Mn-X(1)	2.3316(5)	2.4753(3)	2.6814(2)
Mn-X(2)	2.3476(5)	2.4820(3)	2.6905(2)
P(1)-O(1)	1.4993(11)	1.5024(10)	1.5042(11)
P(1)-N(11)	1.6444(15)	1.6375(13)	1.6368(13)
P(1)-N(12)	1.6366(16)	1.6468(13)	1.6478(14)
P(1)-C(11)	1.7883(17)	1.7898(14)	1.7894(15)
P(2)-O(2)	1.4905(12)	1.5009(10)	1.5023(11)
P(2)-N(21)	1.6354(17)	1.6408(13)	1.6379(14)
P(2)-N(22)	1.6186(18)	1.6395(13)	1.6422(13)
P(2)-C(21)	1.827(2)	1.7990(15)	1.7977(16)
X(1)-Mn-X(2)	121.40(2)	119.633(10)	117.981(9)
O(1)-Mn-O(2)	100.70(5)	104.05(4)	105.06(5)
O(1)-Mn-X(1)	105.38(4)	109.18(3)	108.17(3)
O(2)-Mn-X(1)	110.10(4)	111.43(3)	112.22(3)
O(1)-Mn-X(2)	109.31(4)	103.71(3)	105.36(3)
O(2)-Mn-X(2)	107.98(4)	107.51(3)	107.10(3)
P(1)-O(1)-Mn	140.42(8)	137.91(6)	140.53(7)
P(2)-O(2)-Mn	139.53(7)	152.77(7)	153.53(8)
O(1)-P(1)-N(12)	117.98(7)	118.69(6)	118.33(7)

O(1)-P(1)-N(11)	107.97(7)	108.26(6)	108.41(7)
N(12)-P(1)-N(11)	104.42(8)	104.81(7)	104.95(7)
O(1)-P(1)-C(11)	110.67(7)	108.40(6)	108.31(7)
N(12)-P(1)-C(11)	104.82(8)	105.20(7)	105.48(7)
N(11)-P(1)-C(11)	110.77(8)	111.45(7)	111.31(7)
O(2)-P(2)-N(21)	107.80(8)	118.53(6)	118.76(7)
O(2)-P(2)-N(22)	119.44(9)	108.42(6)	108.13(7)
N(21)-P(2)-N(22)	106.34(9)	103.93(6)	103.93(7)
O(2)-P(2)-C(21)	106.29(8)	108.76(6)	108.66(7)
N(21)-P(2)-C(21)	111.59(9)	104.93(7)	105.00(7)
N(22)-P(2)-C(21)	105.42(9)	112.29(7)	112.40(7)
C(111)-N(11)-C(112)	112.82(16)	111.71(13)	111.74(14)
C(111)-N(11)-P(1)	117.36(12)	120.12(10)	119.71(11)
C(112)-N(11)-P(1)	118.52(14)	120.19(11)	120.13(11)
C(114)-N(12)-C(113)	112.78(16)	112.79(13)	112.92(14)
C(113)-N(12)-P(1)	119.18(14)	118.39(11)	118.26(12)
C(114)-N(12)-P(1)	120.19(13)	120.60(11)	120.32(11)
C(211)-N(21)-C(212)	113.19(17)	112.13(12)	112.54(13)
C(211)-N(21)-P(2)	122.53(13)	118.71(10)	119.80(11)
C(212)-N(21)-P(2)	121.23(14)	120.09(10)	120.23(11)
C(213)-N(22)-C(214)	111.51(19)	112.52(13)	112.85(14)
C(213)-N(22)-P(2)	120.07(15)	121.27(11)	121.34(11)
C(214)-N(22)-P(2)	119.35(14)	120.40(11)	120.44(12)

Table B4. Selected bond lengths [Å] and angles [°] for [MnX$_2${O=P(NMe$_2$)$_2$Cbz}$_2$], X = Cl, Br, I.

	X = Cl	X = Br	X = I	
Mn-O(1)	2.047(6)	2.042(2)	2.033(2)	2.035(3)
Mn-O(2)	2.035(6)	2.0423(19)	2.037(2)	2.041(3)
Mn-X(1)	2.329(3)	2.4748(5)	2.6644(6)	2.6761(6)
Mn-X(2)	2.340(3)	2.4619(6)	2.6843(6)	2.6857(6)
O(1)-P(1)	1.485(6)	1.484(2)	1.493(3)	1.492(3)
P(1)-N(11)	1.688(7)	1.680(2)	1.692(3)	1.687(3)
P(1)-N(12)	1.620(8)	1.616(2)	1.618(3)	1.618(3)
P(1)-N(13)	1.627(7)	1.619(2)	1.626(3)	1.624(3)
P(2)-O(2)	1.498(6)	1.4874(19)	1.489(3)	1.492(3)
P(2)-N(21)	1.689(7)	1.694(2)	1.692(3)	1.691(3)
P(2)-N(22)	1.616(8)	1.616(2)	1.622(3)	1.615(3)
P(2)-N(23)	1.616(7)	1.621(2)	1.630(3)	1.631(3)
O(2)-Mn-O(1)	95.2(3)	95.79(8)	97.92(10)	96.92(10)

O(2)-Mn-X(1)	112.5(2)	112.65(6)	111.67(7)	106.02(8)
O(2)-Mn-X(2)	112.2(2)	113.12(6)	105.09(7)	116.61(7)
O(1)-Mn-X(1)	113.5(2)	109.78(6)	108.31(7)	110.24(7)
O(1)-Mn-X(2)	109.3(2)	113.39(7)	110.32(7)	109.65(7)
X(1)-Mn-X(2)	112.92(10)	111.244(18)	121.02(2)	115.58(2)
P(1)-O(1)-Mn	151.6(4)	152.31(13)	118.12(15)	109.98(16)
P(2)-O(2)-Mn	151.2(4)	149.79(13)	148.89(16)	150.95(17)

Table B5. Selected bond lengths [Å] and angles [°] for [$MnX_2\{O=P(OPh)_2(NMe_2)\}_2$], X = Br, I.

	X = Br	X = I
Mn-X(1)	2.4479(4)	2.6788(9)
Mn-X(2)	2.4760(4)	2.6786(9)
Mn-O(11)	2.0416(14)	2.029(4)
Mn-O(21)	2.0525(14)	2.035(4)
P(1)-N(1)	1.6104(18)	1.623(5)
P(1)-O(11)	1.4755(14)	1.477(4)
P(1)-O(12)	1.5773(14)	1.580(4)
P(1)-O(13)	1.5692(14)	1.567(4)
P(2)-O(21)	1.4767(14)	1.474(4)
P(2)-O(22)	1.5721(14)	1.576(4)
P(2)-O(23)	1.5818(14)	1.572(4)
P(2)-N(2)	1.6102(17)	1.620(5)
X(1)-Mn-X(2)	117.168(14)	112.28(3)
O(11)-Mn-O(21)	97.90(6)	93.39(19)
O(11)-Mn-X(1)	112.74(4)	111.40(12)
O(11)-Mn-X(2)	108.86(4)	113.53(12)
O(21)-Mn-X(1)	105.40(4)	113.58(12)
O(21)-Mn-X(2)	113.12(4)	111.38(13)
P(1)-O(11)-Mn	176.14(10)	175.2(3)
P(2)-O(21)-Mn	164.73(10)	174.7(3)

Table B6. Selected bond lengths [Å] and angles [°] for $[MnX_2\{\mu{-}O{=}P(NMe_2)_2(res)(NMe_2)_2P{=}O\}]_n$, X = Br (n = 2), I.

	X = Br	X = I
Mn-X(1)	2.4653(17)	2.6742(7)
Mn-X(2)	2.4597(18)	2.6489(7)
Mn-O(11)	2.047(7)	2.035(3)
Mn-O(22^{i})	2.053(7)	2.036(3)
P(1)-N(11)	1.614(9)	1.618(4)
P(1)-N(12)	1.643(9)	1.626(4)
P(1)-O(11)	1.479(8)	1.490(3)
P(1)-O(12)	1.596(7)	1.587(3)
P(2)-N(21)	1.601(11)	1.620(4)
P(2)-N(22)	1.605(9)	1.620(4)
P(2)-O(21)	1.590(7)	1.585(3)
P(2)-O(22)	1.486(7)	1.495(3)
X(1)-Mn-X(2)	119.66(7)	114.27(2)
O(11)-Mn-O(22^{i})	101.2(3)	99.42(13)
O(11)-Mn-X(1)	110.9(2)	110.52(9)
O(11)-Mn-X(2)	105.3(2)	107.30(9)
O(22^{i})-Mn-Br(1)	105.4(2)	111.71(9)
O(22^{i})-Mn-Br(2)	113.0(2)	112.50(9)
P(1)-O(11)-Mn	148.3(5)	143.4(2)
P(2)-O(22)-Mn^{ii}	138.5(5)	145.7(2)

Symm. Op.: For X = Br: i=ii, 2-x, 1-y, 1-z; for X = I, O(22i) should be read as O(12i): i, 0.5-x, y-0.5, 1.5-z; ii, 0.5-x, y+0.5, 1.5-z.

Table B7. Selected bond lengths [Å] and angles [°] for O=PPh(S-BINOL).

P(1)-O(1)	1.4619(13)
P(1)-O(3)	1.5985(12)
P(1)-O(2)	1.6028(12)
P(1)-C(31)	1.7770(17)
O(1)-P(1)-O(3)	109.81(7)
O(1)-P(1)-O(2)	117.13(8)
O(3)-P(1)-O(2)	102.79(6)
O(1)-P(1)-C(31)	114.91(8)
O(3)-P(1)-C(31)	108.85(7)
O(2)-P(1)-C(31)	102.37(7)

Table B8. Selected bond lengths [Å] and angles [°] for $[Mn(bpyO_2)_3][ClO_4]_2$.

Mn(1)-O(32)	2.132(4)	Mn(2)-O(62)	2.123(4)	Mn(3)-O(72)	2.100(5)
Mn(1)-O(12)	2.144(4)	Mn(2)-O(52)	2.140(4)	Mn(3)-O(81)	2.125(4)
Mn(1)-O(31)	2.148(4)	Mn(2)-O(51)	2.140(4)	Mn(3)-O(92)	2.133(5)
Mn(1)-O(21)	2.150(5)	Mn(2)-O(42)	2.147(4)	Mn(3)-O(82)	2.134(4)
Mn(1)-O(11)	2.152(4)	Mn(2)-O(61)	2.154(5)	Mn(3)-O(71)	2.147(5)
Mn(1)-O(22)	2.156(4)	Mn(2)-O(41)	2.168(5)	Mn(3)-O(91)	2.171(5)
O(32)-Mn(1)-O(12)	175.70(17)	O(62)-Mn(2)-O(52)	178.52(18)	O(72)-Mn(3)-O(81)	100.1(2)
O(32)-Mn(1)-O(31)	83.53(16)	O(62)-Mn(2)-O(51)	94.99(17)	O(72)-Mn(3)-O(92)	83.2(2)
O(12)-Mn(1)-O(31)	92.16(17)	O(52)-Mn(2)-O(51)	83.89(16)	O(81)-Mn(3)-O(92)	173.8(2)
O(32)-Mn(1)-O(21)	91.08(17)	O(62)-Mn(2)-O(42)	88.63(17)	O(72)-Mn(3)-O(82)	174.9(2)
O(12)-Mn(1)-O(21)	93.20(17)	O(52)-Mn(2)-O(42)	92.57(17)	O(81)-Mn(3)-O(82)	84.69(16)
O(31)-Mn(1)-O(21)	172.24(16)	O(51)-Mn(2)-O(42)	173.77(17)	O(92)-Mn(3)-O(82)	91.87(19)
O(32)-Mn(1)-O(11)	96.15(17)	O(62)-Mn(2)-O(61)	84.72(18)	O(72)-Mn(3)-O(71)	86.7(2)
O(12)-Mn(1)-O(11)	84.22(16)	O(52)-Mn(2)-O(61)	94.39(17)	O(81)-Mn(3)-O(71)	88.18(18)
O(31)-Mn(1)-O(11)	95.79(18)	O(51)-Mn(2)-O(61)	94.05(18)	O(92)-Mn(3)-O(71)	97.3(2)
O(21)-Mn(1)-O(11)	90.33(17)	O(42)-Mn(2)-O(61)	91.33(18)	O(82)-Mn(3)-O(71)	95.48(18)
O(32)-Mn(1)-O(22)	88.51(17)	O(62)-Mn(2)-O(41)	99.98(19)	O(72)-Mn(3)-O(91)	89.8(2)
O(12)-Mn(1)-O(22)	91.63(17)	O(52)-Mn(2)-O(41)	81.00(18)	O(81)-Mn(3)-O(91)	89.87(18)
O(31)-Mn(1)-O(22)	91.47(17)	O(51)-Mn(2)-O(41)	89.44(17)	O(92)-Mn(3)-O(91)	84.8(2)
O(21)-Mn(1)-O(22)	82.79(17)	O(42)-Mn(2)-O(41)	84.93(17)	O(82)-Mn(3)-O(91)	88.31(18)
O(11)-Mn(1)-O(22)	171.77(17)	O(61)-Mn(2)-O(41)	173.91(19)	O(71)-Mn(3)-O(91)	175.6(2)

Table B9. Selected bond lengths [Å] and angles [°] for [Cu(κ^2–BH$_4$)(DPEphos)].

Cu(1)-B(1)	2.170(2)	Cu(2)-B(2)	2.1564(18)
Cu(1)-P(11)	2.2495(4)	Cu(2)-P(21)	2.2300(4)
Cu(1)-P(12)	2.2777(5)	Cu(2)-P(22)	2.2541(5)
Cu(1)-H(13)	1.73(2)	Cu(2)-H(23)	1.75(2)
Cu(1)-H(14)	1.67(3)	Cu(2)-H(24)	1.73(2)
B(1)-H(11)	1.08(2)	B(2)-H(22)	1.07(2)
B(1)-H(12)	1.11(3)	B(2)-H(21)	1.15(2)
B(1)-H(14)	1.14(3)	B(2)-H(23)	1.17(2)
B(1)-H(13)	1.15(2)	B(2)-H(24)	1.20(2)
P(11)-Cu(1)-P(12)	111.663(17)	P(21)-Cu(2)-P(22)	116.190(17)
H(13)-Cu(1)-H(14)	62.7(12)	H(23)-Cu(2)-H(24)	66.3(10)
H(13)-Cu(1)-P(11)	123.6(8)	H(23)-Cu(2)-P(21)	113.5(7)
H(14)-Cu(1)-P(11)	126.6(9)	H(24)-Cu(2)-P(21)	126.7(7)
H(13)-Cu(1)-P(12)	111.8(8)	H(23)-Cu(2)-P(22)	113.8(7)
H(14)-Cu(1)-P(12)	112.1(9)	H(24)-Cu(2)-P(22)	110.3(7)
B(1)-Cu(1)-P(11)	136.08(6)	B(2)-Cu(2)-P(21)	130.05(5)
B(1)-Cu(1)-P(12)	112.20(6)	B(2)-Cu(2)-P(22)	112.92(5)
H(14)-Cu(1)-B(1)	31.2(9)	H(24)-Cu(2)-B(2)	33.8(7)
H(13)-Cu(1)-B(1)	31.9(8)	H(23)-Cu(2)-B(2)	32.9(7)
H(11)-B(1)-H(12)	113.2(18)	H(22)-B(2)-H(21)	115.8(16)
H(11)-B(1)-H(14)	112.5(18)	H(22)-B(2)-H(23)	109.6(15)
H(12)-B(1)-H(14)	108.3(18)	H(21)-B(2)-H(23)	108.7(15)
H(11)-B(1)-H(13)	108.4(17)	H(22)-B(2)-H(24)	107.0(15)
H(12)-B(1)-H(13)	112.9(18)	H(21)-B(2)-H(24)	109.1(15)
H(14)-B(1)-H(13)	100.9(17)	H(23)-B(2)-H(24)	106.2(15)

Table B10. Selected bond lengths [Å] and angles [°] around C1 for CHPh(btz)$_2$ and CH(btz)$_3$.

CHPh(btz)$_2$		CH(btz)$_3$	
C(1)-N(11)	1.4511(16)	C(1)-N(31)	1.4392(16)
C(1)-N(21)	1.4595(16)	C(1)-N(21)	1.4650(17)
C(1)-C(2)	1.5199(17)	C(1)-N(11)	1.4394(16)
N(11)-C(1)-N(21)	110.45(10)	N(31)-C(1)-N(11)	113.28(10)
N(11)-C(1)-C(2)	114.23(10)	N(11)-C(1)-N(21)	109.40(10)
N(21)-C(1)-C(2)	112.20(10)	N(31)-C(1)-N(21)	109.96(10)

Table B11. Selected bond lengths [Å] and angles [°] for the cation [Cu{CHPh(ind)$_2$}$_2$]$^+$.

Cu-N(12)	2.032(2)
Cu-N(42)	2.026(2)
Cu-N(22)	2.030(2)
Cu-N(52)	2.033(2)
N(12)-Cu-N(22)	92.19(8)
N(12)-Cu-N(52)	116.99(8)
N(22)-Cu-N(52)	112.28(9)
N(12)-Cu-N(42)	113.93(9)
N(22)-Cu-N(42)	130.87(8)
N(42)-Cu-N(52)	92.62(8)

Table B12. Selected bond lengths [Å] and angles [°] for trz^{OMe}-btz and trz^{OPh}-btz.

trz^{OMe}-btz				trz^{OPh}-btz	
N(11)-C(112)	1.3205(13)	N(21)-C(112)	1.3188(13)	N(11)-C(21)	1.398(5)
C(114)-O(112)	1.3277(12)	C(214)-O(212)	1.3252(12)	C(23)-O(1)	1.343(5)
C(116)-O(111)	1.3208(12)	C(216)-O(211)	1.3223(12)	C(25)-O(2)	1.339(5)
O(111)-C(117)	1.4492(12)	O(211)-C(217)	1.4526(12)	O(1)-C(31)	1.413(5)
O(112)-C(118)	1.4501(12)	O(212)-C(218)	1.4489(12)	O(2)-C(41)	1.424(5)
C(116)-O(111)-C(117)	117.45(8)	C(216)-O(211)-C(217)	117.02(8)	C(23)-O(1)-C(31)	119.5(3)
C(114)-O(112)-C(118)	117.10(8)	C(214)-O(212)-C(218)	116.91(8)	C(25)-O(2)-C(41)	118.8(3)

Table B13. Selected bond lengths [Å] and angles [°] for [Cu(py-btz)(PPh$_3$)$_2$][BF$_4$] and [Cu(pym-btz)(PPh$_3$)$_2$][BF$_4$].

	[Cu(py-btz)(PPh$_3$)$_2$][BF$_4$]	[Cu(pym-btz)(PPh$_3$)$_2$][BF$_4$]
Cu-N(1)	2.0670(10)	2.1309(17)
Cu-N(12)	2.1160(11)	2.0710(17)
Cu-P(1)	2.2540(4)	2.2642(6)
Cu-P(2)	2.2279(3)	2.2316(5)
N(1)-Cu-N(12)	78.51(4)	78.03(7)
N(1)-Cu-P(1)	117.03(3)	102.27(5)
N(1)-Cu-P(2)	111.66(3)	119.58(5)
N(12)-Cu-P(1)	101.08(3)	106.68(5)

N(12)-Cu-P(2)	120.82(3)	120.86(5)
P(1)-Cu-P(2)	120.417(13)	120.71(2)

Table B14. Selected bond lengths [Å] and angles [°] for [Cu(py-btz)(DPEphos)][BF_4] and [Cu(pym-btz)(P^iPr_3)]$_2$[BF_4].

	[Cu(py-btz)(DPEphos)][BF_4]		[Cu(pym-btz)(P^iPr_3)]$_2$[BF_4]
Cu-N(1)	2.0886(17)	2.0526(19)	2.159(4)
Cu-N(12)	2.0532(17)	2.0423(19)	2.156(4)
Cu-P(1)	2.2803(6)	2.1932(5)	2.3001(13)
Cu-P(2)	2.2360(6)	2.280(2)	2.3026(13)
		2.279(3)	
N(1)-Cu-N(12)	78.42(6)	79.23(8)	75.58(14)
N(1)-Cu-P(1)	125.02(5)	130.17(5)	105.91(11)
N(1)-Cu-P(2)	110.46(5)	102.34(8)	113.19(11)
		97.20(11)	
N(12)-Cu-P(1)	110.35(5)	117.67(5)	111.75(11)
N(12)-Cu-P(2)	104.95(5)	98.76(12)	102.84(11)
		108.82(14)	
P(1)-Cu-P(2)	118.21(2)	118.76(5)	132.95(5)
		117.00(7)	

Table B15. Selected bond lengths [Å] and angles [°] for the dimeric [Cu(pym-btz)(μ–dppe)]$_2$[BF_4]$_2$ complex.

Cu-N(1)	2.090(3)
Cu-N(12)	2.072(4)
Cu-P(1')	2.2480(11)
Cu-P(2)	2.2435(11)
N(12)-Cu-N(1)	78.10(14)
N(12)-Cu-P(2)	112.48(10)
N(1)-Cu-P(2)	122.57(10)
N(12)-Cu-P(1')	112.58(11)
N(1)-Cu-P(1')	112.51(10)
P(2)-Cu-P(1')	113.54(4)

Symmetry transformations used to generate equivalent atoms: i: 1-x; 1-y, 1-z

Table B16. Selected bond lengths [Å] and angles [°] for the complexes $[Cu(trz^{OMe}\text{-}btz)(P^{i}Pr_3)_2][BF_4]$, $[Cu(trz^{OEt}\text{-}btz)(DPEphos)][BF_4]$ and $[Cu(trz^{OPh}\text{-}btz)(DPEphos)][BF_4]$.

	$[Cu(trz^{OMe}\text{-}btz)(P^{i}Pr_3)_2][BF_4]$	$[Cu(trz^{OEt}\text{-}btz)(DPEphos)][BF_4]$	$[Cu(trz^{OPh}\text{-}btz)(DPEphos)][BF_4]$
Cu-N(11)	2.1505(11)	2.080(4)	2.0792(10)
Cu-N(2)	2.1672(11)	2.087(4)	2.0814(11)
Cu-P(1)	2.2744(4)	2.2040(12)	2.2555(3)
Cu-P(2)	2.2853(4)	2.2820(12)	2.2482(3)
N(11)-Cu-N(2)	74.70(4)	77.94(15)	77.46(4)
N(11)-Cu-P(1)	108.78(3)	123.45(11)	110.97(3)
N(11)-Cu-P(2)	107.08(3)	99.79(11)	118.95(3)
N(2)-Cu-P(1)	110.96(3)	127.69(10)	120.88(3)
N(2)-Cu-P(2)	110.61(3)	100.72(11)	114.54(3)
P(1)-Cu-P(2)	130.506(14)	118.22(5)	110.717(13)

Table B17. Selected bond lengths [Å] and angles [°] for $[Cu(BTD)(PPh_3)_2][X]$, $X^- = BF_4^-$, ClO_4^-.

$[Cu(BTD)(PPh_3)_2][BF_4]$		$[Cu(BTD)(PPh_3)_2][ClO_4]$	
Cu-N(1)	2.0940(17)	Cu(1)-N(1)	2.0945(11)
Cu-P(1)	2.2488(5)	Cu(1)-P(1)	2.2497(4)
Cu-P(2)	2.2686(6)	Cu(1)-P(2)	2.2799(4)
Cu-F(1)	2.3321(13)	Cu(1)-O(1)	2.2513(11)
N(1)-S(2)	1.6356(18)	N(1)-S(1)	1.6328(12)
N(1)-C(9)	1.357(3)	N(1)-C(1)	1.3552(17)
N(3)-S(2)	1.6060(19)	N(2)-S(1)	1.6116(12)
N(3)-C(8)	1.346(3)	N(2)-C(6)	1.3467(18)
B(1)-F(1)	1.412(3)	Cl(1)-O(1)	1.4553(11)
B(1)-F(2)	1.392(3)	Cl(1)-O(2)	1.4182(11)
B(1)-F(3)	1.389(3)	Cl(1)-O(3)	1.370(3) 1.525(5)
B(1)-F(4)	1.381(3)	Cl(1)-O(4)	1.518(4) 1.347(4)
N(1)-Cu-P(1)	118.67(5)	N(1)-Cu(1)-P(1)	113.65(3)
N(1)-Cu-P(2)	104.98(5)	N(1)-Cu(1)-P(2)	104.57(3)
P(1)-Cu-P(2)	127.93(2)	P(1)-Cu(1)-P(2)	130.008(14)
N(1)-Cu-F(1)	78.29(6)	N(1)-Cu(1)-O(1)	86.57(5)
P(1)-Cu-F(1)	101.85(4)	P(1)-Cu(1)-O(1)	104.49(4)
P(2)-Cu-F(1)	114.14(4)	P(2)-Cu(1)-O(1)	108.89(3)

Table B18. Selected bond lengths [Å] and angles [°] for $[Cu_2(BTD)(NCCH_3)(\mu\text{-}dppm)_2][BF_4]_2$.

Cu(1)-N(1)	2.089(3)	Cu(2)-N(2)	1.967(3)
Cu(1)-P(1)	2.2230(11)	Cu(2)-P(2)	2.2593(12)

Cu(1)-P(3)	2.2314(11)	Cu(2)-P(4)	2.2518(11)
Cu(1)-F(11)	2.541(2)	Cu(1)-Cu(2)	3.3135(7)
B(1)-F(11)	1.418(5)	B(2)-F(21)	1.381(7)
B(1)-F(12)	1.384(5)	B(2)-F(22)	1.385(6)
B(1)-F(13)	1.397(5)	B(2)-F(23)	1.372(7)
B(1)-F(14)	1.392(5)	B(2)-F(24)	1.376(7)
N(1)-S(2)	1.634(4)	S(2)-N(3)	1.605(4)
N(1)-C(9)	1.354(6)	N(3)-C(8)	1.356(6)
N(2)-C(1)	1.141(5)	C(1)-C(2)	1.457(6)
N(1)-Cu(1)-P(1)	106.89(10)	N(2)-Cu(2)-P(2)	117.31(11)
N(1)-Cu(1)-P(3)	99.34(10)	N(2)-Cu(2)-P(4)	120.65(11)
P(1)-Cu(1)-P(3)	152.43(4)	P(4)-Cu(2)-P(2)	121.50(4)
N(1)-Cu(1)-F(11)	89.33(12)	N(2)-Cu(2)-Cu(1)	94.55(10)
P(1)-Cu(1)-F(11)	86.81(7)	P(4)-Cu(2)-Cu(1)	91.58(3)
P(3)-Cu(1)-F(11)	85.11(7)	P(2)-Cu(2)-Cu(1)	91.26(3)
N(1)-Cu(1)-Cu(2)	169.60(10)	C(1)-N(2)-Cu(2)	168.1(3)
P(1)-Cu(1)-Cu(2)	77.94(3)	N(2)-C(1)-C(2)	178.6(4)
P(3)-Cu(1)-Cu(2)	77.64(3)		
F(11)-Cu(1)-Cu(2)	100.25(6)		

Table B19. Selected bond lengths [Å] and angles [°] for $[ZnX_2\{O{=}P(NMe_2)_2Ind\}_2]$ (X = Cl, Br, I).

	X = Cl	X = Br	X = I	X = I(*)
Zn-O(1)	1.9891(8)	1.9668(10)	1.9840(15)	1.9692(14)
Zn-O(2)	1.9782(8)	1.9859(10)	1.9698(14)	1.9720(15)
Zn-X(1)	2.2173(3)	2.3571(3)	2.5455(3)	2.5609(3)
Zn-X(2)	2.2200(3)	2.3543(2)	2.5404(3)	2.5390(3)
P(1)-O(1)	1.4942(8)	1.4835(10)	1.4863(15)	1.4813(15)
P(1)-N(11)	1.6838(10)	1.6801(12)	1.6918(19)	1.6735(18)
P(1)-N(12)	1.6278(10)	1.6262(12)	1.622(2)	1.6286(18)
P(1)-N(13)	1.6246(11)	1.6253(12)	1.629(2)	1.6210(18)
P(2)-O(2)	1.4950(9)	1.4917(10)	1.4920(15)	1.4898(15)
P(2)-N(21)	1.6858(10)	1.6786(12)	1.6781(18)	1.6724(18)
P(2)-N(22)	1.6255(11)	1.6257(12)	1.6233(18)	1.6163(18)
P(2)-N(23)	1.6177(11)	1.6250(12)	1.6176(19)	1.6394(19)
X(1)-Zn-X(2)	116.687(12)	120.014(9)	121.211(11)	120.952(11)
O(1)-Zn-O(2)	96.48(3)	104.49(4)	97.01(6)	100.19(6)
O(1)-Zn-X(1)	110.10(3)	110.44(3)	108.49(4)	107.55(4)
O(1)-Zn-X(2)	109.40(3)	105.55(3)	109.67(4)	109.58(4)

O(2)-Zn-X(1)	110.46(3)	107.80(3)	110.47(5)	108.98(5)
O(2)-Zn-X(2)	111.86(3)	107.47(3)	107.29(4)	107.62(5)
P(1)-O(1)-Zn	134.14(5)	165.75(7)	146.30(10)	163.92(10)
O(1)-P(1)-N(11)	107.18(5)	108.73(6)	105.91(9)	108.81(8)
O(1)-P(1)-N(12)	111.26(5)	111.61(6)	111.31(10)	112.91(9)
O(1)-P(1)-N(13)	116.07(5)	112.83(6)	118.98(10)	111.36(9)
N(11)-P(1)-N(12)	107.23(5)	107.29(6)	111.82(10)	104.45(9)
N(11)-P(1)-N(13)	103.69(5)	105.61(6)	102.10(10)	108.47(9)
N(12)-P(1)-N(13)	110.70(6)	110.43(6)	106.41(11)	110.51(9)
P(2)-O(2)-Zn	140.40(6)	145.23(6)	143.94(10)	152.55(10)
O(2)-P(2)-N(21)	107.39(5)	108.14(6)	105.77(9)	108.28(9)
O(2)-P(2)-N(22)	118.10(5)	115.09(6)	110.54(9)	112.36(9)
O(2)-P(2)-N(23)	110.94(5)	110.44(6)	117.85(10)	114.60(9)
N(21)-P(2)-N(22)	101.90(5)	104.16(6)	109.73(9)	107.00(9)
N(21)-P(2)-N(23)	108.94(6)	107.94(6)	106.57(10)	110.94(10)
N(22)-P(2)-N(23)	108.91(6)	110.63(6)	106.16(9)	102.91(9)

Table B20. Selected bond lengths [Å] and angles [°] for [ZnBr$_2$(DOPO)$_2$].

Zn-O(11)	1.9975(12)	Zn-O(21)	1.9952(12)
Zn-Br(1)	2.3489(3)	Zn-Br(2)	2.3379(3)
P(1)-O(11)	1.4851(13)	P(2)-O(21)	1.4907(13)
P(1)-O(12)	1.5761(14)	P(2)-O(22)	1.5812(13)
P(1)-C(11)	1.7668(18)	P(2)-C(21)	1.7661(18)
O(11)-Zn-O(21)	98.16(5)	Br(2)-Zn-Br(1)	123.531(11)
O(21)-Zn-Br(1)	109.61(4)	O(21)-Zn-Br(2)	105.91(4)
O(11)-Zn-Br(1)	106.51(4)	O(12)-Zn-Br(2)	110.20(4)
O(11)-P(1)-O(12)	114.68(8)	O(21)-P(2)-O(22)	112.04(7)
O(11)-P(1)-C(12)	112.51(8)	O(21)-P(2)-C(21)	115.26(8)
O(12)-P(1)-C(11)	105.56(8)	O(22)-P(2)-C(21)	103.90(7)
C(112)-O(12)-P(1)	126.34(12)	C(212)-O(22)-P(2)	119.72(11)
P(1)-O(11)-Zn	143.27(9)	P(2)-O(21)-Zn	134.80(8)

Table B21 Selected bond lengths [Å] and angles [°] for [Cu(CNXyl)$_3$][BF$_4$].

Cu-C(11)	1.9078(14)	Cu-C(21)	1.9127(14)
Cu-C(31)	1.9188(14)		
C(11)-N(11)	1.1511(18)	N(11)-C(12)	1.4039(17)
C(21)-N(21)	1.1521(18)	N(21)-C(22)	1.4036(16)
C(31)-N(31)	1.1494(18)	N(31)-C(32)	1.3991(17)

C(11)-Cu-C(21)	125.96(6)	C(11)-Cu-C(31)	117.31(6)
C(21)-Cu-C(31)	116.12(6)		
N(11)-C(11)-Cu	171.37(12)	C(11)-N(11)-C(12)	174.63(14)
N(21)-C(21)-Cu	174.73(12)	C(21)-N(21)-C(22)	175.68(13)
N(31)-C(31)-Cu	176.56(13)	C(31)-N(31)-C(32)	178.86(14)

Table B22 Selected bond lengths [Å] and angles [°] for [Pd(COMe)Cl(BTD$^{\mathrm{NPy}}$)].

Pd(1)-C(21)	1.9518(16)
Pd(1)-N(2)	2.2914(12)
Pd(1)-N(1)	2.0833(12)
Pd(1)-Cl(1)	2.3343(4)
C(21)-Pd(1)-N(1)	93.45(6)
C(21)-Pd(1)-N(2)	171.13(5)
N(1)-Pd(1)-N(2)	77.75(5)
C(21)-Pd(1)-Cl(1)	84.75(5)
N(1)-Pd(1)-Cl(1)	176.46(3)
N(2)-Pd(1)-Cl(1)	103.96(3)